
Particle Physics
STFC Rutherford Appleton Laboratory

Illustrations by F. Cairo

The missing pieces in the Higgs Puzzle at the LHC and Beyond

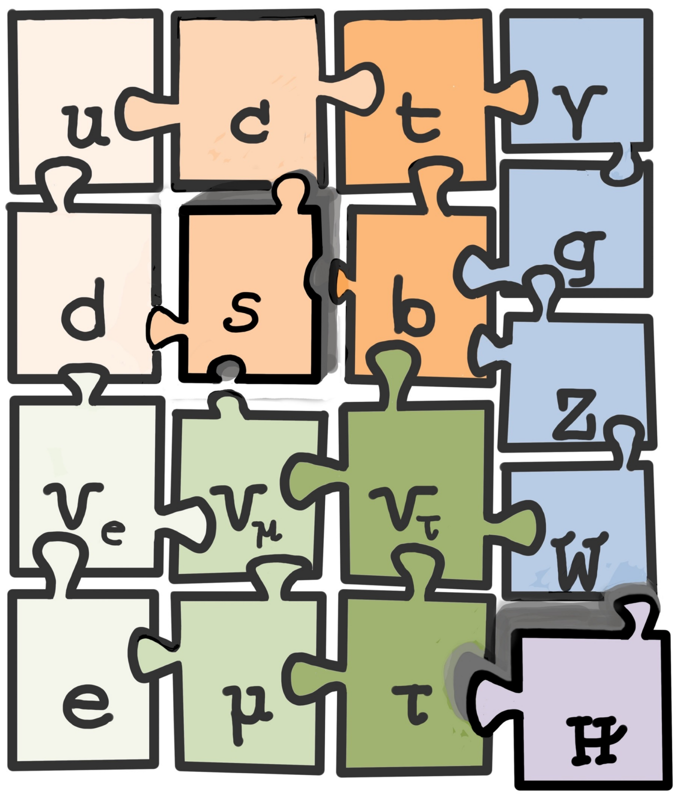

Valentina Maria Martina Cairo

May 11th 2022

CERN

10 years HIGGS boson discovery

The Post Higgs boson era

2012 → **Now**

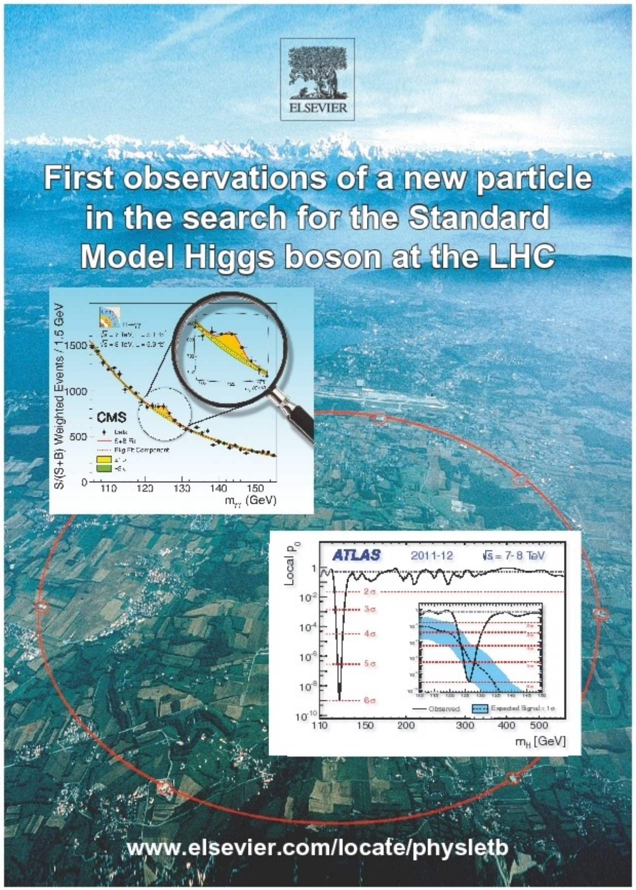

ATLAS-CONF-2020-027

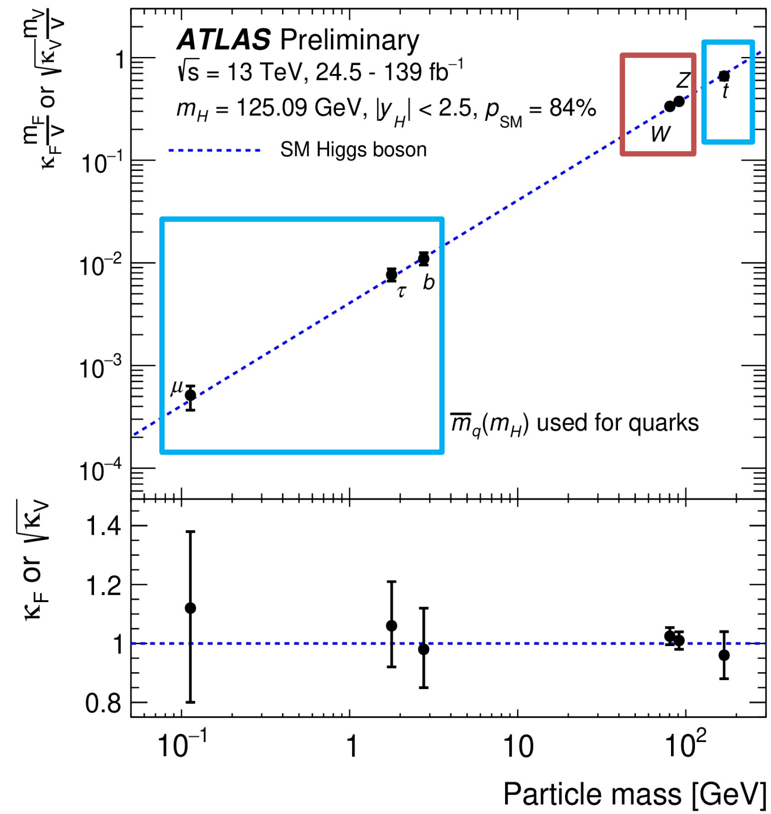

ATLAS-CONF-2020-027

A Higgs boson-like particle was found!

So far, the SM rules, but the exploration has just begun…

The Post Higgs boson era

2012 → **Now**

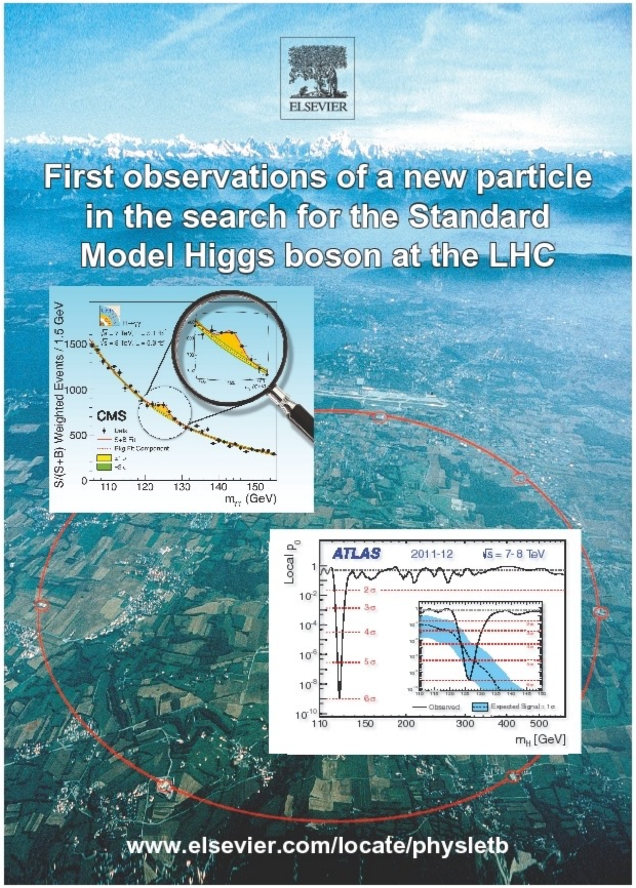

ATLAS-CONF-2020-027

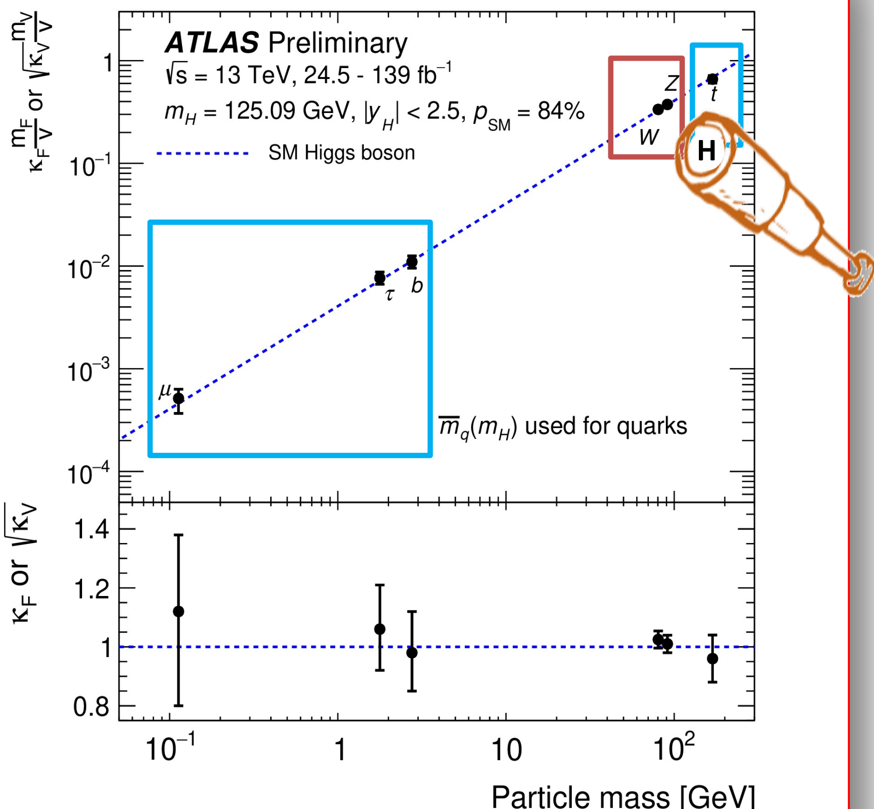

ATLAS-CONF-2020-027

A Higgs boson-like particle was found!

How does the Higgs boson couple to itself?

Piece #1

The Higgs self-coupling at the LHC and beyond

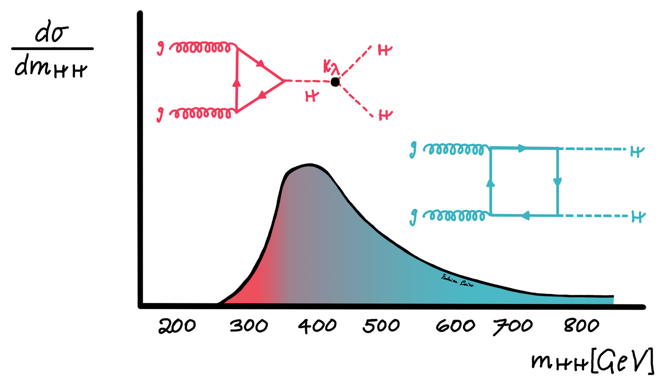

A very popular research topic…

Video

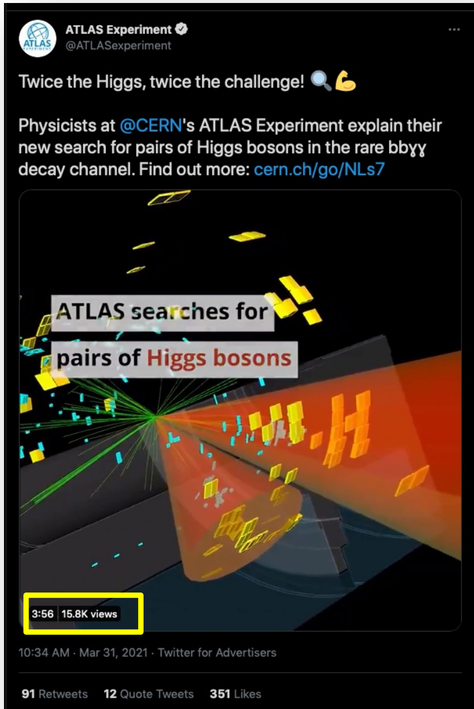

Twice-higgs-twice-challenge

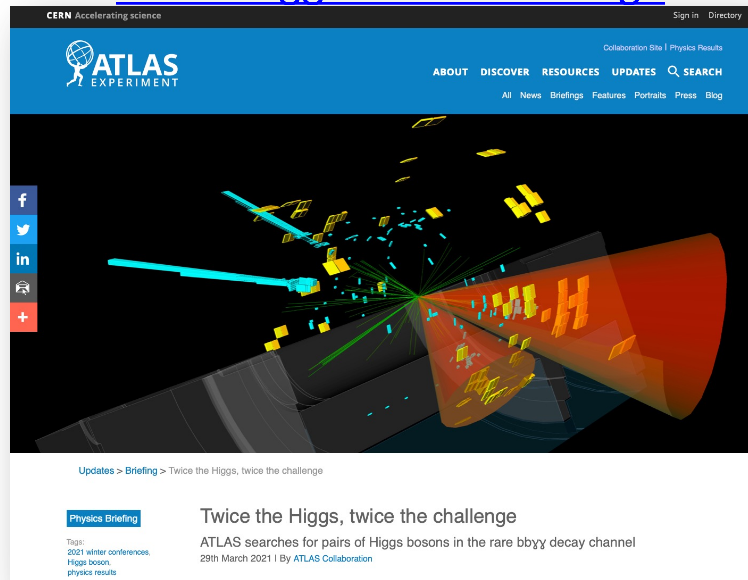

CERN Bulletin (April 2021)

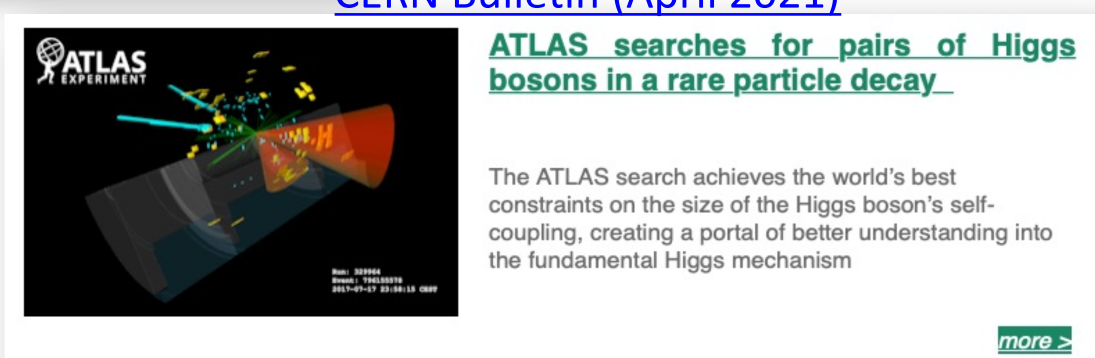

A very popular research topic…

Video

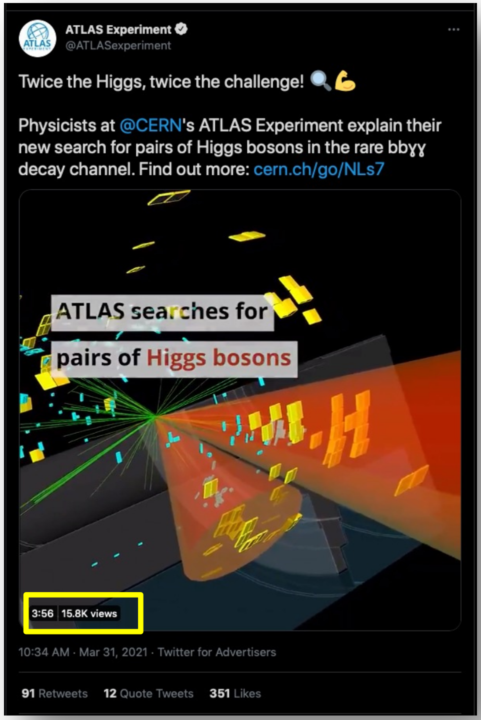

Twice-higgs-twice-challenge

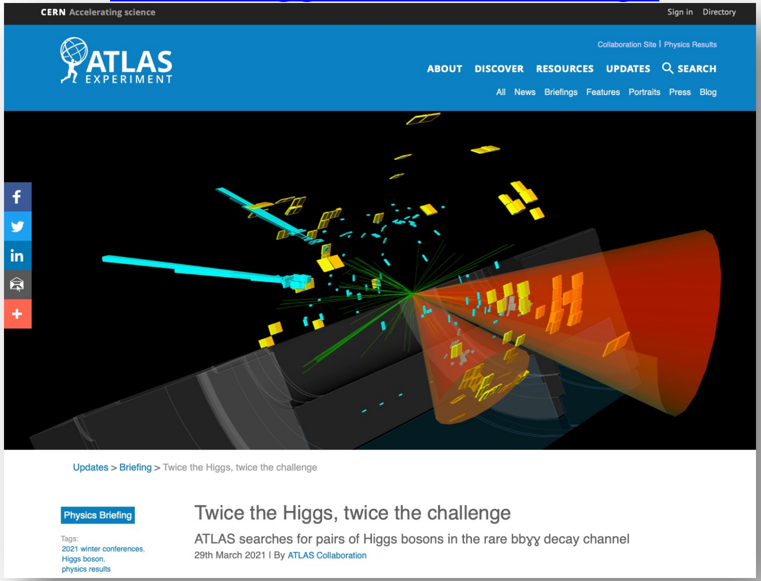

CERN Bulletin (April 2021)

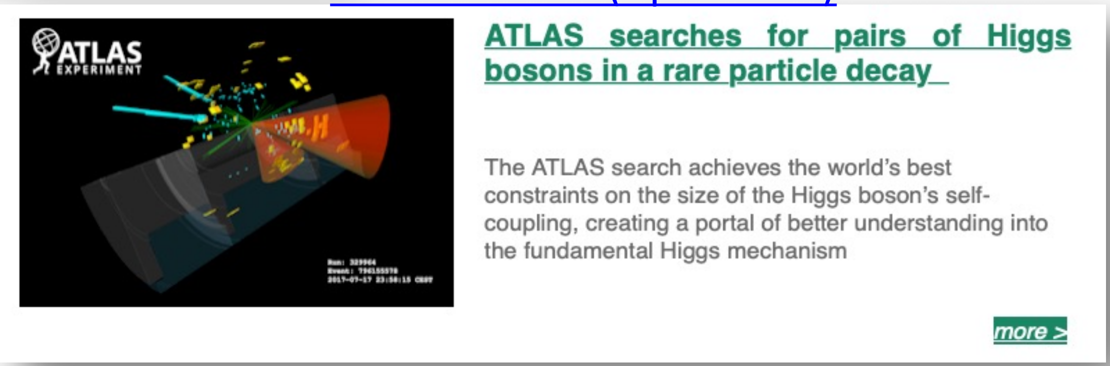

Why so exciting?

The Theory…

F. Cairo, From *Conn(ll)ecting the dots*

The Higgs Potential and Self-Coupling

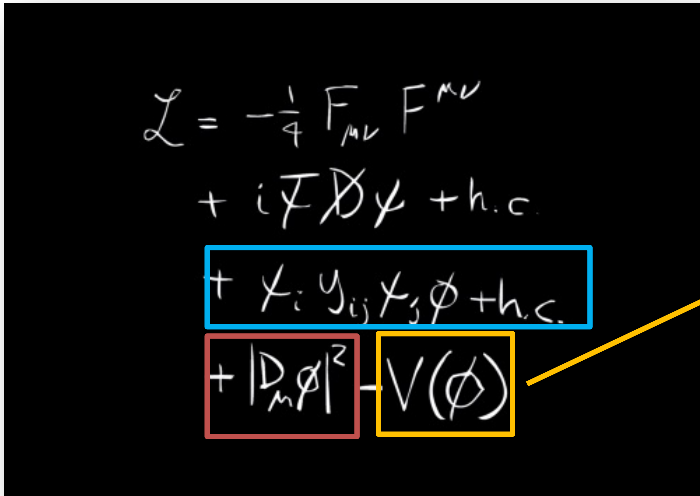

$$
\begin{aligned}
V(\phi^\dagger\phi) &= \mu^2\phi^\dagger\phi + \lambda(\phi^\dagger\phi)^2 \\
&\supset \lambda v^2 H^2 + \lambda v H^3 + \frac{\lambda}{4} H^4
\end{aligned}
$$

$$m_H = \sqrt{2\lambda v^2}$$

$$v \simeq 246 \text{ GeV}$$

$$\kappa_\lambda = \lambda_{HHH}/\lambda_{SM}$$

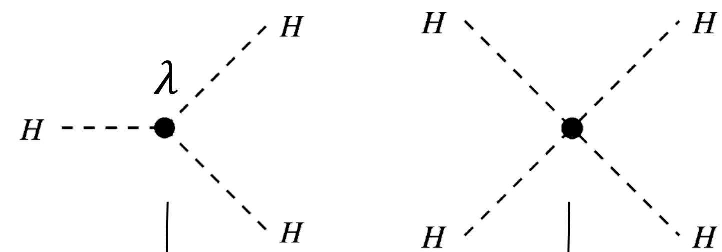

Direct access to λ in HH pair production

Out of reach even for HL-LHC

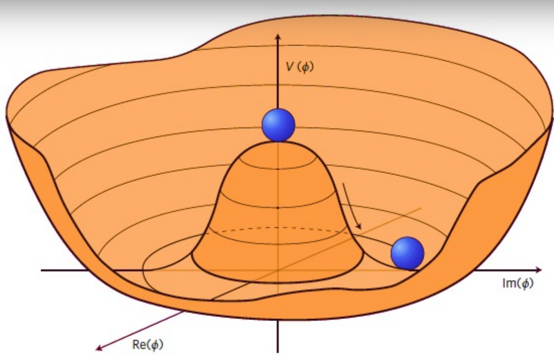

Known m_H (~125 GeV), SM predicts λ (~0.13)

New physics can alter this number → Implications on the stability of the Universe

→ Probing the **Higgs-self coupling** is a **key goal for HL-LHC** and much can be done now!

...the tools...

F. Cairo, From *Conn(ll)ecting the dots*

The Large Hadron Collider

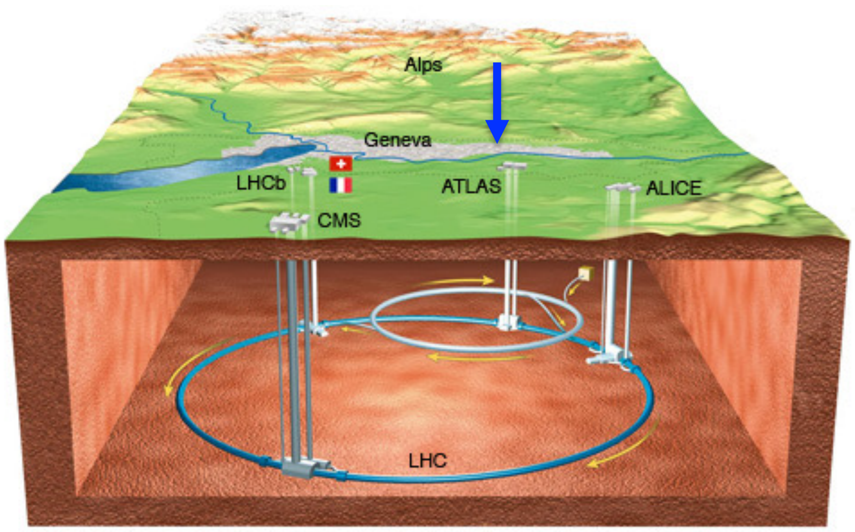

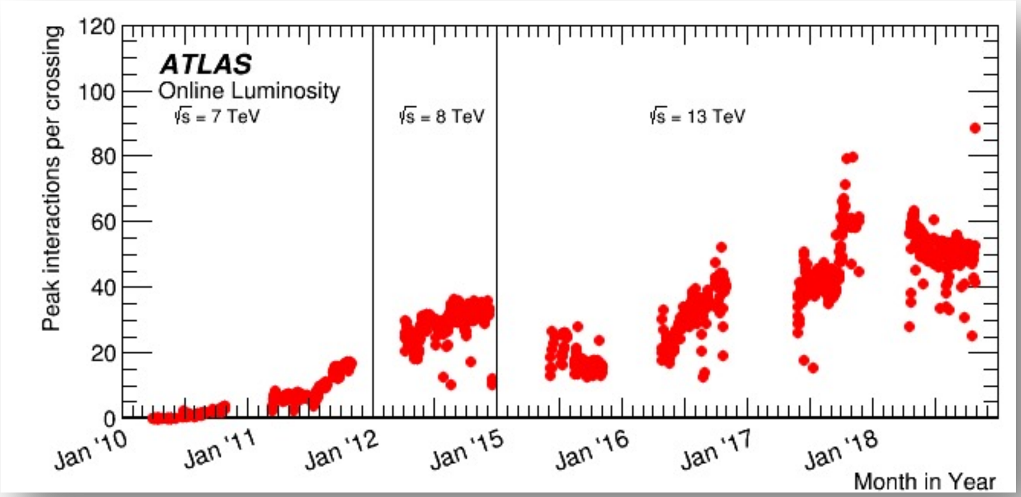

Outperformed specifications during **Run 2**:

- **Peak Luminosity**: x2 (2.14 x 10^{34} $cm^{-2}s^{-1}$)
- **Integrated Luminosity**: 140 fb^{-1}
- **Avg interaction per crossing** $< \mu >$: x2 ($\sim$40)

Two more runs to go:

- **Run 3**: 13.6 TeV, $< \mu > \sim 60$
- **Run 4**: 14 TeV, $< \mu > \sim 200$

The ATLAS Detector

Physics benchmarks drove the design of the detector

- Excellent stand-alone reconstruction capabilities

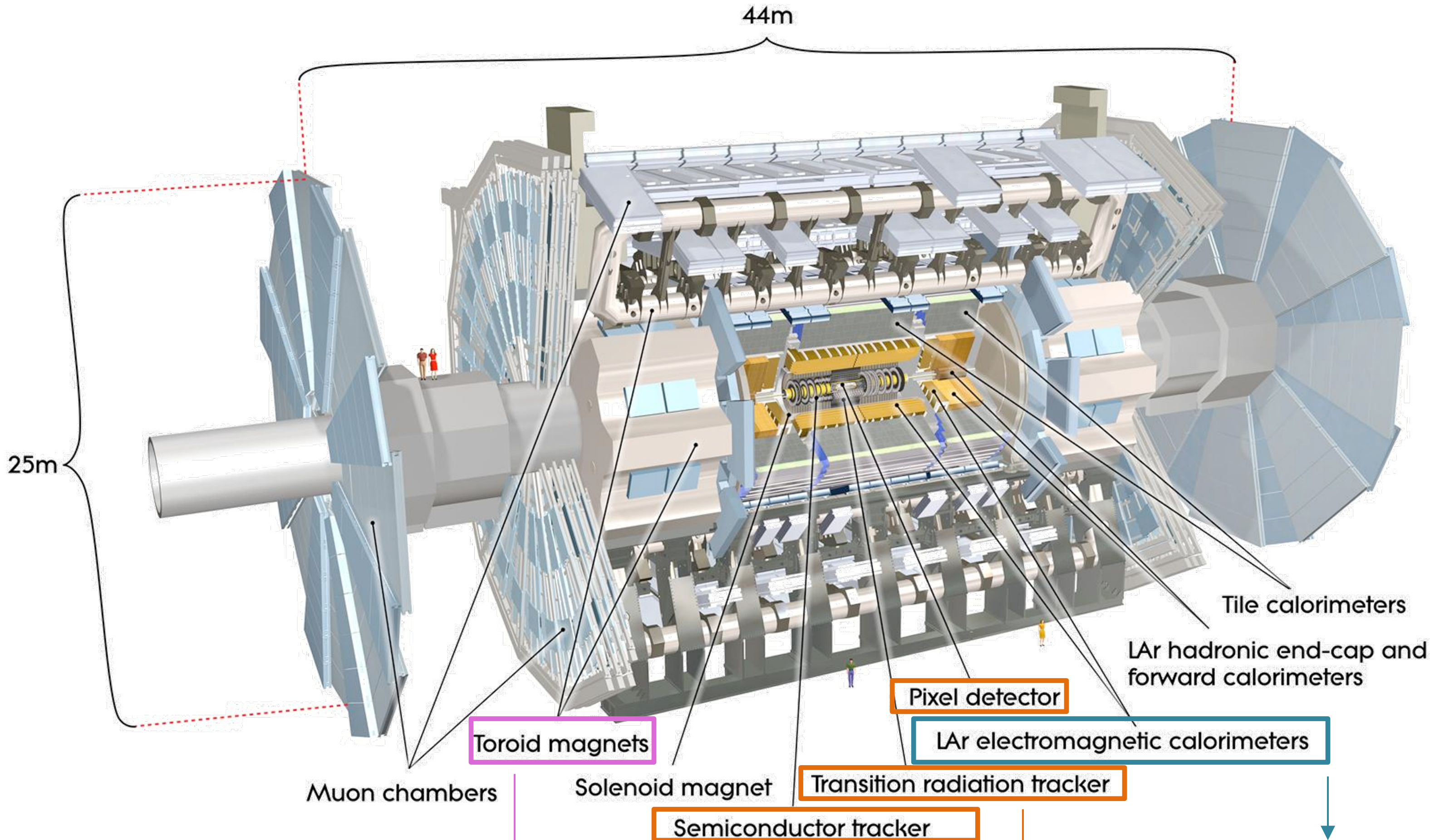

maximize $H \rightarrow \gamma\gamma$ sensitivity

Determines the ATLAS geometry

Combined technologies

The ATLAS Timeline

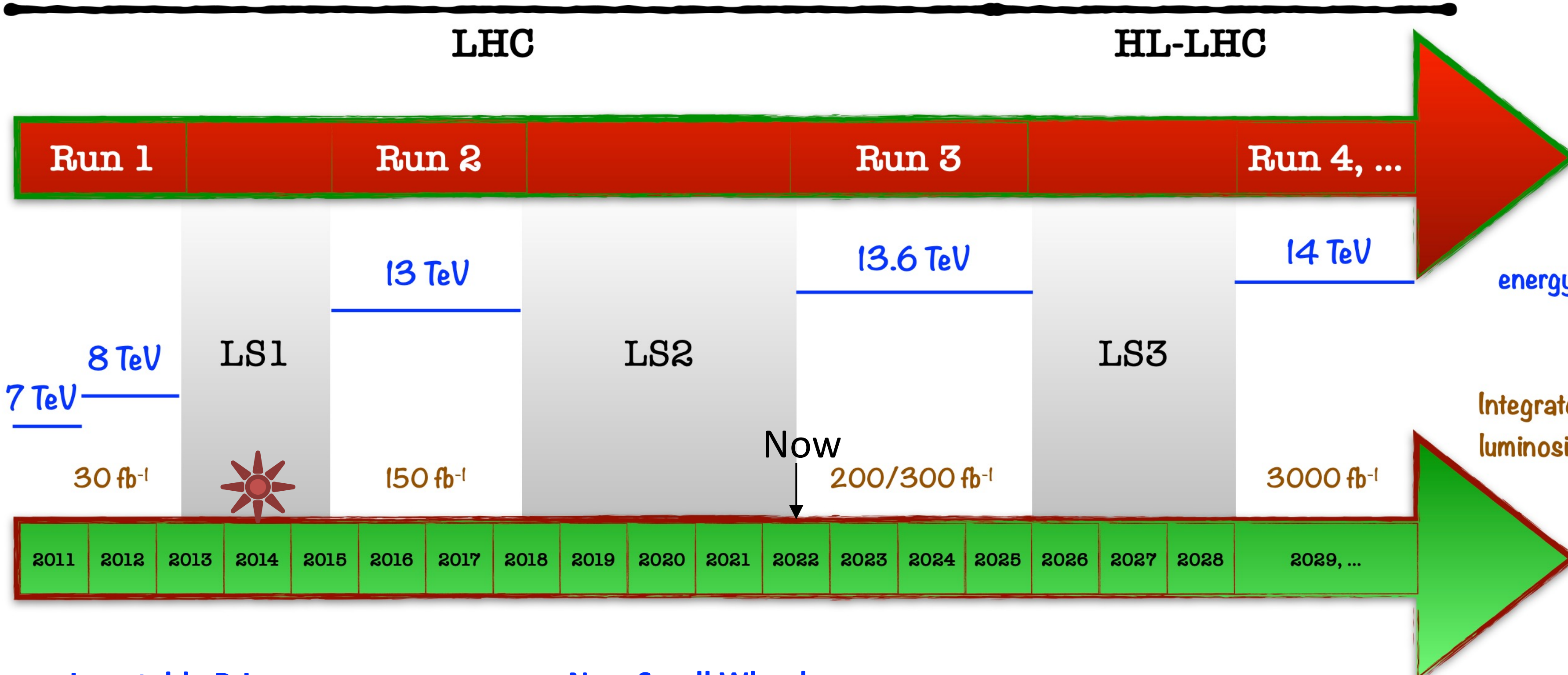

Insertable B-Layer

source

New Small Wheels

source

Inner Tracker

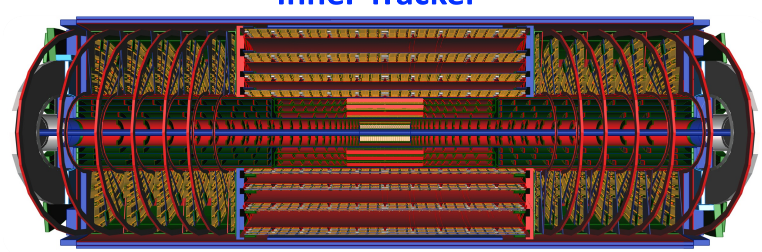

source

...the work...

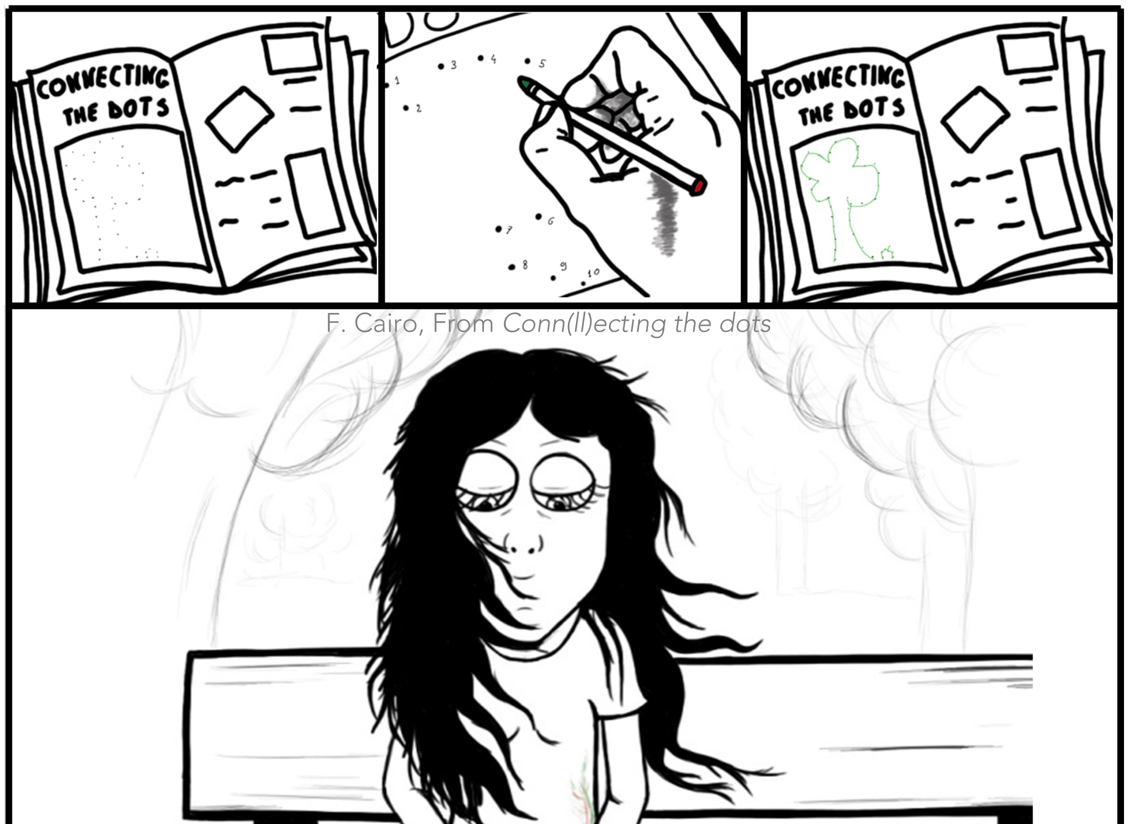

F. Cairo, From *Conn(ll)ecting the dots*

Higgs Self-Coupling

λ_{HHH} can be measured in two complementary ways

Today's focus

di-Higgs

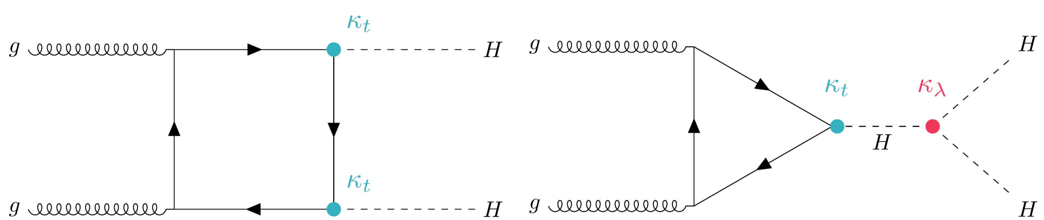

Single-Higgs

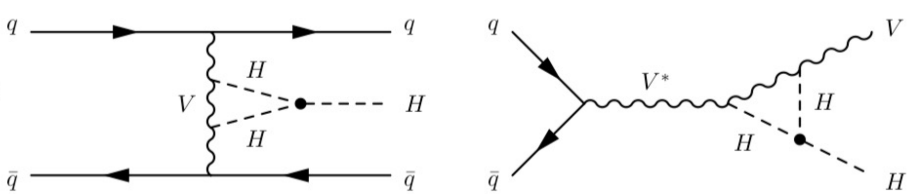

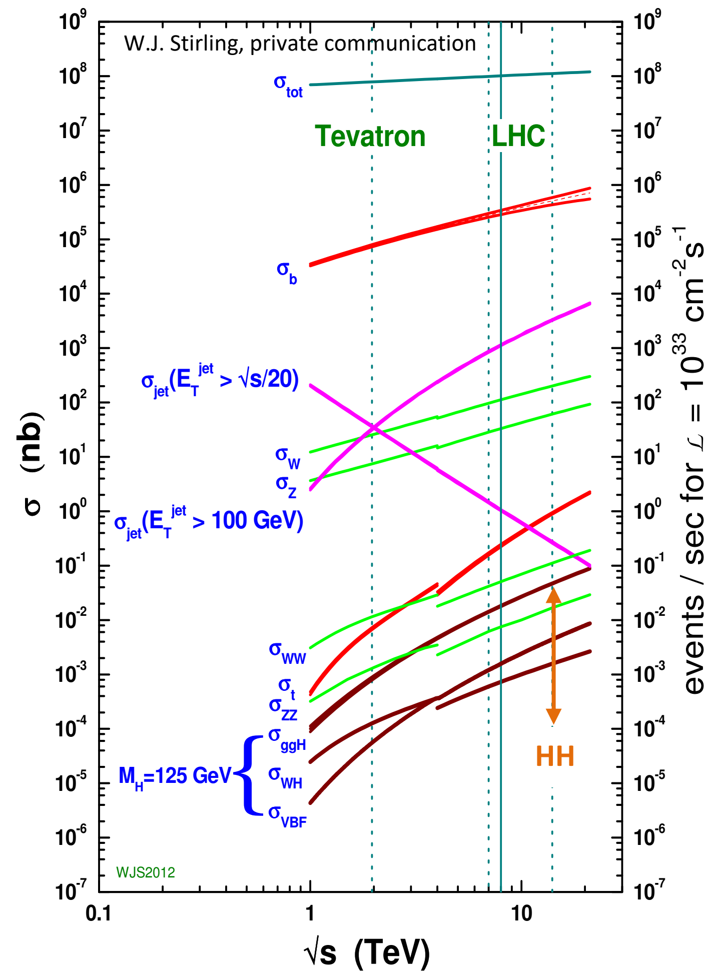

HH Production at the LHC

Non-resonant σ^{ggF}_{HH} = 31.05 fb at 13 TeV for m_H = 125.00 GeV

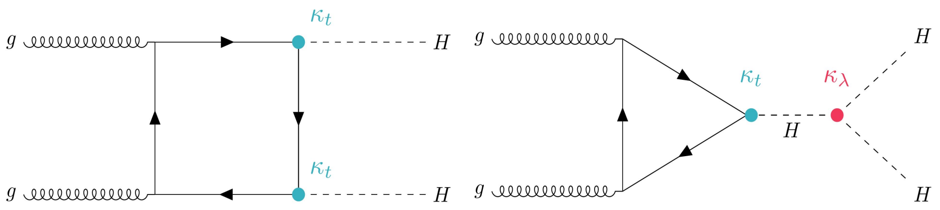

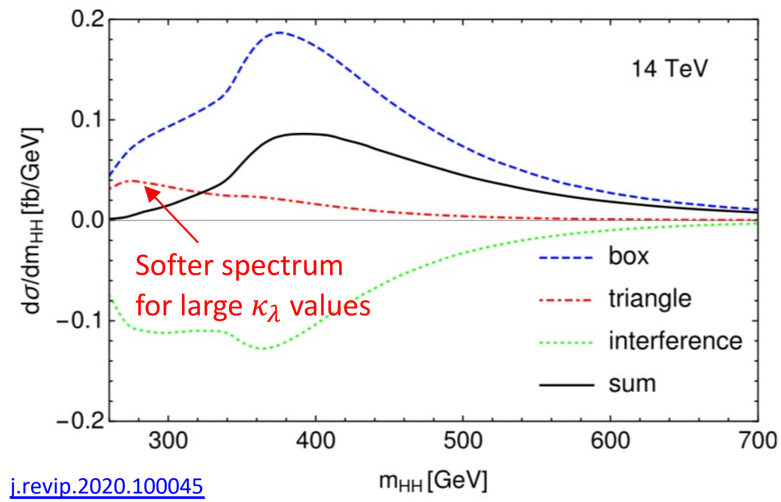

j.revip.2020.100045

HH Production at the LHC

Non-resonant σ_{HH}^{ggF} = 31.05 fb at 13 TeV for m_H = 125.00 GeV

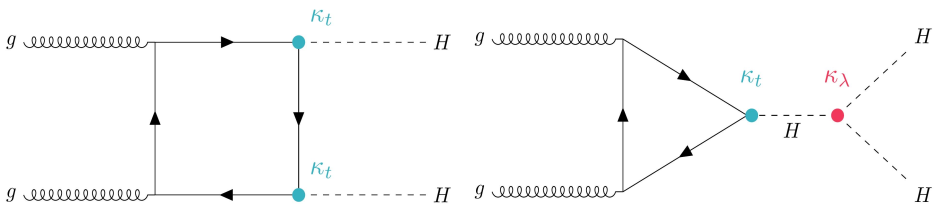

Non-resonant σ_{HH}^{VBF} = 1.73 fb at 13 TeV for m_H = 125.00 GeV

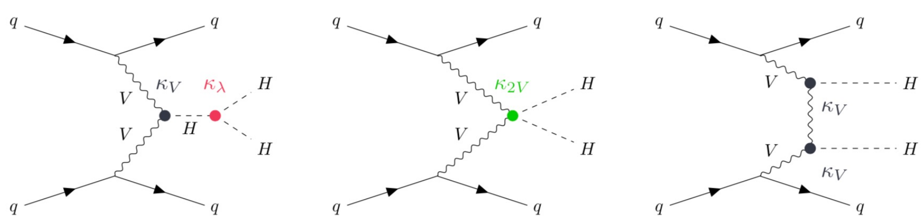

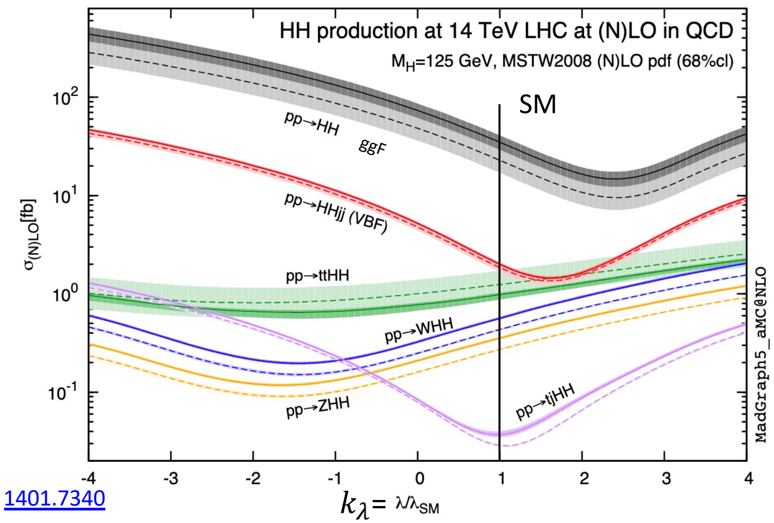

1401.7340

HH Production at the LHC

Non-resonant σ_{HH}^{ggF} = 31.05 fb at 13 TeV for m_H = 125.00 GeV

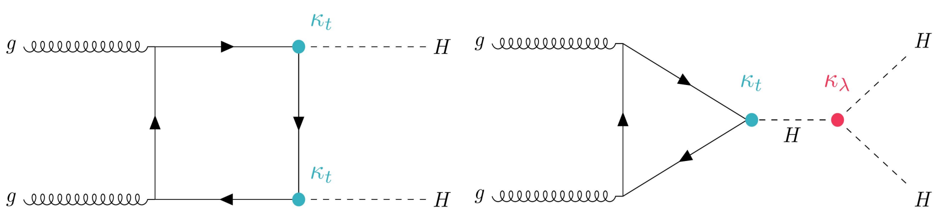

Non-resonant σ_{HH}^{VBF} = 1.73 fb at 13 TeV for m_H = 125.00 GeV

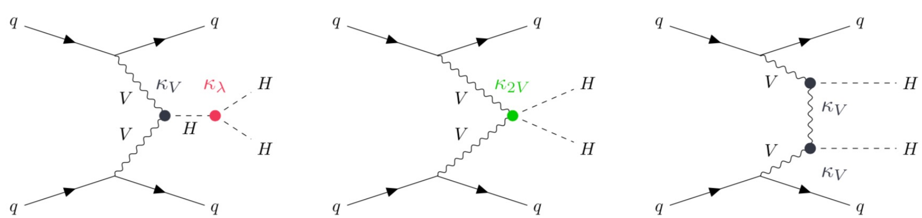

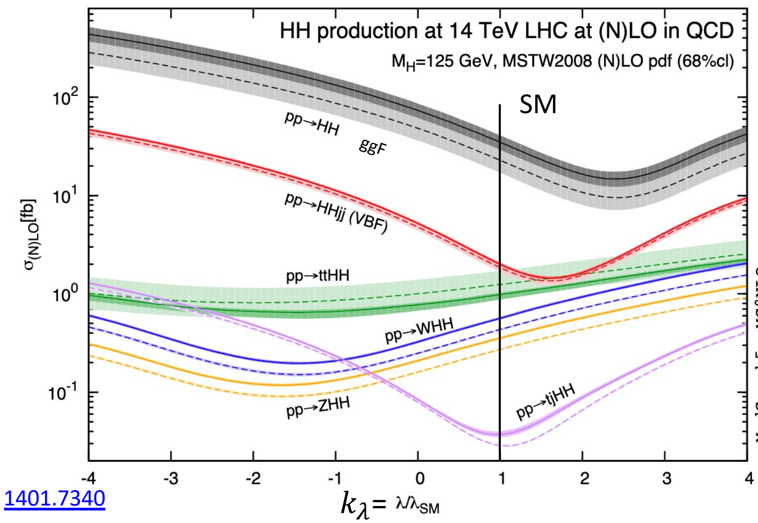

1401.7340

Run 2 $\int L \sim$ **140 fb^{-1}**

$\sim$ **4k HH** events

Scales up to about **10^5 in HL-LHC**

HH Production at the LHC

Non-resonant σ_{HH}^{ggF} = 31.05 fb at 13 TeV for m_H = 125.00 GeV

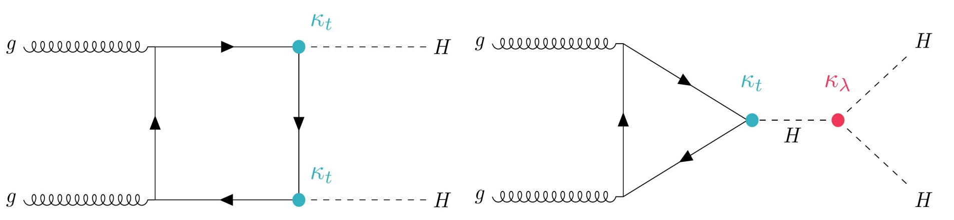

Non-resonant σ_{HH}^{VBF} = 1.73 fb at 13 TeV for m_H = 125.00 GeV

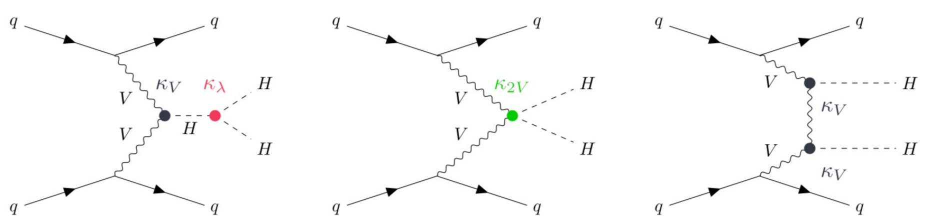

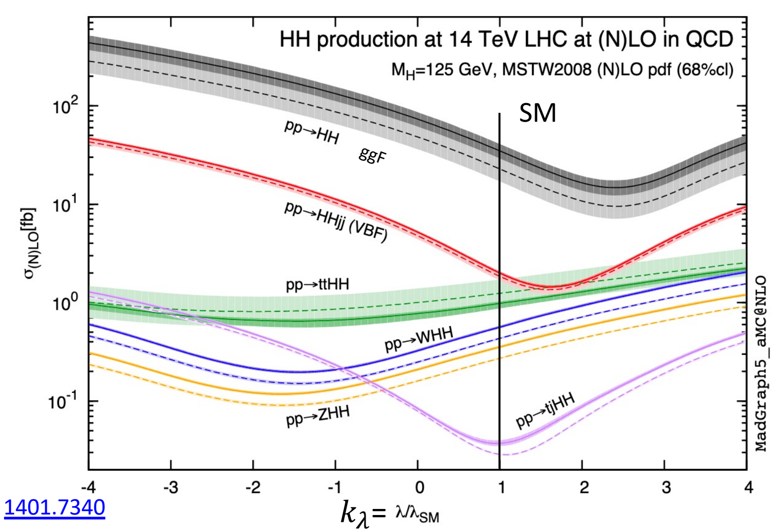

1401.7340

Run 2 $\int L$ ~ **140 fb^{-1}**

~ **4k HH** events

Scales up to about **10^5 in HL-LHC**

$\boldsymbol{\sigma_{HH}}$ and **kinematics** depend on the **couplings**

New physics can manifest as deviation in $\boldsymbol{\sigma_{HH}}$

HH Final States

Branching Ratio	bb	WW	ττ	ZZ	γγ
bb	33%				
WW	25%	4.6%			
ττ	7.4%	2.5%	0.39%		
ZZ	3.1%	1.2%	0.34%	0.076%	
γγ	0.26%	0.10%	0.029%	0.013%	0.0005%

Combination
(and complementarity)
of various final states
fundamental for
observation!

Most final states rely on
b-tagging

Most recent full Run 2 ATLAS Results:

$HH \rightarrow b\bar{b}\gamma\gamma$ (non-resonant & resonant)

$HH \rightarrow b\bar{b}\tau\tau$ (non-resonant & resonant)

$HH \rightarrow b\bar{b}b\bar{b}$ (resonant)

$HH \to b\bar{b}\gamma\gamma$

ATLAS EXPERIMENT

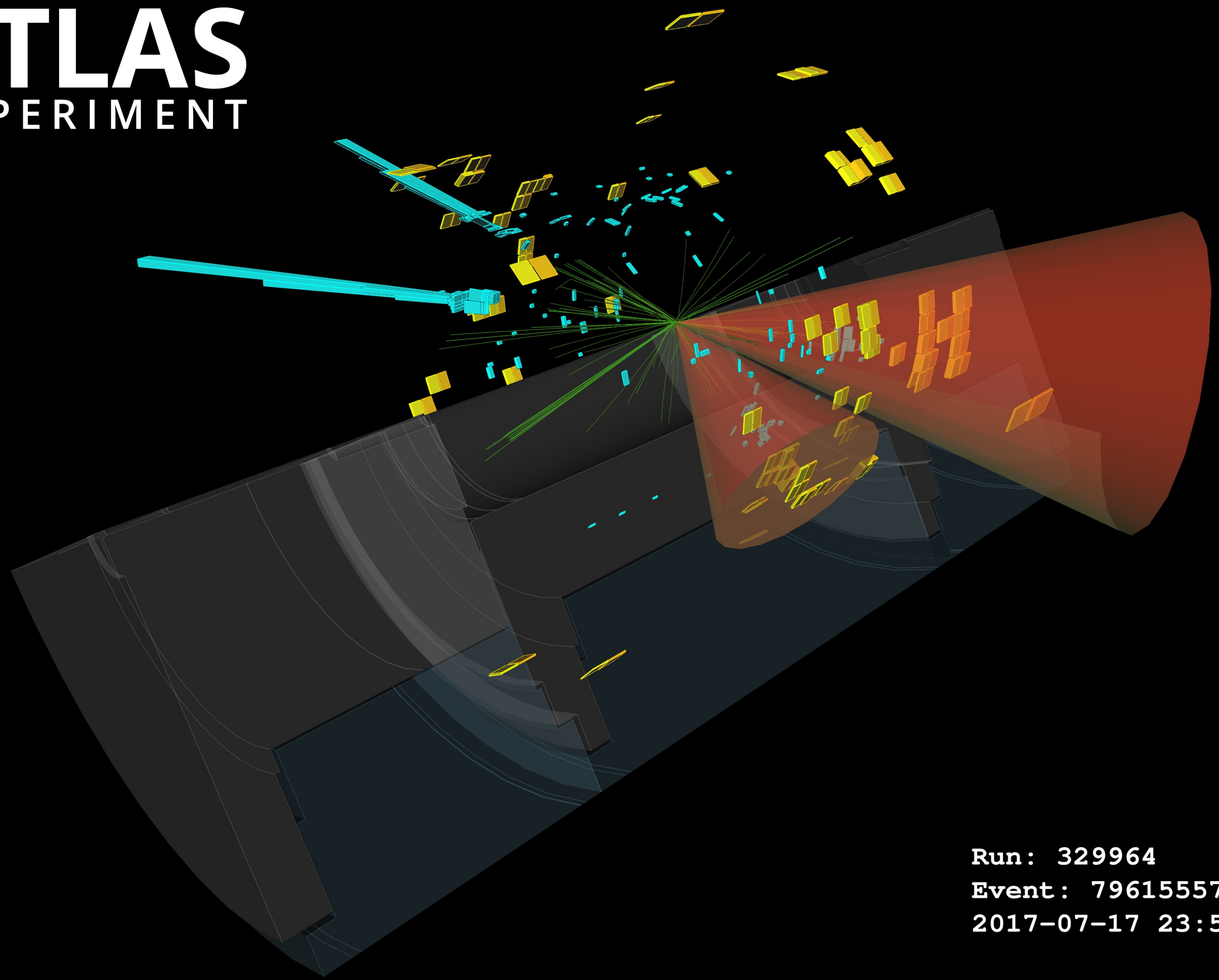

Run: 329964
Event: 796155578
2017-07-17 23:58:15 CEST

Publication: HDBS-2018-34
Physics Briefing: https://atlas.cern/updates/briefing/twice-higgs-twice-challenge

$HH \to b\bar{b}\gamma\gamma$ analysis in a nutshell

Small BR, but fully **reconstructable** final state, **no combinatoric issues, clean signal extraction**

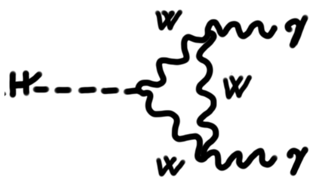

2 photons

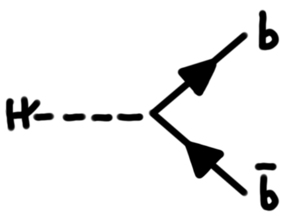

2 b-jets

Object selection

Event categorization

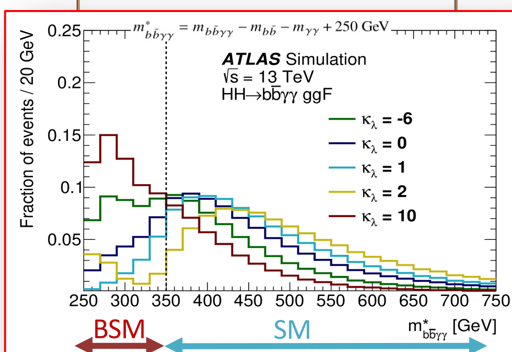

MVA approach,
4 categories

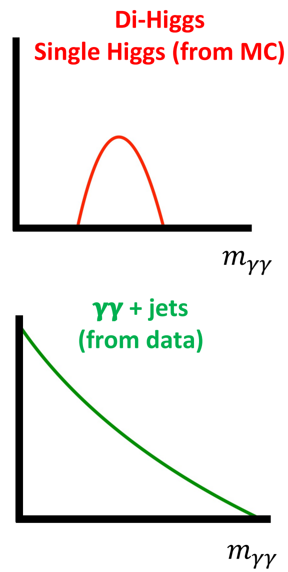

Modeling of discriminant variable

Simultaneous likelihood fit to all categories

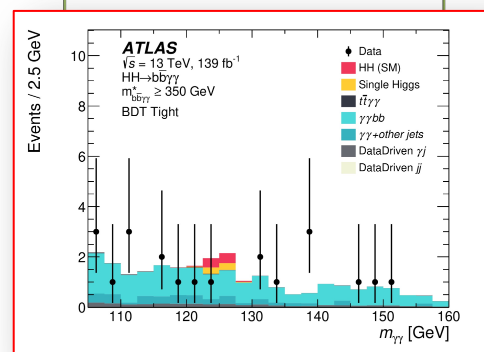

SM σ limits and
σ vs k_λ

Non-Resonant $HH \to b\bar{b}\gamma\gamma$ results

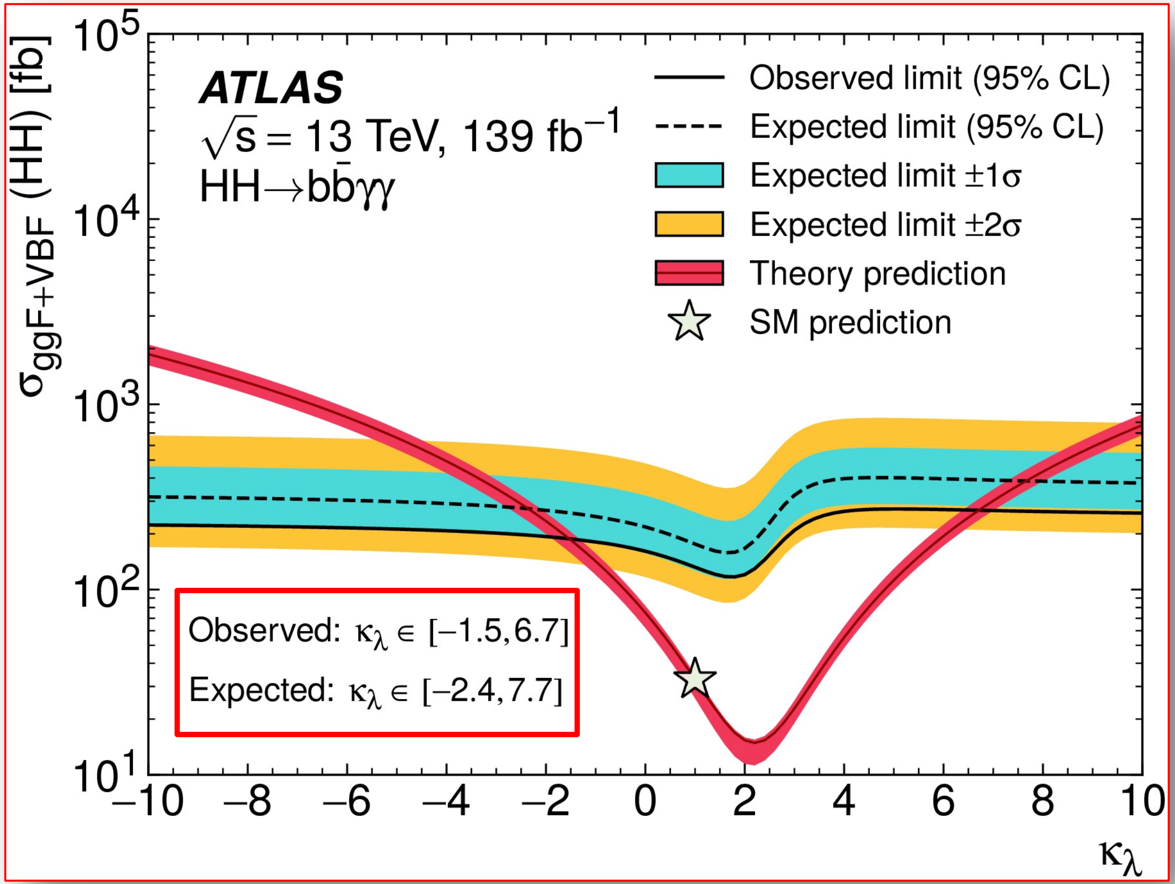

4.1 (5.5) x SM σ_{HH}

5x improvement wrt previous result (~ 26 x SM), ~3x due to analysis techniques

driven by m_{HH} categorization & MVA as well as b-jet corrections

Statistically dominated, few % impact from systematics

Putting everything together

ATLAS-CONF-2021-052

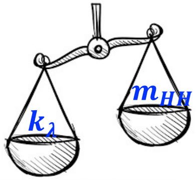

Non-resonant

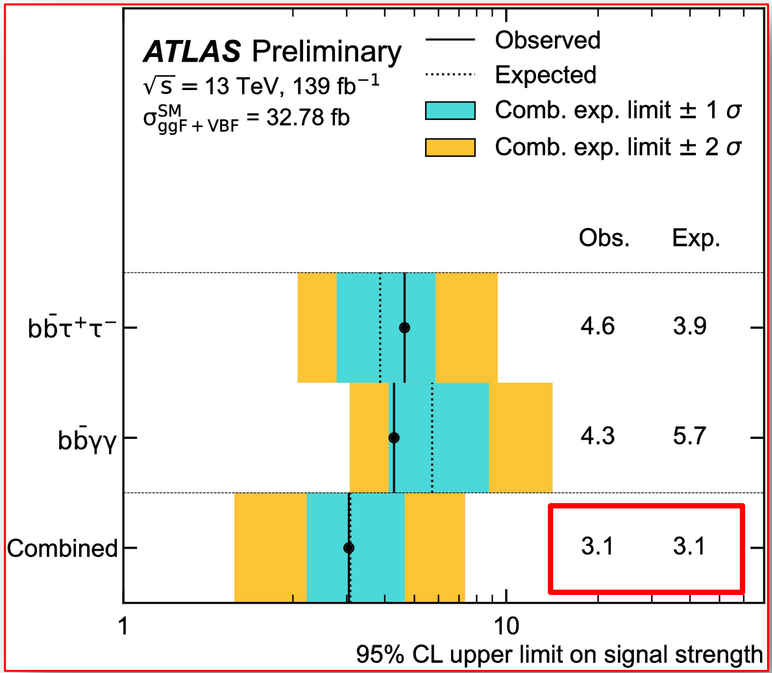

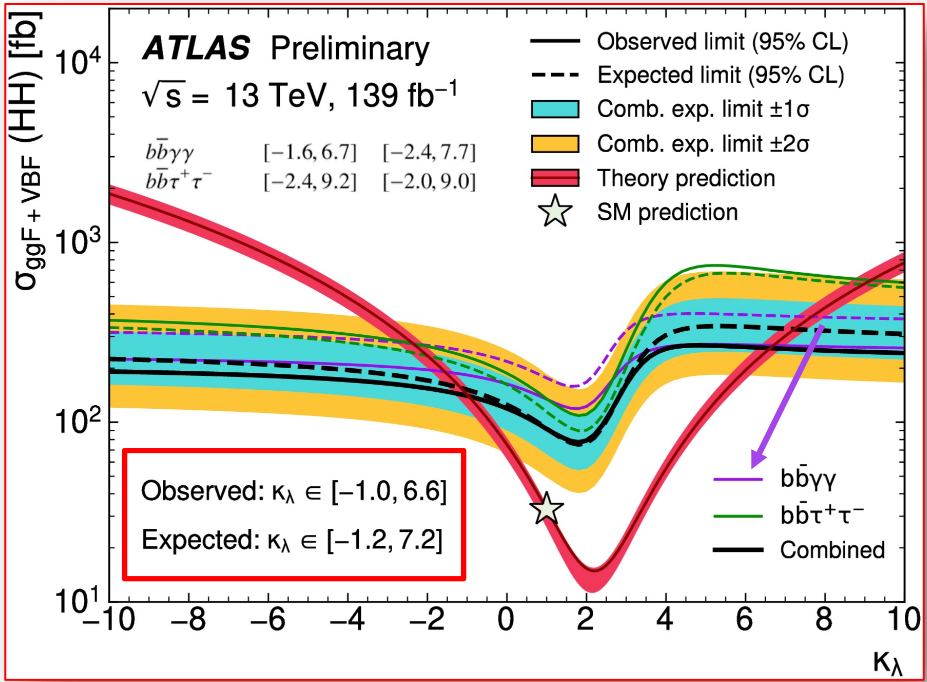

Single channels are now even **better than the 36 fb^{-1} HH combination(*)**

$(HH \rightarrow b\bar{b}b\bar{b}$ still to come)

World's best constraints to date on Higgs boson's self coupling

$HH \rightarrow b\bar{b}\gamma\gamma$ drives the sensitivity at large k_λ!

(*) HH σ^{SM} 6.9 Obs, 10 Exp; Observed $k_\lambda \in [-5, 12.0]$, Expected $k_\lambda \in [-5.8, 11.5]$

An exciting time ahead

Run 3 coming up!

Run 3: σ_{HH} @ 13.6 TeV $\approx +11\%\ \sigma_{HH}$ @ 13 TeV , $\int L \approx$ **+300 fb^{-1} ? $\approx$ +10k HH events!**

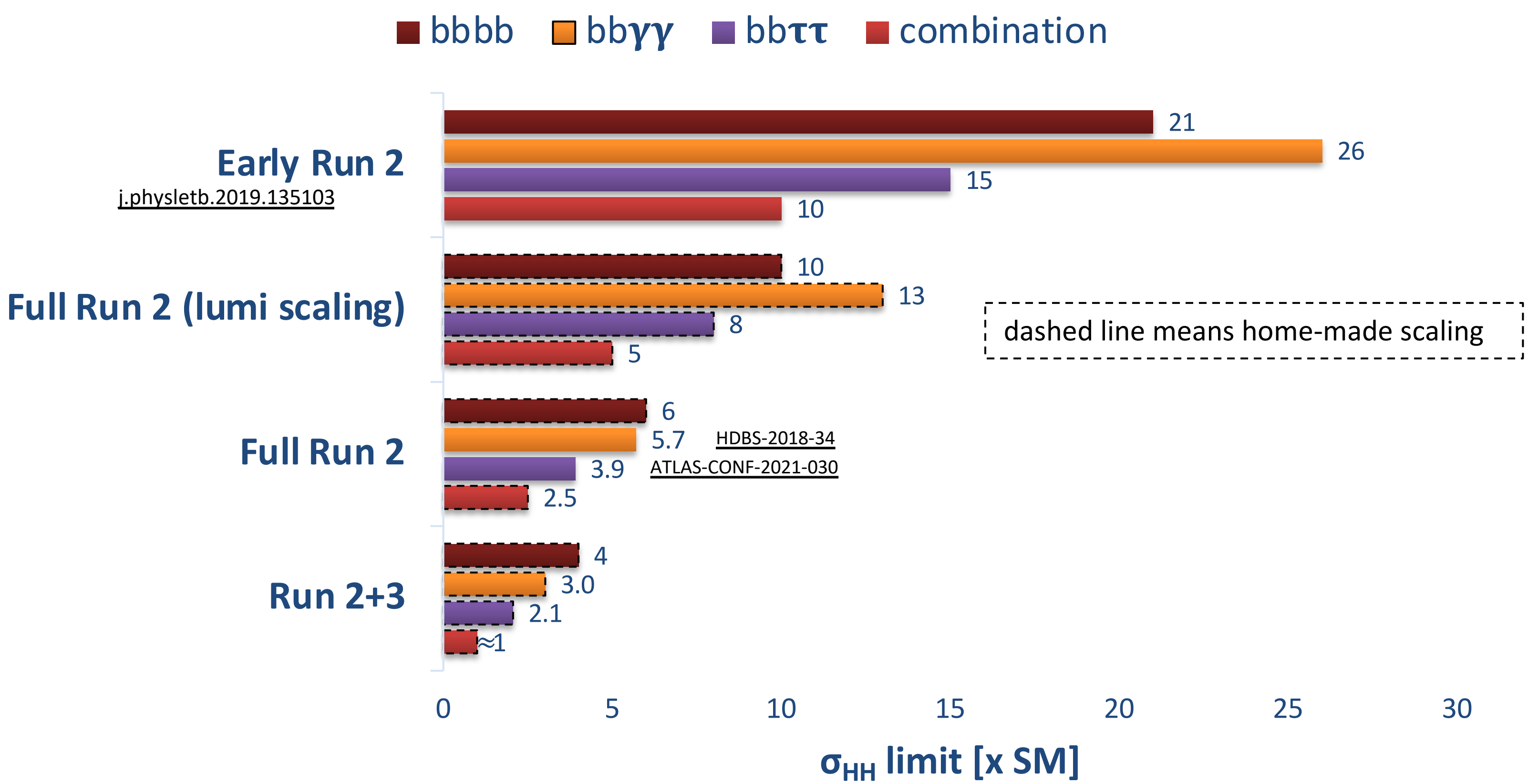

An exciting time ahead

Run 3 coming up!

Run 3: σ_{HH} @ 13.6 TeV ≈ +11% σ_{HH} @ 13 TeV , $\int L$ ≈ **+300 fb^{-1} ?** ≈ **+10k HH events!**

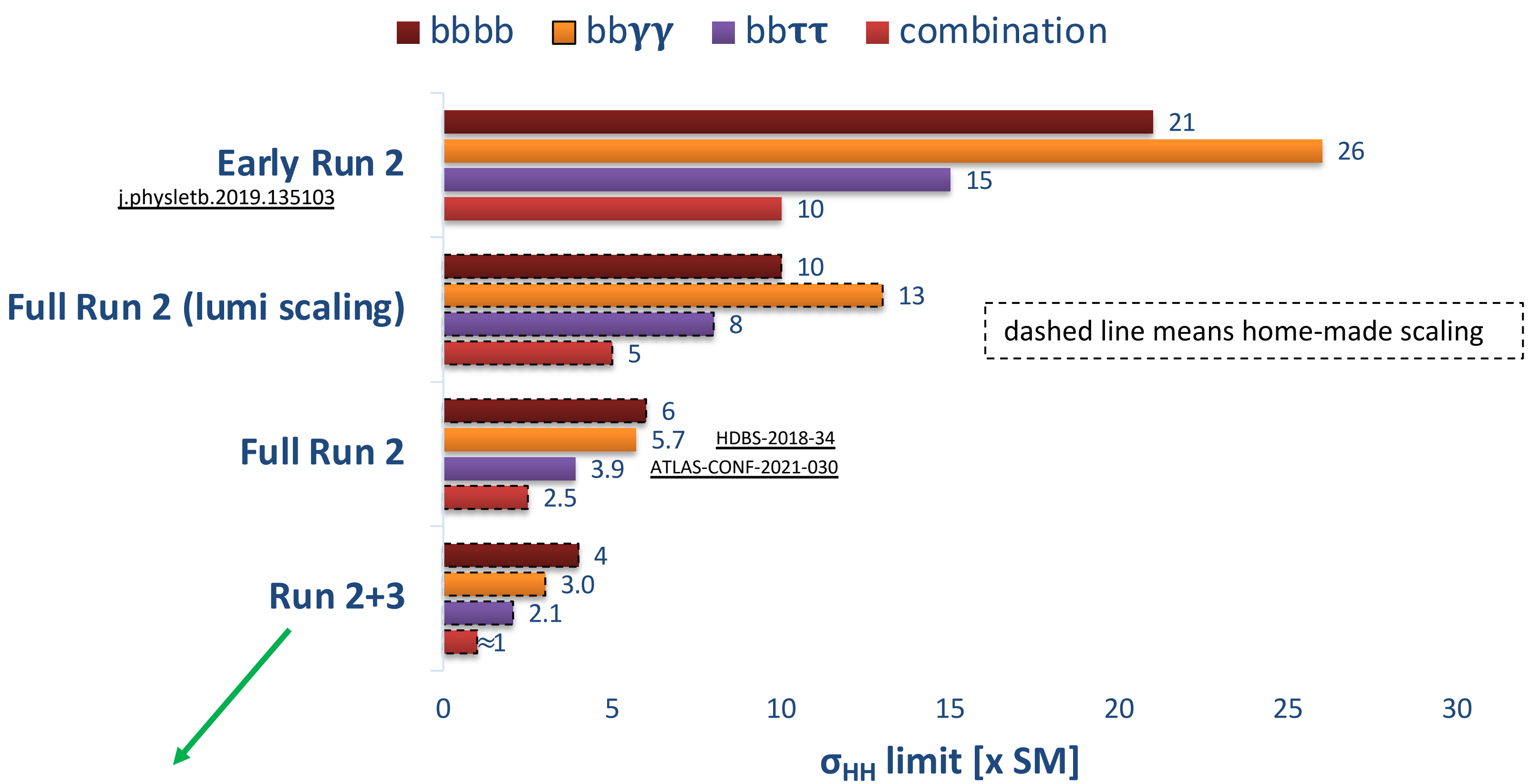

Can already be a game changer for HH!!!

Preparing for Run 3

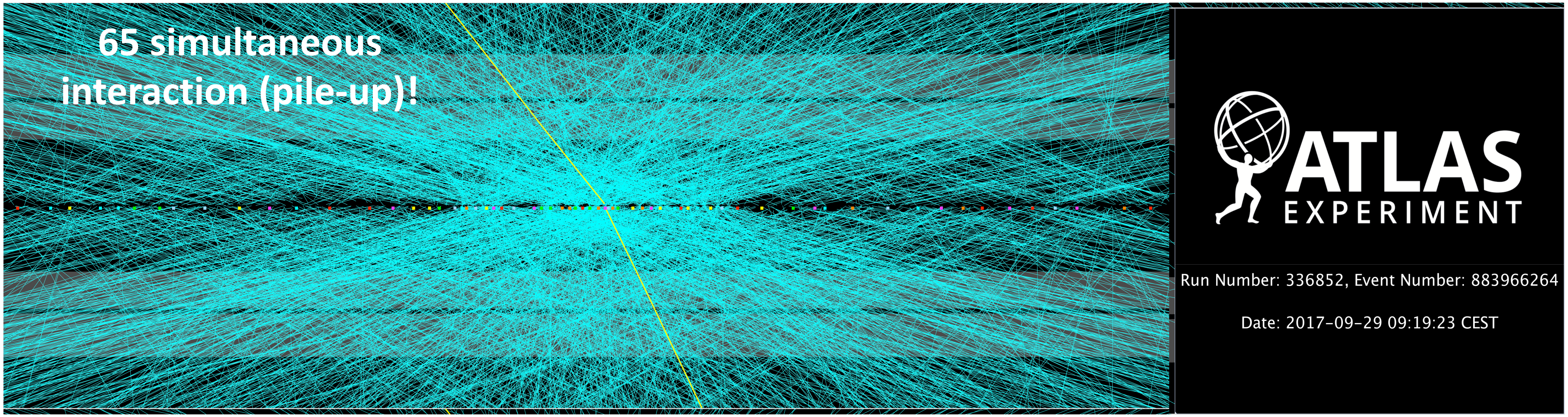

Performance Highlights

- **Tracking and Vertexing are key ingredients for physics analyses**
- **Run 1 → Run 2**: upgraded detector
  - 2x better IP resolution, 4-5x better light-jet rejection in b-tagging
- **Run 2 → Run 3** : aging detector and more challenging pile-up conditions
  - e.g. all physics objects must be reconstructed wrt the correct primary vertex
  - **New primary vertexing algorithm** deployed to improve pile-up robustness

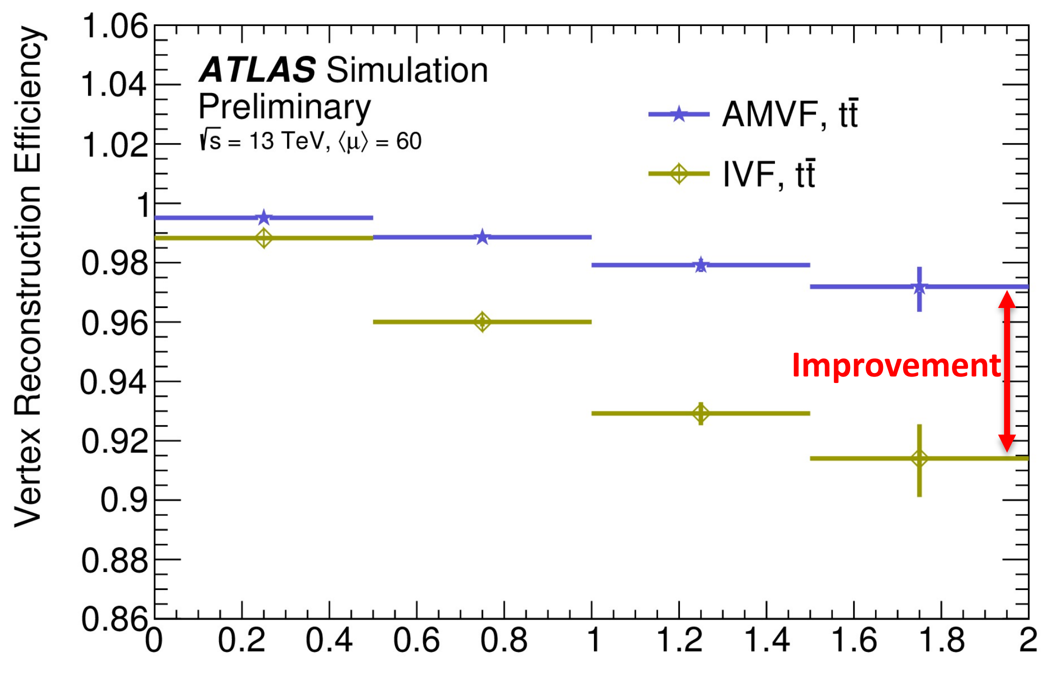

ATL-PHYS-PUB-2019-015

All relevant for **the HL-LHC ATLAS silicon Inner Tracker (ITk)**

Preparing for Run 4

F. Cairo, From *Conn(ll)ecting the dots*

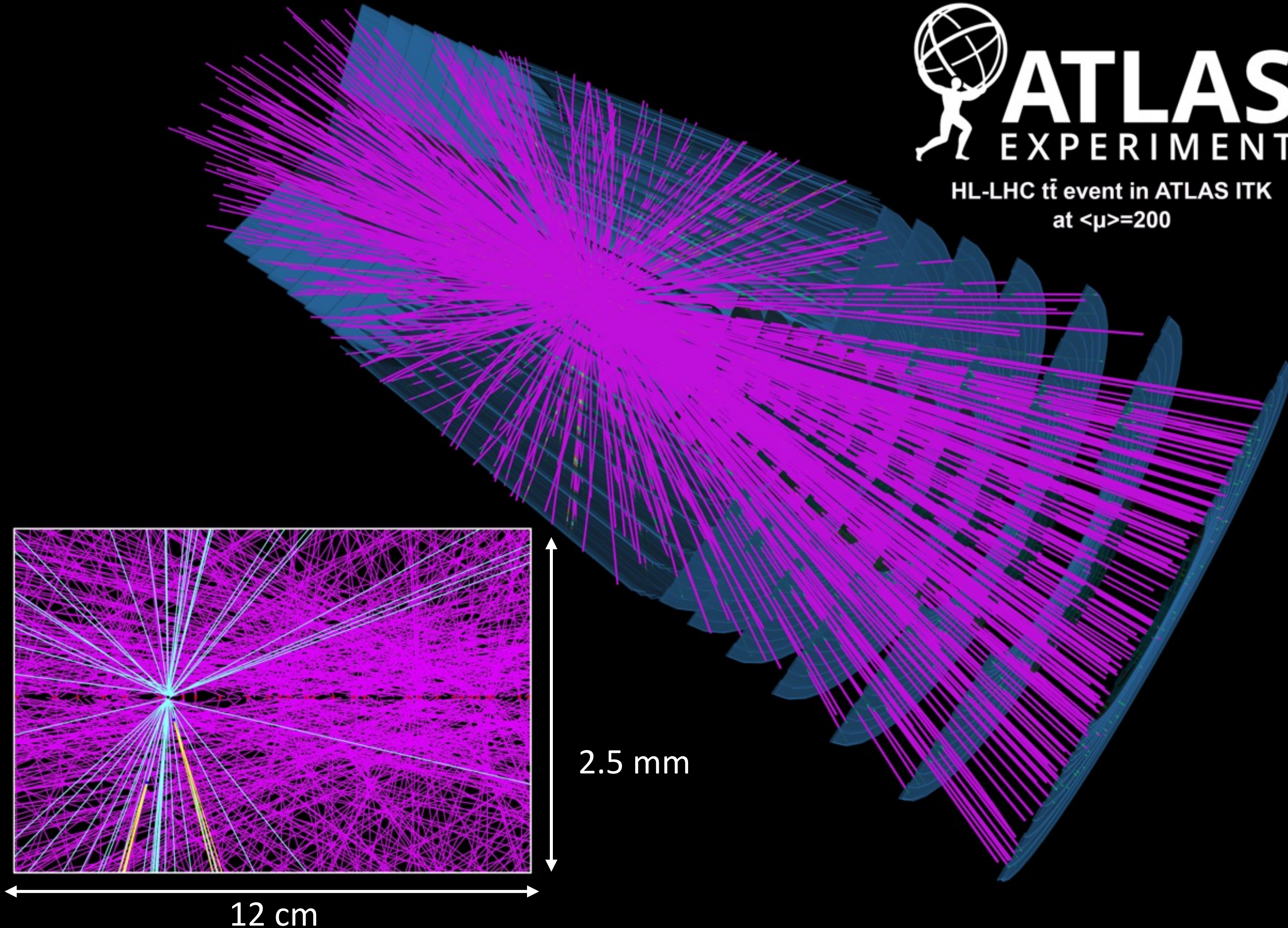

HL-LHC $t\bar{t}$ event in ATLAS ITK
at <μ>=200

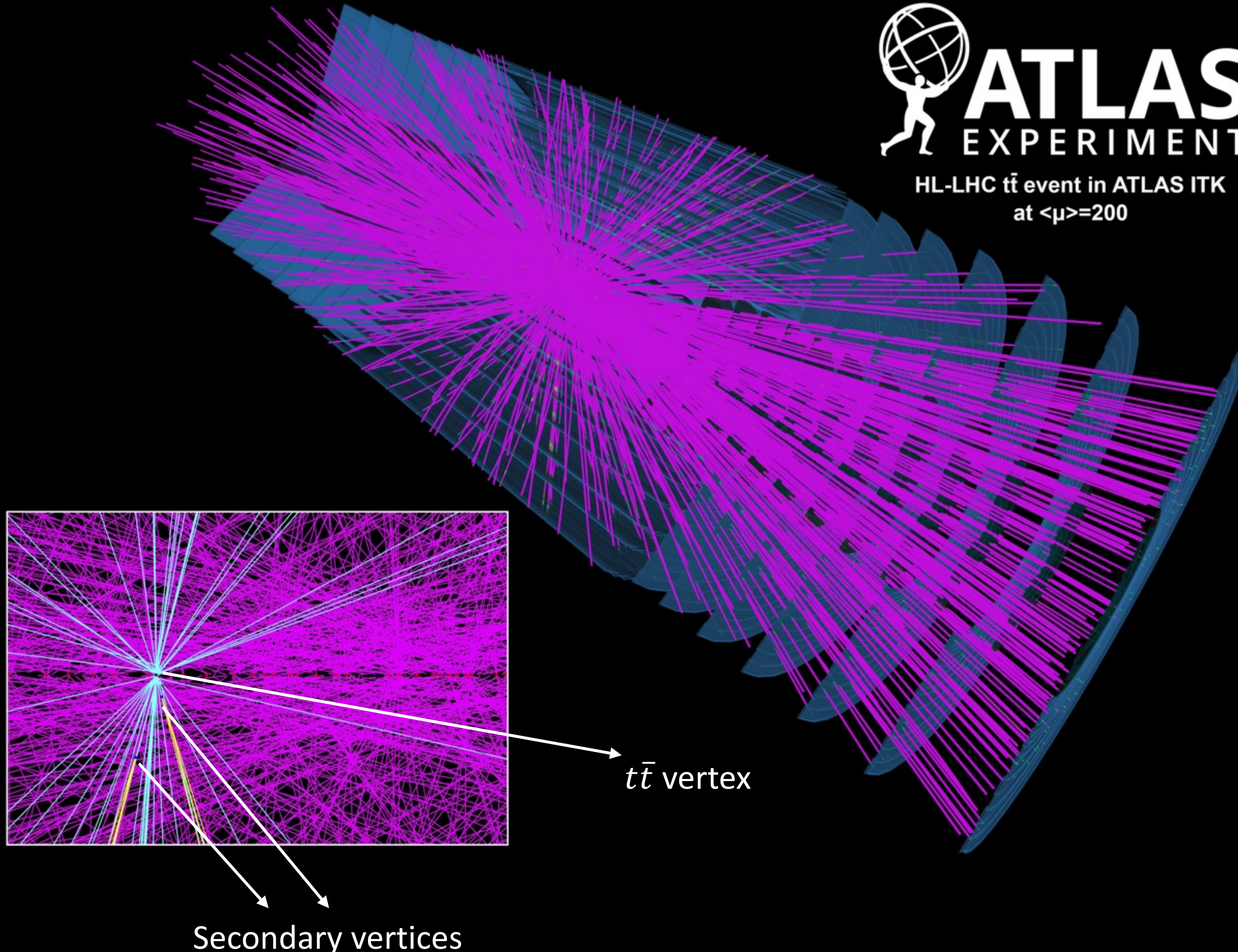
ATLAS
EXPERIMENT
HL-LHC $t\bar{t}$ event in ATLAS ITK
at <μ>=200
$t\bar{t}$ vertex
Secondary vertices

The ATLAS Run 4 Inner Tracker

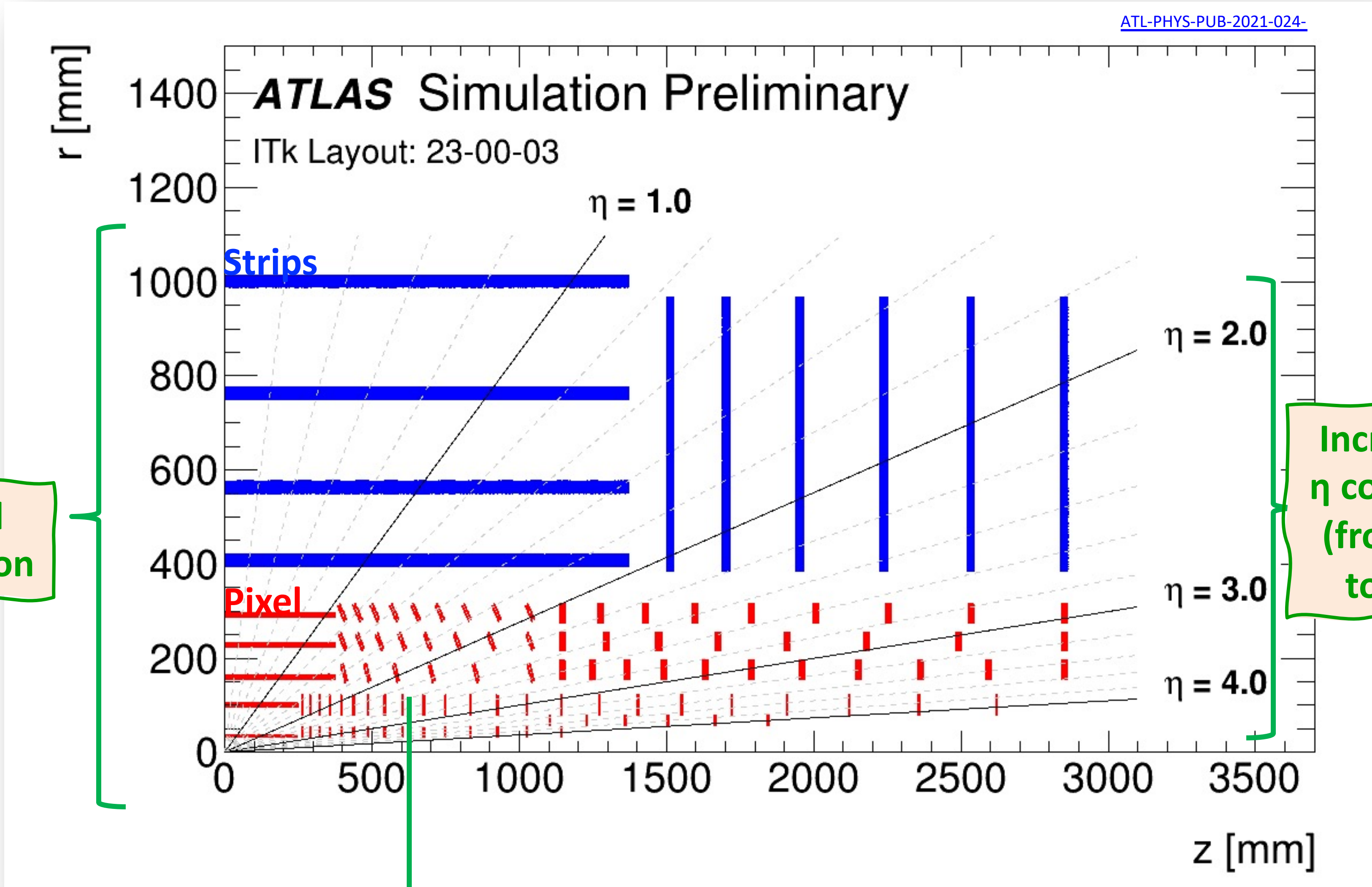

All silicon

Increased η coverage (from 2.4 to 4.0)

Inclined layout

The ATLAS Run 4 Inner Tracker

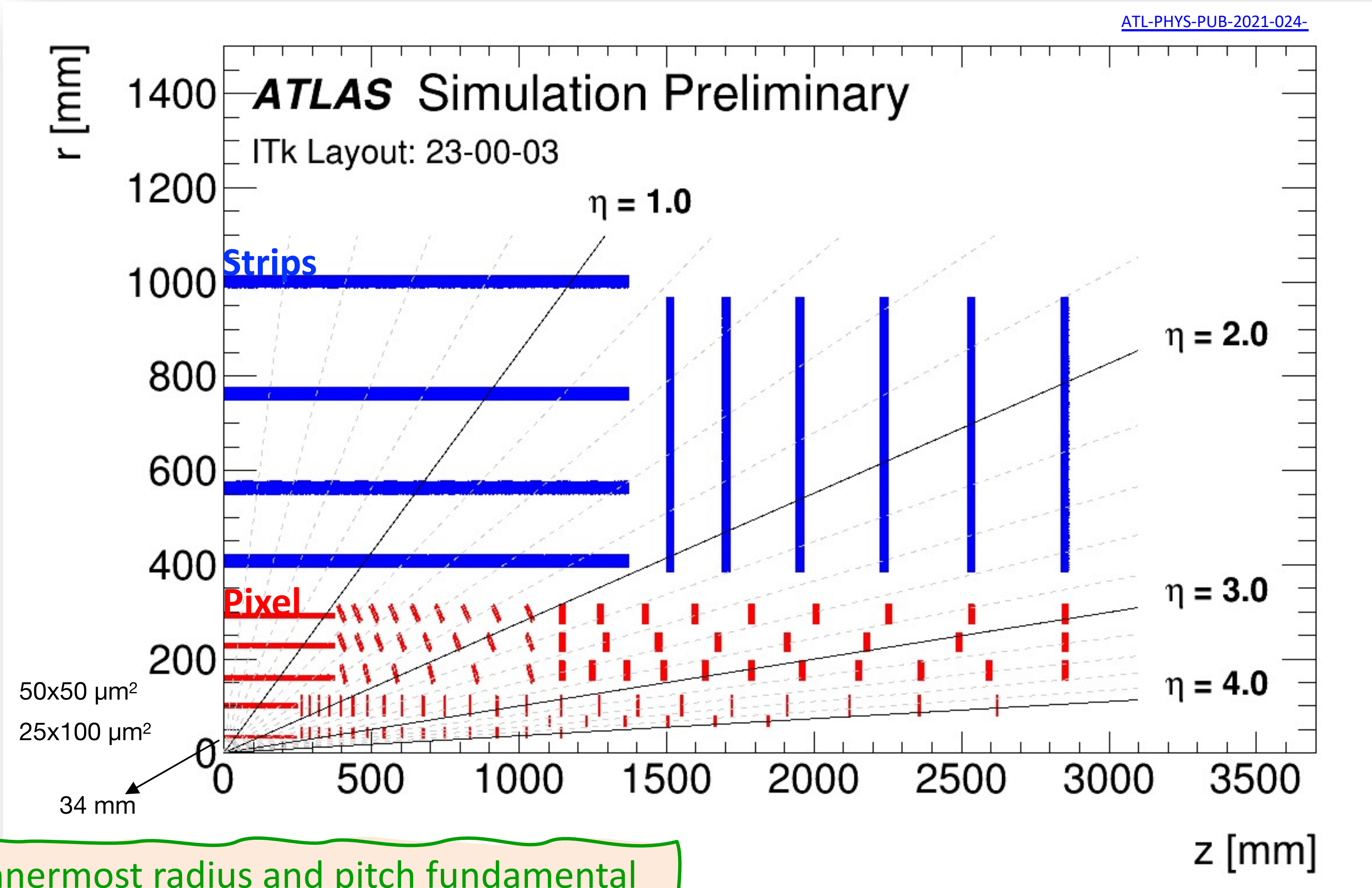

Innermost radius and pitch fundamental for **impact parameter** determination and thus **b-tagging performance**!

The ATLAS Run 4 Inner Tracker

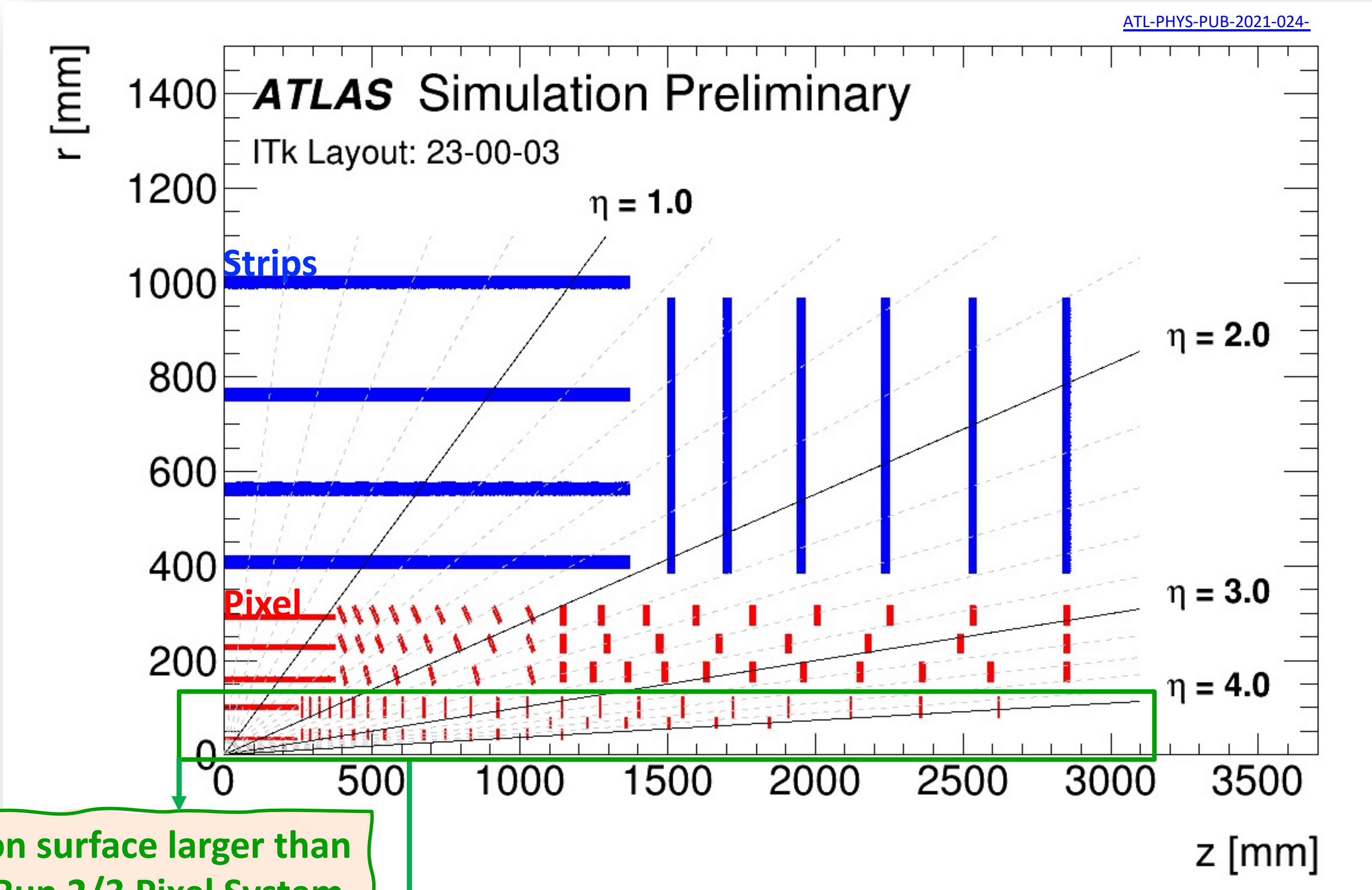

Silicon surface larger than the Run 2/3 Pixel System

Extractable & Replaceable

Radiation hardness up to 10-15 MGy

Run 4 Performance Highlights

High-Level ML b-taggers utilize low-level taggers' outputs

- Impact Parameter based
- Secondary Vertex finding
- Decay chain Multi-Vertex Algorithm

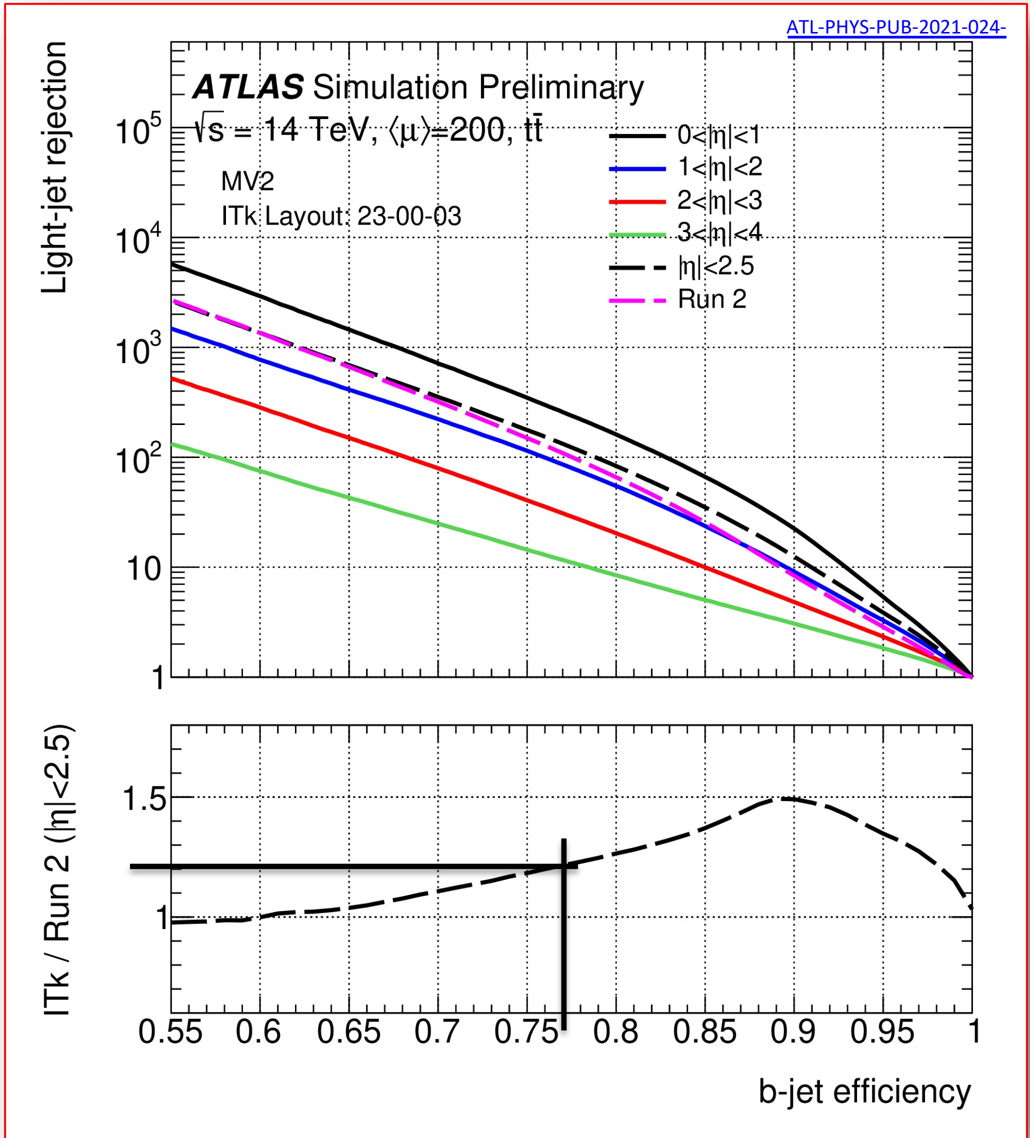

ITk vs Run 2:
20% improvement in light-jet rejection at the 77% b-tag WP

About 1 order of magnitude lower fake rate compared to Tevatron! Ref 1, 2

High-Luminosity LHC projections

ATL-PHYS-PUB-2022-005

- **HL-LHC projections** updated for $HH \to b\bar{b}\gamma\gamma$ & $HH \to b\bar{b}\tau\tau$

Uncertainty scenario	Significance [σ] $b\bar{b}\gamma\gamma$	$b\bar{b}\tau^+\tau^-$	Combination
No syst. unc.	2.3 ~~2.1~~	4.0 ~~2.3~~	4.6 ~~3.3~~
Baseline	2.2 ~~2.0~~	2.8 ~~2.0~~	3.2

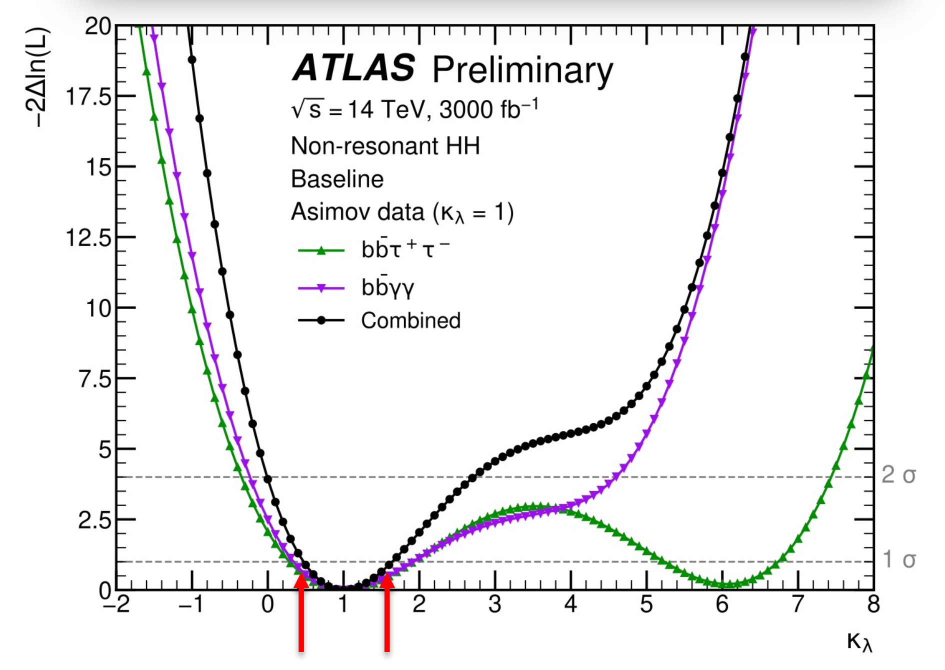

$0.5 \lesssim k_\lambda \lesssim 1.6$ at 1σ,
comparable to previous ATLAS+CMS combination!

What's next?

Relative view point, by F. Cairo

Future Colliders

[Symmetry]

Illustration by Sandbox Studio, Chicago

Future Colliders

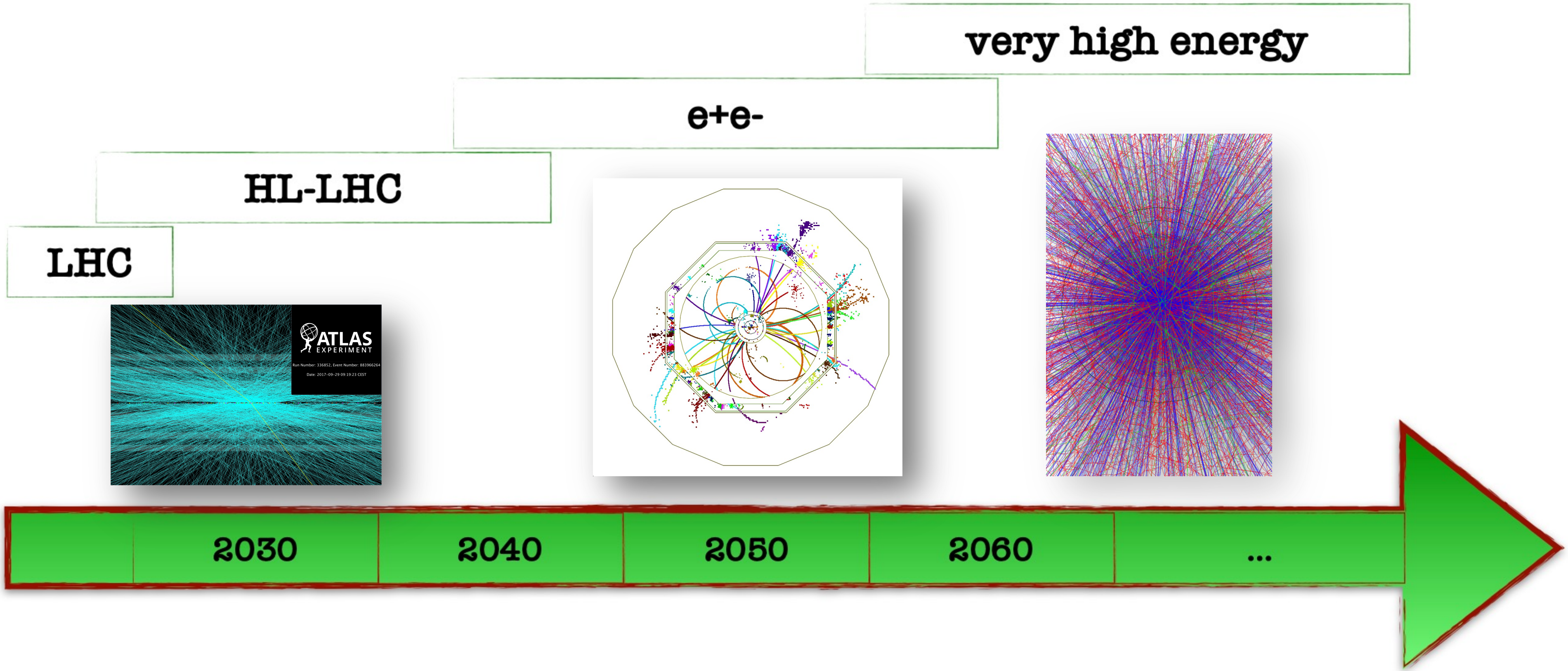

- pp: high energy → ideal for HH (Higgs self-coupling)
- e^+e^-: clean environment, initial states well defined → ideal for precision measurments and for probing light Yukawas

Di-Higgs Prospects for the far future

- **Probing λ: high priority** for particle physics both at the LHC and beyond
- **di-Higgs** require advanced reconstruction techniques & detector technologies
  - Benchmark for the **future HEP machines and driver for their detector design**!

collider	single-H	HH	combined
HL-LHC	100-200%	50%	50%
CEPC_{240}	49%	–	49%
ILC_{250}	49%	–	49%
ILC_{500}	38%	27%	22%
ILC_{1000}	36%	10%	10%
CLIC_{380}	50%	–	50%
CLIC_{1500}	49%	36%	29%
CLIC_{3000}	49%	9%	9%
FCC-ee	33%	–	33%
FCC-ee (4 IPs)	24%	–	24%
HE-LHC	-	15%	15%
FCC-hh	-	5%	5%

j.revip.2020.100045

Run 3: 100% precision?

Di-Higgs Prospects for the far future

As an example: arXiv:1907.02078v2

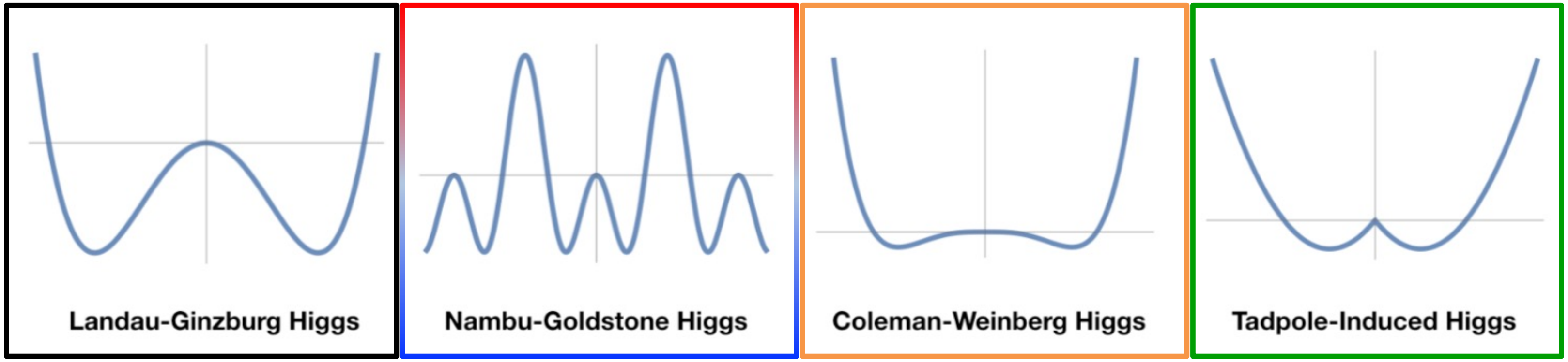

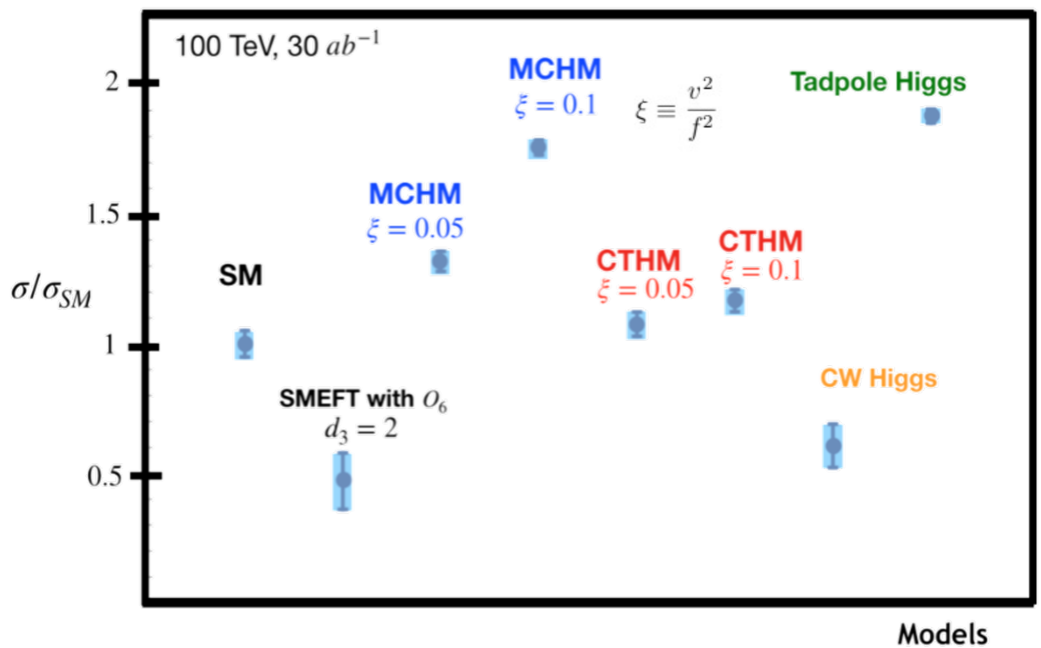

Di-Higgs Prospects for the far future

As an example: [arXiv:1907.02078v2]

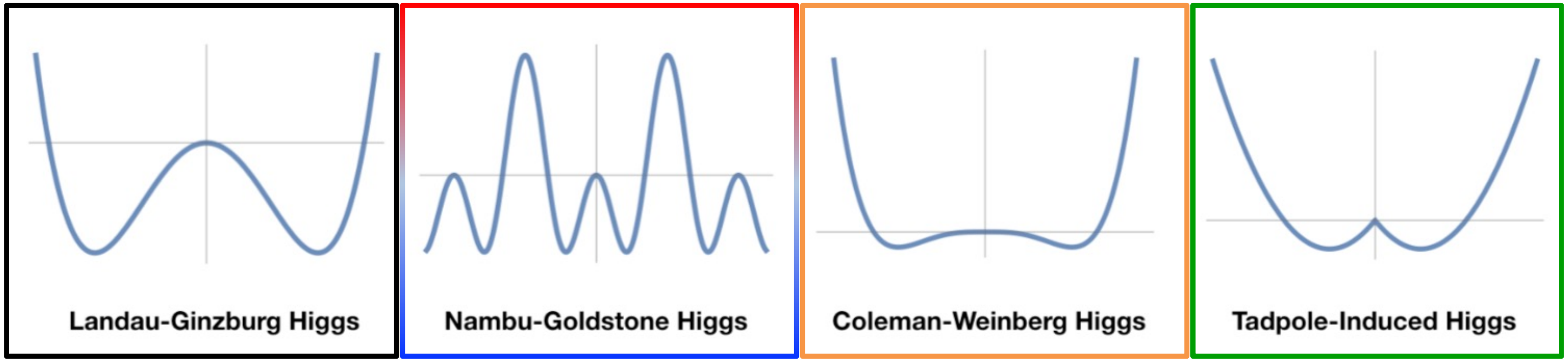

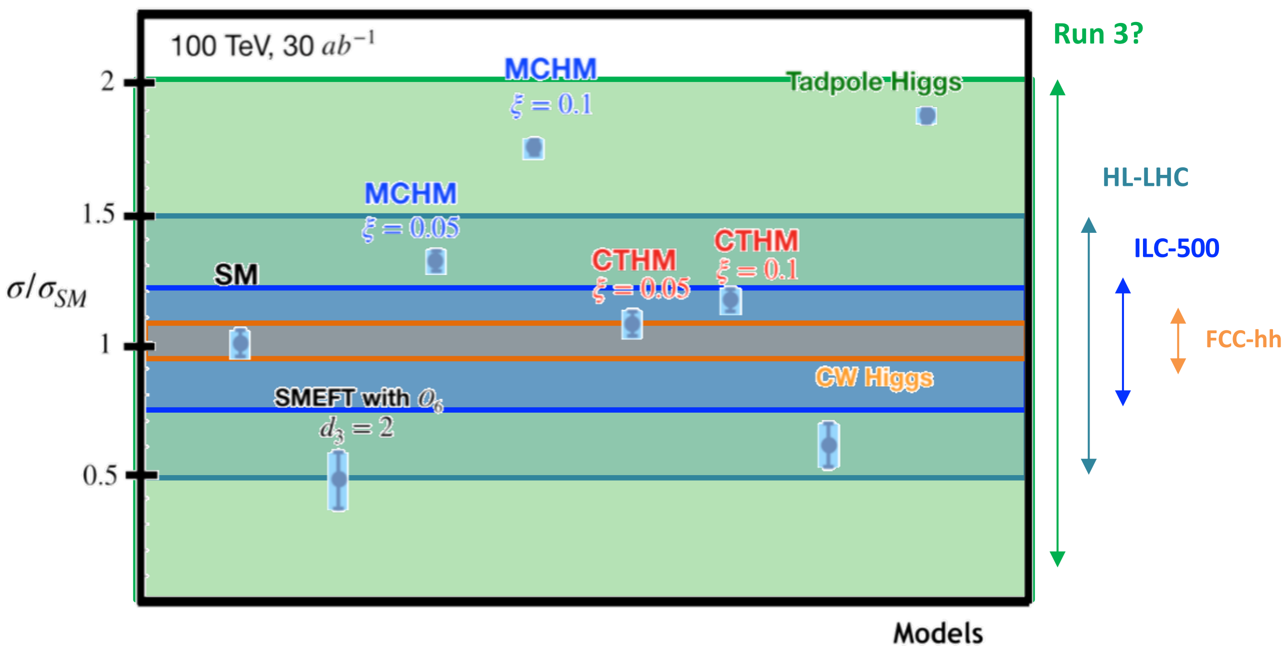

The Post Higgs boson era

Now → **Future**

ATLAS-CONF-2020-027

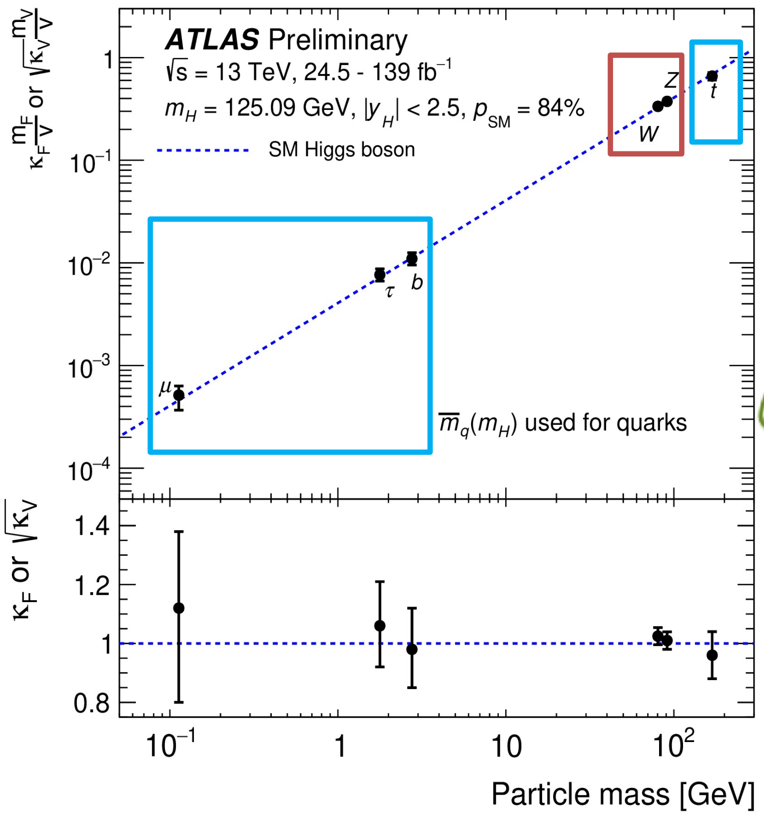

ATLAS-CONF-2020-027

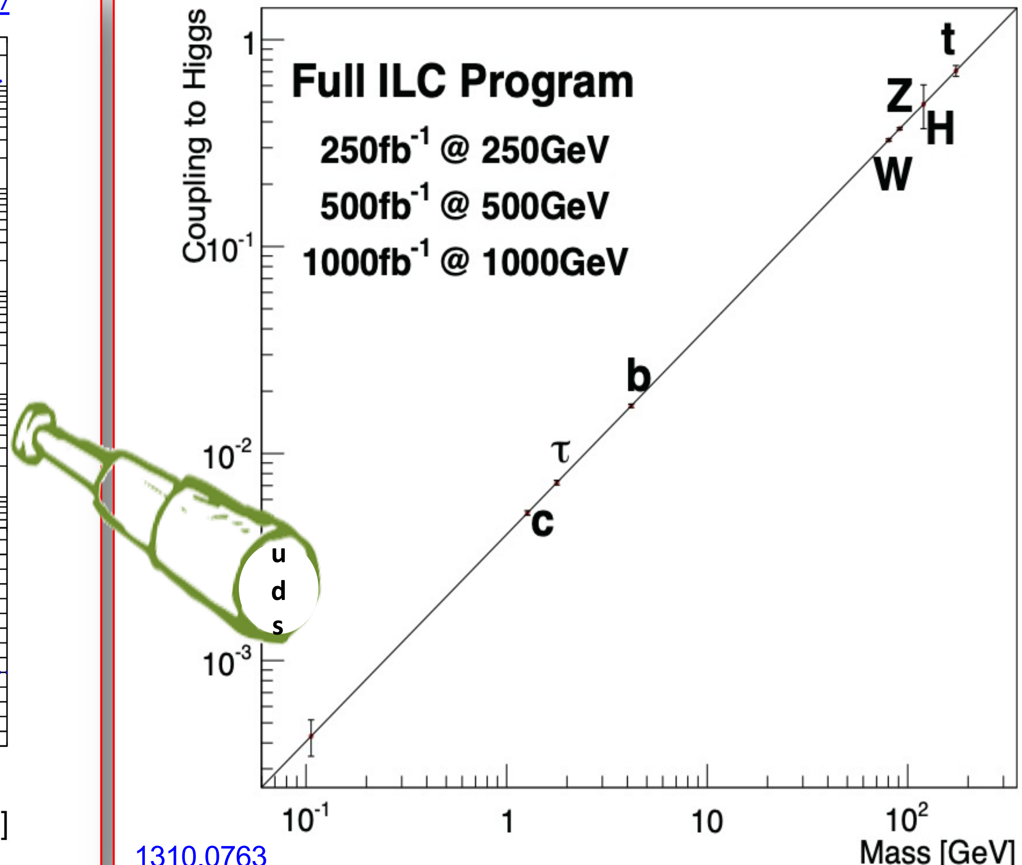

1310.0763

Is **Yukawa coupling really universal** between families?

Higgs and Flavors in the far future

- Higgs to **top-quarks**
  - No big gain from HL-LHC to e+e- machines (low $\sqrt{s}$)
- Higgs to **b-quarks**
  - ~ 2% at HL-LHC
  - ~ 0.5-1% in future e^+e^- machines
    - x2–4 better than HL-LHC
- Higgs to **c-quarks**
  - HL-LHC able to probe the SM?
  - ~1% in future e^+e^- machines
- Higgs to **light-quarks**
  - Only upper bounds

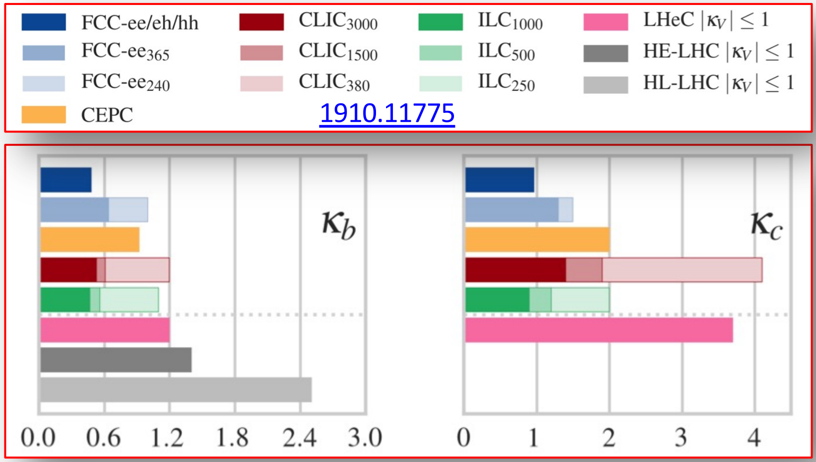

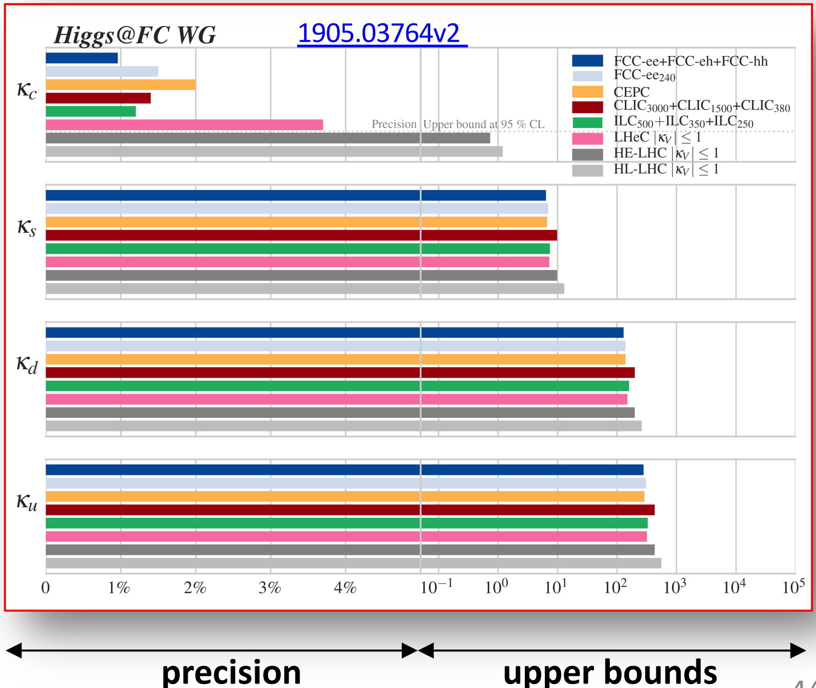

Piece #2

The Strange Yukawa coupling at e^+e^- colliders

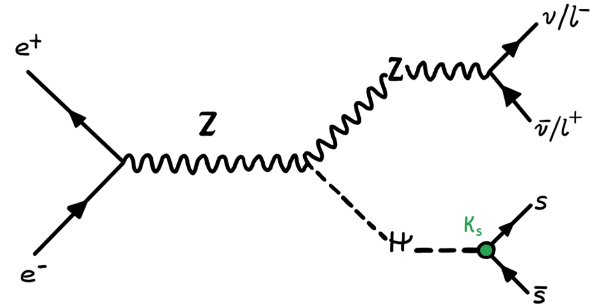

The Strange quark as a probe for New Physics

SM Higgs

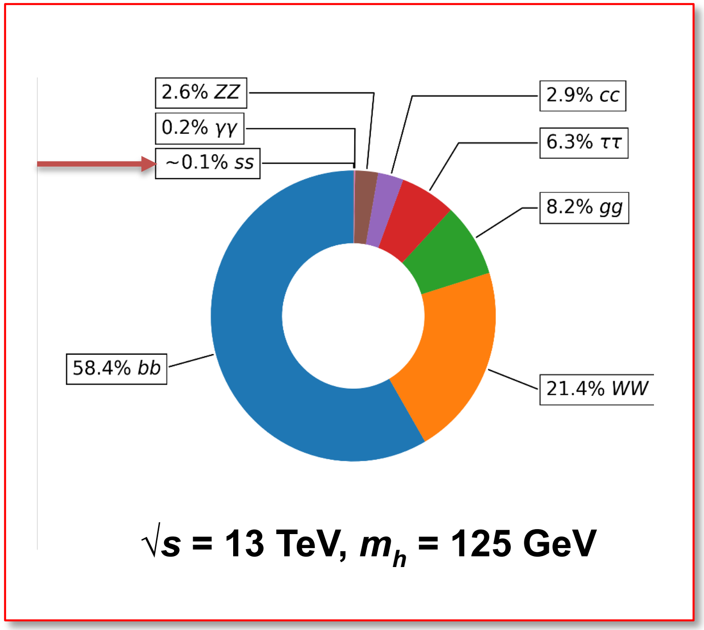

BSM Charged Higgs

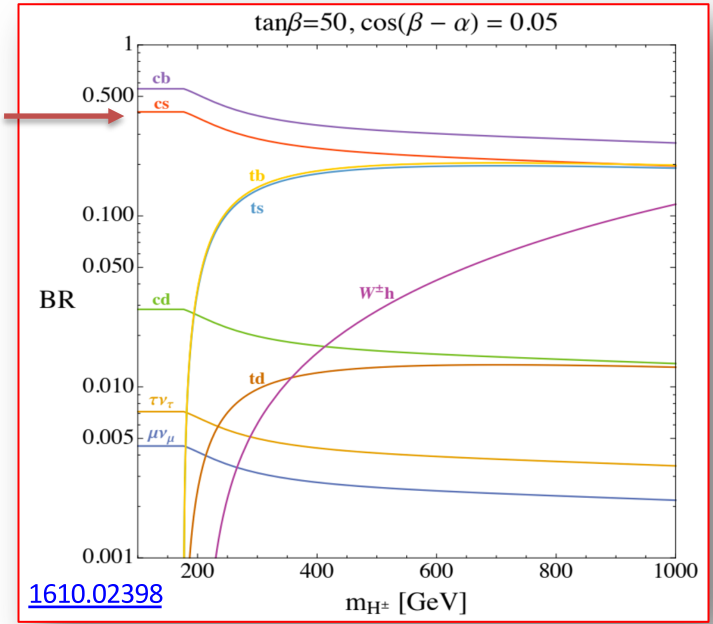

1610.02398

The Strange quark as a probe for New Physics

SM Higgs

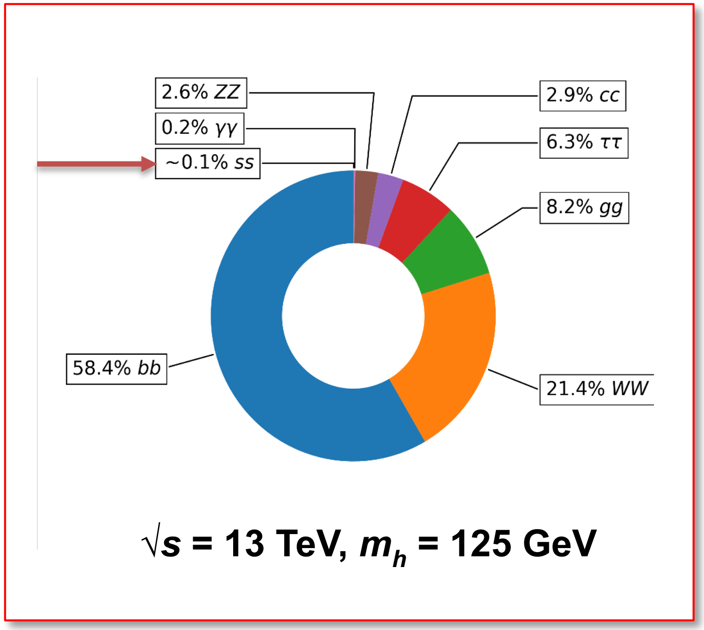

BSM Charged Higgs

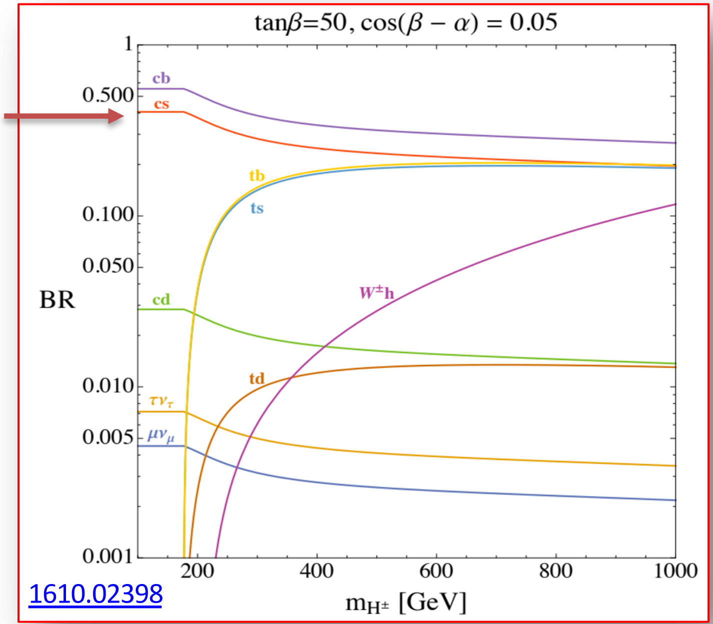

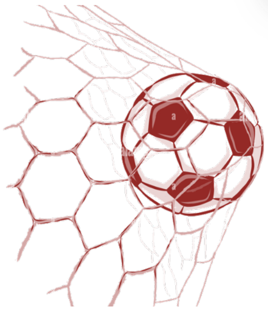

Assess the sensitivity of Higgs to strange couplings(*) at future Higgs Factories and study detector design enabling strange jet tagging

(*)many more SM analyses would benefit from strange tagging, e.g. $ee \rightarrow ss$, $Z \rightarrow ss$, $W \rightarrow cs$, etc!

Experimental Handles for Flavor Tagging

T. Tanabe's presentation

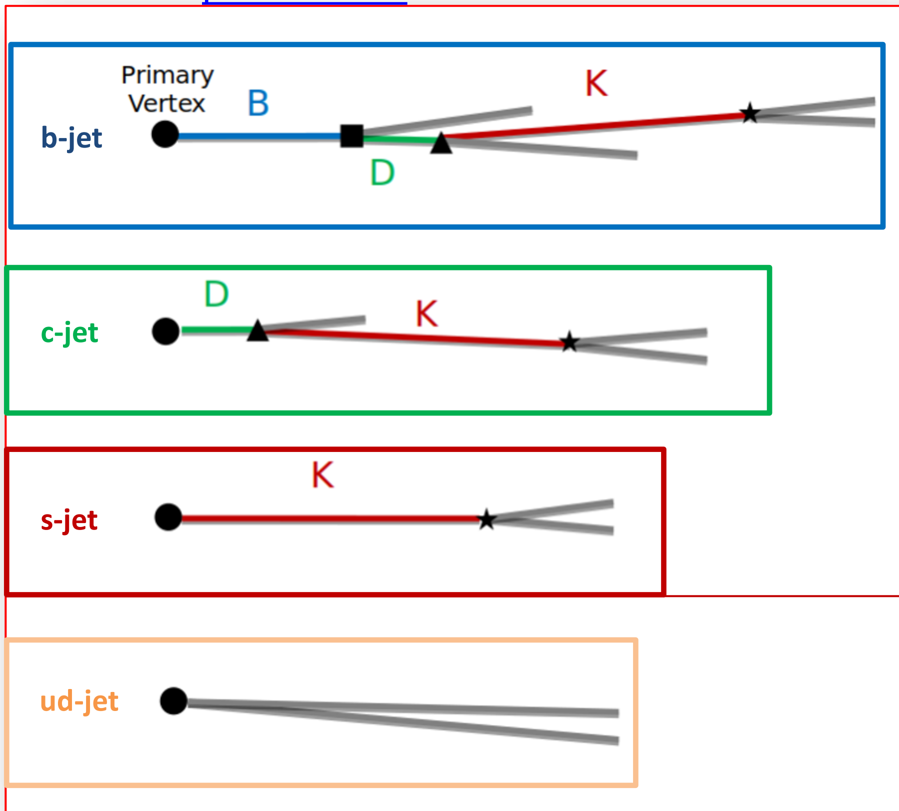

	# of secondary vertices (excluding V^0)	# of strange hadrons ($K^{\pm}$, K_L^0, K_S^0, Λ^0)
b	2	≥1
c	1	≥1
s	0	≥1
ud	0	0

Strange Hadron reconstruction

- $K^{\pm}$ [PID]
- $K_S^0 \rightarrow \pi^+\pi^-$ [Vertex] (BF ~69.2%)
- $\Lambda^0 \rightarrow p\pi^-$ [Vertex] (BF ~64%)
- K_L^0 [Particle Flow]

…and SLD actually measured strange hadrons from $Z \rightarrow s\bar{s}$!

See SLD A_s PRL 85 (2000), 5059

Detector Requirements

Key ingredients for b/c-tagging:

- Track Impact Parameters
- Secondary Vertices
- Multi-Vertex Decay chain

Need tracking & vertexing detectors with:

- excellent spatial resolution
- layers close to IP
- light weight

How about strange-tagging then?

The *strange* features

2203.07535

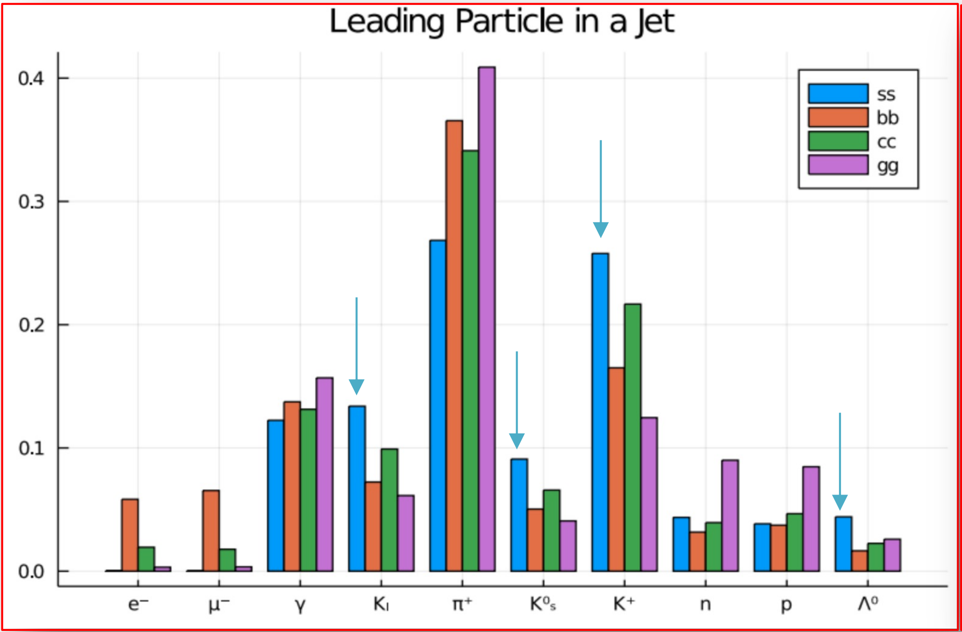

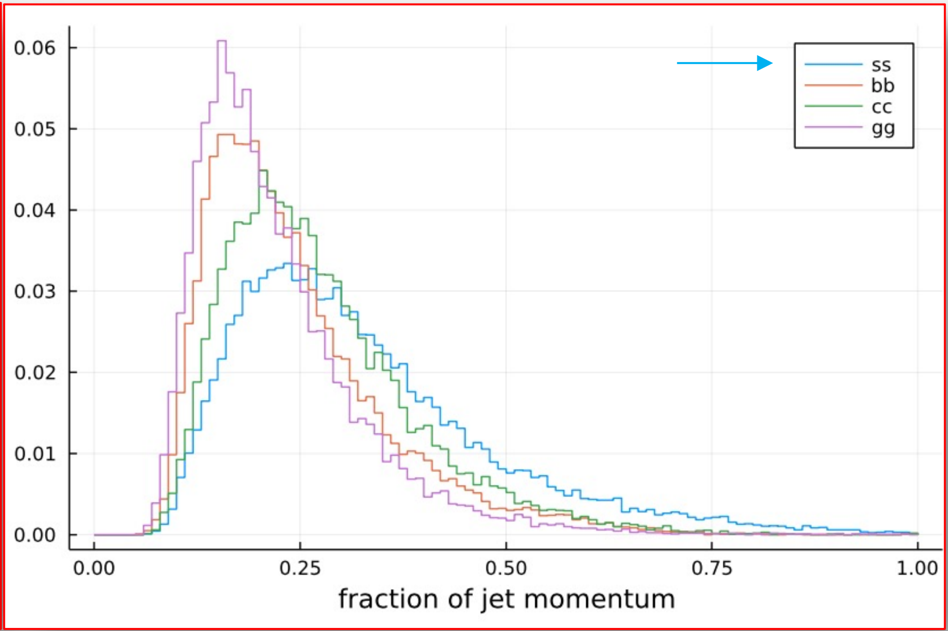

Particle Identification is crucial!

Need **π/K discrimination** over a momentum range of approximately (0.2-0.7) x 0.5 x 125 ≅ **12 to 50 GeV**

[2203.07535](2203.07535)

Impact of PID on Strange Tagging

- Use a Recurrent Neural Net tagger for classifying jet-flavour, train on **full ILD(*) simulation** $(Z \to inv)(H \to qq/gg)$ samples and include **per-jet level inputs** & **variables** on the **10 leading particles** in each jet, **including PDG-based PID** → general validity!

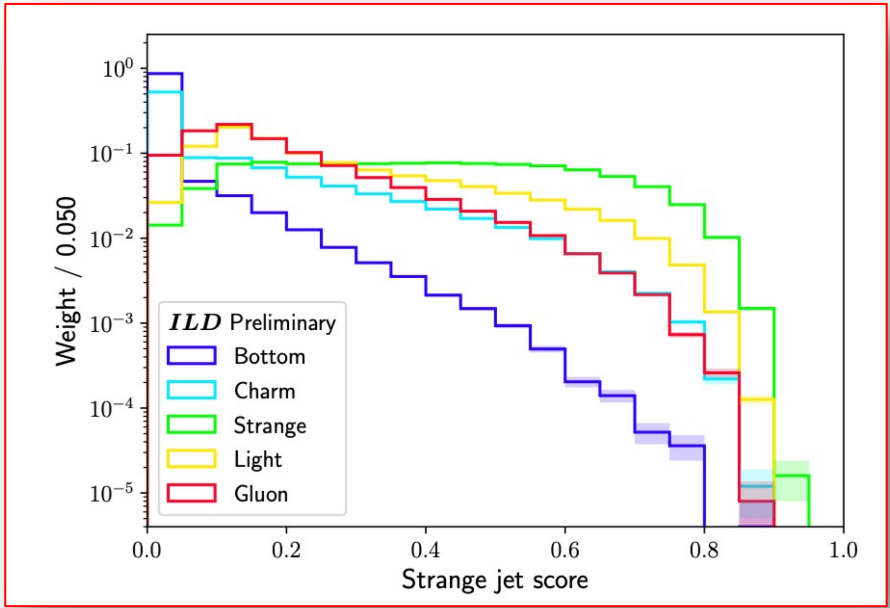

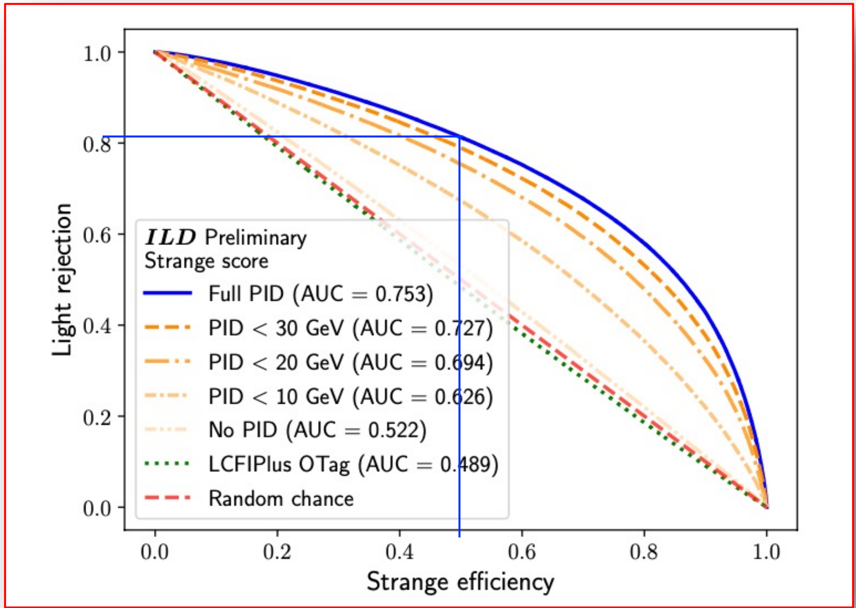

Good discrimination of *s*-jets from u/d- and *g*-jets

@50% s-jet tagging efficiency, >80% u/d-jet rejection with Full PID

(*) **ILD** = multi-purpose **International Large Detector** concept @ the International Linear Collider

Impact of PID on Strange Tagging

2203.07535

- Use a Recurrent Neural Net tagger for classifying jet-flavour, train on **full ILD simulation** $(Z \rightarrow inv)(H \rightarrow qq/gg)$ samples and include **per-jet level inputs** & **variables** on the **10 leading particles** in each jet, **including PDG-based PID** → general validity!

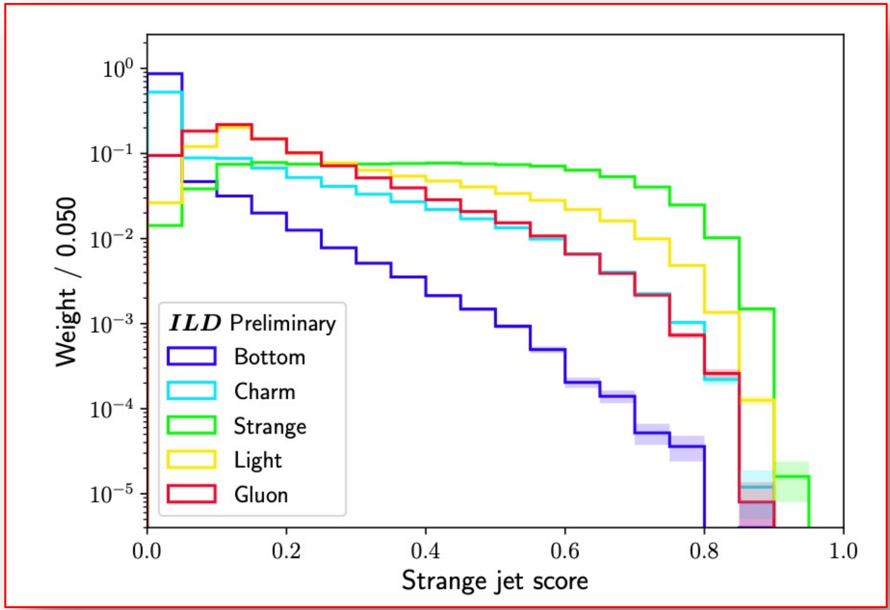

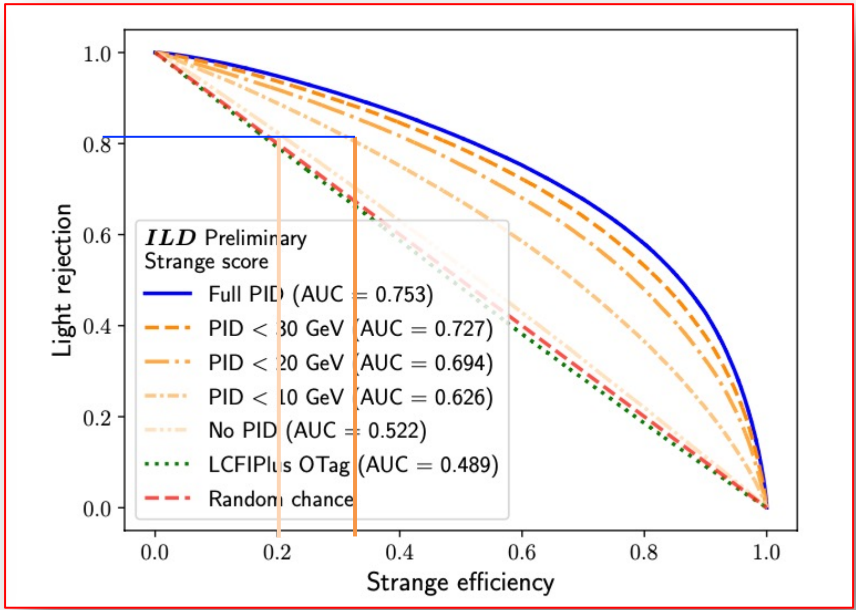

Good discrimination of *s*-jets from u/d- and *g*-jets

At fixed light rejection:
No PID to PID < 10 GeV: ~1.5x efficiency

Impact of PID on Strange Tagging

2203.07535

- Use a Recurrent Neural Net tagger for classifying jet-flavour, train on **full ILD simulation** $(Z \to inv)(H \to qq/gg)$ samples and include **per-jet level inputs** & **variables** on the **10 leading particles** in each jet, **including PDG-based PID** → general validity!

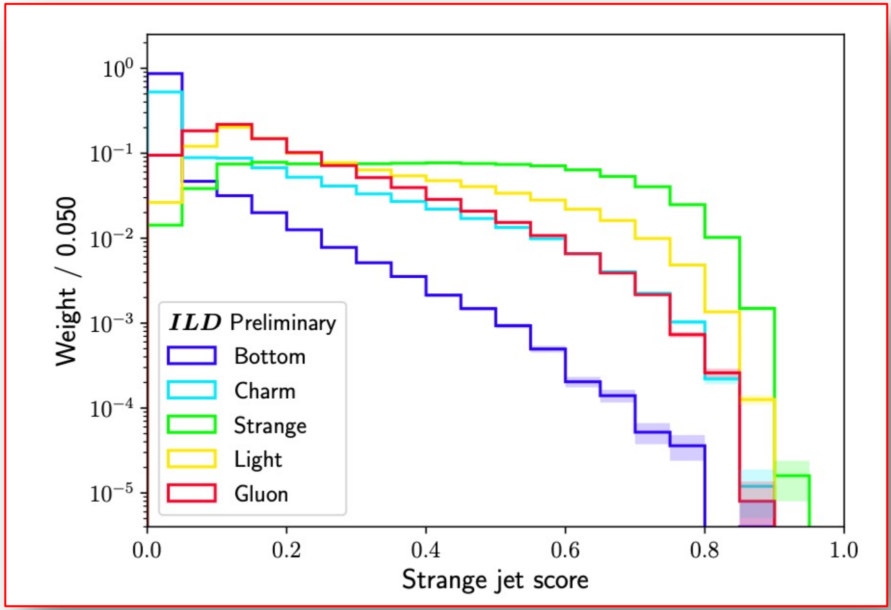

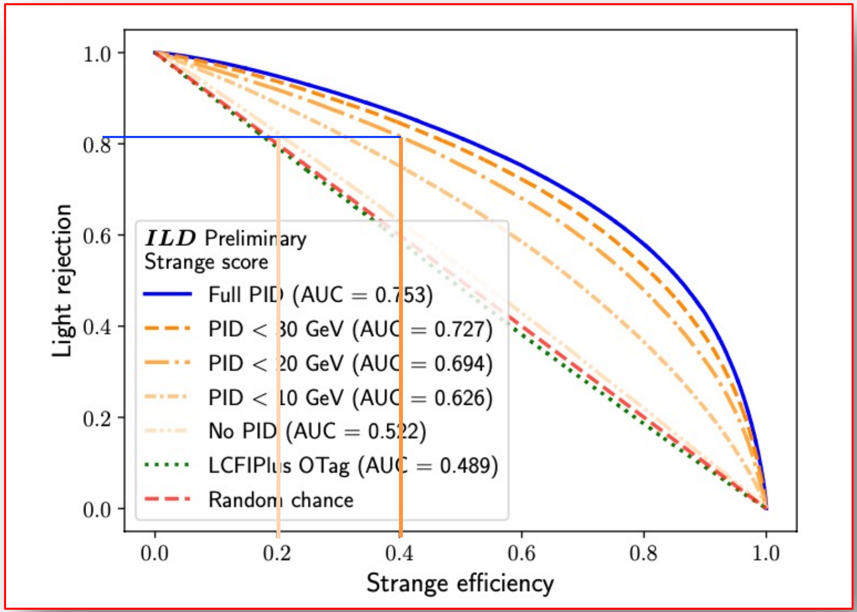

Good discrimination of *s*-jets from u/d- and *g*-jets

At fixed light rejection:
No PID to PID < 10 GeV: ~1.5x efficiency
No PID to PID < 20 GeV: ~2.0x efficiency

Impact of PID on Strange Tagging

2203.07535

- Use a Recurrent Neural Net tagger for classifying jet-flavour, train on **full ILD simulation** $(Z \to inv)(H \to qq/gg)$ samples and include **per-jet level inputs** & **variables** on the **10 leading particles** in each jet, **including PDG-based PID** → general validity!

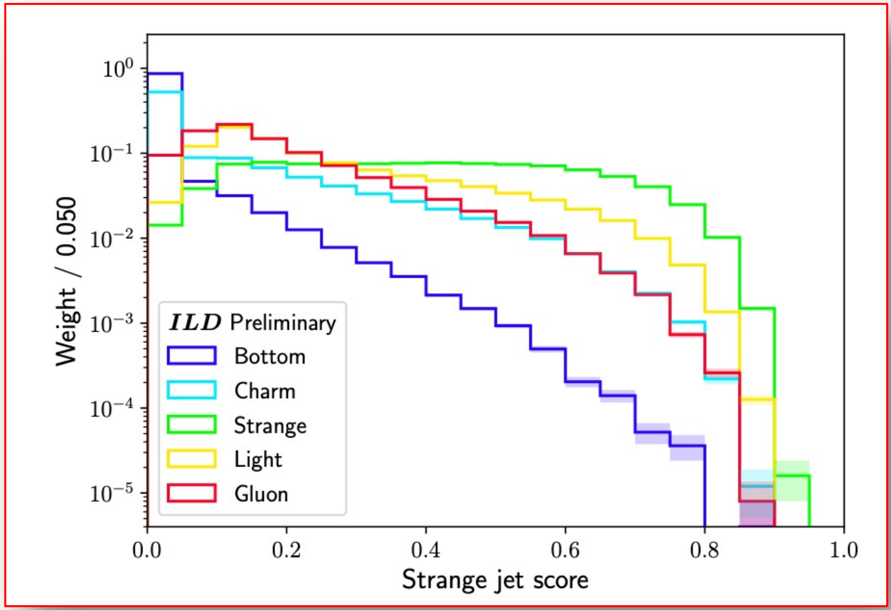

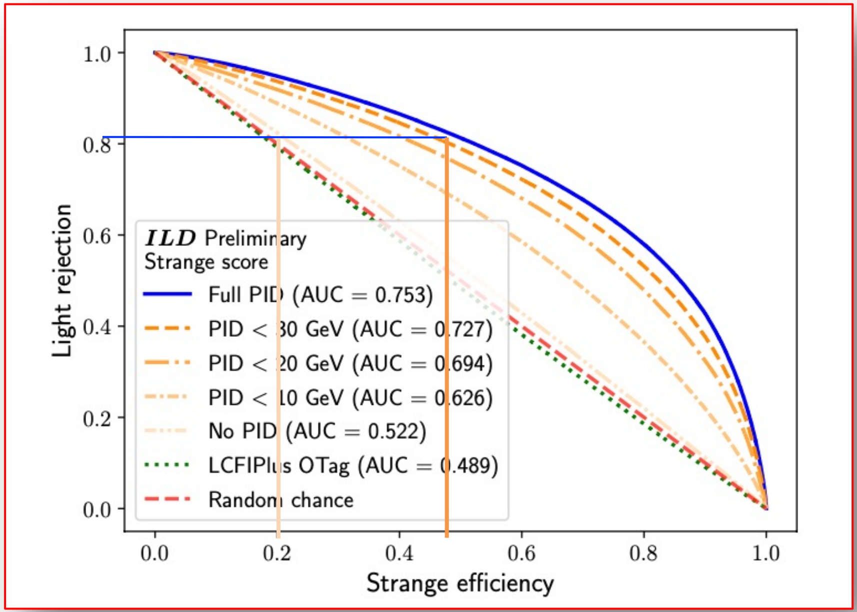

Good discrimination of *s*-jets from u/d- and *g*-jets

At fixed light rejection:
No PID to PID < 10 GeV: ~1.5x efficiency
No PID to PID < 20 GeV: ~2.0x efficiency
No PID to PID < 30 GeV: ~2.5x efficiency

Impact of PID on Strange Tagging

2203.07535

- Use a Recurrent Neural Net tagger for classifying jet-flavour, train on **full ILD simulation** $(Z \to inv)(H \to qq/gg)$ samples and include **per-jet level inputs** & **variables** on the **10 leading particles** in each jet, **including PDG-based PID** → general validity!

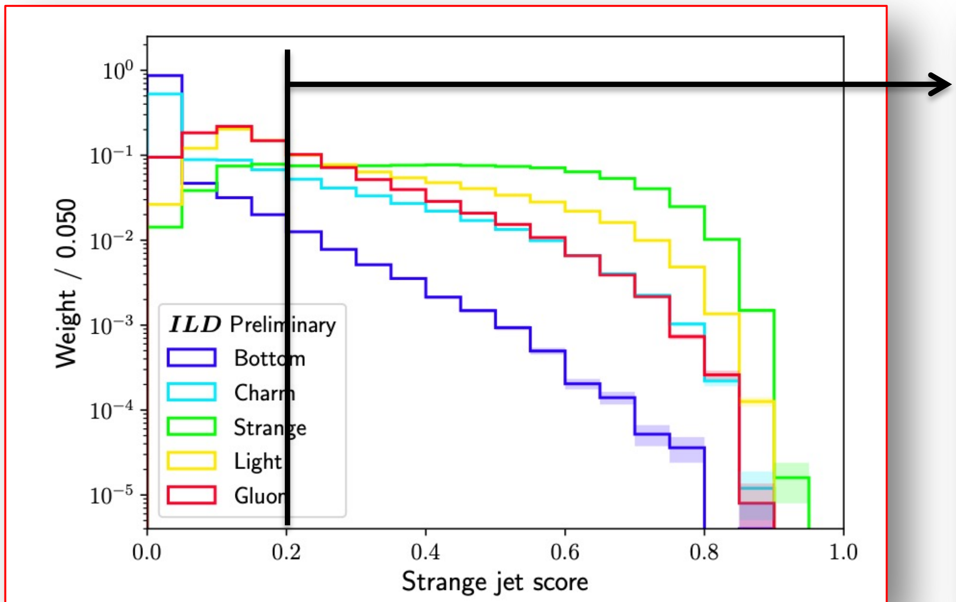

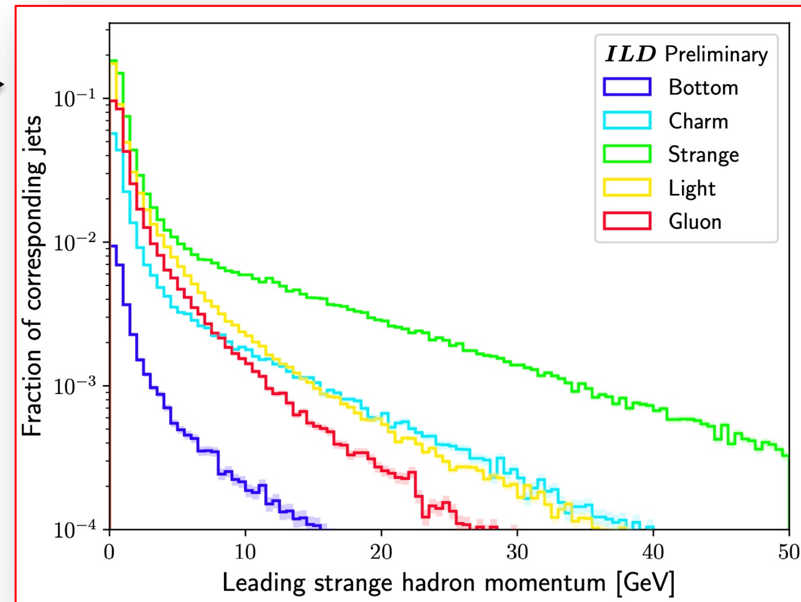

The tighter the cut on the s-tag score,
the more energetic the leading strange hadron!

A physics benchmark: $h \to s\bar{s}$ analysis @ the International Linear Collider

Foreseen to run at several $\sqrt{s}$, dedicated 250 GeV run for Higgs couplings studies

σ_H @ $\sqrt{s} = 250\ \mathrm{GeV} \sim 200\ \mathrm{fb}$ (dominated by ZH production)

2000 fb^{-1} collected in 10y by ILC

→ $\sim$ 400k Higgs → $\sim$ 80 $h \to ss$

But of course, new physics boosts these numbers!

$e^+e^- \rightarrow Zh \rightarrow \mu^+\mu^-h$

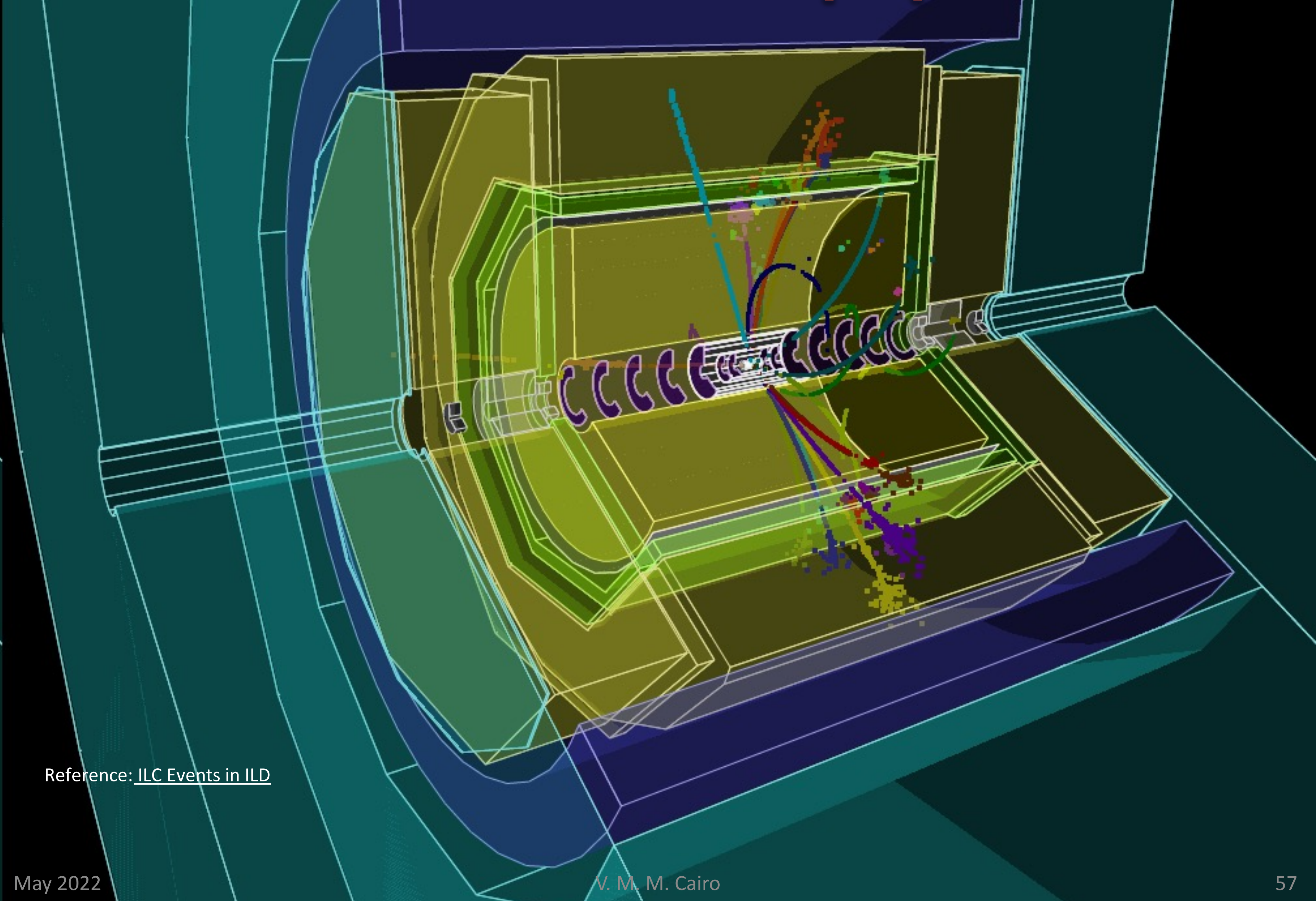

Reference: ILC Events in ILD

2203.07535

$h \to s\bar{s}$ analysis in a nutshell

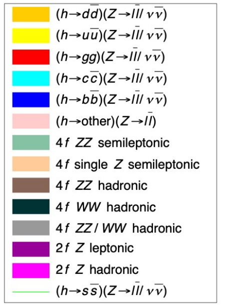

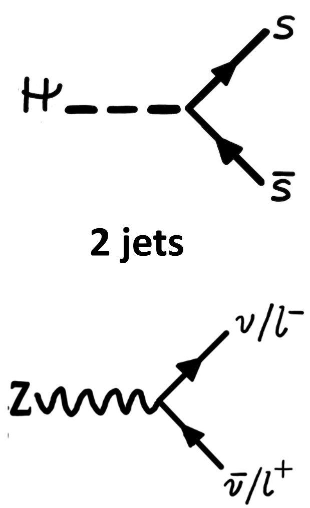

2 jets

0 or 2 SFOS leptons

Object definition

Event selection

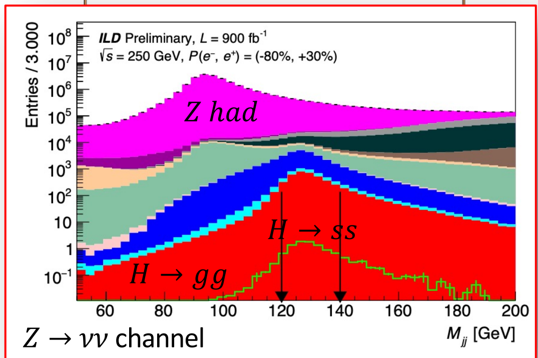

Cut-based approach, reject

$ZH(!\,ss), V, VV$

Sum of

$jet_0 + jet_1$

strange tagging scores

Signal discriminant

s-Yukawa constraints

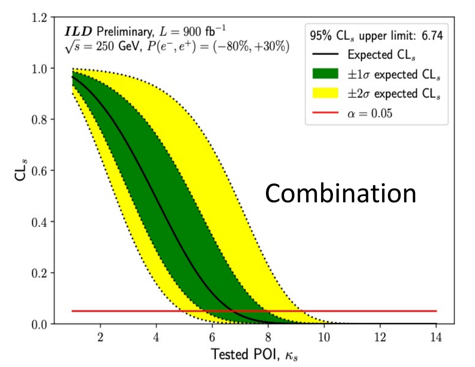

k_s **< 6.74 x SM**

- If we can tag strange jets, we can probe the **Higgs strange Yukawa** coupling…

But **we need π/K discrimination at high momenta**!

- This triggered recent studies of what may be possible with a system that pioneered particle ID: the **RICH**

Particle Identification techniques

- Hadrons are identified by their **mass**, in turn determined by combining **momentum** and **velocity**
- Assuming that momentum is inferred from radius of curvature in magnetic field, the remaining issue is to measure the velocity

  - Can be determined via:
    - **Time-of-flight** (TOF)
    - **Ionization losses** (dE/dx or dN/dx)
    - **Transition radiation**
    - **Cherenkov radiation**

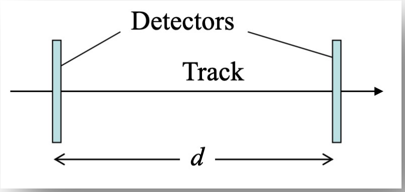

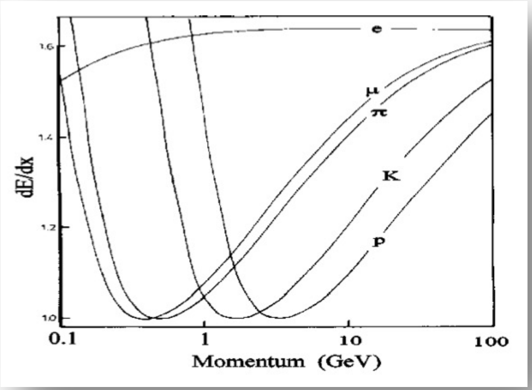

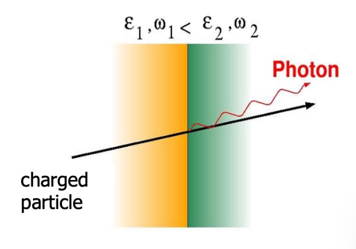

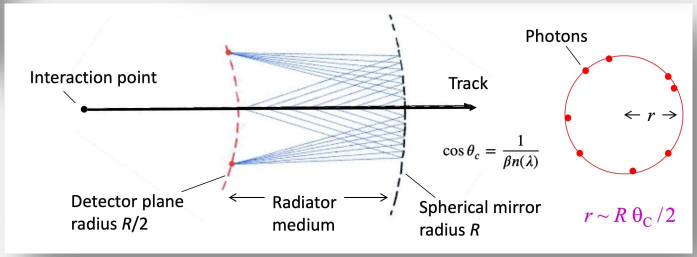

N.B. Detection of photons is needed by many of the detectors performing particle ID.
Requirements: single photon sensitivity, high efficiency, good spatial granularity

The International Large Detector @ the International Linear Collider

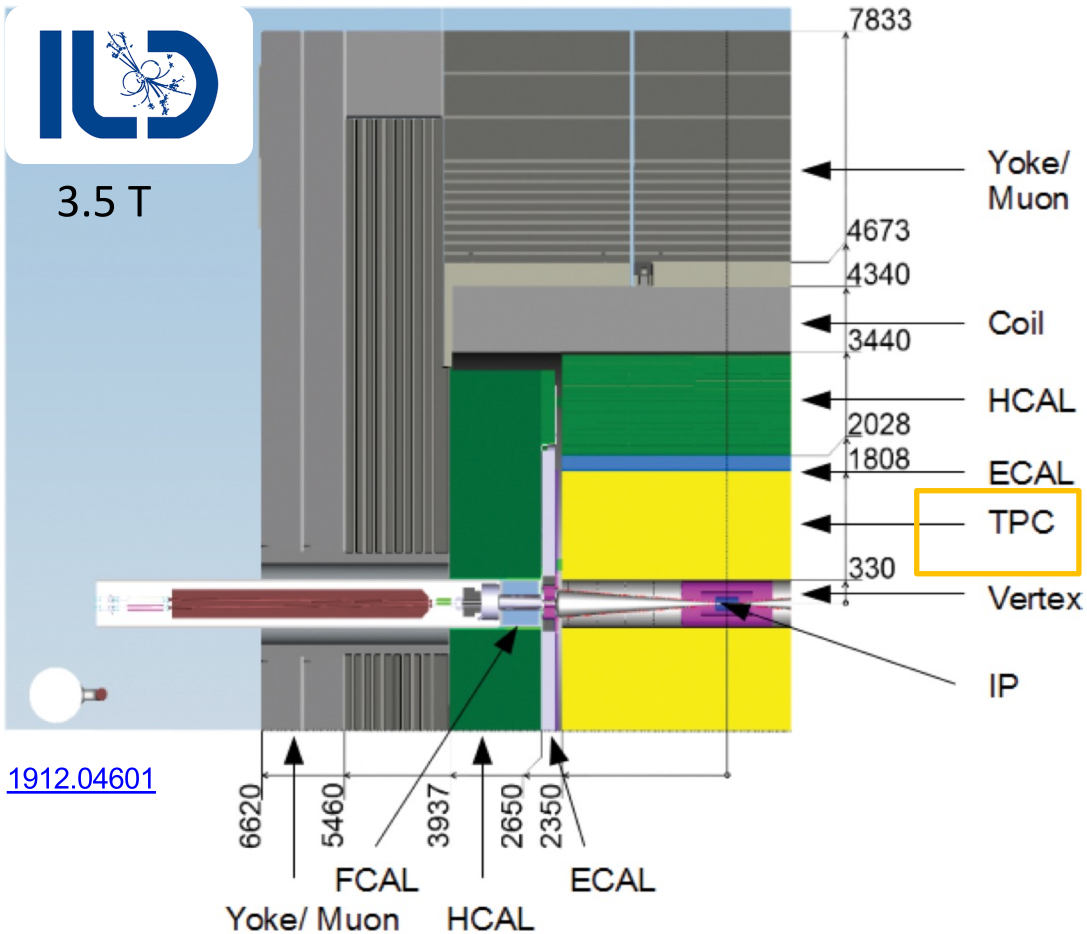

1912.04601

Intrinsic PID capabilities through dE/dx + TOF from silicon wrappers

Extending PID capabilities

TOF or dE/dX have great PID capabilities, but cover only the low momentum regime (unless very large tracker volumes are used)

TOF, dE/dX

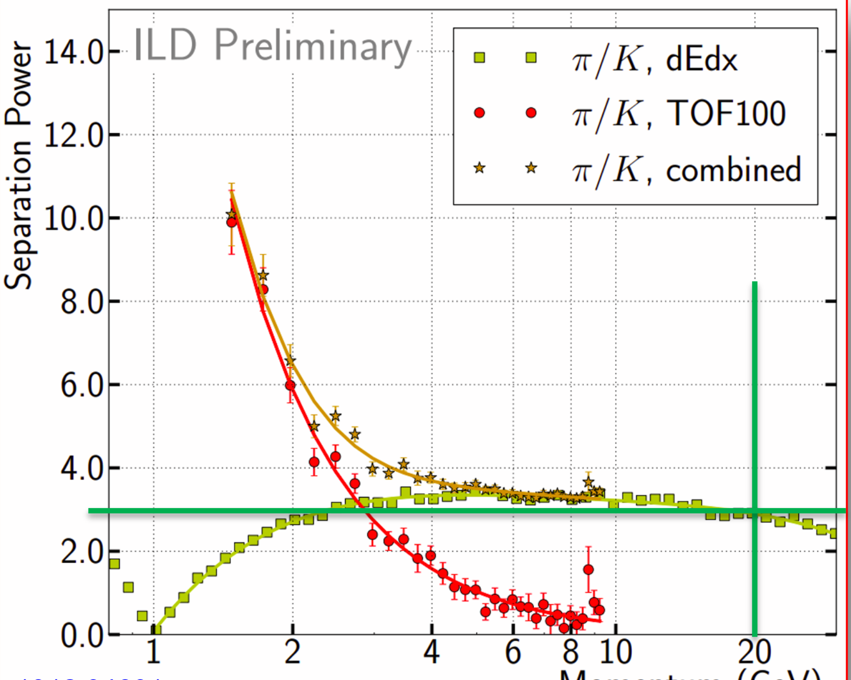

1912.04601

RICH

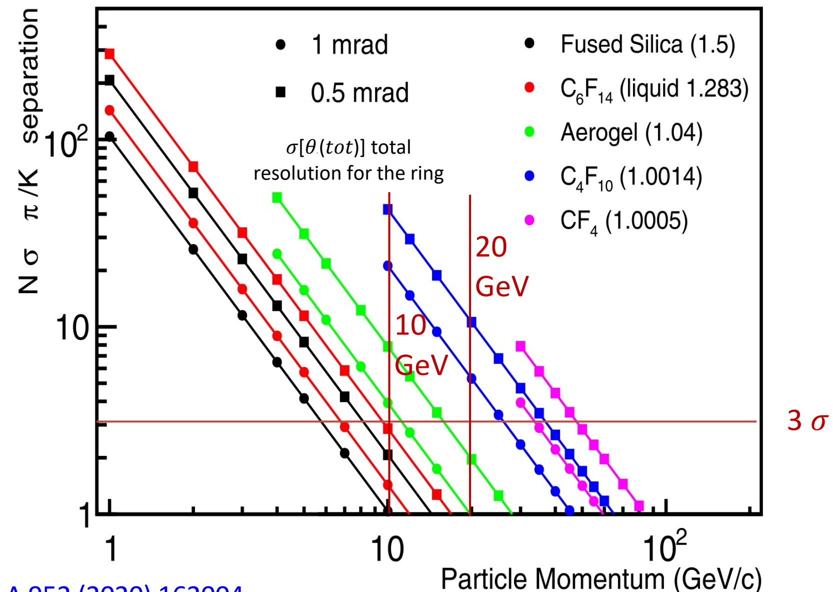

NIM,A 952 (2020) 162004

Fig. 2. The number standard deviations in $\pi - K$ separation versus momentum for different radiators and two different Cherenkov angle resolutions.

Ring Imaging Cherenkov Detectors (RICH) is a favourable approach at high momentum

PID Technology comparison

3σ *separation for* π/K				
dE/dx in silicon	TOF via Fast Timing in silicon envelopes or calorimetry	dE/dx in Time Projection or Drift Chambers	dN/dx	RICH
$\lesssim$ 5 GeV	$\lesssim$ 5 GeV	$\lesssim$ 30 GeV (scales with volume)	O(tens of GeV)	O(tens of GeV)

Momentum →

PID Technology comparison

3σ *separation for* π/K				
dE/dx in silicon	TOF via Fast Timing in silicon envelopes or calorimetry	dE/dx in Time Projection or Drift Chambers	dN/dx	RICH
$\lesssim$ 5 GeV	$\lesssim$ 5 GeV	$\lesssim$ 30 GeV (scales with volume)	O(tens of GeV)	O(tens of GeV)

Momentum →

Will it be possible to accommodate a compact RICH system while preserving performance in tracking and calorimetry?

The past and the future RICH

[2203.07535](https://arxiv.org/abs/2203.07535)

- **Can a RICH work in limited (how limited?) radial space?**
  - Needs to be large enough to detect photons

Past

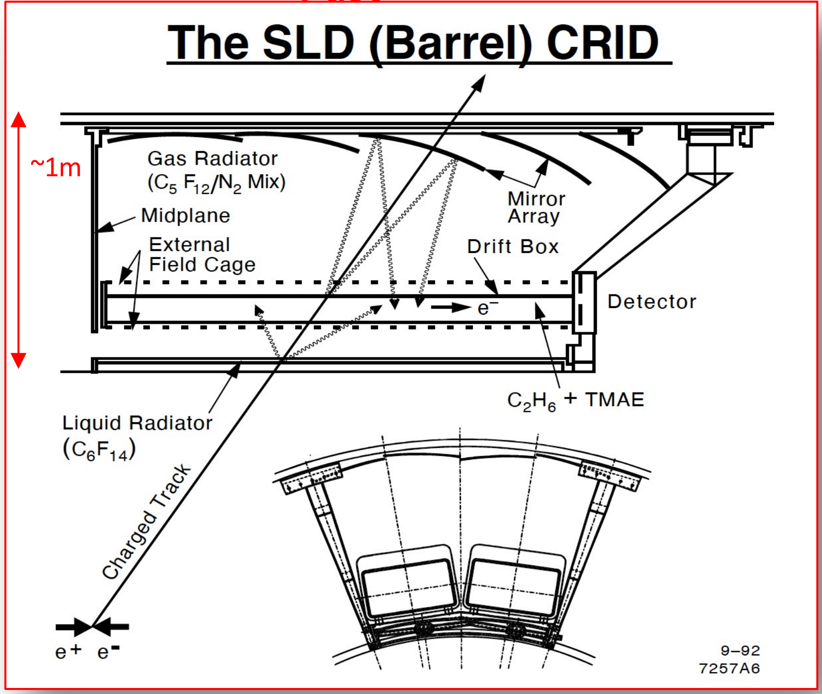

Future

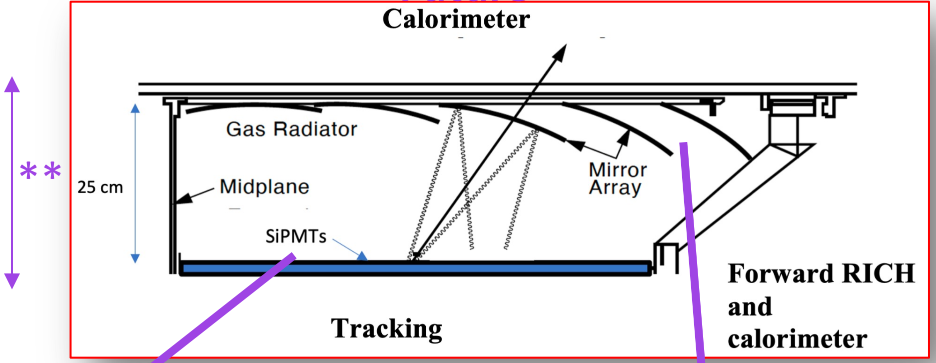

SiPMTs or new detector ideas!
See C. Damerell's article

Extremely thin but excellent optical quality mirrors

** Needed radiator thickness will evolve downwards, as Quantum Efficiency of photodetectors advances

- **Past** → **Future**: Much **smaller** radial length, **SiPMTs** rather than TPCs with TMAE for photon detection improve PID by a factor of 2
- **Many parameters to investigate!**

2203.07535

Compact Gaseous RICH with SiPMTs

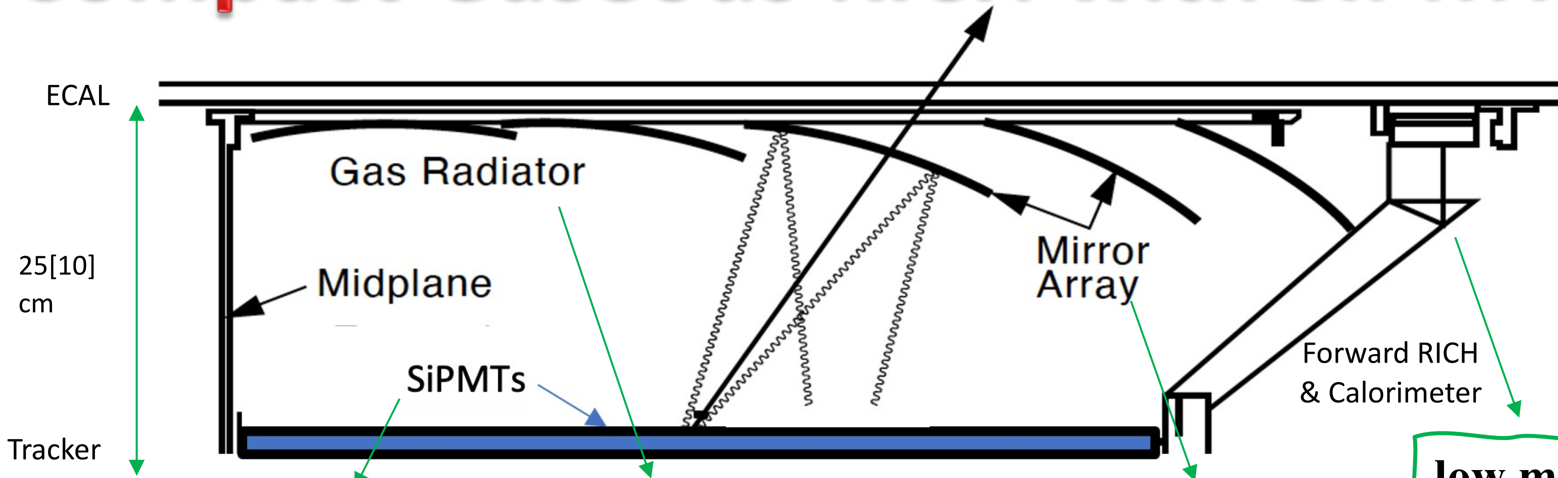

Fast timing device (<100 ps) to provide ToF covering the lower p range and complementing the RICH

Pure **C_4F_{10}** at 1 bar (boiling point -1.9 C at 1 bar, good refraction index)

Beryllium with reflective coating

low mass carbon-composite material for the structure

# of sigmas = $\dfrac{\theta_\pi - \theta_K}{\sigma_\theta/\sqrt{N}}$

σ_θ is total Cherenkov angle resolution

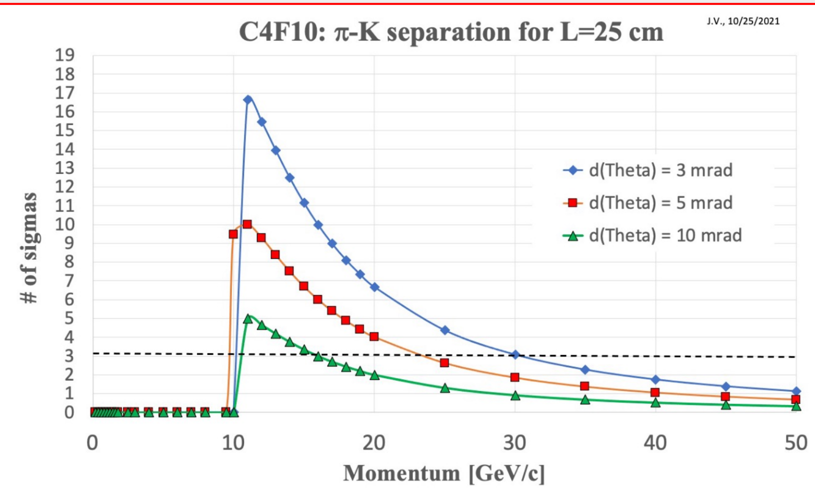

Can reach $3\sigma\ \pi/K$ separation up to 30 GeV with state-of-the-art technology!

A more *optimistic* RICH layout

R. Forty's slides

ARC:
an Aerogel RICH Cellular detector

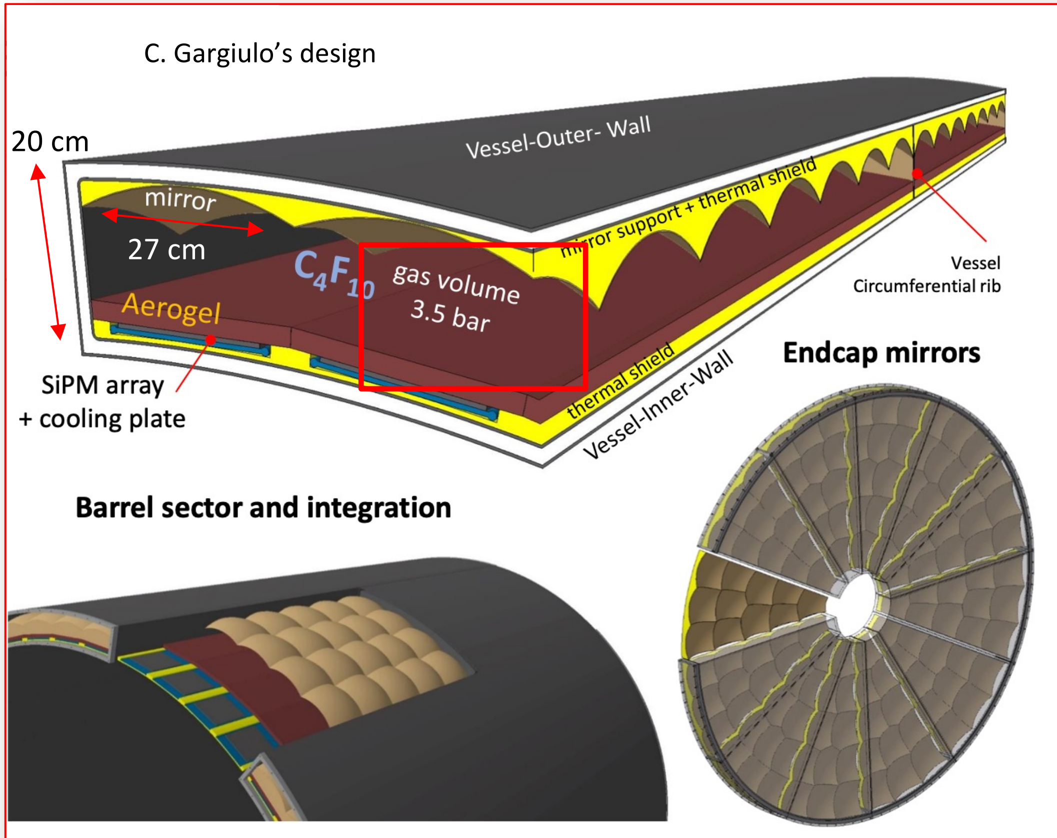

Material budget estimate

Detector component	X/X_0
2 x vessel wall	5 %
Photosensor array/electronics	1 %
Cooling plate (3 mm CF)	1 %
Aerogel (2 cm, *n* = 1.03)	1 %
C_4F_{10} gas (13 cm @ 3.5 bar)	1 %
Focusing mirror	1 %
Total	10 %

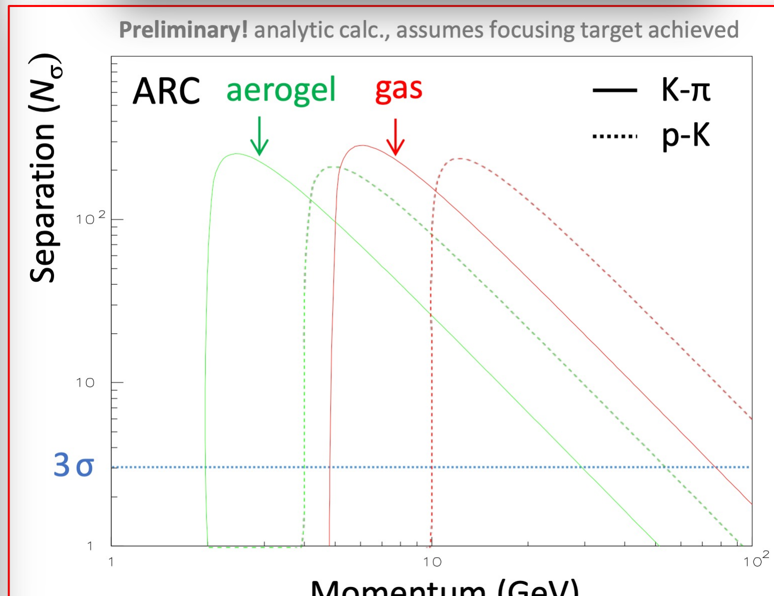

Can reach $3\sigma\ \pi/K$ separation up to tens of GeV!

The importance of *strange* science

- Many unexplored physics benchmarks rely on **strange tagging**, in turn enabled by $\boldsymbol{\pi/K}$ **PID at high momenta**
  - Higgs *& friends* Factories: **Z, W, top, flavor physics in general…**
- The ordinary matter is composed by electron and light quarks – **none of the Higgs boson couplings to such particles has been verified yet!**
- Testing Yukawa universality is a **key benchmark** for future Higgs factories
- The most stringent constraints on the **strange Yukawa** have been derived via a direct SM $\boldsymbol{h \to ss}$ search: phase space for new physics reduced to $\boldsymbol{k_s \sim 6x\ SM}$

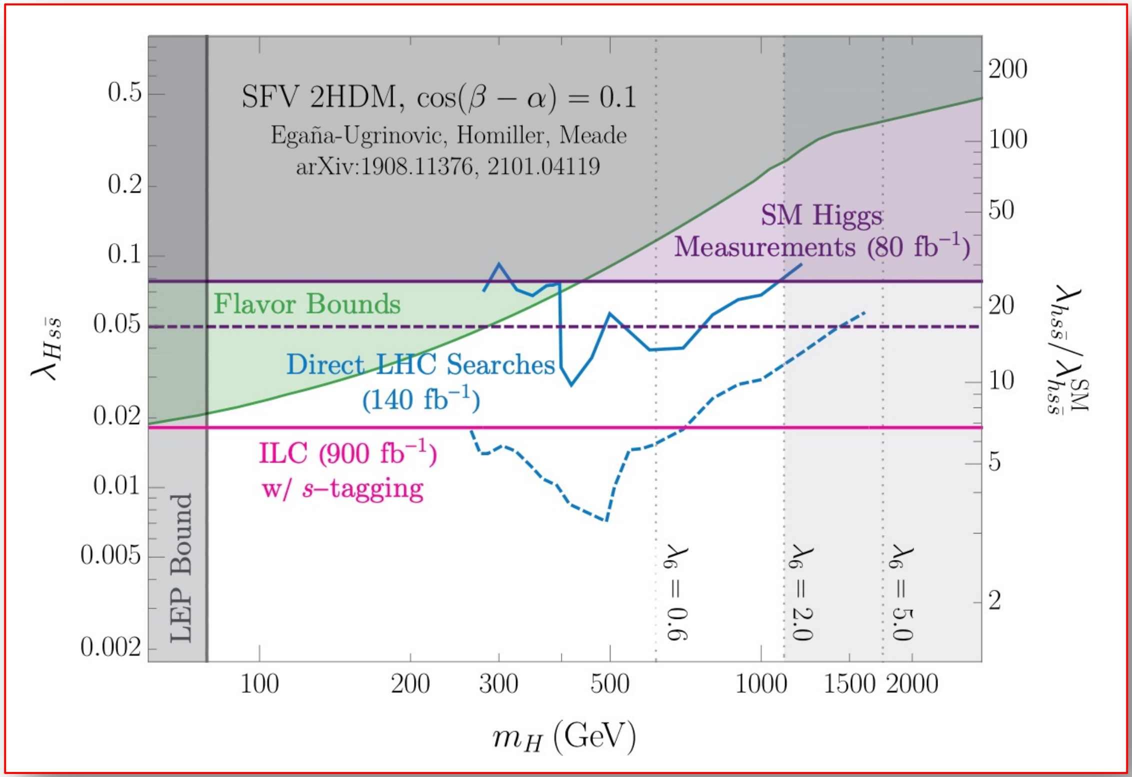

Wrap-up

- Higgs self-coupling: key HL-LHC goal
  - Need to tag b-jets effectively
    - New full-silicon Inner Tracker for ATLAS in HL-LHC

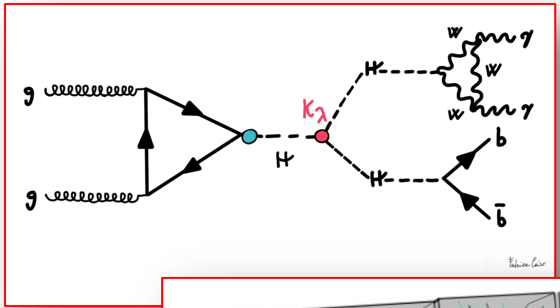

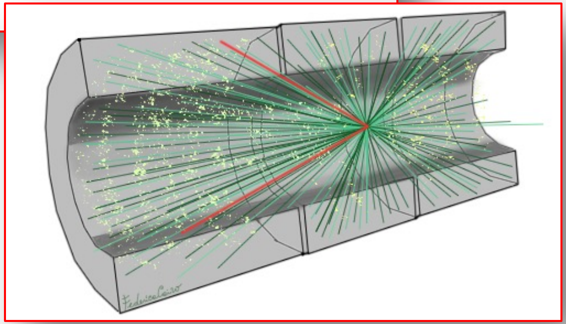

- Strange Yukawa coupling: a challenge for Future Colliders
  - Need to tag s-jets effectively
  - Relies on Particle ID at high momentum
    - Compact RICH Detectors?

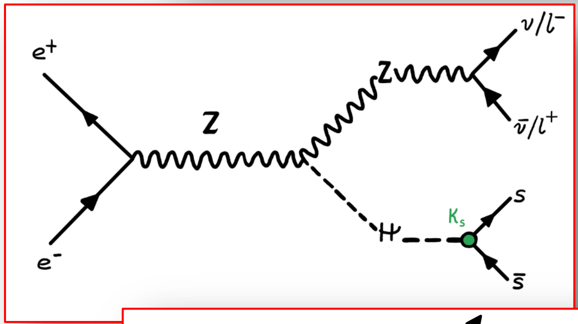

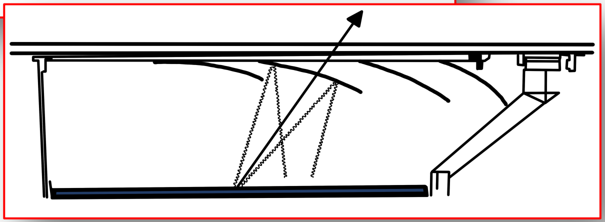

Illustrations by F. Cairo

Conclusions

- Exciting science ahead to solve some of the yet-to-be answered questions in Particle Physics

- Interplay between detector design, performance & analysis techniques is of paramount importance!

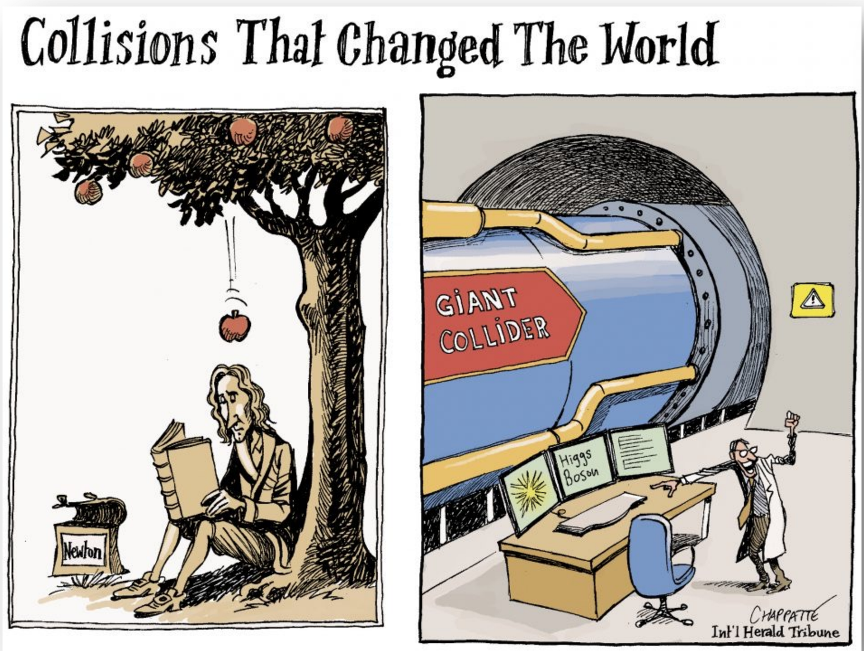

Thanks for your attention!

Valentina Maria Martina Cairo

CERN

Extra Slides

Strange Yukawa

The International Linear Detector @ the International Linear Collider

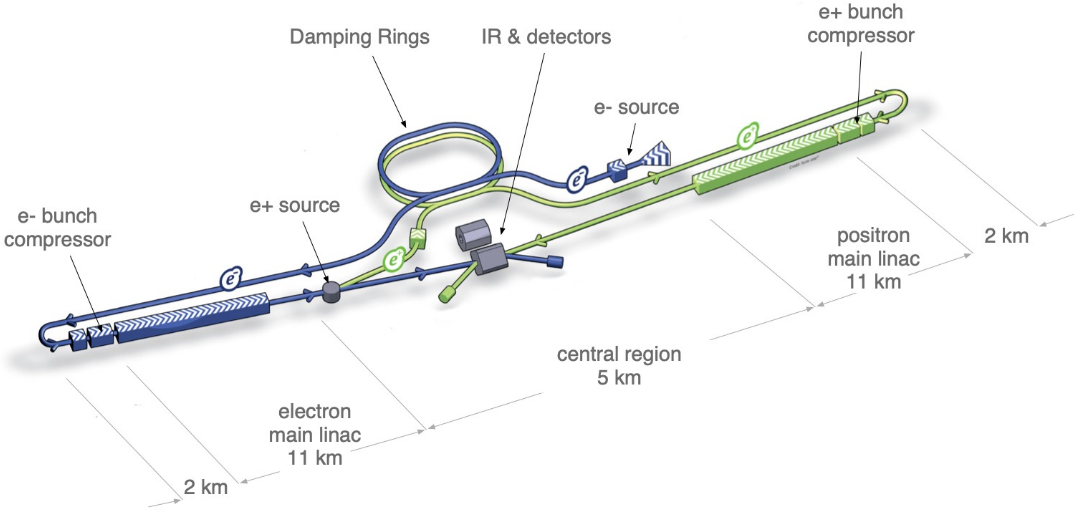

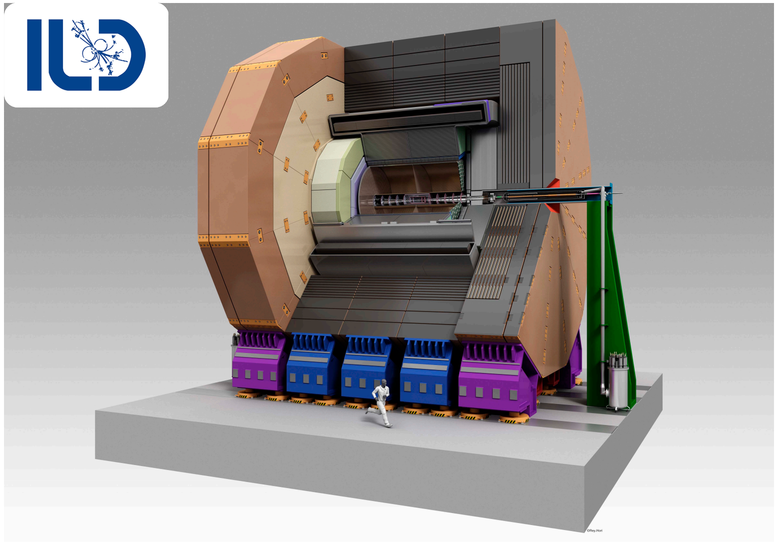

- Foreseen to run at several $\sqrt{s}$
- Dedicated 250 GeV run for Higgs couplings studies

ILD

International Large Detector

- 3 double-layer pixel detectors for vertexing
- Time projection chamber (TPC) for tracking with inner/outer Si layers
  - Low material assists in low-p tracking
- High granularity sampling calorimeters for particle flow reconstruction
  - Challenge is reconstructing neutral hadrons
  - Precise EM/hadronic design still under study
- Tracking/calorimetry contained in 3.5 T field

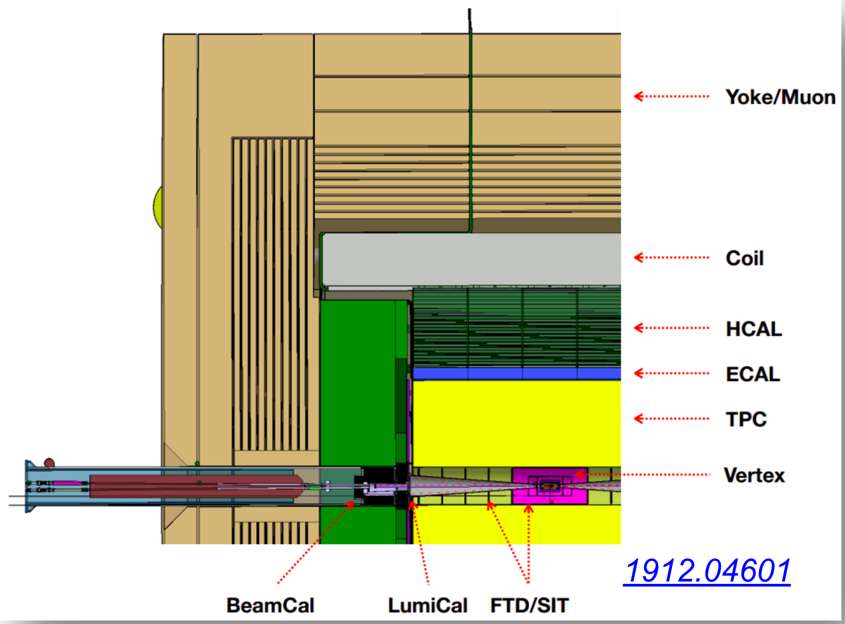

1912.04601

Cross-sections

https://arxiv.org/pdf/1310.0763.pdf

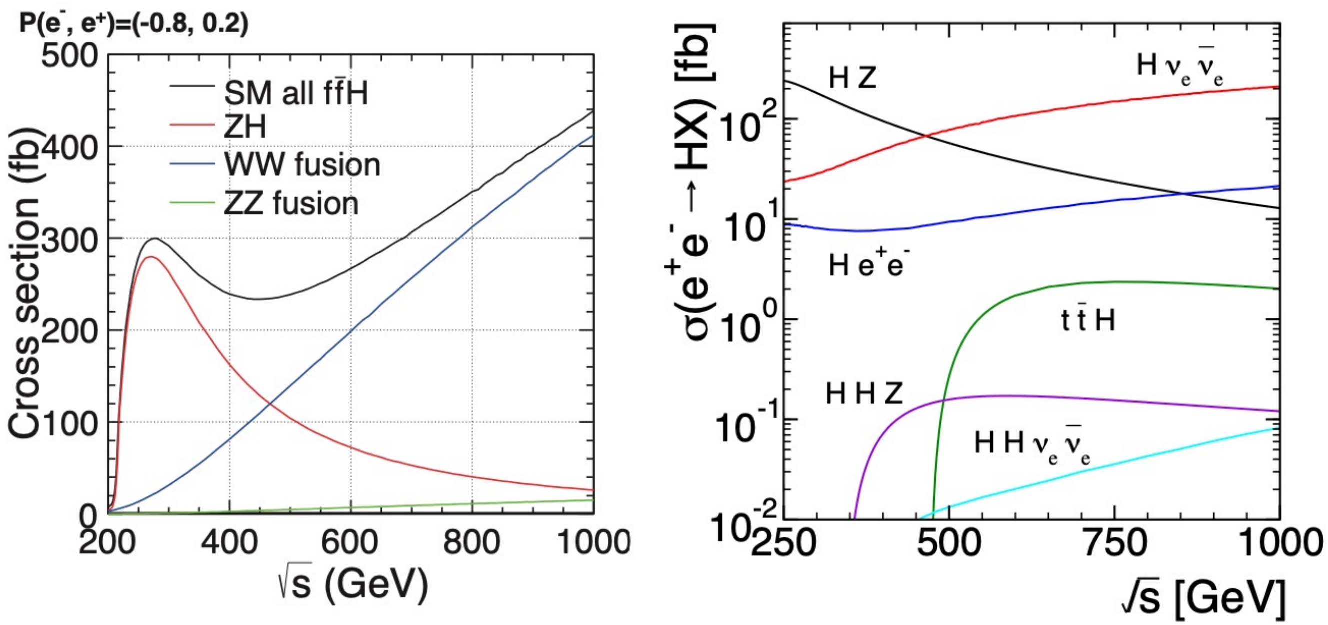

~200fb

If we consider 2000 fb-1 data after 10 years, we have 400k Higgs out of which only 40 will decay to ssbar

Figure 1.4. (Left)The production cross sections of the Higgs boson with the mass of 125 GeV at the ILC as a function of the collision energy $\sqrt{s}$. Polarization of the electron beam (80%) and the positron beam (20%) is assumed. (Right) The cross sections of the production processes $e^+e^- \to hZ$, $e^+e^- \to H\nu_e\bar{\nu}_e$, $e^+e^- \to He^+e^-$, $e^+e^- \to t\bar{t}H$, $e^+e^- \to HHZ$ and $e^+e^- \to HH\nu_e\bar{\nu}_e$ as a function of the collision energy for the mass of 125 GeV. No polarization is assumed for the initial electron and positron beams.

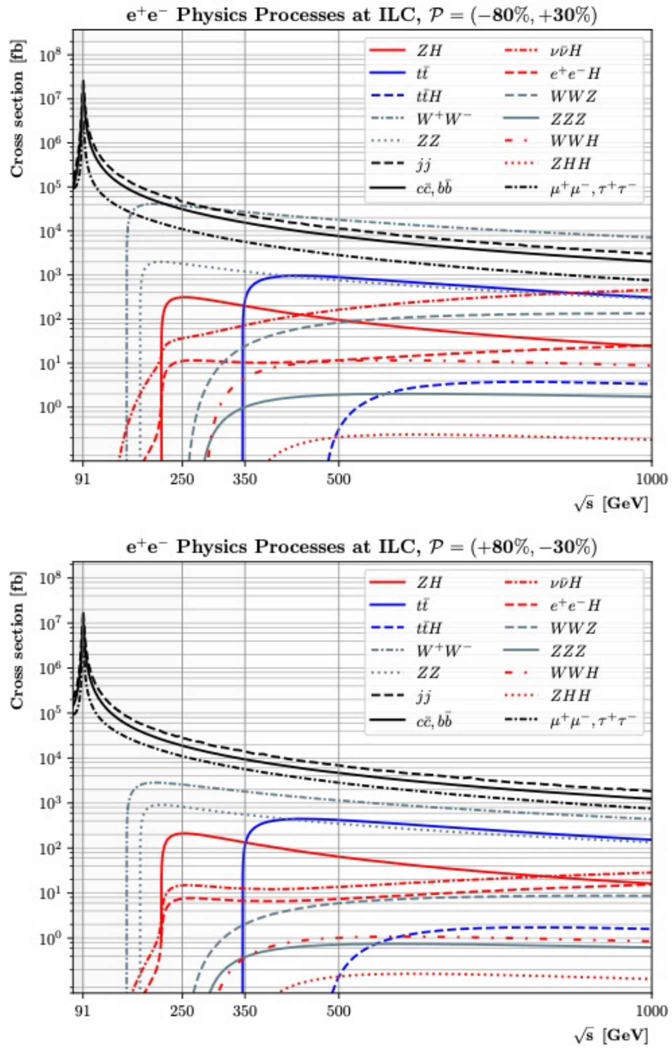

Figure 5.1: Cross sections of the most important Standard Model processes in e^+e^- annihilation in the energy range of the ILC. Initial state radiation is included, and cross section are plotted for reactions in which the annihilation retains > 90% of the nominal CM energy. The cross sections are shown for predominantly left-handed beam polarization (−80%/ + 30% for e^-/e^+) (top) and for predominantly right-handed beam polarization (+80%/ − 30%) (bottom). It is instructive to compare the two plots, which have subtle and not-so-subtle differences.

Luminosity

https://indico.cern.ch/event/838435/contributions/3635820/attachments/1971441/3279557/Complementarity.pdf

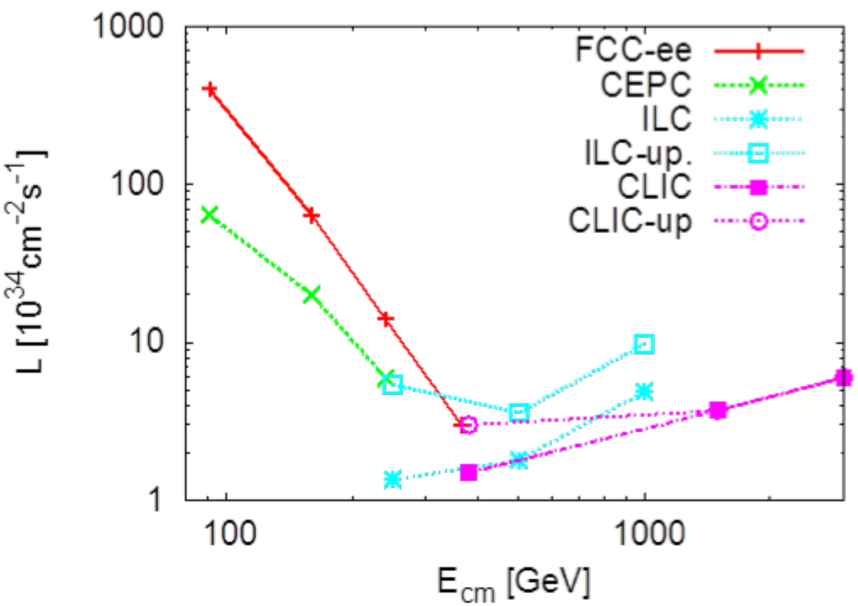

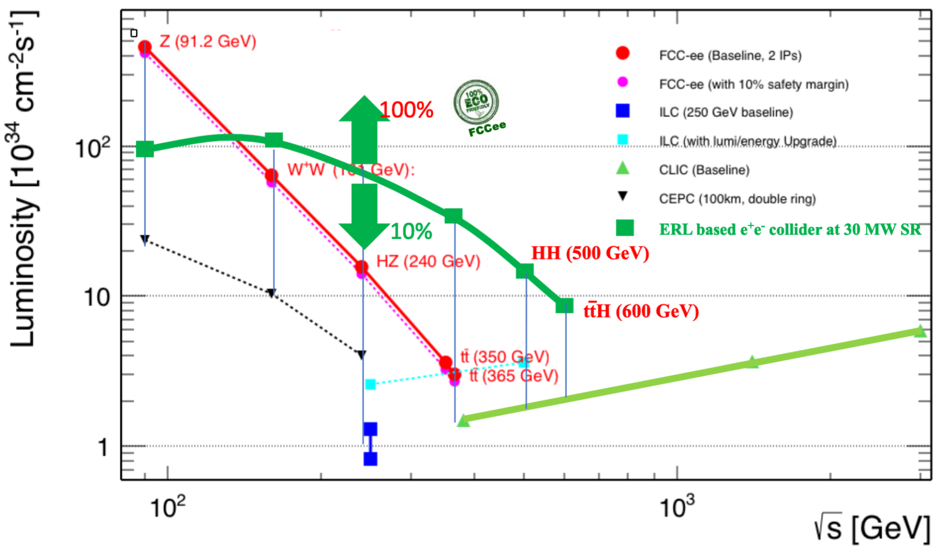

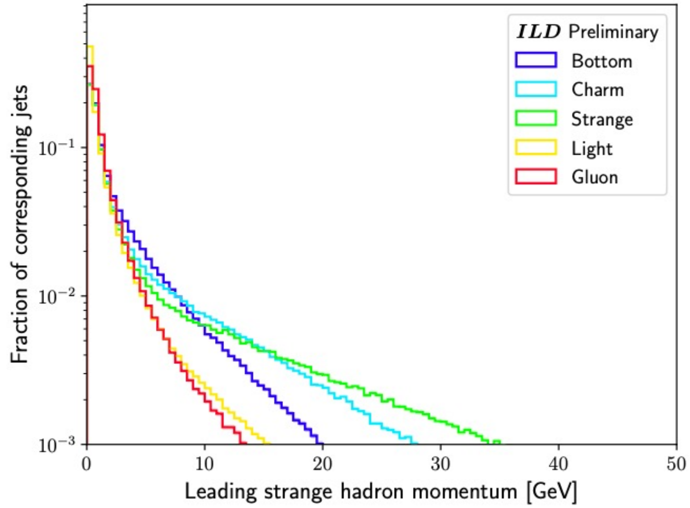

(a) Differential

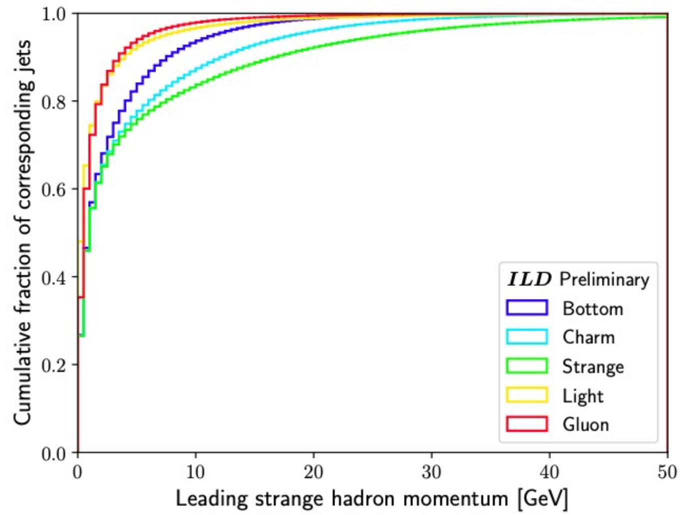

(b) Cumulative

Figure 2: Differential and cumulative distributions of the momentum of the leading strange particle in the leading or subleading momentum jet of the $h(\rightarrow q\bar{q}/gg)Z(\rightarrow \nu\bar{\nu})$ events described in Table 2. The choice of leading or subleading jet is random. The leading strange particle is identified by iterating over the momentum-ordered PFOs in the jet and selecting the first PFO which is truth-matched to a strange hadron. If no strange particle is found, a momentum of 0 GeV is assigned. The sum-of-weights for each class is normalised to 1.

NN Architecture

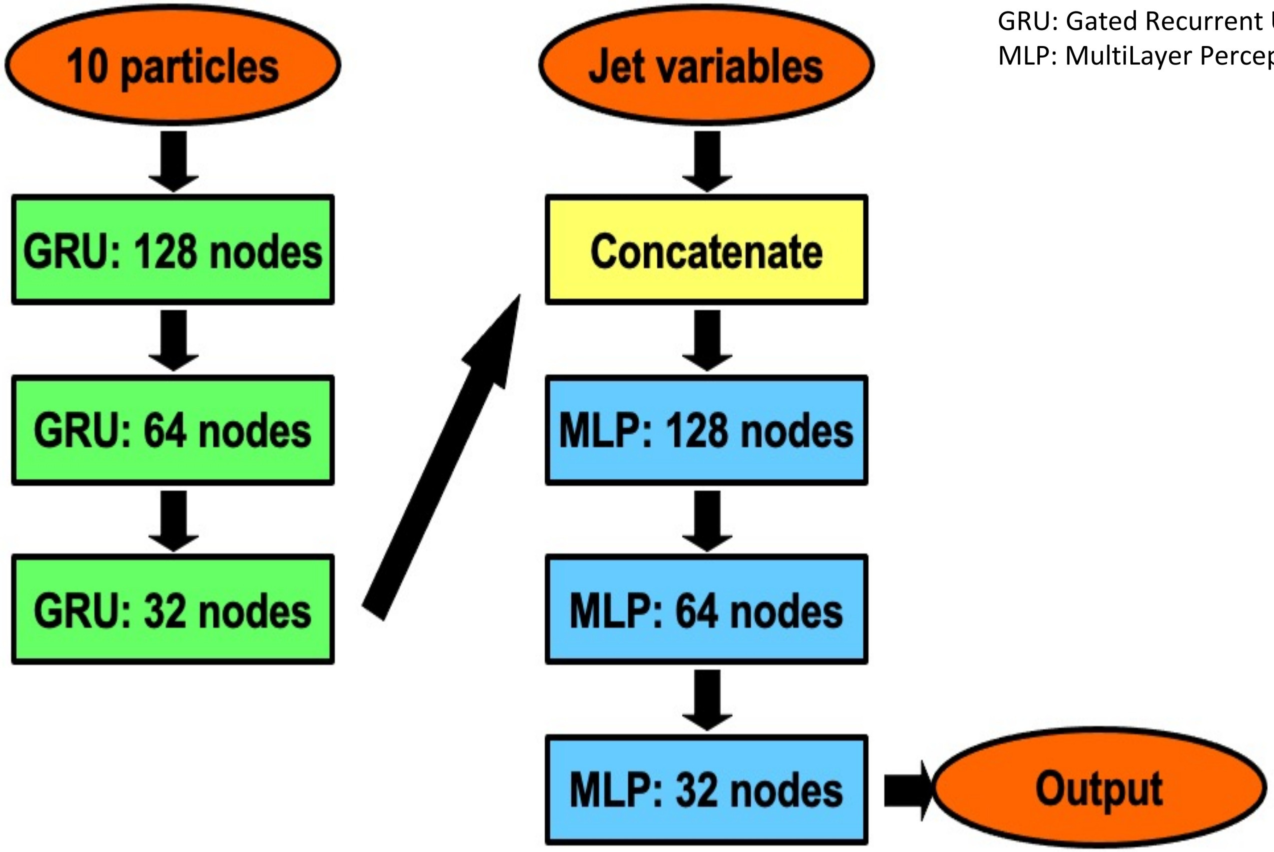

GRU: Gated Recurrent Units
MLP: MultiLayer Perceptron

NN Inputs in ILD

The training is performed on the $Z(\to \nu\bar{\nu})h(\to q\bar{q}/gg)$ samples from table 2. All events are required to have $N_{\text{jets}} \geq 2$ and $N_{\text{leptons}} = 0$. The training is performed using only one jet per event, where the leading or subleading momentum jet is randomly chosen. Per process, 250,000 raw MC events are used – additionally, the $h \to u\bar{u}$ and $h \to d\bar{d}$ processes are combined into a single class, $h \to$ light.

As input to the ANN, several jet-level variables are chosen:

Jets

- kinematics: momentum p, pseudorapidity η, polar angle ϕ, and mass m;
- LCFIPlus tagger results: b- ("BTag"), c- ("CTag"), and o-tag ("OTag") scores as well as jet category;
- number of Particle Flow Objects (PFOs – these are the particles which are grouped into the jet).

In addition to jet-level variables, it is prudent to include variables at the level of the PFOs contained within the jet. The 10 leading momentum particles contained within the jet have their kinematics redefined relative to the jet's axis and their momentum and mass scaled by the momentum of the jet. Per-particle, the following variables are also chosen as inputs:

Tracks

- kinematics: p, η, ϕ, and m;
- charge q;
- truth likelihoods: $L(e^{\pm})$, $L(\mu^{\pm})$, $L(\pi^{\pm})$, $L(K)$, $L(p^{+})$.

The ILD detector will provide PID information per PFO, including electron ($e^{\pm}$), muon ($\mu^{\pm}$), pion ($\pi^{\pm}$), kaon (K), and proton (p^{+}) likelihoods, L. However, the reconstructed likelihoods utilising the dE/dx and TOF information were not available in the inputs at the time of the study. *Truth* likelihoods are assigned instead, representing a best-case scenario in terms of PID. The 5 truth likelihoods are assigned a binary number by comparing the absolute value of PDG ID [39] of the PFO to the PDG ID(s) of each particle class:

PID

- electrons: 11;
- muons: 13;
- pions: 211;
- kaons: 310, 321, and 3122 (includes V^0's: K_s^0 and Λ^0);
- protons: 2212;

where 1 is assigned if one of the PDGs match and 0 is assigned otherwise.

NN Inputs in ILD

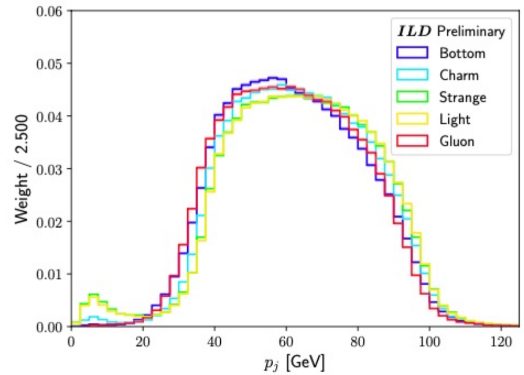

(a) Momentum p_j

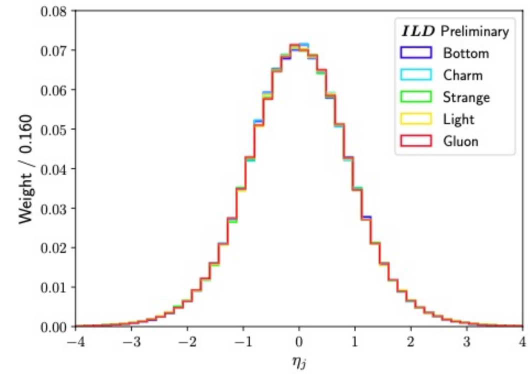

(b) Pseudorapidity η_j

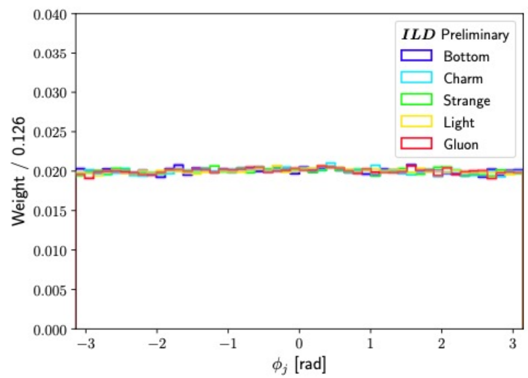

(c) Azimuthal angle ϕ_j

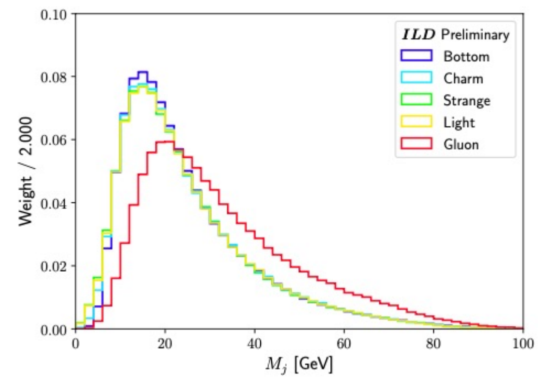

(d) Mass M

Figure A1: Distributions of the jet-level inputs for the ANN described in Section 4. The sum-of-weights for each class is normalised to 1. The error bars correspond to MC statistical uncertainties.

NN Inputs in ILD

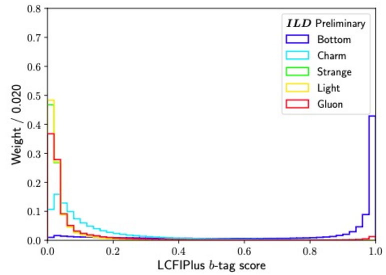

(a) LCFIPlus b-tag score

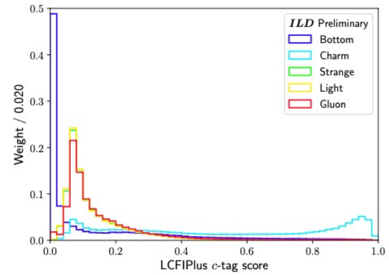

(b) LCFIPlus c-tag score

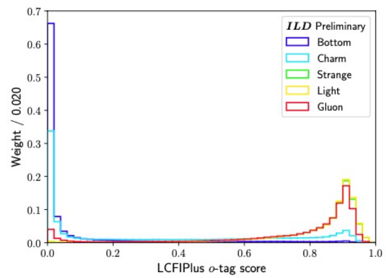

(c) LCFIPlus o-tag score

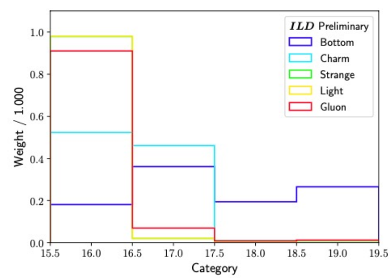

(d) Category

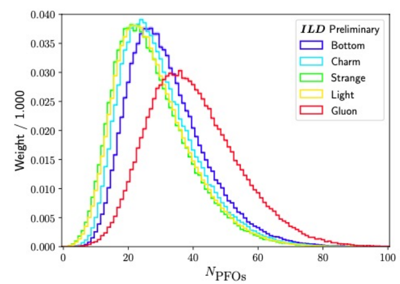

(e) Number of PFOs N_{PFOs}

Figure A2: Distributions of the jet-level inputs for the ANN described in Section 4. The sum-of-weights for each class is normalised to 1. The error bars correspond to MC statistical uncertainties. A continuation of Fig. A1.

NN Inputs in ILD

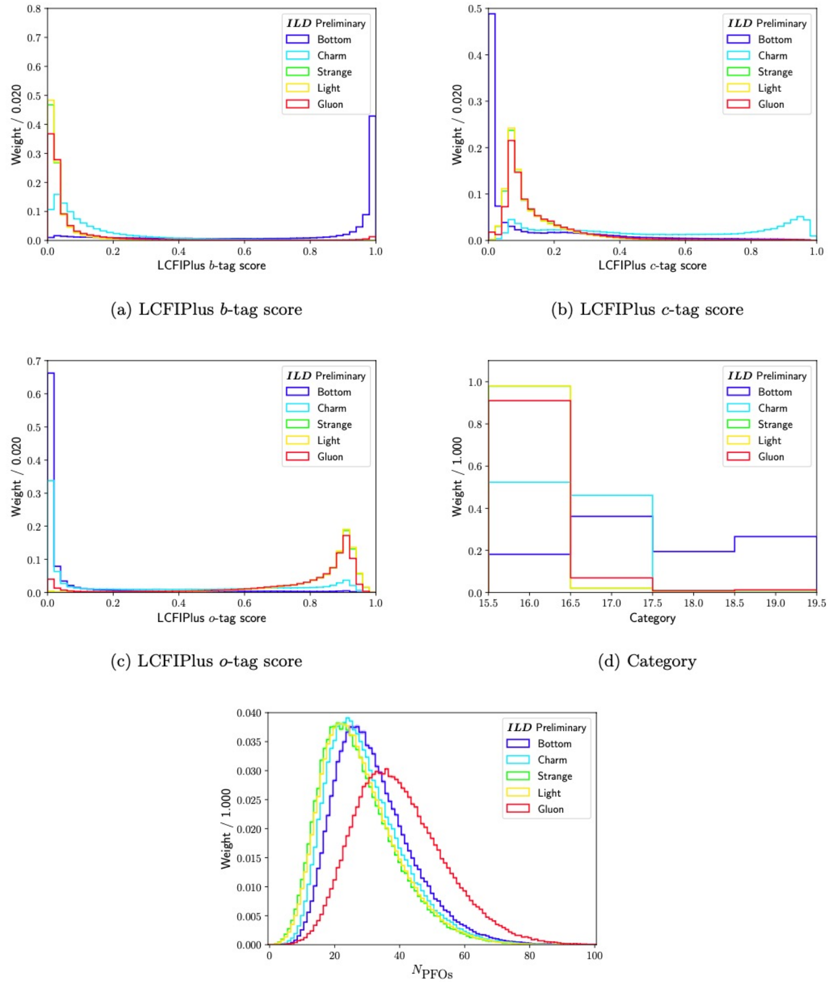

(a) LCFIPlus b-tag score

(b) LCFIPlus c-tag score

(c) LCFIPlus o-tag score

(d) Category

(e) Number of PFOs N_{PFOs}

Figure A2: Distributions of the jet-level inputs for the ANN described in Section 4. The sum-of-weights for each class is normalised to 1. The error bars correspond to MC statistical uncertainties. A continuation of Fig. A1.

NN Inputs in ILD

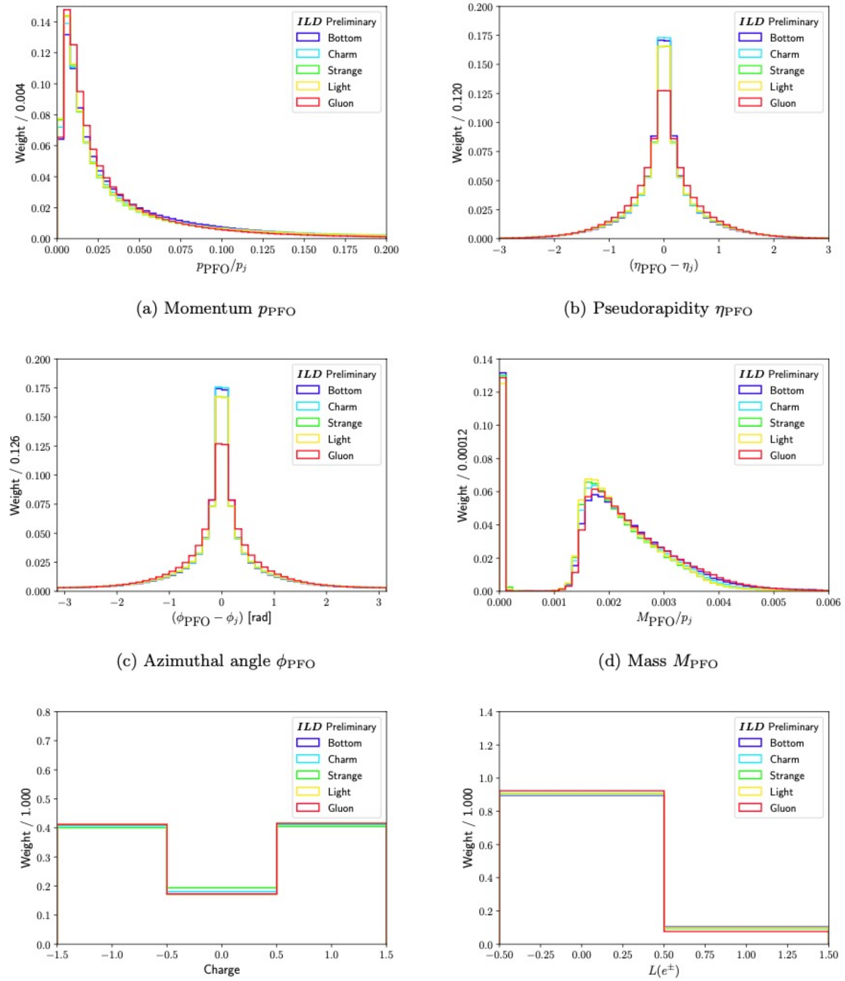

(a) Momentum p_{PFO}

(b) Pseudorapidity η_{PFO}

(c) Azimuthal angle ϕ_{PFO}

(d) Mass M_{PFO}

(e) Charge

(f) Electron truth likelihood $L(e^{\pm})$

Figure A3: Distributions of the PFO-level inputs for the ANN described in Section 4. The sum-of-weights for each class is normalised to 1. The error bars correspond to MC statistical uncertainties.

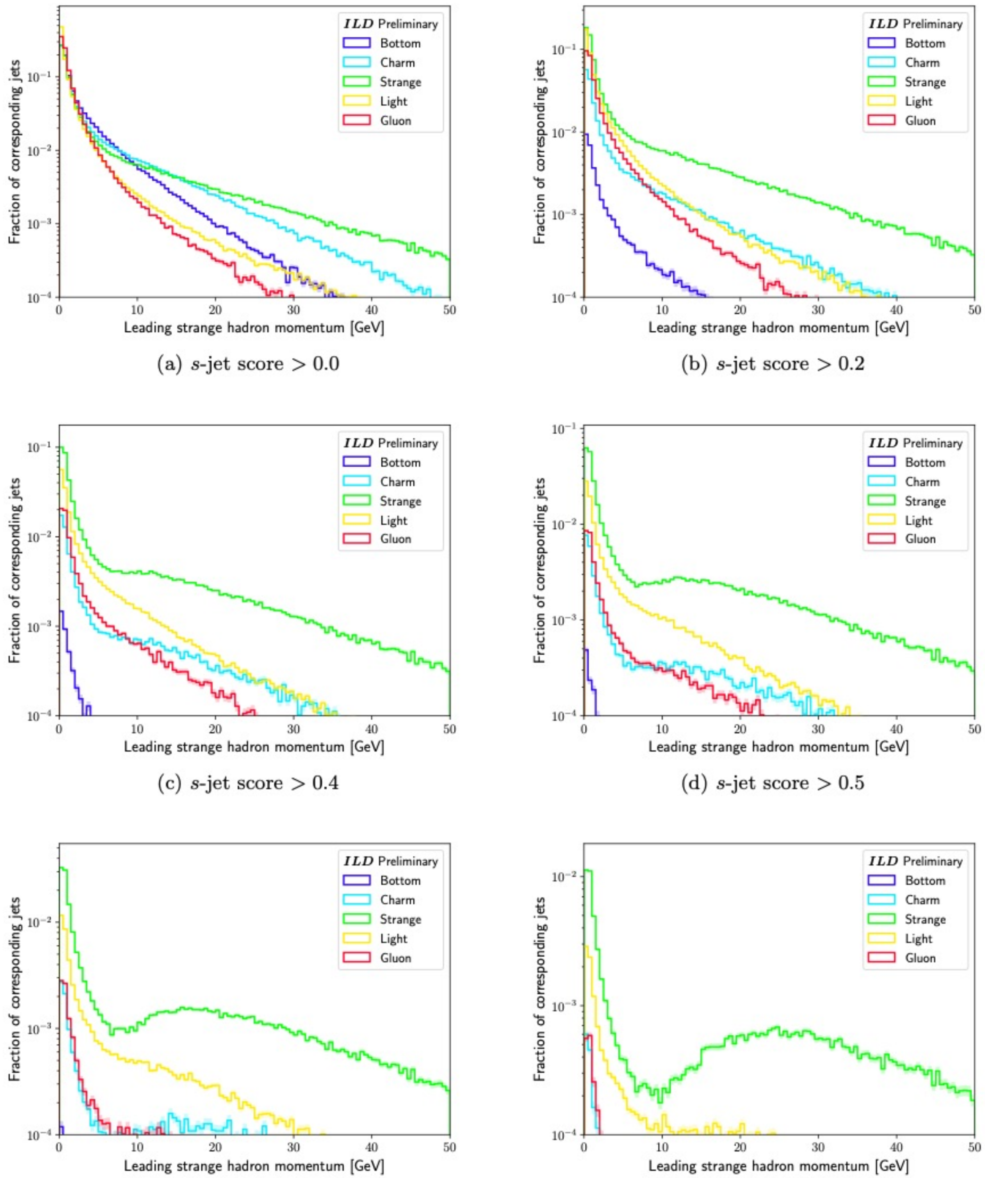

(a) s-jet score > 0.0

(b) s-jet score > 0.2

(c) s-jet score > 0.4

(d) s-jet score > 0.5

(e) s-jet score > 0.6

(f) s-jet score > 0.7

Figure 7: Distributions of the momentum of the leading strange particle in jets from $h(\to q\bar{q}/gg)Z(\to \nu\bar{\nu})$ events. The distributions are shown for different choices of cut on s-jet score of the described jet flavour tagger, Eq. 5. The momentum of the leading strange particle is determined by following the same procedure as for Fig. 2. The sum-of-weights for each class is normalised to 1 in (a) but is *not* renormalised following the application of cuts in (b) through (e).

2203.07535

$h \to s\bar{s}$ analysis in a nutshell

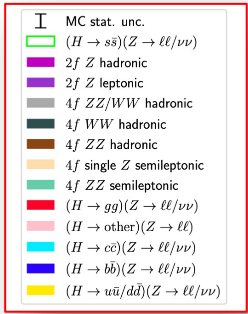

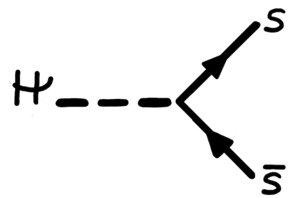

2 jets

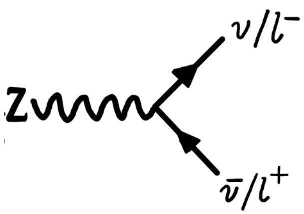

0 or 2 SFOS leptons

Object definition

Event selection

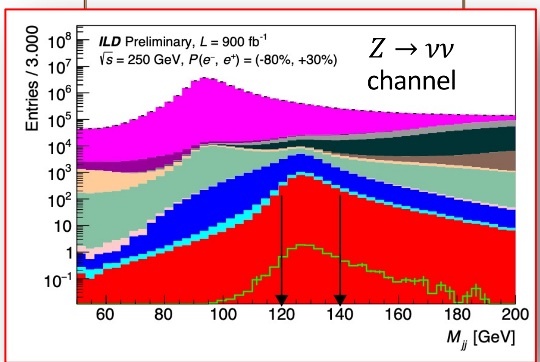

Cut-based approach, reject $ZH(!ss), V, VV$

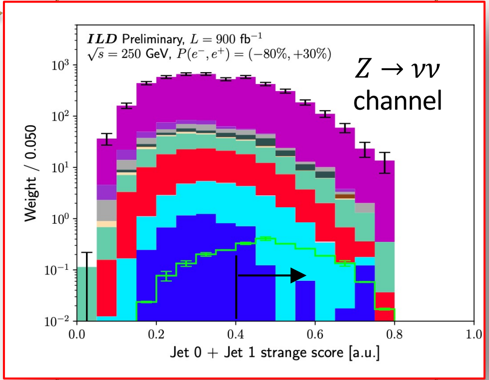

Sum of the s-jet scores

Signal discriminant

s-Yukawa constraints

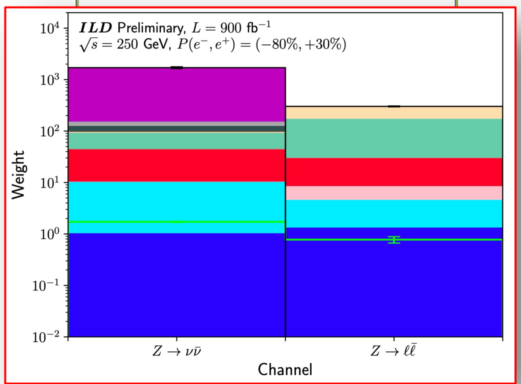

k_s < 6.74 x SM

Analysis overview & results

See also M. Basso's talk at Higgs2021

Define Signal/Bkg

- Signal: Z(inv)H(ss)+: Z(ll)H(ss)
- Bkg: Z(inv/ll)H(bb,cc,gg), Z(qq & semil), ZZ(qqqq &semil), ZZ/WW(had), WW(had)

Select Events

Most powerful cut on M_{jj} (see extra-slides for more details)

Build Signal discriminant

Sum of leading and sub-leading strange-jet score

s-Yukawa coupling

Probe various BSM regimes

Z->inv

The signal efficiency for our selections is **14%** while our background efficiency is **0.005%.** Even with the high background rejection, $Z \rightarrow q\bar{q}$ is still highly dominant with ~16,000 events compared to the ~9 events expected for $h \rightarrow s\bar{s}$. Therefore, improvements to the sensitivity of the analysis are expected to be accompanied by improved rejection of $Z \rightarrow q\bar{q}$. The $h \rightarrow gg$ process is the dominant Higgs background with ~400 events.

Z->ll

The signal efficiency for our selections is **6%** while our background efficiency is **0.001%.** The 4f single Z and ZZ backgrounds are the dominant backgrounds, with ~3,000 events compared to the ~4 events expected for $h \rightarrow s\bar{s}$. As with the $Z \rightarrow \nu\bar{\nu}$ channel, the $h \rightarrow gg$ process is the dominant Higgs background with ~700 events.

Analysis

The jet flavour tagger described in section 4 is applied to a search for SM Higgs decaying to strange quarks ($h \to s\bar{s}$), using all of the MC samples described in table 2. The parameter of interest (POI) for the analysis is the Higgs-strange quark coupling strength modifier, κ_s, which tunes the SM $h \to s\bar{s}$ BR, $\mathrm{BR}[h \to s\bar{s}]_{\mathrm{SM}}$, as:

$$\mathrm{BR}[h \to s\bar{s}] = \mu(\kappa_s^2) \times \mathrm{BR}[h \to s\bar{s}]_{\mathrm{SM}} \,, \tag{6}$$

where $\mathrm{BR}[h \to s\bar{s}]$ is the modified BR and $\mu(\kappa_s^2)$ is our POI as a function of κ_s^2, given by[2]:

$$\mu(\kappa_s^2) = \frac{\kappa_s^2}{\kappa_s^2 \times \mathrm{BR}[h \to s\bar{s}]_{\mathrm{SM}} + (1 - \mathrm{BR}[h \to s\bar{s}]_{\mathrm{SM}})} \,. \tag{7}$$

The coupling strength modifier is understood within the context of the kappa framework, the experimental tool for exploring the properties of the Higgs [47, 48]. When $\kappa_s = 1$, the SM BR is recovered.

Event Selection

Table 3: Kinematic selections for $Z \to \nu\bar{\nu}$ and $Z \to \ell\ell$ channels of the $h \to s\bar{s}$ analysis. The selections are grouped into categories serving specific purposes.

Category	Selection	$Z \to \nu\bar{\nu}$	$Z \to \ell\ell$
Object counting	Number of leptons, N_{leptons}	0	≥ 2
	Number of jets, N_{jets}	≥ 2	≥ 2
	Leading 2 leptons are SFOS[2]	–	True
$2f$ Z rejection	Leading jet momentum, p_{j_0}	$\in [40, 110]$ GeV	$\in [60, 110]$ GeV
	Subleading jet momentum, p_{j_1}	$\in [30, 80]$ GeV	$\in [30, 75]$ GeV
	Dijet mass, M_{jj}	$\in [120, 140]$ GeV	$\in [115, 145]$ GeV
	Dijet energy, E_{jj}	$\in [125, 155]$ GeV	$\in [130, 160]$ GeV
	Missing mass, M_{miss}	$\in [75, 120]$ GeV	–
	Dijet/missing-p^μ angular separation, $\Delta R_{jj,\text{miss}}$[3]	$\in [3.1, 4.0]$[4]	–
	Dijet azimuthal separation, $\Delta\phi_{jj}$	> 1.25	> 1.75
	Leading lepton momentum, p_{ℓ_0}	–	$\in [40, 90]$ GeV
	Subleading lepton momentum, p_{ℓ_1}	–	$\in [20, 60]$ GeV
	Dilepton mass, $M_{\ell\ell}$	–	$\in [70, 100]$ GeV
	Dilepton energy, $E_{\ell\ell}$	–	$\in [85, 115]$ GeV
$h \to b\bar{b}/c\bar{c}$ rejection	Leading jet LCFIPlus BTag score, $\text{score}_b^{j_0}$	< 0.20	< 0.1
	Subleading jet LCFIPlus BTag score, $\text{score}_b^{j_1}$	< 0.20	< 0.1
	Leading jet LCFIPlus CTag score, $\text{score}_c^{j_0}$	< 0.35	< 0.3
	Subleading jet LCFIPlus CTag score, $\text{score}_c^{j_1}$	< 0.35	< 0.3
$4f$ VV rejection	$2 \to 3$ jet transition variable, y_{23}	< 0.010	< 0.050
	$2 \to 3$ jet transition variable, y_{34}	< 0.002	< 0.005
$h \to gg$ rejection	Number of PFOs in event, $N_{\text{PFOs}}^{\text{event}}$	$\in [30, 60]$	$\in [20, 80]$
	Number of PFOs in leading jet, $N_{\text{PFOs}}^{j_0}$	$\in [10, 40]$	$\in [5, 50]$
	Number of PFOs in subleading jet, $N_{\text{PFOs}}^{j_1}$	$\in [9, 37]$	$\in [5, 50]$

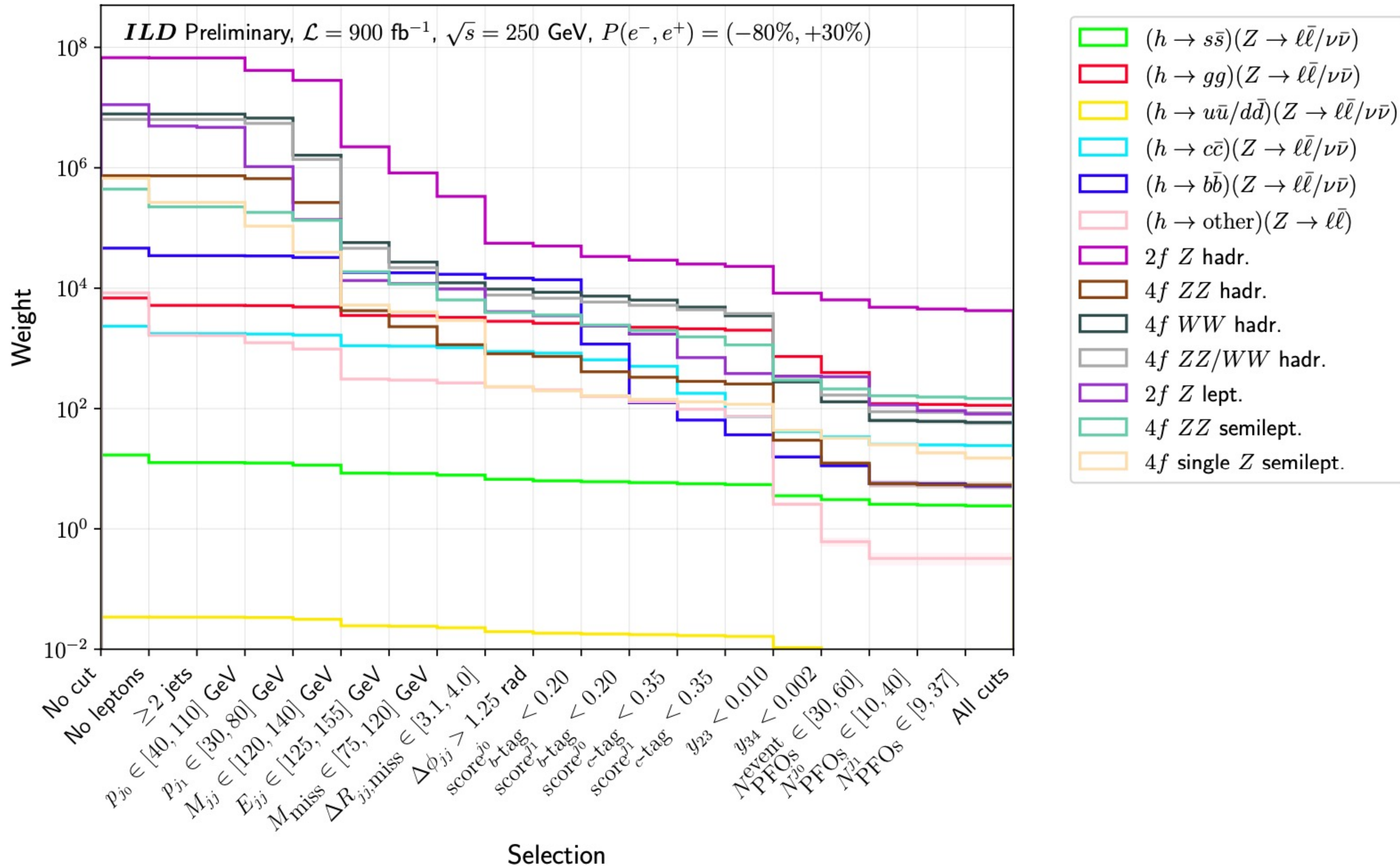

(a) $Z \to \nu\bar{\nu}$ channel

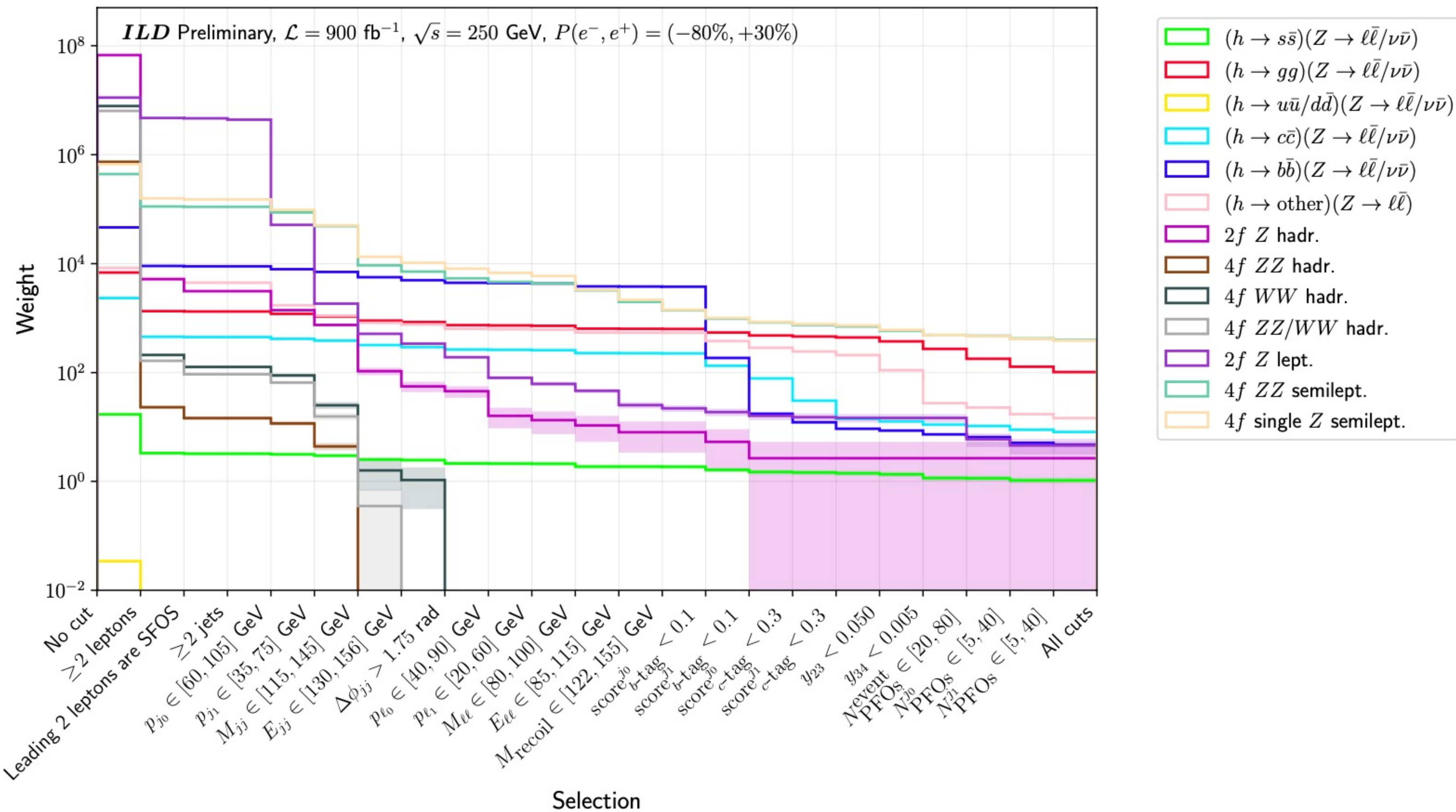

(b) $Z \to \ell\bar{\ell}$ channel

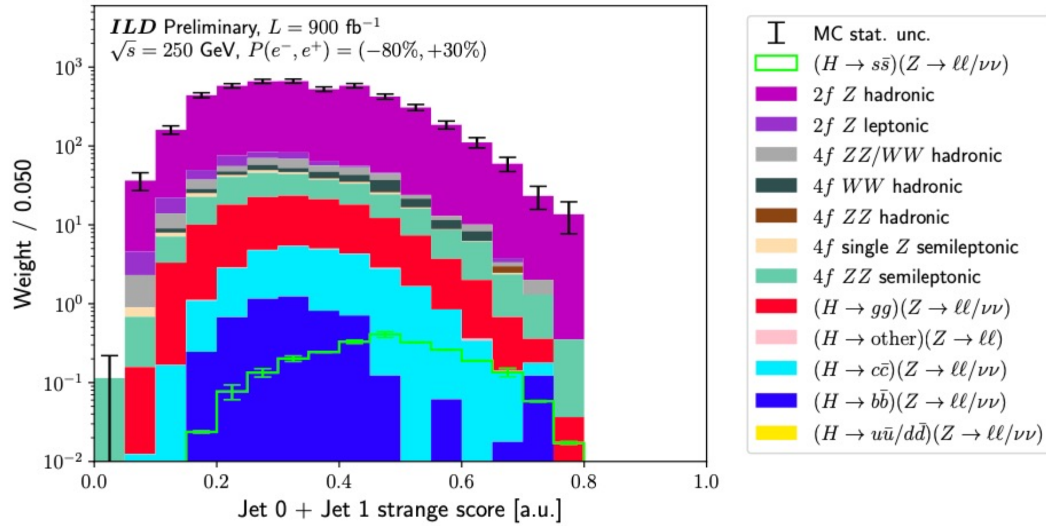

(a) $Z \to \nu\bar{\nu}$ channel

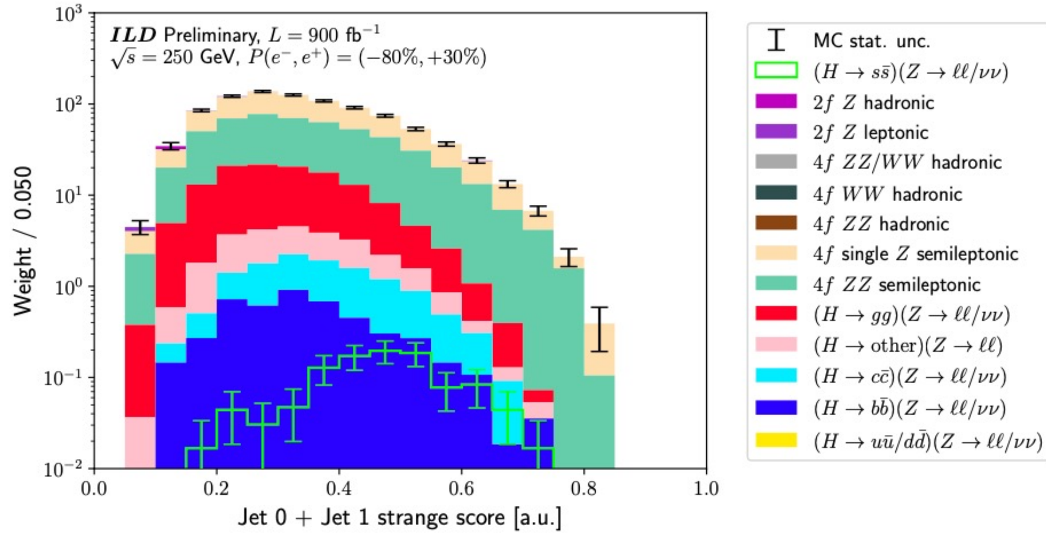

(b) $Z \to \ell\bar{\ell}$ channel

Figure 17: Fit discriminants for each channel of the SM $h \to s\bar{s}$ analysis: ($0.5\times$) the sum of the strange scores for leading and subleading jets, using the jet flavour tagger described in section 4. Each histogram is produced at the level of the last selection of their respective channel in Table 3. The error bars represent the MC statistical uncertainties. The sum-of-weights per process is normalised to the SM cross section. N.B. the $h(\to s\bar{s})Z(\to \ell\bar{\ell}/\nu\bar{\nu})$ signal is unstacked.

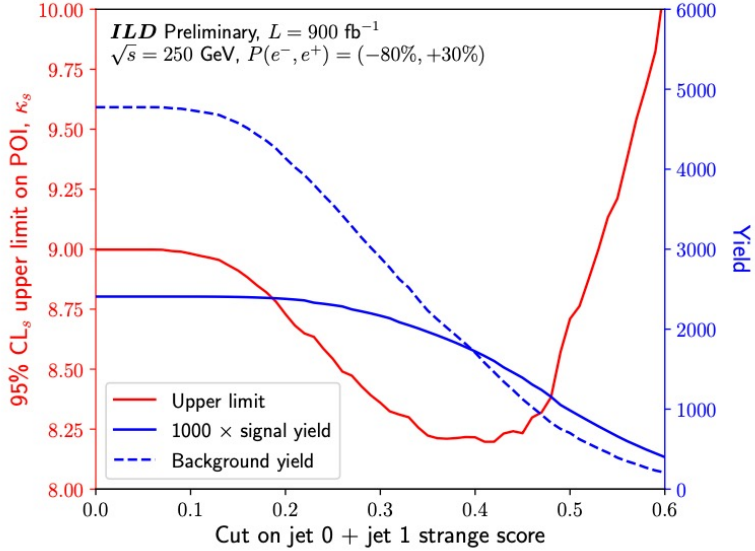

(a) $Z \to \nu\bar{\nu}$ channel

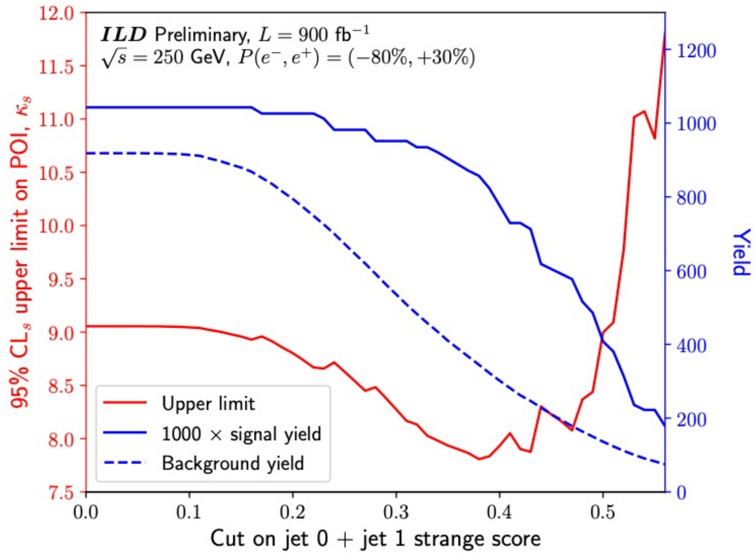

(b) $Z \to \ell\bar{\ell}$ channel

Figure 18: Scans of the 95% CL$_s$ upper limit for the Higgs-strange coupling strength modifier κ_s, obtained by varying the choice of the lower thresholds on the discriminants shown in Fig. 17. Also shown are the signal (i.e., $h(\to s\bar{s})Z(\to \ell\bar{\ell}/\nu\bar{\nu})$) and background (i.e., non-$h(\to s\bar{s})Z(\to \ell\bar{\ell}/\nu\bar{\nu})$) yields in the resulting regions.

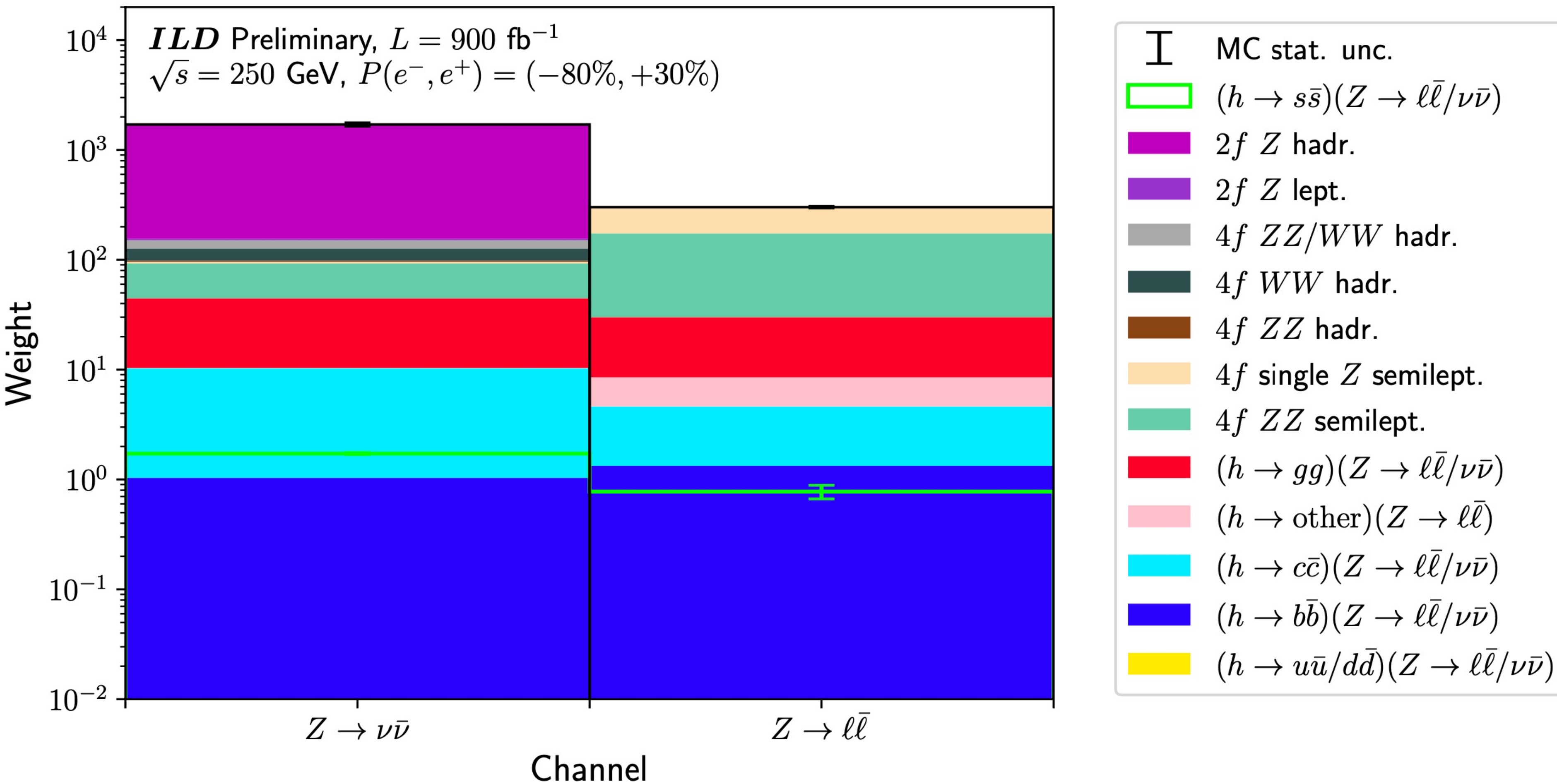

ILD Preliminary, $L = 900$ fb^{-1}
$\sqrt{s} = 250$ GeV, $P(e^-, e^+) = (-80\%, +30\%)$
Weight
10^4
10^3
10^2
10^1
10^0
10^{-1}
10^{-2}
$Z \to \nu\bar{\nu}$
$Z \to \ell\bar{\ell}$
Channel
MC stat. unc.
$(h \to s\bar{s})(Z \to \ell\bar{\ell}/\nu\bar{\nu})$
$2f$ Z hadr.
$2f$ Z lept.
$4f$ ZZ/WW hadr.
$4f$ WW hadr.
$4f$ ZZ hadr.
$4f$ single Z semilept.
$4f$ ZZ semilept.
$(h \to gg)(Z \to \ell\bar{\ell}/\nu\bar{\nu})$
$(h \to \text{other})(Z \to \ell\bar{\ell})$
$(h \to c\bar{c})(Z \to \ell\bar{\ell}/\nu\bar{\nu})$
$(h \to b\bar{b})(Z \to \ell\bar{\ell}/\nu\bar{\nu})$
$(h \to u\bar{u}/d\bar{d})(Z \to \ell\bar{\ell}/\nu\bar{\nu})$

Limits

With PID | Without PID

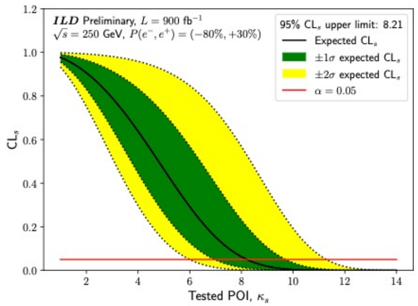

(a) $Z \to \nu\bar{\nu}$ channel

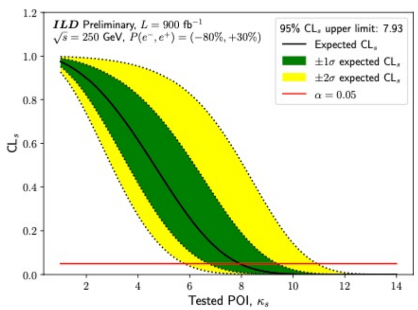

(b) $Z \to \ell\bar{\ell}$ channel

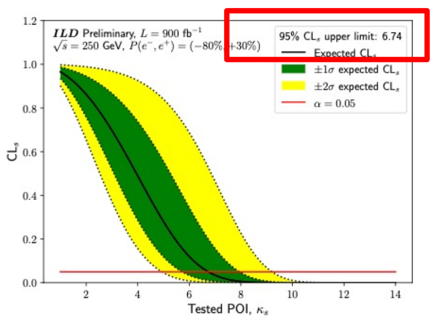

(c) Combined

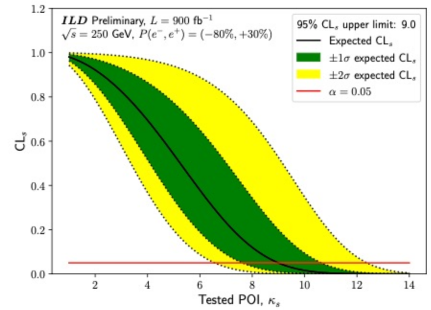

(a) $Z \to \nu\bar{\nu}$ channel

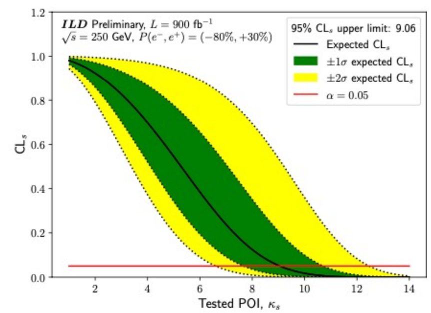

(b) $Z \to \ell\bar{\ell}$ channel

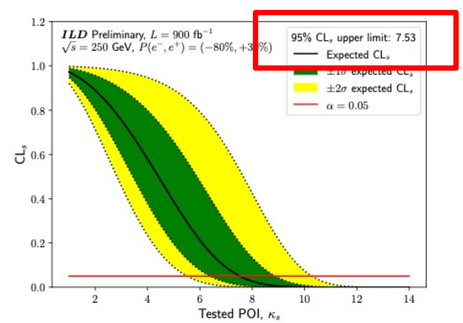

(c) Combined

~15% weaker compared to PID (only 900 fb-1 analysed)

Alternative score to reduce gluons

- Uncertainty on *h→gg* rate could be *significant*
  - Assigning ±100% uncertainty **affects** the *Z→ll* channel, where the absolute uncertainty is comparable to the counting uncertainty in data

    21 gluon events and 301 total bkg with a stat unc. of 17

In Z->inv, the total background is 1706, which has a stat error of 40
The gluons are 34 events
So even 100% uncertainty is less than the stats

Z→νν channel **Z→ll channel**

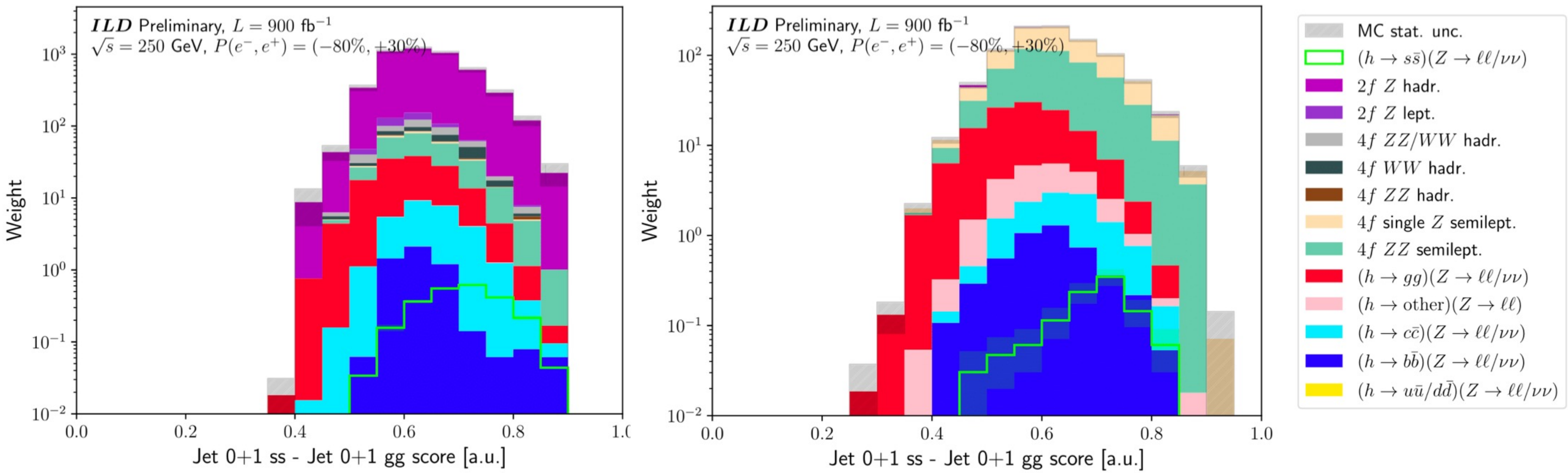

Provides slightly stronger separation of *h→ss* from *h→gg*, but limits should be explicitly computed to confirm

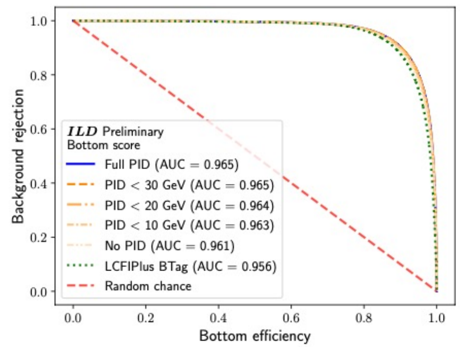

(a) b-jet score

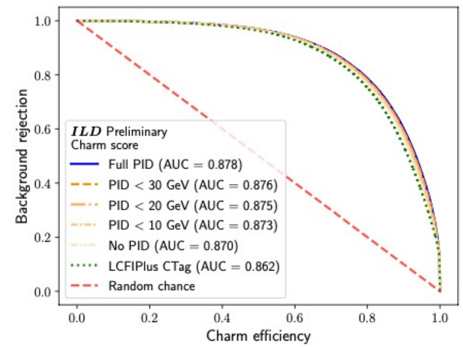

(b) c-jet score

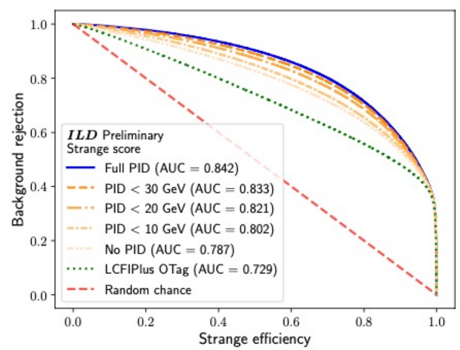

(c) s-jet score

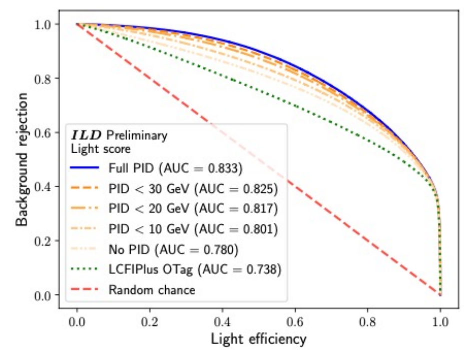

(d) Light-jet score

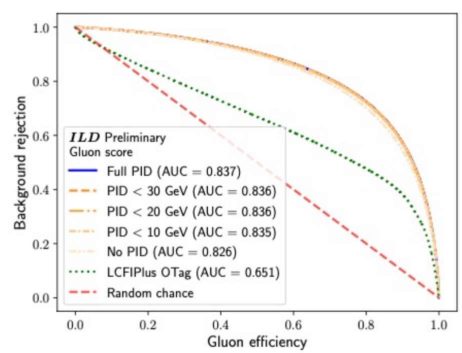

(e) g-jet score

Figure B3: ROC curves for each output node of the jet flavour tagger with full PID ("Full PID"), as described in Section 4, as well as for the jet flavour taggers without PID ("No PID") and with partial PID ("PID $< X$ GeV"), as described in Appendix B. The sum-of-weights for each class is normalised to 1. The "Background" in a given plot corresponds to all classes not targeted by that node of the tagger. N.B. the blue and orange curves lie nearly on top of one another in (a), (b), and (e).

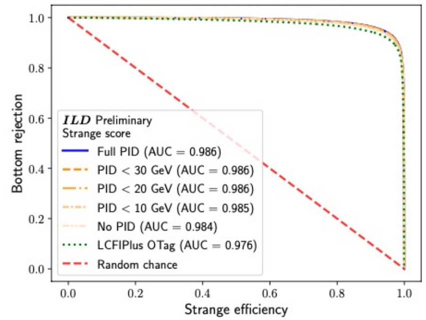

(a) Strange vs. bottom, using s-jet score

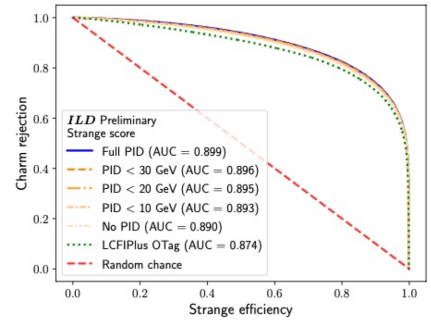

(b) Strange vs. charm, using s-jet score

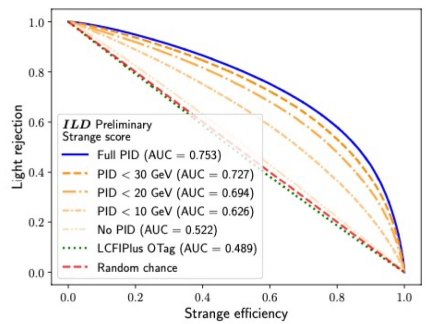

(c) Strange vs. light, using s-jet score

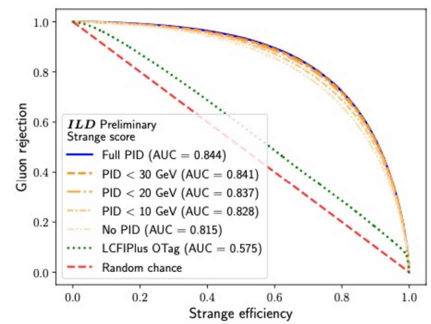

(d) Strange vs. gluon, using s-jet score

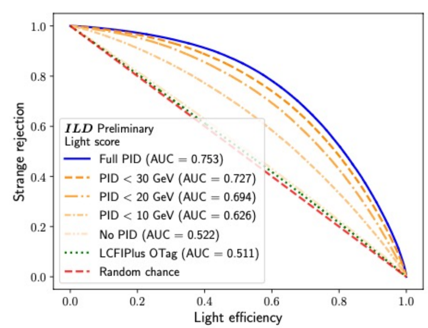

(e) Light vs. strange, using light-jet score

Figure B4: Pairwise ROC curves for various output nodes of the jet flavour tagger with full PID ("Full PID"), as described in Section 4, as well as for the jet flavour taggers without PID ("No PID") and with partial PID ("PID $< X$ GeV"), as described in Appendix B. The sum-of-weights for each class is normalised to 1. N.B. the blue and orange curves lie nearly on top of one another in (a) and (b).

Flavour Tagging with ILD

2202.03285

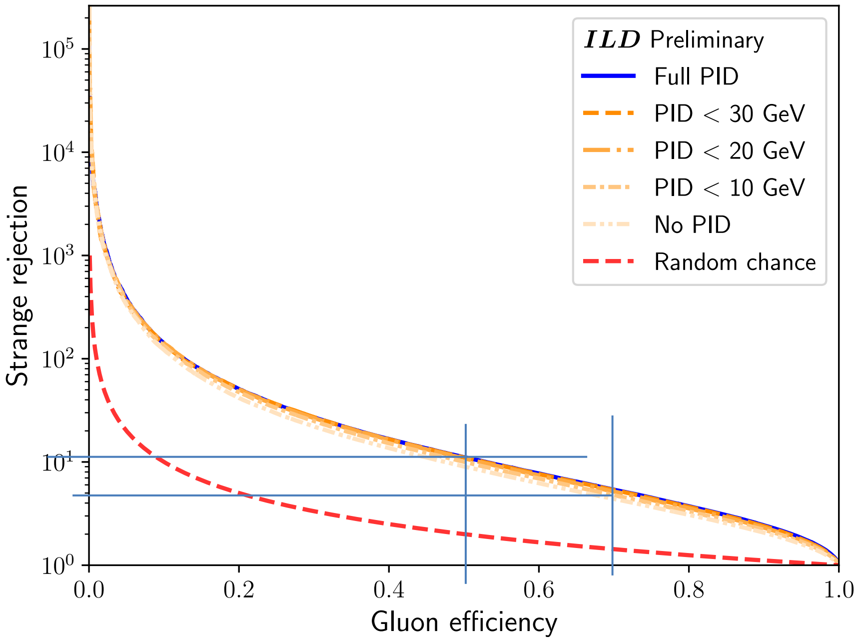

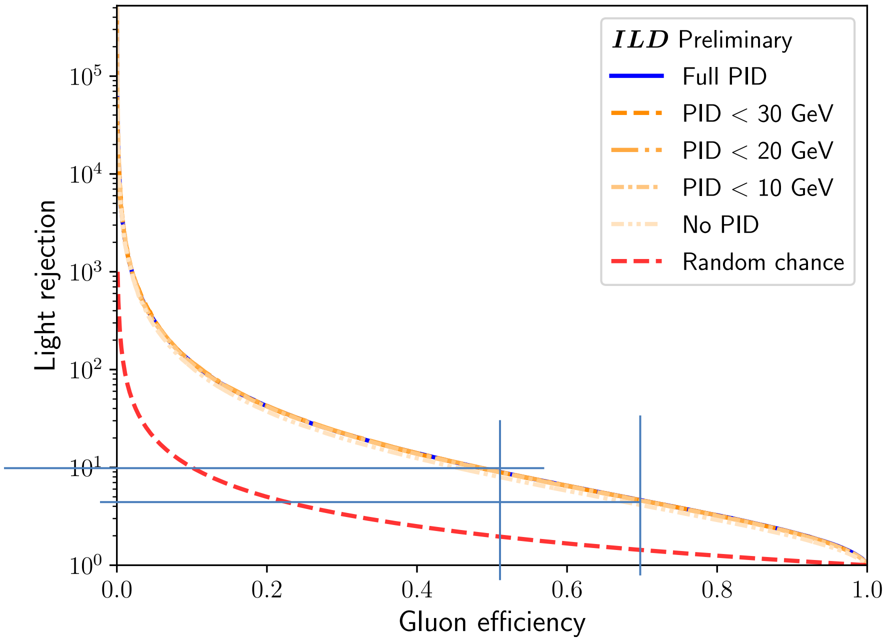

Detector Studies

Sketching the ideal detector…

- **dE/dx not useful in Si-driven trackers (à la SiD):** it needs ~1 m track length in gas and is disfavoured for solids including silicon due to the density effect, which suppresses the K/π difference in the needed momentum range

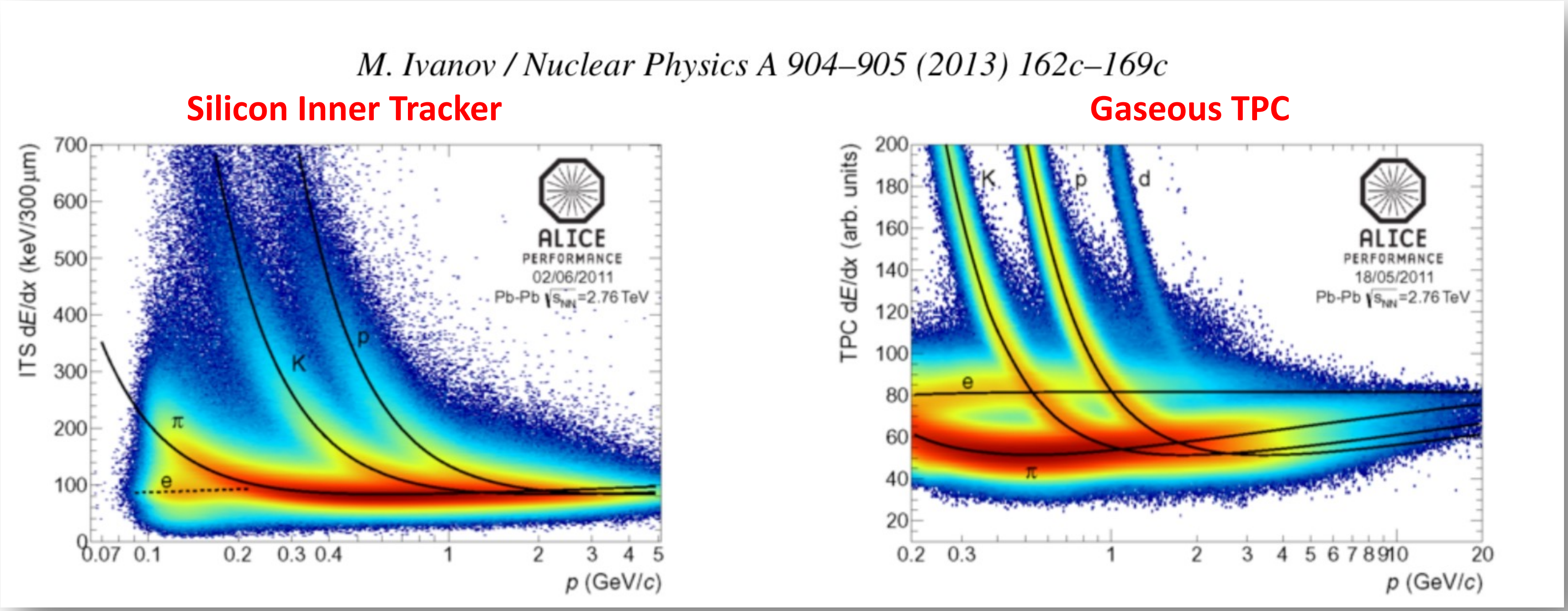

Sketching the ideal detector…

- **TOF** also covers only the very low momentum range
- Larger momentum range covered by **RICH**…
  - See also previous presentation by [Jerry]

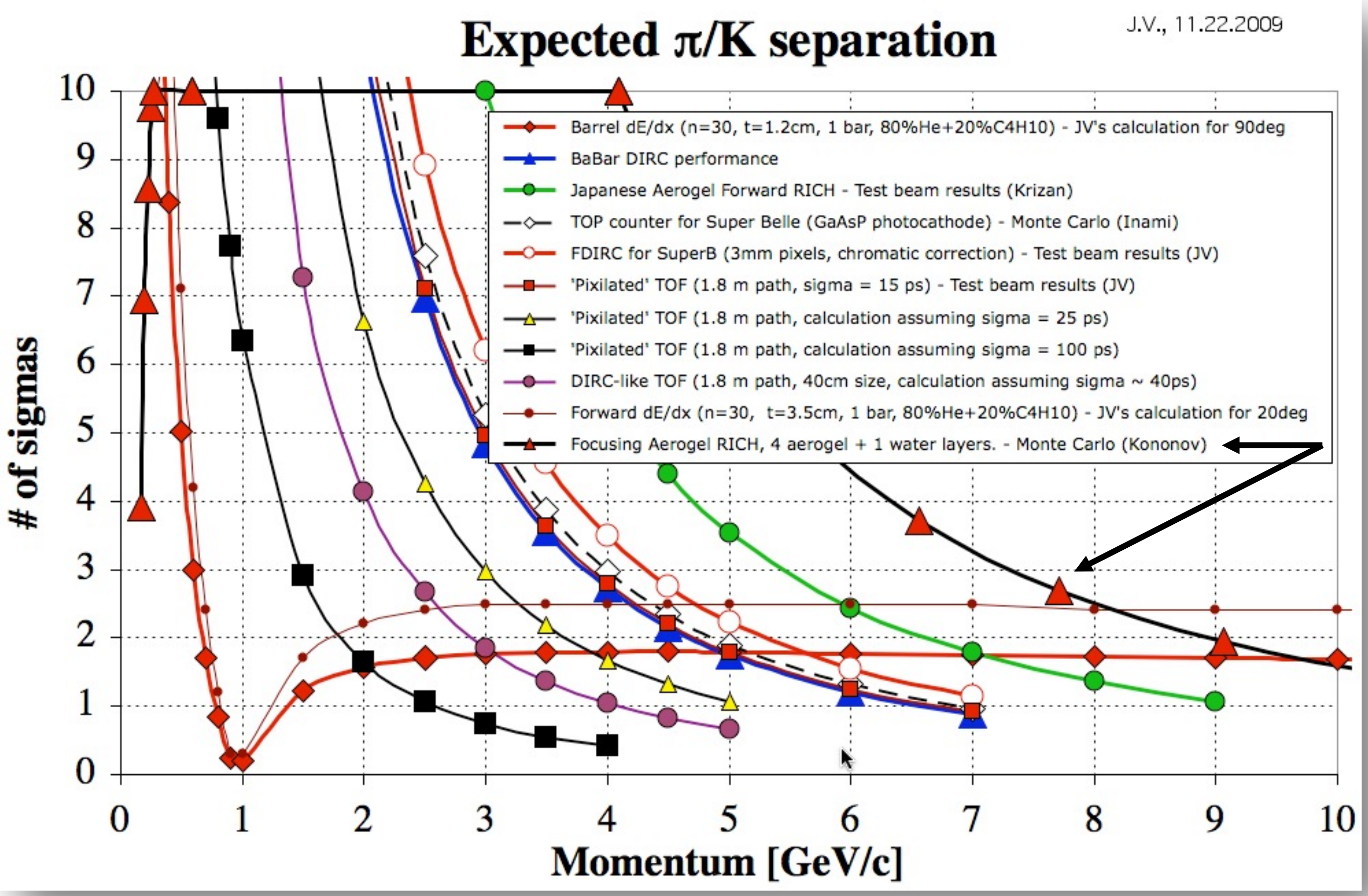

Sketching the ideal detector…

- **Ring Imaging Cherenkov Detectors (RICH)** is the only realistic approach
  - Electron Ion Collider people making impressive progress with an aerogel radiator, but for our momentum range, a **gaseous radiator** is the most promising option
    - Requires excellent Cerenkov angle resolution

Historical Note: CRID@SLD used a design with two radiators: a liquid layer of C_6F_{14} working in proximity focusing and a gas volume filled with C_4F_{10}

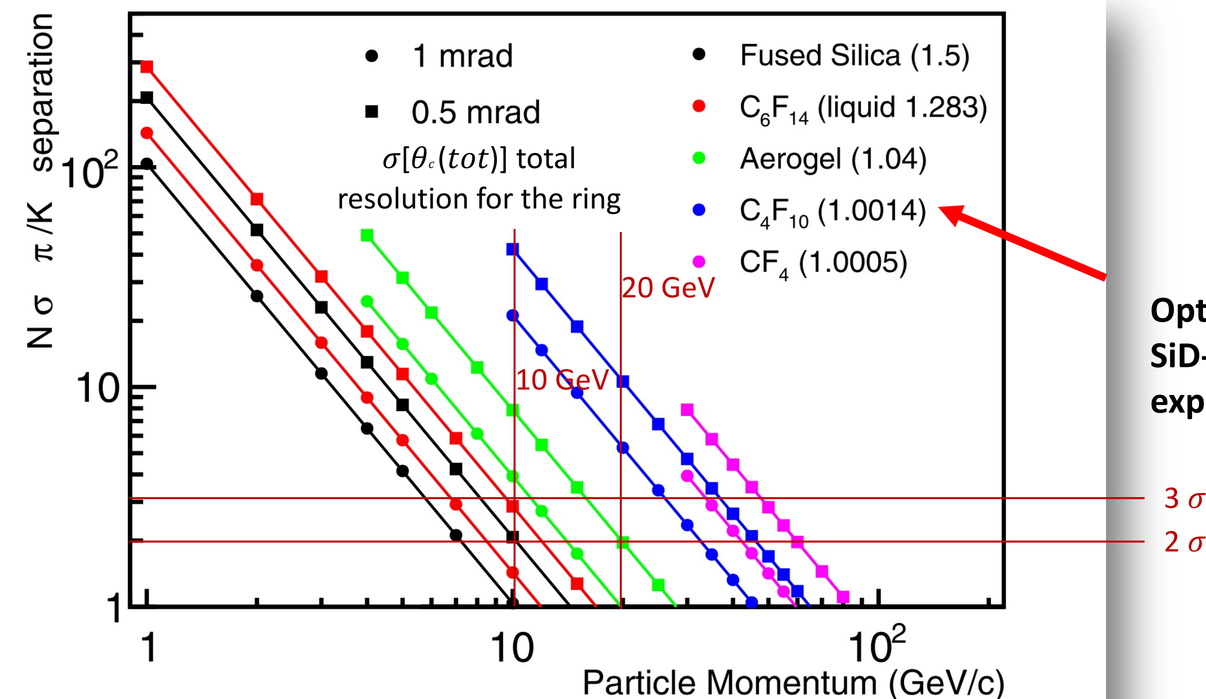

Fig. 2. The number standard deviations in $\pi - K$ separation versus momentum for different radiators and two different Cherenkov angle resolutions.

Optimal for a SiD-like experiment

A. Papanestis, NIM,A 952 (2020) 162004

Gaseous RICH with SiPMTs – gas

- **Low mass vessel** (total detector weight is small compared to CRID @ SLC - no liquid radiator, no heavy mirrors, etc)

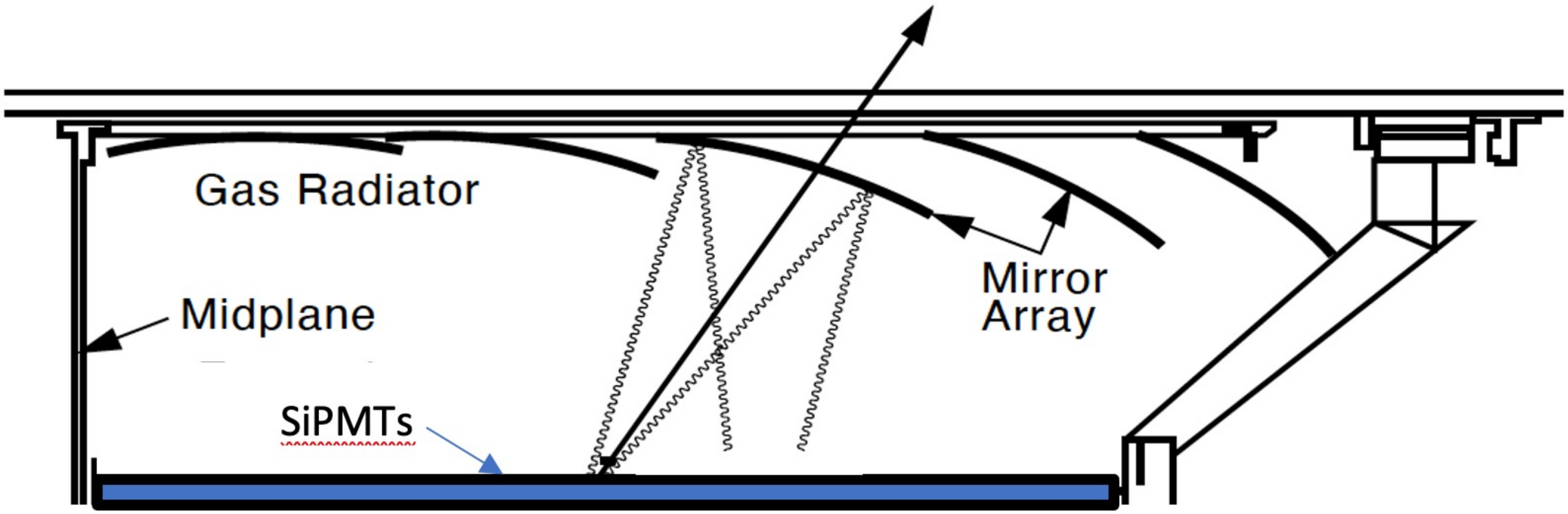

6.1.1 Gas choices

(a) Pure C_5F_{12} gas at 1 bar requires a detector temperature of 40 °C since the boiling point of this gas is 31 °C at 1 bar. That could prove to be difficult since SiPMs need to be cooled.

(b) A gas choice of pure C_4F_{10} at 1 bar allows detector operation at a few degrees Celsius since boiling point of this gas is -1.9 °C at 1 bar. This is presently our *preferred* choice.

(c) A choice of C_2F_6 gas at 1 bar would allow detector operation even below 0 °C since the boiling point of this gas is -70.2 °C at 1 bar. However, this gas would deliver insufficient number of photoelectrons in the geometry shown in Fig. 21 and therefore it was not considered.

(d) A choice of C_3F_8 gas at 1 bar would allow detector operation at -30 °C since the boiling point of C_3F_8 is -37 °C. The detector's PID performance will be between C_2F_6 and C_4F_{10}. It is certainly worthwhile to look into this solution.

Gaseous RICH with SiPMTs – performance

- Reach of PID performance depends on the **Cherenkov angle resolution**
  - Effects of chromaticity, bending of tracks, pixel size, tracking precision, noise, etc.).
- See Jerry's updates here and here

# of sigmas = $\dfrac{\theta_\pi - \theta_K}{\sigma_\theta/\sqrt{N}}$

σ_θ is total Cherenkov angle resolution = f(p); it is a total error, which included chromatic effect, bending effect, pixel size effect and other expected systematic effects

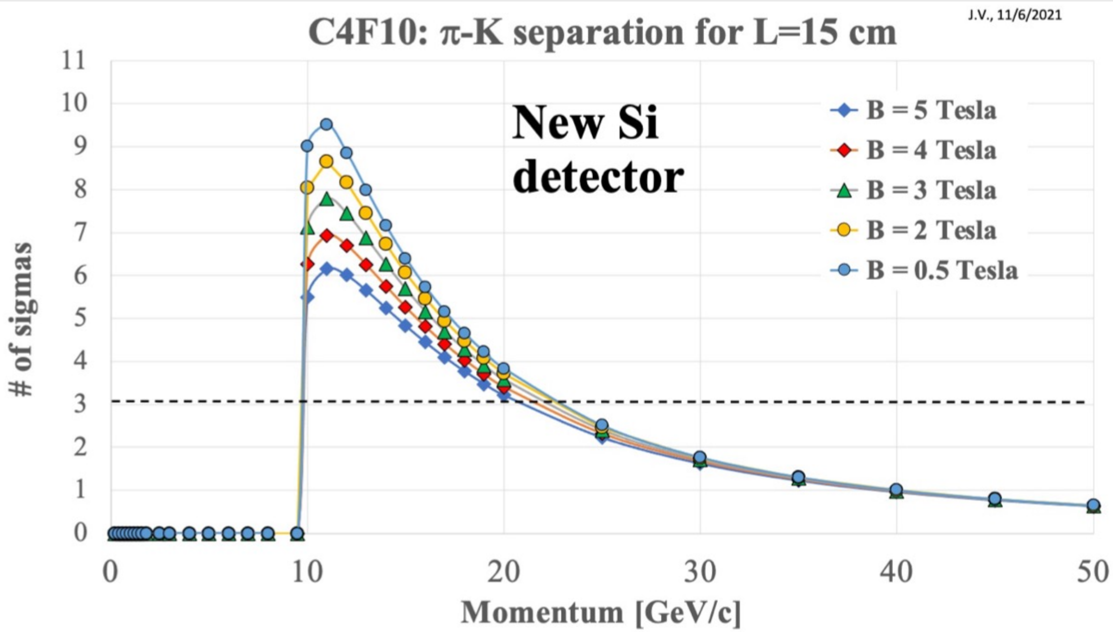

- **15 cm long radiator; PDE of a hypothetical Si detector has 1.5 x PDE$_{\mathrm{SiPMT}}$.**
- **This detector does not exist yet.**

11/17/21 J. Va'vra 18

Gaseous RICH with SiPMTs – refraction index, mirror reflectivity, PDE

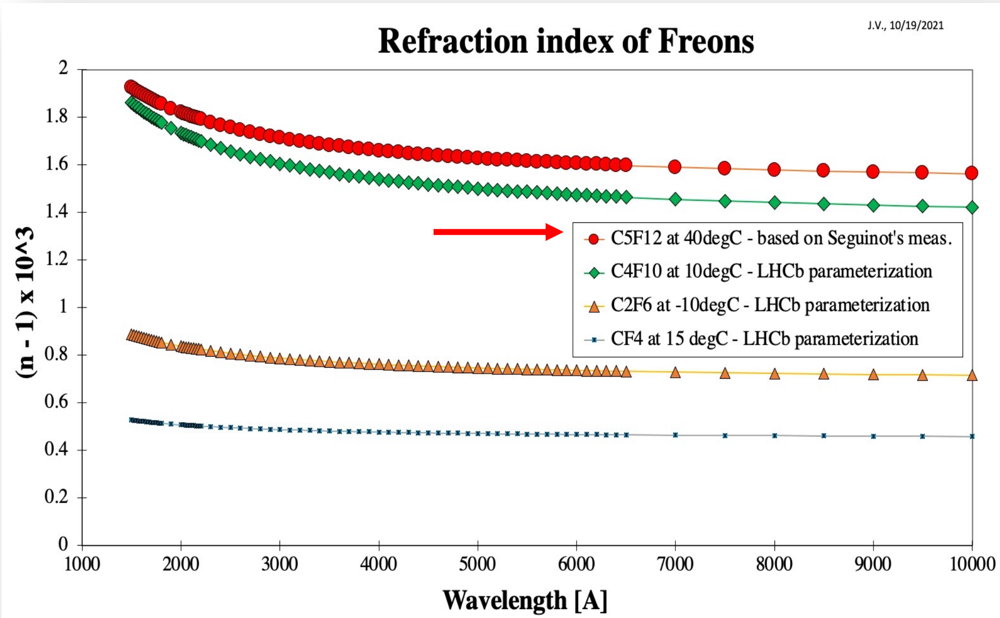

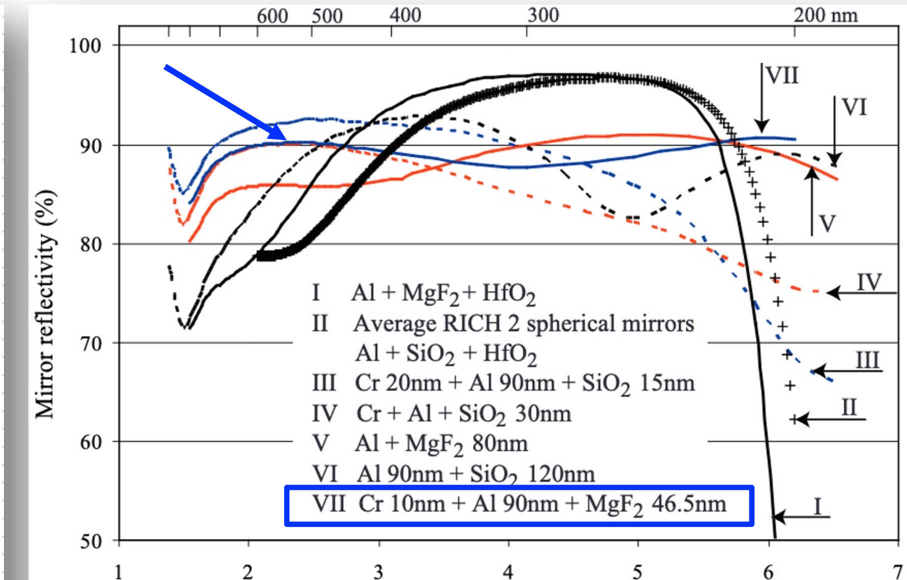

LHCb, JINST 3 S08005, 2008

P. Krizan et al.,NIMA 990(2020)163804, and R. Klanner, arXiv:1809.04346v2, 2018

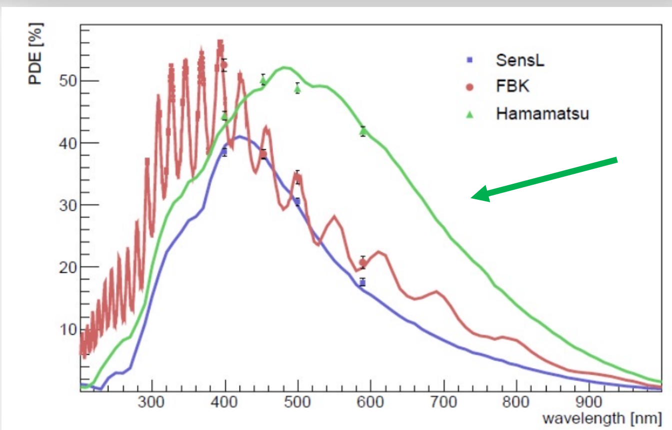

PDE = Photon detection efficiency:

$$PDE = FF \times QE(\lambda) \times P_T(V_{bias}, \lambda)$$

$QE(\lambda)$ – QE of Si
FF – Fill factor within one SiPMT
$P_T(V_{bias}, \lambda)$ – Trigger efficiency

In addition, a SiPMT array has losses due to gaps between pixel elements.
Jerry used **65%** in his calculations, could jump to 100% with back-illumination.

Gaseous RICH with SiPMTs – performance

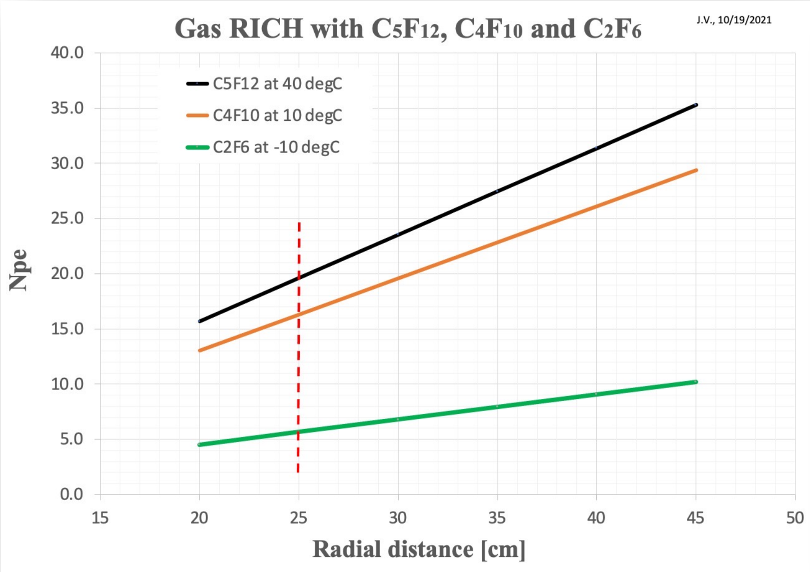

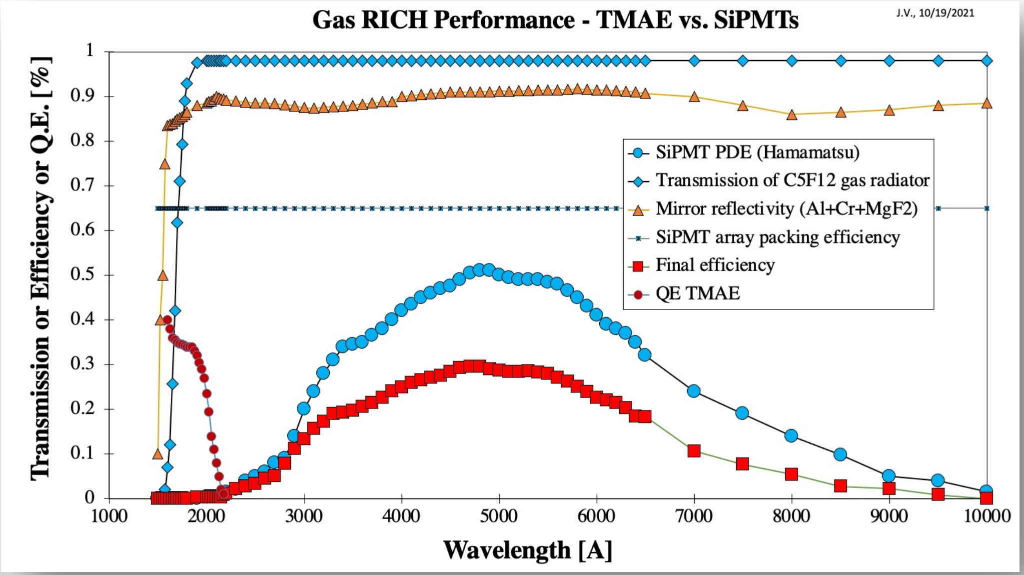

C_4F_{10} seems a possible solution with SiPMT readout even for 20-25 cm radial distance!

Much better Cherenkov Photon Detection efficiency over a wider wavelength compared to TMAE

Why didn't we do this before?
No SiPMT!

Gaseous RICH with SiPMTs – performance

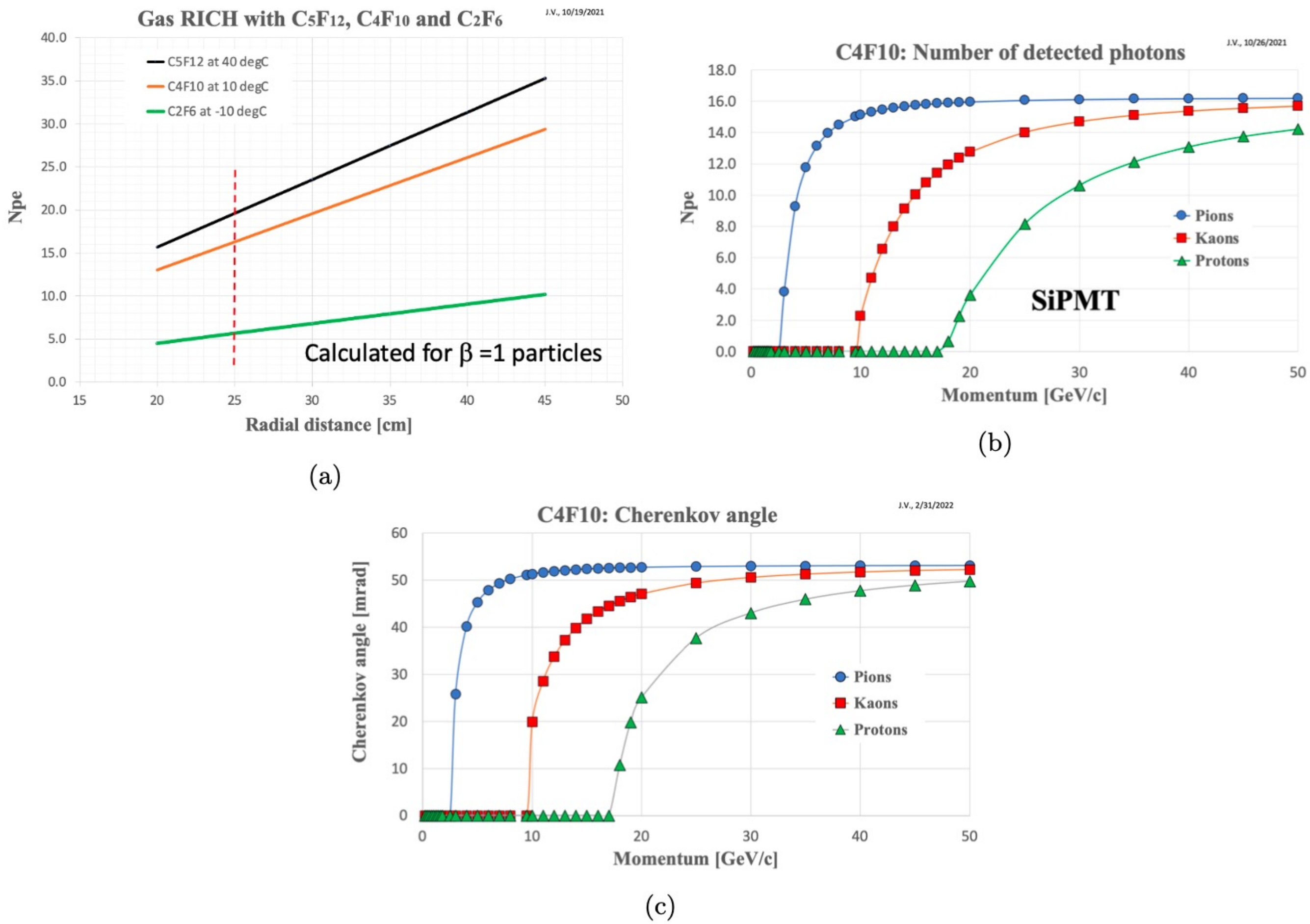

Figure 23: (a) Calculated number of photoelectrons per ring as a function of radiator length L. (b) Calculated number of photoelectrons and (c) Cherenkov angle as a function of momentum for pions, kaons, and protons. One can see that the kaon threshold is $\sim$10 GeV for C_4F_{10} gas and the expected number of photoelectrons per ring is about 16 for $L = 25$ cm and $\beta \sim 1$.

Drift chamber in IDEA vs SiD@ILC

2T

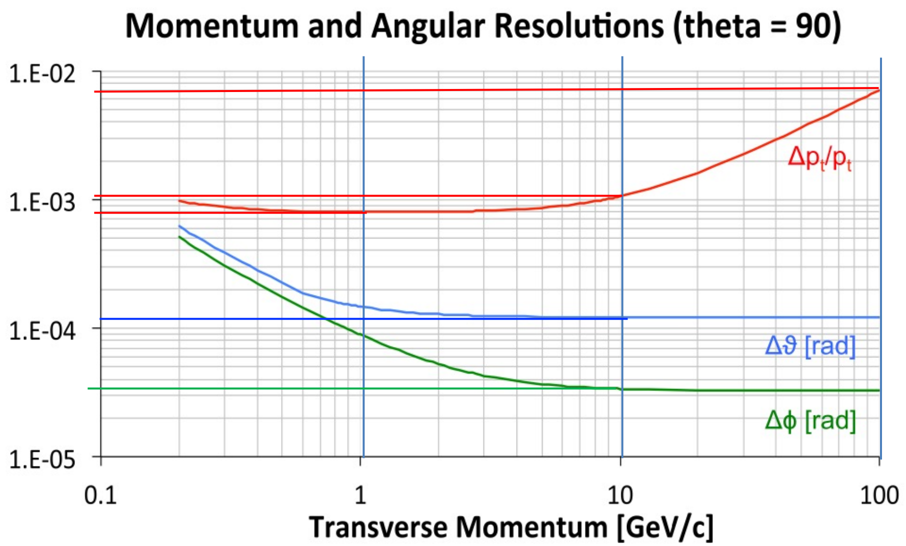

5T

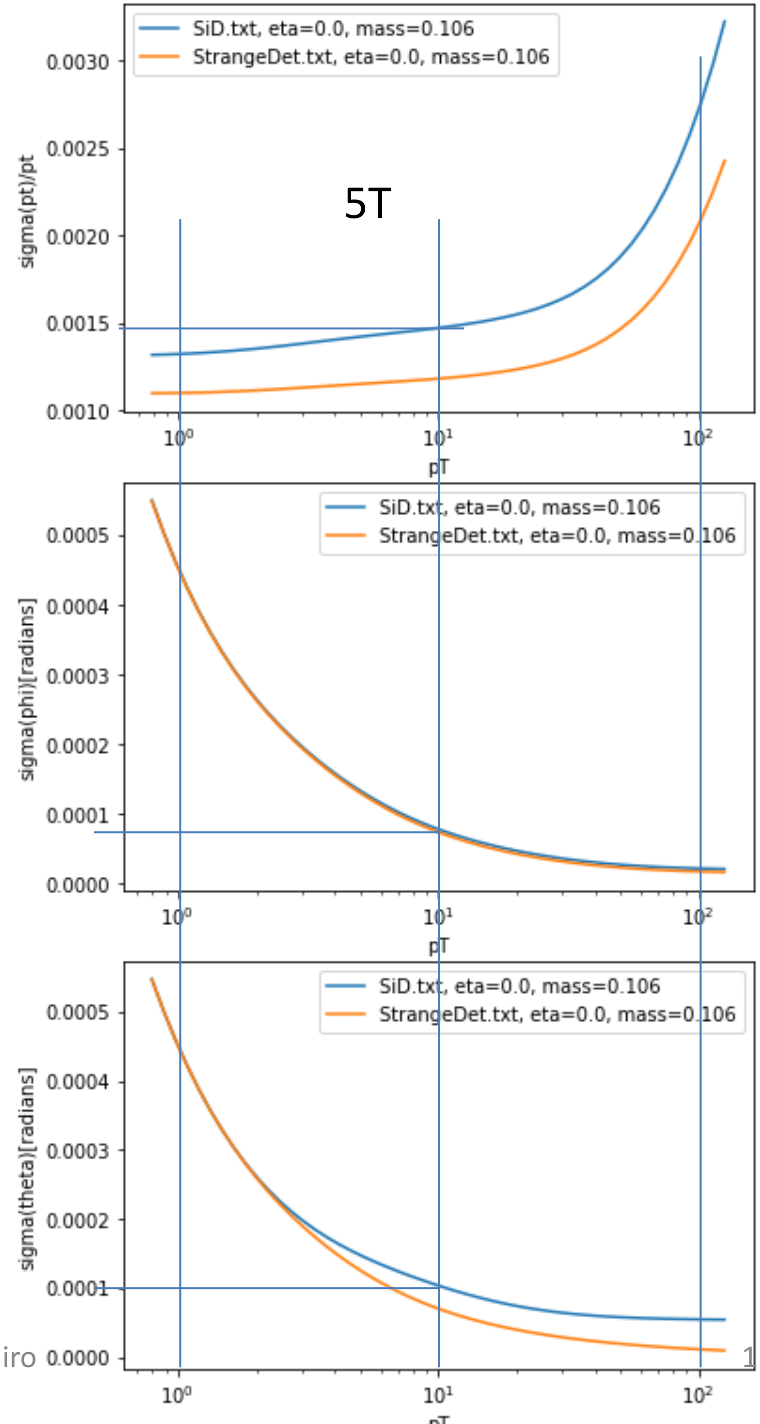

CLD@FCC vs SiD@ILC

2T

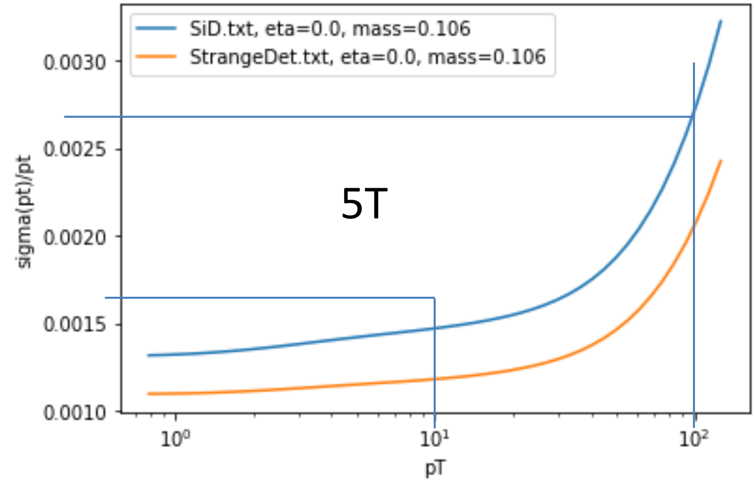

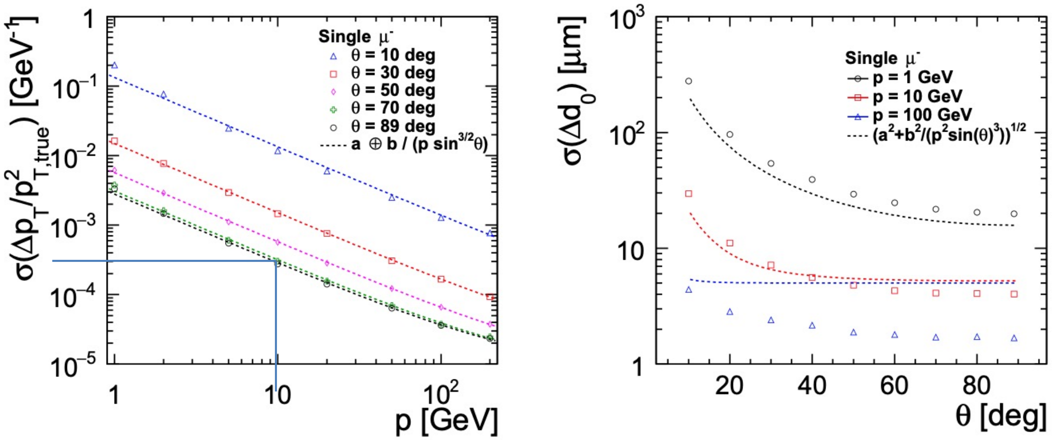

Fig. 7.6. Transverse momentum resolution for single muons as a function of momentum at fixed polar angle $\theta = 10, 30, 5070$ and 89° (left); Impact parameter resolution for single muons as a function of polar angle, at fixed momentum $p = 1$, 10, and 100 GeV (right). The dashed lines show the resolution goals.

Gaseous RICH with SiPMTs – performance

- Reach of PID performance depends on the **Cherenkov angle resolution**
  - Effects of chromaticity, bending of tracks, pixel size, tracking precision, noise, etc.).
- See Jerry's updates here and here

Total Cherenkov angle error in CRID for L = 45 cm

- Chromatic error with C_5F_{12}/N_2 gas and TMAE: ~0.4 mrad
- Pixel size effect: ~(0.15cm/√12)/(1.5 x 45 cm) ~0.48 mrad
- Error due to track bending: ~1-2 mrad
- Mirror misalignment: ~0.5 mrad
- Gas pressure variations, flow changes, distortions, etc.: a few mrad

- **Total: $\sigma_\theta \sim$ 4.3 mrad (per single photoelectron)**

Gaseous RICH with SiPMTs – performance

- Track bending effects: here
- Photon can be produced anywhere along the track segment along path L, which smears the Cherenkov angle
- Bending effects have been evaluated for various $\theta_{dip} = 90°, 86°, 70°$

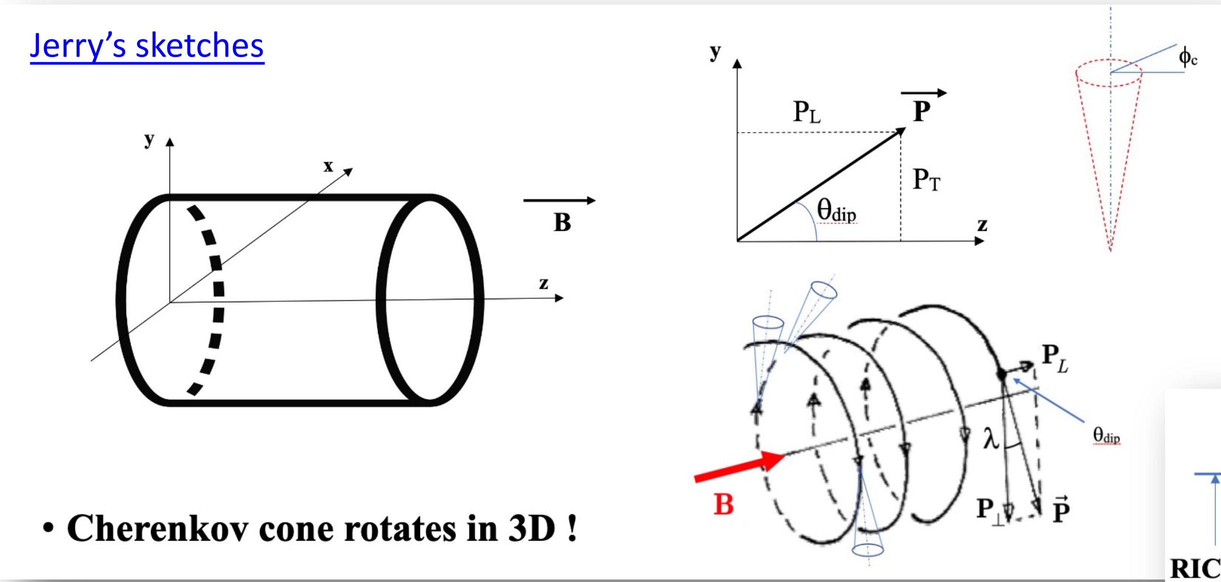

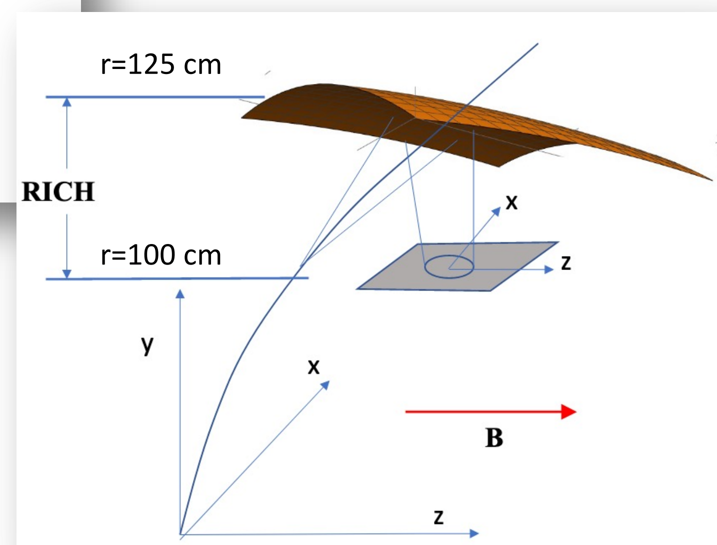

Smearing effects in CRID

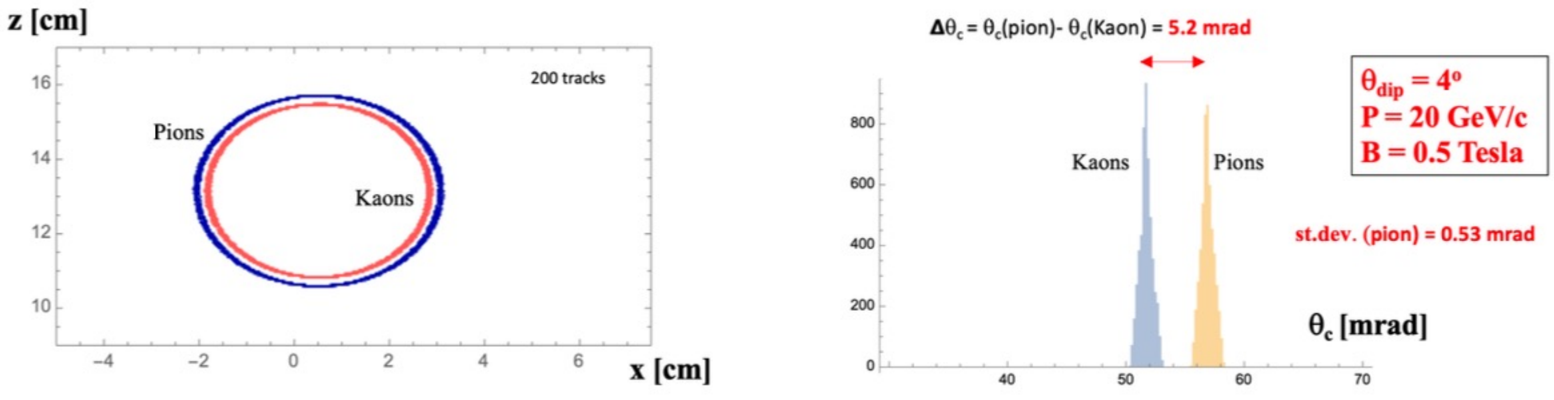

(a) (b)

Figure 23: Smearing effect in the SLD CRID gaseous RICH for $\theta_{\text{dip}} = 4°$, $p = 20\,\text{GeV}$, $B = 0.5\,\text{T}$, and $L = 45\,\text{cm}$. (a) Cherenkov rings imaged as 2D-hits, $\{x_{\text{final}}[i], z_{\text{final}}[i]\}$, in the SiPMT detector plane with no cuts and no fitting, showing the smearing effect alone. (b) A plot of the Cherenkov angle θ_c = (Cherenkov radius) / (focal length), where the Cherenkov radius $= \sqrt{(x_{\text{final}}[i] - x_0)^2 + (z_{\text{final}}[i] - z_0)^2}$. We tune x_0 and z_0 to obtain the smallest possible standard deviation.

Smearing effects in RICH at SiD/ILD

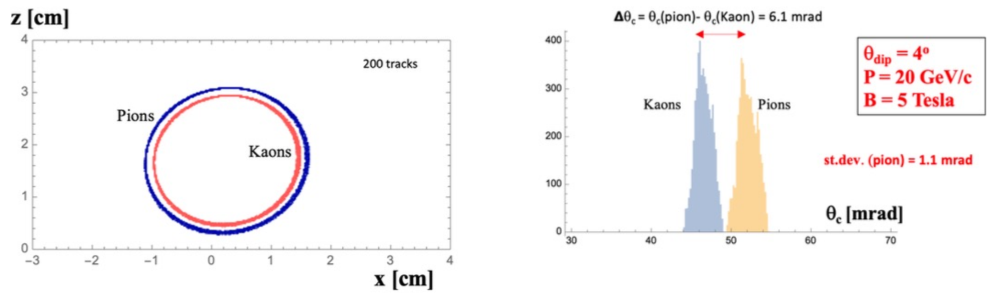

(a) $\theta_{\text{dip}} = 4^\circ$

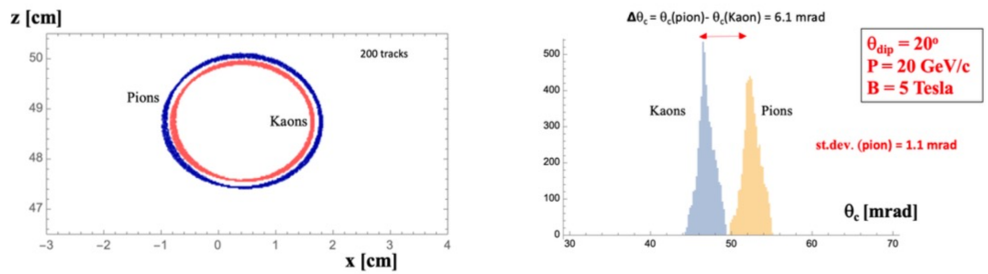

(b) $\theta_{\text{dip}} = 20^\circ$

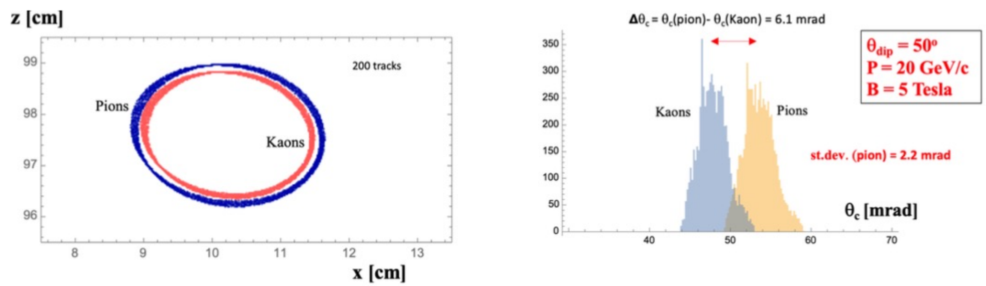

(c) $\theta_{\text{dip}} = 50^\circ$

Figure 24: Smearing effect in the SiD/ILD RICH for $p = 20\,\text{GeV}$, $B = 5\,\text{T}$, and $L = 25\,\text{cm}$. Cherenkov rings are imaged in the detector plane and plots of all 2D-hits, $\{x_{\text{final}}[i], z_{\text{final}}[i]\}$, with no cuts and no fitting are shown for (a) $\theta_{\text{dip}} = 4^\circ$, (b) $\theta_{\text{dip}} = 20^\circ$, and (c) $\theta_{\text{dip}} = 50^\circ$.

Smearing effects in RICH at SiD/ILD

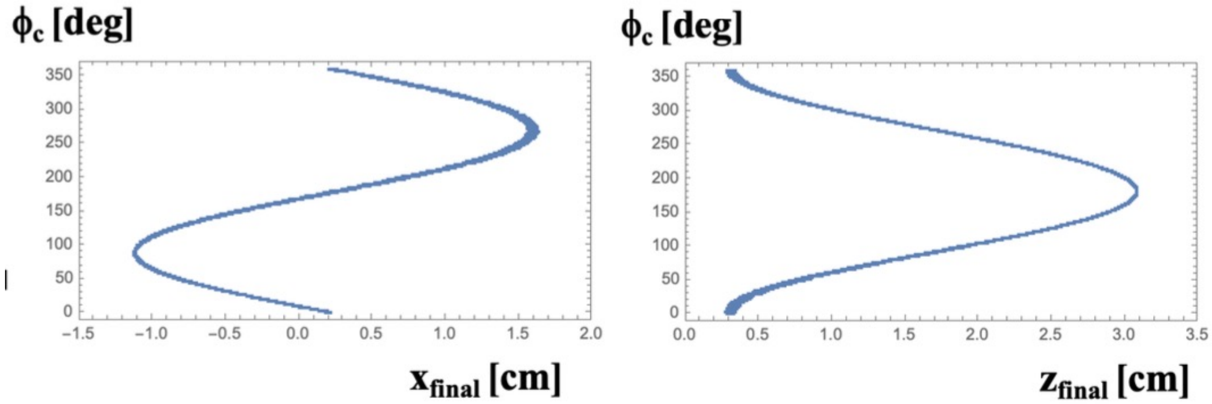

(a) $\theta_{\text{dip}} = 4°$

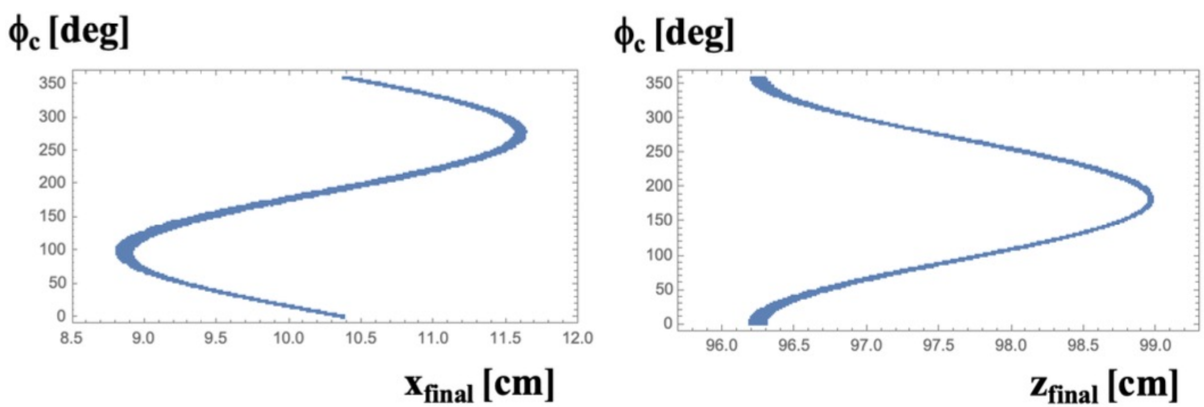

(b) $\theta_{\text{dip}} = 50°$

Figure 25: Smearing effect in the SiD/ILD RICH for $p = 20\,\text{GeV}$, $B = 5\,\text{T}$, and $L = 25\,\text{cm}$. The effects manifests itself as a variation in the Cherenkov angle resolution in x and z final positions as a function of Cherenkov azimuthal angle ϕ_c for (a) $\theta_{\text{dip}} = 4°$ and (b) $\theta_{\text{dip}} = 50°$.

Gaseous RICH with SiPMTs – performance

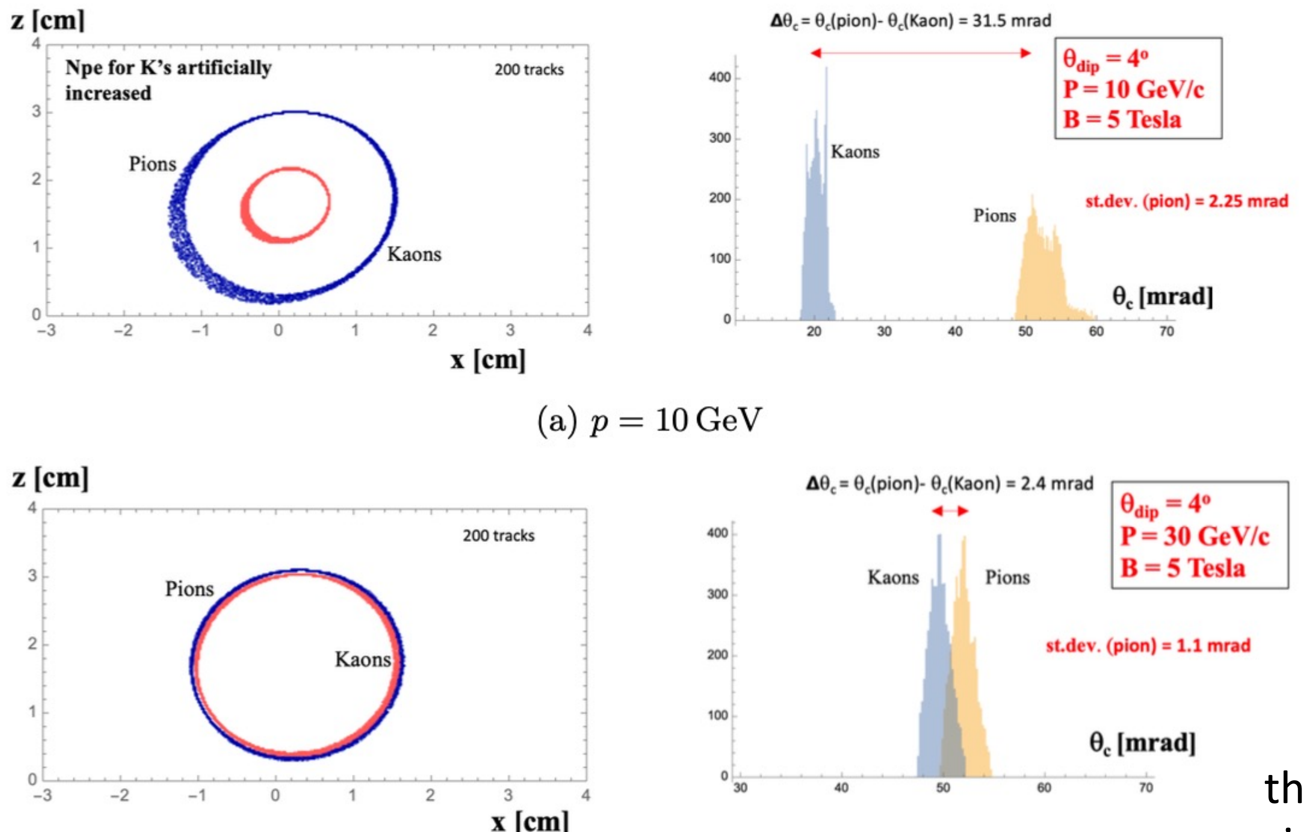

(a) $p = 10\,\text{GeV}$

(b) $p = 30\,\text{GeV}$

Figure 26: Smearing effect in the SiD/ILD RICH for $\theta_{\text{dip}} = 4°$, $B = 5\,\text{T}$, and $L = 25\,\text{cm}$. Cherenkov rings are imaged in the detector plane and plots of all 2D-hits, $\{x_{\text{final}}[i], z_{\text{final}}[i]\}$, with no cuts and no fitting are shown for (a) $p = 10\,\text{GeV}$ and (b) $p = 30\,\text{GeV}$.

the smearing effect is a significant contribution to PID at 30 GeV

Do SiPMTs actually work at 5 Tesla ?

- Contact Robert Klanner.
- **My question to him:** Did anybody tried to run SiPMTs at 4−5 Tesla ? Would they work ? In this application, the field would be tangential to face, i.e., SiPMTs would be placed on a barrel.

- **His answer:** No effects are expected. Measurements at 7 T:
  S. Espan a et al.,
  https://core.ac.uk/download/pdf/30044497.pdf (NIM)

  Greetings,
  Robert

11/17/21 J. Va'vra 3

Compressed Tracker

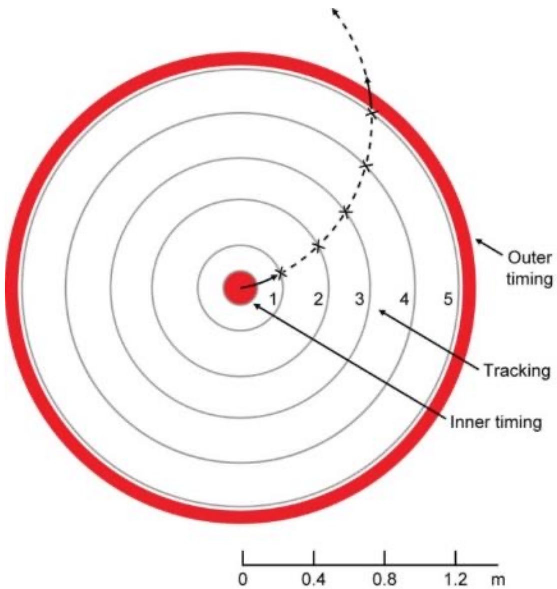

K Stefanov, Pixel tracker for SiD, LCWS2021

(first proposed at LCWS Sendai, 2008)

- **Tracking layers** are ~0.6% X_0 per layer
- 50 μm pixels, 5-bit amplitude digitisation, giving 5 μm precision in rϕ and z
  - This needs to be simulated – delicate balance between thickness of epi layer and depletion depth
- <100 W dissipation, so air cooled
- **Timing layers** (150 μm pixels, O(ns)) are close to ECAL, so material less critical
- 500 W dissipation, so air cooling may be OK (based on recent CLIC studies)
- Layout of Barrels 1-5 directly follow the old SiD microstrip tracker. It may be possible to reduce somewhat the radius of the pixel tracker, while preserving adequate performance for physics (to be simulated).

Comparison with previous SiD Tracker

SiD Vertexing+Tracking Detector

```
#X0    xyRes[m]    zRes[m]    radialPos[m]
#SiD based on ILC TDR https://arxiv.org/pdf/1306.6329.pdf
#vertexing detector (section 2.2 for position and for the material "The simulation described in the following chapters assume
s 0.1% radiation length per layer excluding cables and 20 x 20 µm pixels for the forward tracker disks"
0.001 5.0e-6 5.0e-6 0.014
0.001 5.0e-6 5.0e-6 0.022
0.001 5.0e-6 5.0e-6 0.035
0.001 5.0e-6 5.0e-6 0.048
0.001 5.0e-6 5.0e-6 0.060
#tracking detector (section 3.2 for position, 3.3.1 for material "Excluding overlaps, the material presented by a single barr
el layer is approximately 0.9% X0 for tracks at normal incidence")
#strips of 25um in the sensitive direction, so we use 7um pitch
0.009 7.0e-6 1.0e-4 0.22
0.009 7.0e-6 1.0e-4 0.47
0.009 7.0e-6 1.0e-4 0.72
0.009 7.0e-6 1.0e-4 0.97
0.009 7.0e-6 1.0e-4 1.22
```

Is this z resolution reasonable?

Strange Detector: same vertexing as SiD + squarePixelTracker

```
#X0    xyRes[m]    zRes[m]    radialPos[m]
#vertexing detector (section 2.2 for position and for the material "The simulation described in the following chapters assume
s 0.1% radiation length per layer excluding cables and 20 x 20 µm pixels for the forward tracker disks"
0.001 5.0e-6 5.0e-6 0.014
0.001 5.0e-6 5.0e-6 0.022
0.001 5.0e-6 5.0e-6 0.035
0.001 5.0e-6 5.0e-6 0.048
0.001 5.0e-6 5.0e-6 0.060

#tracking detector (using same positions as SiD)
0.006 5e-6 5e-6 0.22
0.006 5e-6 5e-6 0.47
0.006 5e-6 5e-6 0.72
0.006 5e-6 5e-6 0.97
0.006 5e-6 5e-6 1.22
```

Same position as in SiD, only changes are: rad length & resolutions

Momentum Resolution

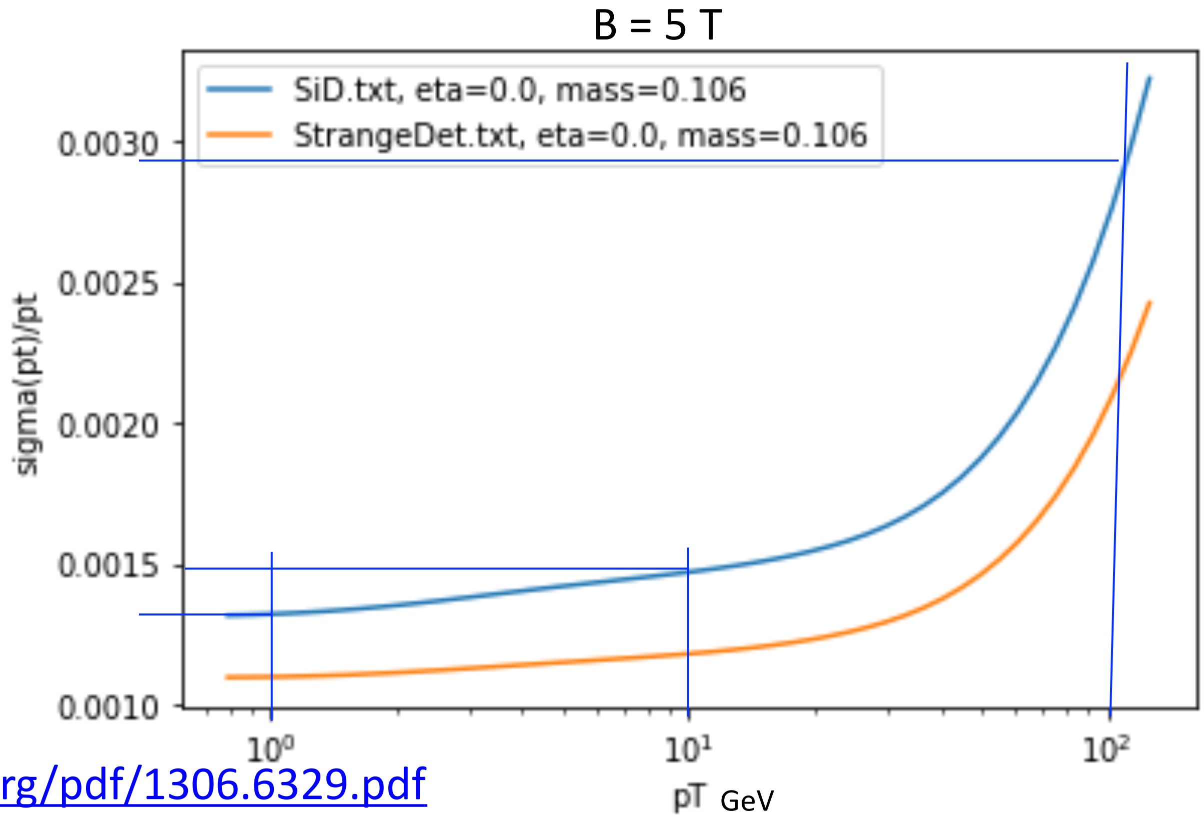

https://arxiv.org/pdf/1306.6329.pdf

Figure II-3.9 Normalised transverse momentum resolution for single-muon events in SIDLOI3 as function of momentum. The dashed lines indicate a fit to the parametrisation given in Equation II-3.1.

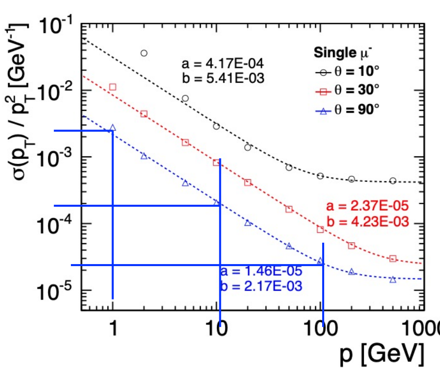

Theta=90 → eta=0, so focus on blue line for comparison

Results from our tool are compatible with ILC TDR

(please note that ILC TDR shows sigma(pT)/pt2, while we show sigma(pT)/pt)

d0 Resolution

B = 5 T

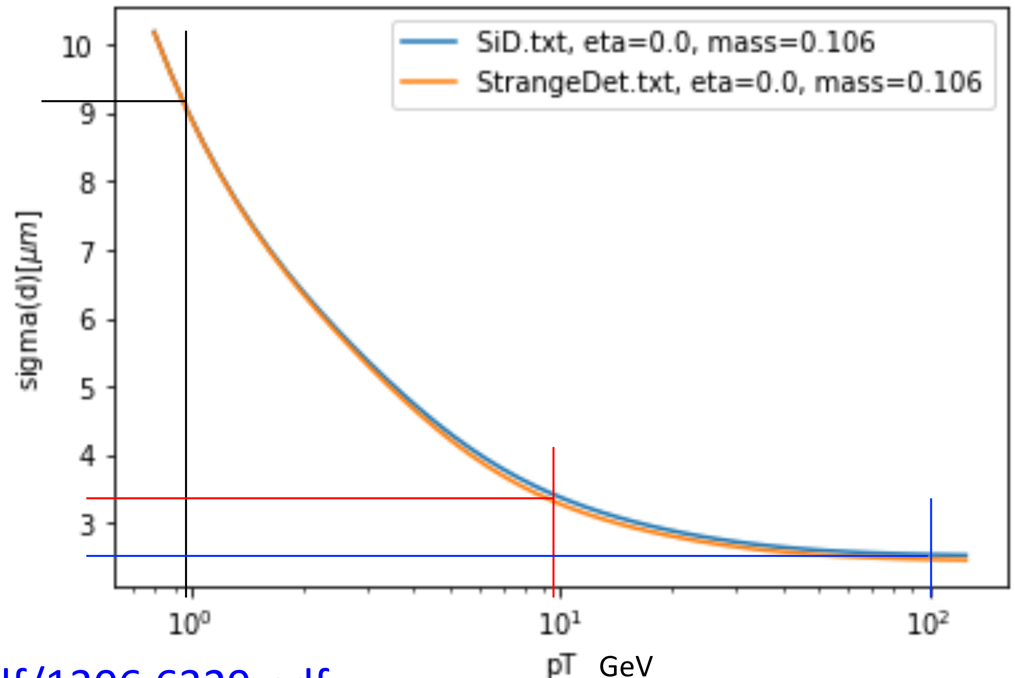

https://arxiv.org/pdf/1306.6329.pdf

Figure II-3.10
Impact parameter resolution $\sigma(d_0)$ (left) and $\sigma(z_0)$ (right) for single muon events in SIDLOI3 as function of the polar angle θ.

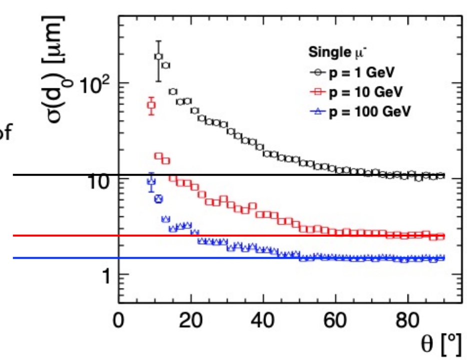

Theta=90 → eta=0

Results from our tool are compatible with ILC TDR

z Resolution

B = 5 T

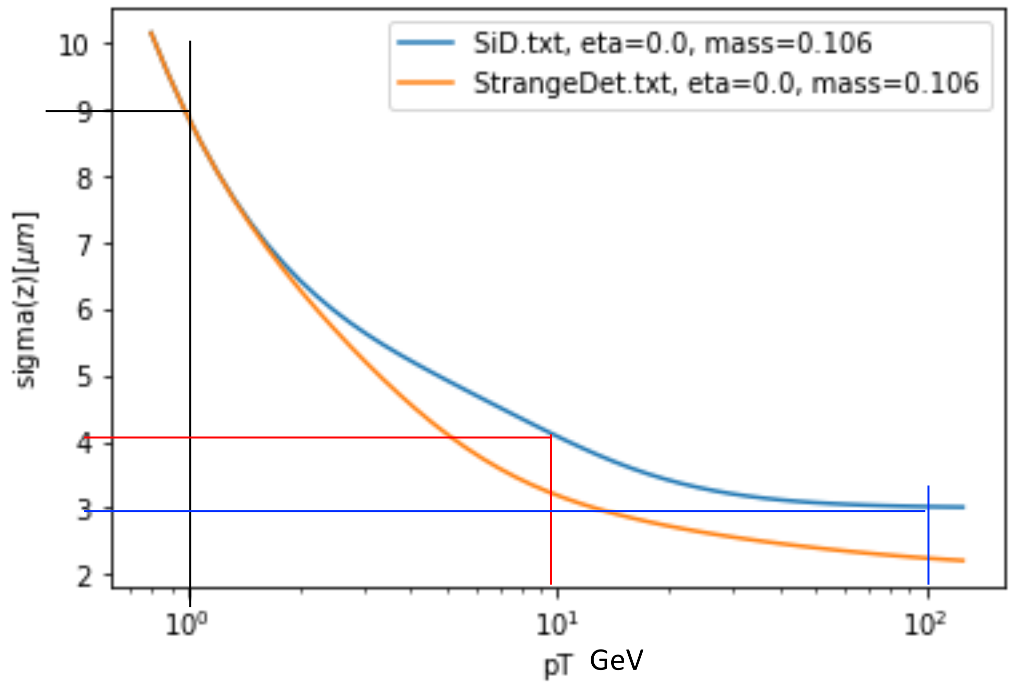

https://arxiv.org/pdf/1306.6329.pdf

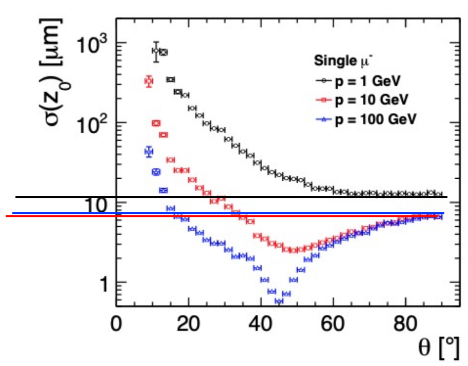

Theta=90 → eta=0

Results from our tool are compatible with ILC TDR at low pT, not very precise at higher momentum

TMAE

https://books.google.fr/books?id=V9o6DAAAQBAJ&pg=PA60&lpg=PA60&dq=TMAE+RICH&source=bl&ots=gFHVLGOUlp&sig=ACfU3U0n6oeMOqP-DK-bDqbA2ZzRQjXXyw&hl=it&sa=X&ved=2ahUKEwj80MTxmunzAhUKKBoKHf33AQgQ6AF6BAgLEAM#v=onepage&q=TMAE%20RICH&f=false

2.4 TMAE

For many years, photosensitive gaseous detectors used the photosensitive vapours described above: benzene, toluene, TMA, TEA or EF. Other vapours were also tested, but with less favorable results, e.g. cis-2-butene (E_i= 9.35 eV), acetone (E_i= 9.65 eV), ammonia (E_i= 10.3 eV), isobutane (E_i= 10.6 eV), DMA (E_i=8.3 eV) etc.

The real boom in this field happened when David Anderson introduced tetrakis (dimethylamino) ethylene, a vapour more often called TMAE and pronounced "Tammy" (Anderson, 1980). TMAE has a photoionization potential as low as 5.36 eV, and it is photosensitive to photons with a wavelength of up to 231 nm. It is an oily fluid with a melting point of -4°C. It was originally used and manufactured by US Naval Ammunition Department (Nakato, 1972). TMAE oxidizes rapidly in air and produces a strong fluorescence light. In large quantities it can light up the whole sky, which is probably why it was of interest for military use.

During oxidation in air TMAE also produces a dense white smoke. Actually, a bottle of TMAE closed down the international airport of El Paso, Texas, for 7 hours in 1993. One of the authors (T. Francke) had a bottle of TMAE shipped from CERN to the US to be used in a space experiment. The transportation firm dropped the package at El Paso airport and the bottle of TMAE broke. Unfortunately, it broke just next to an air inlet for the ventilation system and the thick white smoke quickly filled the whole airport. No one was injured. This put TMAE on the front page of El Paso Times.

G. Charpak describes his first encounter with TMAE in his book "Research on particle imaging detectors" (Charpak, 1995):

He (D. Anderson) had found a prolific stock in the US Army of tetrakis (dimethylamino)-ethylene (TMAE), which has the lowest ionization potential, 5.36 eV, of all known vapours. In the liquid form it was easy to obtain in large quantities. The vapour pressure was easy to control at moderate temperatures and it had considerable quantum efficiency in the VUV range. I invited him to join our group at CERN. He came with his own counter and found the support of a group which had some expertise in gaseous detectors. He discovered with us that in high-energy physics the small overlap between the emission spectrum of BaF_2 and the range of sensitivity of TMAE vapour was sufficient for the conception of a new style of fast electromagnetic calorimeters.

However, TMAE found its most important use in RICH detectors rather than in calorimeters. The low ionization threshold of TMAE allowed a wide choice of solid, liquid and gaseous Cherenkov radiators combined with cheap, large area fused quartz windows. One of the most impressive implementations of a TMAE based detector was the DELPHI RICH detector built at CERN. This detector as well as some other Cherenkov detectors which used TMAE will be described in great detail in the application chapters.

The TMAE vapour pressure at room temperature is not as high as for TMA and TEA, see Figure 8, but it is much higher than for EF. Nevertheless, for efficient recording of UV light a detector filled with TMAE should be heated, typically to 40-60 °C.

SLD

0.5 T

https://indico.slac.stanford.edu/event/6617/contributions/1443/attachments/683/1978/s-tag-SLD.pdf

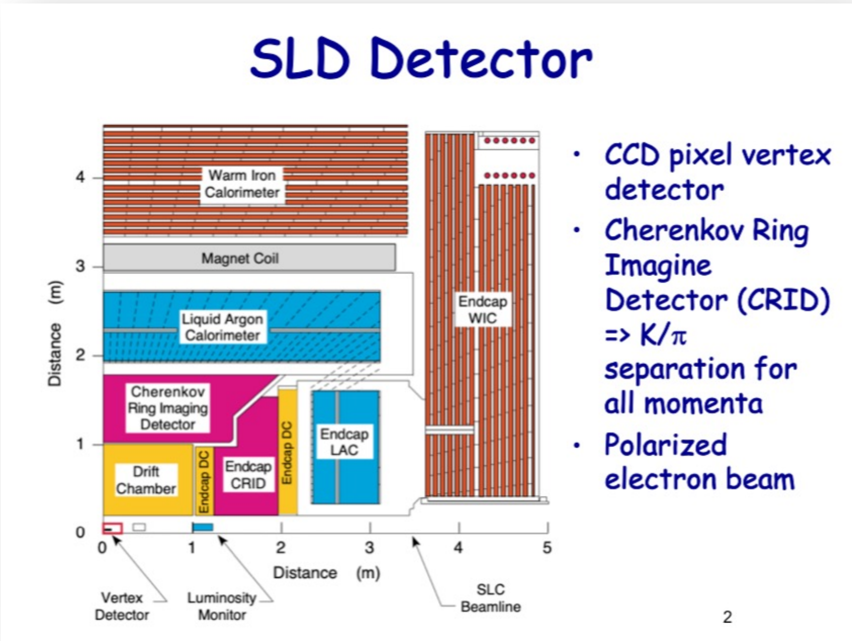

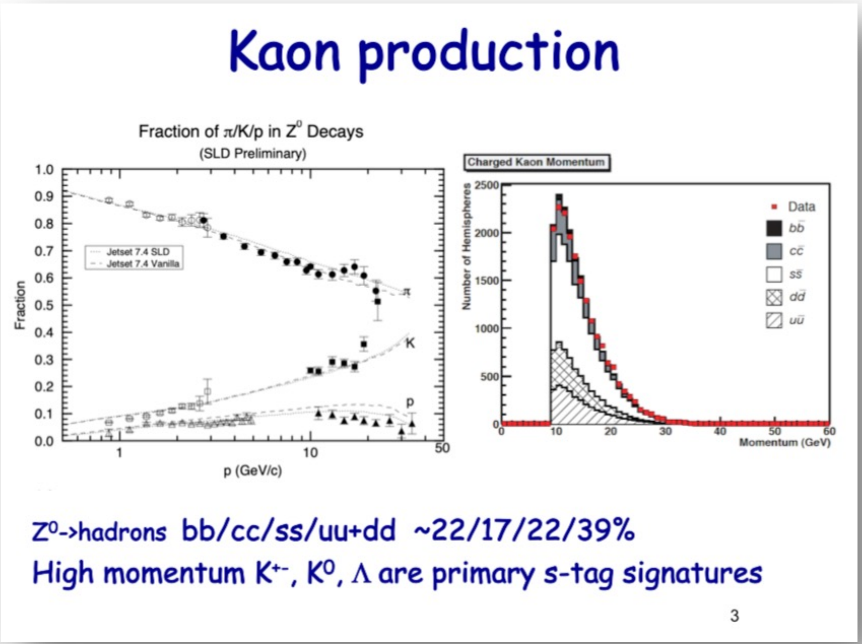

SLD CRID Perfomance

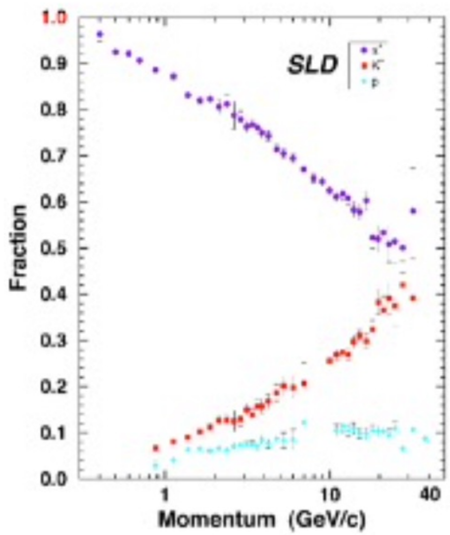

(a)

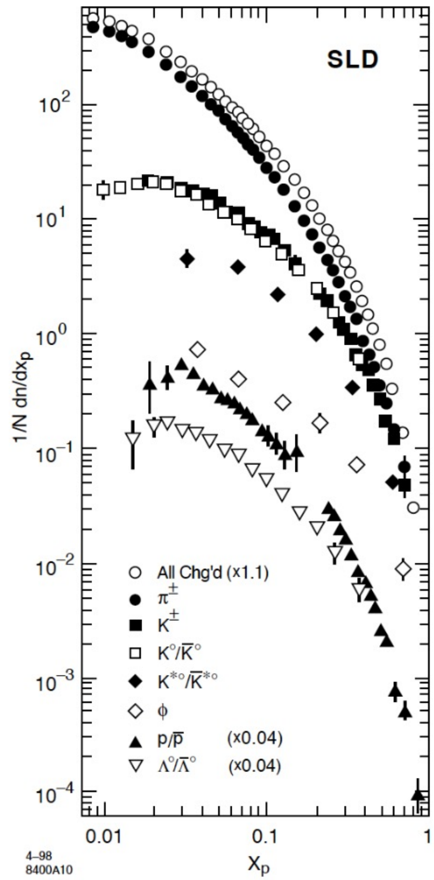

(b)

Figure D1: (a) $\pi/K/p$ fractions determined by the SLD CRID [63]. (b) Differential cross sections as a function of hadronic momentum fraction x_p per hadronic Z^0 decay, by all SLD detectors [64].

ILD & SiD

https://linearcollider.org/files/images/pdf/Executive%20Summary.pdf

SiD

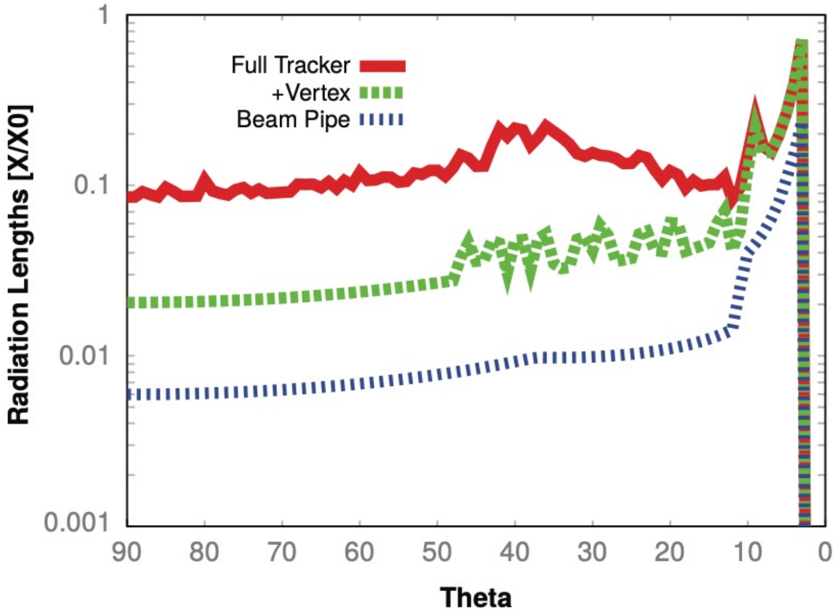

ILD

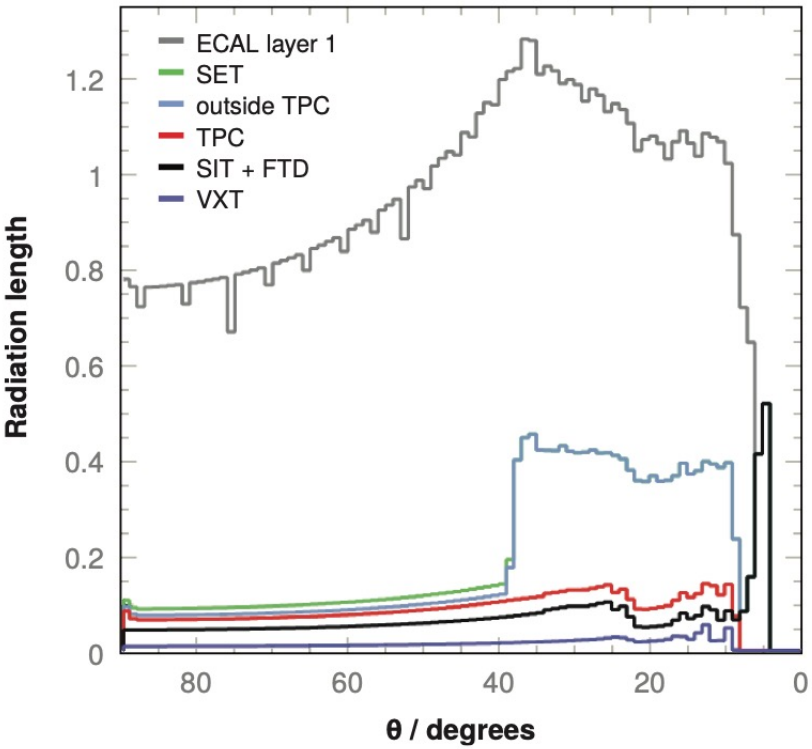

Two examples: IDEA @ FCC-ee & ILD @ ILC

IDEA @ FCC-ee

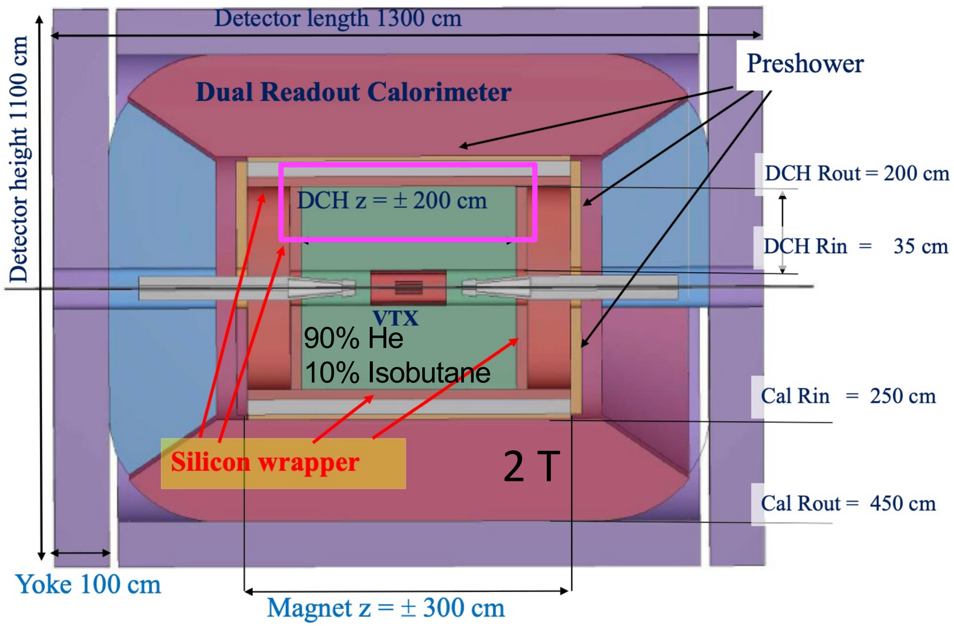

e2019-900045-4

ILD @ ILC

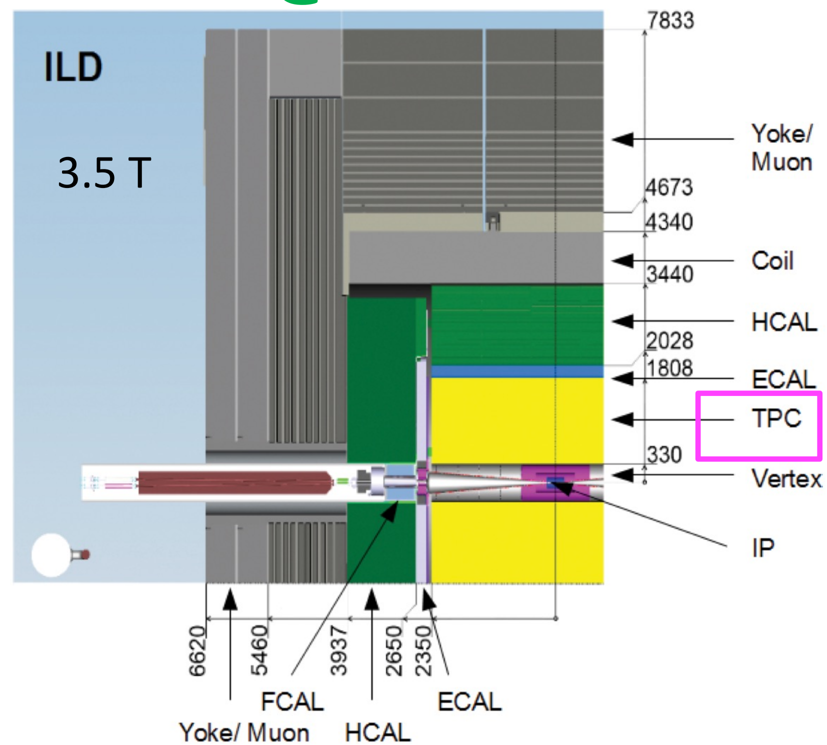

1912.04601

Two examples:
IDEA @ FCC-ee & ILD @ ILC

IDEA @ FCC-ee

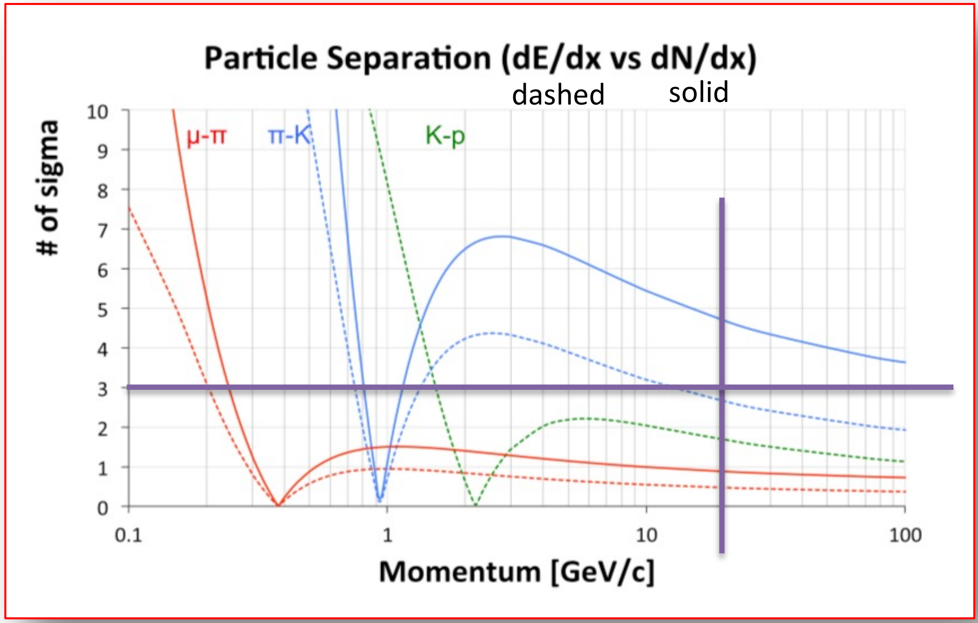

Analitical calculations

[e2019-900045-4](e2019-900045-4)

ILD @ ILC

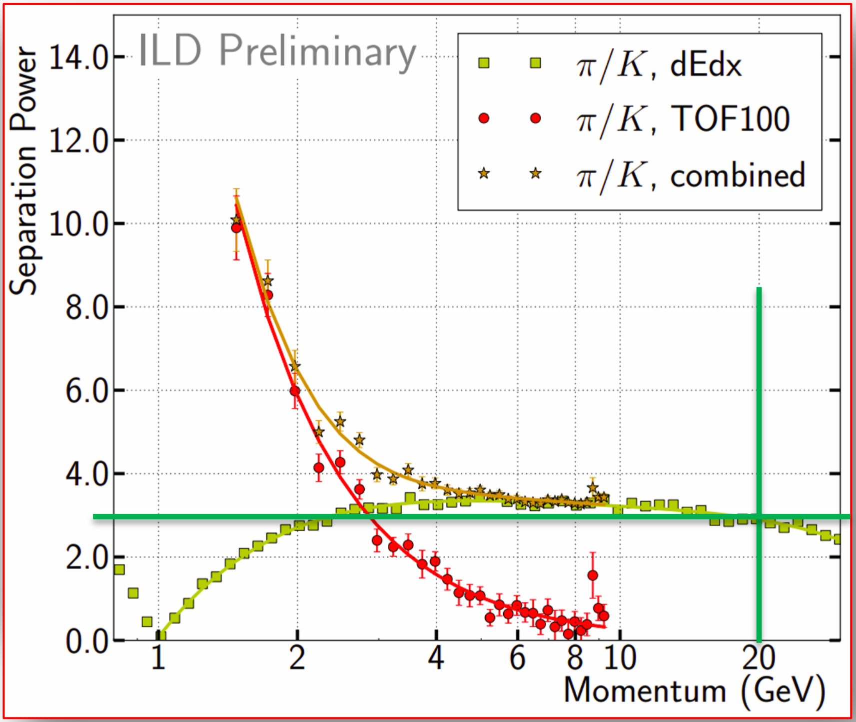

[1912.04601](1912.04601)

Comparable dE/dx performance at e.g. 20 GeV, boost from dN/dx

Strange Tagging with IDEA

Variable	Description
	Kinematics
$E_{\text{const}}/E_{\text{jet}}$	energy of the jet constituent divided by the jet energy
θ_{rel}	polar angle of the constituent with respect to the jet momentum
ϕ_{rel}	azimuthal angle of the constituent with respect to the jet momentum
	Displacement
d_{xy}	transverse impact parameter of the track
d_z	longitudinal impact parameter of the track
SIP_{2D}	signed 2D impact parameter of the track
$\text{SIP}_{\text{2D}}/\sigma_{\text{2D}}$	signed 2D impact parameter significance of the track
SIP_{3D}	signed 3D impact parameter of the track
$\text{SIP}_{\text{3D}}/\sigma_{\text{3D}}$	signed 3D impact parameter significance of the track
d_{3D}	jet track distance at their point of closest approach
$d_{\text{3D}}/\sigma_{d_{\text{3D}}}$	jet track distance significance at their point of closest approach
C_{ij}	covariance matrix of the track parameters
	Identification
q	electric charge of the particle
$m_{\text{t.o.f.}}$	mass calculated from time-of-flight
dN/dx	number of primary ionisation clusters along track
isMuon	if the particle is identified as a muon
isElectron	if the particle is identified as an electron
isPhoton	if the particle is identified as a photon
isChargedHadron	if the particle is identified as a charged hadron
isNeutralHadron	if the particle is identified as a neutral hadron

Strange Tagging with IDEA

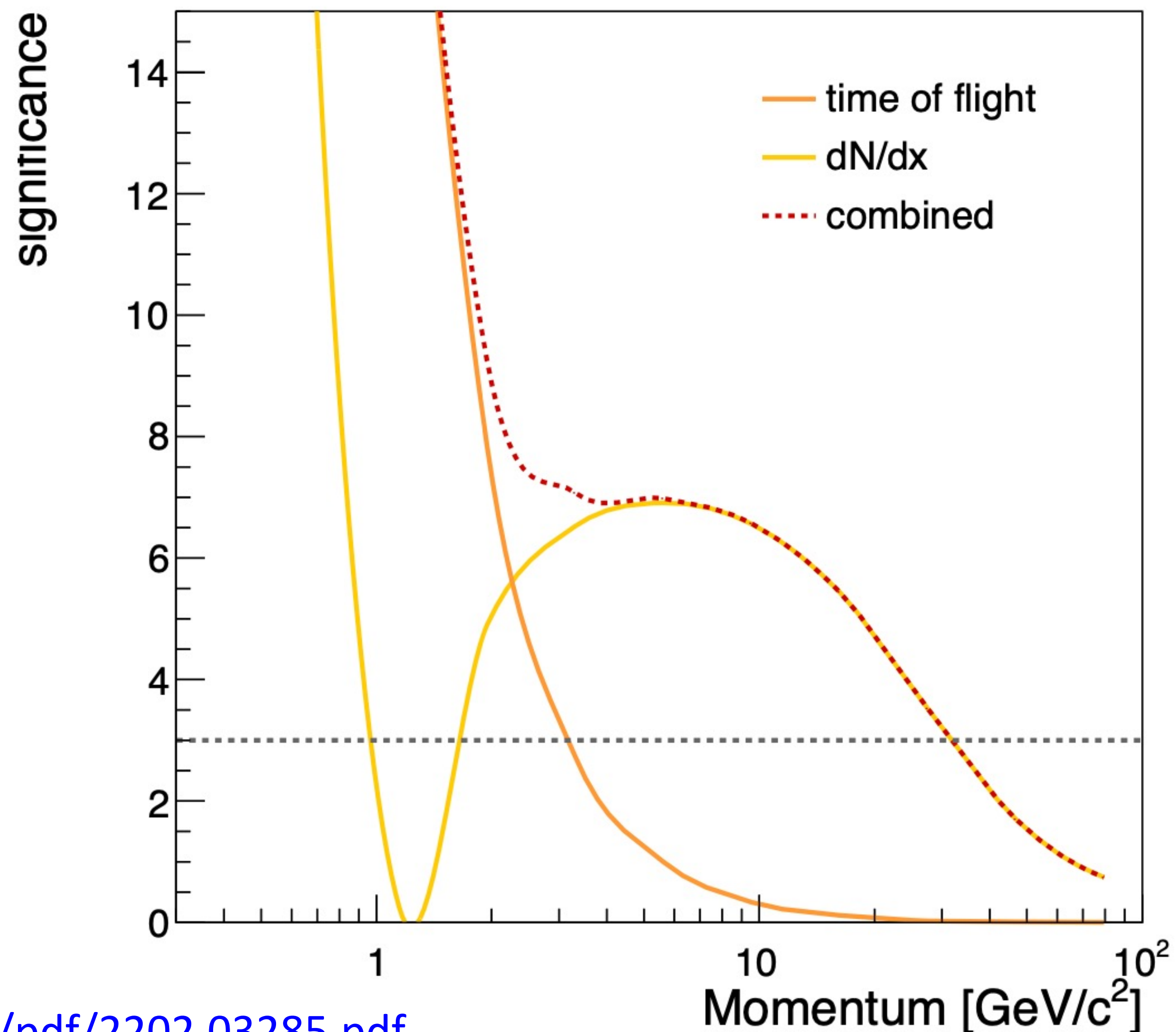

https://arxiv.org/pdf/2202.03285.pdf

Strange Tagging with IDEA

https://arxiv.org/pdf/2202.03285.pdf

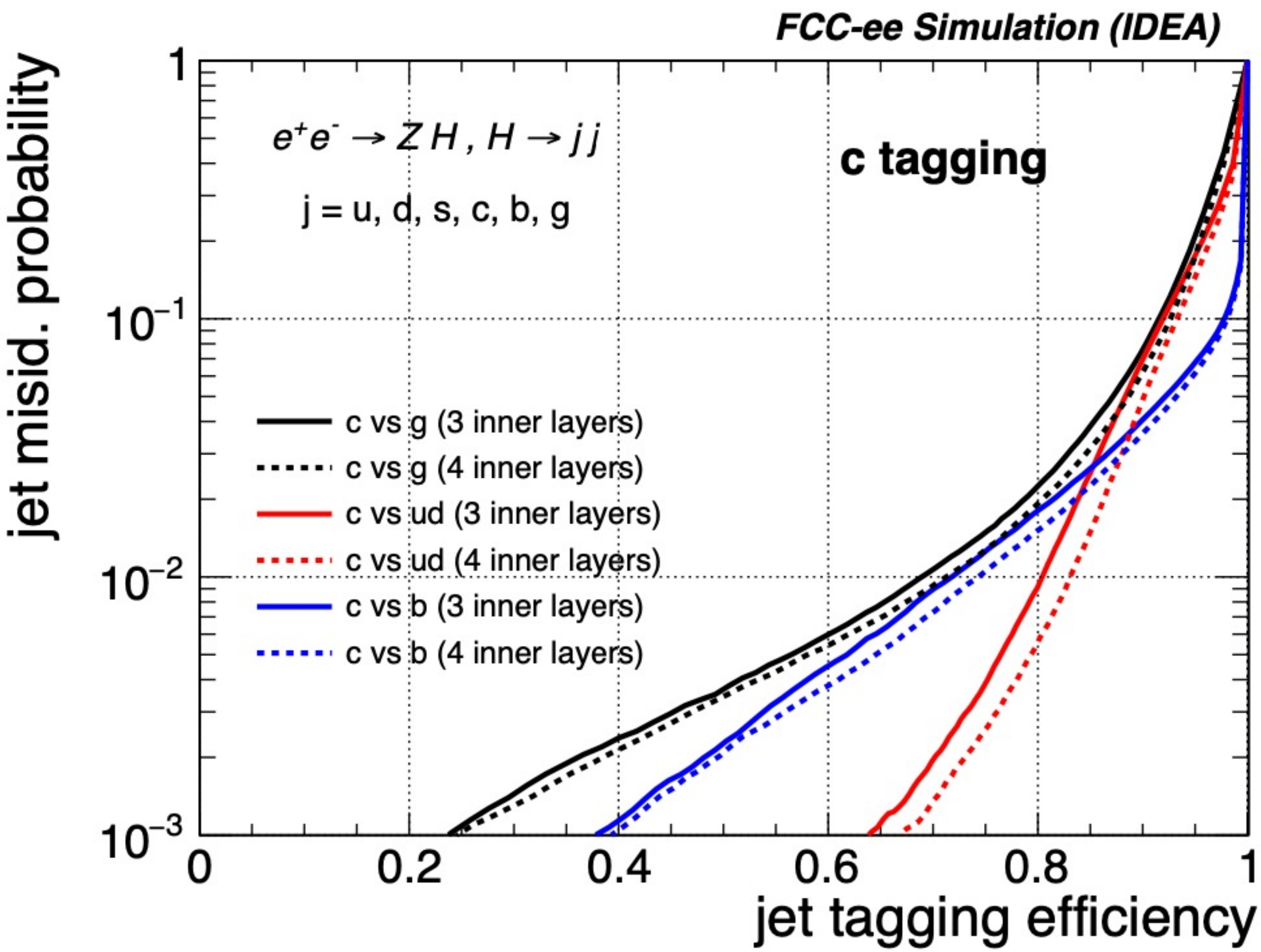

3 layer config: 1st layer at 1.5 cm

4 layer config: 1st layer at 1.0 cm

Strange Tagging with IDEA

2202.03285

- Use a Graph Neural Net *ParticleNetIdea*: jets represented as an un-ordered set of particles
- Train on $(Z \to inv)(H \to qq/gg)$ samples, **per-jet and per-particle level inputs** & **variables** (kinematics, displacement, identification)
- TOF and dN/dx (**3σ < 30 GeV**) considered
- **Fast Simulation and Fast Tracking**

Could probably be removed and show only the ILD work

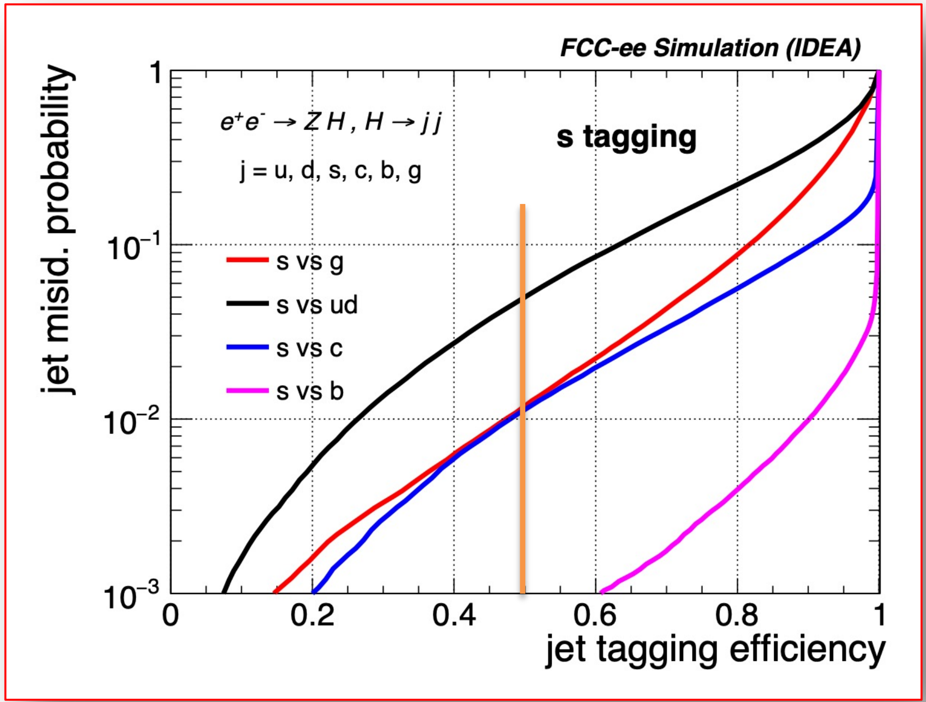

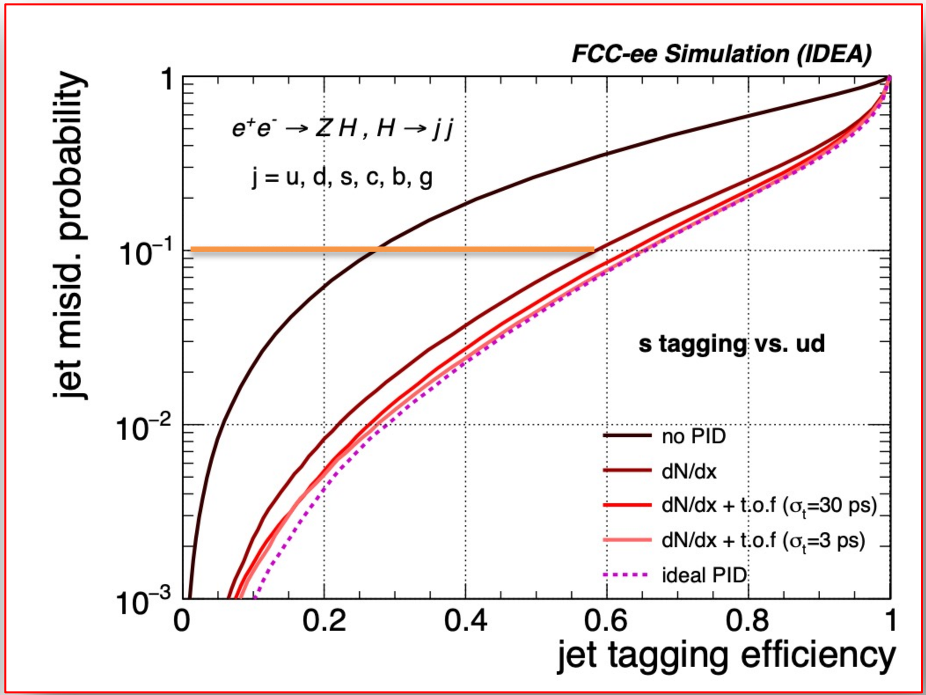

No PID to PID with dN/dx → at fixed mistag, **efficiency doubles**

Gluon Tagging with IDEA

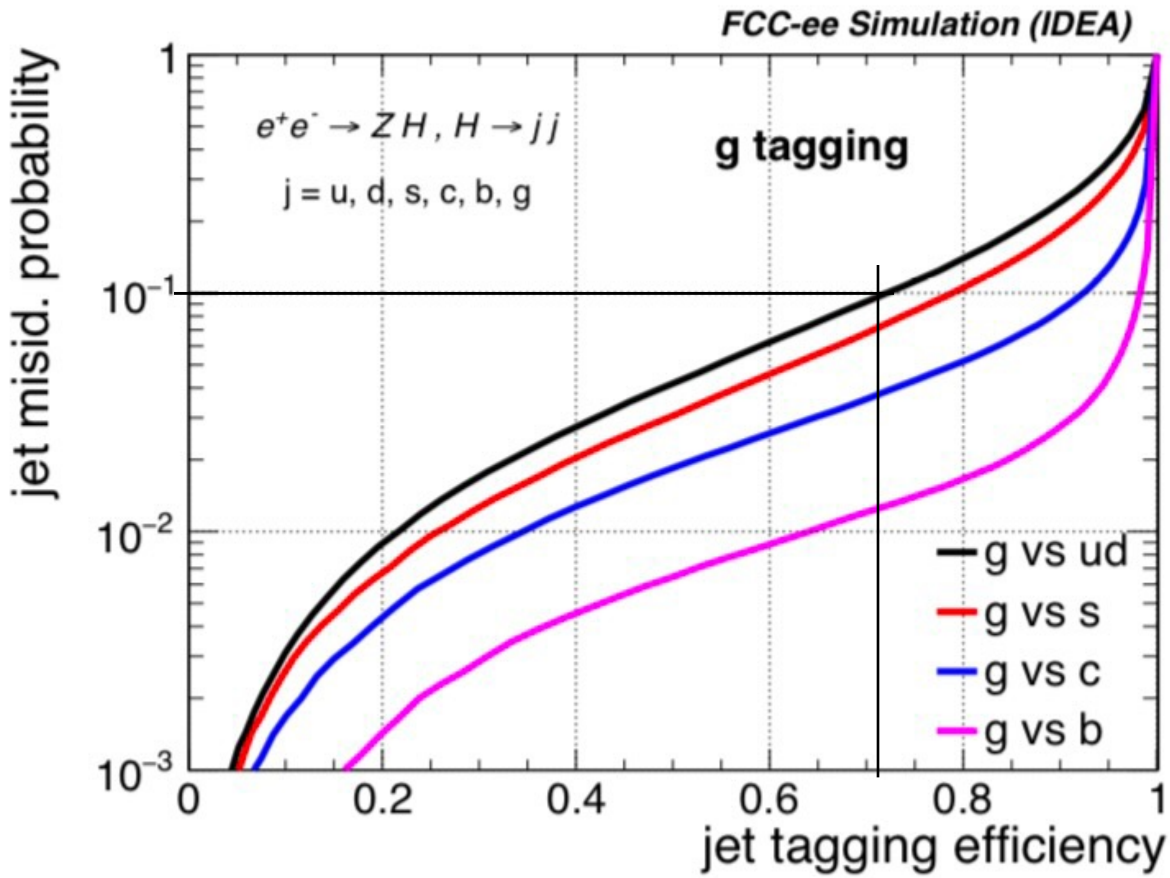

dN/dx

F. Grancagnolo's slides

2105.07064

- Cluster counting (**dN/dx**): counting the multiplicity of the primary ionization clusters produced along the track in gaseous detectors

Move to back-up? And only add a note in the previous slide aboyt the existing of this method

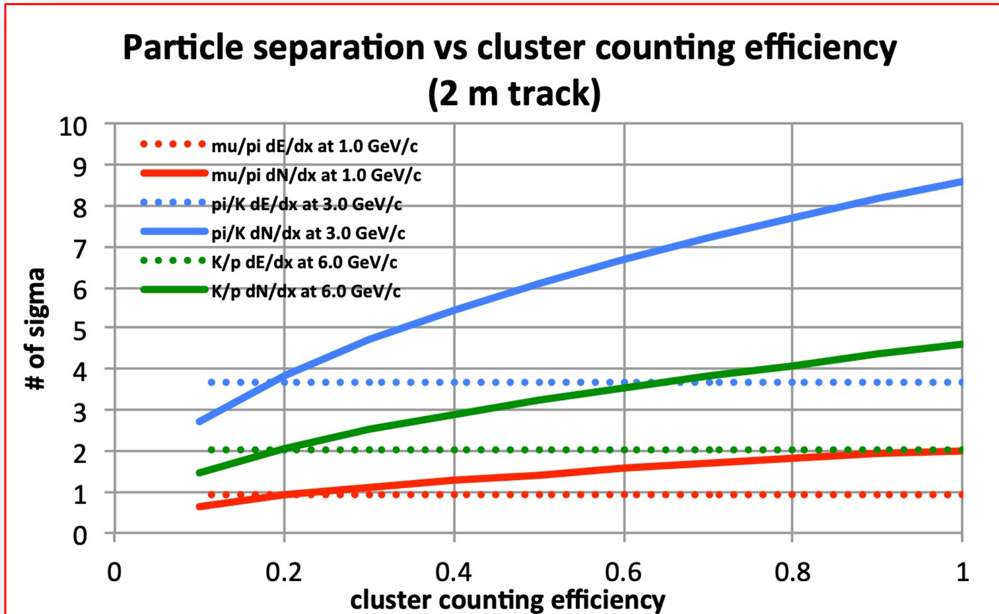

Potentially, **x2 better** than **dE/dx**

- **σ(dE/dx)/(dE/dx) =4.3%**
- 80% cl.counting efficiency **σ(dN_{cl}/dx)/(dN_{cl}/dx) =2.3%**

dN/dx

- Cluster counting (**dN/dx**): counting the multiplicity of the primary ionization clusters produced along the track in gaseous detectors

Move to back-up? And only add a note in the previous slide aboyt the existing of this method

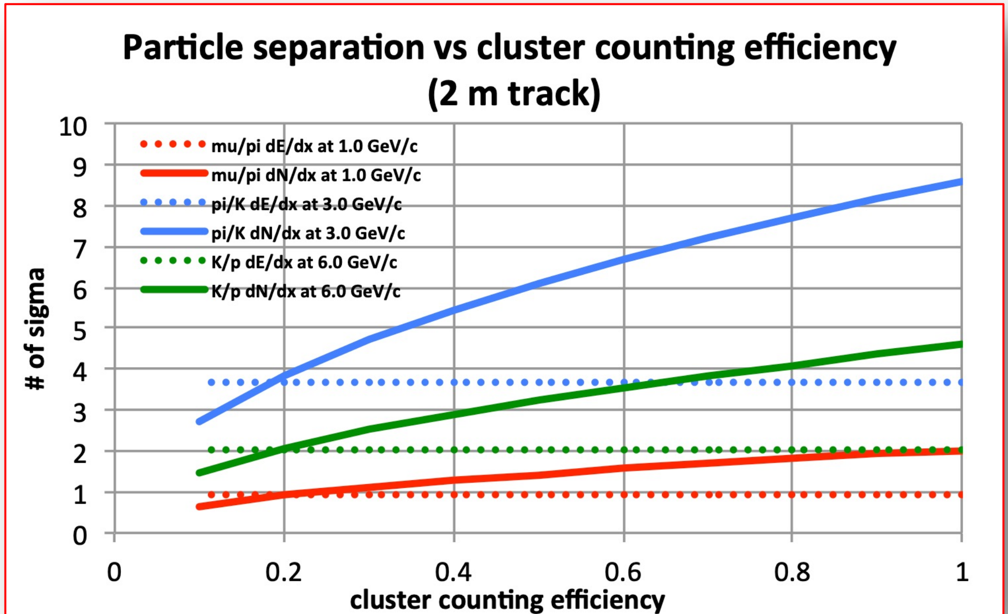

- **Based on analytical calculations, longstanding efforts to demonstrate benefits and feasibility!**
- **Garfield++** can describe properties and performance of a drift chamber single cell, but not suitable to simulate large-scale detectors and study collider events, which instead relies on **Geant4**
- **Various algorithms studied, none of them reproduces the predictions perfectly → Set up test beams**
  - **Use the results to tune cluster counting in Delphes and Full Sim**

Potentially, **x2 better** than **dE/dx**

- **σ(dE/dx)/(dE/dx) =4.3%**
- 80% cl.counting efficiency **σ(dN_{cl}/dx)/(dN_{cl}/dx) =2.3%**

Sketching the ideal detector…

2203.07535

TOF or dE/dX have great PID capabilities, but cover only the low momentum regime (unless very large tracker volumes are used)

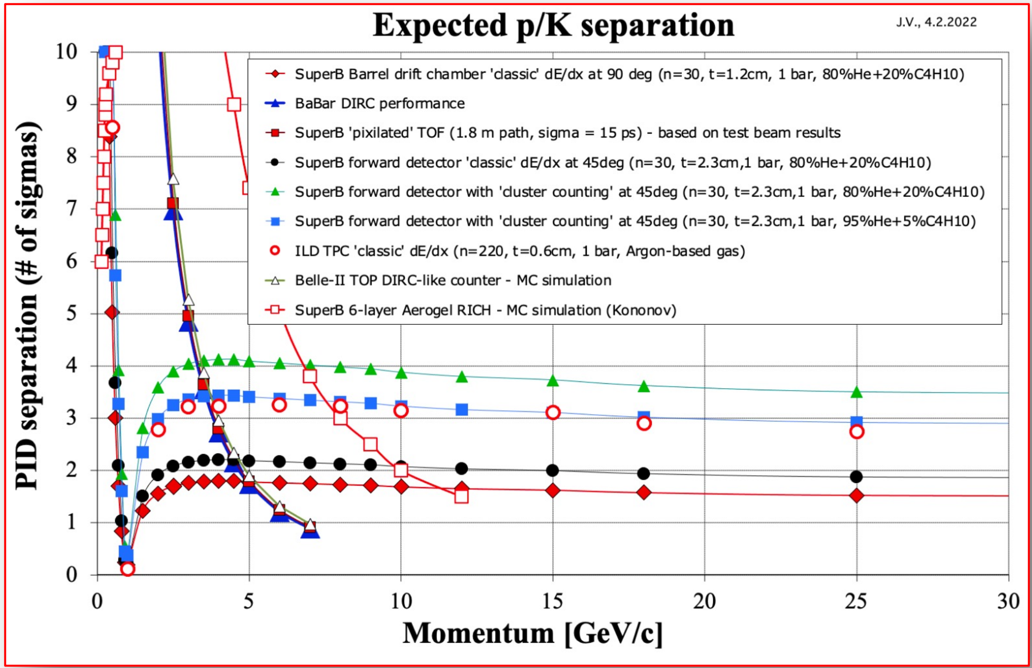

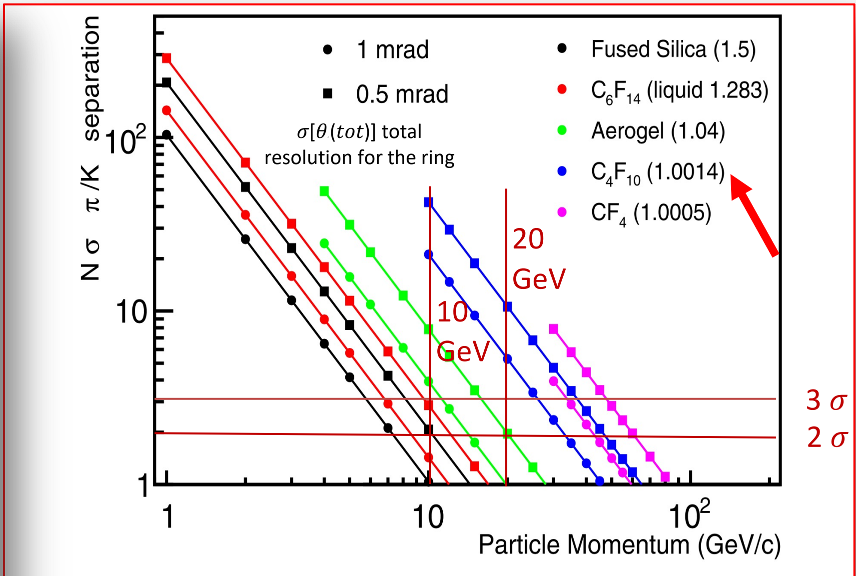

Fig. 2. The number standard deviations in $\pi - K$ separation versus momentum for different radiators and two different Cherenkov angle resolutions.

A. Papanestis, NIM,A 952 (2020) 162004

Ring Imaging Cherenkov Detectors (RICH) is a favourable approach at high momentum

TOF for various resolutions

https://agenda.linearcollider.org/event/8067/contributions/43101

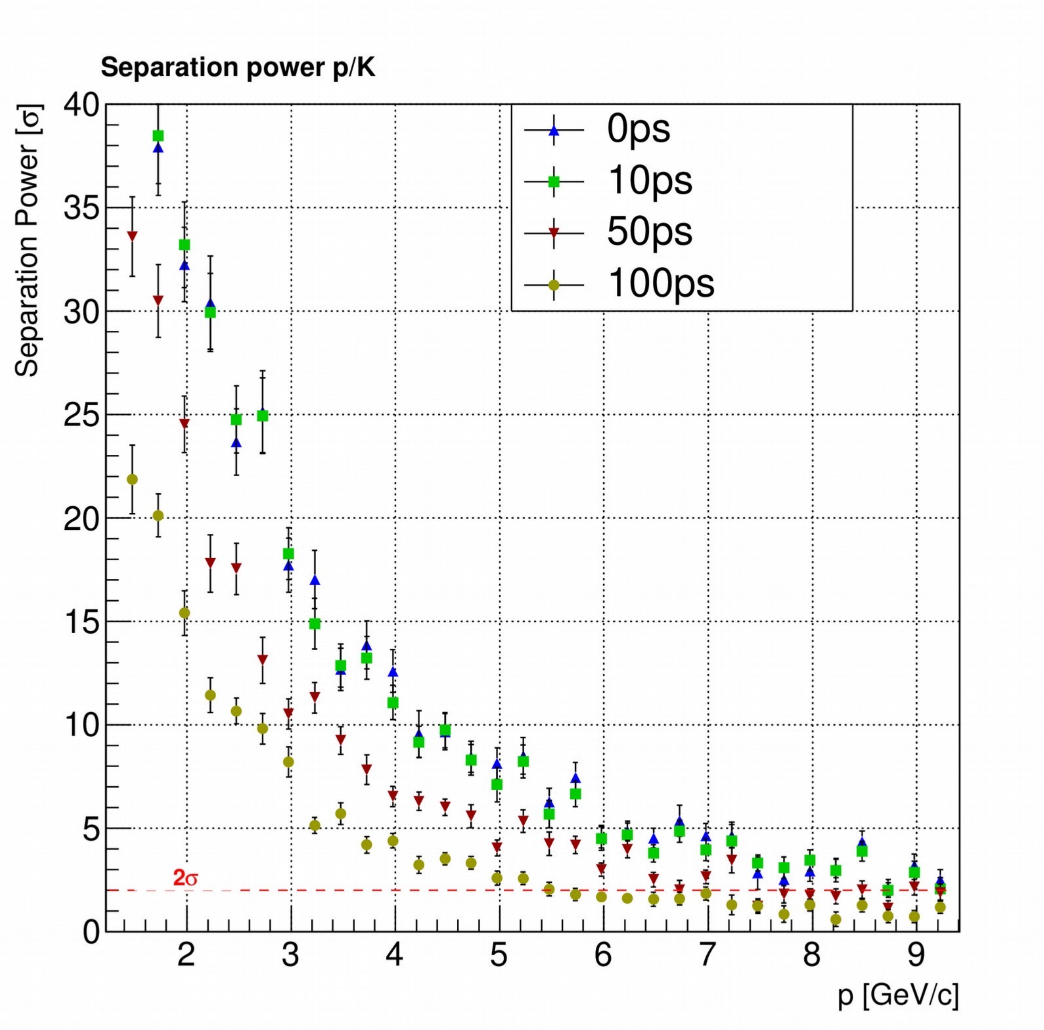

Sketching the ideal detector…

Cherenkov radiation is light produced when a charged particle traverses a medium with a refractive index at a speed higher than the speed of light in that medium. The threshold speed for the production of Cherenkov radiation depends on the refractive index and is given by the equation:

$$\beta_{th} = \frac{v_{th}}{c} = \frac{1}{n(\lambda)} \tag{1}$$

Where n is the refractive index and $n(\lambda)$ shows the dependence on the wavelength.

The light is emitted at an angle that depends on the particle speed and refractive index:

$$\cos\theta_c = \frac{1}{\beta n(\lambda)} \tag{2}$$

The emitted photon spectrum is continuous, the number of photons per unit length depends on the square of the charge and is given by the equation:

$$\frac{N_{photons}}{L} = \frac{\alpha}{\hbar c} Z^2 \int \sin^2\theta_c(E)\, dE \tag{3}$$

Maximizing the number of detected photons is of particular interest as it can improve the measurement of the Cherenkov angle and the particle identification.

A. Papanestis, NIM,A 952 (2020) 162004

Sketching the ideal detector…

For two particles well above the Cherenkov threshold the significance of the identification depends on the particle masses, the refractive index of the radiator and the resolution of Cherenkov angle measurement and can be approximated with [3]:

$$N_\sigma \approx \frac{|m_1^2 - m_2^2|}{2P^2\sigma[\theta_c(tot)]\sqrt{n^2-1}} \tag{4}$$

where N_σ is the number of σ in particle differentiation, P is the particle momentum and $\sigma[\theta_c(tot)]$ is the total resolution for the ring and includes the chromatic effect and the number of photons per ring.

A. Papanestis, NIM,A 952 (2020) 162004

RICH

Mpion = 140 MeV
Mkaon = 500 MeV
Mproton = 1 GeV

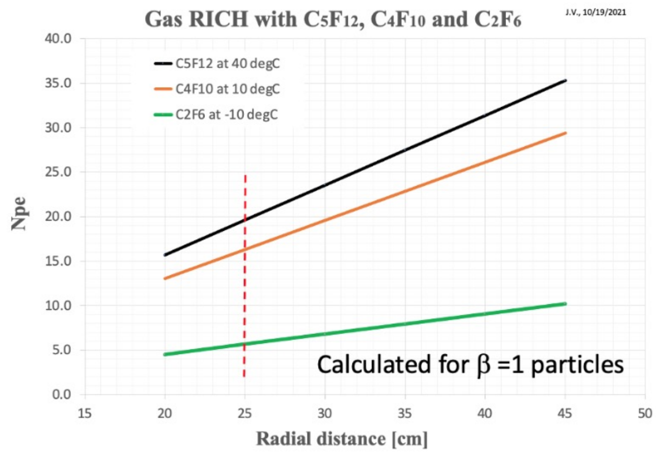

(a)

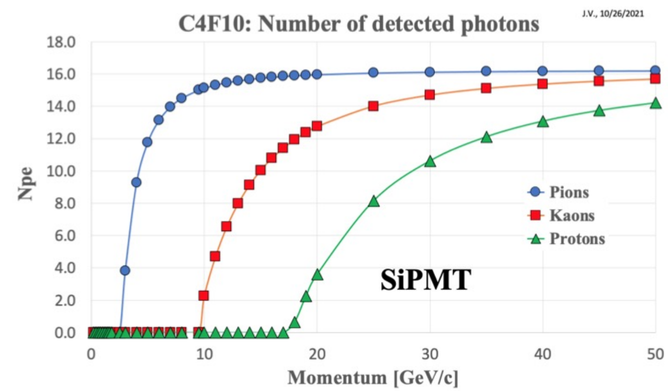

(b)

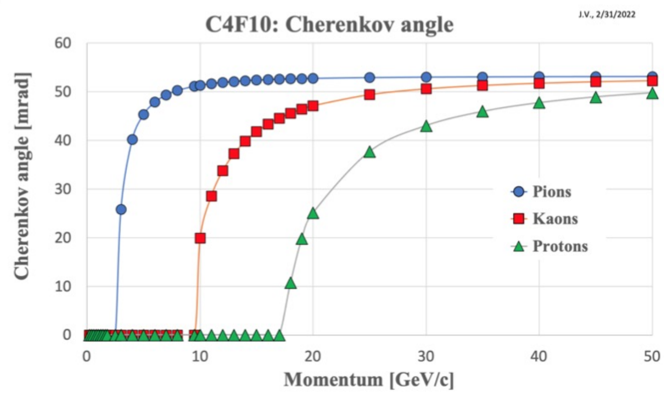

(c)

$$\cos\theta_c = \frac{1}{\beta n(\lambda)}$$

Figure 25: (a) Calculated number of photoelectrons per ring as a function of radiator length L. (b) Calculated number of photoelectrons and (c) Cherenkov angle as a function of momentum for pions, kaons, and protons. One can see that the kaon threshold is $\sim$10 GeV for C_4F_{10} gas and the expected number of photoelectrons per ring is about 16 for $L = 25$ cm and $\beta \sim 1$.

PID

https://www.slac.stanford.edu/~jjv/activity/Vavra_lecture_III.pdf

Summary of PID techniques for SuperB

Method	My personal comment
dE/dx - charge integration	Now a standard technique; good π/K PID bellow ~0.8 GeV/c; no PID near cross-over near ~1 GeV/c; relatively poor PID performance in the relativistic rise region above 1 GeV/c
dE/dx - cluster counting	Nobody has tried it yet; possible with introduction of wave form digitizing electronics; a factor of up to 2x of improvement over the standard dE/dx technique; should be tried.
FDIRC RICH	Thanks to focusing features, the focusing optics is much smaller than the SOB in BaBar; new MaPMTs will allow compact and highly pixelized detector, thus improving the angular resolution; absence of water will make the maintenance easier; the size and much faster timing will help the background issues; a timing resolution of σ ~200ps will allow the chromatic corrections; the overall performance should be better than that of BaBar DIRC by 20-30% ?
TOP counter (latest version: pixelized)	"On-paper" performance about the same as that of FDIRC; however, the MCP-PMT detector must deliver a TTS resolution of σ ~40 ps for the scheme to operate; t0 must be also good to ~25 ps; possibly large rate load on pixels if backgrounds large; sensitive to chromatic effects; GaAsP photocathode probably will not be avaolable; timing MUST work !
Forward Aerogel RICH	Truly excellent PID performance for~0.2-10 GeV/c; one really does not need this much of performance; large number of MCP-PMTs operating at high gain in a high rate environment - as of now unexplored challenge; large number of pixels; mass in front of calorimeter.
Forward TOF (pixelized)	Good for π/K PID bellow 2-3 GeV/c; it has a better chance to work than the DIRC-like TOF scheme; large number of MCP-PMTs required; more expensive; nobody has done it on such a large scale before; aging and rate effects reduced by running a very low gain on these tubes; to reach σ ~25ps will require a large effort as everything has to be done right, including a t0 signal; to reach σ ~ 50ps is easier, still a lot of work !!
Forward TOF (DIRC-like)	Good for π/K PID bellow 2-3 GeV/c; must have tracking; very difficult data analysis; MCP-PMT have to run at high gain; aging & rate effects more difficult than in the "pixilated" TOF scheme.

12/10/2009 J. Va'vra, Frascatti PID lecture III 57

PID Performance of the Compact RICH with SiPMTs

- Smearing effects increase with magnetic field and dip angles while decrease with momenta.
  - The contribution of various effects has been estimated, see much more in the back-up slides

Single photon error source	SiD/ILD RICH detector [mrad]	SLD CRID detector [mrad]
Chromatic error	~0.9	~0.4
Pixel size error (1mm^2 - 3mm^2)	0.8 - 2.3	~0.5
Smearing effect due to magnetic field	1.5 - 2.5 B = 5 T	~0.5 B = 0.5 T
Mirror alignment	< 1	~1
Tracking angular error	< 1	~0.8 [9]
Other systematic errors	a few mrad	a few mrad
Total	**< 5**	**~ 4.3**

These results justify a full Geant 4 simulation!

PID

https://indico.cern.ch/event/995850/contributions/4406336/attachments/2274813/3864163/ARC-presentation.pdf

Collider RICH layout

- To be concrete, based the design on the current **CLD** experiment concept for FCC-ee [N. Bacchetta et al., arXiv:1911.12230]
- Target a radial depth of 20 cm, and material budget of 10% X_0

CLD tracker

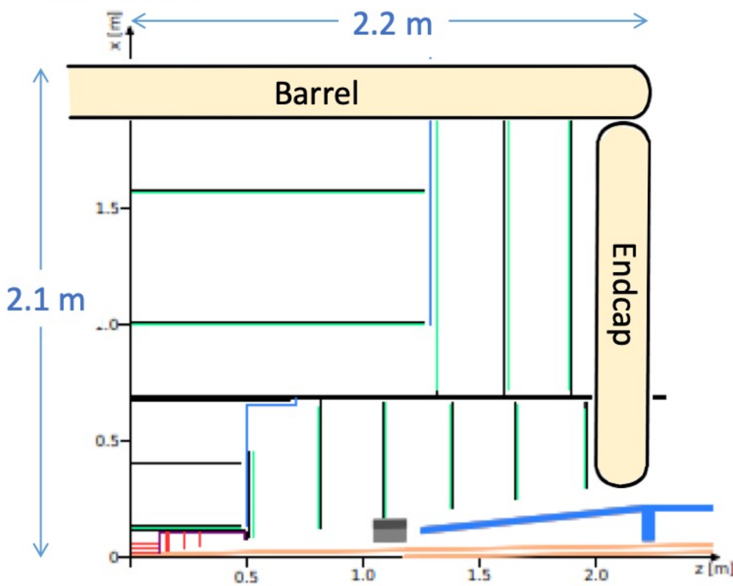

RICH pressure vessel
(Barrel + Endcaps)
= solids of revolution around the beam axis

Tracker would need to be re-optimized using 10% less radial space (already studied in Appendix B of CLD note: intended to make calorimeter smaller and save money…)

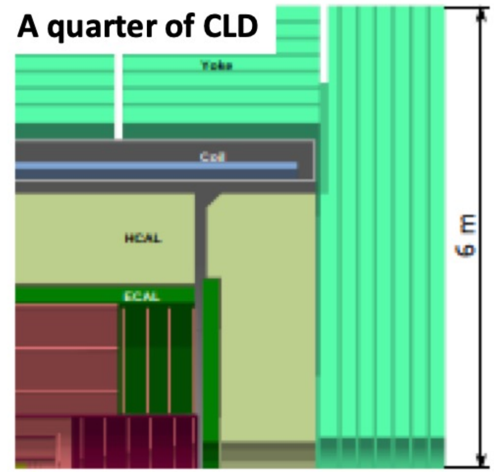

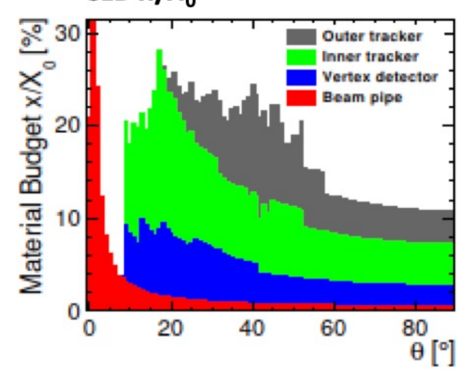

Roger Forty ARC: a solution for particle ID at FCC-ee 5

PID

https://indico.cern.ch/event/995850/contributions/4406336/attachments/2274813/3864163/ARC-presentation.pdf

Pressure vessel

- Lightweight vessels for cryostats currently under intensive R&D, strong synergy with aerospace (e.g. for composite fuel tanks)

Corrado Gargiulo, ECFA TF8, 31/3/2021

- Working group in CERN-EP future detector R&D programme led by Corrado Gargiulo who also convenes related Task Force on Integration for the ECFA R&D Roadmap

→ Corrado has developed a first design:

Barrel

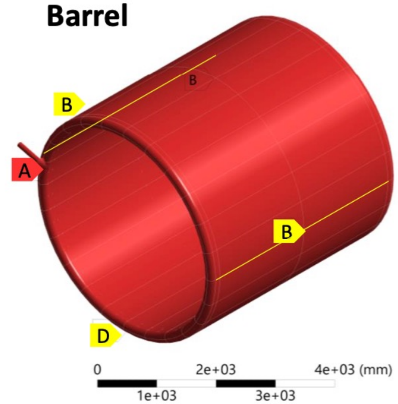

External wall hidden to show reinforcing ribs

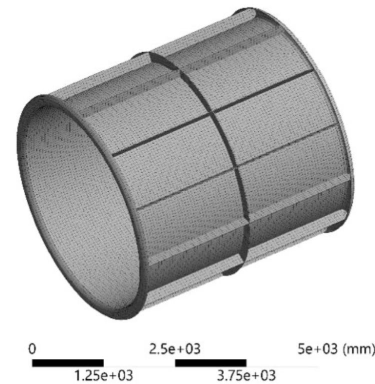

Endcap

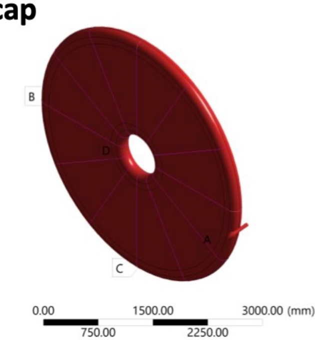

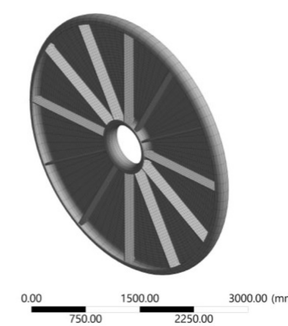

Roger Forty ARC: a solution for particle ID at FCC-ee 6

PID

https://indico.cern.ch/event/995850/contributions/4406336/attachments/2274813/3864163/ARC-presentation.pdf

Construction

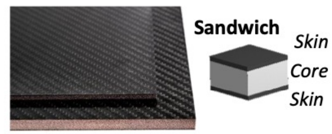

- Propose to use carbon-fibre composite sandwich with foam core: stiff + light
- 12-fold symmetry adopted for stiffening ribs → **sectors**
  Two options for construction, to be further analyzed:
  1. Vessel constructed as single unit, detector elements inserted from outer-end for each sector, on rails
  2. Sectors each constructed separately, then integrated to form overall vessel → smaller units to be constructed, but would expect slightly higher material budget for the walls

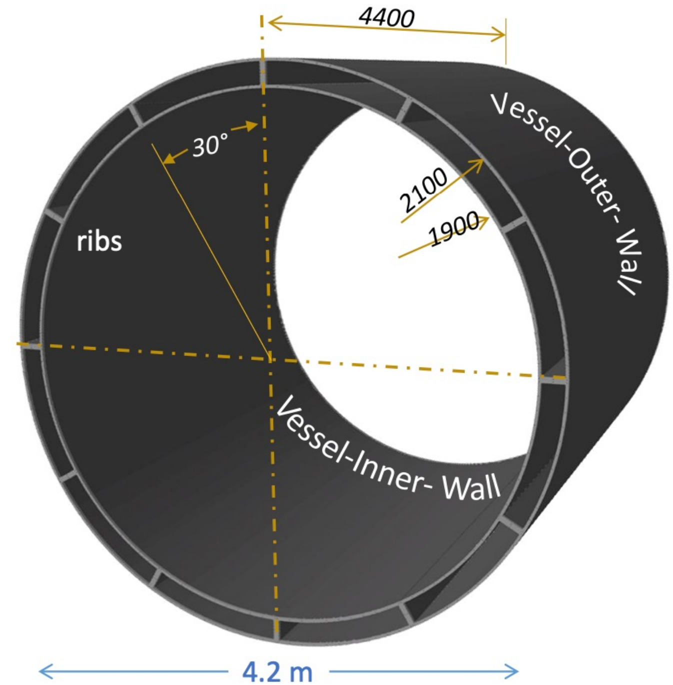

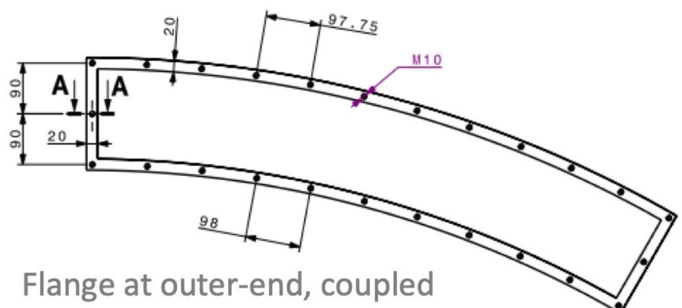

Flange at outer-end, coupled to wall (both 20 mm thick)

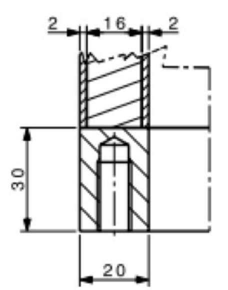

A-A

Side-view at end: removable semi-elliptical caps

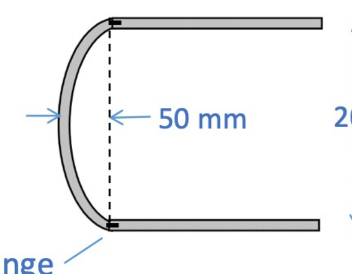

Roger Forty ARC: a solution for particle ID at FCC-ee 7

PID

https://indico.cern.ch/event/995850/contributions/4406336/attachments/2274813/3864163/ARC-presentation.pdf

Finite-element analysis

- Performed by Corrado using ANSYS, at 4 bar pressure, i.e. less than bicycle tyre but large volume:
  ~ 8.8 m^3 (Barrel), 1.7 m^3 (each Endcap)
- Maximum deflection of walls under pressure: 4 mm (Barrel), 7 mm (Endcap)
  Safety factor ≈ 2*, may need further checks to ensure compliance with pressure vessel safety regulations
- Achieved with 20 mm-thick walls, with remarkably low material budget: 2.7% X_0 (per wall); room for further optimization e.g. more aggressive material option available (UHM + honeycomb: 1.8% X_0)
- R&D needed to ensure leak tightness of CF walls (linerless), out-of-autoclave curing to avoid need of large autoclave, etc.

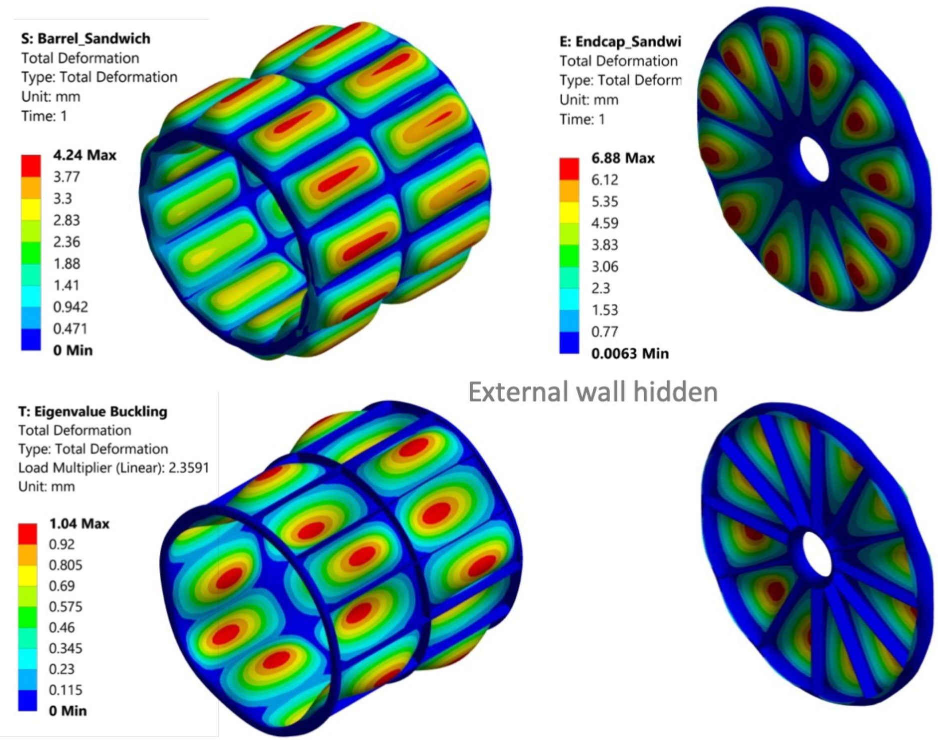

*Taking into account only pressure load: complete set of loads + boundary conditions must be considered for detailed analysis

Roger Forty   ARC: a solution for particle ID at FCC-ee   8

PID

https://indico.cern.ch/event/995850/contributions/4406336/attachments/2274813/3864163/ARC-presentation.pdf

Detector cell

- Challenge to arrange optical elements so that Cherenkov light focused onto a single sensor plane, as the detector radial thickness is reduced
- Concept inspired by the compound-eye of an insect: tile the plane with many separate cells, each with its own mirror and sensor array
- Use spherical focusing mirrors: focal length = radius-of-curvature/2
  → select radius-of-curvature $R \approx 30$ cm for radiator thickness of 15 cm

https://www.findlight.net/blog/2019/01/23/artificial-compound-eyes/

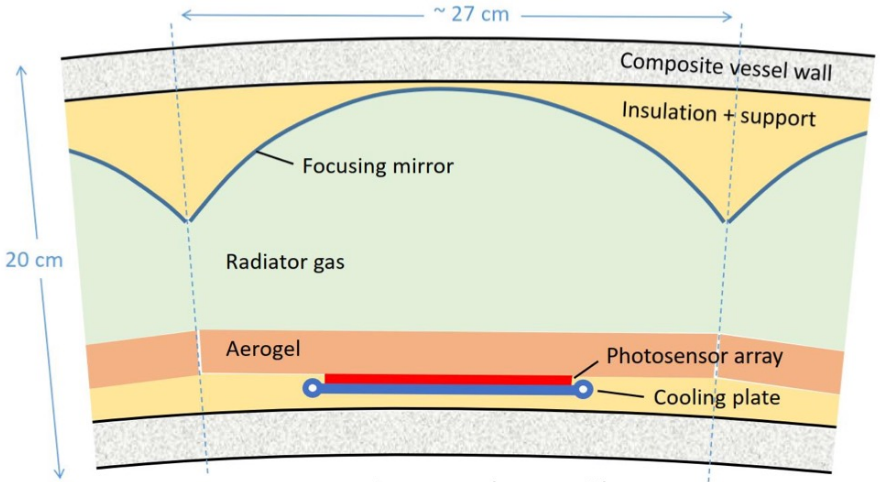

ARC detector (one cell)

Simulate tracks from IP crossing detector uniformly over acceptance and ray trace Cherenkov photons to sensor plane: (here for $\theta \approx 90°$)

Ring radii = $R \cdot \theta_C / 2$ = 1.5 cm (3.6 cm) for gas (aerogel)

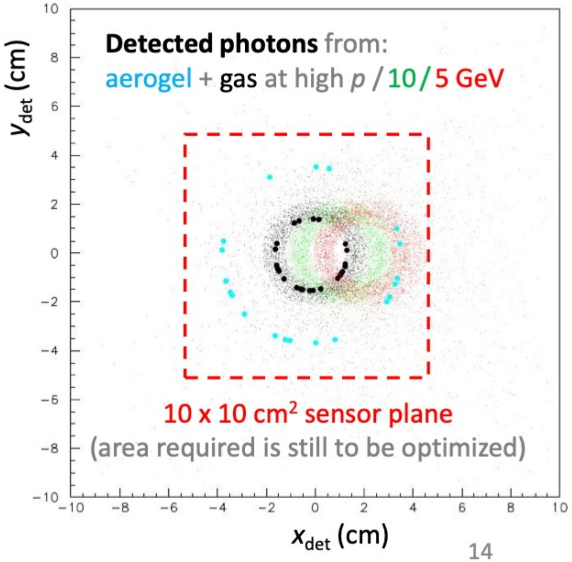

Roger Forty   ARC: a solution for particle ID at FCC-ee   14

PID

https://indico.cern.ch/event/995850/contributions/4406336/attachments/2274813/3864163/ARC-presentation.pdf

Optical layout

- As move away from normal incidence, i.e. $\theta = 90°$ (Barrel) or 0° (Endcap), need to adjust focusing
  Either mirrors kept parallel, radius-of-curvature adjusted (R-half); or tilted and/or parabolic mirrors (L)
  For first solution, add a plane mirror at the end, to keep ring images inside the detector volume

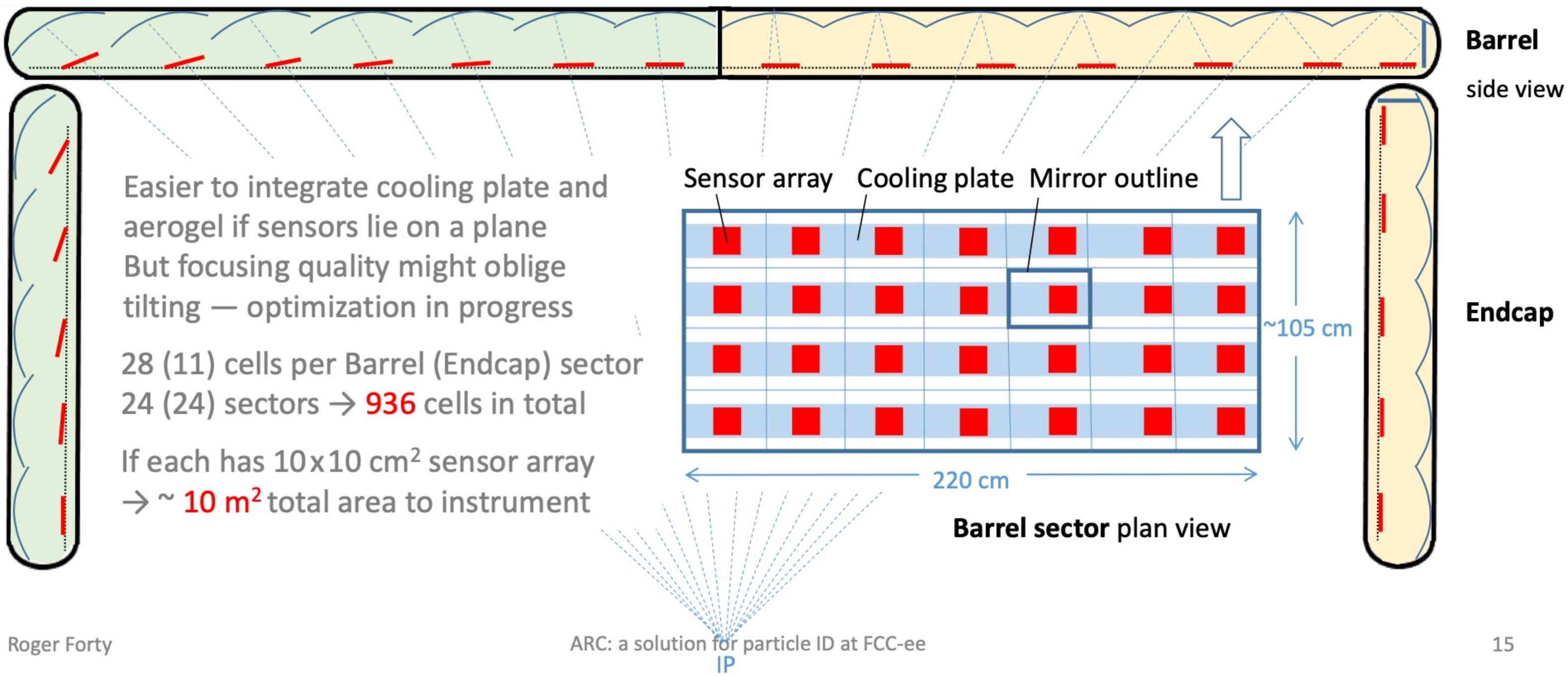

Easier to integrate cooling plate and aerogel if sensors lie on a plane
But focusing quality might oblige tilting — optimization in progress

28 (11) cells per Barrel (Endcap) sector
24 (24) sectors → 936 cells in total

If each has 10x10 cm^2 sensor array
→ ~ 10 m^2 total area to instrument

Roger Forty ARC: a solution for particle ID at FCC-ee 15

PID

https://indico.cern.ch/event/995850/contributions/4406336/attachments/2274813/3864163/ARC-presentation.pdf

Alternative layouts

- Current proposal has been outlined assuming the use of aerogel is necessary for thermal insulation of photosensor + readout electronics from gas volume: named **ARC**, for **A**erogel **R**ICH **C**ellular detector

4 cells to a sector (transverse view)

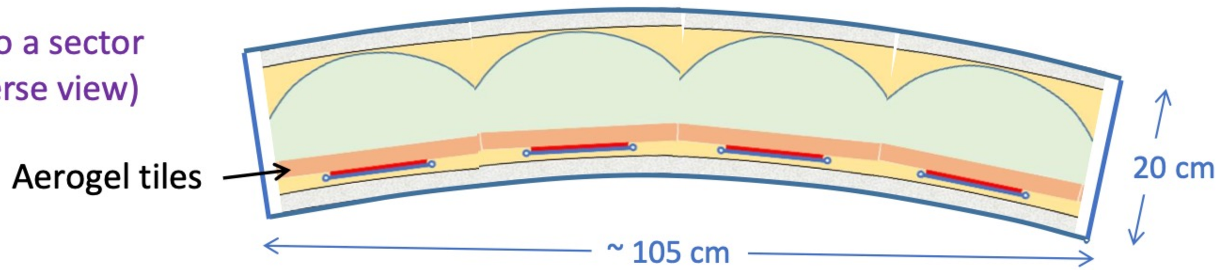

- If (with further study) a photosensor is found which could operate at the same temperature as the gas, or e.g. if higher momentum range is targeted for the particle ID, then the aerogel might not be needed
→ the radial depth could be squeezed further using a similar "cellular pressurized RICH" design:

e.g. 6 cells to a sector

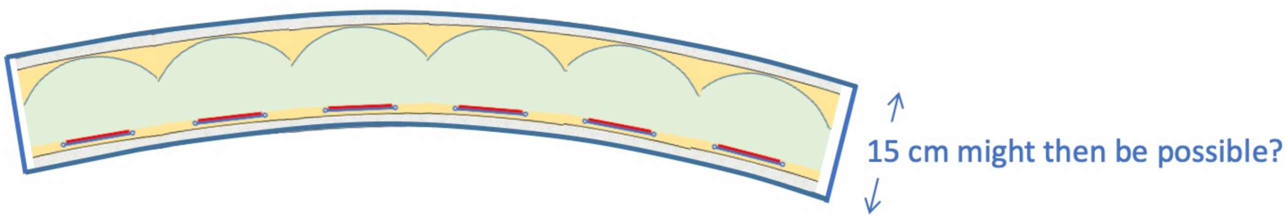

Roger Forty ARC: a solution for particle ID at FCC-ee 18

ARC vs Compact RICH

ARC	Compact RICH
C4F10 at 3.5 bar	C4F10 at 1 bar
~10% X0	~4-5% X0
SIMPTs at -30 (C4F10 condenses at +2degC. Aerogel on top of SiPMT will act as an insulation/radiator.)	SIMPTS at room temperature
Gaps between active SiPMT sensor segments	continuous coverage with only small gaps between SiPMT sensors (similar to CRID)
chromatic error ~0.5 mrad (possibly having Aerogel helps as it is acting as a UV filter, thus removing part of the wavelength acceptance and therefore reducing chromatic error.)	chromatic error ~0.9 mrad
tracking resolution ~**0.3 mrad**	tracking resolution ~**0.8 mrad** based on SLD experience
1 mrad for angular resolution thanks to **0.5mm^2 pixels**	error from final size pixels **~0.8-2.3 mrad** if we use **1mm^2 or 3mm^2** pixel sizes
No smearing due to magnetic field (2 T)	~1.5-2.5 mrad smearing due to magnetic field (5 T)
25 photoelectrons for 20 cm (higher QE using NUV-HD SiPMTs)	16 photoelectrons per ring at beta = 1 and 25 cm radiator length
SIMPTs with **10 ps** timing resolution	SIMPTs with **~100 ps** timing resolution

SLD Results

https://arxiv.org/abs/2203.07535

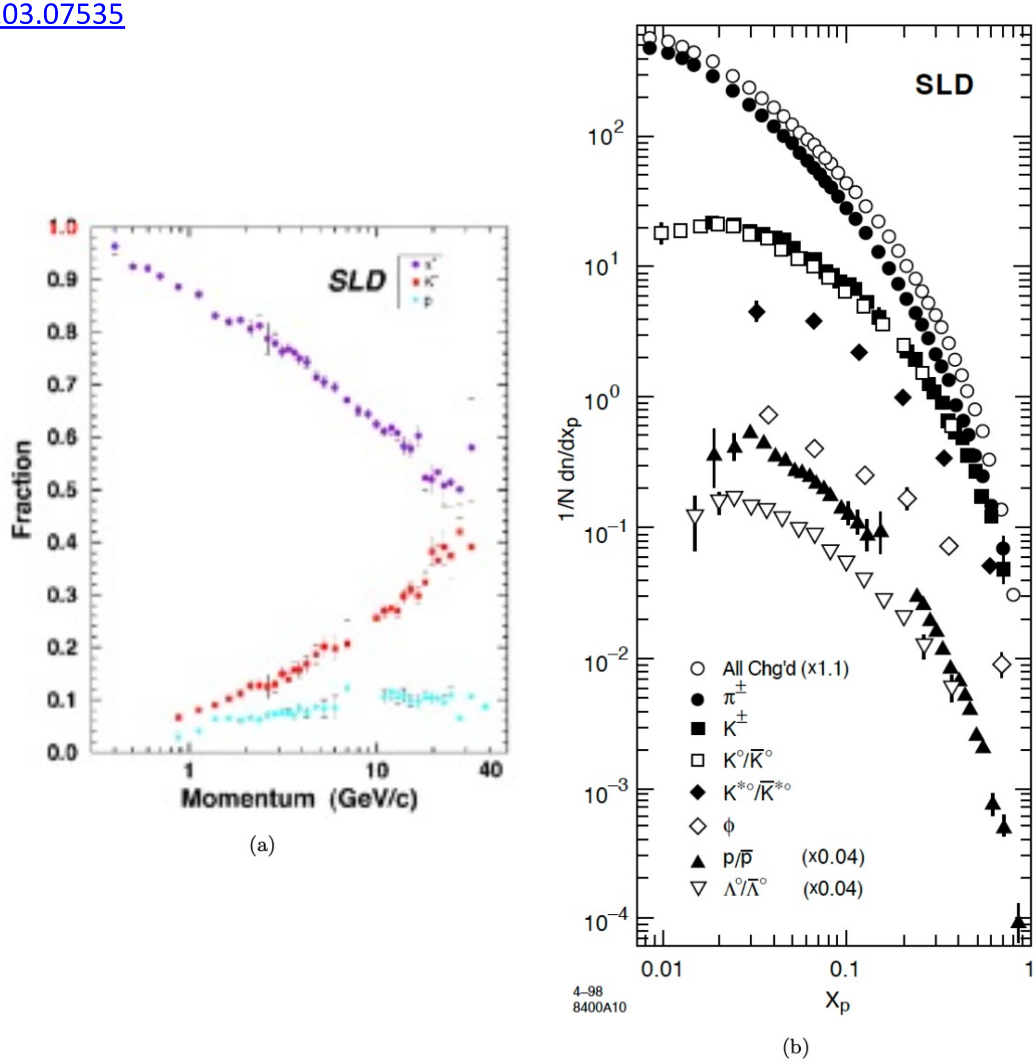

Figure E1: (a) $\pi/K/p$ fractions determined by the SLD CRID [90]. (b) Differential cross sections as a function of hadronic momentum fraction x_p per hadronic Z^0 decay, by all SLD detectors [91].

Not only Higgs: $Z \to s\bar{s}$

[F. Blekman, F. Canelli, K. Gautam, E. Plörer, A.R. Sahasransu, L. Vanhecke's slides]

- $Z \to s\bar{s}$ decay width measurement
- Train a **Convolutional Neural Network** on Zuds events with jet images from different categories with the IDEA detector

Performance

Three working points defined at fake rates of 10%, 5%, and 1%, respectively

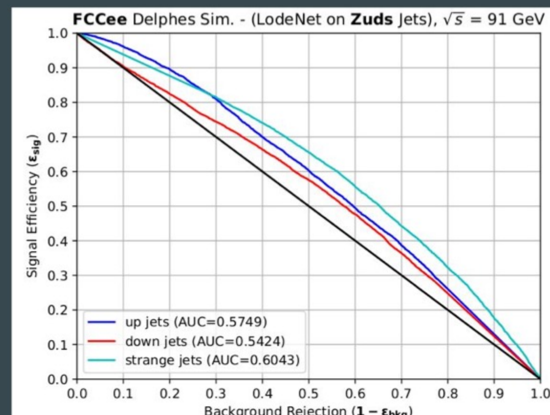

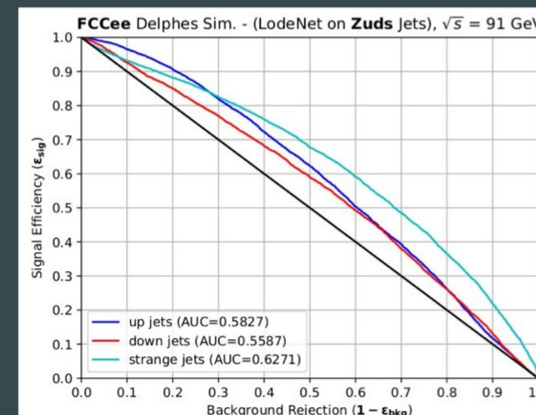

Signal Efficiency	10% fake rate	5% fake rate	1% fake rate
Generator	47.2%	27.7%	7.5%
PF only	17.7%	9.7%	2.0%
PF + Ks	21.9%	12.9%	4.4%
PF + Ks + K+-	39.5%	24.8%	7.0%

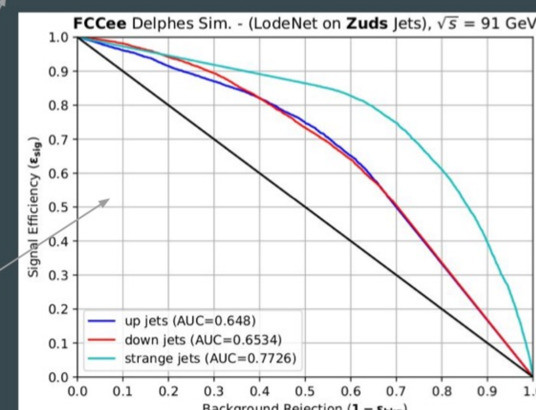

16

Not only Higgs: $Z \to s\bar{s}$

[F. Blekman, F. Canelli, K. Gautam, E. Plörer, A.R. Sahasransu, L. Vanhecke's slides]

- $Z \to s\bar{s}$ decay width measurement
- Train a **Convolutional Neural Network** on Zuds events with jet images from different categories with the IDEA detector

Truth-level Z peak

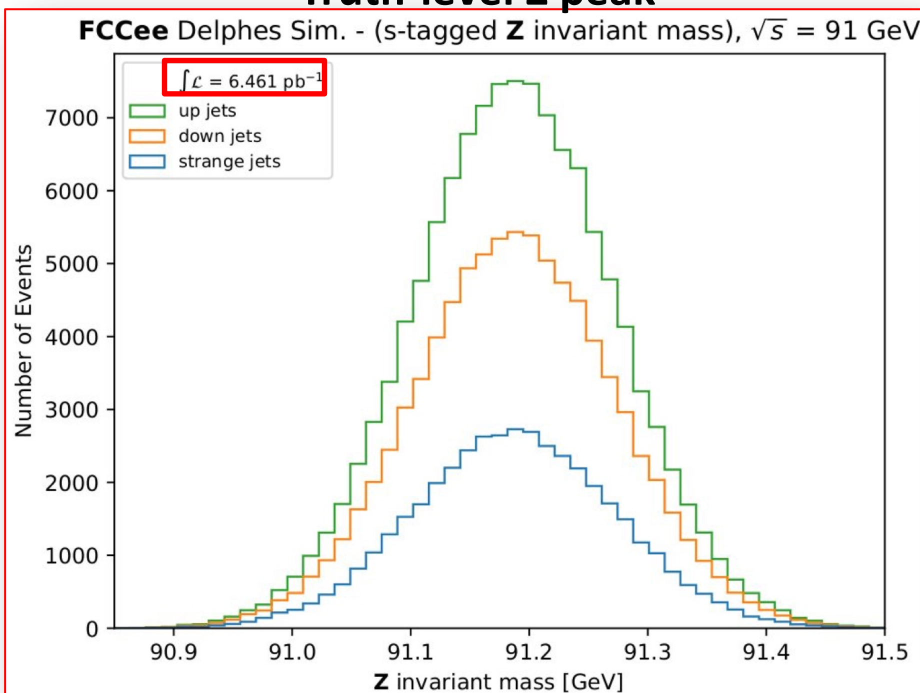

Z peak after tagging @ 10% mistag rate

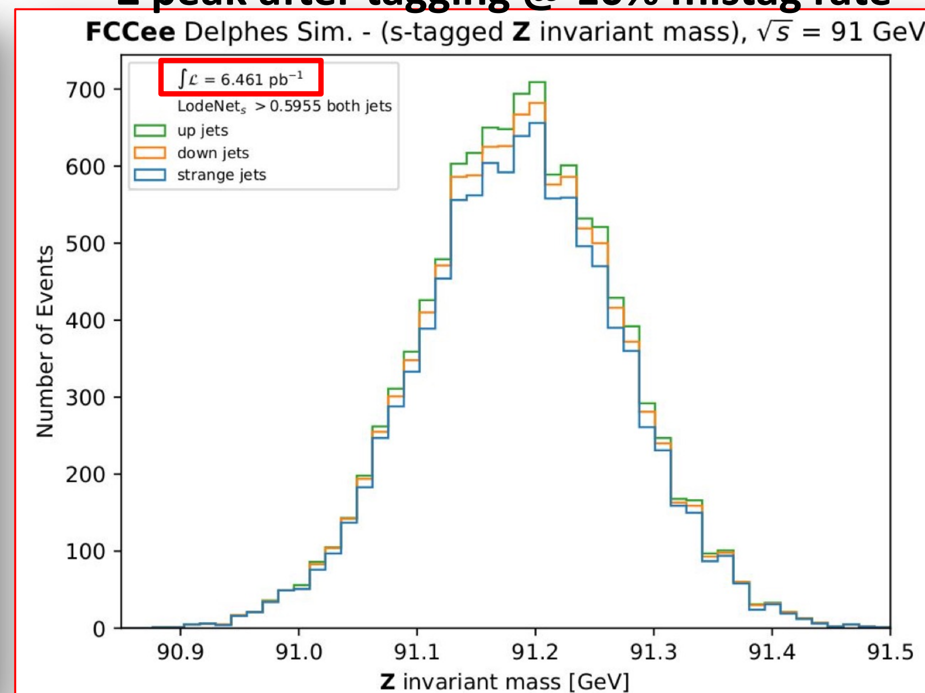

Even on a small sample, clear $Z \to s\bar{s}$ peak after applying s-tagging

Not only Higgs: $e^+e^- \to s\bar{s}$

Y. Okugawa's slides

- Di-fermion production @ ILD to study Z^0/γ couplings at 250 GeV, eL pR, 120 fb-1
- Couplings extracted from helicity amplitudes included in the differential cross-section

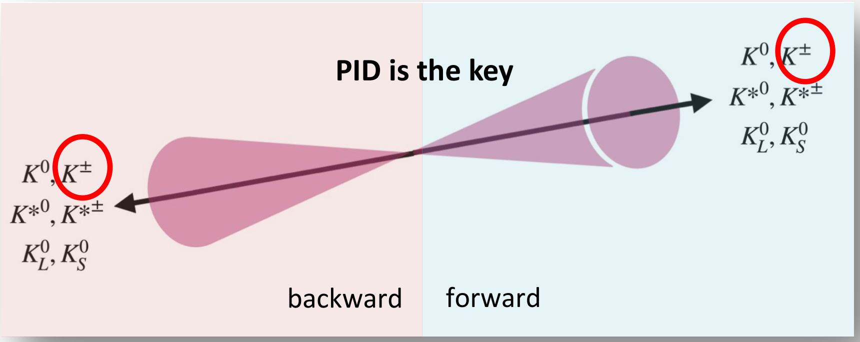

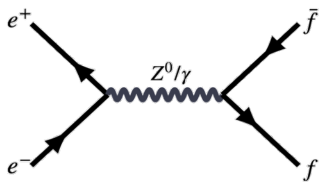

- $s\bar{s}$ back-to-back, $120 < E_s, E_{\bar{s}} < 127$ GeV, lead. particle in s-jet [20,60] GeV

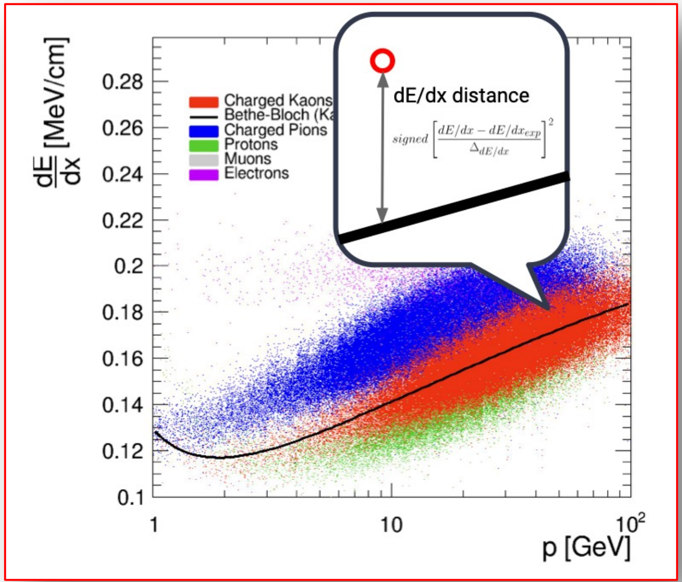

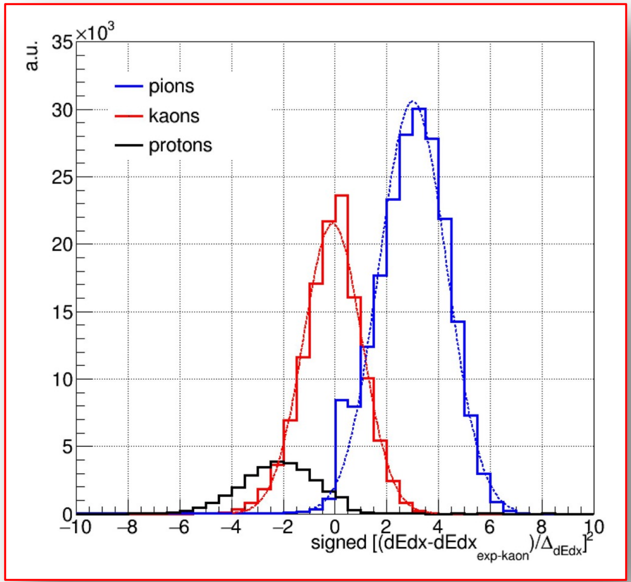

- Very challenging analysis: with K^+/K^-, to obtain > 95 purity, the efficiency reduces to 1%!

U. Einhaus's Thesis in prep. & slides on $W \to cs$,

P. Malek's Thesis in prep. & slides on $Z \to q\bar{q}$

$W \to cs$

U. Einhaus's Thesis in prep. & slides

Measure Vcs *without* assumption of unitarity

- Samples used: 500 GeV center-of-mass, $e^+e^- \to \nu\nu$ H, with H $\to$ WW*, and semileptonic WW* decays
- Use only same-generational decays
- Reject events with taus
- Re-reconstructed events using different dE/dx resolutions
  - 4.5 %: default
  - 2.6 %: best possible
  - 7 %, 10 %: for comparison

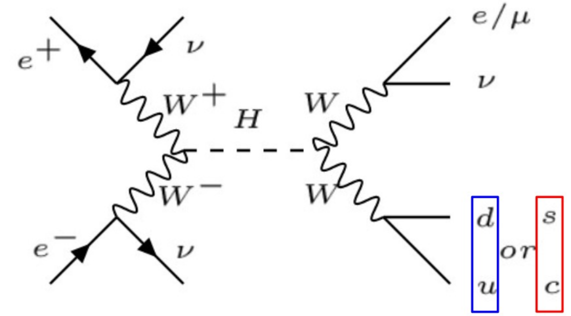

24.11.21 PhD Defense 42

DELPHI Analysis with 120 W bosons, with 10^8 W bosons @ILC, statistical precision of 0.0003 possible

$$|V_{cs}| = 0.94^{+0.32}_{-0.26}(\text{stat}) \pm 0.13(\text{syst})$$

$W \to cs$

U. Einhaus's Thesis in prep. & slides

- Build a BDT with 20 PID-related observables based on number & momentum of jet particles and if they are leading

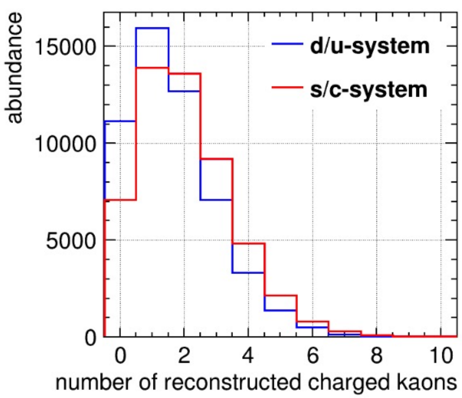

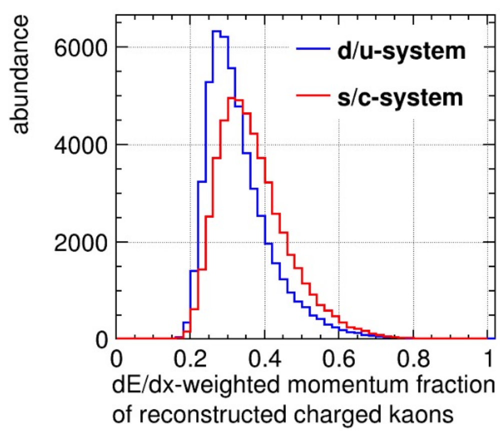

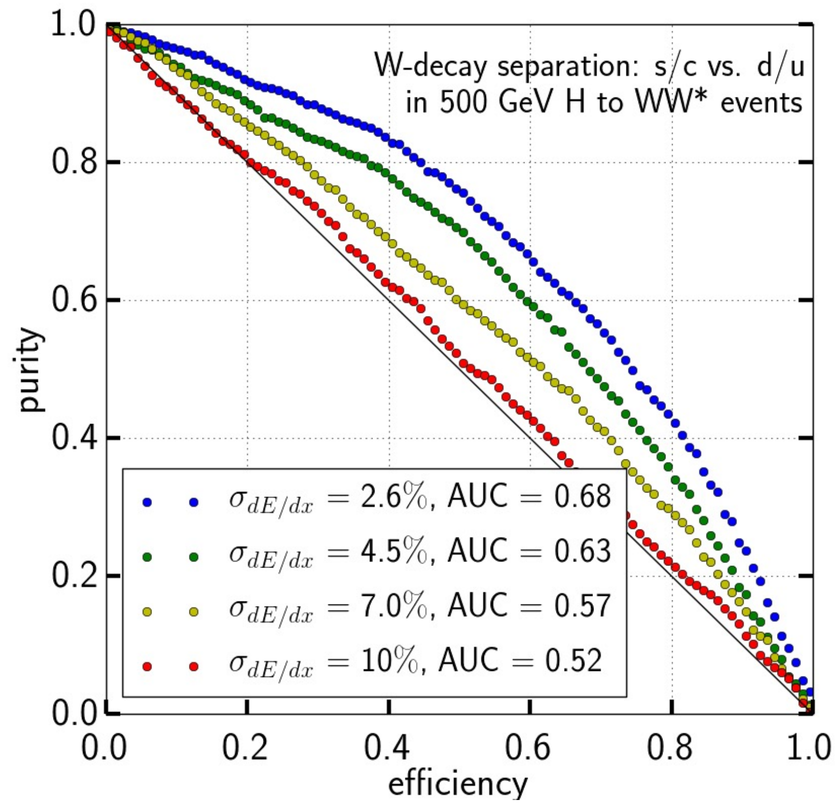

$W \rightarrow cs$

U. Einhaus's Thesis in prep. & slides

Add f-tag info from PFlow

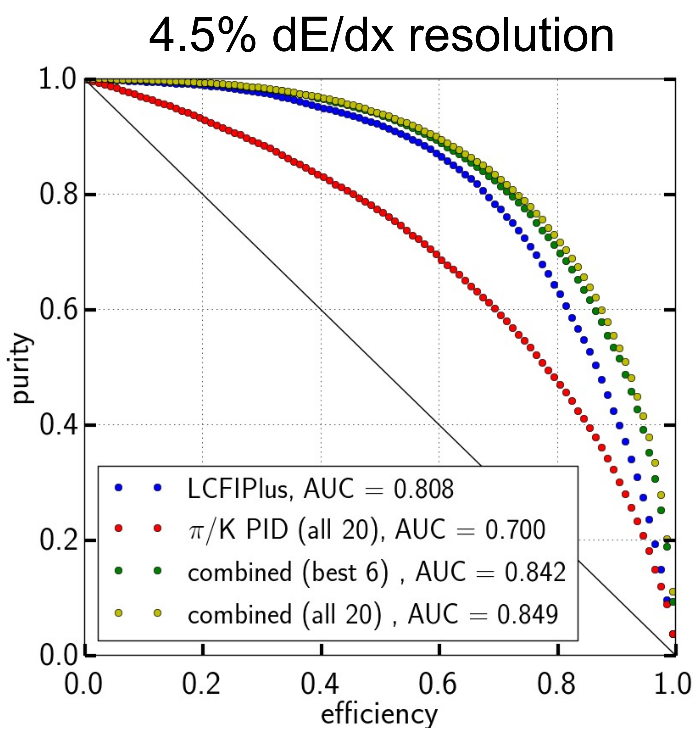

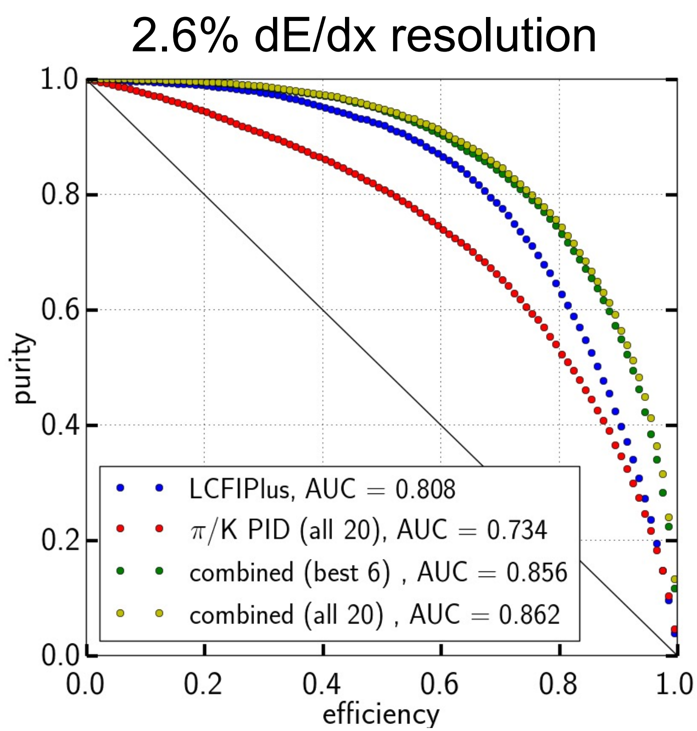

$W \to cs$

U. Einhaus's Thesis in prep. & slides

Improvement after adding PID

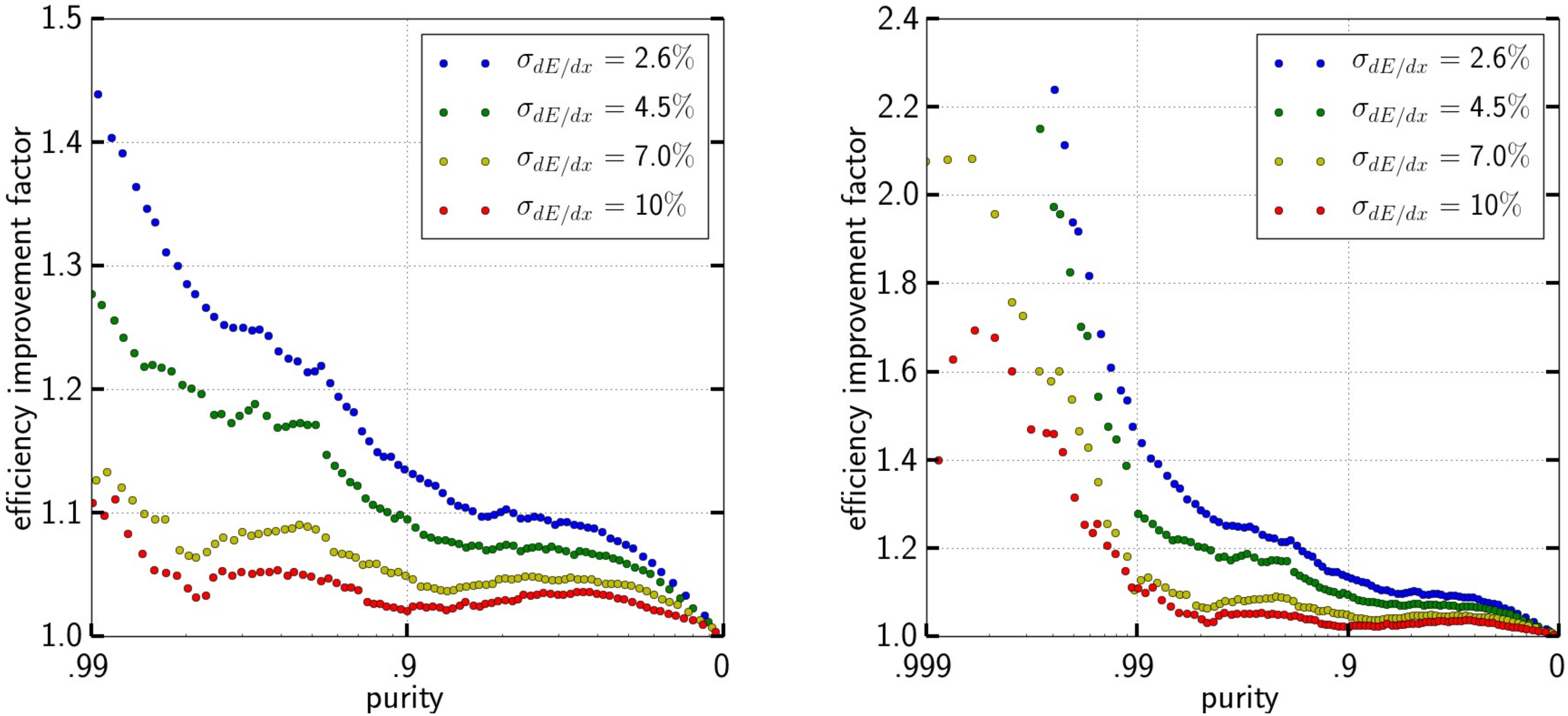

$Z \to qq$

P. Malek's Thesis in prep. & slides

- $\mathcal{B}(Z \to q\bar{q})$ for u,d,s known to 4.2 % (OPAL)
  - [Z. Phys. C 76, (1997)]
  - violation of flavour universality?
  - important SM background
- issue: $e^+e^- \to q\bar{q}$ at 250 GeV contains photon contribution
  ➔ use radiative return to Z
- ILC: 74M Z-return events
  - cf. OPAL 4.3M events

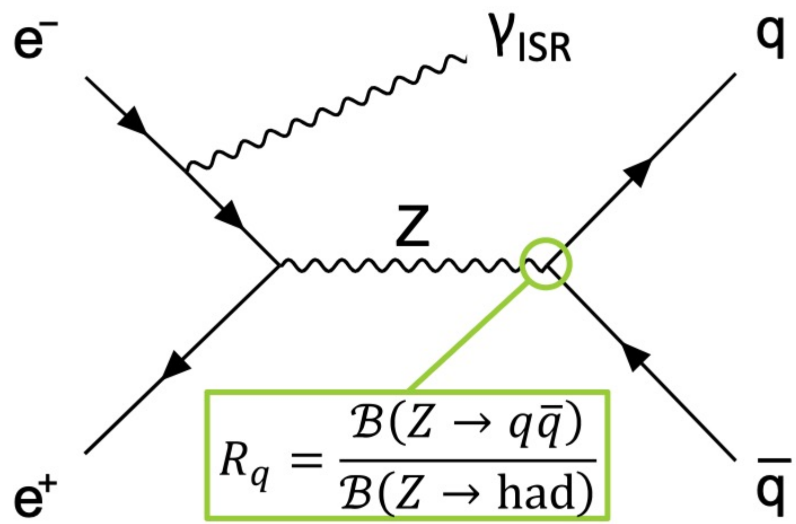

$$R_q = \frac{\mathcal{B}(Z \to q\bar{q})}{\mathcal{B}(Z \to \text{had})}$$

$Z \to qq$

P. Malek's Thesis in prep. & slides

Analysis Result

- unweighted data: similar errors as OPAL
  - even with smaller data set (1.8M : 4.3M)
- weighted fit uncertainty of $R_{d,s}$: 1.2 %
  - OPAL: 4.2 %
- systematics benefit from higher statistics & better detector
  - e.g. contribution of c-quarks to leading kaons
    - OPAL determined from MC
    - now high eff. c-tags allow measurement

➔ total uncertainty of $\mathcal{O}(1\ \%)$ reachable

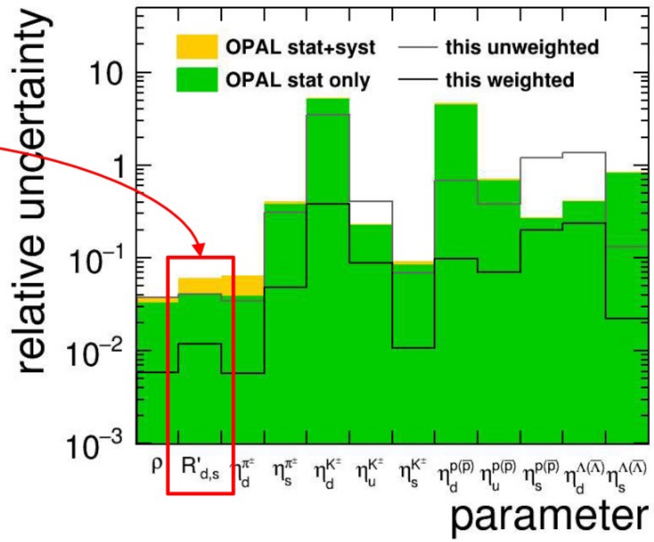

11.02.2022 DISPUTATION, PAUL MALEK 37

High Granularity

"Double-hit separation and dE/dx resolution of a time projection chamber with GEM readout" by the LCTPC collaboration.
[Slides]

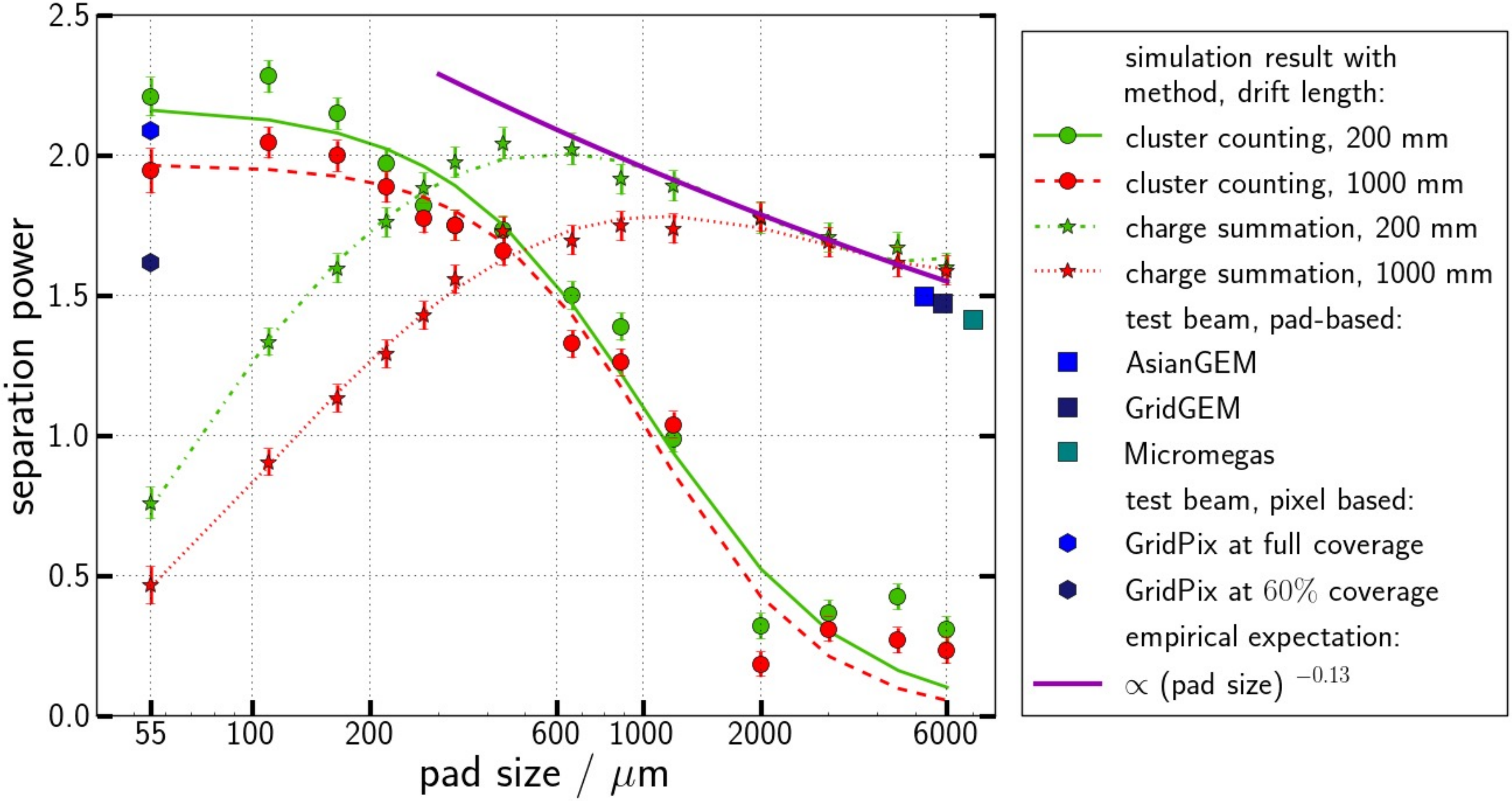

High Granularity

"Double-hit separation and dE/dx resolution of a time projection chamber with GEM readout" by the LCTPC collaboration.
Slides

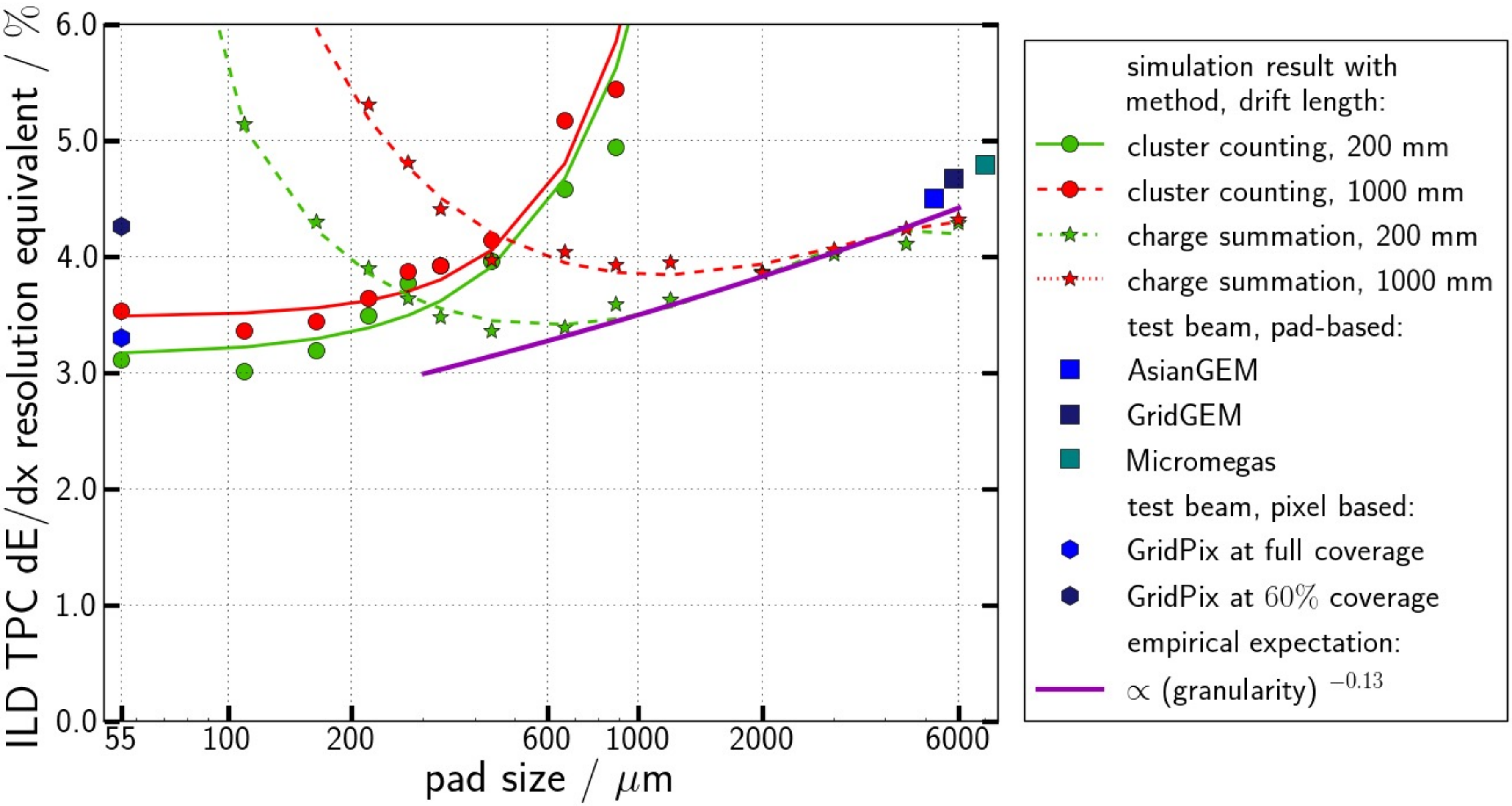

Vts

If we have 200 fb-1 at about ~100 fb cross section, we would have ~20 t->Ws events

https://arxiv.org/pdf/hep-ph/0508097.pdf

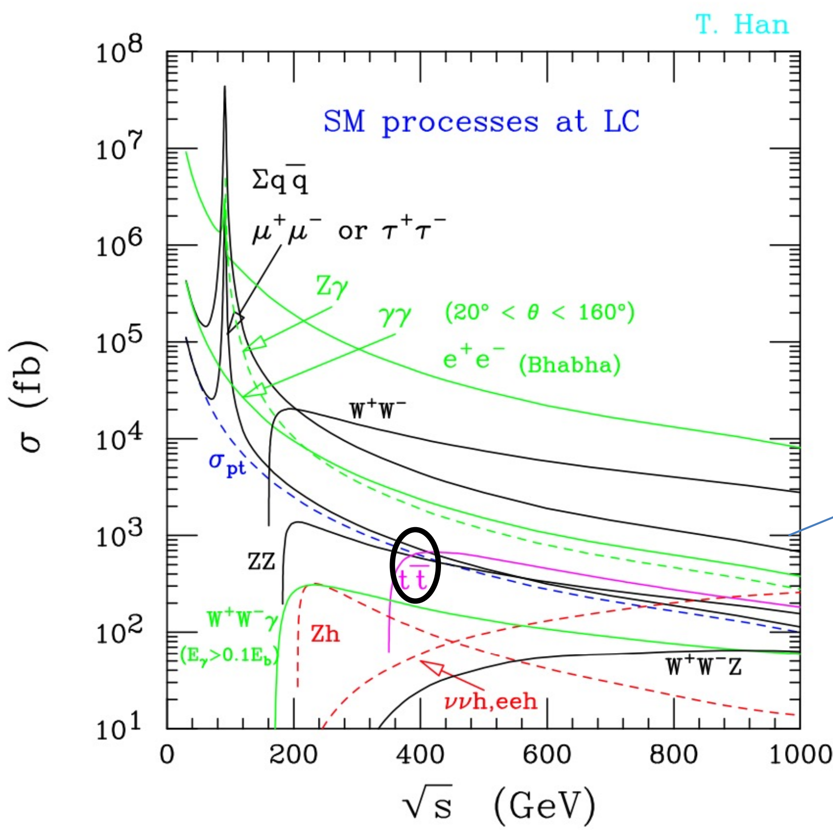

FIG. 2: Scattering cross sections versus c.m. energy for the SM processes in e^+e^- collisioins. The Higgs boson mass has been taken as 120 GeV.

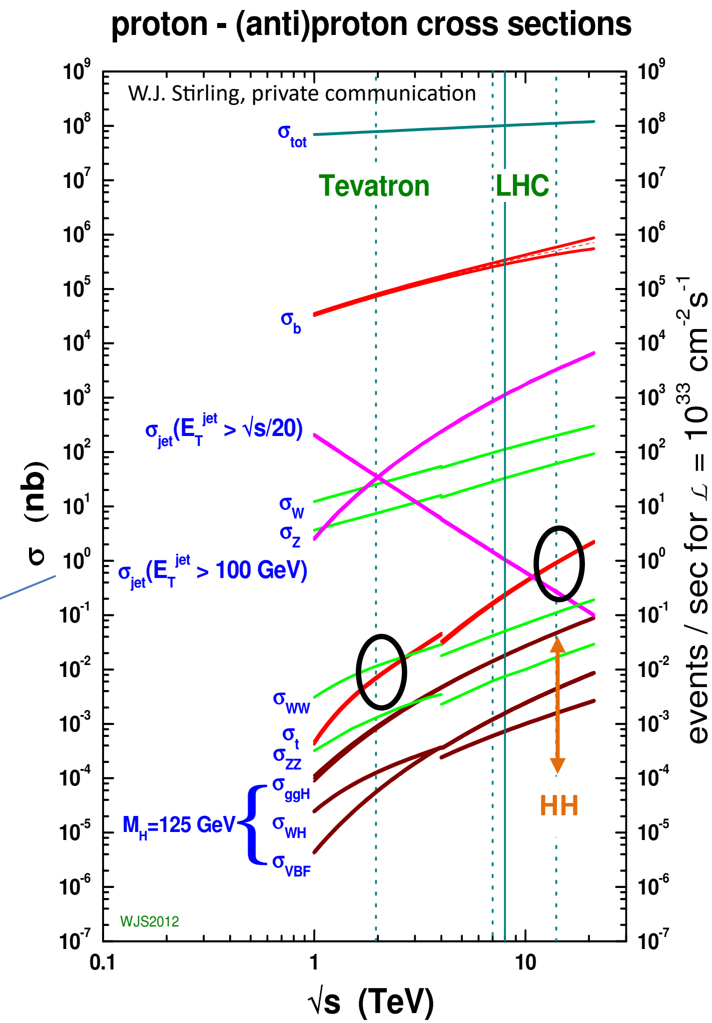

ECFA

ECFA Detector R&D roadmap:

Sect. 4.3.1 “The limited space of the interaction region for hermetic-coverage collider experiments (mandatory at the EIC and FCC-ee) requires designing performant RICH detectors with a total length shorter than a metre”

The Higgs self-coupling

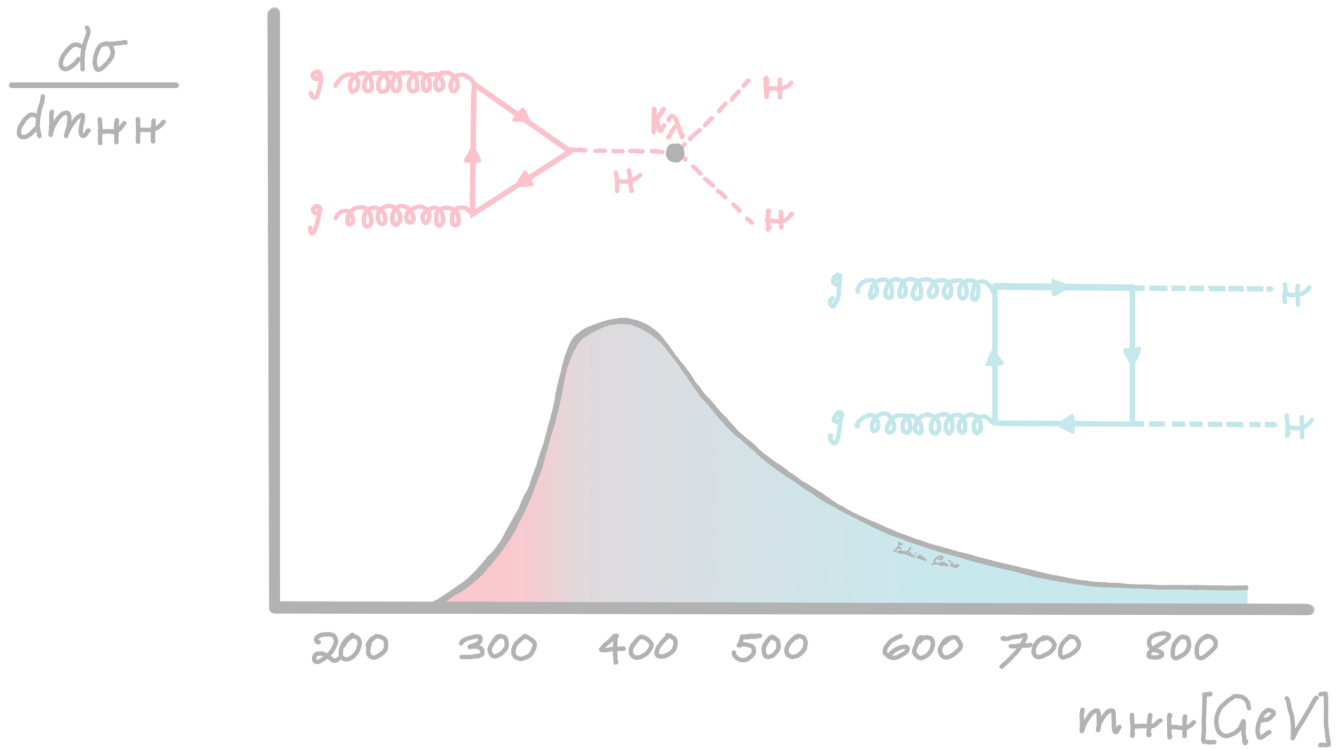

HH Production at the LHC

Non-resonant σ_{HH}^{ggF} = 31.05 fb at 13 TeV for m_H = 125.00 GeV

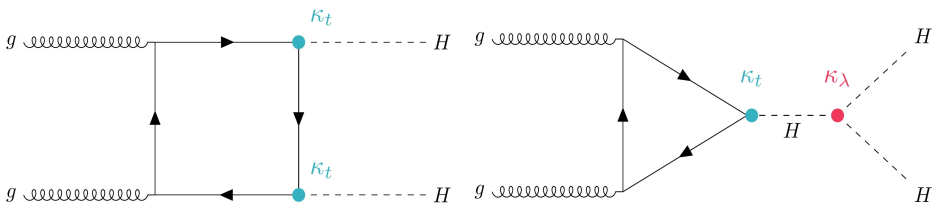

Non-resonant σ_{HH}^{VBF} = 1.73 fb at 13 TeV for m_H = 125.00 GeV

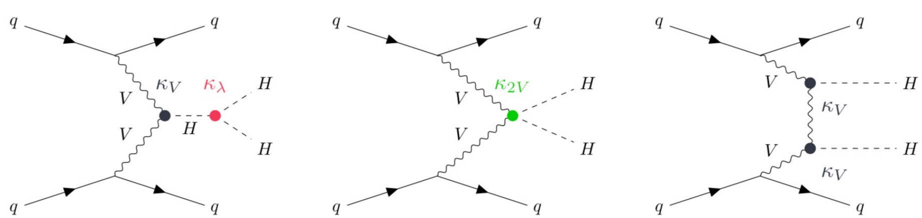

Resonant ggF

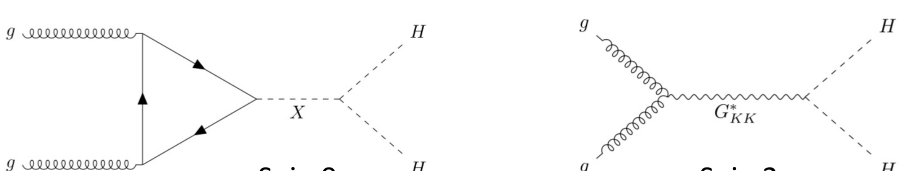

Spin 0

Spin 2

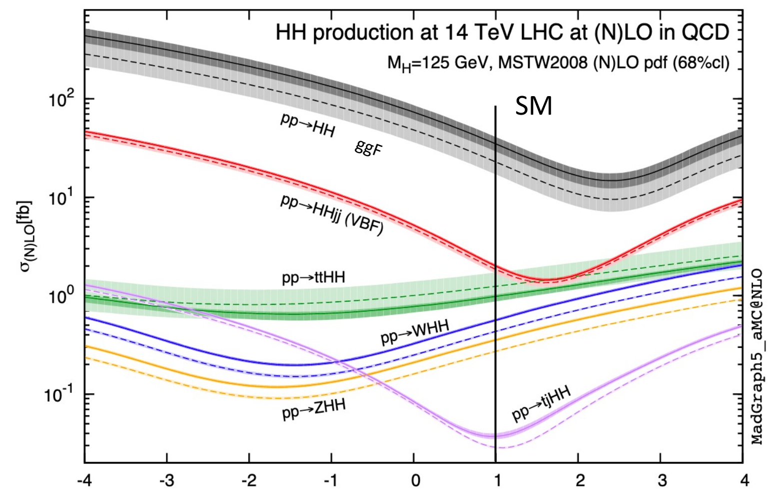

1401.7340

σ_{HH} and **kinematics** depend on the **couplings** and presence of new **resonances**

New physics can manifest as deviation in σ_{HH}

$HH \to b\bar{b}\gamma\gamma$ analysis in a nutshell

Small BR, but fully **reconstructable** final state, **clean signal extraction**

Di-photon triggers with **E_T > 35, 25 GeV** (82.9% efficiency for non-resonant signal, 69.5% for m_X = 300 GeV)

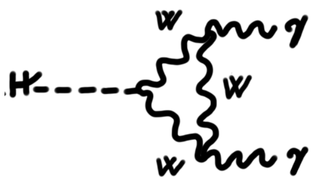

Tight and isolated

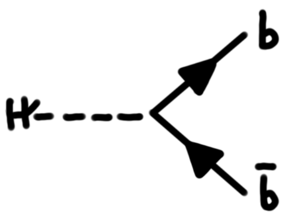

B-jet energy corrections

Object selection

Event categorization

MVA approach

4 categories for non-resonant analysis

1 category per m_X for resonant analysis

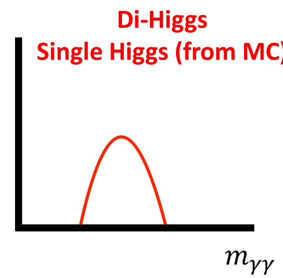

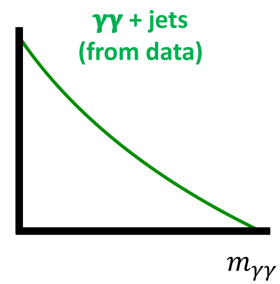

Modeling of discriminant variable

Simultaneous likelihood fit to all categories

SM $\boldsymbol{\sigma}$ limits and

$\boldsymbol{\sigma}$ vs $\boldsymbol{k_\lambda}$

for **non resonant** analysis

$\boldsymbol{\sigma}$ vs $\boldsymbol{m_X}$

for **resonant** analysis

Non-Resonant $HH \to b\bar{b}\gamma\gamma$ (1)

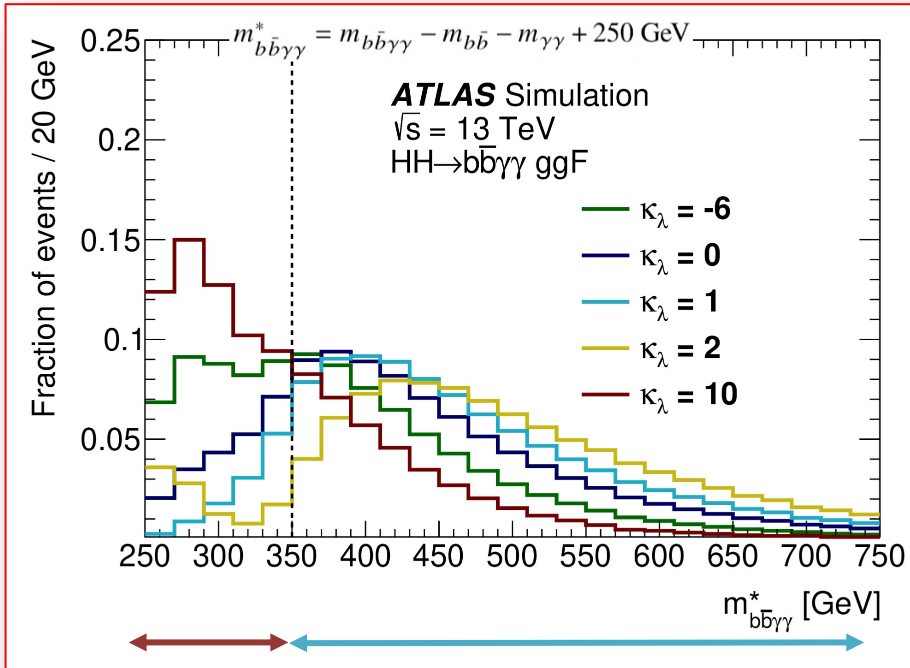

- Low and High $m^*_{b\bar{b}\gamma\gamma}$ (very important!)
  - < 350 GeV for BSM, > 350 GeV for SM

Non-Resonant $HH \to b\bar{b}\gamma\gamma$ (2)

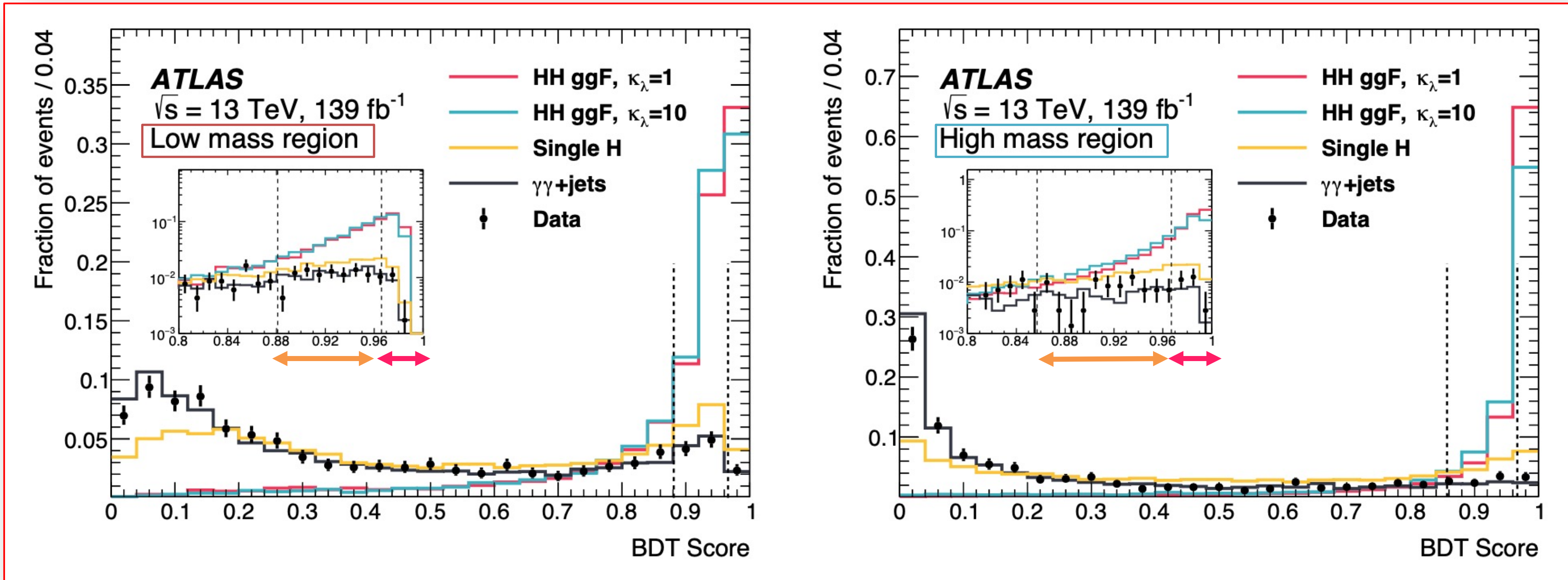

- **BDT to discriminate signal ($k_\lambda = 1, 10$) from backgrounds**
  - m_{bb} with b-jet energy corrections (improves resolution by ~ **20%**)
  - *Topness* (rejects up to 35% ttH)

- **Loose and Tight BDT**
  - Boundaries chosen to maximize combined expected significance

Non-Resonant $HH \to b\bar{b}\gamma\gamma$ (3)

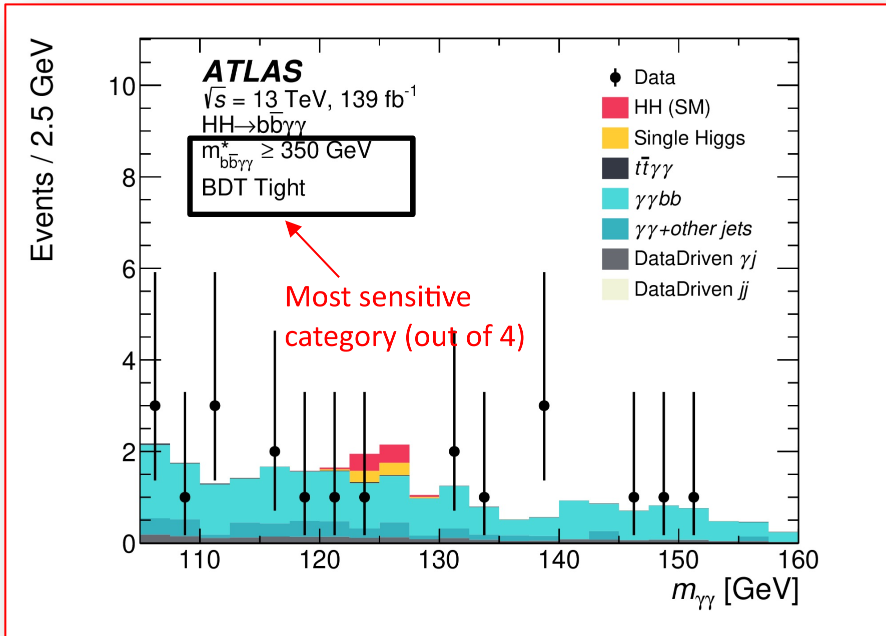

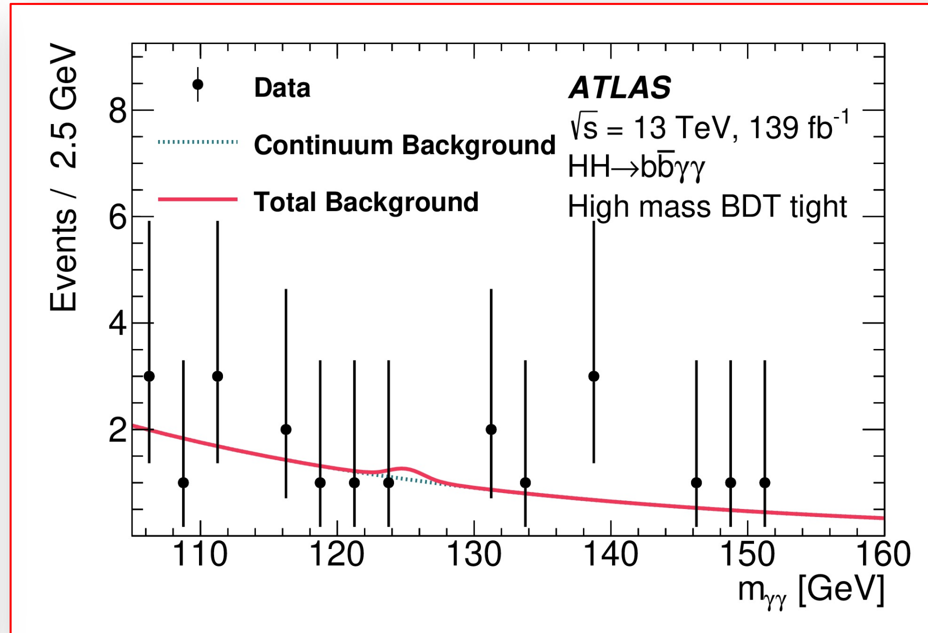

Main Single Higgs backgrounds

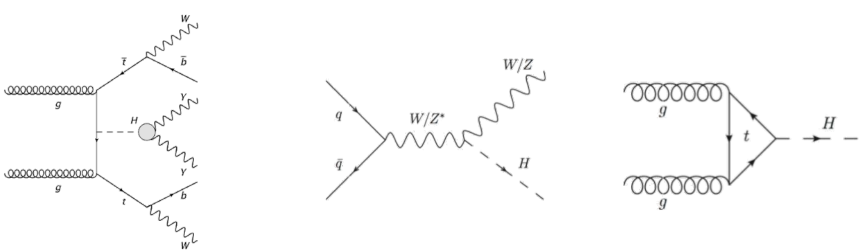

Maximum likelihood fit of $m_{\gamma\gamma}$ performed simultaneously over all categories

Non-Resonant $HH \to b\bar{b}\gamma\gamma$ results

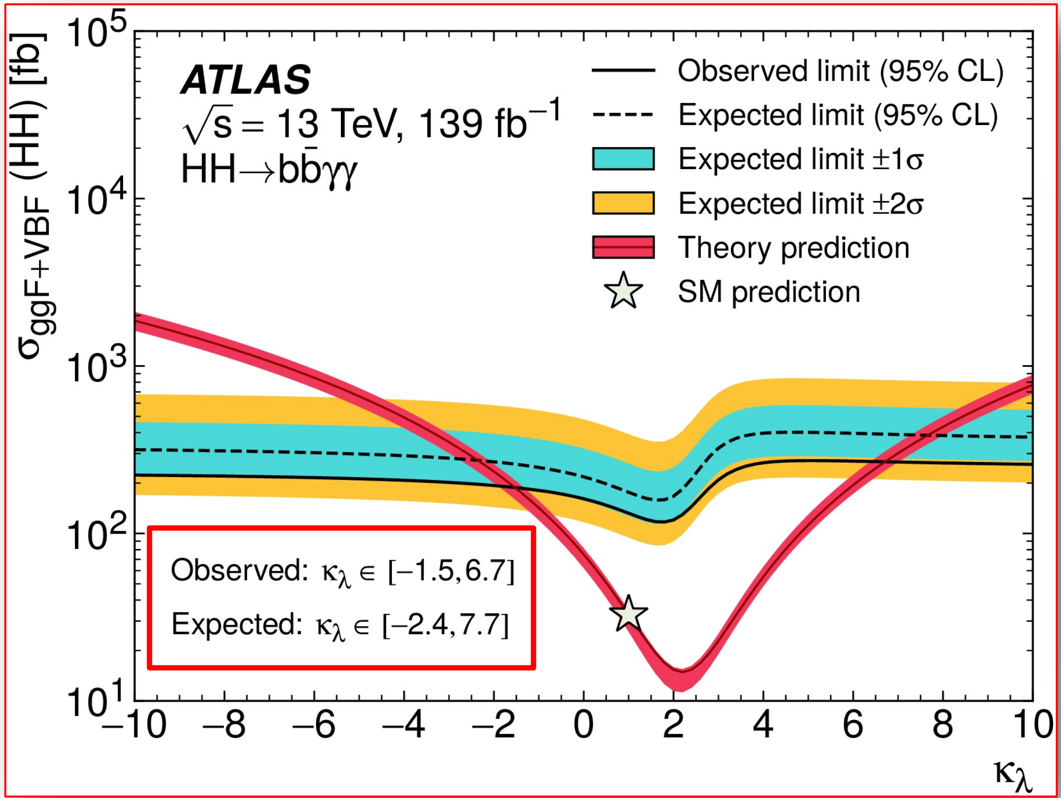

Earlier ATLAS results

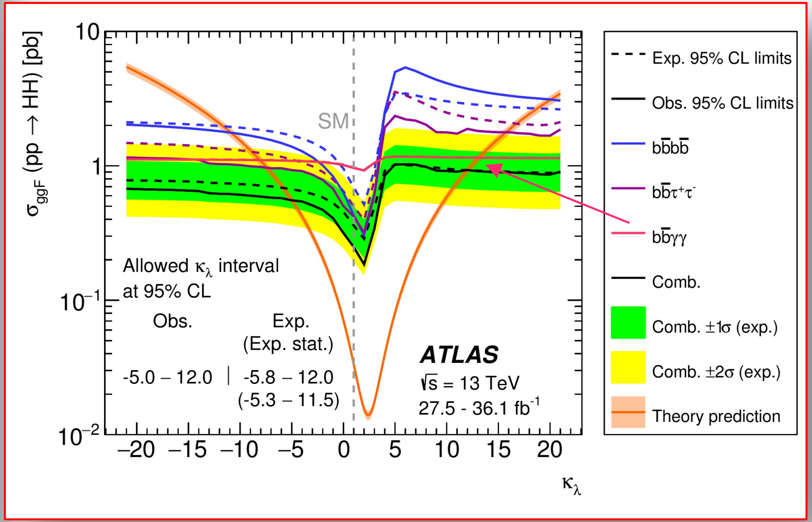

4.1 (5.5) x SM σ_{HH}

5x improvement wrt previous result (~ 26 x SM), ~3x due to analysis techniques

driven by m_{HH} categorization & MVA as well as b-jet corrections

Statistically dominated, few % impact from systematics

World's best constraints to date on Higgs boson's self coupling!

Resonant $HH \to b\bar{b}\gamma\gamma$ results

- **Single BDT for all resonances (mass dependent cut), 2 BDTs** to separate signal vs **continuum** and **single Higgs** backgrounds, scores combined in BDT_{tot}, signal extracted from $m_{\gamma\gamma}$

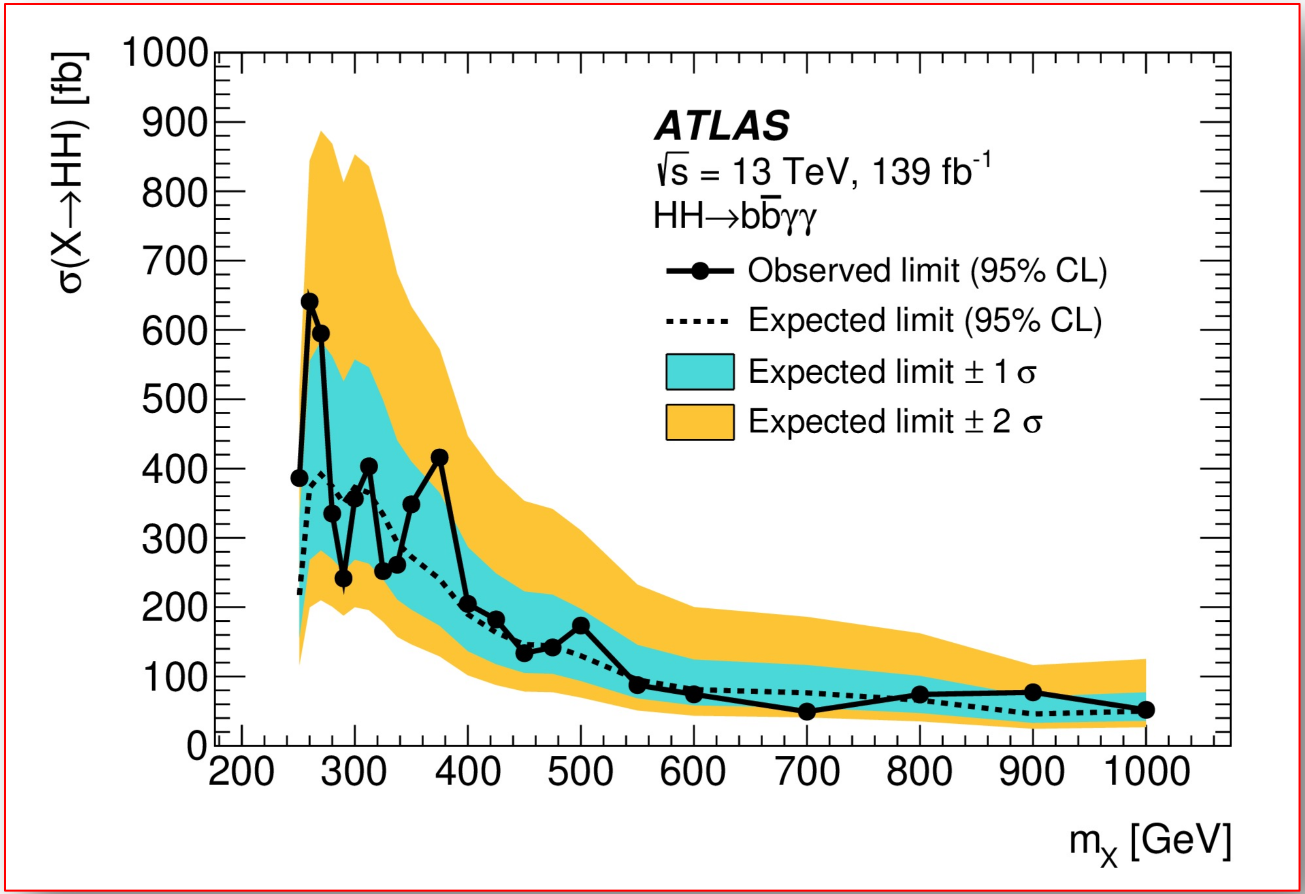

~ 30% improvement from BDT strategy on top of luminosity increase wrt 36 fb⁻¹ results

$HH \to b\bar{b}\tau\tau$

$\tau_{had} - \tau_{had}$

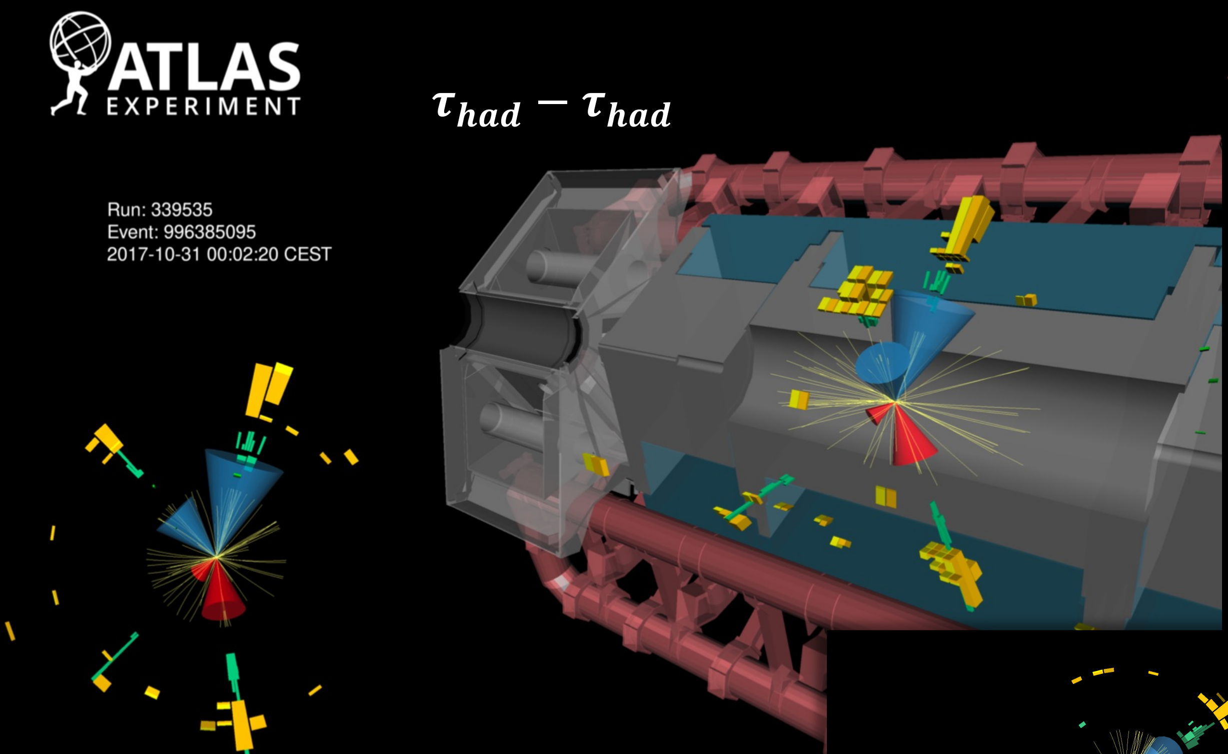

$\tau_{lep} - \tau_{had}$

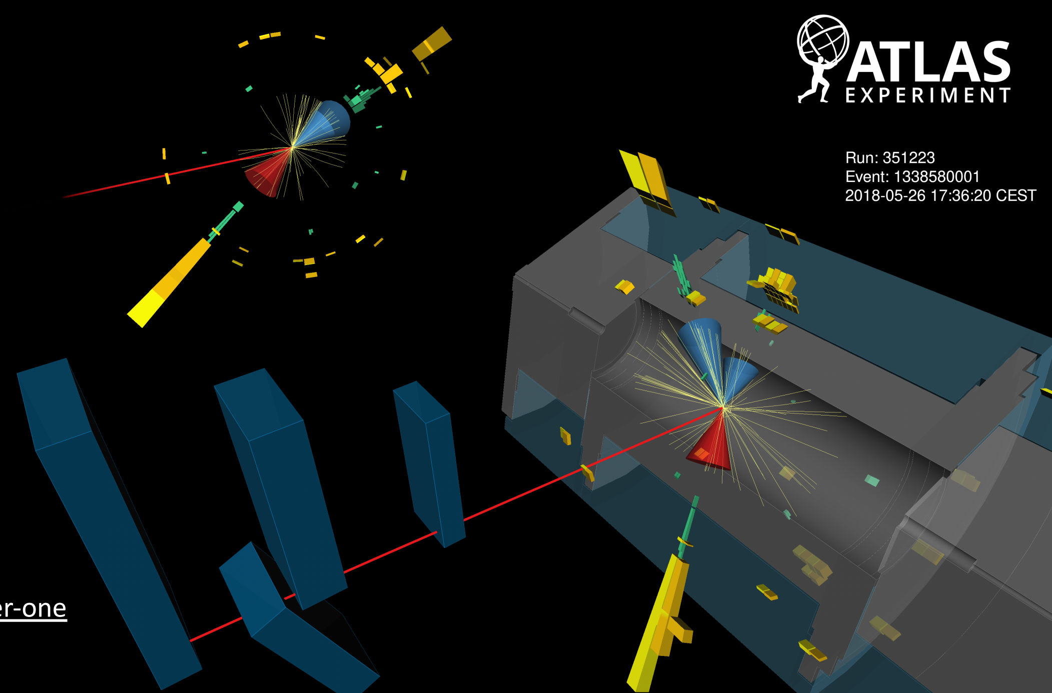

Publication: ATLAS-CONF-2021-030

Physics Briefing: https://atlas.cern/updates/briefing/two-Higgs-better-one

$HH \to b\bar{b}\tau\tau$ analysis in a nutshell

Relatively large BR and **relatively clean final state**
Single Tau Trigger & **Di-Tau** Trigger **for** $\tau_{had}\,\tau_{had}$
Single Lepton Trigger (SLT) and **Lepton+Tau Trigger** (LTT) **in** $\tau_{lep}\,\tau_{had}$

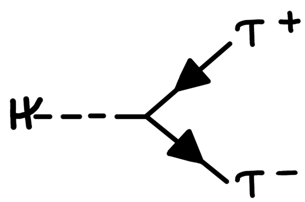

Hadronic & Leptonic

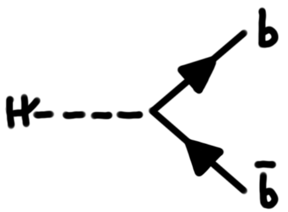

B-jet energy corrections

Object selection

Event categorization

MVA in 3 categories:

$\tau_{had}\,\tau_{had}$
(opp. charged)

$\tau_{lep}\,\tau_{had}$ (e/μ & opp. charged τ) **LTT**
SLT

Control region Z+HF (m_{ll})

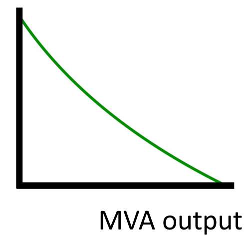

BDT($\tau_{had}\,\tau_{had}$) &
NN($\tau_{lep}\,\tau_{had}$) for
non-resonant

Parametric (by m_X)
NNs for resonant

m_{HH}, m_{bb}, $m_{\tau\tau}$, etc.

Multi-variable signal extraction

Simultaneous likelihood fit to all categories

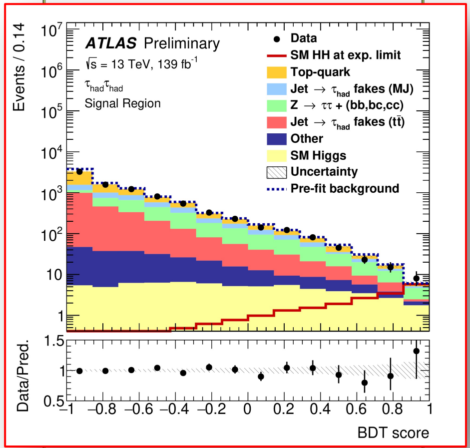

Non-resonant $HH \to b\bar{b}\tau\tau$ results

Non-resonant analysis thoroughly optimized for SM cross-section limit!

		Observed	$-2\,\sigma$	$-1\,\sigma$	Expected	$+1\,\sigma$	$+2\,\sigma$
$\tau_{had}\tau_{had}$	$\sigma_{ggF+VBF}$ [fb]	145	70.5	94.6	131	183	245
	$\sigma_{ggF+VBF}/\sigma^{SM}_{ggF+VBF}$	4.95	2.38	3.19	4.43	6.17	8.27
$\tau_{lep}\tau_{had}$	$\sigma_{ggF+VBF}$ [fb]	265	124	167	231	322	432
	$\sigma_{ggF+VBF}/\sigma^{SM}_{ggF+VBF}$	9.16	4.22	5.66	7.86	10.9	14.7
Combined	$\sigma_{ggF+VBF}$ [fb]	135	61.3	82.3	114	159	213
	$\sigma_{ggF+VBF}/\sigma^{SM}_{ggF+VBF}$	4.65	2.08	2.79	3.87	5.39	7.22

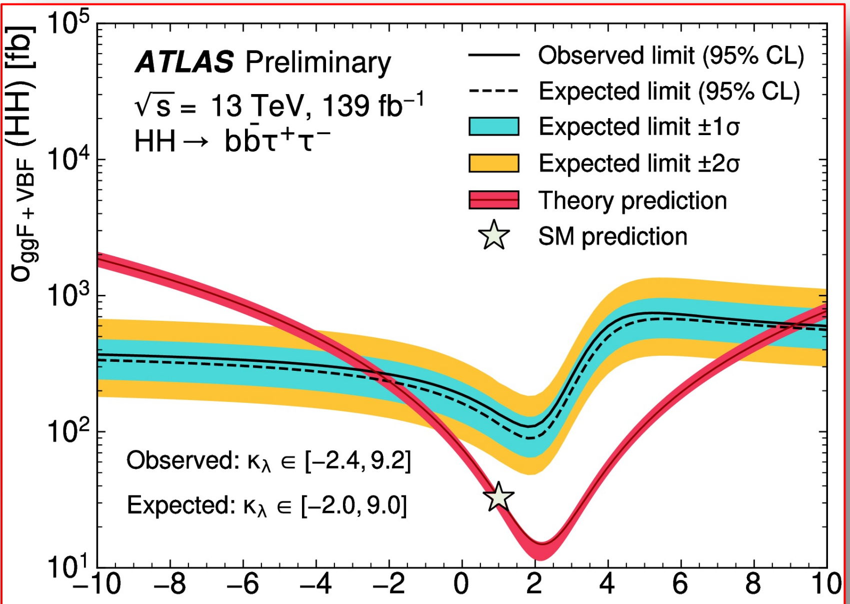

ATLAS-CONF-2021-052

4x improvement wrt to previous results! (12.7 x SM),

2x due to the τ and *b*-jet reconstruction and identification improvements and to analysis techniques (MVA & fake-τ estimation methods).

- Statistically dominated, largest systematics from background modeling

Resonant $HH \to b\bar{b}\tau\tau$ results

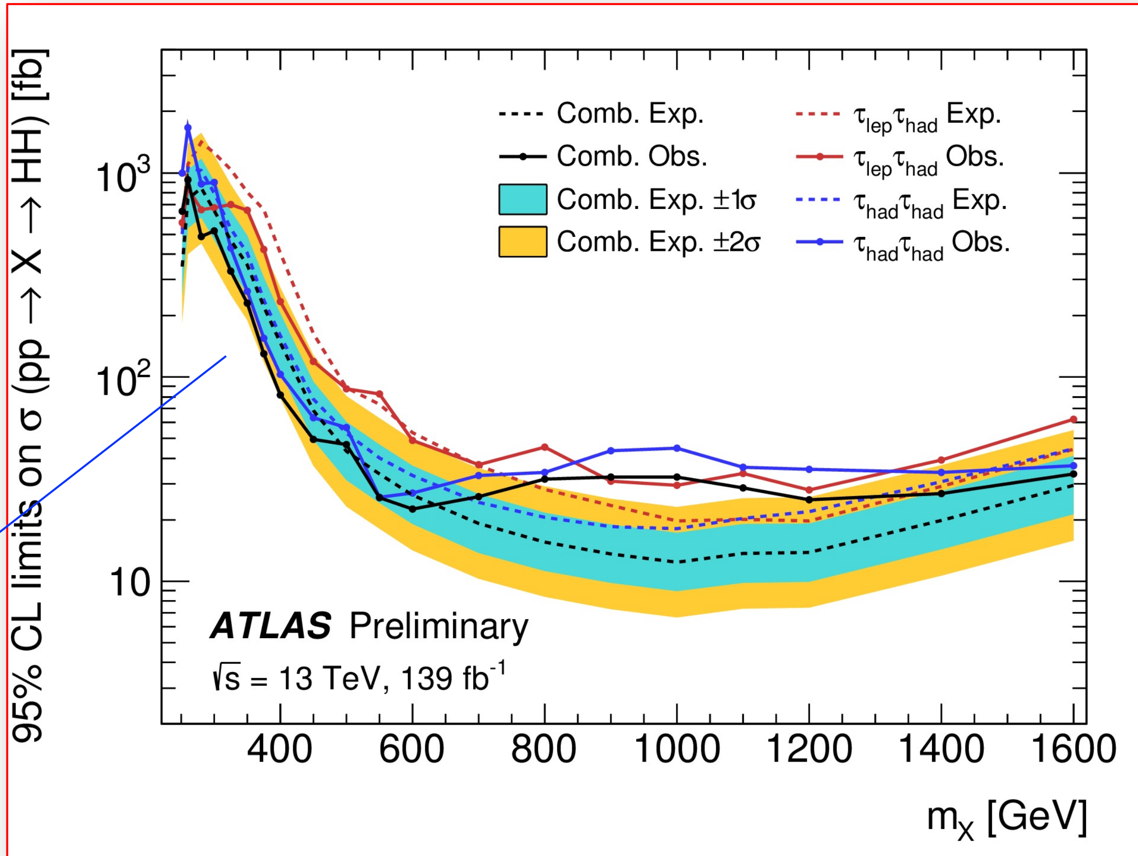

$\tau_{had}\,\tau_{had}$

Better sensitivity below 1 TeV

- Broad excess @ 700 GeV < m_X < 1.2 TeV.
- Most significant excess for $\tau_{had}\,\tau_{had}$ ($\tau_{lep}\,\tau_{had}$) found @ 1 TeV (1.1 TeV), local significance of 2.8 σ (1.6 σ).
- Combined: @1 TeV, local significance 3.1 σ, global significance of $2.1^{+0.4}_{-0.2}$ σ.

$HH \to b\bar{b}b\bar{b}$

ATLAS EXPERIMENT

Run: 356259
Event: 311347503
2018-07-22 20:00:32 CEST

Boosted

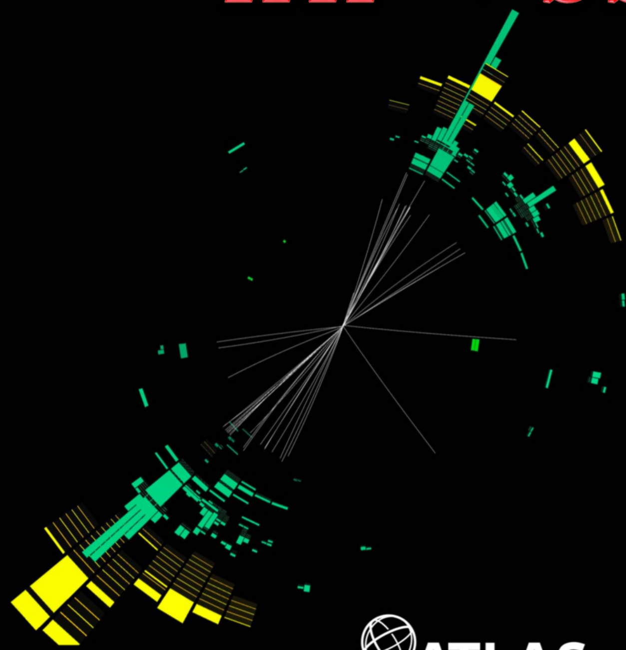

ATLAS EXPERIMENT

Run: 350013
Event: 1556168518
2018-05-11 01:39:26 CEST

Resolved

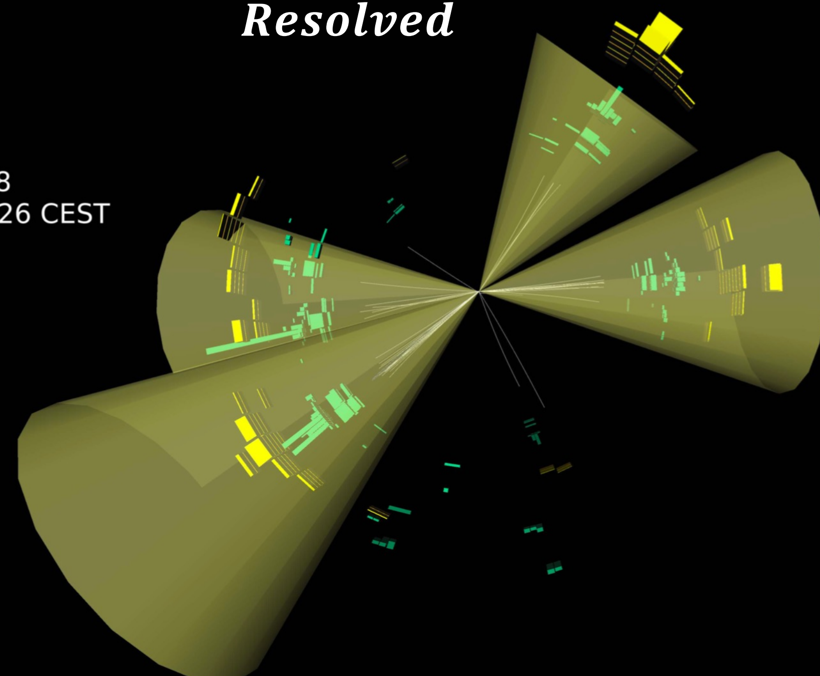

Publication: ATLAS-CONF-2021-035
Physics Briefing: https://atlas.cern/updates/briefing/double-Higgs-to-bottoms

$HH \rightarrow b\bar{b}b\bar{b}$

Largest BR, but **large multi-jet backgrounds** and challenging combinatorics
Only ggF **resonant** production considered

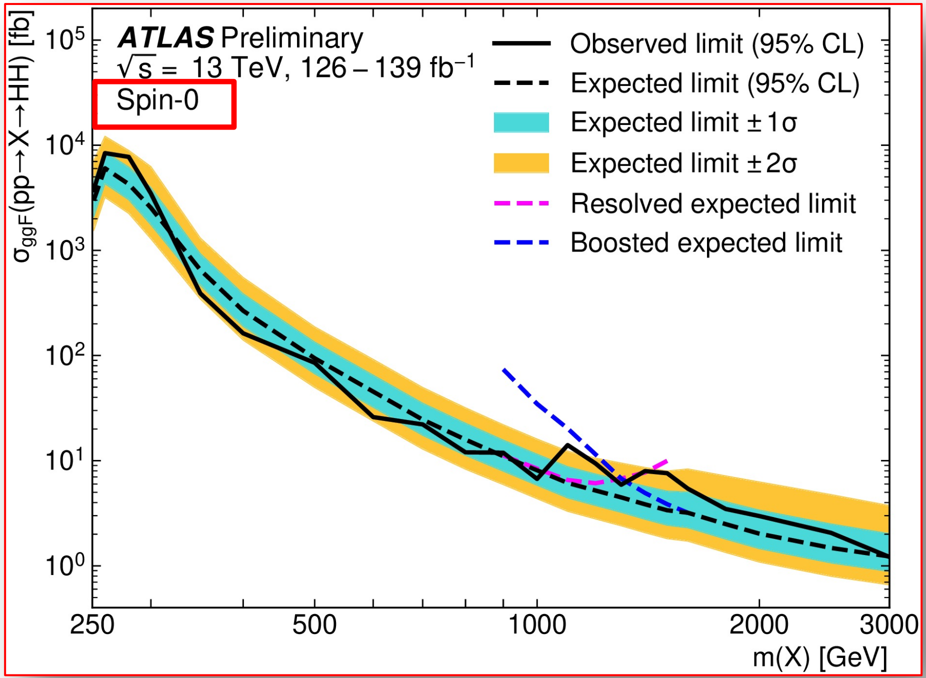

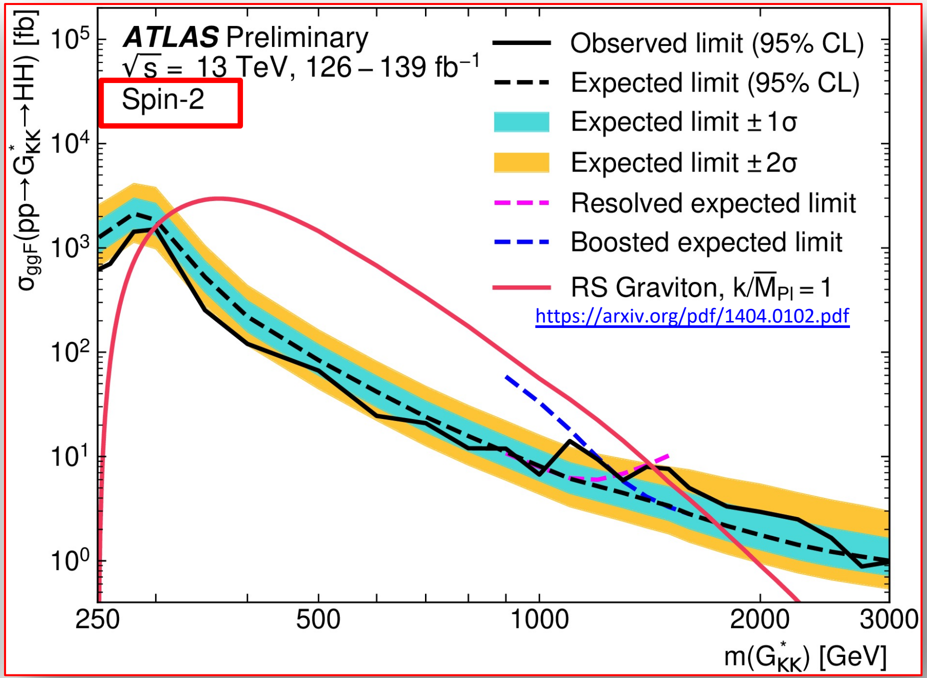

model excluded for graviton masses between 298 GeV and 1440 GeV.

Excess @ 1.1 TeV,
local (global) significance = 2.6σ (1.0 σ) for *spin-0* and 2.7σ (1.2 σ) for *spin-2*.
Statistically dominated results, systematic effects up to ~16%, mostly from background modeling

Putting everything together

Non-resonant

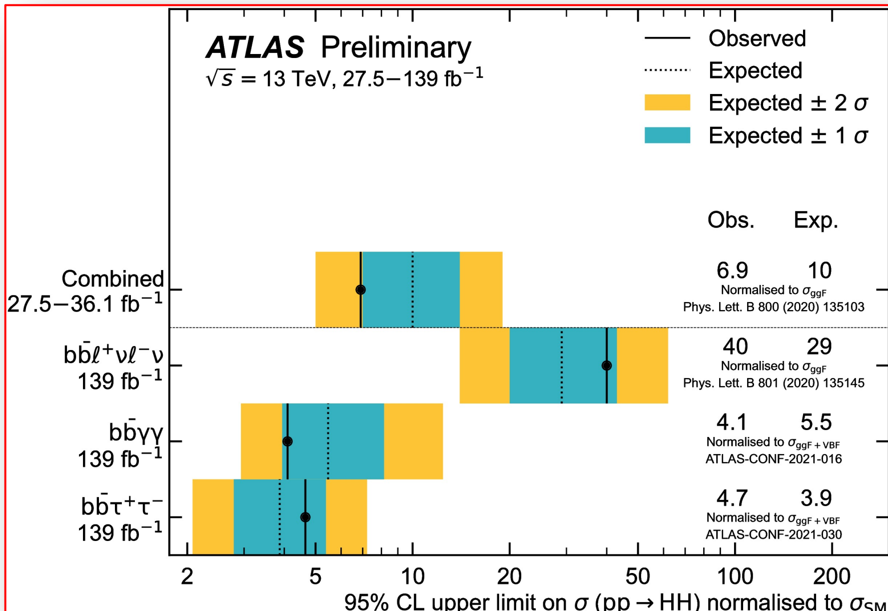

Resonant

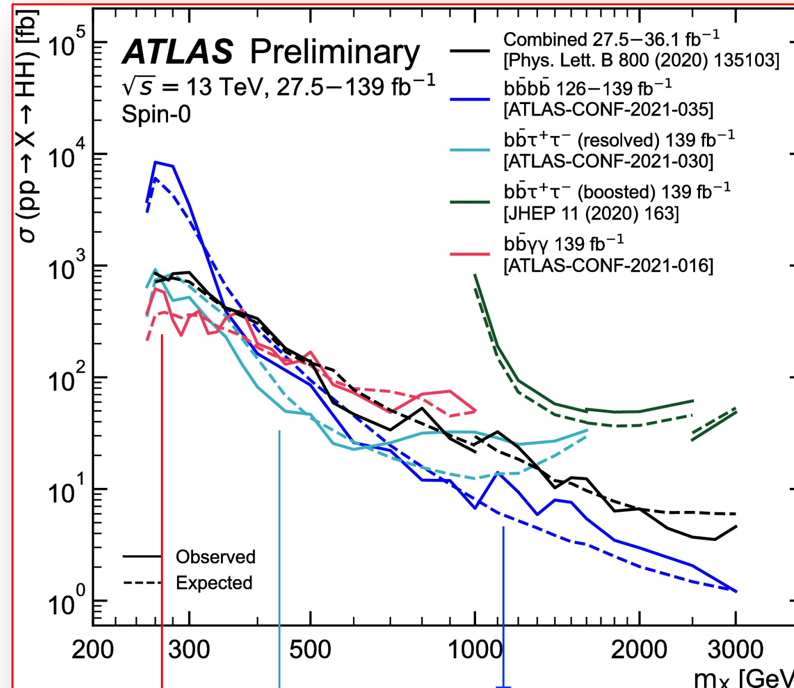

Single channels are now even better than the 36 fb^{-1} HH combination!

$b\bar{b}\gamma\gamma$ dominates the sensitivity at low m_X

$b\bar{b}b\bar{b}$ dominates the sensitivity at high m_X

$b\bar{b}\tau\tau$ dominates the sensitivity at medium m_X

Putting everything together

ATLAS-CONF-2021-052

Resonant

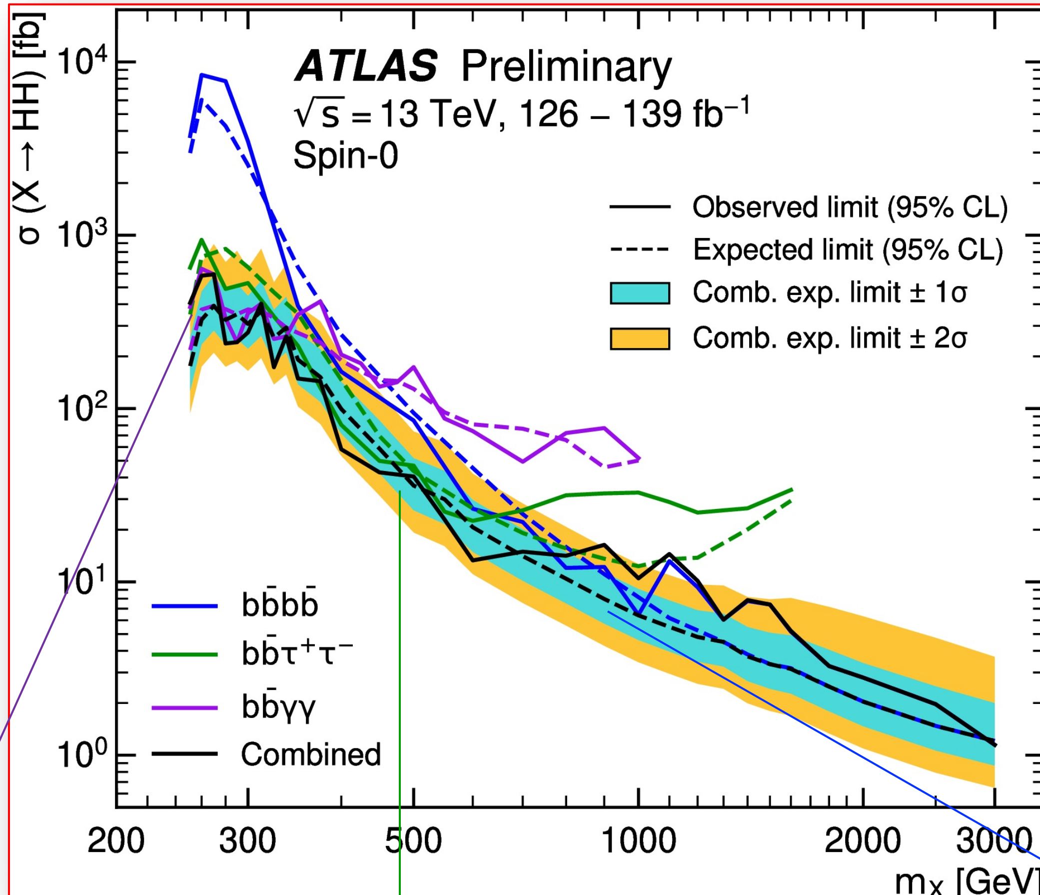

$b\bar{b}\gamma\gamma$ dominates the sensitivity at low m_X

$b\bar{b}b\bar{b}$ dominates the sensitivity at high m_X

$b\bar{b}\tau\tau$ dominates the sensitivity at medium m_X

B-jet energy corrections

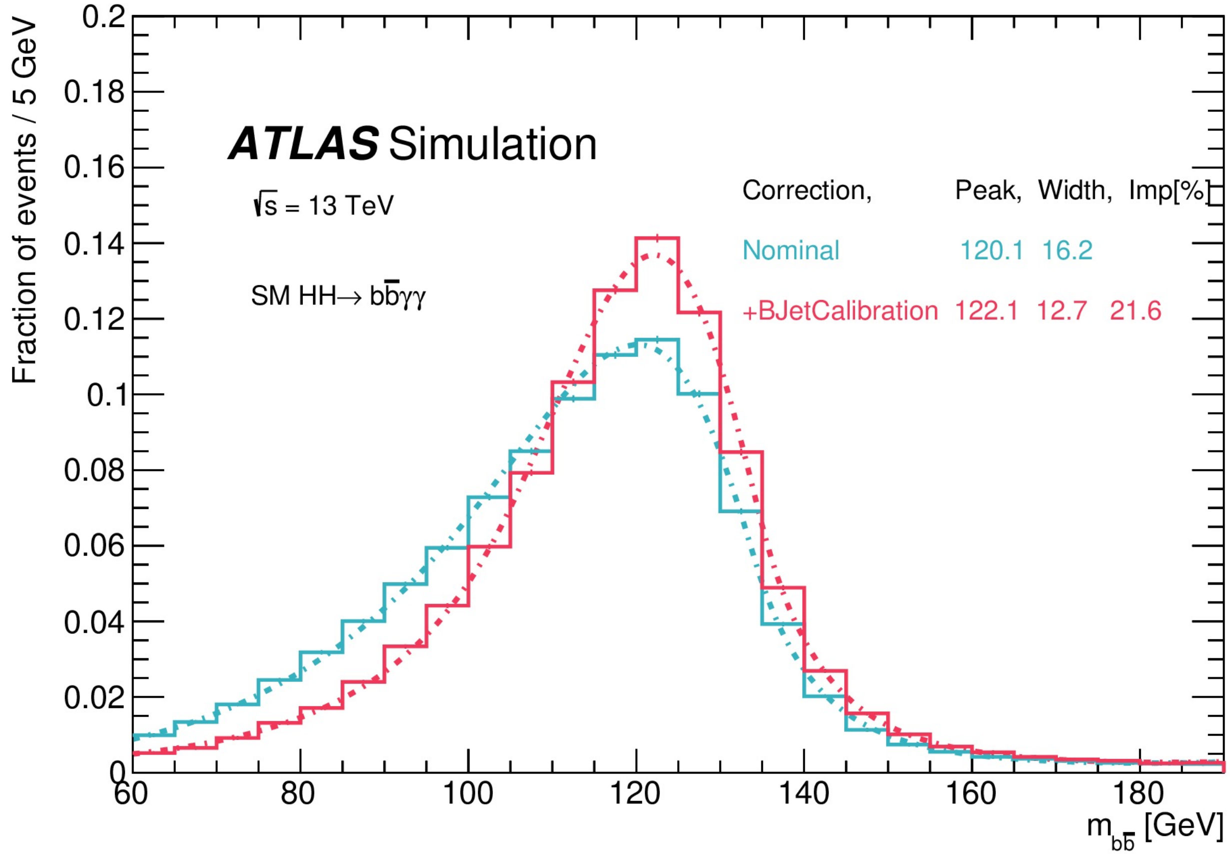

Topness

$$\chi_{Wt} = \min\sqrt{\left(\frac{m_{j_1j_2} - m_W}{m_W}\right)^2 + \left(\frac{m_{j_1j_2j_3} - m_t}{m_t}\right)^2},$$

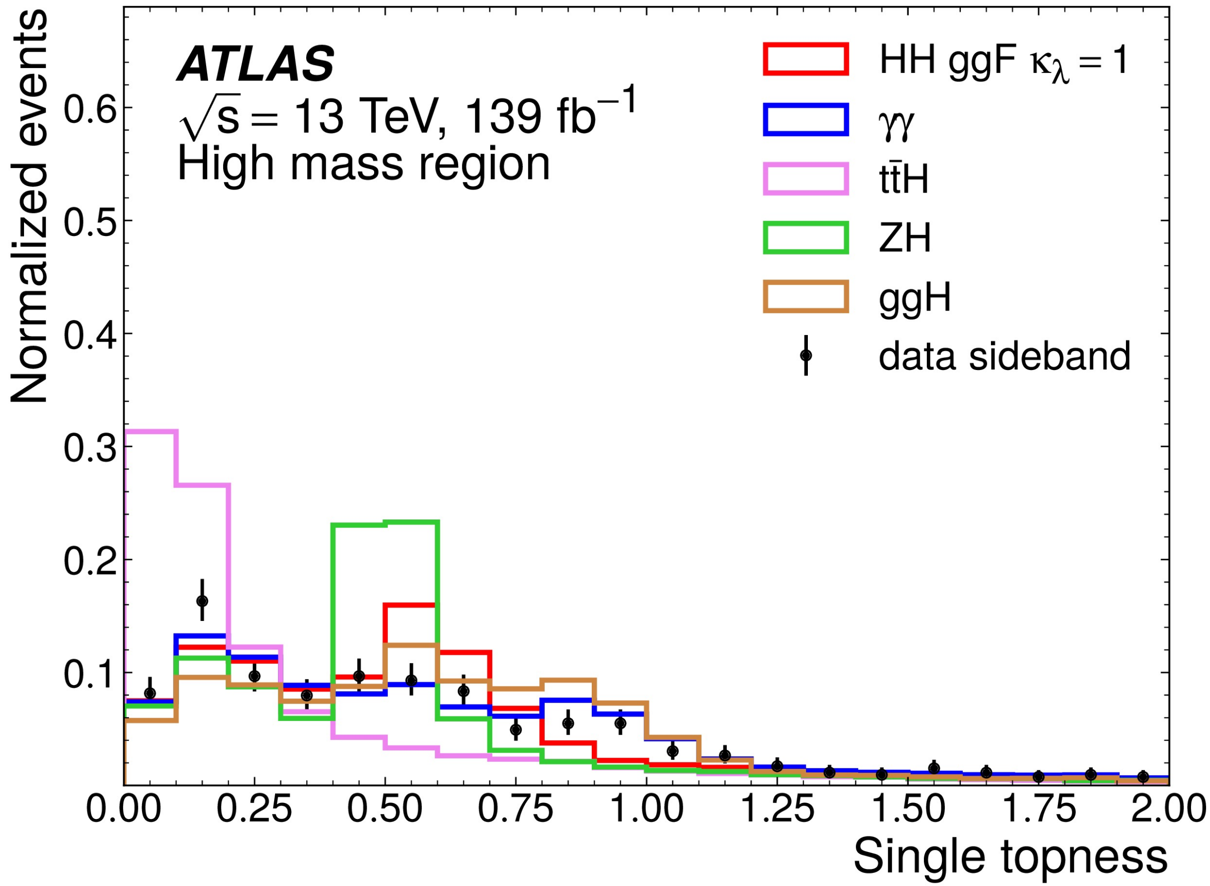

Categories & Significances

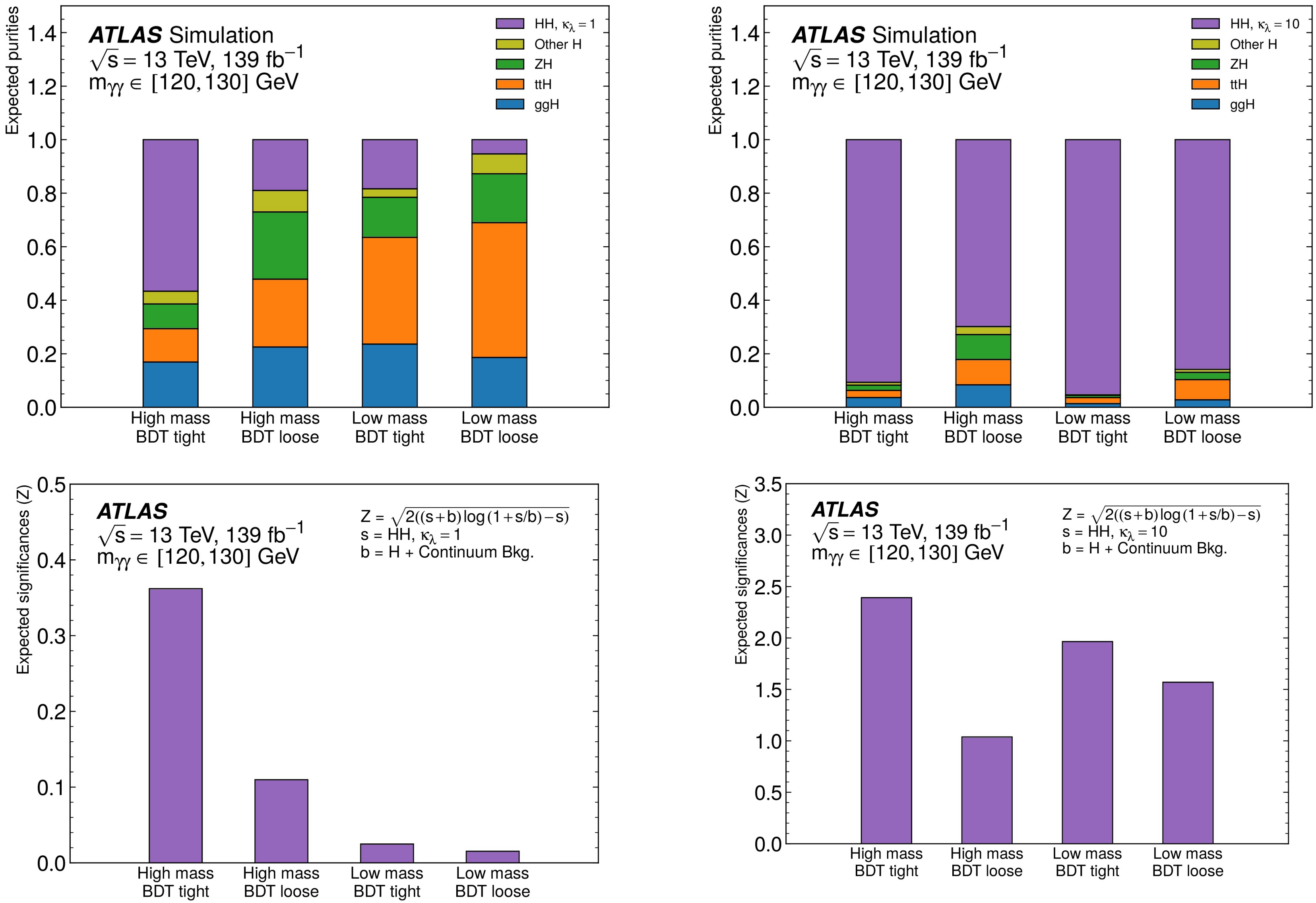

Acceptance x Efficiency

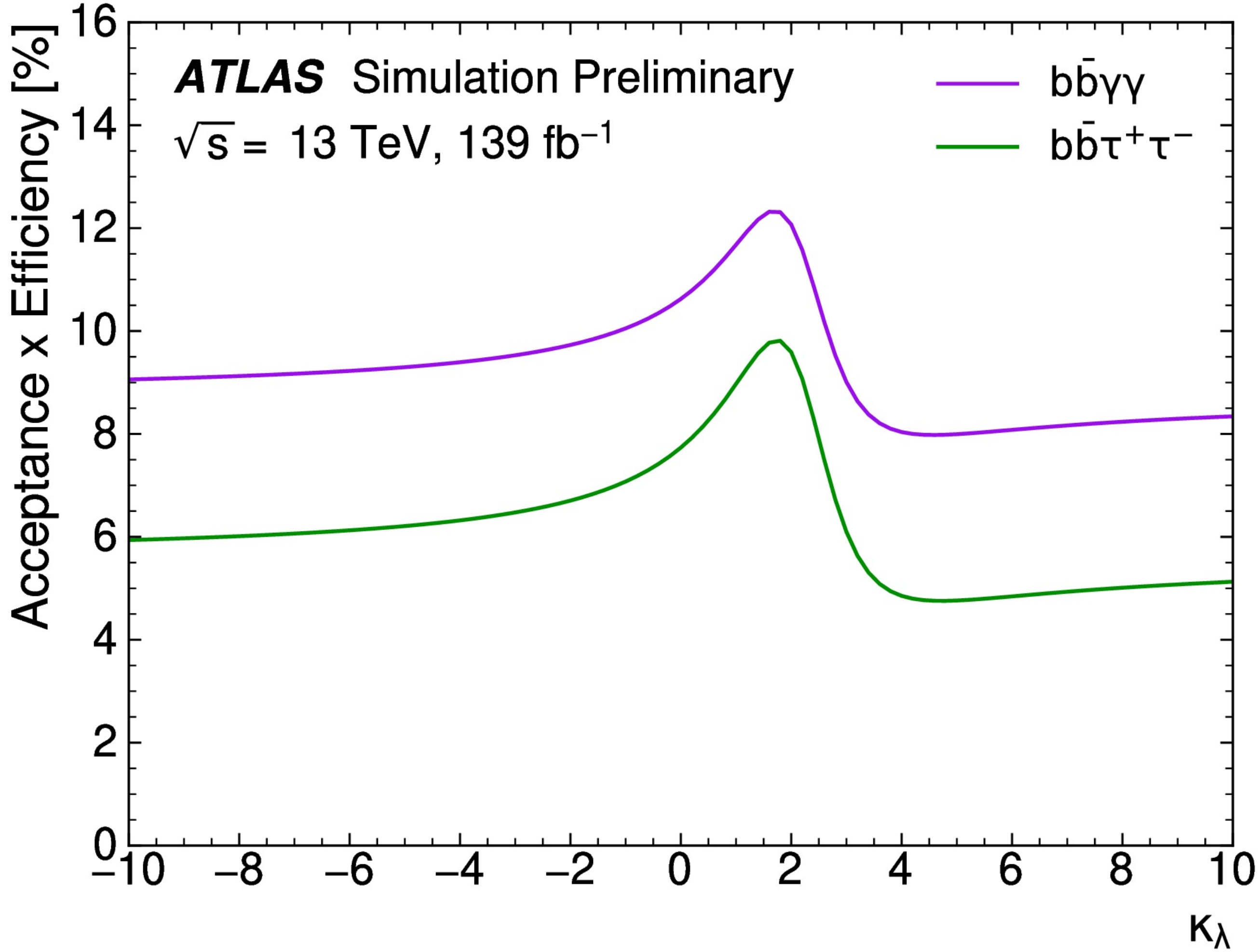

Pvalue

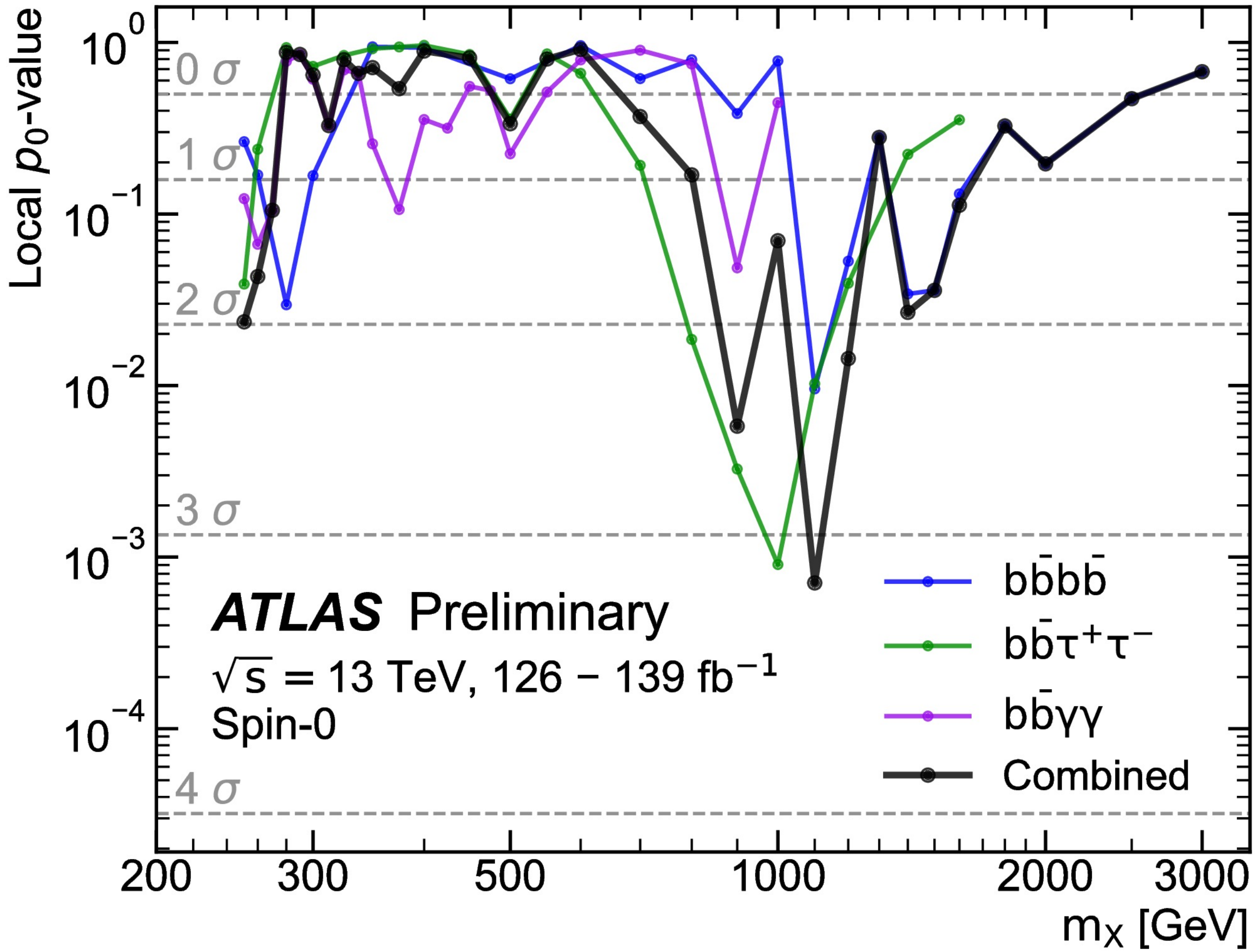

Local p_0-value
10^0
10^{-1}
10^{-2}
10^{-3}
10^{-4}
0 σ
1 σ
2 σ
3 σ
4 σ
ATLAS Preliminary
$\sqrt{s}$ = 13 TeV, 126 − 139 fb^{-1}
Spin-0
$b\bar{b}b\bar{b}$
$b\bar{b}\tau^+\tau^-$
$b\bar{b}\gamma\gamma$
Combined
200
300
500
1000
2000
3000
m_X [GeV]

Run 2/3

The ATLAS Run2/3 Inner Detector

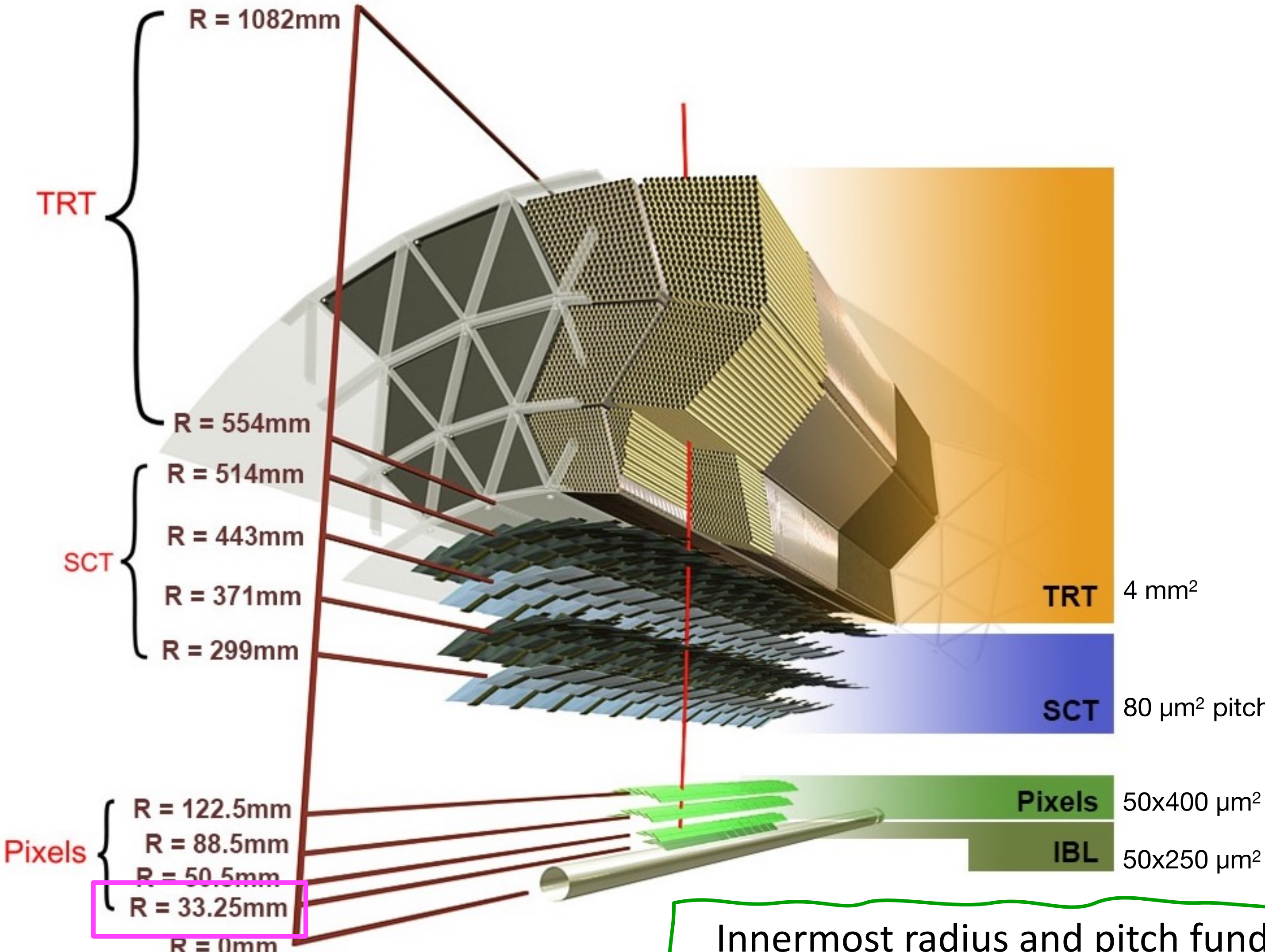

Innermost radius and pitch fundamental for **impact parameter** determination and thus **b-tagging performance**!

What is a b-jet in ATLAS?

High-Level ML b-taggers utilize low-level taggers' outputs

- Impact Parameter based
- Secondary Vertex finding
- **Decay chain Multi-Vertex Algorithm** (JetFitter)

CERN-THESIS-2010-027

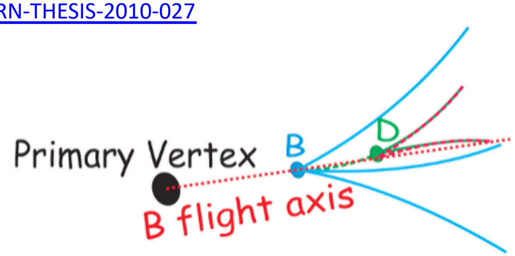

Sensitive to primary vertex reconstruction

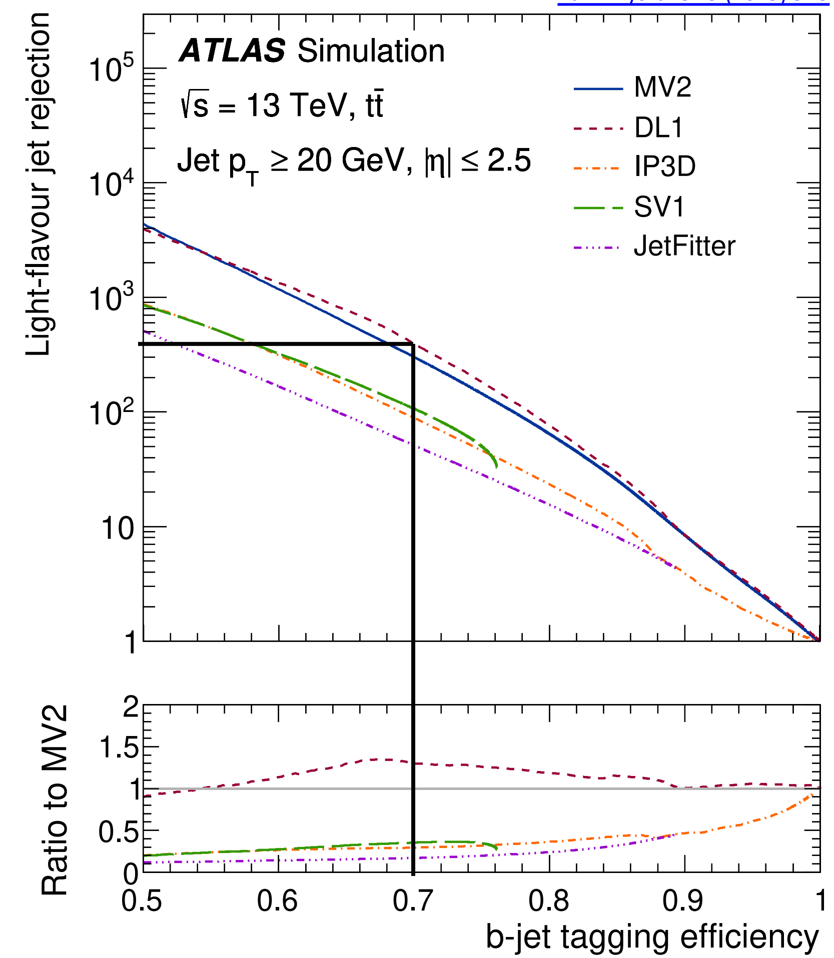

70% b-tag efficiency, ~0.3% light-jet

About 1 order of magnitude lower fake rate compared to Tevatron! Ref 1, 2

Run 2 Performance Highlights

- **Tracking and Vertexing are key ingredients for physics analyses**
- **Run 1** → **Run 2**: upgraded detector
  - 2x better IP resolution, 4-5x better light-jet rejection in b-tagging

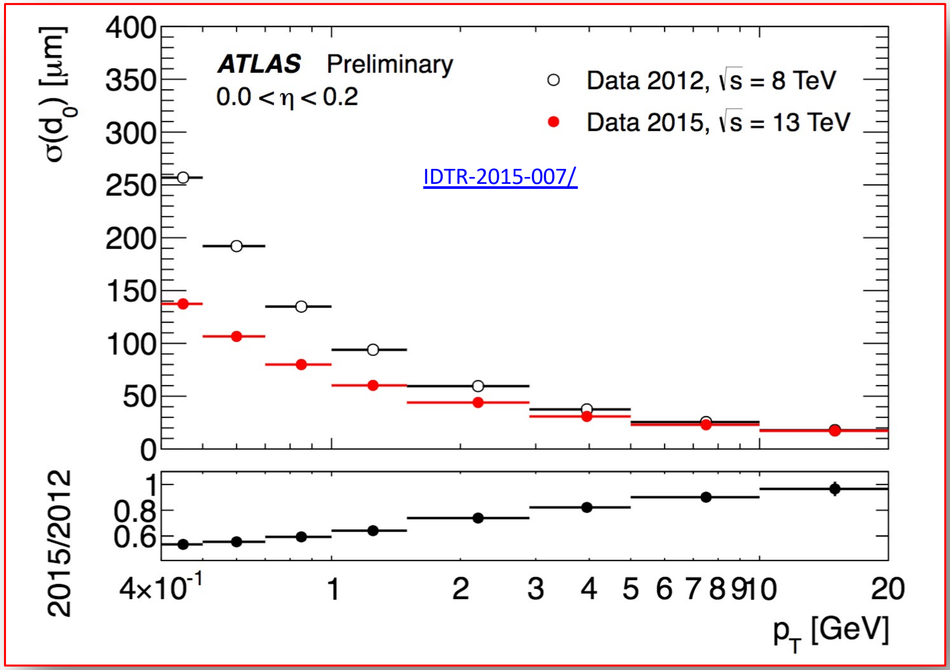

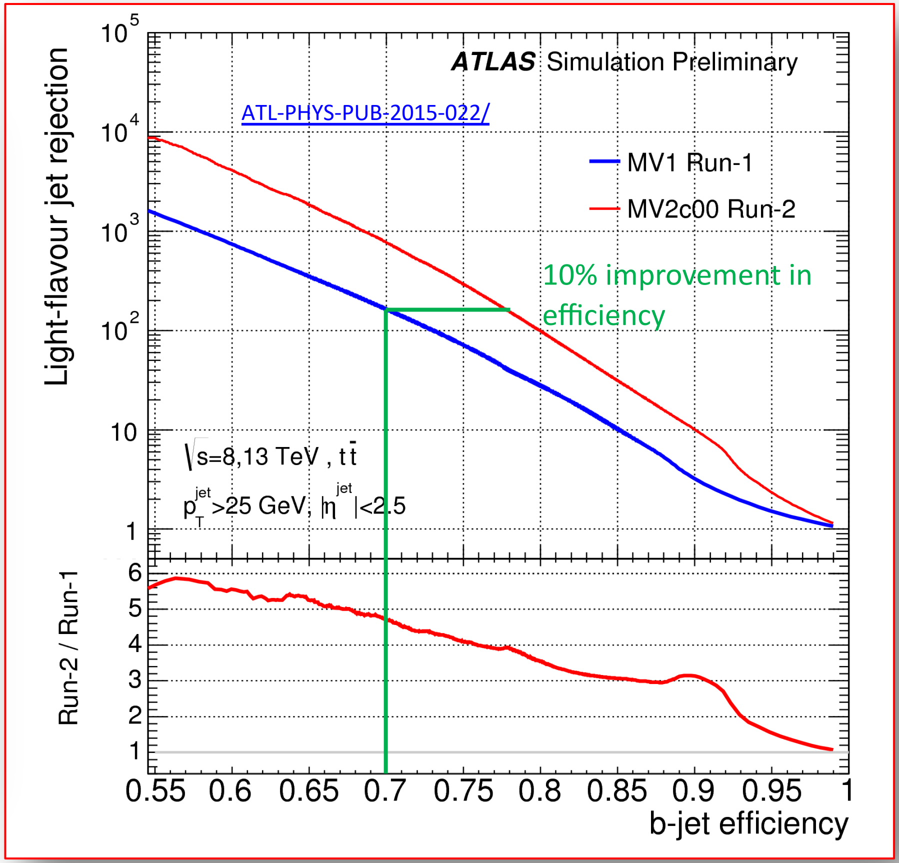

Run 3 Performance Highlights

- **Run 2** → **Run 3** : aging detector and more challenging pile-up conditions
- All physics objects must be reconstructed wrt the correct primary vertex
- **New primary vertexing algorithm** deployed to improve pile-up robustness

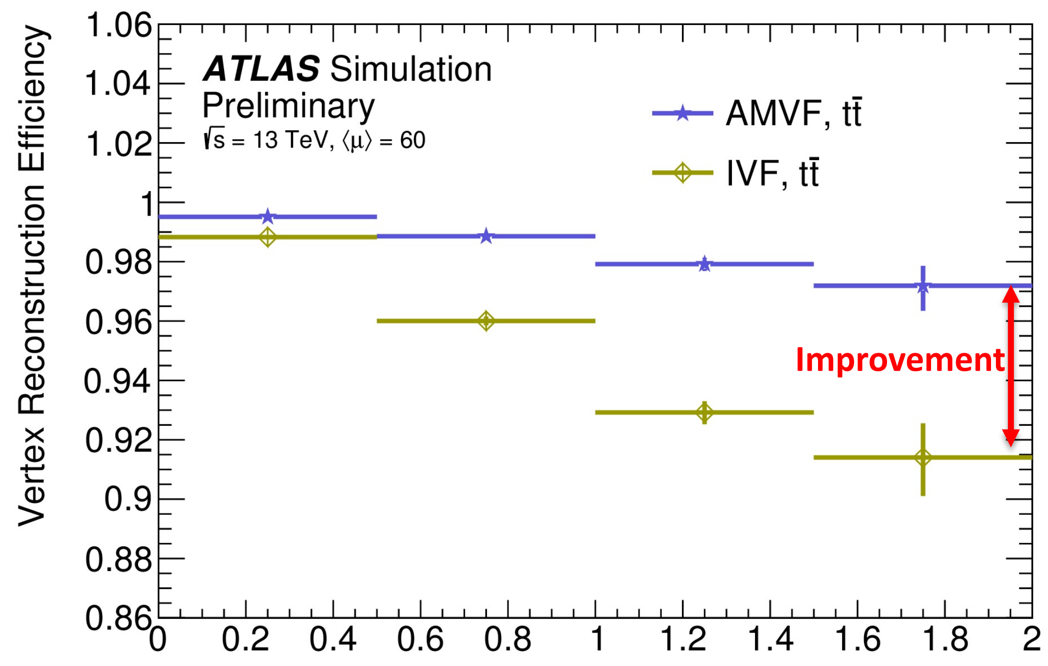

ATL-PHYS-PUB-2019-015

Significant performance improvements:

~**10**% better vertex selection efficiency, ~**20**% better longitudinal resolution,

~**30%** inclusive efficiency recovery

All relevant for **the HL-LHC ATLAS silicon Inner Tracker (ITk)**

HL-LHC Extrapolations

High-Luminosity LHC timeline

From J. Mnich's presentation

Long-term Schedule

Run 3 will be extended by 1 year until end 2025 and LS3 by ½ year until end 2028

Note:

- no further extension of Run 3 or LS3 possible! For technical and political reasons
- the HL-LHC goal of providing 3000/fb integrated luminosity to ATLAS and CMS would require HL-LHC operation until ≈ 2041
- ending HL-LHC in 2038 would provide ≈ 2500/fb per experiment

Final decision on the long-term HL-LHC schedule will have to be taken at the next (or next-to-next?) strategy update in light of:

- performance and results from the LHC, progress with the next project (FCC), …

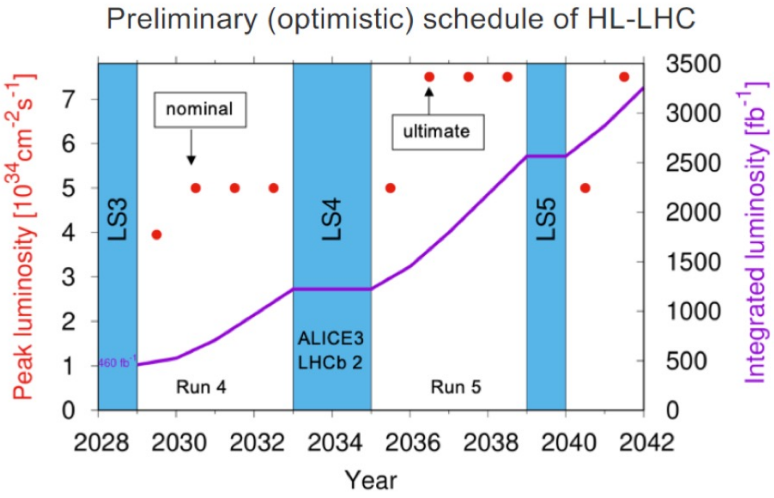

07.02.2022 J. Mnich 4

500 fb^{-1} can have an impact on HH!

HL-LHC Extrapolations

- Various systematics scenarios studied

Table 1: Summary of HL-LHC scale factors for relevant systematic uncertainties according to the most up-to-date ATLAS conventions for HL-LHC projections .

Source	**HL-LHC Scale Factor**
Experimental Uncertainties	
Luminosity	0.6
Photon efficiency (ID, trigger, isolation efficiency)	0.8
Photon energy scale and resolution	1.0
Jet energy scale and resolution, $E_{\mathrm{T}}^{\mathrm{miss}}$	1.0
b-jet tagging efficiency	0.5
c-jet tagging efficiency	0.5
Light-jet tagging efficiency	1.0
Value of m_H	0.08
κ_λ reweighting	0.0
Spurious signal	0.0
Theoretical Uncertainties	0.5

High-Luminosity LHC projections

Table 2: Summary of HL-LHC scale factors for relevant systematic uncertainties according to the recommendations of the ATLAS conventions for HL-LHC projections [39]. A “*" indicates that the uncertainty is considered by the corresponding analysis.

Source	Scale factor	$b\bar{b}\gamma\gamma$	$b\bar{b}\tau^+\tau^-$
Experimental Uncertainties			
Luminosity	0.6	*	*
b-jet tagging efficiency	0.5	*	*
c-jet tagging efficiency	0.5	*	*
Light-jet tagging efficiency	1.0	*	*
Jet energy scale and resolution, $E_{\mathrm{T}}^{\mathrm{miss}}$	1.0	*	*
κ_λ reweighting	0.0	*	*
Photon efficiency (ID, trigger, isolation efficiency)	0.8	*	
Photon energy scale and resolution	1.0	*	
Spurious signal	0.0	*	
Value of m_H	0.08	*	
τ_{had} efficiency (statistical)	0.0		*
τ_{had} efficiency (systematic)	1.0		*
τ_{had} energy scale	1.0		*
Fake-τ_{had} estimation	1.0		*
MC statistical uncertainties	0.0		*
Theoretical Uncertainties	0.5	*	*

High-Luminosity LHC projections

- **HL-LHC projections** updated for **various systematics** scenarios

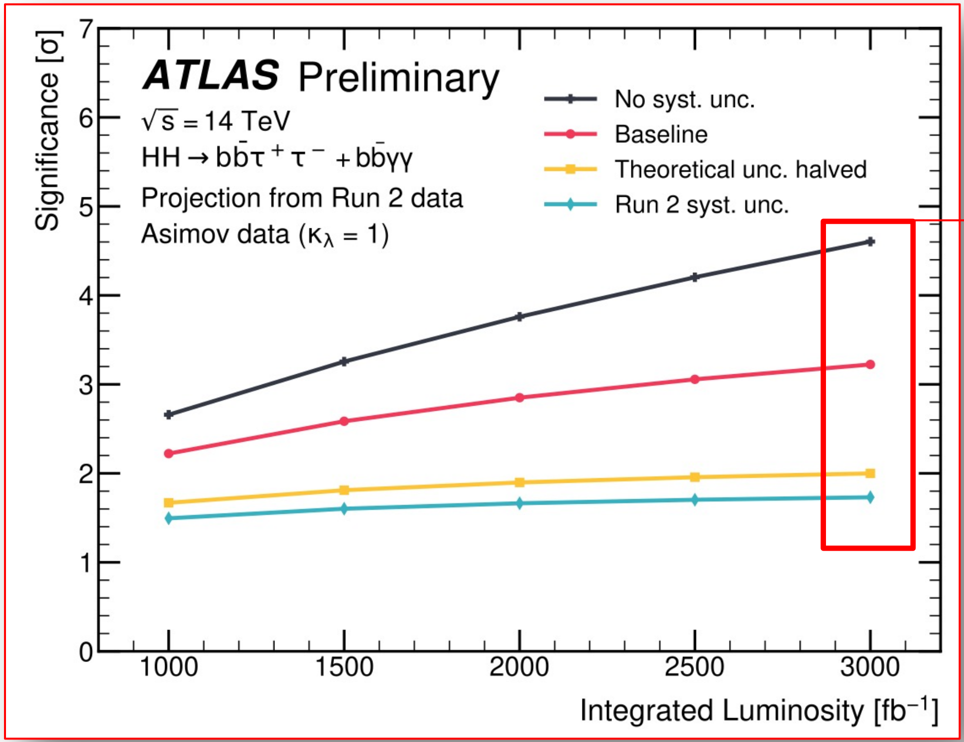

Critical role of **systematic uncertainties,**
e.g. continuum bkg modelling in
$HH \rightarrow bb\gamma\gamma$
Baseline: 0.5 x th. unc. and expected sys in HL-LHC

High-Luminosity LHC projections

- **HL-LHC projections** updated for **various systematics** scenarios

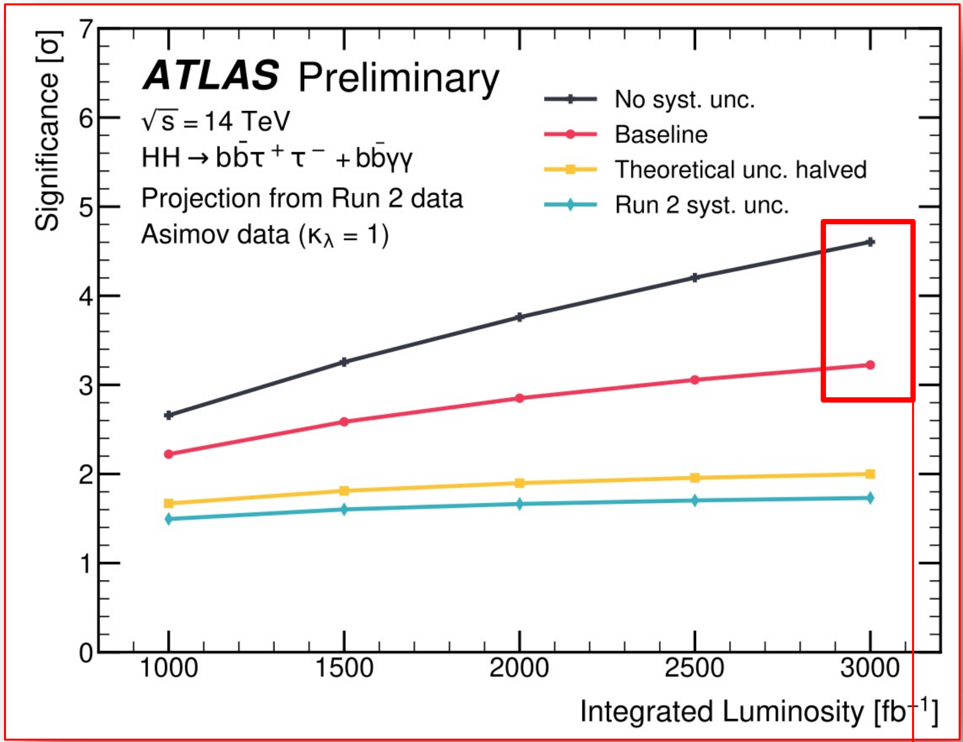

Uncertainty scenario	Significance [σ] $b\bar{b}\gamma\gamma$	$b\bar{b}\tau^+\tau^-$	Combination	Combined signal strength precision [%]
No syst. unc.	2.3 was 2.1	4.0 was 2.3	4.6	$-23/+23$
Baseline	2.2 was 2.0	2.8 was 2.0	3.2	$-31/+34$

Critical role of **systematic uncertainties,**
e.g. continuum bkg modelling in
$HH \to bb\gamma\gamma$

Baseline: 0.5 x th. unc. and expected sys in HL-LHC

High-Luminosity LHC projections

- **Significance** evaluated also **for non-SM scenarios**

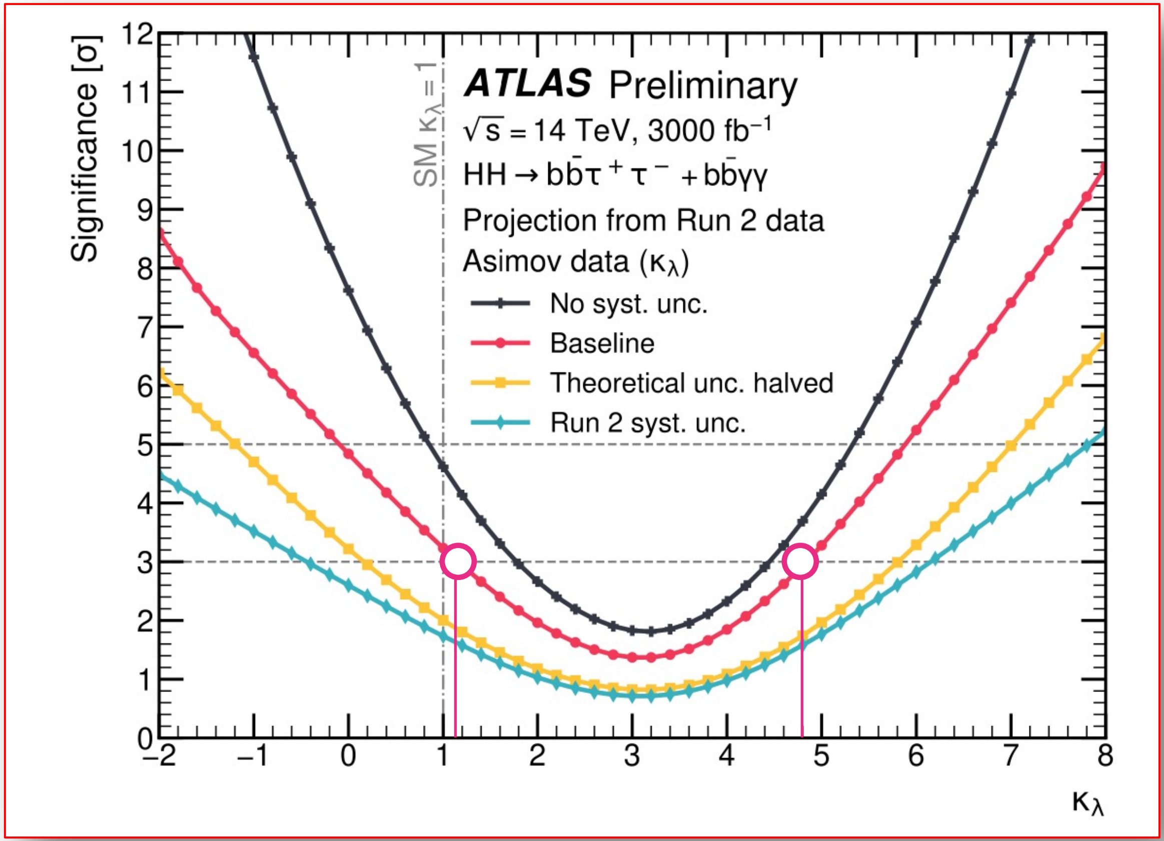

Baseline scenario:
evidence (3 σ)
if $\kappa_\lambda < 1.1$ or $\kappa_\lambda > 4.8$

High-Luminosity LHC projections

- **Significance** evaluated also **for non-SM scenarios**

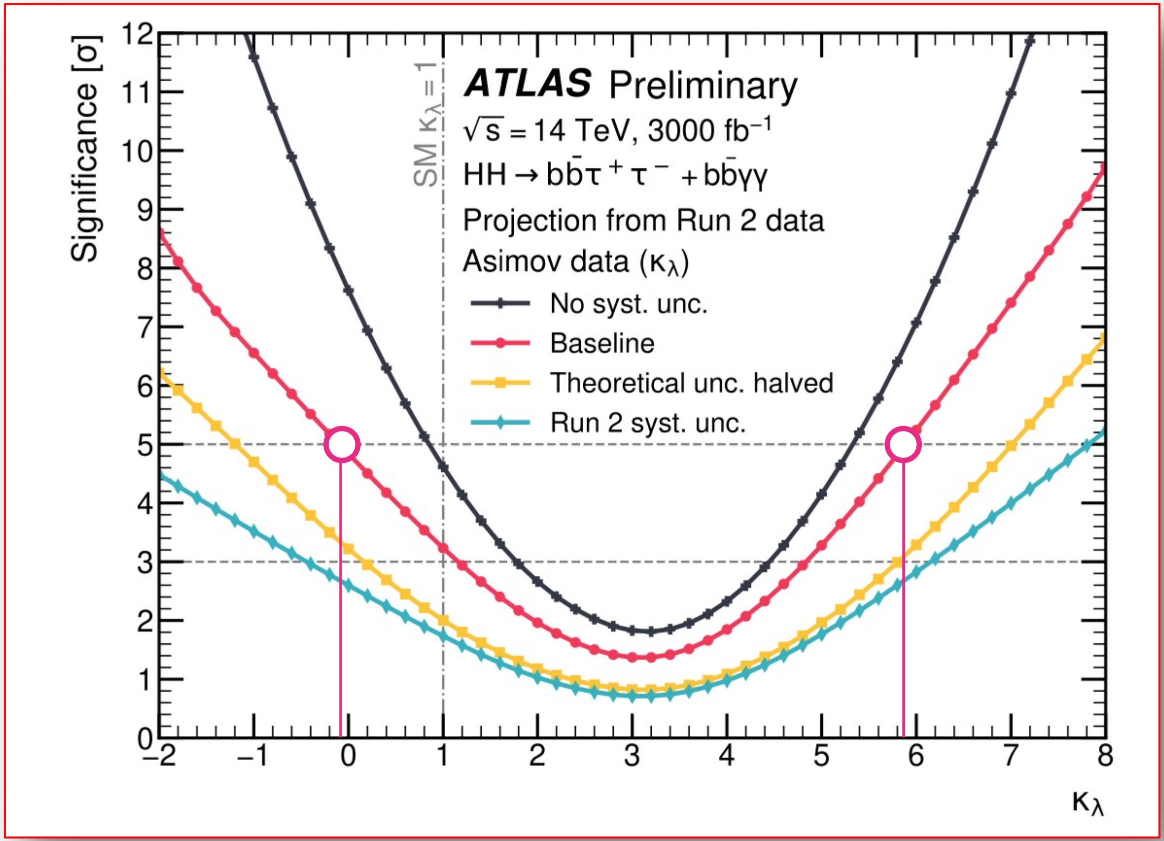

Baseline scenario:
evidence (3 σ)
if $\kappa_\lambda < 1.1$ *or* $\kappa_\lambda > 4.8$,
observation (5 σ)
if $\kappa_\lambda < -0.1$ *or* $\kappa_\lambda > 5.9$

High-Luminosity LHC projections

- Existing **combined** projections based on Early Run 2 results!

ATL-PHYS-PUB-2020-005

ATLAS (old) HL-LHC projections

Channel	Statistical-only	Statistical + Systematic
$HH \to b\bar{b}b\bar{b}$	1.2	0.5
$HH \to b\bar{b}\tau^+\tau^-$	2.3	2.0
$HH \to b\bar{b}\gamma\gamma$	2.1	2.0
Combined	3.3 σ	2.9 σ

ATLAS + CMS
$\sim 4\ \sigma$ (50% precision)
j.revip.2020.100045

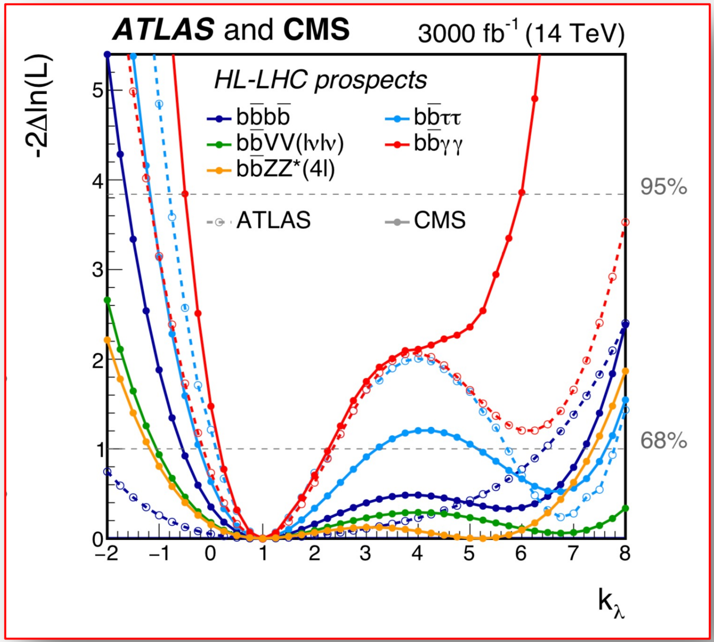

High-Luminosity LHC projections

- Existing **combined** projections based on Early Run 2 results!
  - Now great **analysis improvements** in all final states compared to Early Run 2
  - **Single-channel projections have been updated for various systematics scenarios**

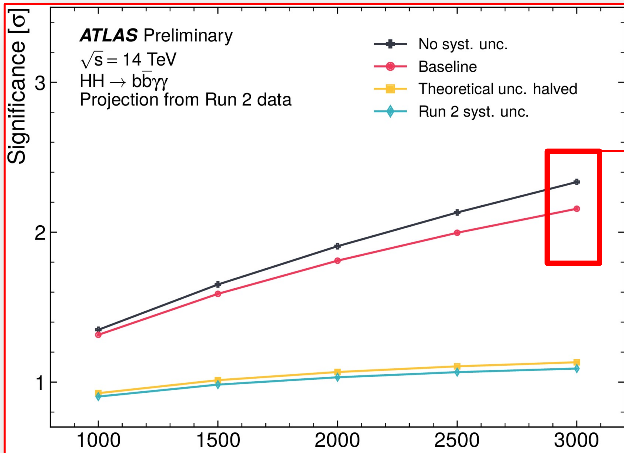

ATL-PHYS-PUB-2022-001/

$HH \to b\bar{b}\gamma\gamma$

Scenario	95% CL Upper Limit	Significance [σ]
No syst. unc.	0.86	2.3 was 2.1
Baseline	0.93	2.2 was 2.0

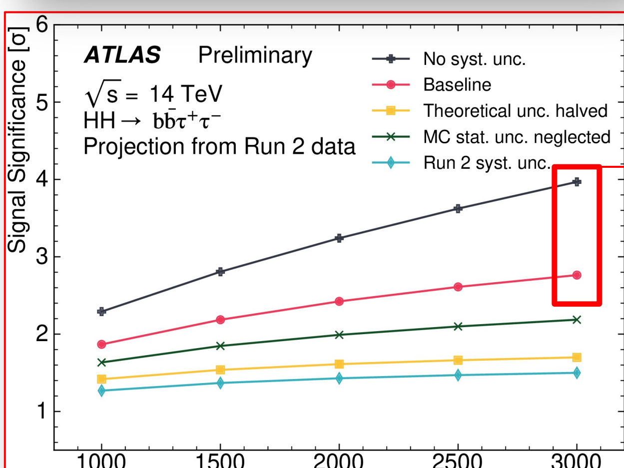

ATL-PHYS-PUB-2021-044/

$HH \to b\bar{b}\tau\tau$

Uncertainty Scenario	95% CL Upper Limit	Significance [σ]
No syst. unc.	0.49	4.0 was 2.3
Baseline	0.71	2.8 was 2.0

High-Luminosity LHC projections

- Statistical limited analysis at the LHC, but systematics start to play a role in HL-LHC!

Background Modeling Uncertainty Scenario	Spurious Signal ($N \times$ Run 2 value)	95% CL Upper Limit	Significance [σ]
No syst. uncert. (optimistic)	0	0.93	2.2
	1	0.93	2.2
Improved syst. uncert. (aggressive)	2	0.94	2.1
	4	0.96	2.1
Improved syst. uncert. (conservative)	10	1.1	1.8
	20	1.5	1.3
Current Run 2 syst. uncert. (pessimistic)	25	1.7	1.1

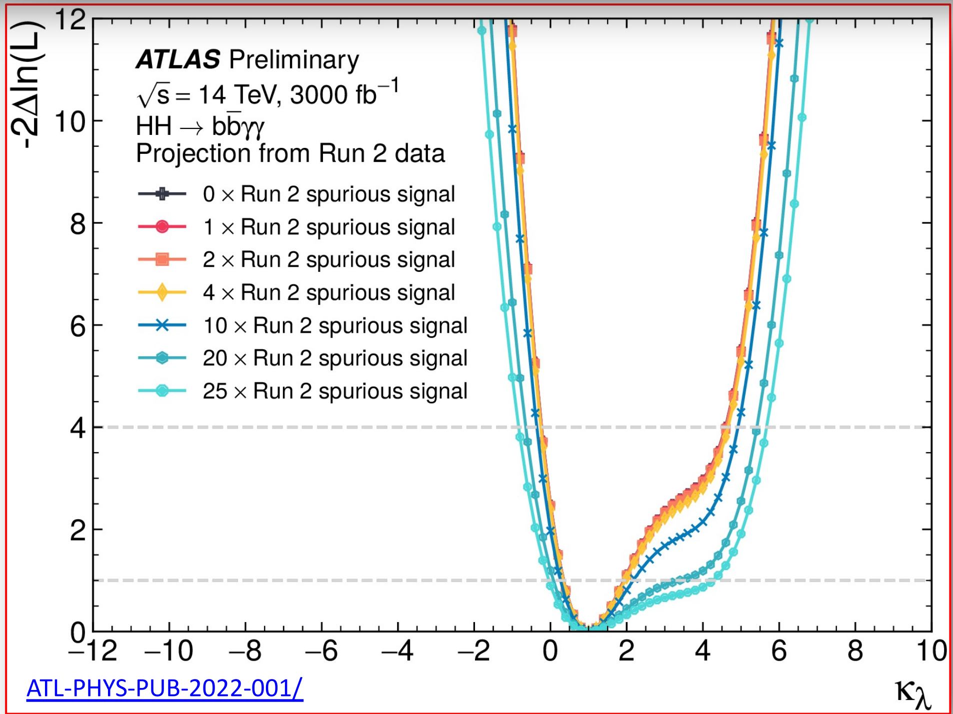

High-Luminosity LHC projections

As the spurious signal is the dominant systematic uncertainty affecting the Run 2 analysis sensitivity, dedicated studies are performed to better understand its impact on the projection results. The value of the Run 2 spurious signal systematic uncertainty consists primarily of two components: the intrinsic bias due to background mismodeling and a part due to statistical fluctuations resulting from the finite size of the MC background template. The former scales in the same manner as the background template, while the latter becomes negligible with increasing MC template statistics. The baseline projection scenario with HL-LHC systematic uncertainties takes the optimistic view that there is no intrinsic background modeling bias, and therefore that the spurious signal uncertainty will be 0 at the HL-LHC. The Run 2 systematic uncertainty and theoretical uncertainties halved scenarios assume the pessimistic scenario that the Run 2 spurious signal is due completely to mismodeling of the background, and therefore that the spurious signal uncertainty will simply scale in the same manner as the continuum background, i.e. by a factor of 25. The true spurious signal value at the HL-LHC likely lies between these two extremes. Studies of template smoothing techniques such as Gaussian Process Regression (GPR) suggest that a large increase to the MC template statistics may reduce the Run 2 spurious signal to approximately 15% of their nominal values for the same background functional forms. In this case, the spurious signal value at the HL-LHC would be approximately 4 times the current Run 2 value. A reduction of 50% on the spurious signal from template smoothing methods, corresponding to a HL-LHC spurious signal of approximately 10 times the Run 2 value, would be a rather conservative possibility.

ATL-PHYS-PUB-2022-001/

HL-LHC Extrapolations

- Degeneracy lifted

ATL-PHYS-PUB-2022-001/

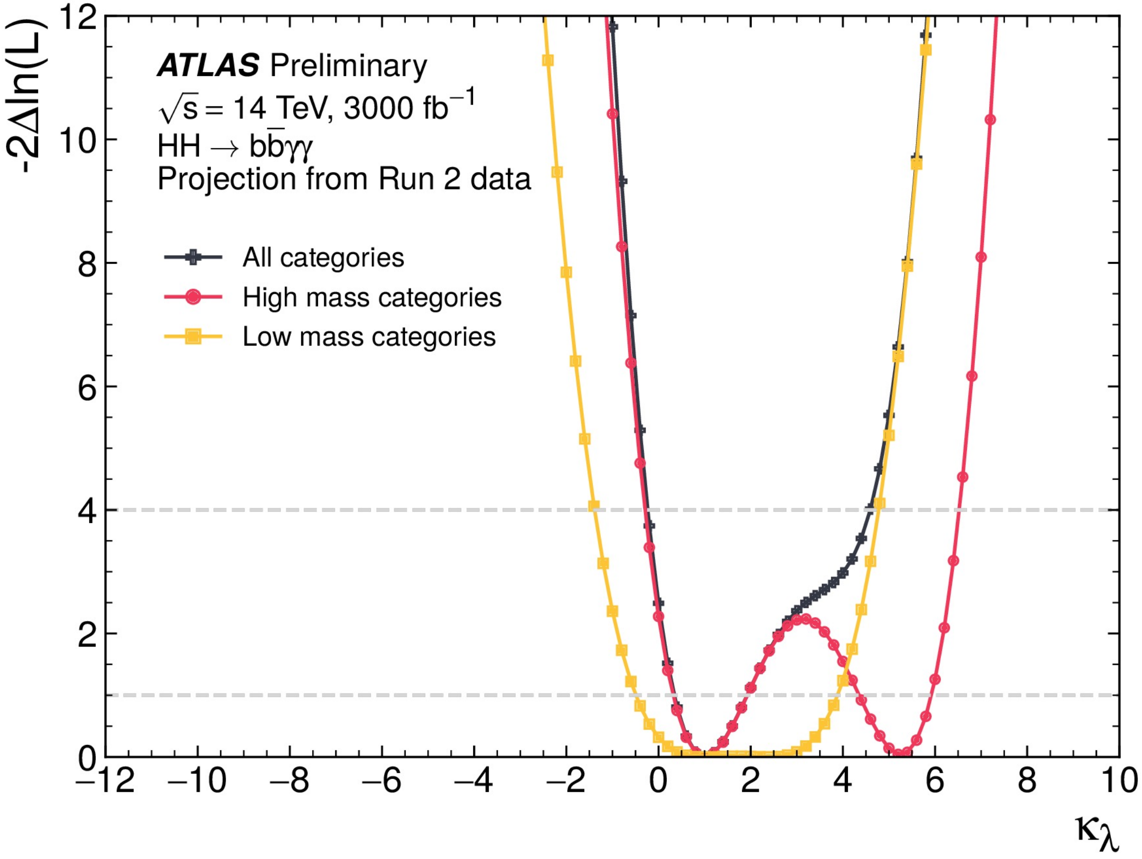

HL-LHC Extrapolations

- Various systematics scenarios studied

bbyy ATL-PHYS-PUB-2022-001/

Scenario	95% CL Upper Limit	Significance [σ]	Signal Strength Precision [%]
No syst. unc.	0.86	2.3	46
Baseline	0.93	2.2	50
Theoretical unc. halved	1.7	1.1	89
Run 2 syst. unc.	1.9	1.1	92

bbtautau ATL-PHYS-PUB-2021-044/

Uncertainty Scenario	95% CL Upper Limit	Significance [σ]	Signal Strength Precision
No syst. unc.	0.49	4.0	0.27
Baseline	0.71	2.8	0.39
Run 2 syst. unc.	1.37	1.5	0.69
MC stat. unc. neglected	0.99	2.2	0.51
Theoretical unc. halved	1.07	1.7	0.58

HL-LHC Extrapolations

ATL-PHYS-PUB-2022-001/

- Various systematics scenarios studied

Background Modeling Uncertainty Scenario	Spurious Signal ($N \times$ Run 2 value)	95% CL Upper Limit	Significance [σ]
No syst. uncert. (optimistic)	0	0.93	2.2
	1	0.93	2.2
Improved syst. uncert. (aggressive)	2	0.94	2.1
	4	0.96	2.1
Improved syst. uncert. (conservative)	10	1.1	1.8
	20	1.5	1.3
Current Run 2 syst. uncert. (pessimistic)	25	1.7	1.1

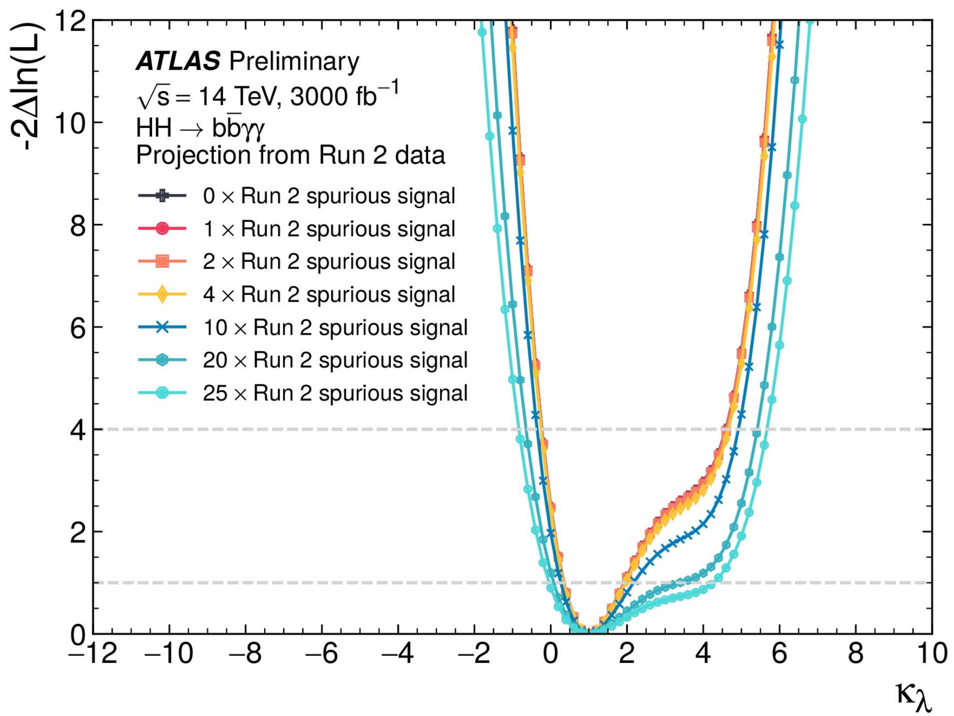

High-Luminosity LHC projections

- Existing **combined** projections based on Early Run 2 results!
  - Now great **analysis improvements** in all final states compared to Early Run 2
  - **Projections are being updated**

ATL-PHYS-PUB-2022-001/

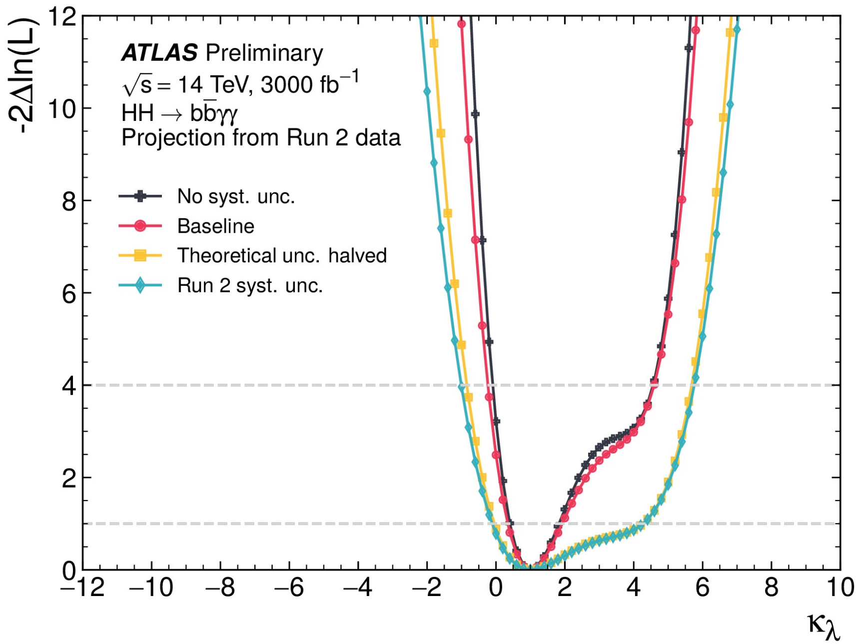

ATL-PHYS-PUB-2021-044/

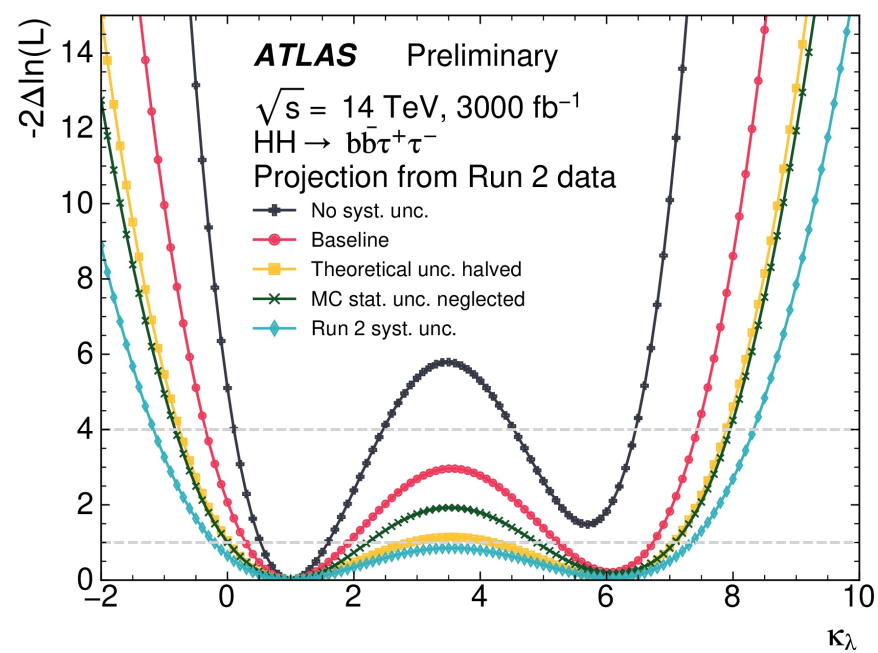

HL-LHC Extrapolations

- Various systematics scenarios studied

ATL-PHYS-PUB-2022-001/

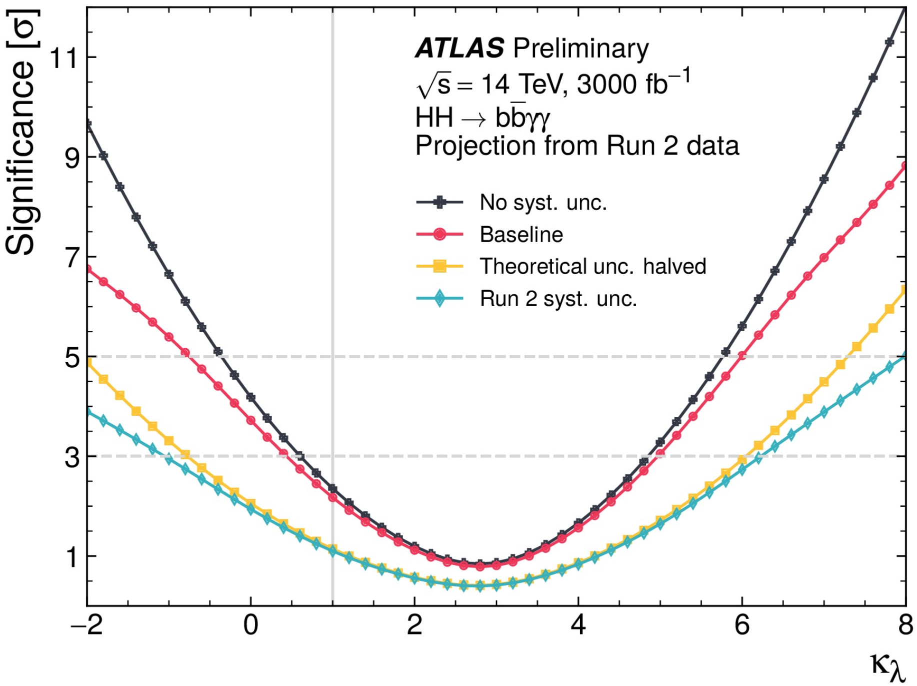

ATL-PHYS-PUB-2021-044/

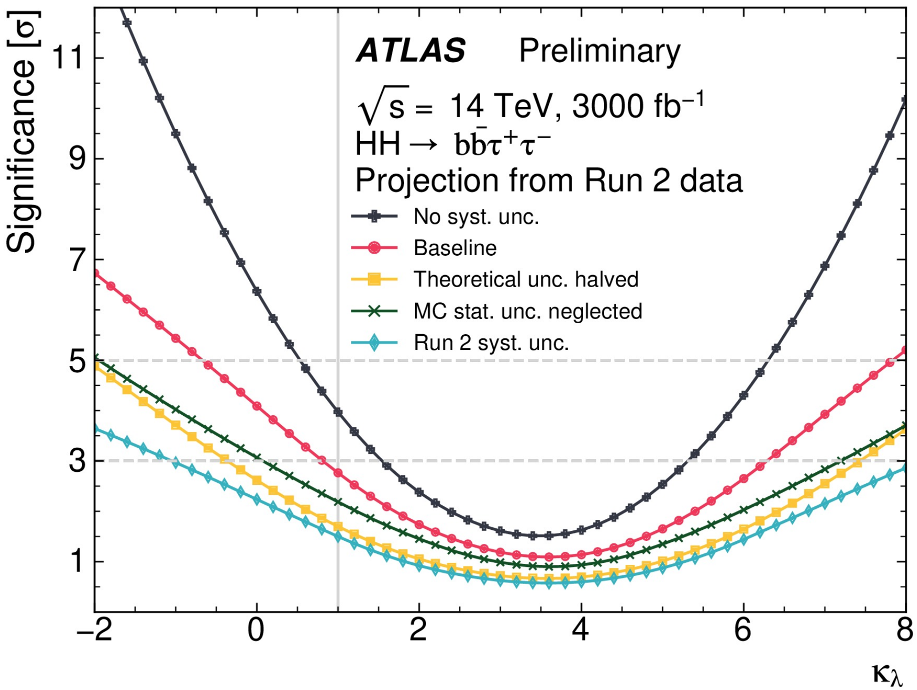

HL-LHC Extrapolations

- Various systematics scenarios studied

ATL-PHYS-PUB-2022-001/

bbyy

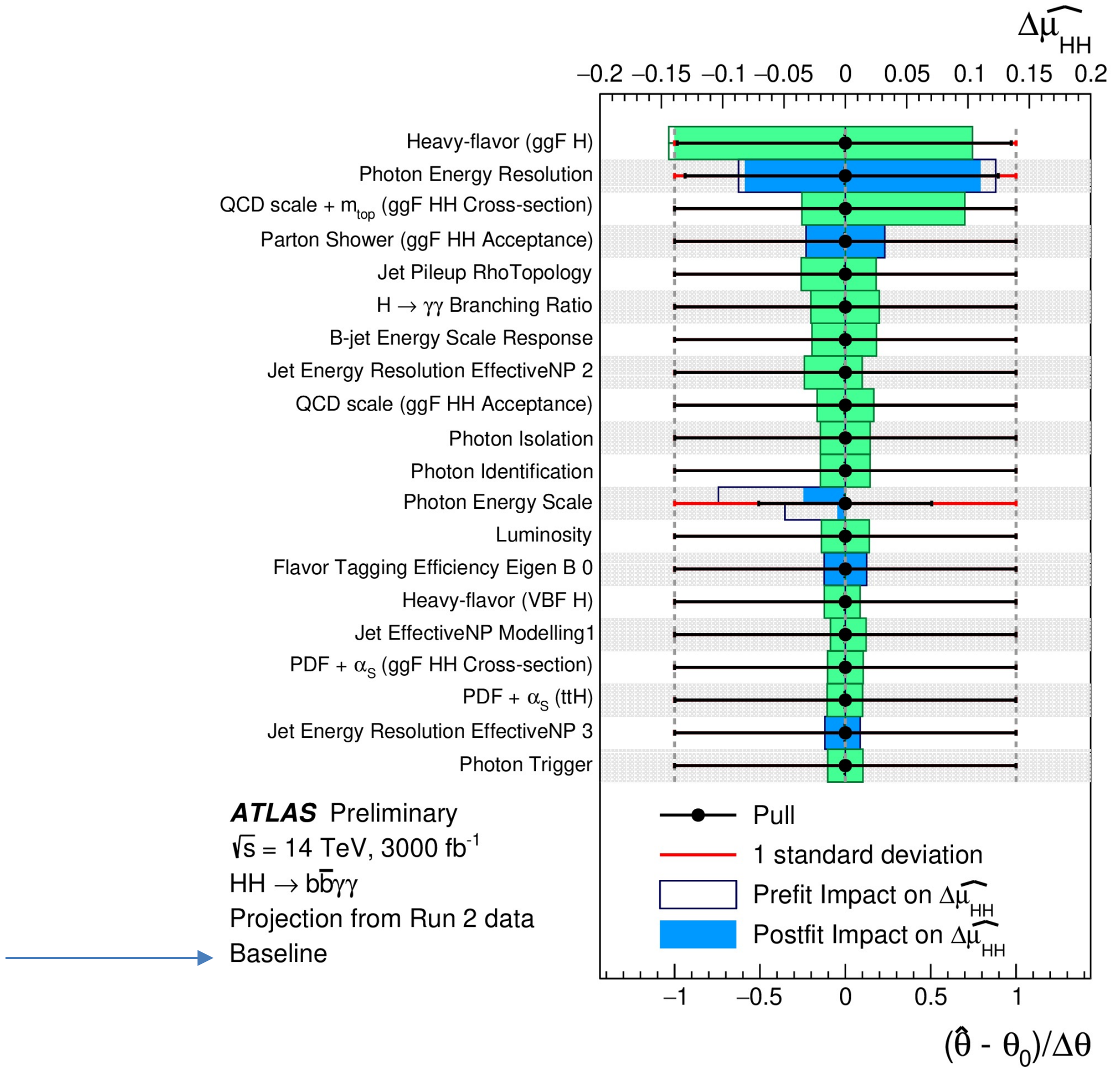

HL-LHC Extrapolations

- Various systematics scenarios studied

ATL-PHYS-PUB-2021-044/

bbtautau

Source	HL-LHC Scale Factor
Experimental Uncertainties	
Luminosity	0.6
Electrons and muons efficiency	1.0
b-jet tagging efficiency	0.5
c-jet tagging efficiency	0.5
Light-jet tagging efficiency	1.0
$\tau_{\text{had-vis}}$ efficiency (statistical)	0.0
$\tau_{\text{had-vis}}$ efficiency (systematic)	1.0
$\tau_{\text{had-vis}}$ energy scale	1.0
Fake-$\tau_{\text{had-vis}}$ estimation	1.0
Jet energy scale and resolution, $E_{\text{T}}^{\text{miss}}$	1.0
κ_{λ} reweighting	0.0
Theoretical Uncertainties	0.5

How to boost analysis sensitivity in HL-LHC?

Reduce systematics, increase signal efficiency for instance via **improved object reconstruction**!

- An example: the $HH \rightarrow \gamma\gamma b\bar{b}$ case

Background Modeling Uncertainty Scenario	Spurious Signal ($N \times$ Run 2 value)	95% CL Upper Limit	Significance [σ]
No syst. uncert. (optimistic)	0	0.93	2.2
	1	0.93	2.2
Improved syst. uncert. (aggressive)	2	0.94	2.1
	4	0.96	2.1
Improved syst. uncert. (conservative)	10	1.1	1.8
	20	1.5	1.3
Current Run 2 syst. uncert. (pessimistic)	25	1.7	1.1

- **Systematics dominated by spurious signal!**
  - Combination of intrinsic bias due to bkg mismodeling & statistical fluctuations in bkg templates (limited MC size)
  - **Strong motivation for improvements in background modelling (**Gaussian Process Regression, dedicated yy+hf in 4FNS samples, etc)

- Run2–like systematics would wash out b-tagging improvements!
- But… a hypothetical **10% improvement in btag. eff.** with HL-LHC systematics would buy us **~0.3 σ**, i.e. ~ 500 fb^{-1}!!!

Old ATLAS-CMS Combination

https://www.sciencedirect.com/science/article/pii/S2405428320300083?via%3Dihub

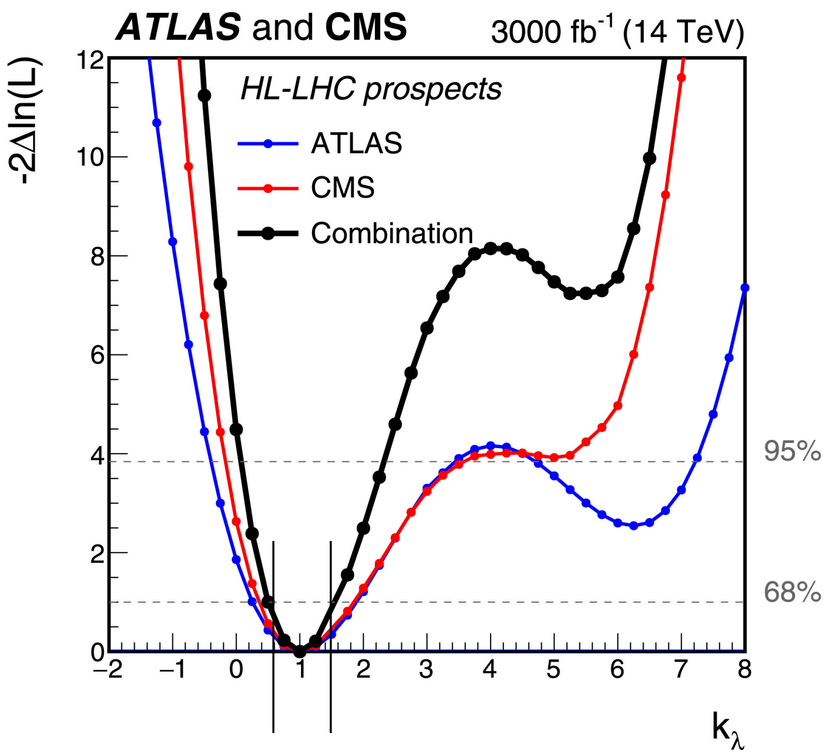

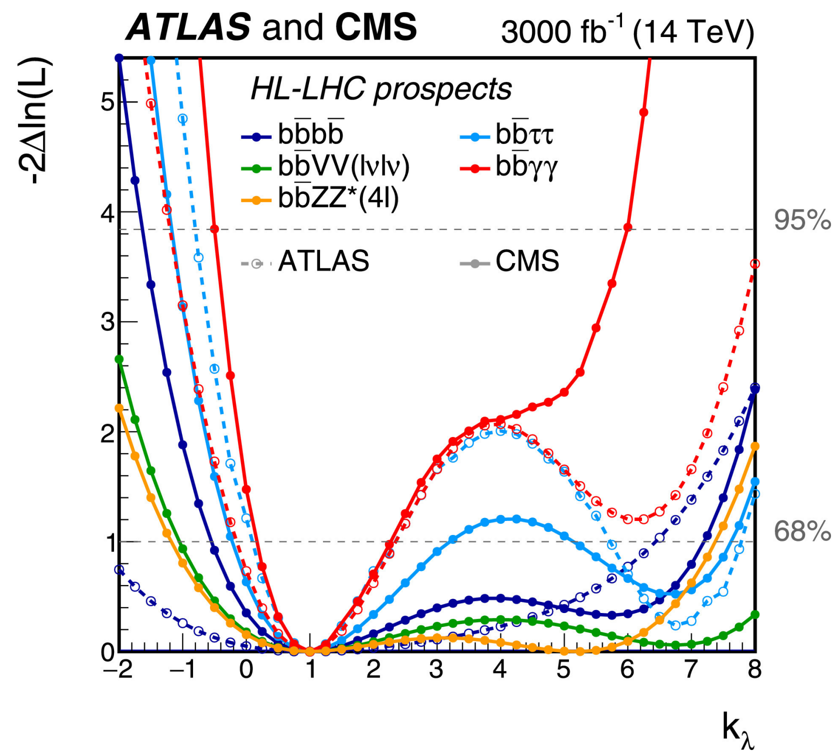

Old ATLAS-CMS Combination

https://www.sciencedirect.com/science/article/pii/S2405428320300083?via%3Dihub

	Statistical-only		Statistical + Systematic	
	ATLAS	CMS	ATLAS	CMS
$HH \to b\bar{b}b\bar{b}$	1.4	1.2	0.61	0.95
$HH \to b\bar{b}\tau^+\tau^-$	2.5	1.6	2.1	1.4
$HH \to b\bar{b}\gamma\gamma$	2.1	1.8	2.0	1.8
$HH \to b\bar{b}VV^*$	-	0.59	-	0.56
$HH \to b\bar{b}ZZ\,(4\ell)$	-	0.37	-	0.37
Combination	3.5	2.8	3.0	2.6
	4.5		4.0	

Objects

What is a jet in ATLAS?

- Jets are reconstructed using the anti-k_t jet clustering algorithm (https://iopscience.iop.org/article/10.1088/1126-6708/2008/04/063) with a radius parameter of 0.4
  - applied to noise-suppressed positive-energy **topological energy clusters** and charged-particle tracks, processed using a **particle-flow algorithm**.

- Jet energies are corrected for contributions from pileup, calibrated using energy- and η-dependent correction factors determined from comparisons of particle-level objects to reconstructed physics objects in simulated events, and then corrections are applied to account for effects due to the initiating parton type and hadron composition.

- In data, a residual *in situ* correction is applied to correct for differences with respect to simulation.

- Jets are required to have $p_T > 20$ GeV and $|\eta| < 2.5$. To reject jets from pileup, jets with $p_T < 60$ GeV and $|\eta| < 2.4$ are required to pass a 'Jet Vertex Tagger' [118] requirement to determine if they originate from the primary vertex [119]. Lastly, jet quality criteria [118] are applied to remove events containing jets from non-collision backgrounds and calorimeter noise, and jets reconstructed from topological calorimeter clusters [115, 116] are used for this purpose.

Jet energy scale

https://arxiv.org/pdf/2007.02645.pdf

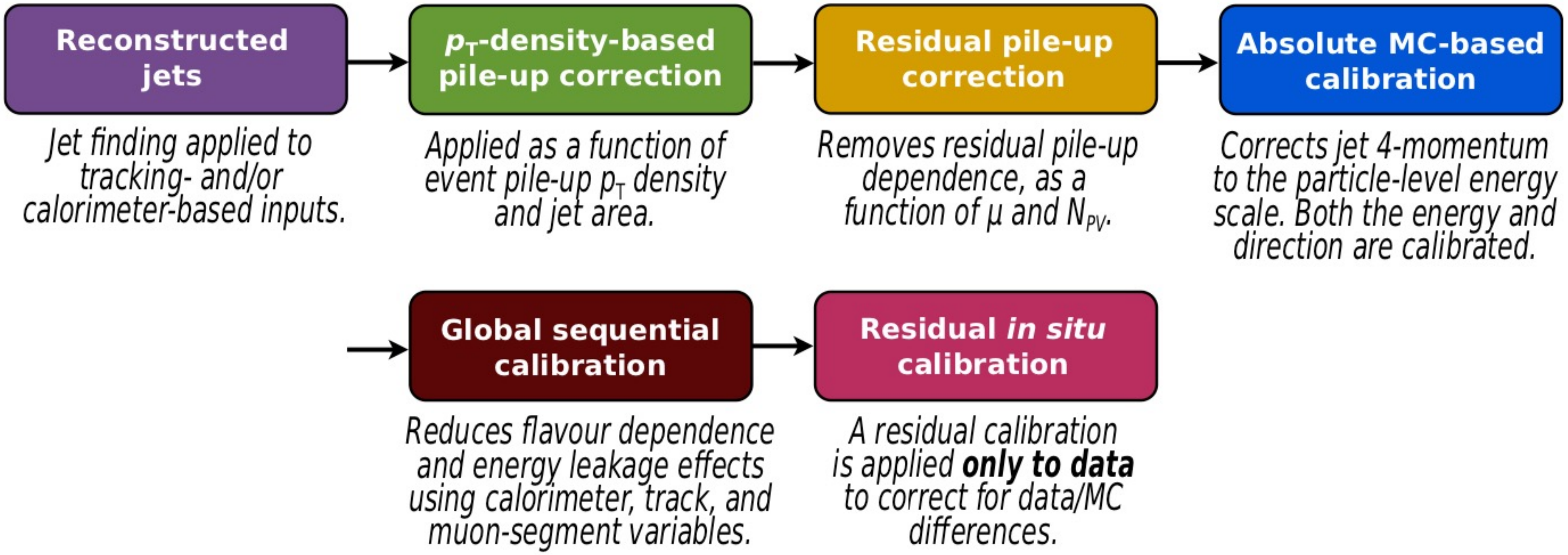

Figure 1: Stages of jet energy scale calibrations. Each one is applied to the four-momentum of the jet.

Jet energy scale

https://arxiv.org/pdf/2007.02645.pdf

Table 2: Sources of uncertainty in the jet energy scale.

Component	Description
	η intercalibration
Systematic mis-modelling	Envelope of the generator, pile-up, and event topology variations
Statistical component	Statistical uncertainty (single component)
Non-closure	Three components describing non-closure at high energy and at $\eta \sim \pm 2.4$
Non-closure, 2018 only	Single component describing non-closure at $\eta \sim \pm 1.5$ due to Tile calibration
	Z + jet
Electron scale	Uncertainty in the electron energy scale
Electron resolution	Uncertainty in the electron energy resolution
Muon scale	Uncertainty in the muon momentum scale
Muon resolution (ID)	Uncertainty in muon momentum resolution in the ID
Muon resolution (MS)	Uncertainty in muon momentum resolution in the MS
MC generator	Difference between MC event generators
JVT cut	Jet vertex tagger uncertainty
$\Delta\phi$ cut	Variation of $\Delta\phi$ between the jet and Z boson
Subleading jet veto	Radiation suppression through second-jet veto
Showering & topology	Modelling energy flow and distribution in and around a jet
Statistical	Statistical uncertainty in 28 discrete p_T terms
	γ + jet
Photon scale	Uncertainty in the photon energy scale
Photon resolution	Uncertainty in the photon energy resolution
MC generator	Difference between MC event generators
JVT cut	Jet vertex tagger uncertainty
$\Delta\phi$ cut	Variation of $\Delta\phi$ between the jet and photon
Subleading jet veto	Radiation suppression through second-jet veto
Showering & topology	Modelling energy flow and distribution in and around a jet
Photon purity	Purity of sample used for γ + jet balance
Statistical	Statistical uncertainty in 16 discrete p_T terms
	Multijet balance
$\Delta\phi$ (lead, recoil system)	Angle between leading jet and recoil system
$\Delta\phi$ (lead, any sublead)	Angle between leading jet and closest subleading jet
MC generator	Difference between MC event generators
p_T^{asym} selection	Second jet's p_T contribution to the recoil system
Jet p_T	Jet p_T threshold
Statistical	Statistical uncertainty in 28 discrete p_T terms
	Pile-up
μ offset	Uncertainty in the μ modelling in MC simulation
N_{PV} offset	Uncertainty in the N_{PV} modelling in MC simulation
ρ topology	Uncertainty in the per-event p_T density modelling in MC simulation
p_T dependence	Uncertainty in the residual p_T dependence
	Jet flavour
Flavour composition	Uncertainty in the proportional sample composition of quarks and gluons
Flavour response	Uncertainty in the response of gluon-initiated jets
b-jets	Uncertainty in the response of b-quark-initiated jets
Punch-through	Uncertainty in GSC punch-through correction
Single-particle response	High-p_T jet uncertainty from single-particle and test-beam measurements
AFII non-closure	Difference in the absolute JES calibration for simulations in AFII

Jet energy resolution

https://arxiv.org/pdf/2007.02645.pdf

The dependence of the relative JER on the transverse momentum of the jet may be parameterized using a functional form expected for calorimeter-based resolutions, with three independent contributions, namely the noise (N), stochastic (S) and constant (C) terms [52]:

$$\frac{\sigma(p_{\mathrm{T}})}{p_{\mathrm{T}}} = \frac{N}{p_{\mathrm{T}}} \oplus \frac{S}{\sqrt{p_{\mathrm{T}}}} \oplus C \,. \tag{4}$$

The noise (N) term is due to the contribution of electronic noise to the signal measured by the detector front-end electronics, as well as that due to pile-up. Since both contribute directly to the energy measured in the calorimeter but are approximately independent of the energy deposited by the showing particles, the contribution to the JER scales like $1/p_{\mathrm{T}}$. The noise term is expected to be significant in the low-p_{T} region, below ~30 GeV. Statistical fluctuations in the amount of energy deposited are captured by the stochastic (S) term, which represents the limiting term in the resolution up to several hundred GeV in jet p_{T}. The S term contribution to the JER scales like $1/\sqrt{p_{\mathrm{T}}}$. The constant (C) term corresponds to fluctuations that are a constant fraction of the jet p_{T}, such as energy depositions in passive material (e.g. cryostats and solenoid coil), the starting point of the hadron showers, and non-uniformities of response across the calorimeter. The constant term is expected to dominate the high-p_{T} region, above approximately 400 GeV.

In order to measure the JER, jet momentum must be measured precisely. This implies that the jets must either recoil against a reference object whose momentum can be measured precisely, or be balanced against one another in a well-defined dijet system [5, 6]. Measurements using the latter approach are presented here, as well as a method for measuring the contributions to the resolution from the noise term (N) due to both pile-up and electronics.

What is a photon in ATLAS?

https://iopscience.iop.org/article/10.1088/1748-0221/14/12/P12006/pdf

Photon reconstruction: dynamic, topological cell clustering-based approach

- Recovers brem effects (electrons radiating photons due to material interactions)
- For photons that convert to electron-positron pairs, superclusters can include more of the energy of the primary photon.
    - photons can produce multiple topo-clusters, which can then be merged into one supercluster. The use of fixed-size clusters is suboptimal in this scenario, as the fixed cluster size cannot properly accommodate the growth of two independent EM showers, particularly when the two clusters share cells.

- the reconstruction algorithm matches tracks to the electron superclusters and conversion vertices to the photon superclusters.
- **electron** = object consisting of a cluster built in the calorimeter (supercluster) and a matched track (or tracks)
- **converted photon** = calorimeter cluster matched to a conversion vertex (or vertices)
- **unconverted photon** = cluster matched to neither an electron track nor a conversion vertex.

About 20% of photons at low $|\eta|$ convert in the ID, and up to about 65% convert at $|\eta| \approx 2.3$.

What is a photon in ATLAS?

https://iopscience.iop.org/article/10.1088/1748-0221/14/12/P12006/pdf

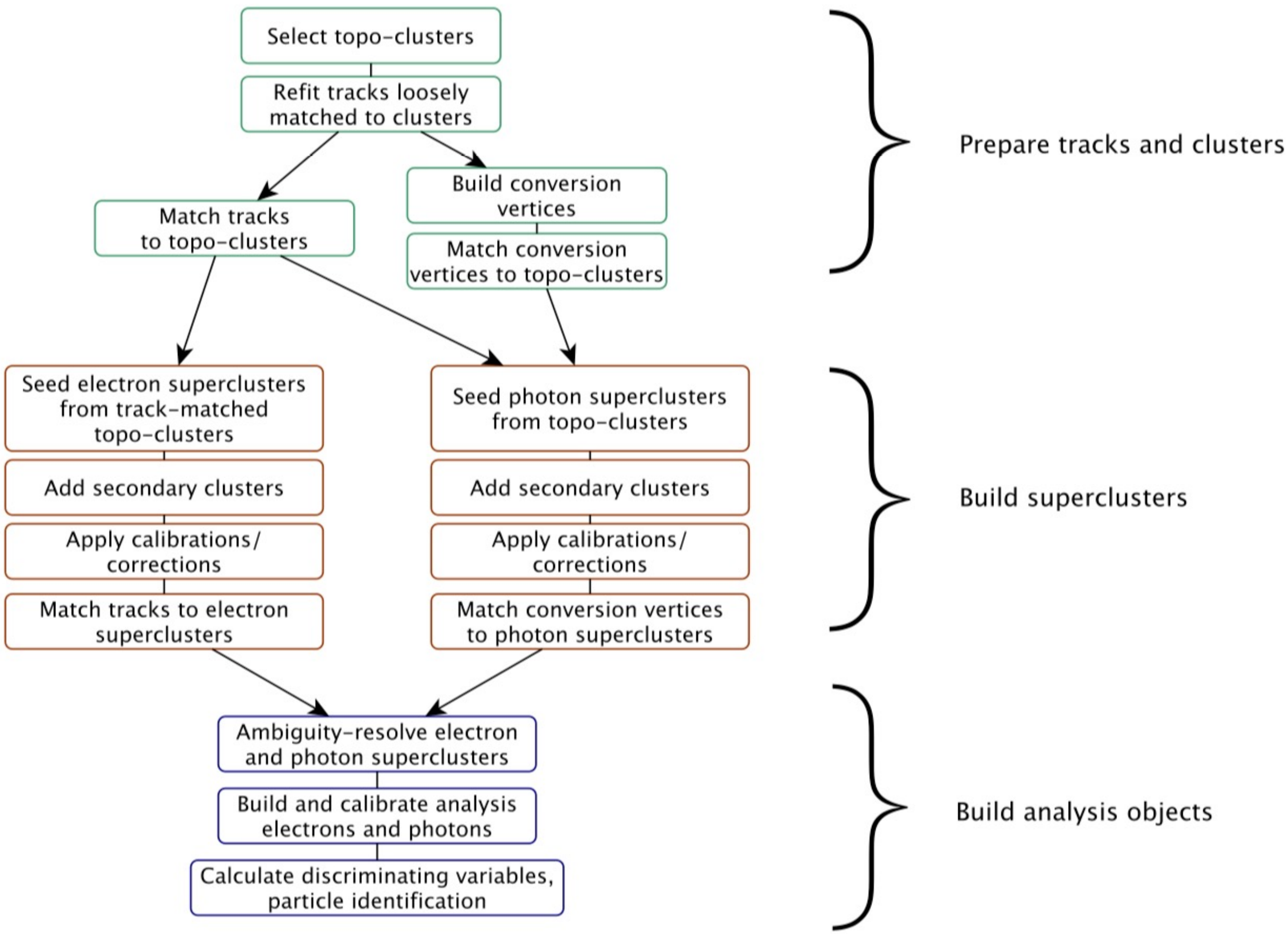

Photon Identification

https://iopscience.iop.org/article/10.1088/1748-0221/14/12/P12006/pdf

- Based on the lateral and longitudinal energy profiles of the shower measured in the calorimeter
- Rectangular cuts are imposed on discriminating variables describes the energy fraction released in the hadronic calorimeter and photon's shower shapes in the EM calorimeter.
- *loose* PID: uses shower shapes in the hadronic calorimeter and the EM calorimeter's second layer, providing a highly efficient selection with quite fair background rejection.
- *tight* PID: uses the full granularity of the EM calorimeter, including the fine segmentation of the first sampling layer, and applies tighter requirements on the shower shapes.

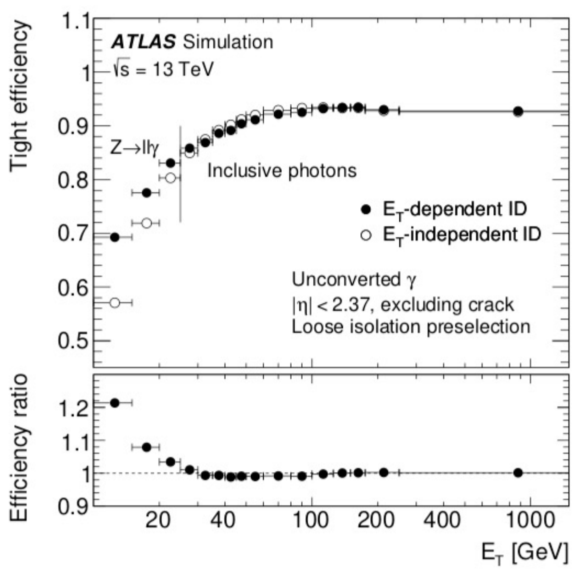

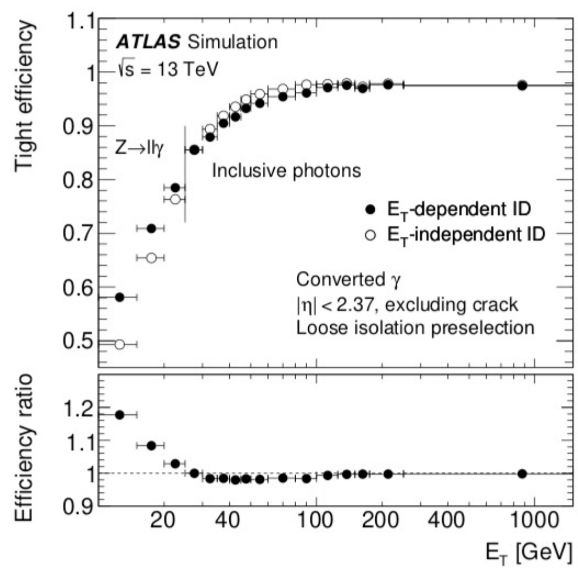

Photon Isolation

https://iopscience.iop.org/article/10.1088/1748-0221/14/12/P12006/pdf

Table 3. Definition of the photon isolation working points.

Working point	Calorimeter isolation	Track isolation
Loose	$E_T^{\text{cone20}} < 0.065 \times E_T$	$p_T^{\text{cone20}}/E_T < 0.05$
Tight	$E_T^{\text{cone40}} < 0.022 \times E_T + 2.45$ GeV	$p_T^{\text{cone20}}/E_T < 0.05$
TightCaloOnly	$E_T^{\text{cone40}} < 0.022 \times E_T + 2.45$ GeV	—

Used in H->yy analysis

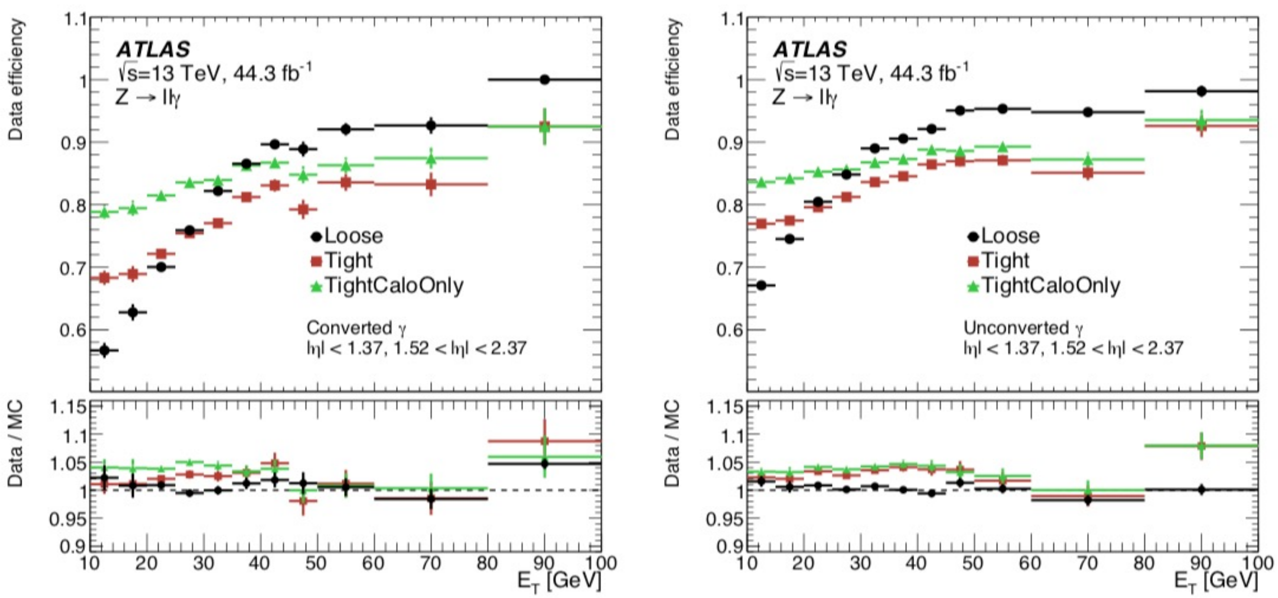

Photon conversions

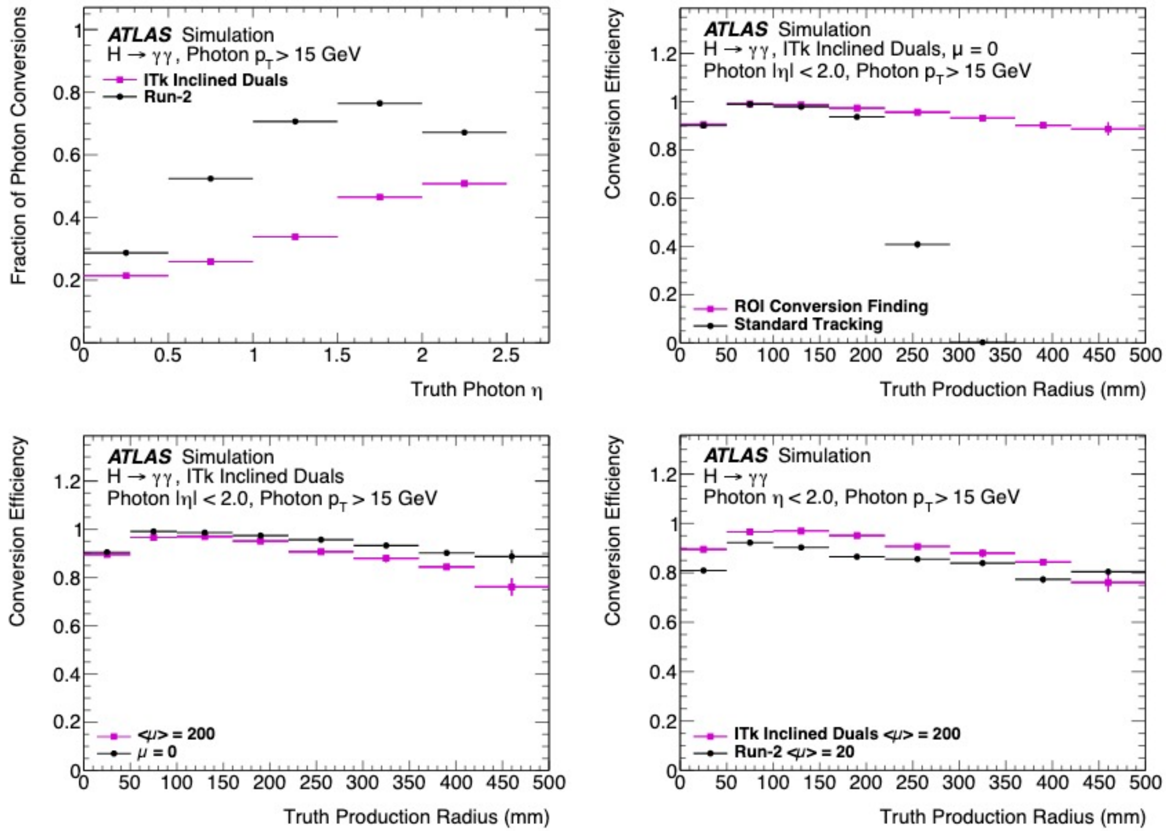

Figure 3.20: Results of a conversion reconstruction study using a sample of $H \to \gamma\gamma$ events for photons with $|\eta| < 2$. **Top left:** Probability for a photon to covert when traversing the detector. **Top right:** Efficiency to reconstruct conversions in the ITk material just using the standard track reconstruction as input, for events without pile-up, compared to the results using a dedicated reconstruction in regions of interest (ROI) defined by high-p_{T} electromagnetic showers. **Bottom left:** Effect of adding an average of 200 pile-up interactions on the conversion reconstruction in the ITk. **Bottom right:** Conversion efficiency using the ITk compared to the result for the current Run 2 detector reconstruction.

Diphoton trigger

https://link.springer.com/article/10.1140/epjc/s10052-019-7500-2/figures/11

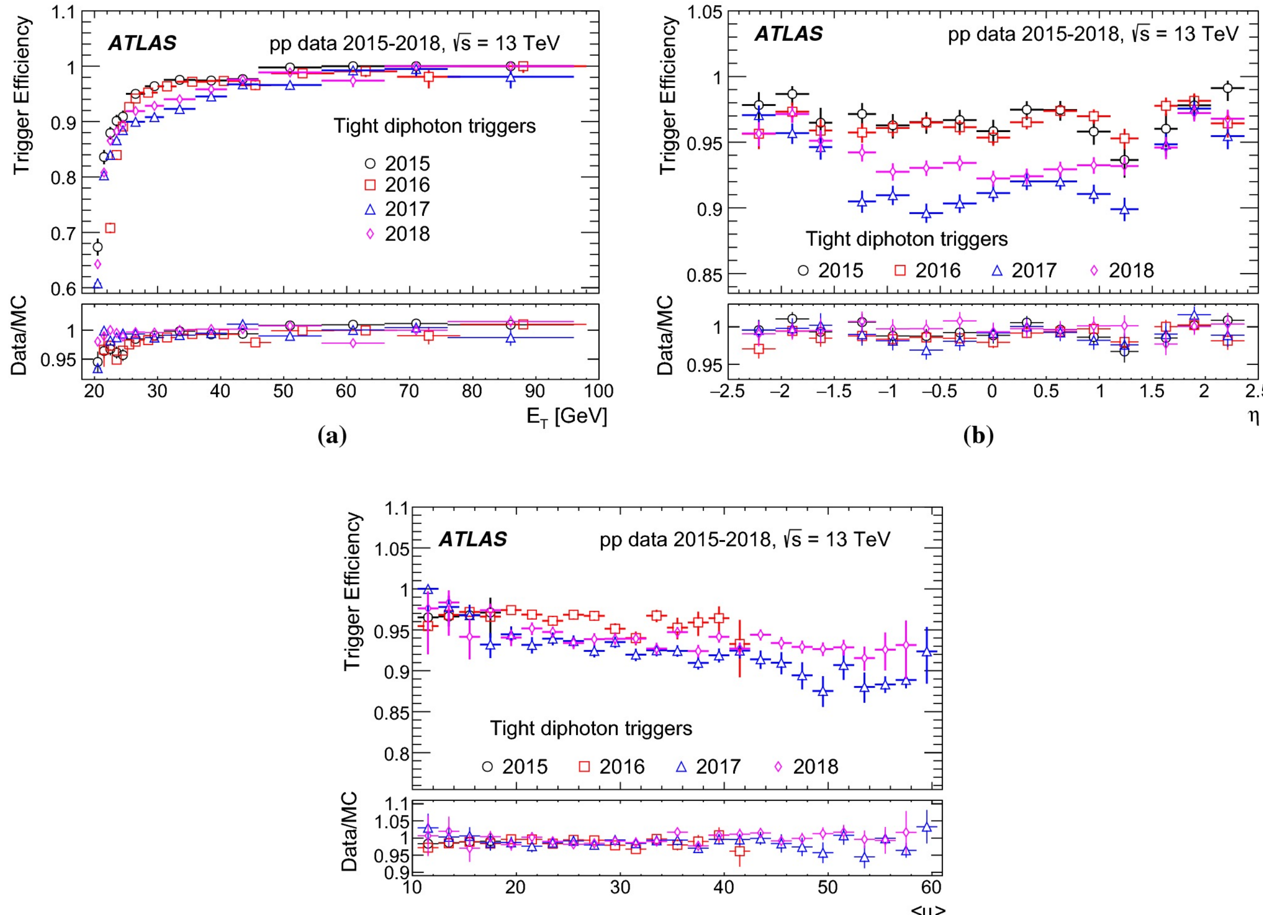

Evolution of efficiencies for tight diphoton trigger legs as a function of the offline photon **a** ETET, **b** ηη, and **c** $\langle\mu\rangle$⟨μ⟩ during Run 2. The changes between years are detailed in Sect. 9.1. The efficiency is computed with respect to offline photons satisfying tight identification criteria and the calorimeter-only tight isolation requirement. The ratios of data to MC simulation efficiencies are also shown. The total uncertainties, shown as vertical bars, are dominated by statistical uncertainties. Offline photon candidates in the calorimeter transition region $1.37<|\eta|<1.52$1.37<|η|<1.52 are not considered. For **b** and **c**, only offline candidates with ETET values 5 GeV GeV above the corresponding trigger threshold are used

What is a tau in ATLAS?

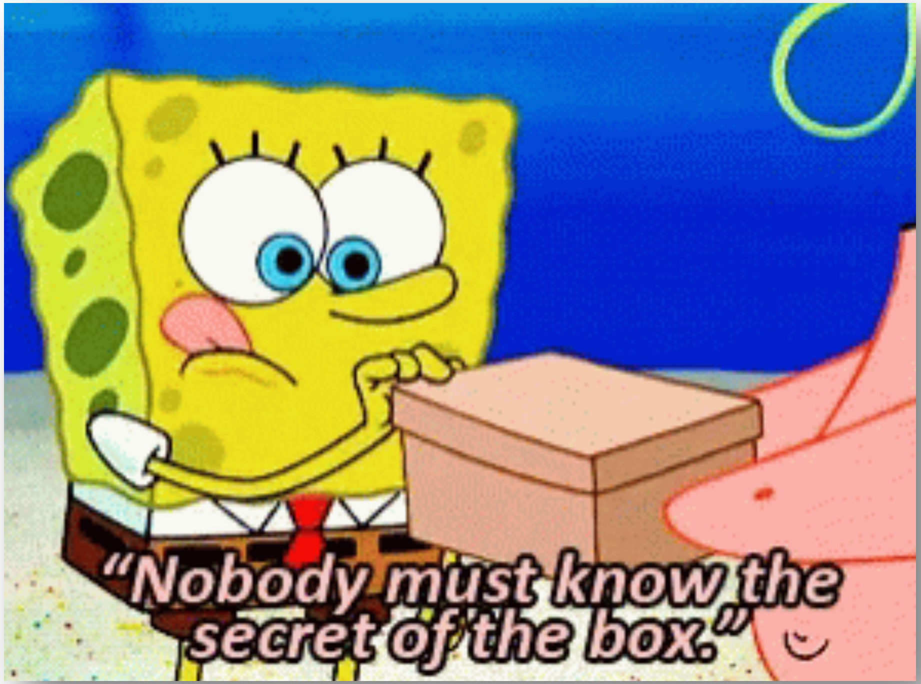

What is a tau in ATLAS?

- **The only lepton that can decay into hadrons (~65% rate)** – the other leptons do not have the necessary mass.
- Like the other decay modes of the tau, the hadronic decay is through the weak interaction
- **Almost all hadronic tau lepton decays include one (72%) or three (22%) charged pions and the majority (68%) include one or more neutral pions.**
  - **Their signature corresponds to that of a narrow jet with one or three tracks in the detector.**
  - **The neutrino from the hadronic tau lepton decay can not be reconstructed and the combination of all visible decay products is referred to as $\tau_{had\text{-}vis}$.**
- The reconstructed $\tau_{had\text{-}vis}$ candidates are seeded by jets (anti-kt 0.4), the $\tau_{had\text{-}vis}$ energy is calibrated using multivariate methods with information from tracks and calorimeter clusters, and they are required to have $p_T > 20$ GeV and $|\eta| < 2.5$, excluding $1.37 < |\eta| < 1.52$.
- Boosted decision trees are used to determine if nearby tracks originate from a τ_{had}, and one or three tracks with a total charge of ±1 are required to pass this selection.
- **The true-$\tau_{had\text{-}vis}$** are discriminated from backgrounds of quark- and gluon-initiated jets using **recurrent neural networks traine to target signatures with either one or three associated tracks** and a loose requirement with an efficiency of around 85% (75% for one-track (three-track) $\tau_{had\text{-}vis}$ candidates is applied.
- A separate boosted decision tree is then used to reject $\tau_{had\text{-}vis}$ candidates originating from electrons, with an efficiency of abc 95%.

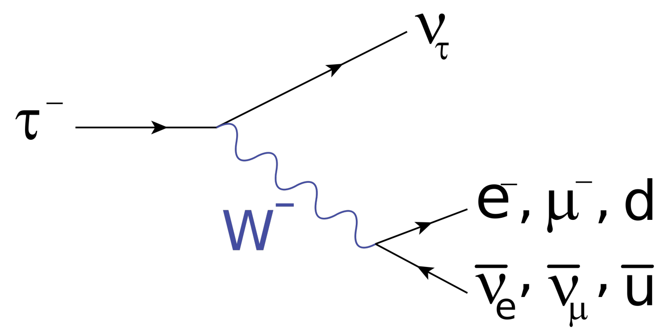

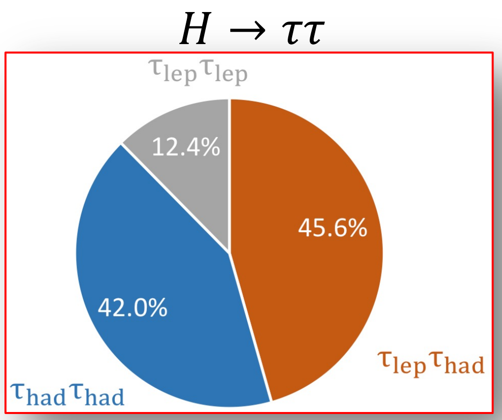

https://arxiv.org/pdf/1510.07488.pdf

Table 1: Approximate branching fractions ($\mathcal{B}$) of different τ decay modes [18]. The generic symbol h^- represents a charged hadron (either a pion or a kaon). Charge conjugation invariance is assumed in this paper.

Decay mode	Meson resonance	$\mathcal{B}$ [%]
$\tau^- \to e^- \bar{\nu}_e \nu_\tau$		17.8
$\tau^- \to \mu^- \bar{\nu}_\mu \nu_\tau$		17.4
$\tau^- \to h^- \nu_\tau$		11.5
$\tau^- \to h^- \pi^0 \nu_\tau$	$\rho(770)$	26.0
$\tau^- \to h^- \pi^0 \pi^0 \nu_\tau$	$a_1(1260)$	9.5
$\tau^- \to h^- h^+ h^- \nu_\tau$	$a_1(1260)$	9.8
$\tau^- \to h^- h^+ h^- \pi^0 \nu_\tau$		4.8
Other modes with hadrons		3.2
All modes containing hadrons		64.8

What is a tau in ATLAS?

During the tau reconstruction process no attempt is made to separate tau leptons from QCD jets. Therefore a dedicated identification procedure is applied.
To reduce the background arising from quark and gluon jets, we exploit the fact that hadronic τ decays result in a lower particle multiplicity, and are more collimated and isolated relative to other particles in the event.

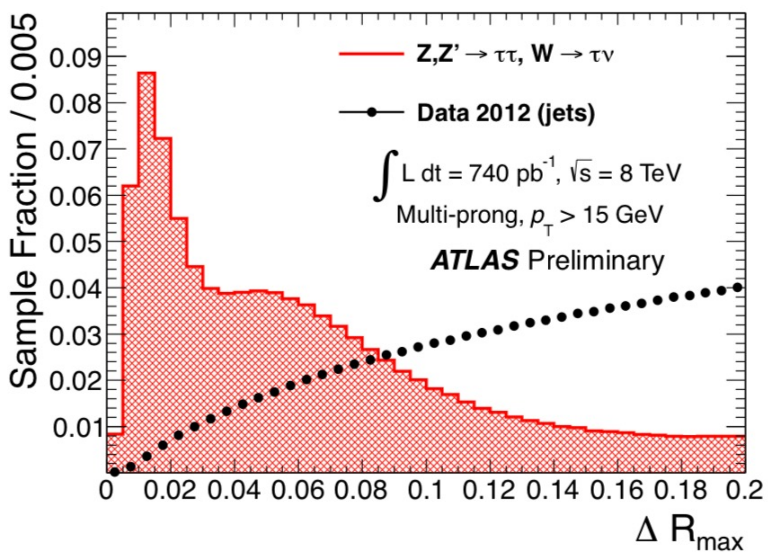

Figure 2: Maximal distance between a track and the tau candidate axis. Only tracks inside a cone of $\Delta R = 0.2$ considered. [3]

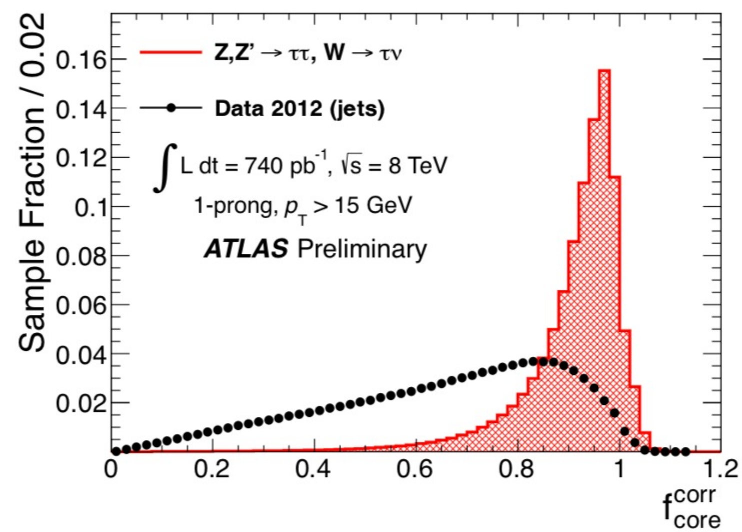

Figure 3: Fraction of the transverse energy of calorimeter cells deposited in a cone of $\Delta R = 0.1$ around the tau candidate axis to those deposited in the region of $\Delta R = 0.2$. [3]

What is a tau in ATLAS?

- The tau reconstruction algorithm provides no discrimination against other particles that result in jet-like signatures in the detector. Therefore, dedicated algorithms are used to identify hardonic tau lepton decays. A set of BDTs was previously used in ATLAS to discriminate jets from tau_had_vis and it is now superseded by an RNN
- The RNN uses a combination of low-level input variables for individual tracks and clusters that are associated to the tau_had_vis candidate as well as high-level quantities calculated from tracks and calorimeter quantities

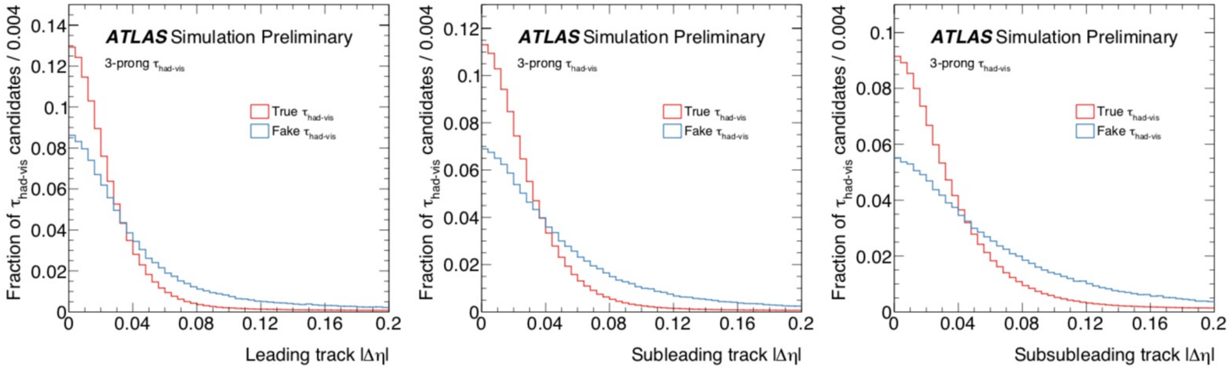

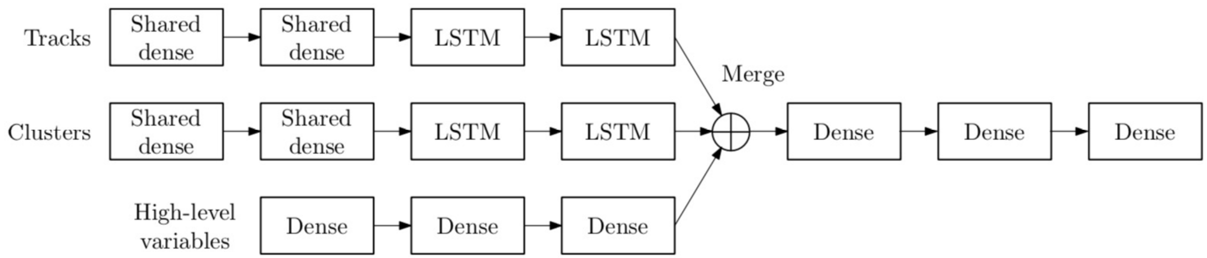

Figure 2: Schematic view of the network architecture used for tau identification. Layers marked as *dense* are fully connected to adjacent layers.

ATL-PHYS-PUB-2019-033

What is a tau in ATLAS?

Table 1: List of observables used as inputs in the different parts of the RNN. The markers indicate which observables are used to identify 1-prong and 3-prong $\tau_{\text{had-vis}}$. See Section 5.1 for the definitions of the observables.

	Observable	1-prong	3-prong
Track inputs	$p_T^{\text{seed jet}}$	•	•
	p_T^{track}	•	•
	$\Delta\eta^{\text{track}}$	•	•
	$\Delta\phi^{\text{track}}$	•	•
	$\lvert d_0^{\text{track}}\rvert$	•	•
	$\lvert z_0^{\text{track}} \sin\theta\rvert$	•	•
	$N_{\text{IBL hits}}$	•	•
	$N_{\text{Pixel hits}}$	•	•
	$N_{\text{SCT hits}}$	•	•
Cluster inputs	$p_T^{\text{jet seed}}$	•	•
	E_T^{cluster}	•	•
	$\Delta\eta^{\text{cluster}}$	•	•
	$\Delta\phi^{\text{cluster}}$	•	•
	λ_{cluster}	•	•
	$\langle\lambda^2_{\text{cluster}}\rangle$	•	•
	$\langle r^2_{\text{cluster}}\rangle$	•	•
High-level inputs	$p_T^{\text{uncalibrated}}$	•	•
	f_{cent}	•	•
	$f^{-1}_{\text{leadtrack}}$	•	•
	ΔR_{max}	•	•
	$\lvert S_{\text{leadtrack}}\rvert$	•	
	S_T^{flight}		•
	$f_{\text{iso}}^{\text{track}}$	•	•
	$f_{\text{track}}^{\text{EM}}$	•	•
	$p_T^{\text{EM+track}}/p_T$	•	•
	$m^{\text{EM+track}}$	•	•
	m^{track}		•

Table 2: List of defined working points with fixed true $\tau_{\text{had-vis}}$ selection efficiencies and the corresponding background rejection factors for misidentified $\tau_{\text{had-vis}}$ in dijet events for the BDT and RNN classifiers.

	Signal efficiency		Background rejection BDT		Background rejection RNN	
Working point	1-prong	3-prong	1-prong	3-prong	1-prong	3-prong
Tight	60%	45%	40	400	70	700
Medium	75%	60%	20	150	35	240
Loose	85%	75%	12	61	21	90
Very loose	95%	95%	5.3	11.2	9.9	16

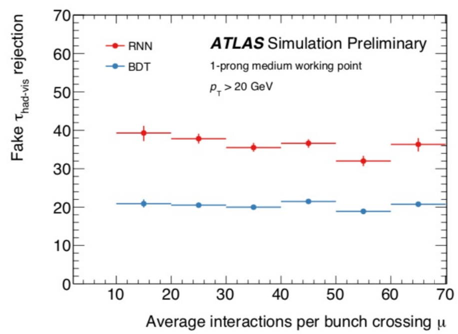

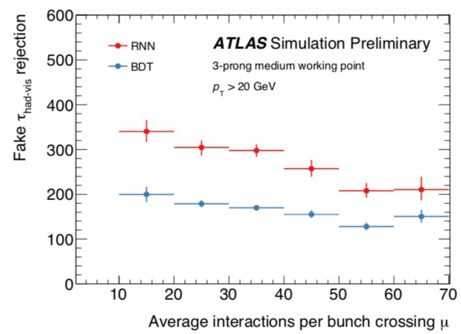

How to improve multiple HH channels?

- Most HH analyses: $HH \rightarrow xxb\bar{b}$
  - **b-tagging improvements are crucial!**
- In ATLAS
  - **High-Level ML taggers** read **low-level taggers' outputs**
    - Impact Parameter based
    - Secondary Vertex Finding
    - **Decay chain Multi-Vertex Algorithm** (JetFitter)
      - **Improved thanks to new PV strategy!**

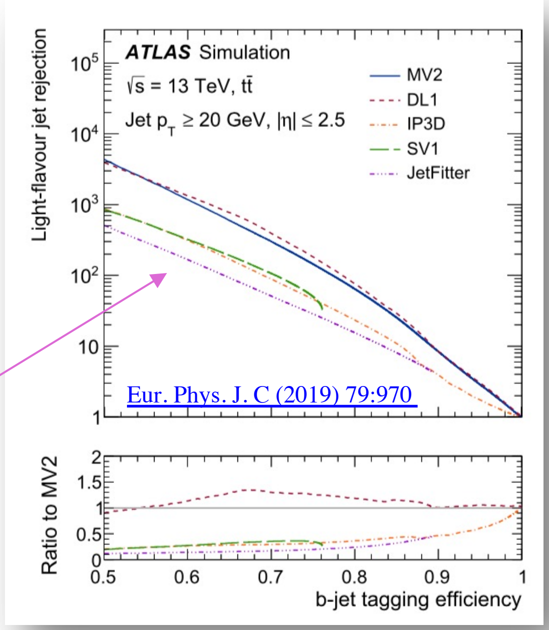

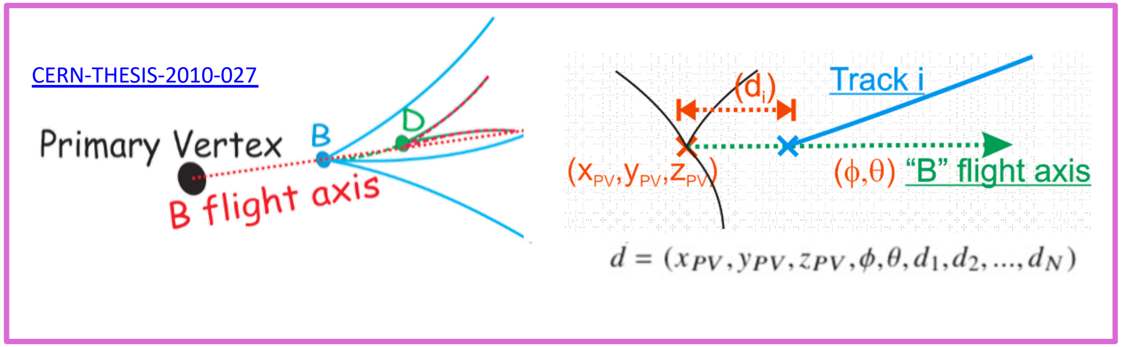

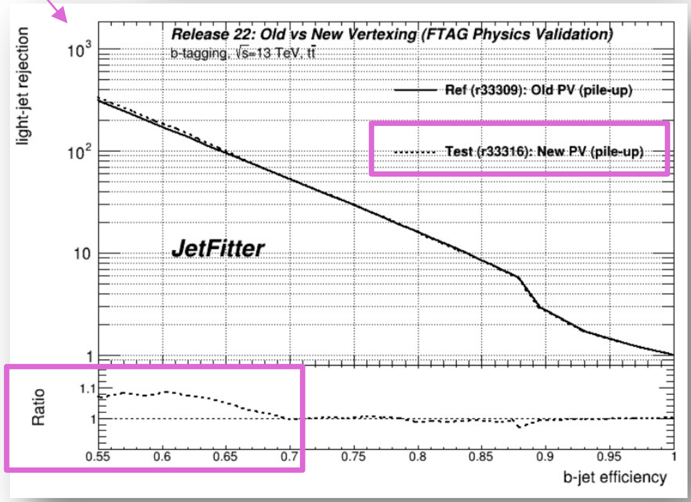

- Reconstructs 1-track vertices
- Assumes B- & D-hadron vertices to lie on the same axis

ATL-PHYS-PUB-2018-025

	JF Vertices All	≥1 Single Trk 0 Multi Trk	0 Single Trk 1 Multi Trk	≥1 Single Trk 1 Multi Trk	2 Multi Trk	≥3 Multi Trk
b-jets	0.893	0.147	0.414	0.227	0.102	0.0040
c-jets	0.556	0.246	0.258	0.044	0.008	0.0001
light jets	0.234	0.155	0.069	0.010	0.001	0.0001

Extra Slides

Eur. Phys. J. C (2019) 79:970

Table 1 Input variables used by the MV2 and the DL1 algorithms. The JETFITTER c-tagging variables are only used by the DL1 algorithm

Input	Variable	Description
Kinematics	p_{T}	Jet p_{T}
	η	Jet $\lvert\eta\rvert$
IP2D/IP3D	$\log(P_b/P_{\text{light}})$	Likelihood ratio between the b-jet and light-flavour jet hypotheses
	$\log(P_b/P_c)$	Likelihood ratio between the b- and c-jet hypotheses
	$\log(P_c/P_{\text{light}})$	Likelihood ratio between the c-jet and light-flavour jet hypotheses
SV1	$m(\mathrm{SV})$	Invariant mass of tracks at the secondary vertex assuming pion mass
	$f_E(\mathrm{SV})$	Energy fraction of the tracks associated with the secondary vertex
	$N_{\mathrm{TrkAtVtx}}(\mathrm{SV})$	Number of tracks used in the secondary vertex
	$N_{\mathrm{2TrkVtx}}(\mathrm{SV})$	Number of two-track vertex candidates
	$L_{xy}(\mathrm{SV})$	Transverse distance between the primary and secondary vertex
	$L_{xyz}(\mathrm{SV})$	Distance between the primary and the secondary vertex
	$S_{xyz}(\mathrm{SV})$	Distance between the primary and the secondary vertex divided by its uncertainty
	$\Delta R(\vec{p}_{\text{jet}}, \vec{p}_{\text{vtx}})(\mathrm{SV})$	ΔR between the jet axis and the direction of the secondary vertex relative to the primary vertex
JETFITTER	$m(\mathrm{JF})$	Invariant mass of tracks from displaced vertices
	$f_E(\mathrm{JF})$	Energy fraction of the tracks associated with the displaced vertices
	$\Delta R(\vec{p}_{\text{jet}}, \vec{p}_{\text{vtx}})(\mathrm{JF})$	ΔR between the jet axis and the vectorial sum of momenta of all tracks attached to displaced vertices
	$S_{xyz}(\mathrm{JF})$	Significance of the average distance between PV and displaced vertices
	$N_{\mathrm{TrkAtVtx}}(\mathrm{JF})$	Number of tracks from multi-prong displaced vertices
	$N_{\mathrm{2TrkVtx}}(\mathrm{JF})$	Number of two-track vertex candidates (prior to decay chain fit)
	$N_{1\text{-trk vertices}}(\mathrm{JF})$	Number of single-prong displaced vertices
	$N_{\geq 2\text{-trk vertices}}(\mathrm{JF})$	Number of multi-prong displaced vertices
JETFITTER c-tagging	$L_{xyz}(\mathrm{2nd/3rdvtx})(\mathrm{JF})$	Distance of 2nd or 3rd vertex from PV
	$L_{xy}(\mathrm{2nd/3rdvtx})(\mathrm{JF})$	Transverse displacement of the 2nd or 3rd vertex
	$m_{\mathrm{Trk}}(\mathrm{2nd/3rdvtx})(\mathrm{JF})$	Invariant mass of tracks associated with 2nd or 3rd vertex
	$E_{\mathrm{Trk}}(\mathrm{2nd/3rdvtx})(\mathrm{JF})$	Energy fraction of the tracks associated with 2nd or 3rd vertex
	$f_E(\mathrm{2nd/3rdvtx})(\mathrm{JF})$	Fraction of charged jet energy in 2nd or 3rd vertex
	$N_{\mathrm{TrkAtVtx}}(\mathrm{2nd/3rdvtx})(\mathrm{JF})$	Number of tracks associated with 2nd or 3rd vertex
	$Y_{\text{trk}}^{\min}, Y_{\text{trk}}^{\max}, Y_{\text{trk}}^{\text{avg}}(\mathrm{2nd/3rdvtx})(\mathrm{JF})$	Min., max. and avg. track rapidity of tracks at 2nd or 3rd vertex

Extra Slides

Eur. Phys. J. C (2019) 79:970

Table 4 Selection and c-jet, τ-jet and light-flavour jet rejections corresponding to the different b-jet tagging efficiency single-cut operating points for the MV2 and the DL1 b-tagging algorithms, evaluated on the baseline $t\bar{t}$ events

ϵ_b	MV2				DL1			
	Selection	Rejection			Selection	Rejection		
		c-jet	τ-jet	Light-flavour jet		c-jet	τ-jet	Light-flavour jet
60%	> 0.94	23	140	1200	> 2.74	27	220	1300
70%	> 0.83	8.9	36	300	> 2.02	9.4	43	390
77%	> 0.64	4.9	15	110	> 1.45	4.9	14	130
85%	> 0.11	2.7	6.1	25	> 0.46	2.6	3.9	29

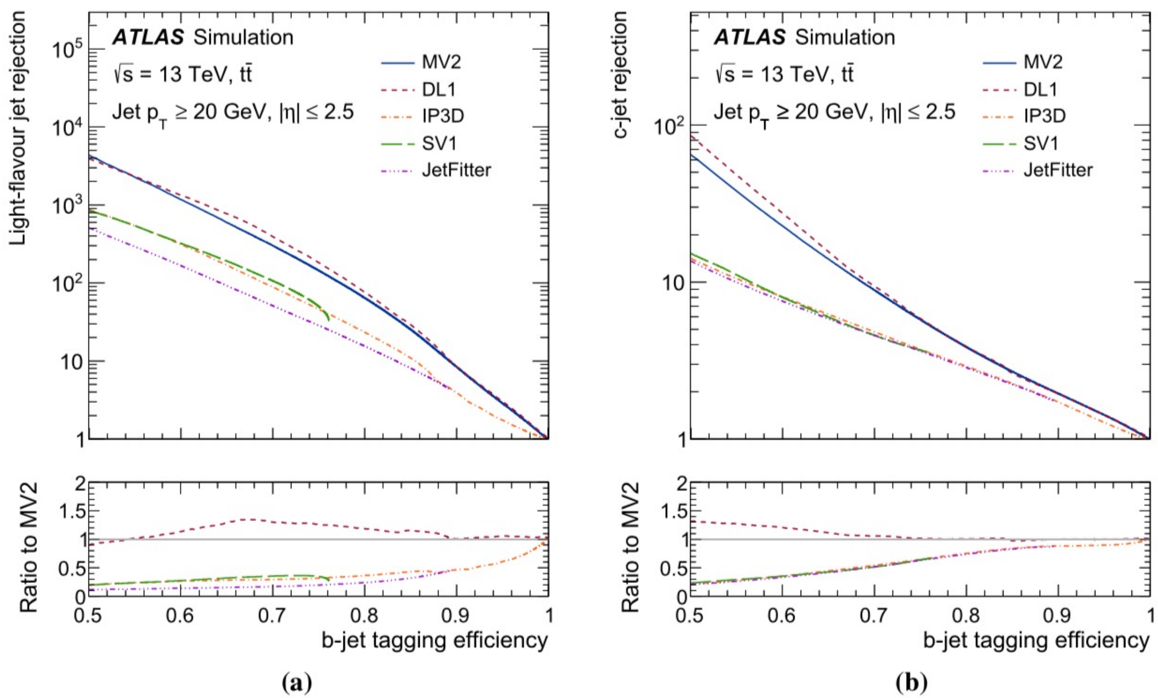

Fig. 2 The **(a)** light-flavour jet and **(b)** c-jet rejections versus the b-jet tagging efficiency for the IP3D, SV1, JetFitter, MV2 and DL1 b-tagging algorithms evaluated on the baseline $t\bar{t}$ events

Extra Slides

Table 4: Input variables used for the three trainings of the multivariate tagging algorithm. All the variables up to the "Baseline" variable set are used as the JetFitter inputs to the ATLAS MV2 tagger [9]. The "Full" variable set brings additional information from to the full topological properties of the reconstructed decay chain.

Input	Variable	Description
Kinematics	p_T	Jet p_T
	η	Jet $\lvert\eta\rvert$
Reduced	m	Invariant mass of tracks from displaced vertices
	f_E	Fraction of the charged jet energy in the secondary vertices
	$\Delta R(\vec{p}_{\mathrm{jet}}, \vec{p}_{\mathrm{vtx}})$	ΔR between jet axis and vectorial sum of momenta of all tracks attached to displaced vertices
	S_{xyz}	Significance of average distance between PV and displaced vertices
	N_{TrkAtVtx}	Number of tracks from multi-prong displaced vertices
Baseline	above variables +	
	N_{2TrkVtx}	Number of 2-track vertex candidates (prior to decay chain fit)
	$N_{\mathrm{1\text{-}trk\ vertices}}$	Number of single-prong displaced vertices
	$N_{\mathrm{\geq 2\text{-}trk\ vertices}}$	Number of multi-prong displaced vertices
Full	above variables +	
	$L_{xyz}(2^{\mathrm{nd}}/3^{\mathrm{rd}}\mathrm{vtx})$	Distance of 2^{nd} or 3^{rd} vertex from PV
	$L_{xy}(2^{\mathrm{nd}}/3^{\mathrm{rd}}\mathrm{vtx})$	Transverse displacement of the 2^{nd} or 3^{rd} vertex
	$m_{\mathrm{Trk}}(2^{\mathrm{nd}}/3^{\mathrm{rd}}\mathrm{vtx})$	Invariant mass of tracks associated to 2^{nd} or 3^{rd} vertex
	$E_{\mathrm{Trk}}(2^{\mathrm{nd}}/3^{\mathrm{rd}}\mathrm{vtx})$	Energy of charged tracks associated to 2^{nd} or 3^{rd} vertex
	$f_E(2^{\mathrm{nd}}/3^{\mathrm{rd}}\mathrm{vtx})$	Fraction of charged jet energy in 2^{nd} or 3^{rd} vertex
	$N_{\mathrm{TrkAtVtx}}(2^{\mathrm{nd}}/3^{\mathrm{rd}}\mathrm{vtx})$	Number of tracks associated to 2^{nd} or 3^{rd} vertex

https://cds.cern.ch/record/2645405/files/ATL-PHYS-PUB-2018-025.pdf?version=1

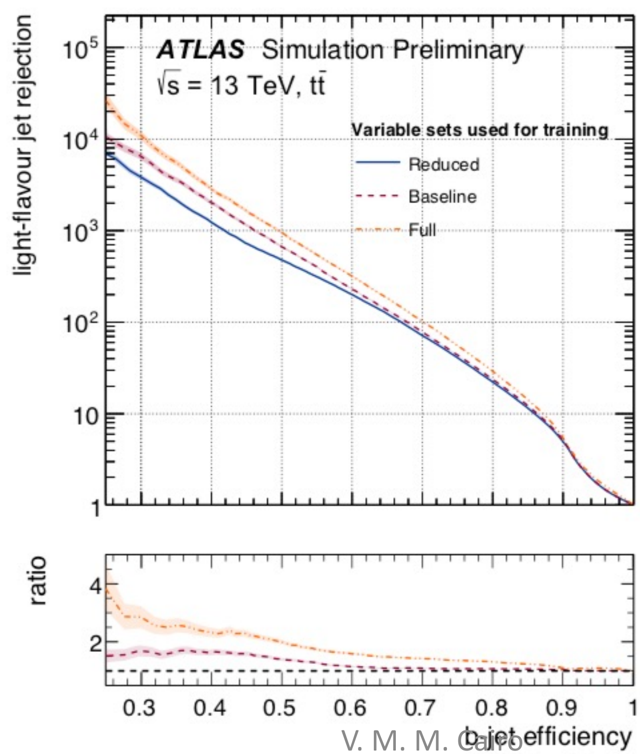

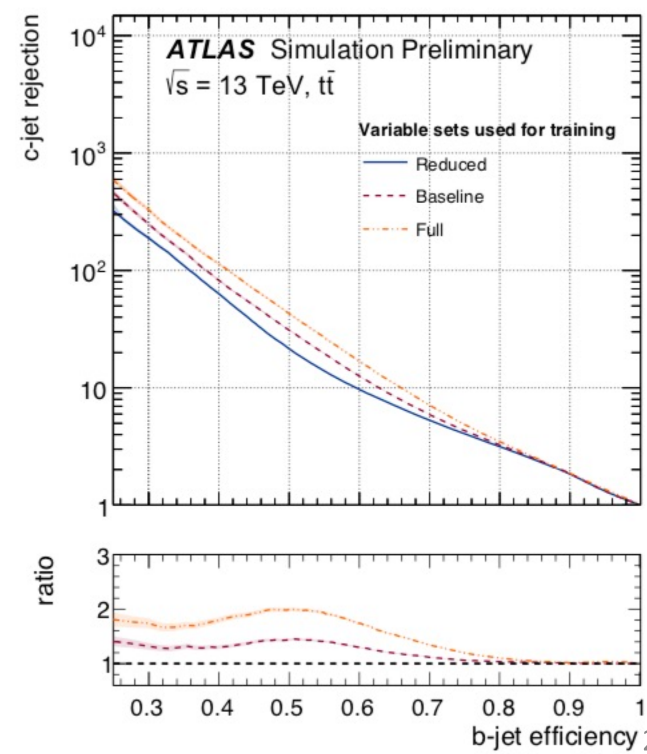

Run 2 Performance Highlights

http://cdsweb.cern.ch/record/2037697/files/ATL-PHYS-PUB-2015-022.pdf

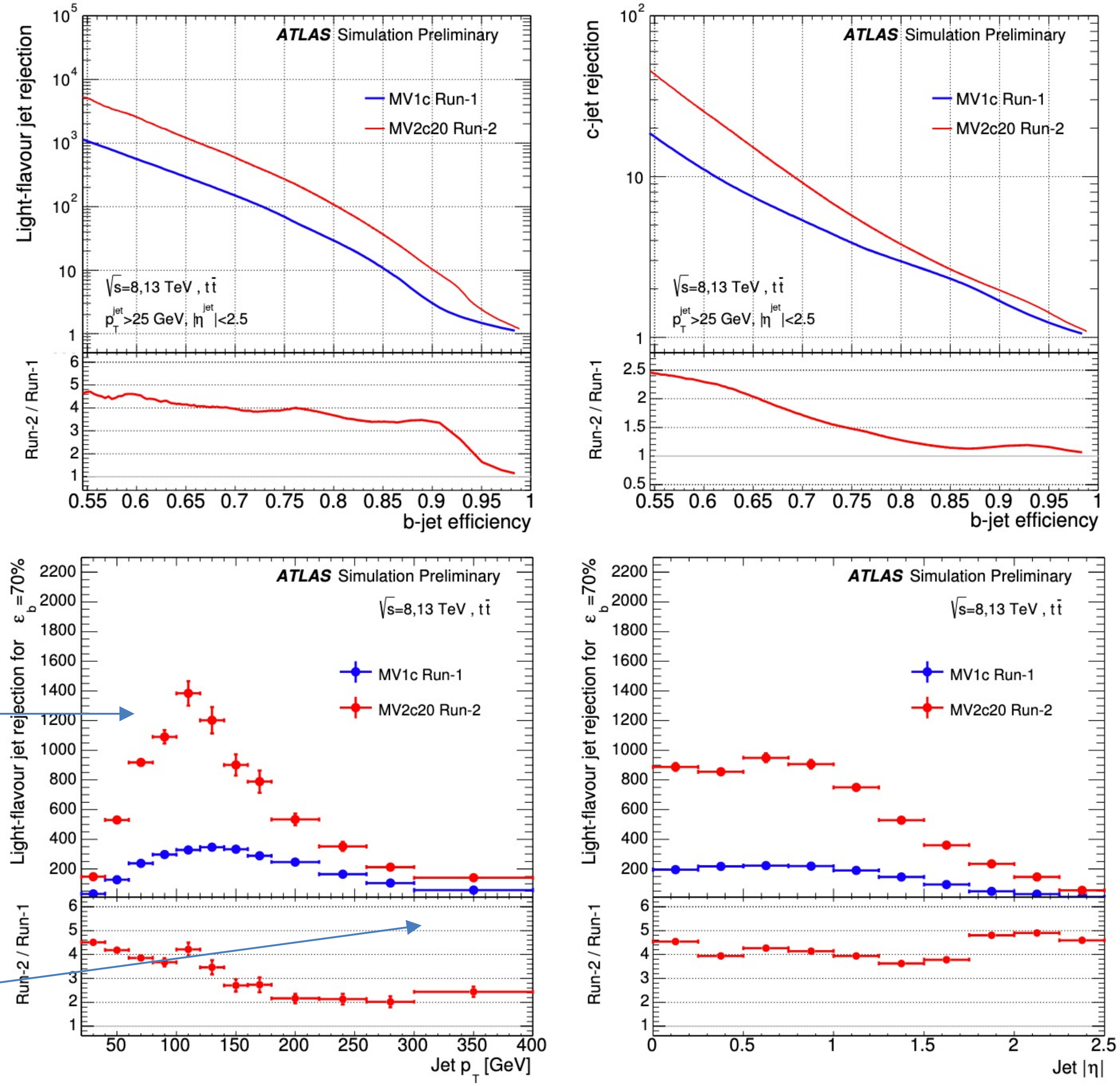

The IBL improves the impact parameter resolution of tracks mostly at pT up to 5-10 GeV, and thus the improvement due to the addition of IBL is concentrated
in the low to medium jet pT region,

while at high jet pT most of the improvement comes from the new algorithms.

Run 2 Performance Highlights

- **Comparing with previous experiments**

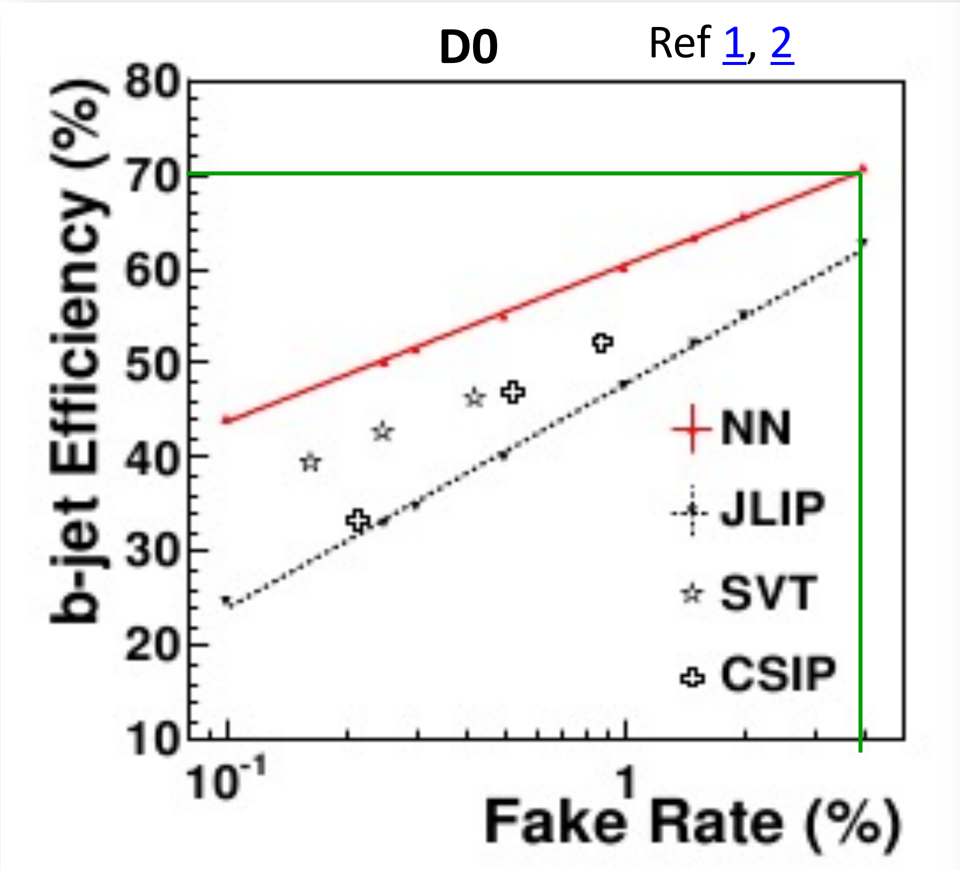

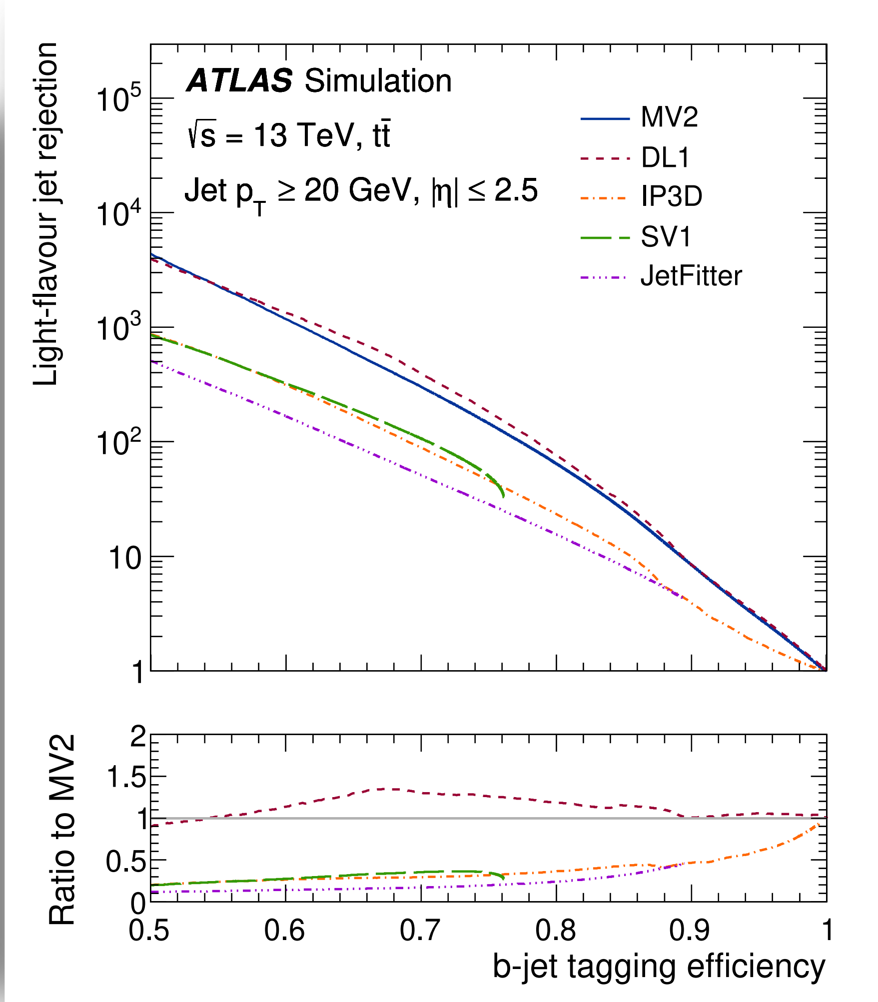

- 1 order of magnitude larger fake rate compared to the ATLAS Run 2
  - Transverse IP resolution about 30-40 microns
- Similar complementarity among algorithms

FTag

http://atlas.web.cern.ch/Atlas/GROUPS/PHYSICS/PLOTS/FTAG-2019-005/

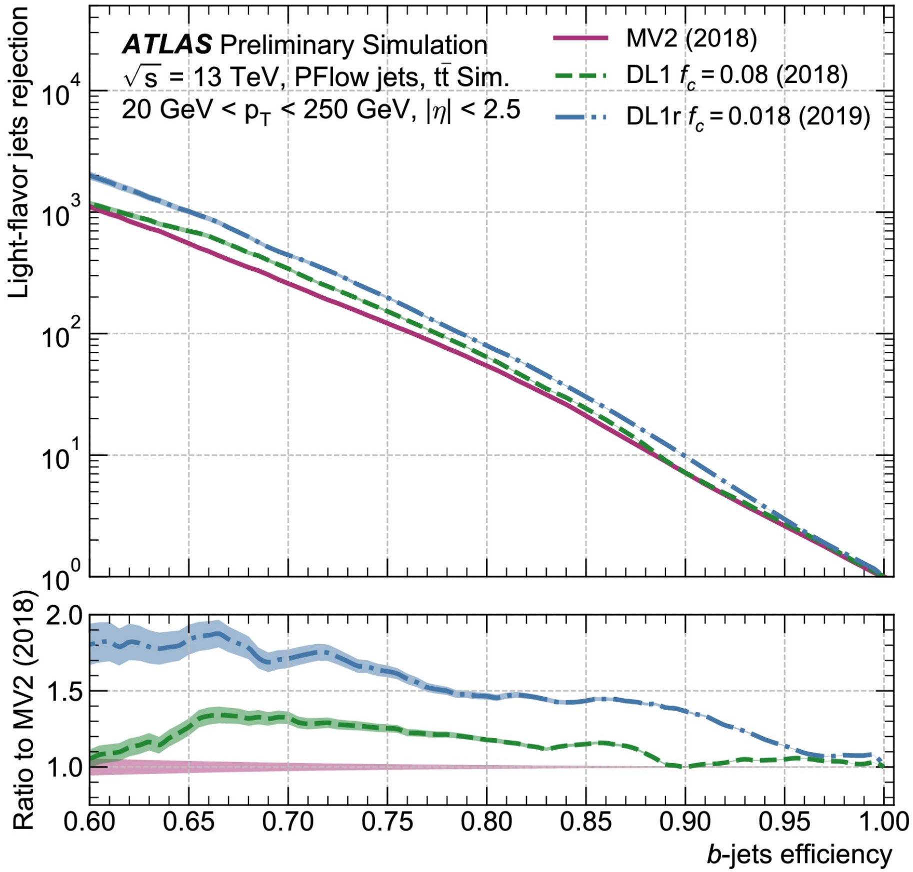

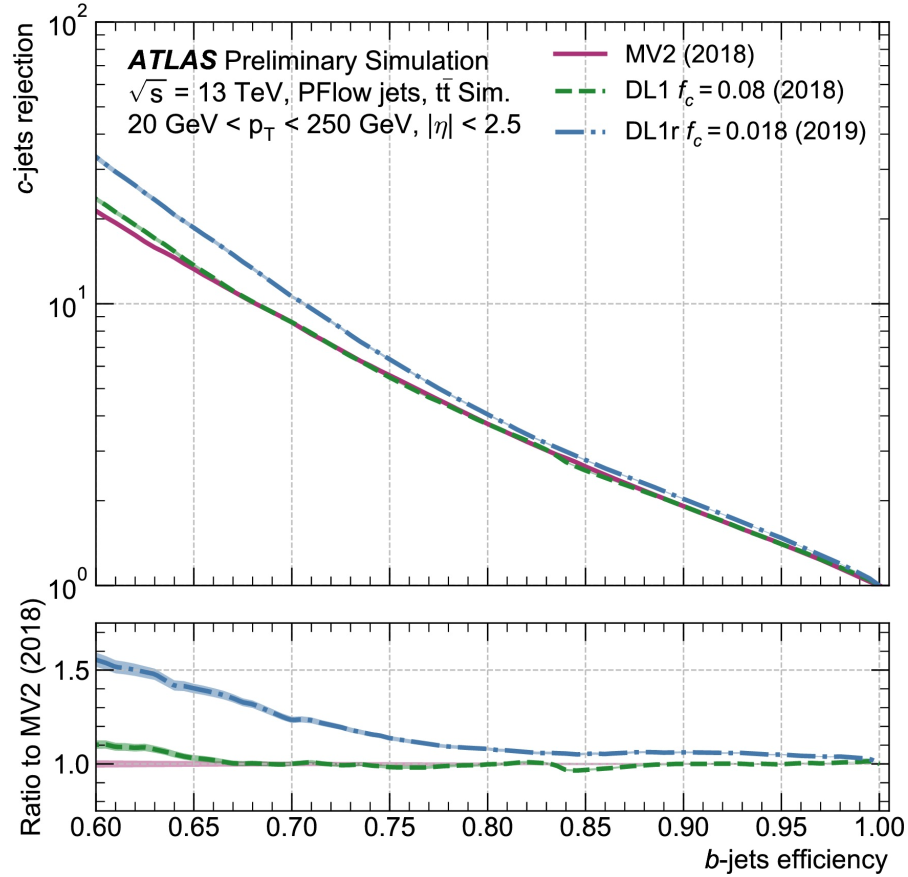

Tau ID

https://cds.cern.ch/record/2688062/files/ATL-PHYS-PUB-2019-033.pdf?version=1

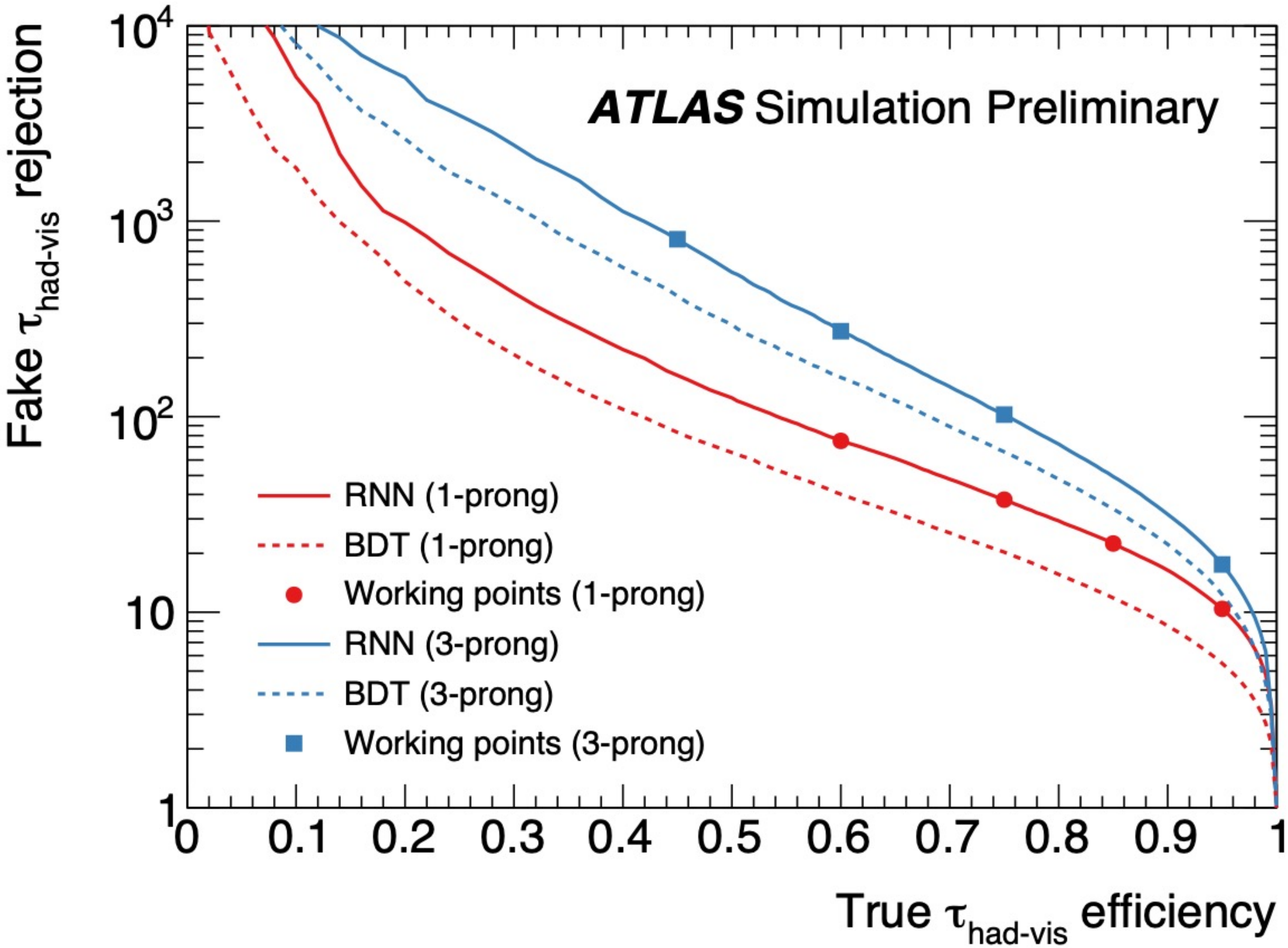

HIGGS

The stability of the Electroweak vacuum

The Higgs-self coupling and, thus, the shape of the Higgs potential, have implications on the stability of the Universe

j.physletb.2012.02.013

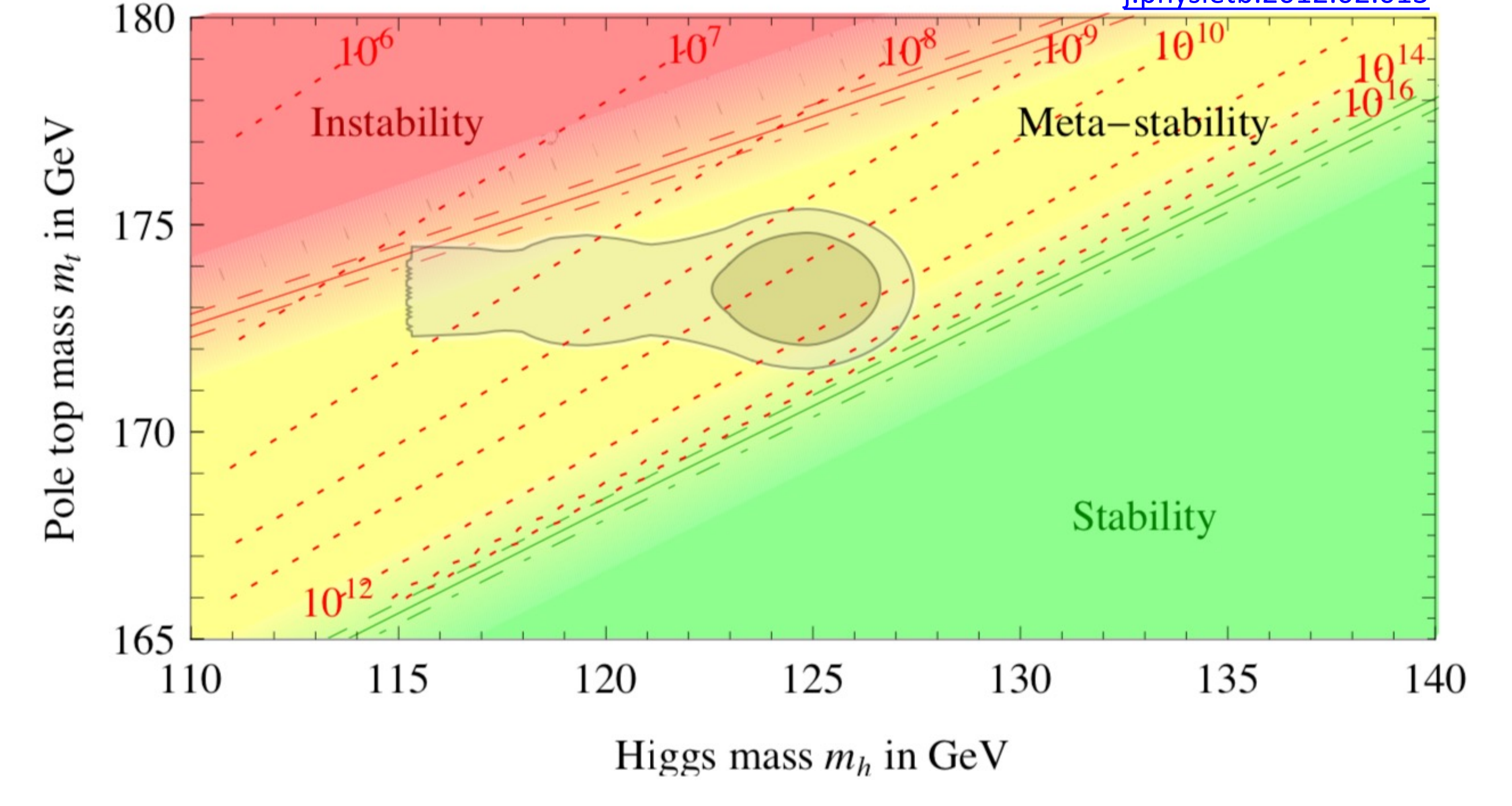

Single Higgs

$$\mu_i = 1 + \delta\sigma_{\lambda_{H^3}}(i), \qquad \mu^f = 1 + \delta \mathrm{BR}_{\lambda_{H^3}}(f),$$

$$\mu_i(\kappa_\lambda) = \frac{\sigma^{\mathrm{BSM}}(i)}{\sigma^{\mathrm{SM}}(i)} = 1 + \delta\mu_i(\kappa_\lambda) + Z_H^{\mathrm{BSM}}(\kappa_i^2 - 1),$$

Takes into account variations to other Higgs couplings (fermions, bosons, etc) or it can be taken = 1 if only the self-coupling is being considered

http://cdsweb.cern.ch/record/2667570/files/ATL-PHYS-PUB-2019-009.pdf

The 95% C.L. interval of κ_λ is $-3.2 < \kappa_\lambda < 11.9$ (observed) and $-6.2 < \kappa_\lambda < 14.4$ (expected). This interval is comparable to the one obtained from the direct *HH* searches using an integrated luminosity of 36.1 fb^{-1}, which is $-5.0 < \kappa_\lambda < 12.1$ (observed) and $-5.8 < \kappa_\lambda < 12.0$ (expected).

In particular, **the sensitivity to κ_λ is not much degraded when determining κ_F at the same time, while it is degraded by 50% (on the expected lower 95% C.L. exclusion limit) when determining simultaneously κ_V and κ_λ**. An even less constrained fit, performed by either fitting simultaneously κ_λ, κ_V and κ_F, or fitting simultaneously κ_λ and a common single Higgs boson coupling modifier ($\kappa = \kappa_V = \kappa_F$), results in nearly no sensitivity to κ_λ within the theoretically allowed range of $|\kappa_\lambda| < 20$.

Single Higgs + HH combination

http://cds.cern.ch/record/2693958/files/ATLAS-CONF-2019-049.pdf?version=2

Analysis	Integrated luminosity (fb^{-1})	Ref.
$H \to \gamma\gamma$ (excluding $t\bar{t}H$, $H \to \gamma\gamma$)	79.8	[21, 22]
$H \to ZZ^* \to 4\ell$ (including $t\bar{t}H$, $H \to ZZ^* \to 4\ell$)	79.8	[23, 24]
$H \to WW^* \to e\nu\mu\nu$	36.1	[25]
$H \to \tau^+\tau^-$	36.1	[26]
VH, $H \to b\bar{b}$	79.8	[27, 28]
$t\bar{t}H$, $H \to b\bar{b}$	36.1	[29]
$t\bar{t}H$, $H \to$ multilepton	36.1	[30]
$HH \to b\bar{b}b\bar{b}$	27.5	[31]
$HH \to b\bar{b}\tau^+\tau^-$	36.1	[32]
$HH \to b\bar{b}\gamma\gamma$	36.1	[33]

The single-Higgs and double-Higgs categories combined in this note have not been designed to be orthogonal to each other. The overlap between them has been studied for this combination. Following the results of the study, the $t\bar{t}H$, $H \to \gamma\gamma$ categories included in Ref. [17] have been removed because there are categories where up to 50% of the selected $t\bar{t}H$, $H \to \gamma\gamma$ events are also selected by the $HH \to b\bar{b}\gamma\gamma$ analysis. When removing the $t\bar{t}H$, $H \to \gamma\gamma$ categories, the expected κ_λ 95% CL interval increases by 4%; this is significantly smaller than the expected interval increase due to the removal of the $HH \to b\bar{b}\gamma\gamma$ categories. The remaining categories have a maximum overlap of less than 2% of the events in the double-Higgs categories, with the maximum being between the VH, $H \to b\bar{b}$ and $H \to \tau^+\tau^-$ single-Higgs categories and the $HH \to b\bar{b}\tau^+\tau^-$ categories. The impact of this overlap on the results has been checked

Single Higgs + HH combination

http://cds.cern.ch/record/2693958/files/ATLAS-CONF-2019-049.pdf?version=2

- inclusive production cross sections, decay branching ratios and differential cross sections (VBF, WH, ZH) are exploited to increase the sensitivity

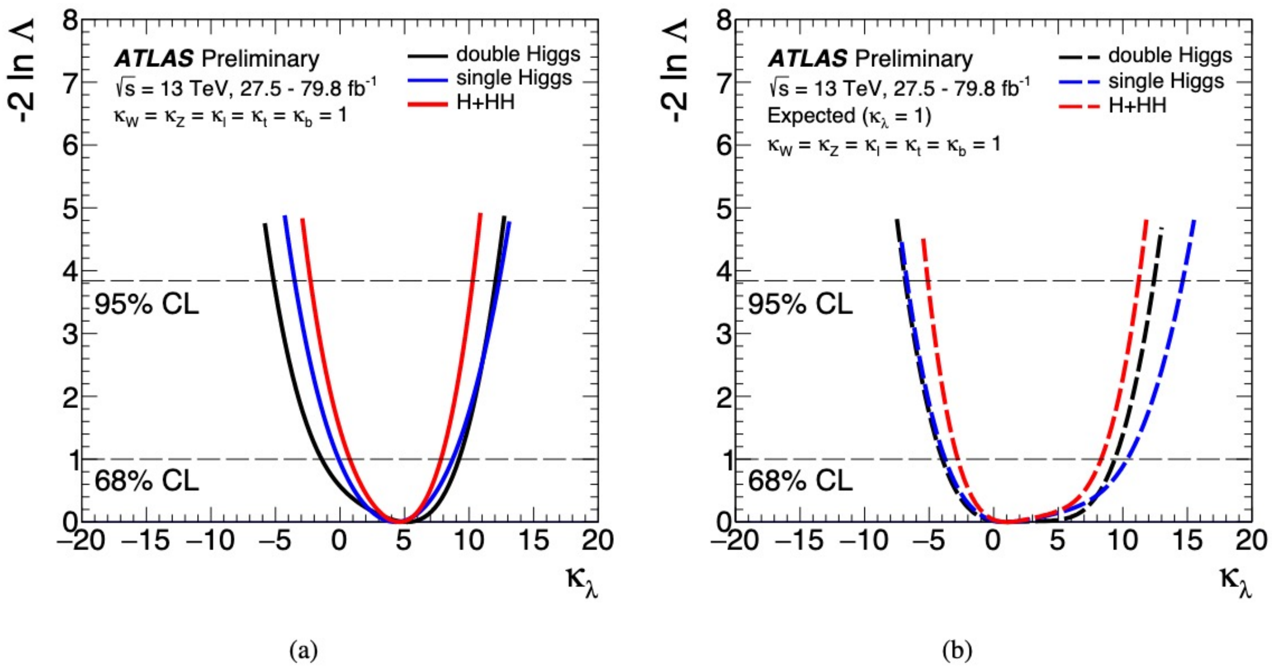

Driven by HH

Figure 3: Value of $-2\ln\Lambda$ as a function of κ_λ for single-Higgs and double-Higgs analyses separately and for the combination of the two analyses: for the data (a) and for the Asimov dataset [50] generated in the SM hypothesis (b). The intersections of the dashed horizontal lines, corresponding to $-2\ln\Lambda = 1$ and $-2\ln\Lambda = 3.84$, with the profile likelihood curve are used to define the $\pm1\sigma$ sigma uncertainty on κ_λ and the 95% CL interval, respectively.

Single Higgs + HH combination

http://cds.cern.ch/record/2693958/files/ATLAS-CONF-2019-049.pdf?version=2

- inclusive production cross sections, decay branching ratios and differential cross sections (VBF, WH, ZH) are exploited to increase the sensitivity

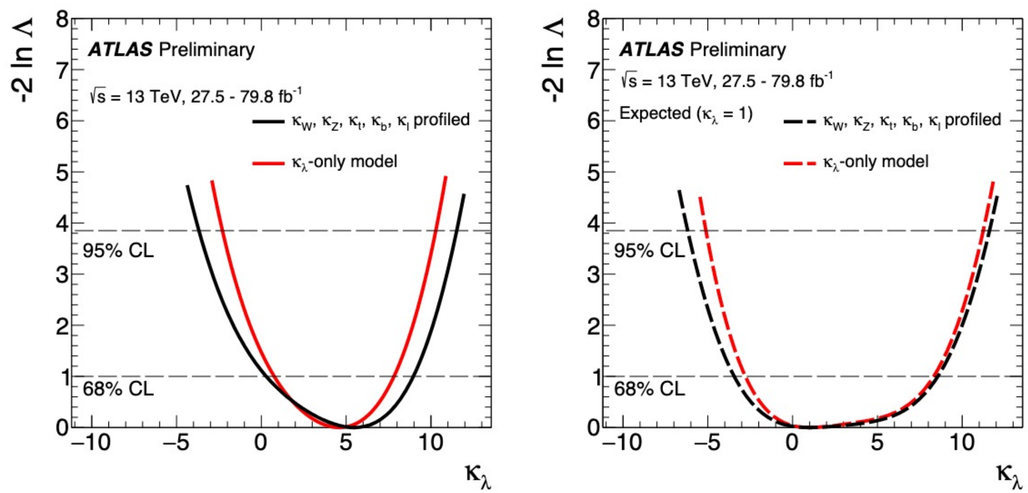

(a) (b)

Figure 5: Value of $-2\ln\Lambda$ as a function of κ_λ with κ_W, κ_Z, κ_t, κ_b, κ_ℓ profiled (i.e., the generic model) for the data (a) and the Asimov dataset [50] generated assuming $\kappa_\lambda = 1$ with the likelihood distribution Λ evaluated with nuisance parameters fixed to the best-fit values obtained from data and the parameters of interest fixed to the SM hypothesis (b). The curves are compared to the κ_λ-only model (where all κ_m modifiers are set to unity). The intersections of the dashed horizontal lines, corresponding to $-2\ln\Lambda = 1$ and $-2\ln\Lambda = 3.84$, with the profile likelihood curve are used to define the $\pm1\sigma$ sigma uncertainty on κ_λ and the 95% CL interval, respectively.

Single Higgs

http://cdsweb.cern.ch/record/2667570/files/ATL-PHYS-PUB-2019-009.pdf

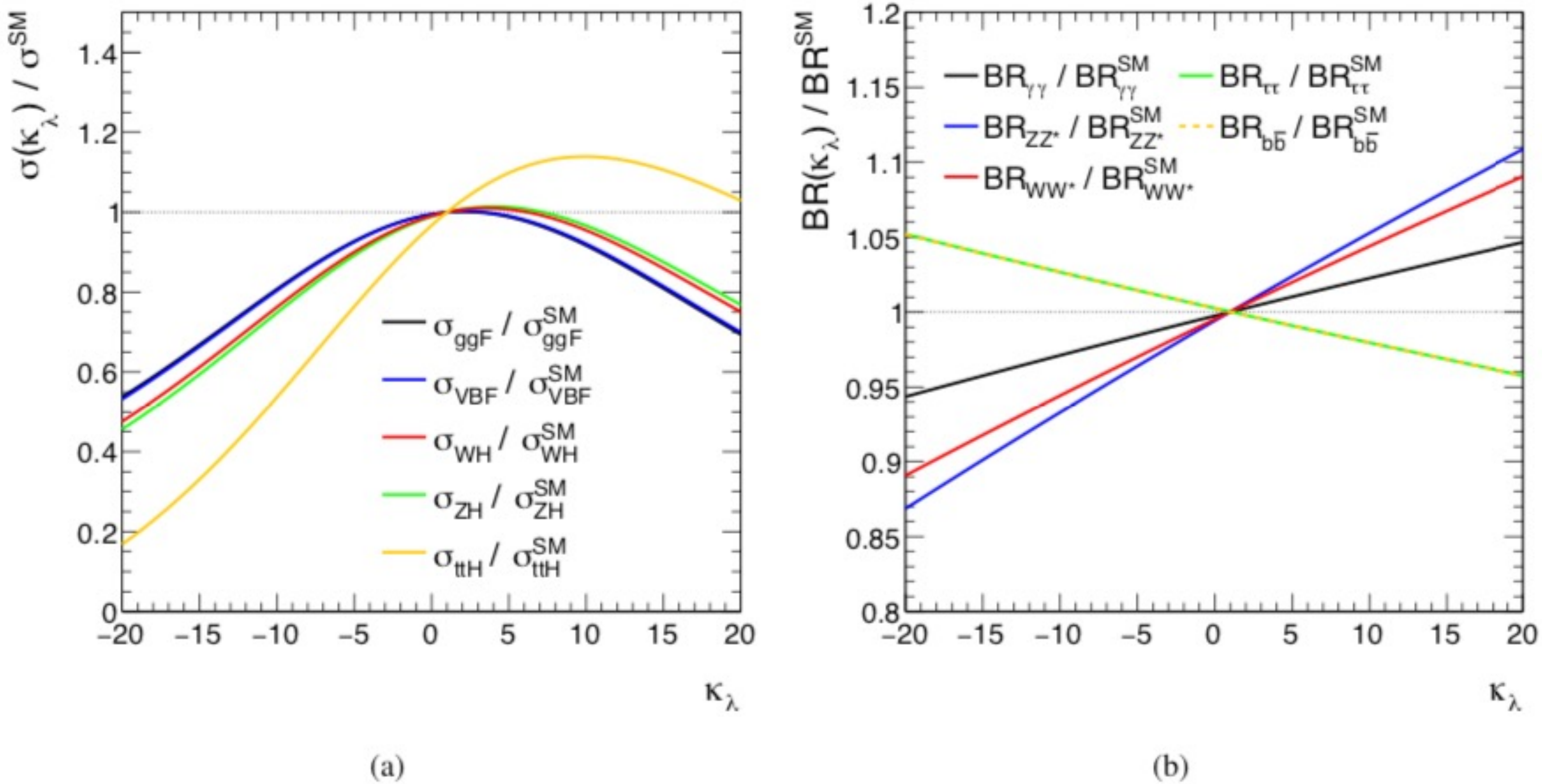

Figure 2: Variation of the cross-sections (a) and branching fractions (b) as a function of the trilinear coupling modifier κ_λ. The plots represent the equations (2) and (4) using the numerical values shown in Tables 3 and 4, all obtained from Ref. [8, 9].

Data and Simulated Samples

- **Full Run 2 data set** (139.0 ± 2.4 fb^{-1})
- **ggF HH signal** ($k_\lambda = 1, 10$) at NLO with **Powheg-Box** v2 PDF4LHC15 + **Pythia 8**
  - Herwig 7 used for PS uncertainty
- **VBF HH signal** ($k_\lambda = 0, 1, 2, 10$) at LO with **MadGraph5_aMC@NLO** v2.6.0 NNPDF3.0nlo + **Pythia 8**
- **Heavy** (251-1000 GeV) **spin 0 resonance** at LO with **MadGraph5_aMC@NLO** v2.6.1 NNPDF2.3lo set of PDFs + **Herwig** v7.1.3
- **Single Higgs** and **continuum backgrounds** summarized in the table below
- Data-driven estimate for ***γ*+jet** and **di-jet** backgrounds
- **PU overlay**: **Pythia 8.1** with NNPDF2.3lo PDF set and **A3** tune

Table 1: Summary of single Higgs boson background samples, split by production modes, and continuum background samples. The generator used in the simulation, the PDF set, and tuned parameters (tune) are also provided.

Process	Generator	PDF set	Showering	Tune
ggF	NNLOPS [61–63] [64, 65]	PDFLHC [38]	Pythia 8.2 [66]	AZNLO [67]
VBF	Powheg-Box v2 [62, 68–75]	PDFLHC	Pythia 8.2	AZNLO
WH	Powheg-Box v2	PDFLHC	Pythia 8.2	AZNLO
$qq \to ZH$	Powheg-Box v2	PDFLHC	Pythia 8.2	AZNLO
$gg \to ZH$	Powheg-Box v2	PDFLHC	Pythia 8.2	AZNLO
$t\bar{t}H$	Powheg-Box v2 [69–71, 75, 76]	NNPDF2.3lo [77]	Pythia 8.2	A14 [78]
bbH	Powheg-Box v2	PDFLHC	Pythia 8.2	A14
$tHqj$	MadGraph5_aMC@NLO	NNPDF3.0nnlo [77]	Pythia 8.2	A14
tHW	MadGraph5_aMC@NLO	NNPDF3.0nnlo [77]	Pythia 8.2	A14
$\gamma\gamma$+jets	Sherpa v2.2.4 [52]	NNPDF3.0nnlo	Sherpa v2.2.4	–
$t\bar{t}\gamma\gamma$	MadGraph5_aMC@NLO	NNPDF2.3lo	Pythia 8.2	–

Object & Event pre-selection

Di-photon triggers with **E_T > 35, 25 GeV**. Trigger efficiency for the non-resonant signal is 82.9% and 69.5% for the resonant signal (using as reference m_X = 300 GeV).

Lepton veto: Events are rejected if they contain medium electrons and/or medium muons

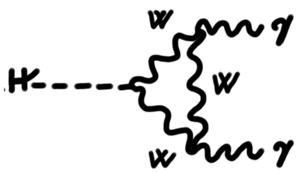

At least **2 photons**:

- Identified (Tight WP)
- Calo- and Track-isolated within a cone of $\Delta R = 0.2$
  - $E_T^{iso} < 0.065 \cdot E_T$ and $p_T^{iso} < 0.05 \cdot E_T$
- 105 GeV < $m\gamma\gamma$ < 160 GeV
- $E_T/m\gamma\gamma$ > 0.35 and 0.25
- **γγ vertex**

$m_{\gamma\gamma}$

Primary Vertex Selection Efficiency

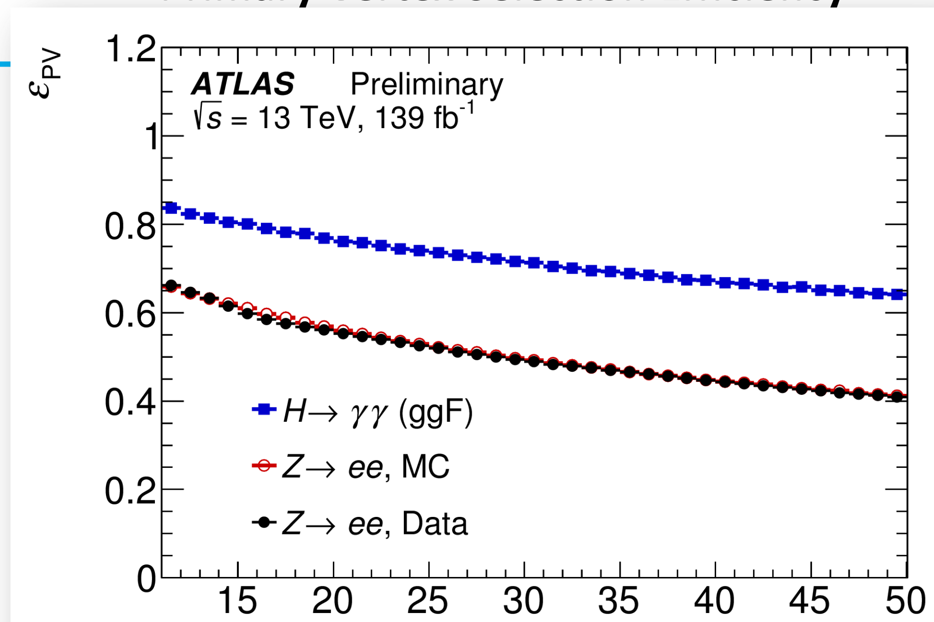

ATLAS-CONF-2019-029/

Object & Event pre-selection

Di-photon triggers with **E_T > 35, 25 GeV**. Trigger efficiency for the non-resonant signal is 82.9% and 69.5% for the resonant signal (using as reference m_X = 300 GeV).

Lepton veto: Events are rejected if they contain medium electrons and/or medium muons

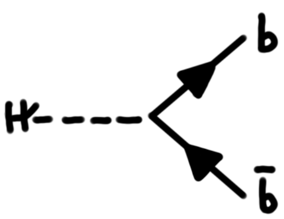

Less than 6 central jets (reduce ttH)

- PFlow jets, anti-kt R=0.4, tight JVT applied

Exactly **2 b-jets**

- DL1r 77% WP
- B-jet energy corrections applied
    - Muon-in-jet
    - pT-reco

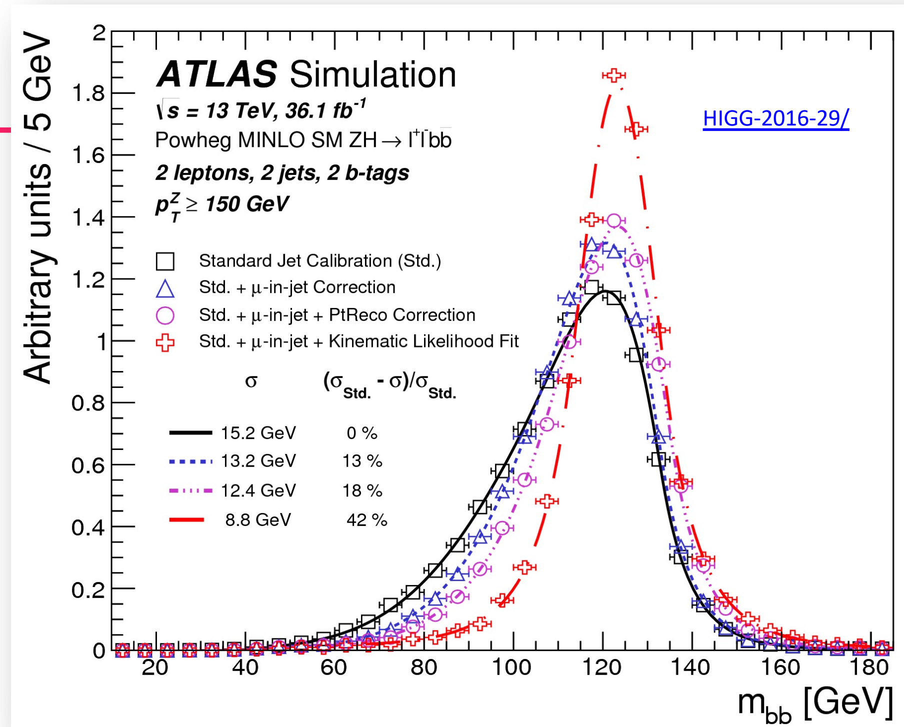

Event Categorization

$$m^*_{b\bar{b}\gamma\gamma} = m_{b\bar{b}\gamma\gamma} - m_{b\bar{b}} - m_{\gamma\gamma} + 250 \text{ GeV}$$

- $m^*_{b\bar{b}\gamma\gamma}$ used in both non-resonant and resonant selections → improves resolution
- **On top of common preselection and $m^*_{b\bar{b}\gamma\gamma}$ cuts, apply BDT-based categorization**
- Require at least 9 expected background events in the $m\gamma\gamma$ **window** (excluding 120-130) to guarantees sufficient events in data side-bands for $m\gamma\gamma$ fit.

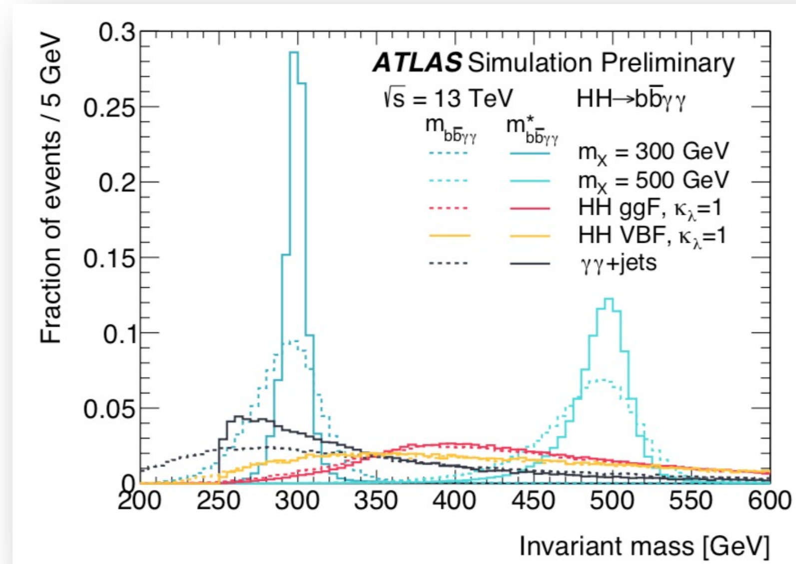

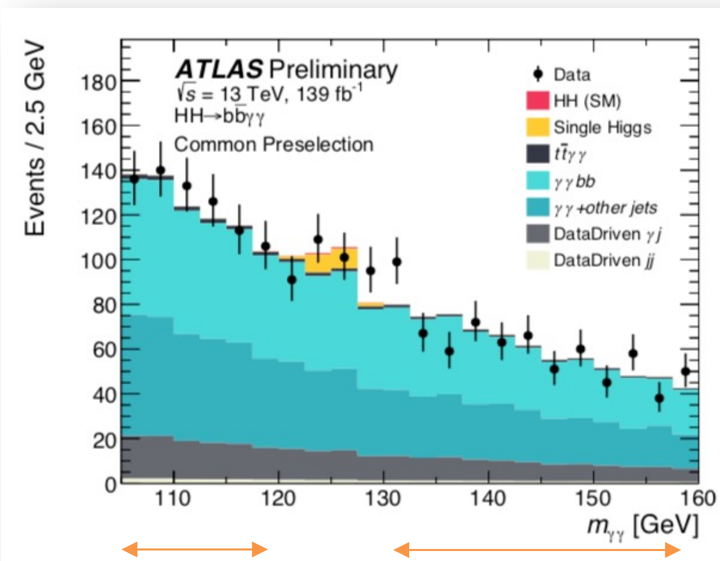

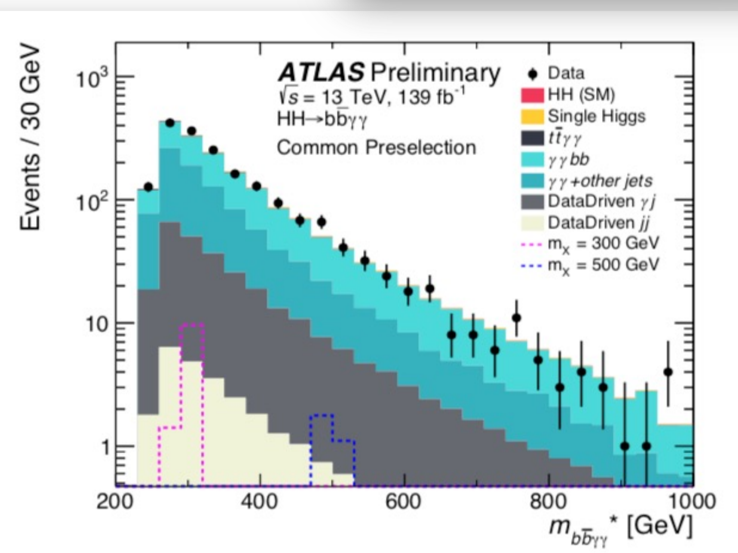

HH->bbyy strategy

Non resonant

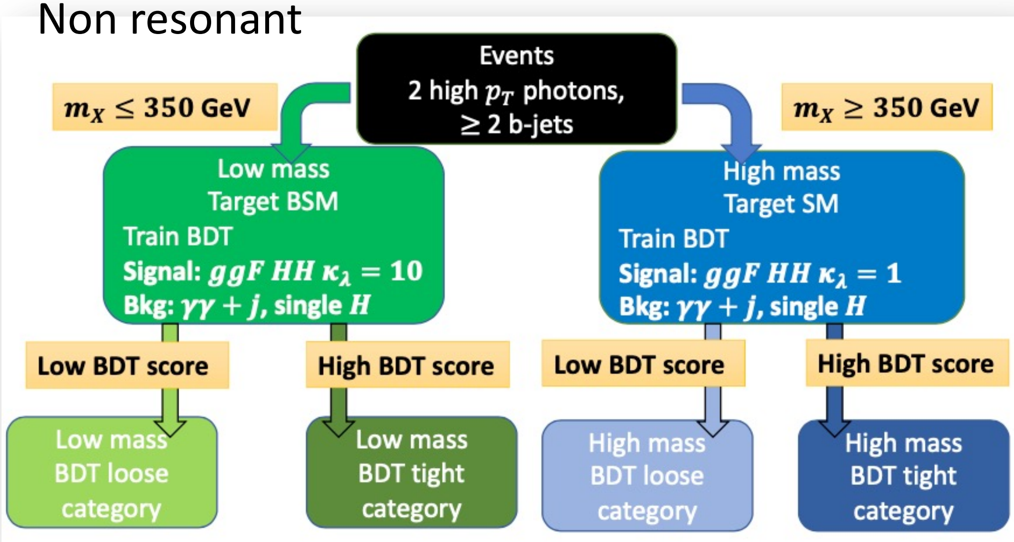

Resonant

Previous paper

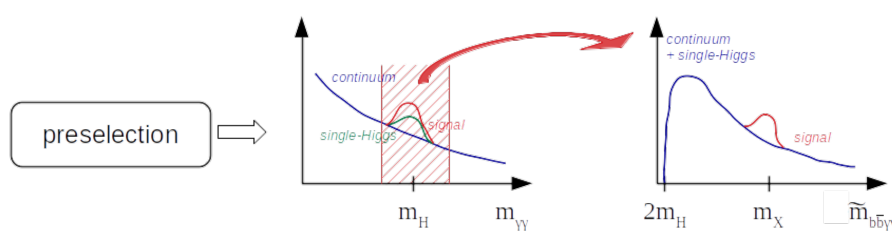

New strategy

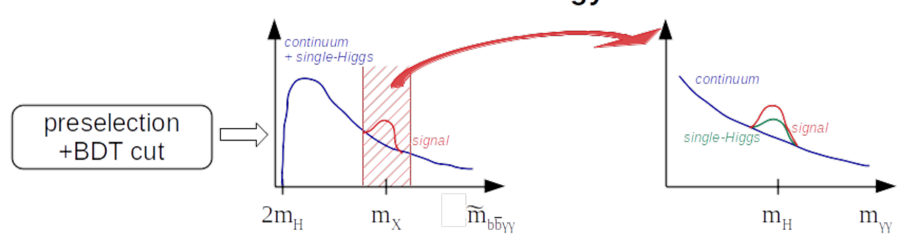

Non-resonant Categorization

4 categories (different wrt previous paper)

- **Low** and **High** $m^*_{b\bar{b}\gamma\gamma}$
  - **< 350 GeV for BSM**
  - **> 350 GeV for SM**
- In each mass region, train BDT to discriminate signal ($k_\lambda = 1, 10$) from continuum + single Higgs backgrounds
- Photon- and jet-level info used in BDT (details in back-up)
  - m_{bb} very powerful
  - "topness" reduces ttH contamination by ~35%

$$\chi_{Wt} = \min \sqrt{\left(\frac{m_{j_1 j_2} - m_W}{m_W}\right)^2 + \left(\frac{m_{j_1 j_2 j_3} - m_t}{m_t}\right)^2}$$

- **Loose** and **Tight BDT**
  - Boundaries chosen to maximize combined expected significance

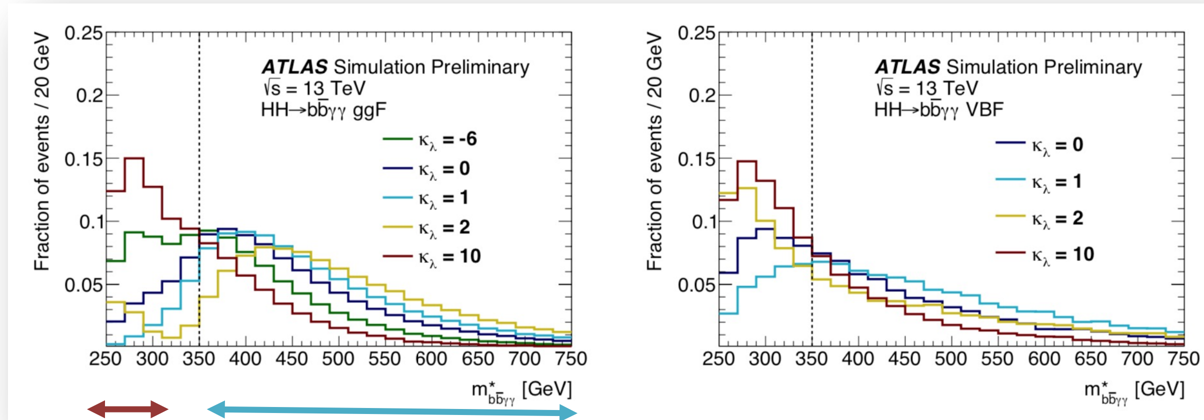

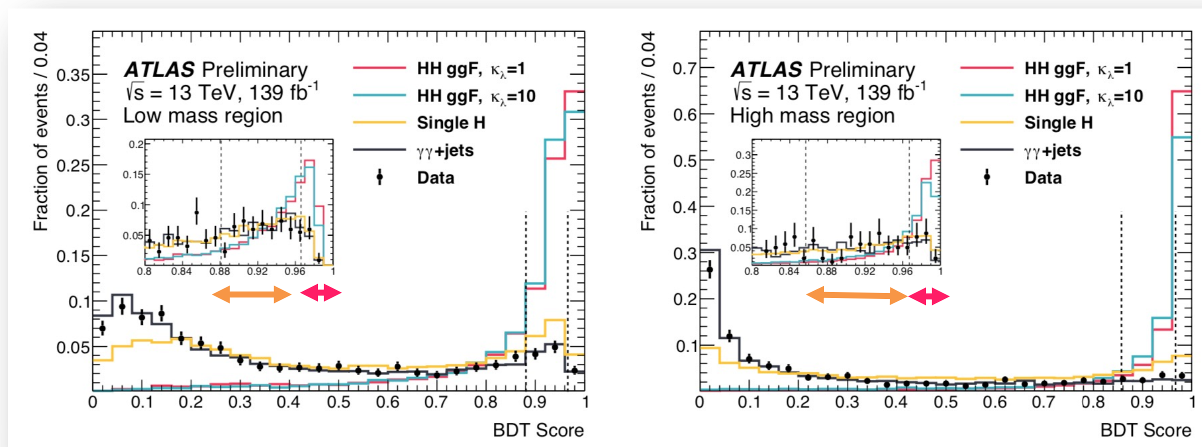

Resonant Categorization

- **Different wrt previous paper**
- **Single BDT for all resonances**
- **2 BDTs** to separate signal from **continuum** and from **single Higgs** backgrounds
- Scores combined in BDT_{tot}

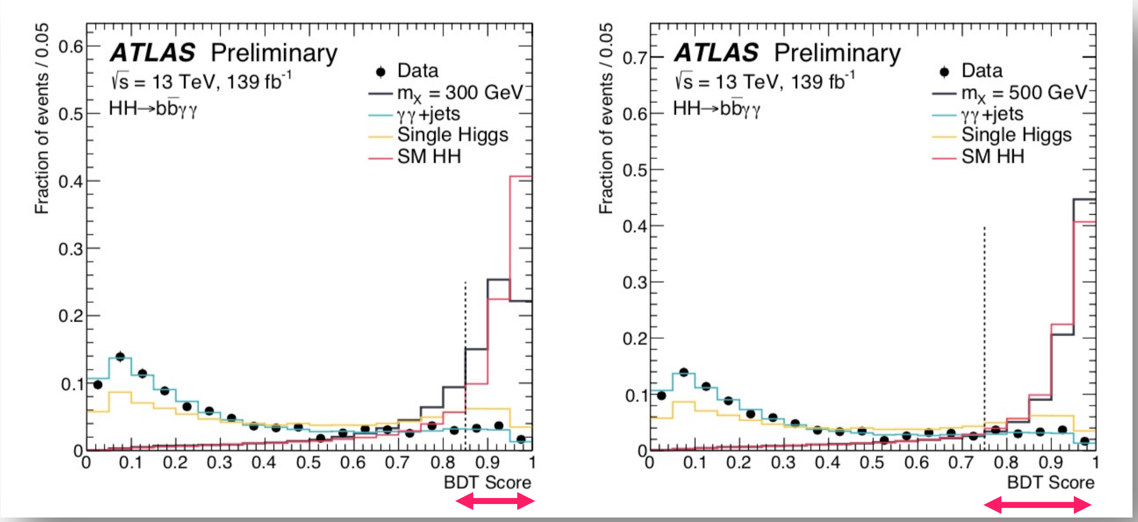

$$\mathrm{BDT_{tot}} = \frac{1}{\sqrt{C_1^2 + C_2^2}} \sqrt{C_1^2 \left(\frac{\mathrm{BDT}_{\gamma\gamma} + 1}{2}\right)^2 + C_2^2 \left(\frac{\mathrm{BDT}_{\mathrm{Single}H} + 1}{2}\right)^2}$$

$$C_1, C_2\ (C_2 = 1 - C_1)$$

- **2-stage optimization**
  1. Maximize significance for each resonance
     - Different coefficients and BDT scores
  2. Select coefficients providing a significance within 5% from the maximum value, for each resonance
     - A common C_1 = 0.65 coefficient is found, individual BDT cuts are used

A cut on $m^*_{b\bar{b}\gamma\gamma}$ is applied at $\pm 2\sigma$ ($\pm 4\sigma$) of the expected mean value for signal events for each resonance (at 900-1000 GeV)

Non-resonant BDT inputs

Table 2: Variables used in the BDT for the non-resonant analysis. The b-tag status identifies the highest fixed btag working point (60%, 70%, 77%) that the jet passes. All vectors in the event are rotated so that the leading photon ϕ is equal to zero.

Variable	Definition
Photon-related kinematic variables	
$p_{\mathrm{T}}/m_{\gamma\gamma}$	Transverse momentum of the two photons scaled by their invariant mass $m_{\gamma\gamma}$
η and ϕ	Pseudo-rapidity and azimuthal angle of the leading and sub-leading photon
Jet-related kinematic variables	
b-tag status	b-tagging score coming from the DL1r algorithm
p_{T}, η and ϕ	Transverse momentum, pseudo-rapidity and azimuthal angle of the two jets with the highest b-tagging score
$p_{\mathrm{T}}^{b\bar{b}}$, $\eta_{b\bar{b}}$ and $\phi_{b\bar{b}}$	Transverse momentum, pseudo-rapidity and azimuthal angle of b-tagged jets system
$m_{b\bar{b}}$	Invariant mass built with the two jets with the highest b-tagging score
H_{T}	Scalar sum of the p_{T} of the jets in the event
Single topness	For the definition, see Eq. 1
Missing transverse momentum-related variables	
$E_{\mathrm{T}}^{\mathrm{miss}}$ and ϕ	Missing transverse momentum and its azimuthal angle

$$\chi_{Wt} = \min\sqrt{\left(\frac{m_{j_1 j_2} - m_W}{m_W}\right)^2 + \left(\frac{m_{j_1 j_2 j_3} - m_t}{m_t}\right)^2},$$

Resonant BDT inputs

Table 4: Variables used in the BDT for the resonant analysis. For variables depending on b-tagged jets, only jets b-tagged using the 77% working point are considered as described in Section 4.1.

Variable	Definition
Photon-related kinematic variables	
$p_T^{\gamma\gamma}$, $y^{\gamma\gamma}$	Transverse momentum and rapidity of the di-photon system
$\Delta\phi_{\gamma\gamma}$ and $\Delta R_{\gamma\gamma}$	Azimuthal angular distance and ΔR between the two photons
Jet-related kinematic variables	
$m_{b\bar{b}}$, $p_T^{b\bar{b}}$ and $y_{b\bar{b}}$	Invariant mass, transverse momentum and rapidity of the b-tagged jets system
$\Delta\phi_{b\bar{b}}$ and $\Delta R_{b\bar{b}}$	Azimuthal angular distance and ΔR between the two b-tagged jets
N_{jets} and $N_{b-\text{jets}}$	Number of jets and number of b-tagged jets
H_T	Scalar sum of the p_T of the jets in the event
Photons and jets-related kinematic variables	
$m_{b\bar{b}\gamma\gamma}$	Invariant mass built with the di-photon and b-tagged jets system
$\Delta y_{\gamma\gamma,b\bar{b}}$, $\Delta\phi_{\gamma\gamma,b\bar{b}}$ and $\Delta R_{\gamma\gamma,b\bar{b}}$	Distance in rapidity, azimuthal angle and ΔR between the di-photon and the b-tagged jets system

Cut flow

Table 9: Cutflow for non-resonant ggF signal sample, yields are normalised to 139 fb^{-1}.

Cuts	Yields	Efficiency [%]
N_{xAOD}	11.37	100
N_{DxAOD}	11.37	100
All events	11.37	99.99
No duplicates	11.37	99.99
GRL	11.37	99.99
Pass trigger	9.43	82.98
Detecctor DQ	9.43	82.98
Has PV	9.43	82.98
2 loose photons	7.00	61.61
$e-\gamma$ ambiguity	7.00	61.58
Trigger match	6.66	58.57
Tight ID	5.86	51.50
Isolation	5.17	45.45
$rel.p_T cuts$	4.65	40.88
$m_{\gamma\gamma} \in [105, 160]$ GeV	4.64	40.85
$N_{lep} = 0$	4.71	41.44
$N_j > 2$	4.69	41.29
N_j central <6	3.95	34.73
$N_j btag < 3$	1.97	17.28
2 b-jets with 77% WP	1.56	13.76
Di-Higgs invariant mass <350 GeV	0.19	1.65
Di-Higgs invariant mass >350 GeV	1.38	12.11

Table 10: Cutflow for resonant signal sample, with m_X = 300 GeV. Yields are normalised to 139 fb^{-1}.

Cuts	Yield	Efficiency [%]
N_{xAOD}	134.07	100
N_{DxAOD}	134.07	100
All events	134.06	99.99
No duplicates	134.06	99.99
GRL	134.06	99.99
Pass trigger	91.90	68.54
Detecctor DQ	91.90	68.54
Has PV	91.90	68.54
2 loose photons	75.69	56.45
$e-\gamma$ ambiguity	75.66	56.43
Trigger match	68.44	51.04
Tight ID	58.70	43.79
Isolation	49.24	36.72
$rel.p_T cuts$	44.47	33.17
$m_{\gamma\gamma} \in [105, 160]$	44.44	33.15
$N_{lep} = 0$	44.44	33.15
$N_j > 2$	44.24	33.00
N_j central <6	33.03	24.63
$N_j btag < 3$ with 77% WP	14.39	10.73
2 b-jet with 77% WP	11.30	8.43
Di-Higgs invariant mass selection	9.80	7.31
$m_{\gamma\gamma} \in [120, 130]$ GeV	5.99	4.47

Resonant BDT score

Table 14: Minimum BDT value of the events passing the selection criteria of the resonant search. The combined BDT score uses $C_1 = 0.65$. Only C_1 is specified since $C_2 = 1 - C_1$.

m_X [GeV]	BDT threshold
251	0.70
260	0.75
270	0.80
280	0.85
290	0.85
300	0.85
312.5	0.85
325	0.85
337.5	0.85
350	0.85
375	0.90
400	0.80
425	0.85
450	0.85
475	0.80
500	0.75
550	0.60
600	0.45
700	0.20
800	0.10
900	0.20
1000	0.05

DSCB resolutions

Table 5: Effective resolution of the the $m_{\gamma\gamma}$ invariant mass spectrum (the smallest mass window that contains 68% of signal, termed σ_{68}) and corresponding statistical uncertainty are given for the non-resonant search categories and for the two benchmark scalar resonant signals.

Category	σ_{68} [GeV]
High mass BDT tight	1.46 ± 0.01
High mass BDT loose	1.61 ± 0.02
Low mass BDT tight	1.72 ± 0.06
Low mass BDT loose	1.81 ± 0.03
Resonant m_X = 300 GeV	1.96 ± 0.02
Resonant m_X = 500 GeV	1.60 ± 0.01

Data/MC comparison

Non-resonant

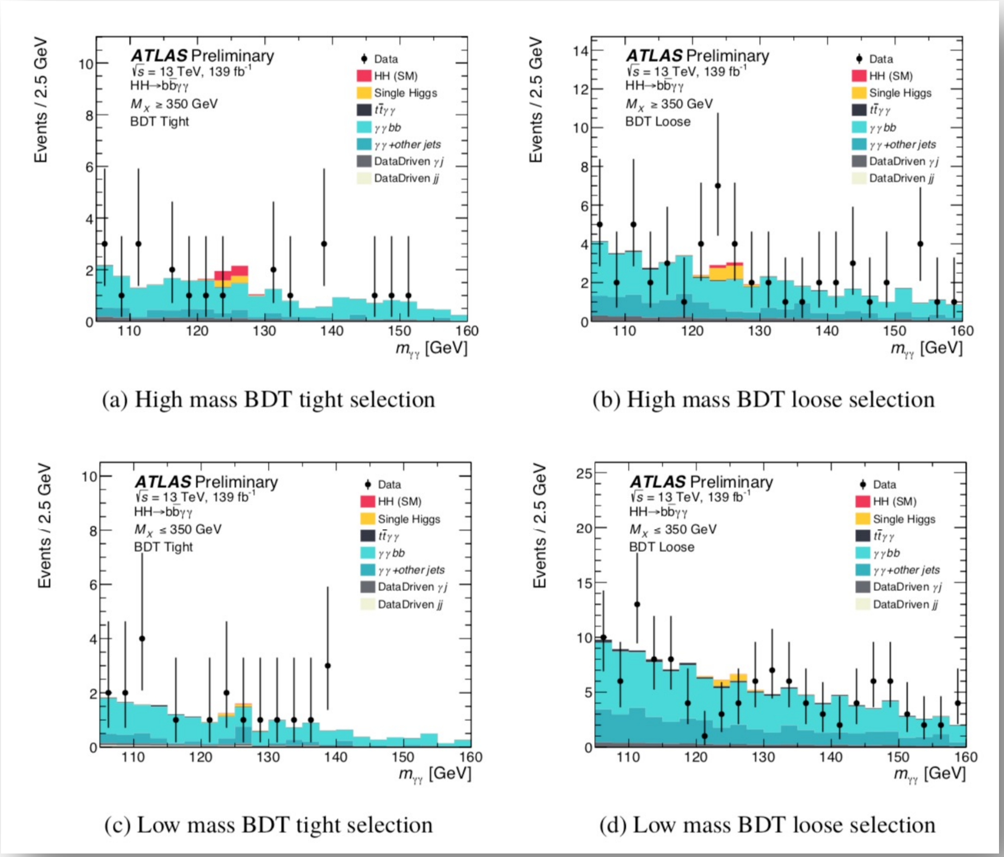

(a) High mass BDT tight selection

(b) High mass BDT loose selection

(c) Low mass BDT tight selection

(d) Low mass BDT loose selection

Dominated by γγbb background (flavor composition from Sherpa)

Data-driven $\gamma\&j$ via 2x2D method based on reverting γ isolation and identification criteria

(only for data/MC comparison)

Resonant

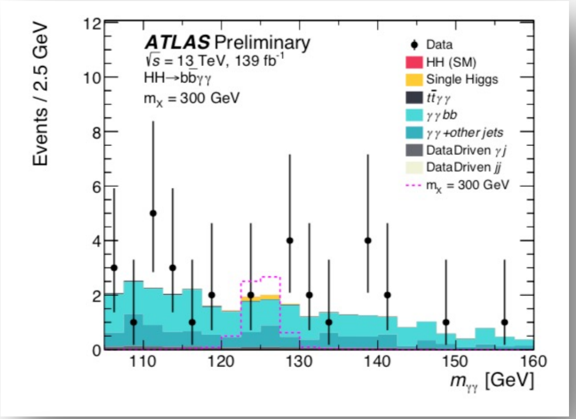

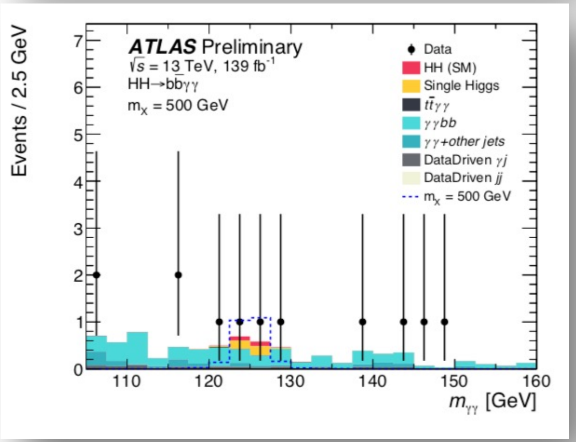

Main SH backgrounds

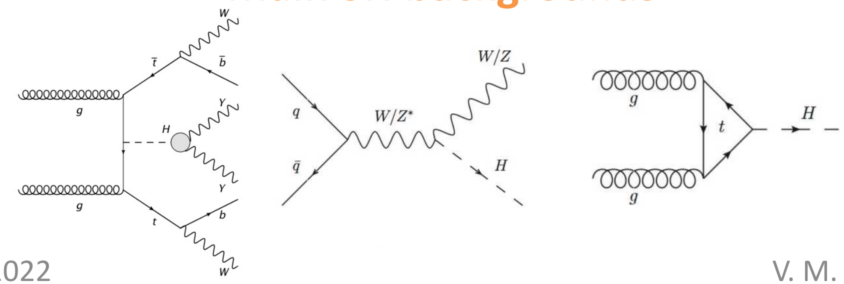

Modeling of the discriminant variable

- $m_{\gamma\gamma}$ for both non-resonant & resonant (different than previous paper, improved resonant limits at low mass thanks to easier background modeling)
- Yields are parameterized with a 2nd order polynomial
- **HH signal and single Higgs background** shape modelled from MC with a **DSCB** function
  - No sizable dependence on k_λ is observed

- **Continuum background** modelled from data side bands
- Systematic uncertainty assigned to the function choice via ***Spurious Signal*** method
  - Estimate signal bias by fitting a background only template with a signal + background function
  - **Exponential function** chosen: similar bias, but minimal number of degrees of freedom
    - Wald test performed in data, no sign of preference for higher degree function

Statistical Analysis

- Maximum likelihood fit of $m_{\gamma\gamma}$ in 105 GeV < $m_{\gamma\gamma}$ < 160 GeV, performed simultaneously over all categories

$$\mathcal{L} = \prod_c \left(\mathrm{Pois}(n_c | N_c(\boldsymbol{\theta})) \cdot \prod_{i=1}^{n_c} f_c(m^i_{\gamma\gamma}, \boldsymbol{\theta}) \cdot G(\boldsymbol{\theta}) \right)$$

Expected #events

$$N_c(\boldsymbol{\theta}) = \mu \cdot N_{HH,c}(\boldsymbol{\theta}^{\mathrm{yield}}_{HH}) + N^{\mathrm{res}}_{\mathrm{bkg,c}}(\boldsymbol{\theta}^{\mathrm{yield}}_{\mathrm{res}}) + N_{\mathrm{SS,c}} \cdot \boldsymbol{\theta}^{\mathrm{SS,c}} + N^{\mathrm{non-res}}_{\mathrm{bkg,c}}$$

PDF

$$f_c(m_{\gamma\gamma}, \boldsymbol{\theta}) = [\mu \cdot N_{HH,c}(\boldsymbol{\theta}^{\mathrm{yield}}_{HH}) \cdot f_{HH,c}(m_{\gamma\gamma}, \boldsymbol{\theta}^{\mathrm{shape}}_{HH}) + N^{\mathrm{res}}_{\mathrm{bkg,c}}(\boldsymbol{\theta}^{\mathrm{yield}}_{\mathrm{res}}) \cdot f^{\mathrm{res}}_{\mathrm{bkg,c}}(m_{\gamma\gamma}, \boldsymbol{\theta}^{\mathrm{shape}}_{\mathrm{res}}) + N_{\mathrm{SS,c}} \cdot \boldsymbol{\theta}^{\mathrm{SS,c}}_{HH} \cdot f_{HH,c}(m_{\gamma\gamma}, \boldsymbol{\theta}^{\mathrm{shape}}_{HH}) + N^{\mathrm{non-res}}_{\mathrm{bkg,c}} \cdot f^{\mathrm{non-res}}_{\mathrm{bkg,c}}(m_{\gamma\gamma}, \boldsymbol{\theta}^{\mathrm{shape}}_{\mathrm{non-res}})] / N_c(\boldsymbol{\theta}^{\mathrm{yield}}_{\mathrm{non-res}})$$

Single Higgs yields fixed to SM values, while μ, non-resonant background shape and nuisance parameters for sys. floating in fit

Non-resonant

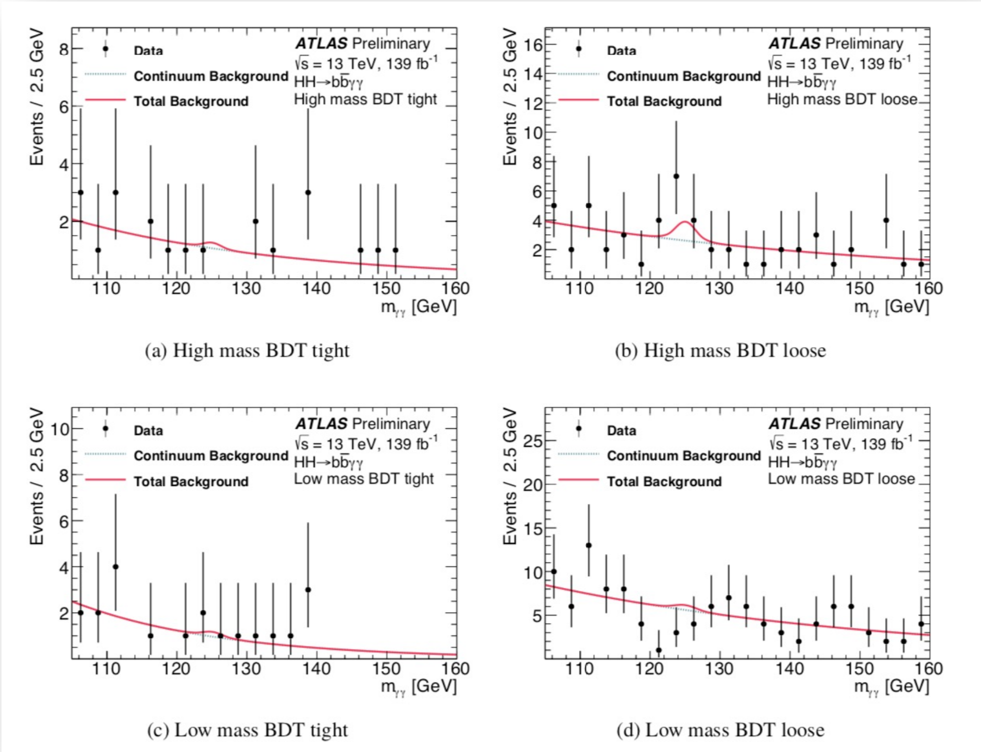

(a) High mass BDT tight
(b) High mass BDT loose
(c) Low mass BDT tight
(d) Low mass BDT loose

Resonant

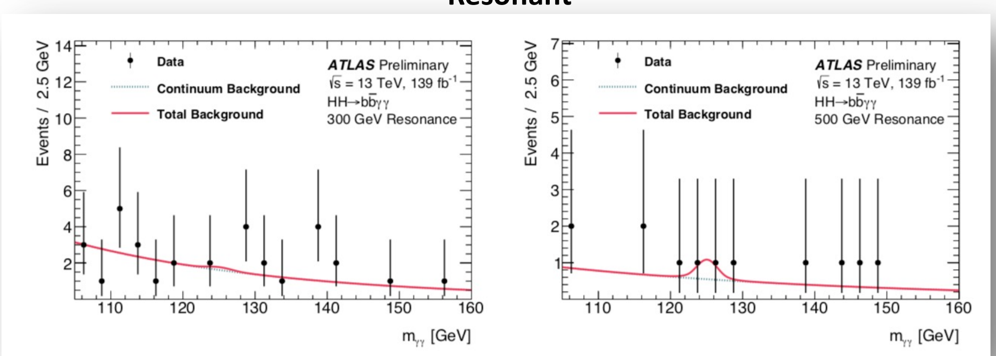

Number of events – non resonant

	High mass BDT tight	High mass BDT loose	Low mass BDT tight	Low mass BDT loose
Continuum background	$4.9^{+1.1}_{-1.3}$	$9.5^{+1.5}_{-1.7}$	$3.7^{+0.9}_{-1.1}$	$24.9^{+2.3}_{-2.5}$
Single Higgs boson background	$0.67^{+0.29}_{-0.13}$	$1.6^{+0.6}_{-0.2}$	$0.23^{+0.09}_{-0.03}$	$1.40^{+0.33}_{-0.16}$
ggF+bbH	$0.26^{+0.28}_{-0.16}$	$0.4^{+0.5}_{-0.2}$	$0.07^{+0.08}_{-0.04}$	$0.27^{+0.27}_{-0.16}$
$t\bar{t}H$	$0.19^{+0.03}_{-0.03}$	$0.49^{+0.09}_{-0.07}$	$0.107^{+0.022}_{-0.017}$	$0.75^{+0.13}_{-0.11}$
ZH	$0.142^{+0.035}_{-0.025}$	$0.48^{+0.09}_{-0.07}$	$0.040^{+0.020}_{-0.014}$	$0.27^{+0.06}_{-0.04}$
Rest	$0.074^{+0.032}_{-0.014}$	$0.16^{+0.07}_{-0.03}$	$0.012^{+0.008}_{-0.004}$	$0.111^{+0.030}_{-0.012}$
SM $HH(\kappa_\lambda = 1)$ signal	$0.87^{+0.10}_{-0.18}$	$0.37^{+0.04}_{-0.07}$	$0.049^{+0.006}_{-0.010}$	$0.078^{+0.008}_{-0.015}$
ggF	$0.86^{+0.10}_{-0.18}$	$0.35^{+0.04}_{-0.07}$	$0.046^{+0.006}_{-0.010}$	$0.072^{+0.008}_{-0.015}$
VBF	$(12.6^{+1.3}_{-1.2}) \cdot 10^{-3}$	$(16.1^{+1.4}_{-1.2}) \cdot 10^{-3}$	$(3.2^{+0.4}_{-0.4}) \cdot 10^{-3}$	$(6.9^{+0.5}_{-0.6}) \cdot 10^{-3}$
Alternative $HH(\kappa_\lambda = 10)$ signal	$6.5^{+1.0}_{-0.8}$	$3.6^{+0.6}_{-0.4}$	$4.5^{+0.7}_{-0.6}$	$8.5^{+1.3}_{-1.0}$
Data	2	17	5	14

Number of events – resonant

	m_X = 300 GeV	m_X = 500 GeV
Continuum background	$5.5^{+1.3}_{-1.5}$	$1.6^{+0.6}_{-0.9}$
Single Higgs boson background	$0.34^{+0.14}_{-0.07}$	$0.40^{+0.18}_{-0.08}$
SM HH background	$0.021^{+0.005}_{-0.009}$	$0.20^{+0.09}_{-0.09}$
$X \to HH$ signal	$6.1^{+0.9}_{-0.8}$	$6.1^{+0.8}_{-0.6}$
Data	6	4

Non-resonant results

No signal is observed, exclusion limits are set via the CLs method with asymptotic approximation

- Observed non-resonant HH production of **130 fb**, while **180 fb** is expected.
  - **4.1 (5.5) x the SM**

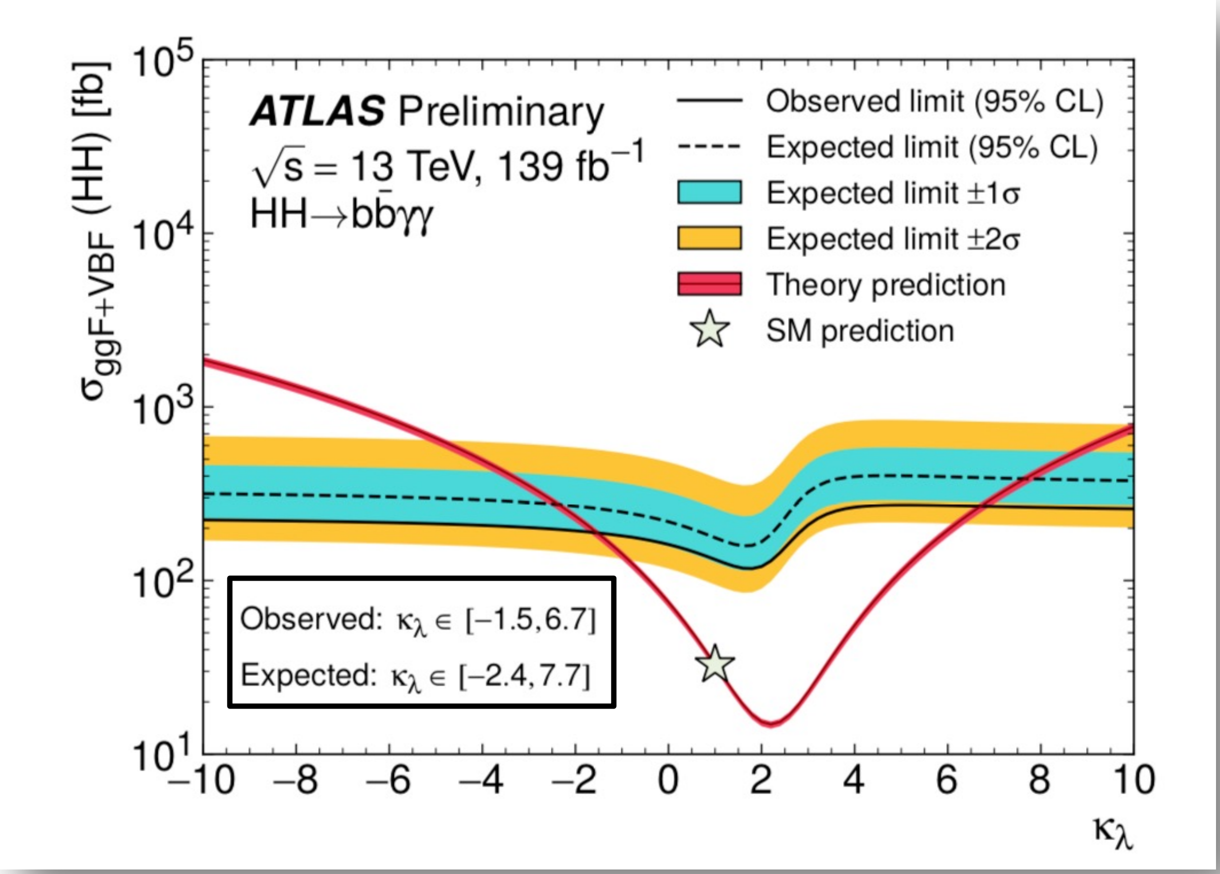

- 36 fb^{-1} results: **22 (28) x SM** observed (expected), $\mathbf{-8.2\ (-8.3)\ <\ k_\lambda\ <\ 13.2\ (13.2)}$
- **Full Run 2 CMS results: 7.7 (5.2) x SM,** $-3.3\ (-2.5) \leq\ k_\lambda \leq\ 8.5\ (8.2)$

Non-resonant results

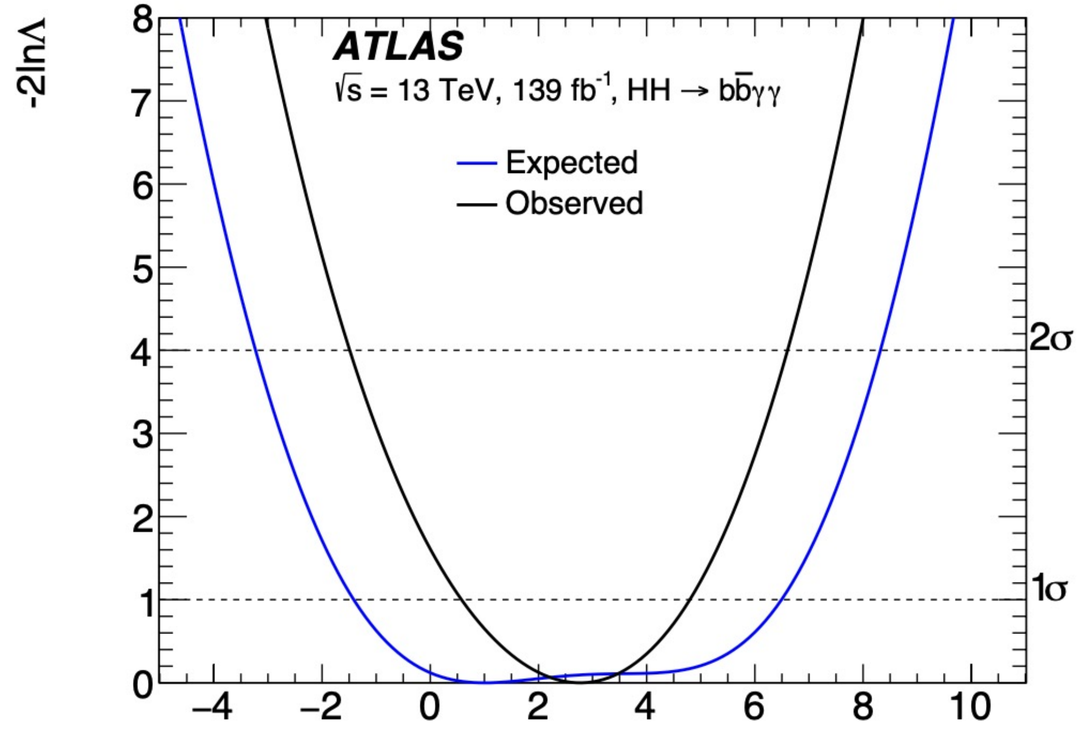

Figure 13: Values of the negative log-profile-likelihood ratio ($-2\ln\Lambda$) as a function of κ_λ evaluated for the combination of all the categories of the nonresonant search. The coupling of the Higgs boson to fermions and gauge bosons is set to SM values in the profile likelihood calculation. The expected result corresponds to a Asimov data set [106] generated under the SM signal-plus-background hypothesis, $\kappa_\lambda = 1$. All systematic uncertainties, including the theoretical uncertainties in the di-Higgs boson production cross section, are included. The intersections of the solid curves and the horizontal dashed lines indicate the 1σ and 2σ confidence-level intervals.

Resonant $HH \to b\bar{b}\gamma\gamma$

- **Different analysis strategy** compared to the early Run 2 analysis
- **single BDT for all resonances, 2 BDTs** to separate signal from **continuum** and from **single Higgs** backgrounds, scores combined in $\mathrm{BDT_{tot}}$

$$\mathrm{BDT_{tot}} = \frac{1}{\sqrt{C_1^2 + C_2^2}} \sqrt{C_1^2 \left(\frac{\mathrm{BDT}_{\gamma\gamma} + 1}{2}\right)^2 + C_2^2 \left(\frac{\mathrm{BDT}_{\mathrm{Single}H} + 1}{2}\right)^2}$$

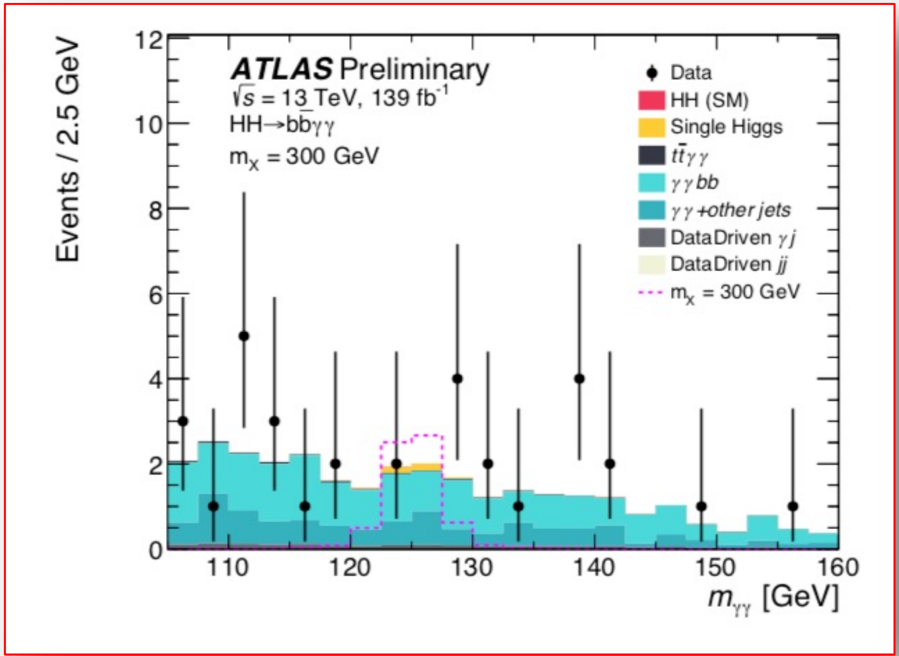

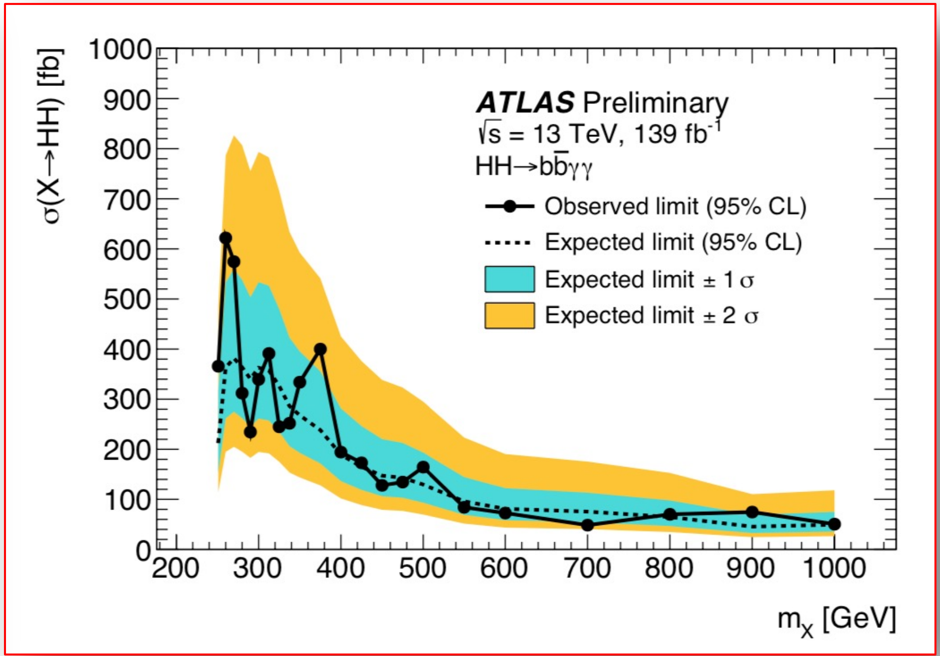

- **~ 30% improvement from BDT strategy, lower mass regime tested**
- 36 fb^{-1} results: Observed (expected) limits between **1.1 pb (0.9 pb) and 0.12 pb (0.15 pb)** in the range **260 GeV < m$_X$ < 1000 GeV**.

Resonant results

No signal is observed, exclusion limits are set via the CLs method with asymptotic approximation

- Observed and expected σ upper limits at 95% CL on the for a narrow width scalar resonance varying between **610–47 fb (360–43 fb)** in **251 GeV ≤ m_X ≤ 1000 GeV**.

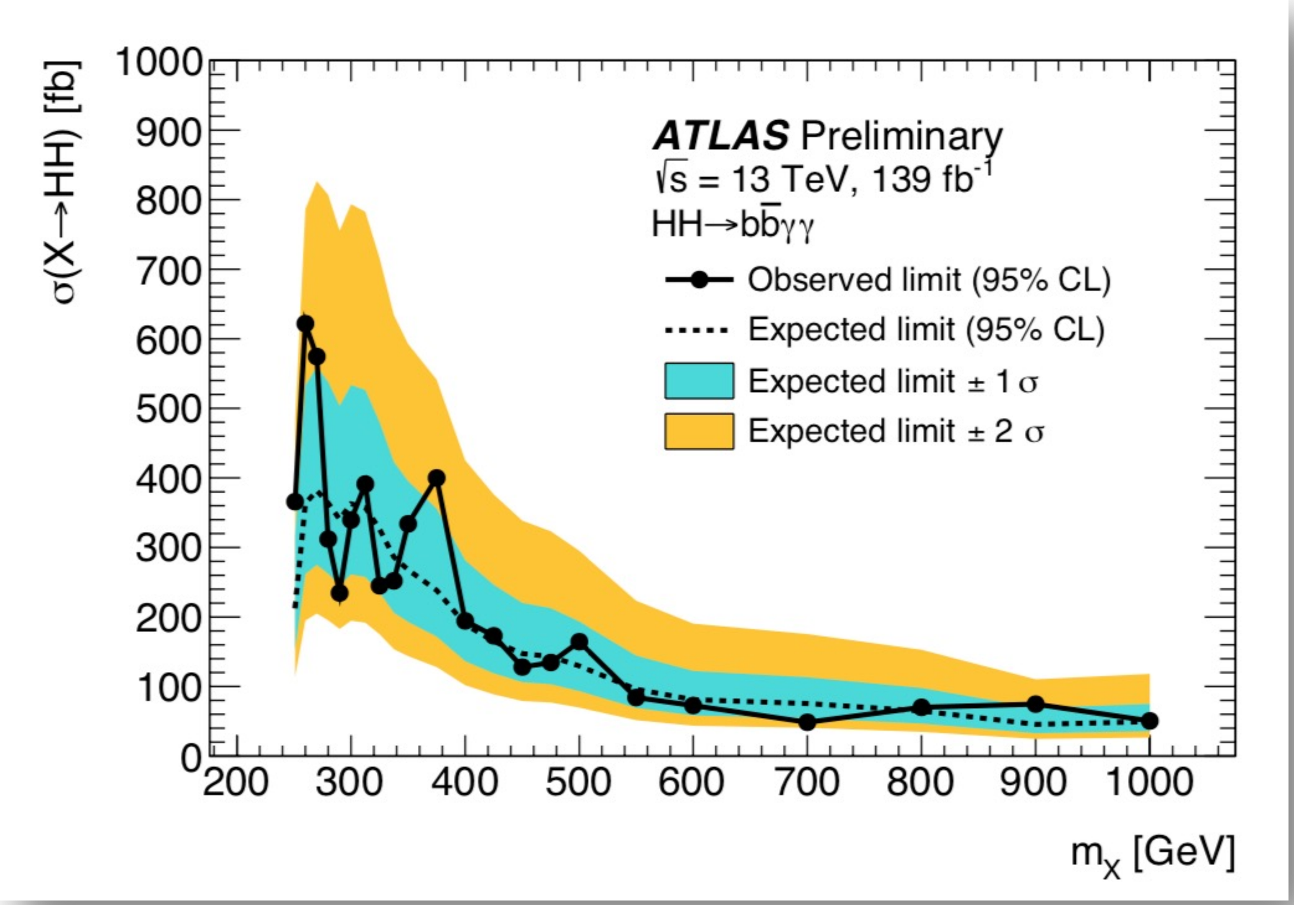

- 36 fb^{-1} results: Observed (expected) limits between **1.1 pb (0.9 pb) and 0.12 pb (0.15 pb)** in the range **260 GeV < m_X < 1000 GeV**.

Systematic Uncertainties

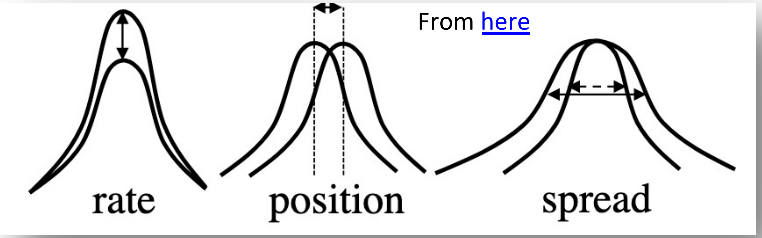

- **Statistically dominated analysis, systematics have a sub-dominant effect**
- Luminosity uncertainty 1.7%
- Continuum background fitted from data, only **spurious signal** uncertainty
- Experimental & theory systematics affect HH non-resonant, HH resonant and Single Higgs

Systematic Uncertainties

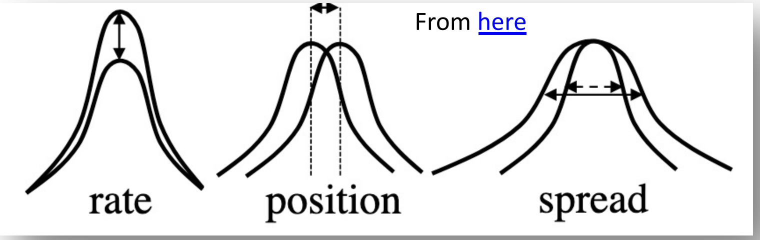

Table 8: Breakdown of the dominant systematic uncertainties. The impact of the uncertainties corresponds to the relative variation of the expected upper limit on the cross section when re-evaluating the profile likelihood ratio after fixing the nuisance parameter in question to its best-fit value, while all remaining nuisance parameters remain free to float. The impact is shown in %. Only systematic uncertainties with an impact of at least 0.2% are shown. Uncertainties of the "Norm. + Shape" type affect both the normalization and the parameters of the functional form. The rest of the uncertainties affect only the yields.

		Relative impact of the systematic uncertainties [%]	
Source	Type	Nonresonant analysis HH	Resonant analysis $m_X = 300$ GeV
Experimental			
Photon energy resolution	Norm. + Shape	0.4	0.6
Jet energy scale and resolution	Normalization	< 0.2	0.3
Flavor tagging	Normalization	< 0.2	0.2
Theoretical			
Factorization and renormalization scale	Normalization	0.3	< 0.2
Parton showering model	Norm. + Shape	0.6	2.6
Heavy-flavor content	Normalization	0.3	< 0.2
$\mathcal{B}(H \to \gamma\gamma, b\bar{b})$	Normalization	0.2	< 0.2
Spurious signal	Normalization	3.0	3.3

k_λ reweighting for ggF samples

Common HH procedure

Truth level *HH* ggF samples with 10 million events are produced for κλ = 0,1,10 and 20 at NLO using Powheg-Box-V2+FT.
A linear combination, described in, of samples with κλ = 0,1 and 20 is used to generate samples with other values of κλ ∈ [-30,30] in increments of 0.2. κλ = 10 used for closure test

Event-level weights in mHH are derived between 20 GeV and 1 TeV

$$w_i = \frac{h^{\kappa_\lambda}_{m_{HH},i}}{h^{SM}_{m_{HH},i}}$$

Due to the variation of the HH cross section depending on the κ_λ, the cross section for the targetted κ_λ sample is calculated at NLO (in fb) following equation 20 as indicated in the LHC Cross Section Working Group twiki (https://twiki.cern.ch/twiki/bin/view/LHCPhysics/LHCHXSWGHH) on October 28th 2020. The full Cross Section × Branching Ratio in pb is then given by equation 21, where $BR(h_1) = BR(h \to \bar{b}b) = 0.5809$ and $BR(h_2) = BR(h \to \gamma\gamma) = 0.002270$ as indicated in the CERN Yellow Report (https://twiki.cern.ch/twiki/bin/view/LHCPhysics/CERNYellowReportPageBR).

$$\sigma_{\kappa_\lambda} = f(\kappa_\lambda) \times \frac{XS(m_{hh} = 125.09)}{XS(m_{hh} = 125)} = 70.3874 - 50.4111 \times \kappa_\lambda + 11.0595 \times \kappa_\lambda^2 \times \frac{31.02}{31.05} \times \frac{31.05}{31.0358} \quad (20)$$

$$\sigma_{\kappa_\lambda} \times BR = f(\kappa_\lambda) \times \frac{XS(m_{hh} = 125.09)}{XS(m_{hh} = 125)} \times 2 \times BR(h_1) \times BR(h_2) \times \frac{1}{1000} \quad (21)$$

$HH \rightarrow b\bar{b}\tau\tau$ analysis (1)

Relatively large BR and **relatively clean final state**

Single Tau Trigger & **Di-Tau** Trigger **for $\tau_{had}\,\tau_{had}$**

Single Lepton Trigger (SLT) and **Lepton+Tau Trigger** (LTT) **in $\tau_{lep}\,\tau_{had}$**

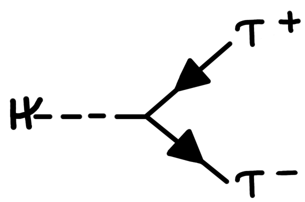

Hadronic & Leptonic

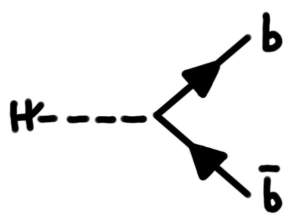

B-jet energy corrections

Object selection

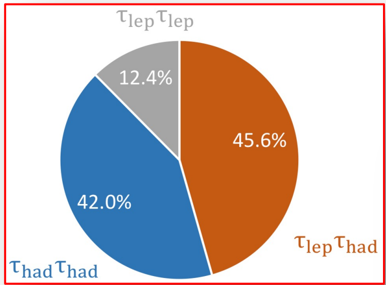

Event categorization

MVA in 3 categories:

$\tau_{had}\,\tau_{had}$ (opp. charged)

$\tau_{lep}\,\tau_{had}$ (e/μ & opp. charged τ) **LTT** **SLT**

Control region for Z+HF (m_{ll})

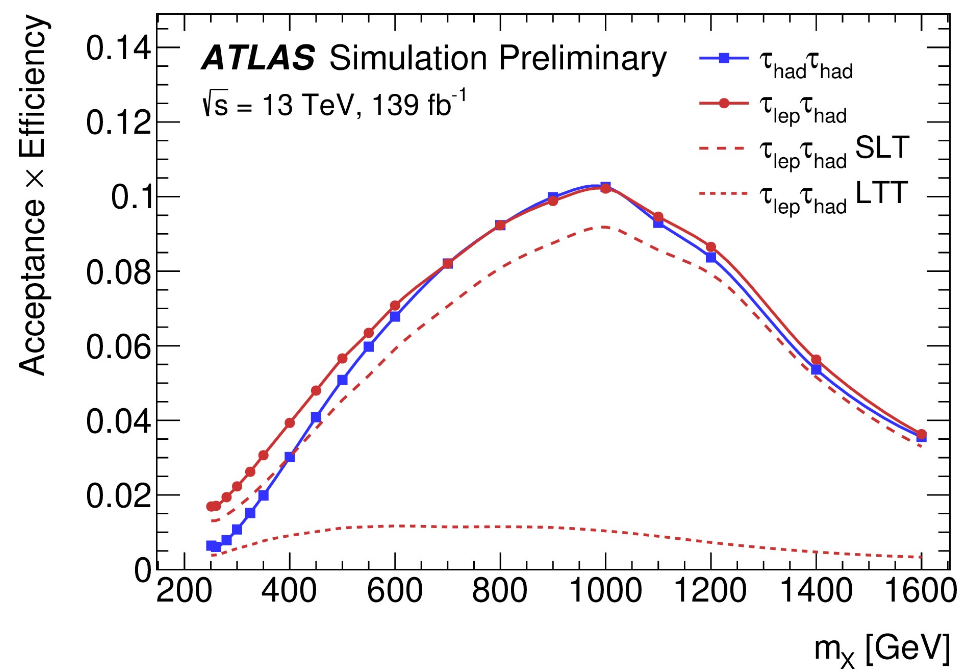

$HH \to b\bar{b}\tau\tau$ analysis (2)

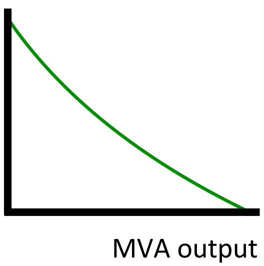

Parametric (by m_X) NNs for resonant

BDT(τ_{had} τ_{had}) & NN(τ_{lep} τ_{had}) for non-resonant

m_{HH}, m_{bb}, $m_{\tau\tau}$, etc.

Multi-variable signal extraction

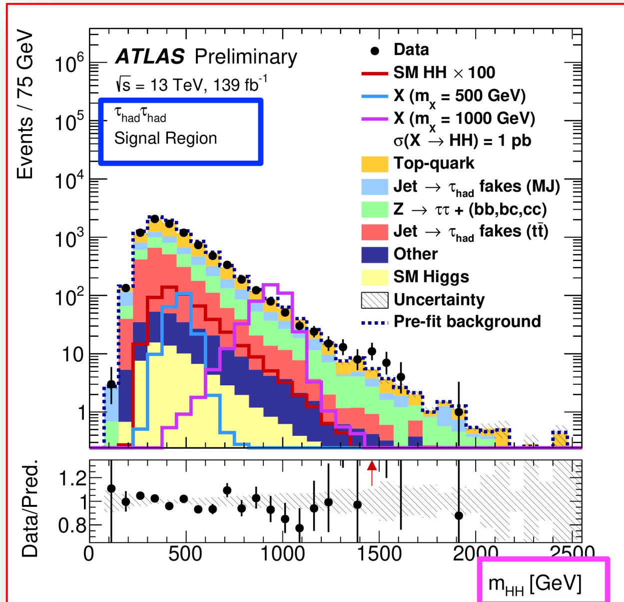

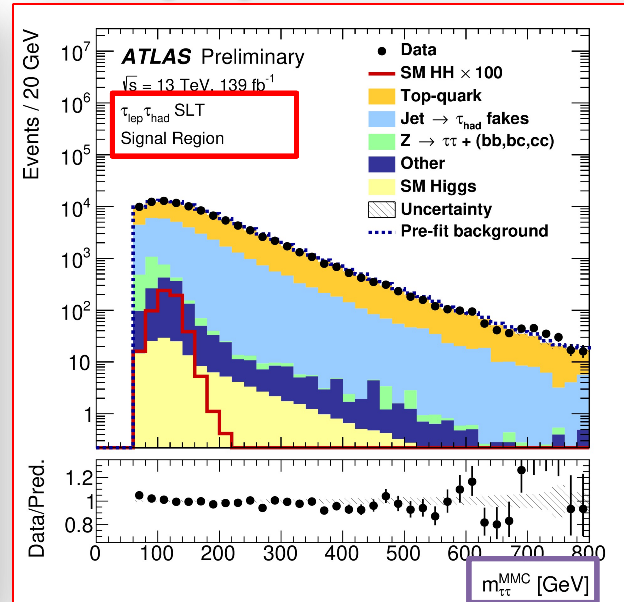

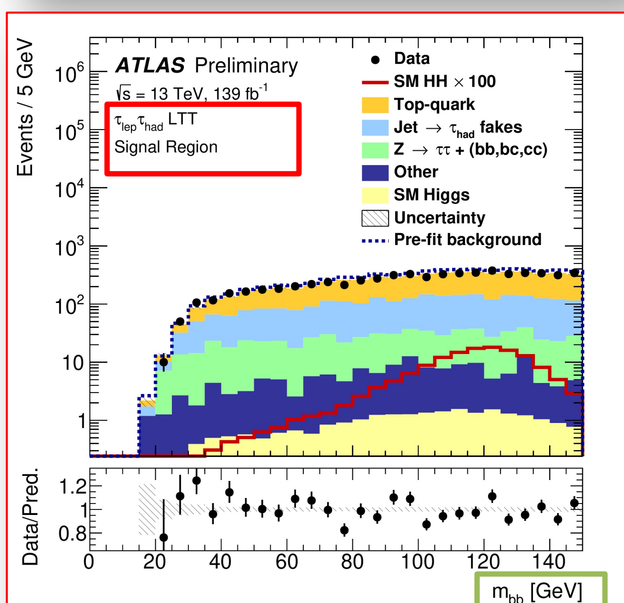

Backgrounds from:

true τ in $t\bar{t}$ and **Z+HF** (from MC, normalization from data)

fake τ in $t\bar{t}$ and **multi-jet** (data-driven)

Non-resonant $HH \to b\bar{b}\tau\tau$ results

Binned maximum-likelihood fit of the MVA score to data (simultaneous in all categories)

Non-resonant analysis thoroughly optimized for SM cross-section limit!

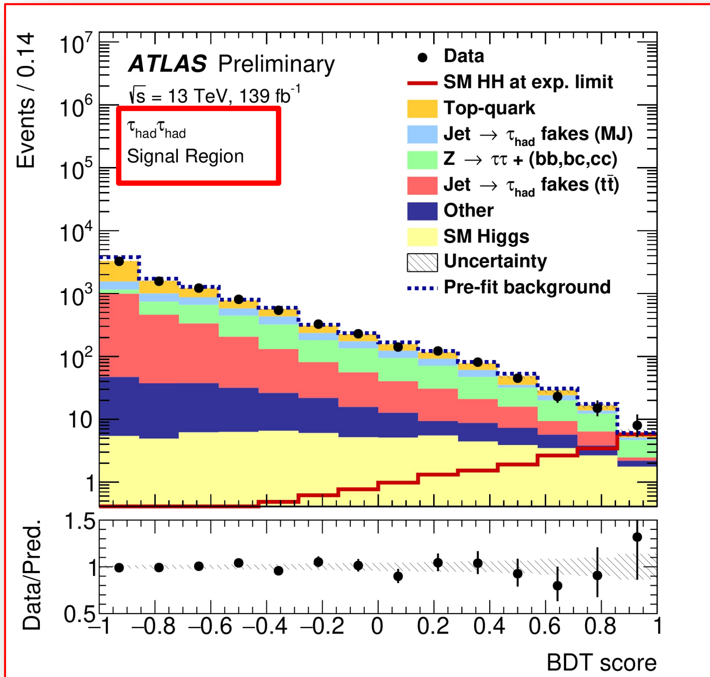

		Observed	$-2\,\sigma$	$-1\,\sigma$	Expected	$+1\,\sigma$	$+2\,\sigma$
$\tau_{\mathrm{had}}\tau_{\mathrm{had}}$	$\sigma_{\mathrm{ggF+VBF}}$ [fb]	145	70.5	94.6	131	183	245
	$\sigma_{\mathrm{ggF+VBF}}/\sigma^{\mathrm{SM}}_{\mathrm{ggF+VBF}}$	4.95	2.38	3.19	4.43	6.17	8.27
$\tau_{\mathrm{lep}}\tau_{\mathrm{had}}$	$\sigma_{\mathrm{ggF+VBF}}$ [fb]	265	124	167	231	322	432
	$\sigma_{\mathrm{ggF+VBF}}/\sigma^{\mathrm{SM}}_{\mathrm{ggF+VBF}}$	9.16	4.22	5.66	7.86	10.9	14.7
Combined	$\sigma_{\mathrm{ggF+VBF}}$ [fb]	135	61.3	82.3	114	159	213
	$\sigma_{\mathrm{ggF+VBF}}/\sigma^{\mathrm{SM}}_{\mathrm{ggF+VBF}}$	4.65	2.08	2.79	3.87	5.39	7.22

4x improvement wrt to previous results! (12.7 x SM),

2x due to the τ and *b*-jet reconstruction and identification improvements and to analysis techniques (MVA & fake-τ estimation methods).

- Statistically dominated, largest systematics from background modeling

$HH \rightarrow b\bar{b}\tau\tau$ analysis (1)

Relatively large BR and **clean final state** (cleaner compared to e.g. 4b)

SingleTau (80<pT<160 GeV)/**DiTau** (35-25 GeV) **triggers for $\tau_{had}\,\tau_{had}$**

SingleLepton (e: 24<E_T<26 GeV, μ: 20<p_T<26 GeV) **/Lepton** (e: E_T>17 GeV, μ: p_T>14 GeV)**+Tau** (μ: p_T>25 GeV) **triggers in $\tau_{lep}\,\tau_{had}$**

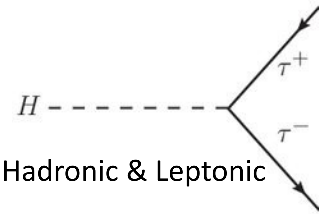

Hadronic & Leptonic

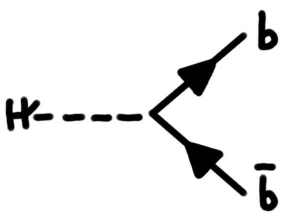

77% btag WP (~1% mistag)
Muon-in-jet+pTReco

Object selection

See extra slides for details on object selection

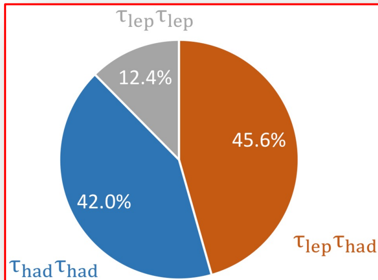

Event categorization

MVA in 3 categories:

$\tau_{had}\,\tau_{had}$ (opp. charged) → High Purity

$\tau_{lep}\,\tau_{had}$ (e/μ & opp. charged τ)

LTT → Low mass sensitivity due to low p_T^l

SLT → High acceptance, large ttbar background

Control region for Z+HF (mll)

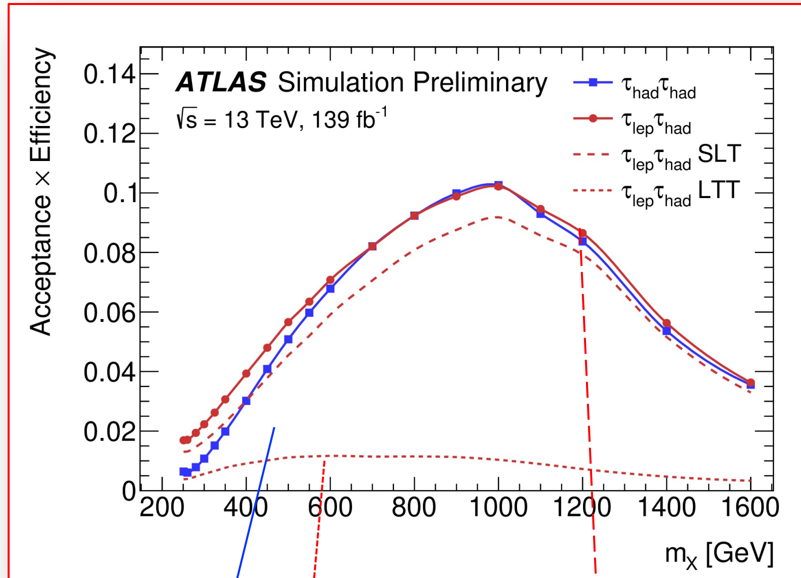

$HH \to b\bar{b}\tau\tau$ analysis (3)

Z+HF & ttbar normalization from mll fit to data

Fake taus:
Fake factor method for $\tau_{lep}\ \tau_{had}$ and $\tau_{had}\ \tau_{had}$ (multi-jet), scale factors for $\tau_{had}\ \tau_{had}$ ttbar

Background modeling

$\tau_{lep}\ \tau_{had}$

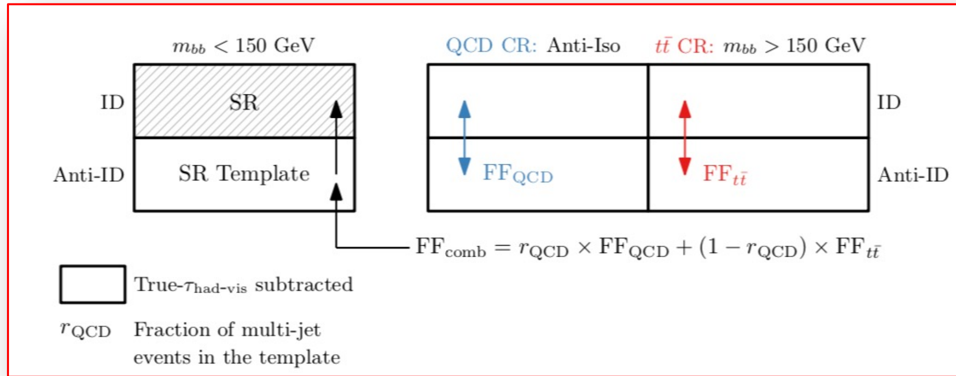

$\tau_{had}\ \tau_{had}$, multi-jet

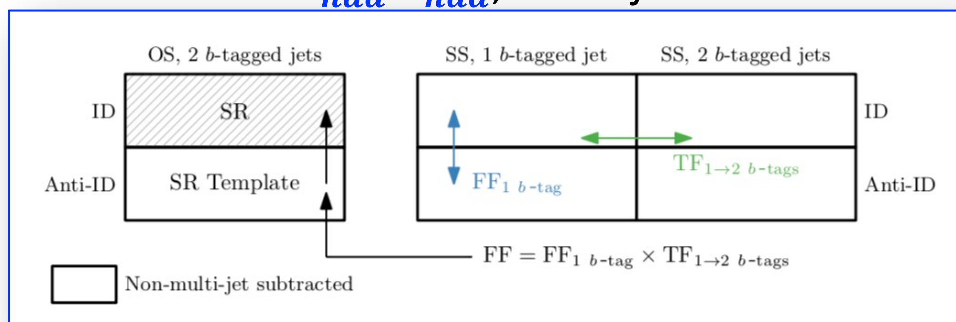

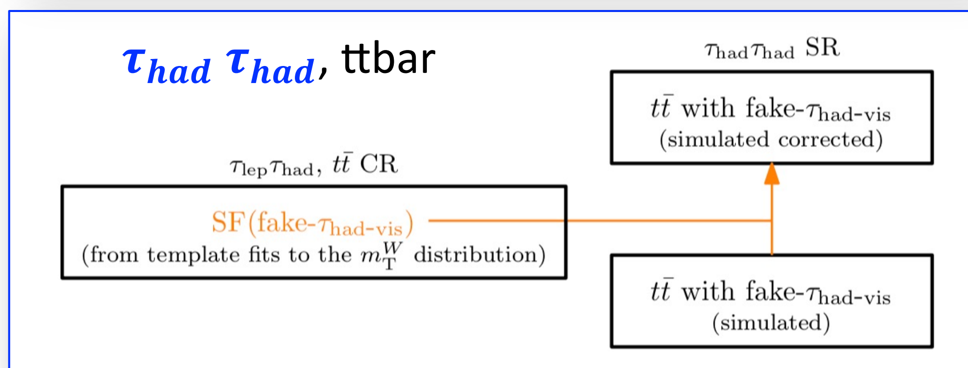

$HH \to b\bar{b}\tau\tau$

Table 1: The generators used for the simulation of the signal and background processes. If not specified, the order of the cross-section calculation refers to the expansion in the strong coupling constant (α_S). The acronyms ME, PS and UE are used for matrix element, parton shower and underlying event, respectively.

The resonant *HH* signal was simulated for 19 values of the resonance mass, m_X, between 251 GeV and 1.6 TeV.

Process	ME generator	ME PDF	PS and hadronisation	UE model tune	Cross section order
Signal					
non-resonant $gg \to HH$ (ggF)	Powheg-Box v2	PDF4LHC15 [73]	Pythia 8.244 [68]	A14	NNLO FTApprox [20]
non-resonant $qq \to qqHH$ (VBF)	MadGraph	NNPDF3.0NLO [74]	Pythia 8.244	A14	N3LO(QCD)
resonant $gg \to X \to HH$	MadGraph	NNPDF2.3LO [70]	Herwig v7.1.3	H7.1-Default	–
Top-quark					
$t\bar{t}$	Powheg-Box v2	NNPDF3.0NLO	Pythia 8.230	A14	NNLO+NNLL [75]
t-channel	Powheg-Box v2	NNPDF3.0NLO	Pythia 8.230	A14	NLO [76]
s-channel	Powheg-Box v2	NNPDF3.0NLO	Pythia 8.230	A14	NLO [77]
Wt	Powheg-Box v2	NNPDF3.0NLO	Pythia 8.230	A14	NLO [78]
$t\bar{t}V$ ($V = W, Z$)	Sherpa 2.2.1	NNPDF3.0NNLO [74]	Sherpa 2.2.1	Default	NLO
Vector boson + jets					
W+jets	Sherpa 2.2.1	NNPDF3.0NNLO	Sherpa 2.2.1	Default	NNLO
Z+jets	Sherpa 2.2.1	NNPDF3.0NNLO	Sherpa 2.2.1	Default	NNLO
Diboson					
WW	Sherpa 2.2.1	NNPDF3.0NNLO	Sherpa 2.2.1	Default	NLO
WZ	Sherpa 2.2.1	NNPDF3.0NNLO	Sherpa 2.2.1	Default	NLO
ZZ	Sherpa 2.2.1	NNPDF3.0NNLO	Sherpa 2.2.1	Default	NLO
Single Higgs boson					
ggF	Powheg-Box v2	NNPDF3.0NLO	Pythia 8.212	AZNLO	N3LO(QCD)+NLO(EW) [79–83]
VBF	Powheg-Box v2	NNPDF3.0NLO	Pythia 8.212	AZNLO	NNLO(QCD)+NLO(EW)
$qq \to WH$	Powheg-Box v2	NNPDF3.0NLO	Pythia 8.212	AZNLO	NNLO(QCD)+NLO(EW) [84–90]
$qq \to ZH$	Powheg-Box v2	NNPDF3.0NLO	Pythia 8.212	AZNLO	NNLO(QCD)+NLO(EW)
$gg \to ZH$	Powheg-Box v2	NNPDF3.0NLO	Pythia 8.212	AZNLO	NLO+NLL
ttH	Powheg-Box v2	NNPDF3.0NLO	Pythia 8.230	A14	NLO

$HH \rightarrow b\bar{b}\tau\tau$ selection

Table 2: Summary of the event selection, shown separately in the different trigger categories. In cases where pairs of reconstructed objects of the same type are required, thresholds on the (sub-)leading p_{T} object are given outside (within) parentheses. When the selection depends on the year of data-taking, the possible values of the requirements are separated by commas, except for the jet selection in the lepton-plus-$\tau_{\text{had-vis}}$ trigger and di-$\tau_{\text{had-vis}}$ triggers which use multiple possible selection criteria, that are described in Section 5.1. The p_{T} trigger thresholds shown correspond to the offline requirements.

$\tau_{\text{had}}\tau_{\text{had}}$ channel		$\tau_{\text{lep}}\tau_{\text{had}}$ channel	
STT	DTT	SLT	LTT
e/μ selection			
No loose e/μ with $p_{\mathrm{T}} > 7$ GeV		Exactly one tight e or medium μ	
		$p_{\mathrm{T}}^{e} > 25, 27$ GeV	18 GeV $< p_{\mathrm{T}}^{e} <$ SLT cut
		$p_{\mathrm{T}}^{\mu} > 21, 27$ GeV	15 GeV $< p_{\mathrm{T}}^{\mu} <$ SLT cut
		$\lvert\eta^{e}\rvert < 2.47$, not $1.37 < \lvert\eta^{e}\rvert < 1.52$	
		$\lvert\eta^{\mu}\rvert < 2.7$	
$\tau_{\text{had-vis}}$ selection			
Two loose $\tau_{\text{had-vis}}$		One loose $\tau_{\text{had-vis}}$	
$\lvert\eta\rvert < 2.5$		$\lvert\eta\rvert < 2.3$	
$p_{\mathrm{T}} > 100, 140, 180$ (25) GeV	$p_{\mathrm{T}} > 40$ (30) GeV	$p_{\mathrm{T}} > 20$ GeV	$p_{\mathrm{T}} > 30$ GeV
Jet selection			
≥ 2 jets with $\lvert\eta\rvert < 2.5$			
$p_{\mathrm{T}} > 45$ (20) GeV	Trigger dependent	$p_{\mathrm{T}} > 45$ (20) GeV	Trigger dependent
Event-level selection			
Trigger requirements passed			
Collision vertex reconstructed			
$m_{\tau\tau}^{\mathrm{MMC}} > 60$ GeV			
Opposite-sign electric charges of $e/\mu/\tau_{\text{had-vis}}$ and $\tau_{\text{had-vis}}$			
Exactly two b-tagged jets			
		$m_{bb} < 150$ GeV	

- LepHad: largely dominated by $t\bar{t}$
  - Preselection signal efficiency: ~ 5%
- HadHad: significant contributions from $t\bar{t}$ (+ fakes) , Z + jets, QCD fakes
  - Pre-selection signal efficiency: ~ 4%

$HH \to b\bar{b}\tau\tau$ MVA

Table 3: Variables used as inputs to the MVAs in the three analysis categories. The same choice of input variables is used for the resonant and non-resonant production modes. The variables are defined in the main text.

Variable	$\tau_{\text{had}}\tau_{\text{had}}$	$\tau_{\text{lep}}\tau_{\text{had}}$ SLT	$\tau_{\text{lep}}\tau_{\text{had}}$ LTT
m_{HH}	✓	✓	✓
$m_{\tau\tau}^{\text{MMC}}$	✓	✓	✓
m_{bb}	✓	✓	✓
$\Delta R(\tau,\tau)$	✓	✓	✓
$\Delta R(b,b)$	✓	✓	
$\Delta p_{\text{T}}(\ell,\tau)$		✓	✓
Sub-leading b-tagged jet p_{T}		✓	
m_{T}^{W}		✓	
$E_{\text{T}}^{\text{miss}}$		✓	
$E_{\text{T}}^{\text{miss}}$ ϕ centrality		✓	
$\Delta\phi(\tau\tau, bb)$		✓	
$\Delta\phi(\ell, E_{\text{T}}^{\text{miss}})$			✓
$\Delta\phi(\ell\tau, E_{\text{T}}^{\text{miss}})$			✓
S_{T}			✓

$HH \to b\bar{b}\tau\tau$ background

$\tau_{lep}\ \tau_{had}$

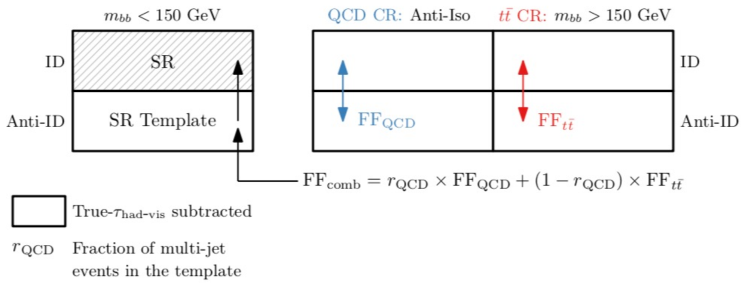

Figure 4: Schematic depiction of the combined fake-factor method used to estimate multi-jet and $t\bar{t}$ background with fake-$\tau_{\text{had-vis}}$ in the $\tau_{\text{lep}}\tau_{\text{had}}$ channel. Backgrounds which are not from events with fake-$\tau_{\text{had-vis}}$ originating from jets are subtracted from data in all control regions. Events in which an electron or a muon is misidentified as a $\tau_{\text{had-vis}}$ are also subtracted, but their contribution is very small. Both sources are indicated by "True-$\tau_{\text{had-vis}}$ subtracted" in the legend.

$\tau_{had}\ \tau_{had}$

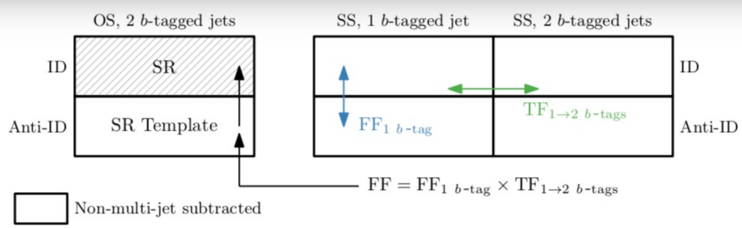

Figure 5: Schematic depiction of the combined fake-factor method to estimate multi-jet background with fake-$\tau_{\text{had-vis}}$ in the $\tau_{\text{had}}\tau_{\text{had}}$ channel. Backgrounds with true-$\tau_{\text{had-vis}}$ which are not from multi-jet events are simulated and subtracted from data in all the control regions. This is indicated by "Non-multi-jet subtracted" in the legend.

$\tau_{had}\ \tau_{had}$

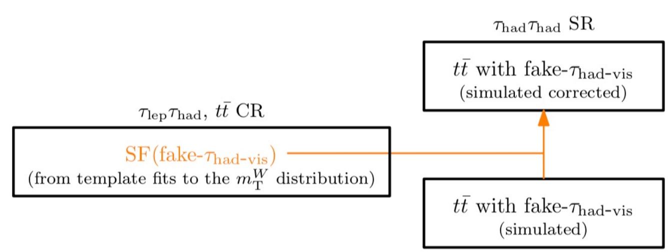

Figure 6: Schematic depiction of the fake-$\tau_{\text{had-vis}}$ scale-factor method to estimate $t\bar{t}$ background with fake-$\tau_{\text{had-vis}}$ in the $\tau_{\text{had}}\tau_{\text{had}}$ channel.

$HH \to b\bar{b}\tau\tau$

- Systematic uncertainties

Table 4: Breakdown of the relative contributions to the uncertainty in the extracted signal yield divided by the MC prediction, as determined in the likelihood fit to data. These are obtained from fixing the relevant nuisance parameters in the likelihood fit, and subtracting the obtained uncertainty on the fitted signal yield divided by the MC prediction in quadrature from the total uncertainty, and then dividing the result by the total uncertainty. The sum in quadrature of the individual components differs from the total uncertainty due to correlations between the groups of uncertainties.

Uncertainty source	Non-resonant HH	Resonant $X \to HH$		
		300 GeV	500 GeV	1000 GeV
Data statistical	83%	75%	89%	88%
Systematic	56%	66%	45%	48%
Experimental				
Jet and $E_{\mathrm{T}}^{\mathrm{miss}}$	7%	28%	5%	4%
b-jet tagging	3%	6%	3%	3%
$\tau_{\text{had-vis}}$	6%	13%	3%	7%
Electrons and muons	3%	3%	2%	1%
Luminosity & Pileup	3%	2%	2%	5%
$t\bar{t}$ and Z + HF normalisations	6%	11%	5%	3%
Theoretical and Modelling				
Fake-$\tau_{\text{had-vis}}$	10%	22%	7%	7%
Top-quark	25%	21%	13%	8%
$Z(\to \tau\tau)$ + HF	10%	22%	10%	15%
Single Higgs boson	30%	2%	15%	14%
Other background	3%	2%	6%	2%
Signal modelling	7%	15%	13%	34%
MC statistical	29%	44%	33%	18%

Resonant $HH \rightarrow b\bar{b}\tau\tau$ results

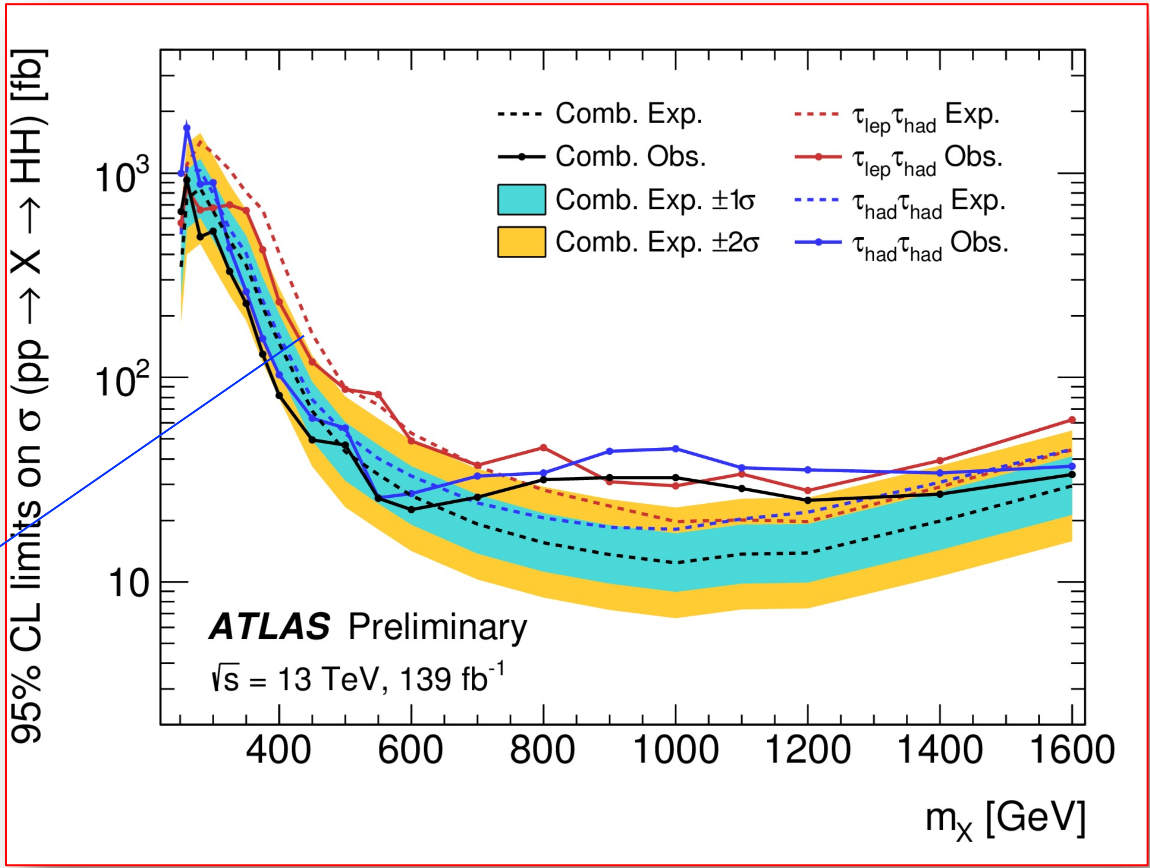

$\tau_{had}\,\tau_{had}$
Better sensitivity below 1 TeV

Statistically dominated, largest sys from signal and background modeling

- Broad excess @ 700 GeV < *m*X < 1.2 TeV.
- Most significant excess for $\tau_{had}\,\tau_{had}$ ($\tau_{lep}\,\tau_{had}$) found @ 1 TeV (1.1 TeV), local significance of 2.8 σ (1.6 σ).
- Combined: @1 TeV, local significance 3.1 σ, global significance of $2.1^{+0.4}_{-0.2}$ σ.
- Deficit @ 280 GeV with a local significance of 2.4 σ.

$HH \to b\bar{b}b\bar{b}$ analysis (1)

Largest BR, but **large multi-jet backgrounds** and challenging combinatorics

Only ggF **resonant** production considered

12 different b-jet & jet triggers for *resolved* (eff up to 80%), single jet trigger for *boosted* (eff ~80%)

Resolved
(251 GeV – 1.5 TeV)
4 b-tagged ΔR=0.4 jets

& Boosted
(900 GeV – 3 TeV)
b-tagged ΔR=1.0 and VR track-jets

Combined in the overlap region

77% btag WP
muon-in-jet+p_T-reco

Object selection

Event categorization

Resolved:
4b signal region (2b category for bkg estimate)

BDT to pair jets from Higgs
(65-100% eff)

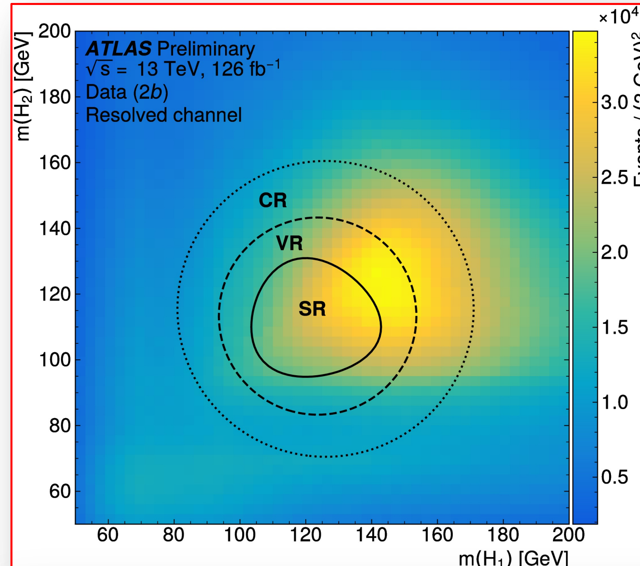

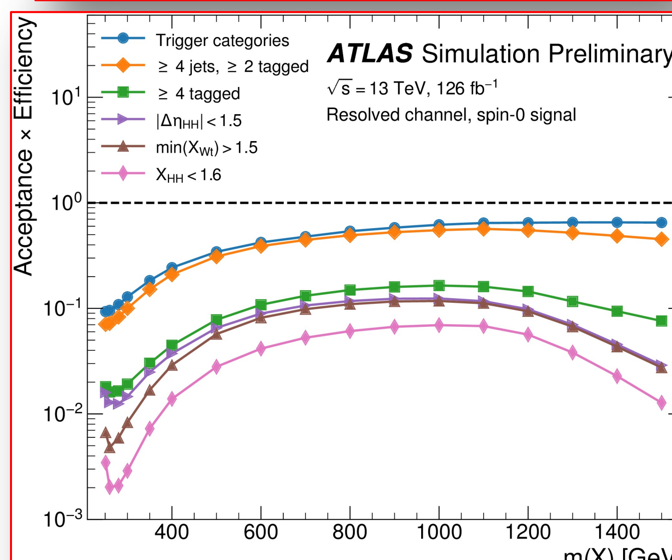

$HH \to b\bar{b}b\bar{b}$ analysis (2)

Largest BR, but **large multi-jet backgrounds** and challenging combinatorics

Only ggF **resonant** production considered

12 different b-jet & jet triggers for *resolved* (eff up to 80%), single jet trigger for *boosted* (eff ~80%)

Resolved
(251 GeV – 1.5 TeV)
4 b-tagged ΔR=0.4 jets

& Boosted
(900 GeV – 3 TeV)
b-tagged ΔR=1.0 and VR track-jets

Combined in the overlap region

77% btag WP
muon-in-jet+p_T-reco

Object selection

Event categorization

Resolved:
4b signal region (2b category for bkg estimate)

BDT to pair jets from Higgs (65-100% eff)

Resolved:
Bkg dominated by multi-jet + ~5% ttbar

Use 2-tag data (and apply NN-based kinematic reweighting) to derive an extrapolation from the CR into the SR.

Background modeling

Statistical analysis

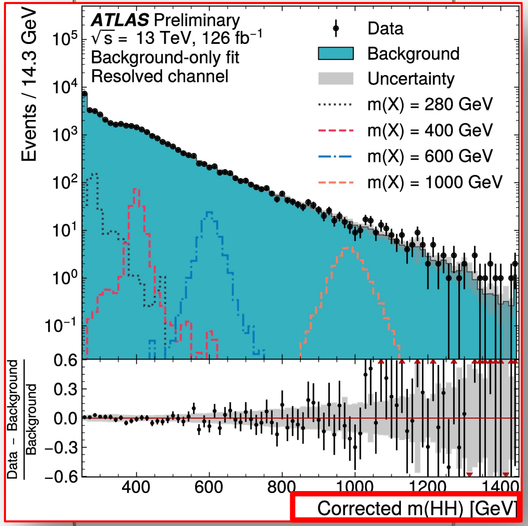

$HH \rightarrow b\bar{b}b\bar{b}$ analysis (3)

Largest BR, but **large multi-jet backgrounds** and challenging combinatorics

Only ggF **resonant** production considered

12 different b-jet & jet triggers for *resolved* (eff up to 80%), single jet trigger for *boosted* (eff ~80%)

Resolved
(251 GeV – 1.5 TeV)
4 b-tagged ΔR=0.4 jets

& Boosted
(900 GeV – 3 TeV)
b-tagged ΔR=1.0 and VR track-jets

Combined in the overlap region

77% btag WP
muon-in-jet+p_T-reco

Object selection

Event categorization

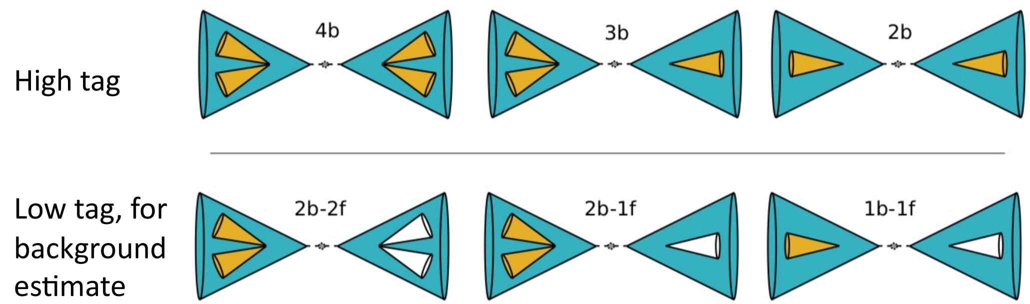

Boosted:
3 signal-enriched categories
4b, 3b, 2b

(b-tag inefficient at high p_T)

Events sorted in CR, VR & SR like in the *resolved* case

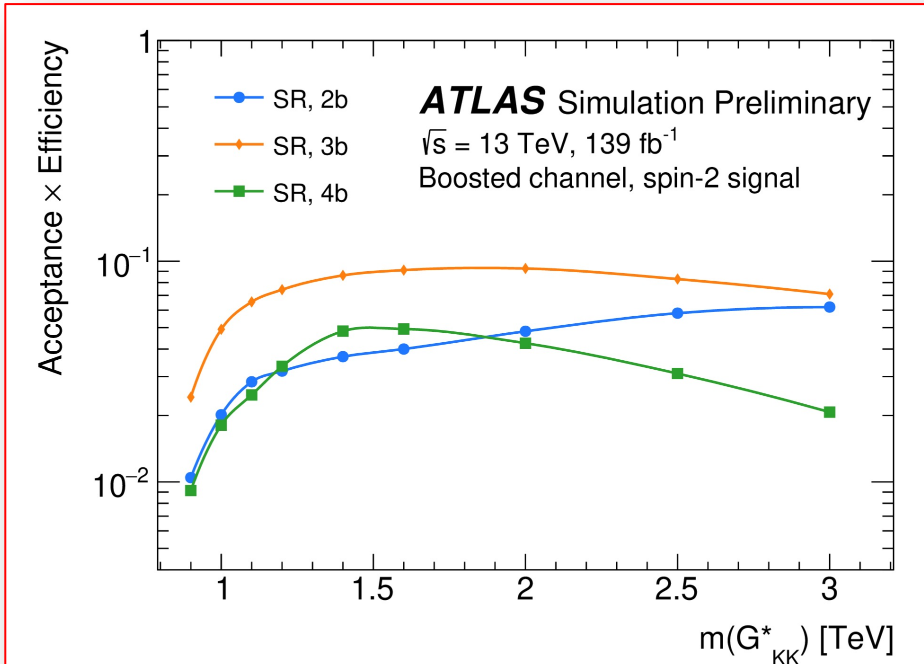

$HH \to b\bar{b}b\bar{b}$ analysis (4)

Largest BR, but **large multi-jet backgrounds** and challenging combinatorics

Only ggF **resonant** production considered

12 different b-jet & jet triggers for *resolved* (eff up to 80%), single jet trigger for *boosted* (eff ~80%)

Resolved (251 GeV – 1.5 TeV)

4 b-tagged ΔR=0.4 jets

& Boosted (900 GeV – 3 TeV)

b-tagged ΔR=1.0 and VR track-jets

Combined in the overlap region

77% btag WP

muon-in-jet+p_T-reco

Object selection

Event categorization

Boosted:

3 signal-enriched categories

4b, 3b, 2b

(b-tag inefficient at high p_T)

Events sorted in CR, VR & SR like in the *resolved* case

Boosted:

Bkg dominated by multi-jet + ~10/15/30% ttbar in the 4/3/2b regions

Data-driven MJ & MC-driven ttbar (data-driven corrections in 2/3 b)

Same reweighting approach as in the [36fb[-1] analysis]()

Background modeling

$$N^{n_b}_{i,\mathrm{data}} = \mu^{n_b}_{\mathrm{MJ}}(N^{n_b-1f}_{i,\mathrm{data}} - N^{n_b-1f}_{i,t\bar{t}}) + \alpha^{n_b}_{t\bar{t}} N^{n_b}_{i,t\bar{t}}.$$

Statistical Analysis (3 categories)

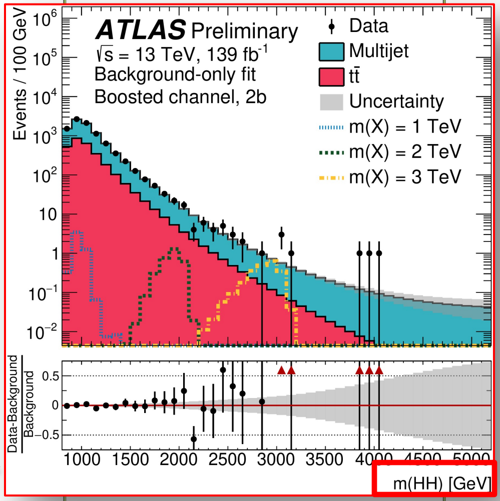

$HH \rightarrow b\bar{b}b\bar{b}$ analysis resolved

$$R_{HH}^{\mathrm{VR}} \equiv \sqrt{\left(m(H_1) - 1.03 \times 120\,\mathrm{GeV}\right)^2 + \left(m(H_2) - 1.03 \times 110\,\mathrm{GeV}\right)^2} < 30\,\mathrm{GeV}.$$

Finally, the *control region* (CR) contains the events not in the SR or VR which satisfy the condition

$$R_{HH}^{\mathrm{CR}} \equiv \sqrt{\left(m(H_1) - 1.05 \times 120\,\mathrm{GeV}\right)^2 + \left(m(H_2) - 1.05 \times 110\,\mathrm{GeV}\right)^2} < 45\,\mathrm{GeV}.$$

The centers of the VR and CR are shifted with respect to the SR to ensure that the mean H candidate masses are equal in the three regions. The shapes of these regions in the $m(H_1)$–$m(H_2)$ plane are shown with the $2b$ data in Figure 2.

After the full selection, the final discriminating variable "corrected $m(HH)$" is constructed. This is obtained by rescaling the four-momenta of the H candidates such that $m(H_1) = m(H_2) = 125\,\mathrm{GeV}$. The corrected $m(HH)$ is then the invariant mass of the sum of the two resulting four-momenta. This procedure improves the scale and resolution of the reconstructed signal mass distribution by correcting for detector effects and physical processes such as radiative emission outside the jet cones. This correction improves the signal mass resolution by up to 25% and shifts the mean of the mass distribution closer to the true value, but has a negligible effect on the background. The signal efficiency times acceptance for the various event selection steps is shown in Figure 3. The efficiency at low resonance masses is mainly limited by the trigger. At high resonance masses the jets start to merge together and the reconstruction and b-tagging efficiencies decrease. The efficiency is substantially larger for the spin-2 model than for the spin-0 model because the corrected $m(HH)$ distribution of the spin-2 model is much broader, particularly on the high-mass side.

$HH \to b\bar{b}b\bar{b}$ analysis resolved: kinematic reweighting

$$w(\vec{x}) = \frac{p_{4b}(\vec{x})}{p_{2b}(\vec{x})},$$

where $p_{2b}(x)$ and $p_{4b}(x)$ are the probability density functions for 2*b* and 4*b* data, respectively, over a set of kinematic variables *x*.

The computation of $w(\vec{x})$ is a density ratio estimation problem, for which a variety of approaches exist. The method employed in this analysis is modified from Refs. [77, 78] and makes use of an artificial neural network (NN). This NN is trained on 2b and 4b CR data to minimize the loss function:

$$\mathcal{L}(w(\vec{x})) = \int d\vec{x} \left[\sqrt{w(\vec{x})}p_{2b}(\vec{x}) + \frac{1}{\sqrt{w(\vec{x})}}p_{4b}(\vec{x}) \right]. \quad (6)$$

$HH \to b\bar{b}b\bar{b}$ analysis resolved: kinematic reweighting

The kinematic variables used to make up *x* are chosen to be sensitive to the differences between the 2*b* and 4*b*

1. $\log(p_{\mathrm{T}})$ of the selected jet with the 2^{nd}-highest p_{T},
2. $\log(p_{\mathrm{T}})$ of the selected jet with the 4^{th}-highest p_{T},
3. $\log(\Delta R)$ between the two selected jets with the smallest ΔR,
4. $\log(\Delta R)$ between the other two selected jets,
5. the average $|\eta|$ of selected jets,
6. $\log(p_{\mathrm{T}})$ of the HH system,
7. ΔR between the two H candidates,
8. $\Delta\phi$ between the jets making up H_1,
9. $\Delta\phi$ between the jets making up H_2,
10. $\log(\min(X_{Wt}))$, and
11. the number of jets in the event with $p_{\mathrm{T}} > 40\,\mathrm{GeV}$ and $|\eta| < 2.5$, including jets that are not selected.

There are two main sources of uncertainties: uncertainties from finite statistics in the CR, and physical differences between the CR and SR.

$HH \to b\bar{b}b\bar{b}$ analysis

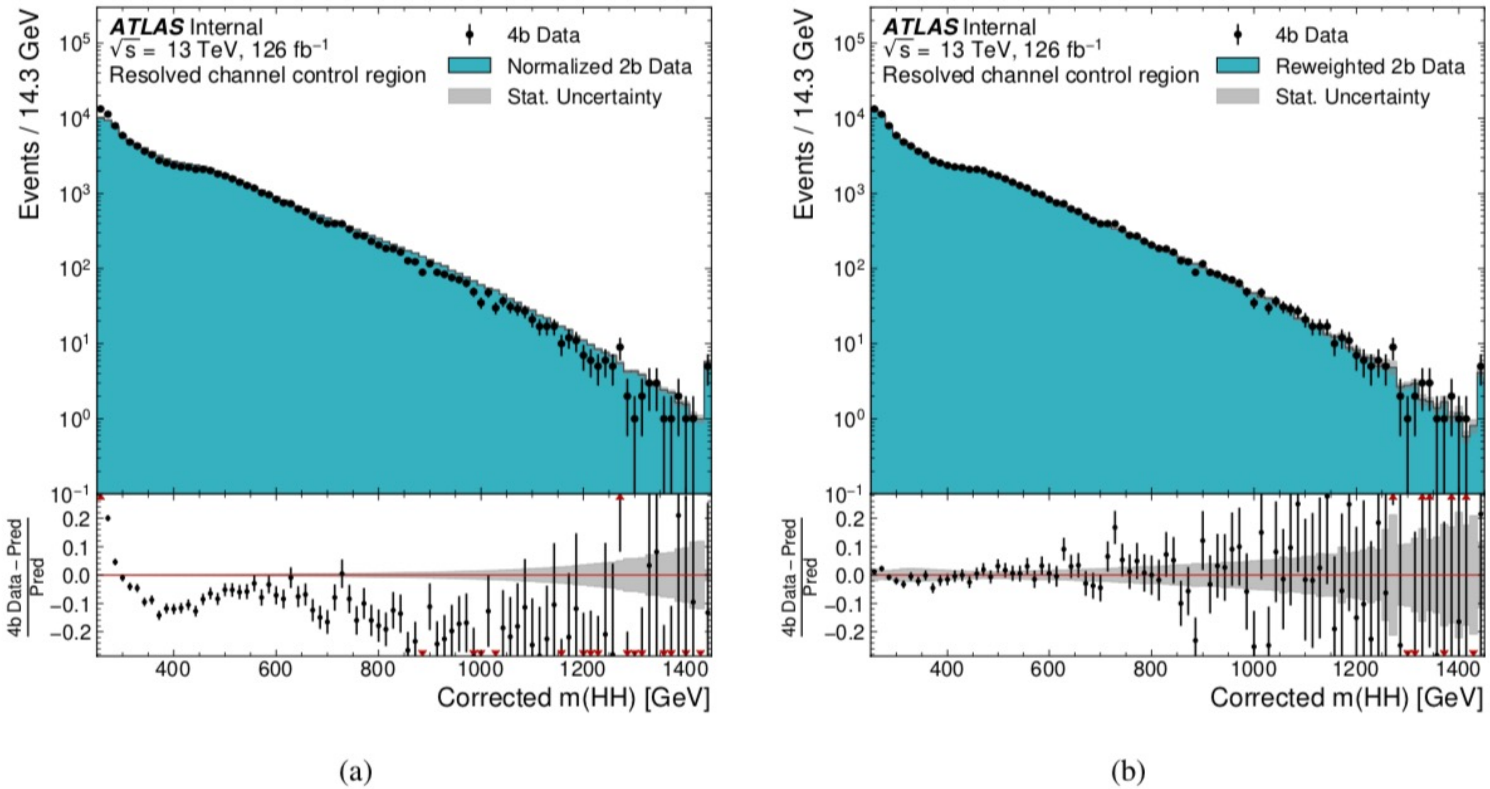

Figure 4: Corrected $m(HH)$ distributions for the $2b$ control region (teal histogram) and $4b$ control region (dots) in the resolved channel. The statistical uncertainty in the $2b$ control region is represented by the grey band. The error bars on the $4b$ points represent the Poisson uncertainties corresponding to their event yields. The $2b$ data are shown (a) before and (b) after the kinematic reweighting procedure. In both cases the $2b$ distributions are normalized to the $4b$ event yields for a pure shape comparison. The final bin of each distribution includes overflow. The bottom panel shows the difference between the $4b$ and $2b$ distributions, normalized to the $4b$ distribution.

$HH \rightarrow b\bar{b}b\bar{b}$ analysis

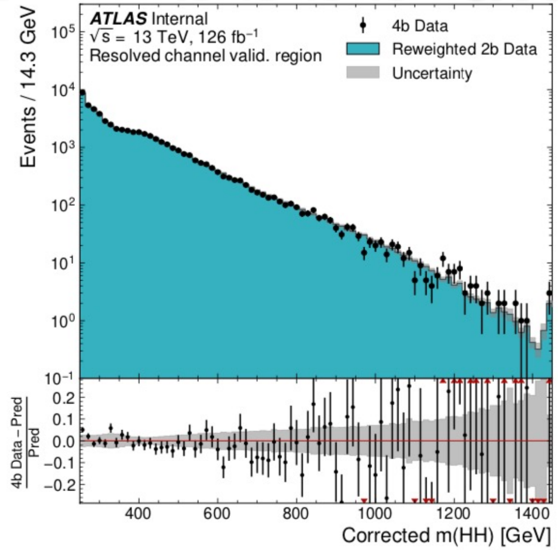

Table 1: Resolved $4b$ signal region data, estimated background, and signal event yields in corrected $m(HH)$ windows containing roughly 90% of each signal, for representative spin-0 mass hypotheses. The signal is normalized to the overall expected limit on its cross-section; its uncertainties are evaluated by adding all individual components in quadrature and are treated as correlated across corrected $m(HH)$ bins. The background yields and uncertainties are evaluated after a background-only fit to the data.

$m(X)$ [GeV]	Corrected $m(HH)$ range [GeV]	Data	Background model	Spin-0 signal model
260	[250, 321)	18 554	18 300 ± 110	503 ± 43
500	[464, 536)	2 827	2 866 ± 22	105.4 ± 5.7
800	[750, 850)	358	366.2 ± 7.3	37.7 ± 1.7
1200	[1079, 1250)	68	52.6 ± 1.7	11.71 ± 0.62

Table 2: Resolved $4b$ signal region data, estimated background, and signal event yields in corrected $m(HH)$ windows containing roughly 90% of each signal, for representative spin-2 mass hypotheses. The signal is normalized to the overall expected limit on its cross-section; its uncertainties are evaluated by adding all individual components in quadrature and are treated as correlated across corrected $m(HH)$ bins. The background yields and uncertainties are evaluated after a background-only fit to the data.

$m(G^*_{\mathrm{KK}})$ [GeV]	Corrected $m(HH)$ range [GeV]	Data	Background model	Spin-2 signal model
260	[250, 393)	26 775	26 650 ± 130	368 ± 25
500	[464, 636)	4 655	4 719 ± 37	138.6 ± 5.7
800	[707, 950)	795	811 ± 13	52.1 ± 1.9
1200	[993, 1279)	146	120.6 ± 2.8	14.45 ± 0.67

$HH \to b\bar{b}b\bar{b}$ analysis boosted

background distribution. The VR contains the events not in the SR which satisfy the condition

$$R_{HH}^{\mathrm{VR}} \equiv \sqrt{\left(m(H_1) - 124\,\mathrm{GeV}\right)^2 + \left(m(H_2) - 115\,\mathrm{GeV}\right)^2} < 33\,\mathrm{GeV}. \tag{9}$$

Finally, the CR contains the events not in the SR or VR which satisfy the condition

$$R_{HH}^{\mathrm{CR}} \equiv \sqrt{\left(m(H_1) - 134\,\mathrm{GeV}\right)^2 + \left(m(H_2) - 125\,\mathrm{GeV}\right)^2} < 58\,\mathrm{GeV}. \tag{10}$$

The CR is shifted to higher masses relative to the signal and validation regions in order to maximize statistics while avoiding the low-mass peak of the multijet background distribution. The definition of these regions in the $m(H_1) - m(H_2)$ plane are shown with the $2b$-$1f$ data in Figure 8.

In order to ensure orthogonality between the resolved and boosted channels, any events passing the resolved signal region selection are vetoed from the boosted channel. This priority choice results in the best signal sensitivity.

$HH \to b\bar{b}b\bar{b}$ analysis boosted

The sizes of the multijet and $t\bar{t}$ estimates are obtained from a normalization fit to the CR data in each category. Two normalization parameters μ_{MJ} and $\alpha_{t\bar{t}}$ per b-tagging category are introduced as follows:

$$N^{n_b}_{i,\mathrm{data}} = \mu^{n_b}_{\mathrm{MJ}}(N^{n_b-1f}_{i,\mathrm{data}} - N^{n_b-1f}_{i,t\bar{t}}) + \alpha^{n_b}_{t\bar{t}} N^{n_b}_{i,t\bar{t}}. \tag{11}$$

Table 3: Best-fit values for μ_{MJ} and $\alpha_{t\bar{t}}$, with statistical uncertainties on the parameters. The linear correlation coefficient between both parameters is also given. The value of $\alpha_{t\bar{t}}$ in the $4b$ region is fixed to 1, since the data are unable to constrain it significantly.

Region	$2b$	$3b$	$4b$
μ_{MJ}	0.05428 ± 0.00057	0.1201 ± 0.0024	0.0269 ± 0.0015
$\alpha_{t\bar{t}}$	0.827 ± 0.011	0.771 ± 0.041	1
Correlation	-0.74	-0.74	0

For $3b$ and $2b$, a kinematic reweighting procedure is applied to each corresponding low-tag category, analogous to the resolved channel. For the $4b$ category, no kinematic reweighting is applied. This is because the effect of mismodelings due to b-tagging is small compared to the size of statistical uncertainties in this category. Instead of an NN for constructing the reweighting function, an iterative spline method based on the one used in Ref. [8] is implemented here.

$HH \to b\bar{b}b\bar{b}$ analysis boosted

The difference between these low-tag and high-tag regions is that the low-tag events have an untagged H candidate (0 b-tagged track jets), while high-tag events instead have a tagged H candidate (exactly 1 b-tagged track jet, since only the $3b$ and $2b$ categories are considered here). Therefore, the reweighting is applied to low-tag events based on their untagged H candidates, with the aim to match the kinematics of the tagged H candidates in high-tag events. This reweighting is derived purely in the low-tag regions; the tagged H candidates in the $1b$-$1f$ category are used to define the target.

The following kinematic distributions are used to construct the reweighting, for which leading and subleading refer to an ordering in p_{T}:

1. p_{T} of the H candidate,
2. p_{T} of the chosen track jet,
3. η of the chosen track jet, and
4. ΔR between the leading and subleading track jets (for H candidates with at least two track jets).

$HH \rightarrow b\bar{b}b\bar{b}$ analysis boosted

The "chosen" track jet is the b-tagged one for tagged H candidates and a random one for untagged H candidates. In tagged H candidates with two track jets, the leading and subleading track jets have roughly equal probabilities to be the b-tagged one, so this random selection does not introduce significant bias. Separate distributions are constructed for leading and subleading H candidates, as well as for leading and subleading track jets.

At each iteration i, cubic splines are fit to the ratios of tagged to untagged distributions, and the weights are updated according to

$$w_i(\vec{x}) = w_{i-1}(\vec{x}) \times \left[\left(\prod_j f_{ij}(x_j) - 1\right) \times r_i + 1\right], \tag{12}$$

$HH \rightarrow b\bar{b}b\bar{b}$ analysis systematics

Table 6: Impacts of the main systematic uncertainties on the expected 95% CL upper limits on the signal cross-section times branching ratio. These are defined as the relative decrease in the expected limit when each relevant nuisance parameter is held fixed to its best-fit value instead of being assigned an uncertainty. The spin-0 signal model is used here.

Uncertainty category	Relative impact (%)		
	280 GeV	600 GeV	1600 GeV
Background $m(HH)$ shape	12	8.7	1.3
Jet momentum/mass scale	0.6	0.1	1.5
Jet momentum/mass resolution	2.1	1.5	7.4
b-tagging calibration	0.7	0.4	1.8
Theory (signal)	0.6	0.6	1.6
Theory ($t\bar{t}$ background)	N/A	N/A	0.7
All systematic uncertainties	16	11	13

$HH \rightarrow b\bar{b}b\bar{b}$ analysis

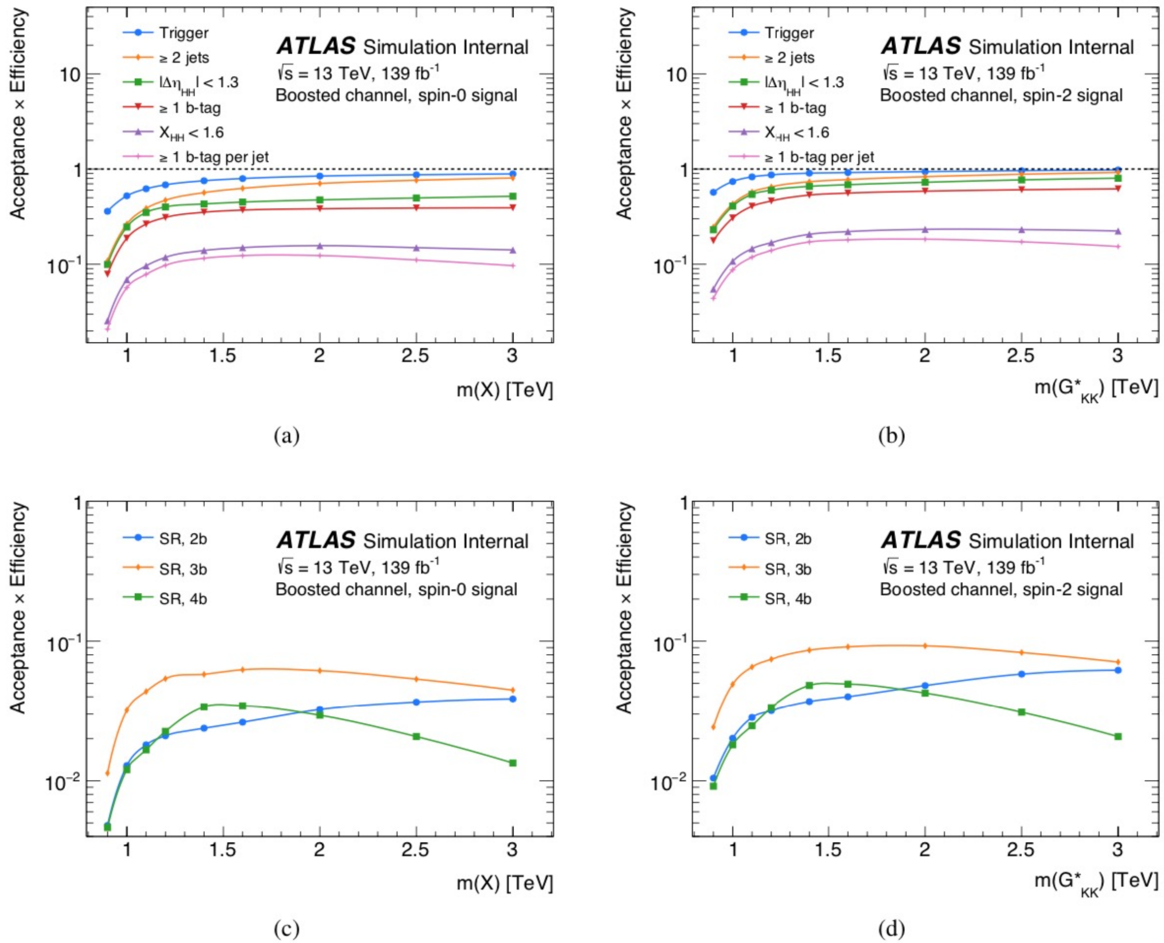

Figure 9: Cumulative signal acceptance times efficiency as a function of the resonance mass for various selection steps in the boosted channel. The steps up to the b-tag categorization are shown for (a) the spin-0 and (b) the spin-2 signal models. The efficiencies of the three b-tag categories are shown for (c) the spin-0 and (d) the spin-2 scenarios; this efficiency is obtained after the other selection steps including the SR definition. The signal efficiency in the 4b region has a maximum around 1.5 TeV. Above that value the track jets starts to merge together, and for the highest resonance masses the 2b category becomes the most efficient.

VBF 4b

https://link.springer.com/article/10.1007/JHEP07(2020)108

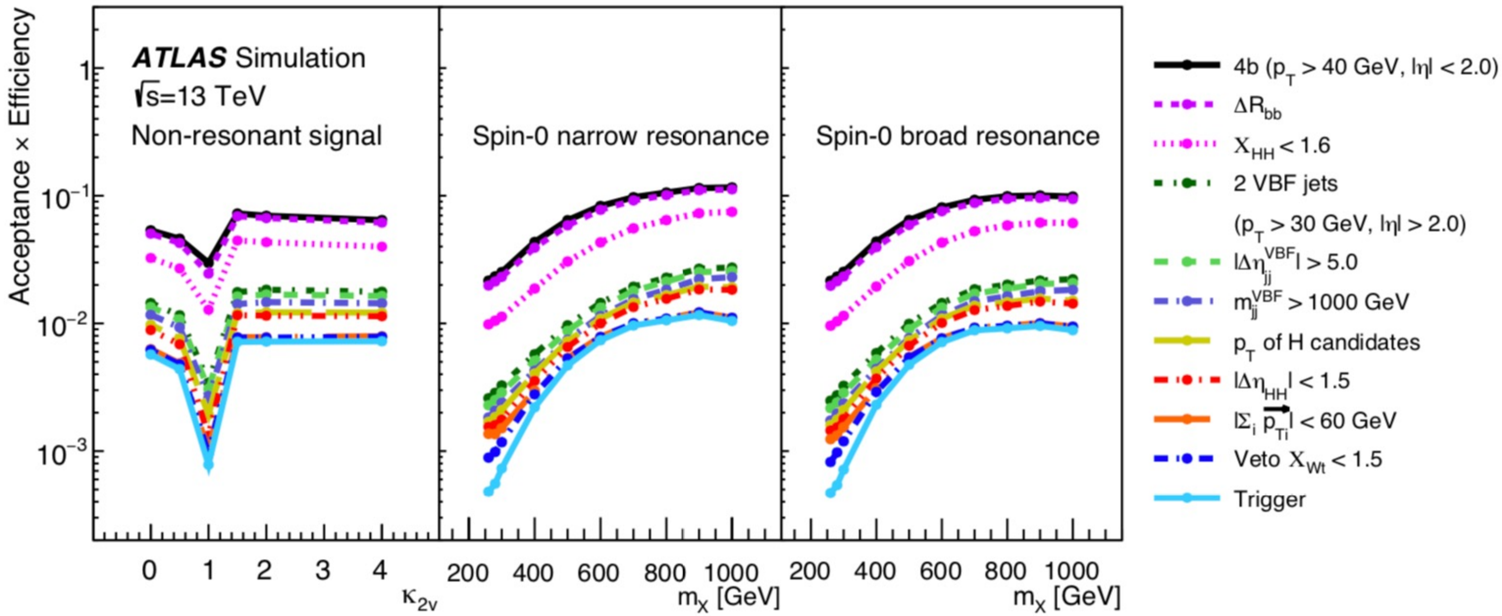

Figure 2: Cumulative acceptance times efficiency at each stage of the event selection, as detailed in Section 5. The number of events surviving the selection divided by the number of generated events is reported separately for the non-resonant signal as a function of the κ_{2V} coupling modifier and for the narrow- and broad-width resonance production hypotheses as a function of the generated mass.

VBF 4b

https://link.springer.com/article/10.1007/JHEP07(2020)108

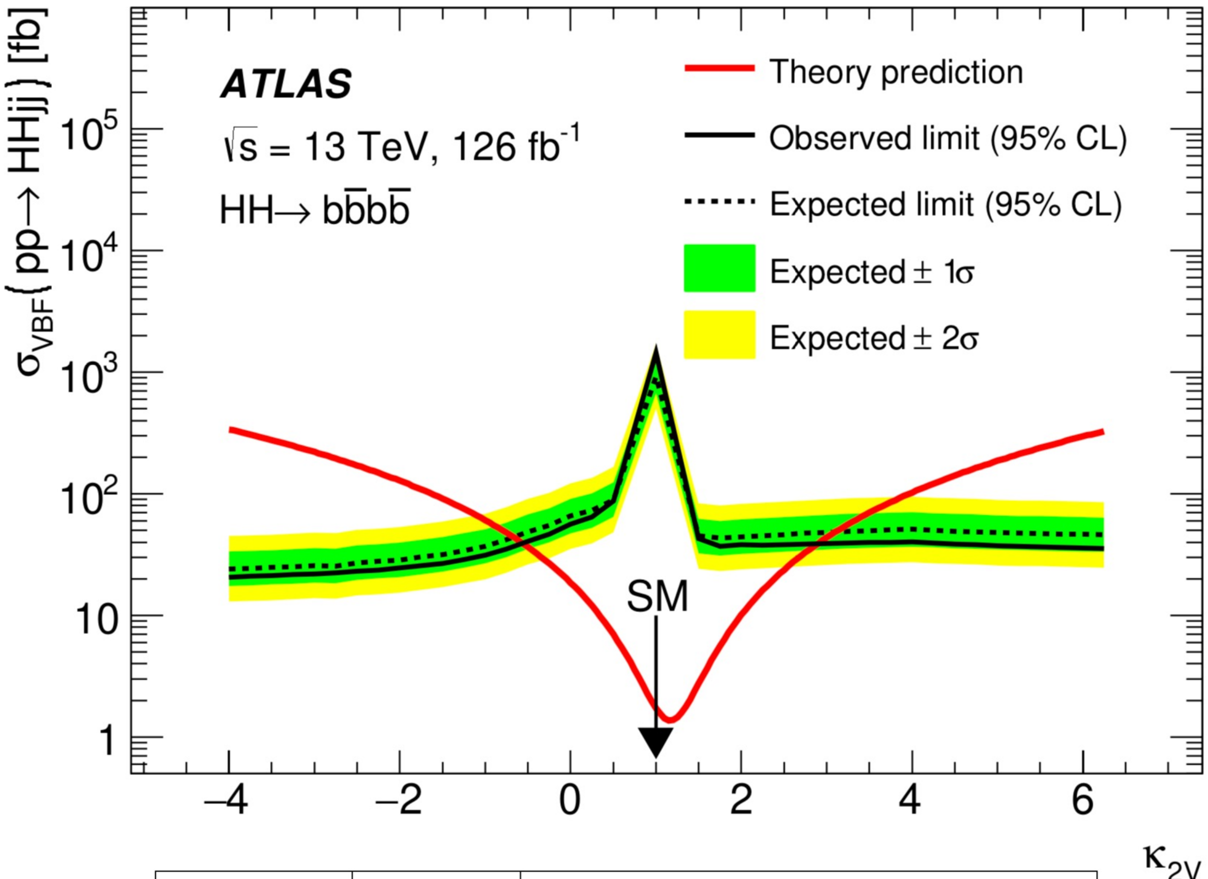

	Observed	-2σ	-1σ	Expected	$+1\sigma$	$+2\sigma$
$\sigma_{\rm VBF}$ [fb]	1450	500	660	920	1280	1720
$\sigma_{\rm VBF}/\sigma_{\rm VBF}^{\rm SM}$	840	290	390	540	750	1000

For κ2V values deviating from the SM prediction, growing non-cancellation effects result in a harder mHH spectrum, and thereby higher-pT b-jets, which in turn lead to increased signal acceptance times efficiency as shown in figure 2. This search is therefore not sensitive to the region close to the SM prediction, corresponding to κ2V = 1 .

$HH \to b\bar{b}b\bar{b}$ analysis (1)

Largest BR, but **large multi-jet backgrounds** and challenging combinatorics

Only ggF **resonant** production considered

12 different b-jet & jet triggers for *resolved* (eff up to 80%), single jet trigger for *boosted* (eff ~80%)

Resolved
(251 GeV – 1.5 TeV)
4 b-tagged ΔR=0.4 jets

& Boosted
(900 GeV – 3 TeV)
b-tagged ΔR=1.0 and
VR track-jets

Combined in the overlap region

B-jet energy corrections

Object selection

Event categorization

4b signal region
2b category for bkg estimate

BDT to pair jets from Higgs
(65-100% eff)

Resolved

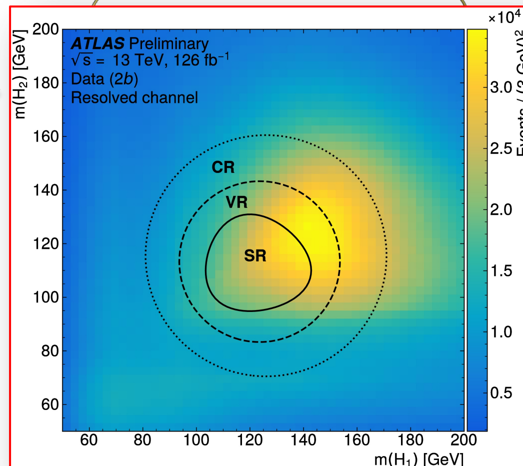

dominated by multi-jet + ∼5% $t\bar{t}$

Background modeling

Resolved

Statistical analysis

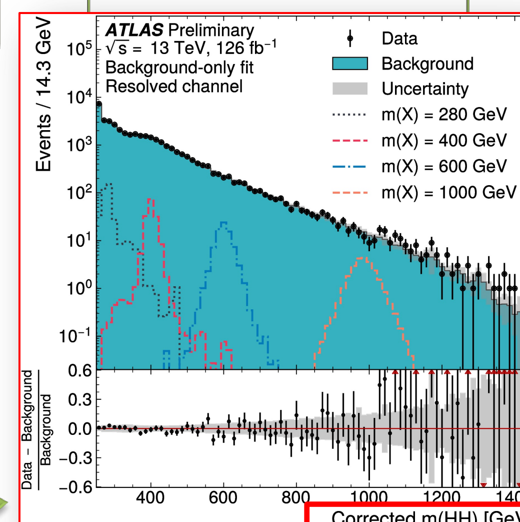

$HH \to b\bar{b}b\bar{b}$ analysis (2)

Largest BR, but **large multi-jet backgrounds** and challenging combinatorics

Only ggF **resonant** production considered

12 different b-jet & jet triggers for *resolved* (eff up to 80%), single jet trigger for *boosted* (eff ~80%)

Resolved
(251 GeV – 1.5 TeV)
4 b-tagged ΔR=0.4 jets

& Boosted
(900 GeV – 3 TeV)
b-tagged ΔR=1.0 and VR track-jets

Combined in the overlap region

B-jet energy corrections

Object selection

Event categorization

signal

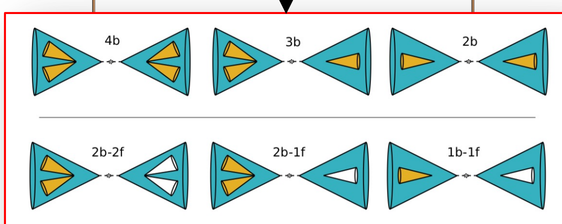

background

CR, VR & SR like in the *resolved* case

Boosted

Bkg dominated by multi-jet + up to 30% $t\bar{t}$

Data-driven multi-jet & MC-driven $t\bar{t}$ (data-driven corrections in 2/3 b region)

Background modeling

Boosted

Statistical Analysis

(3 categories)

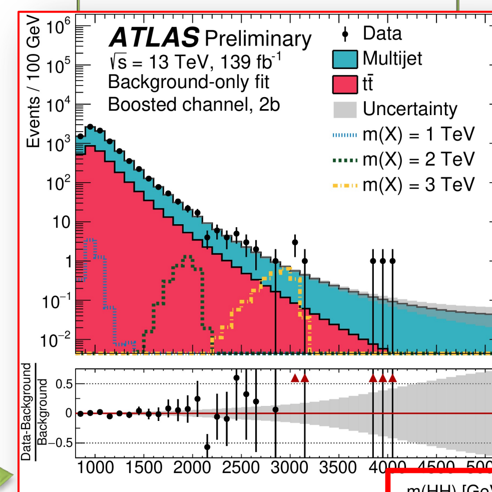

$HH \to b\bar{b}\gamma\gamma$ analysis

Early Run 2 Results
36.1fb^{-1}

- σ_{HH} limits: **22 (28) x SM** observed (expected)
  - Compared to **24 (19) x SM** observed (expected) in **CMS**
- -8.2 (-8.3) < k_λ < 13.2 (13.2)

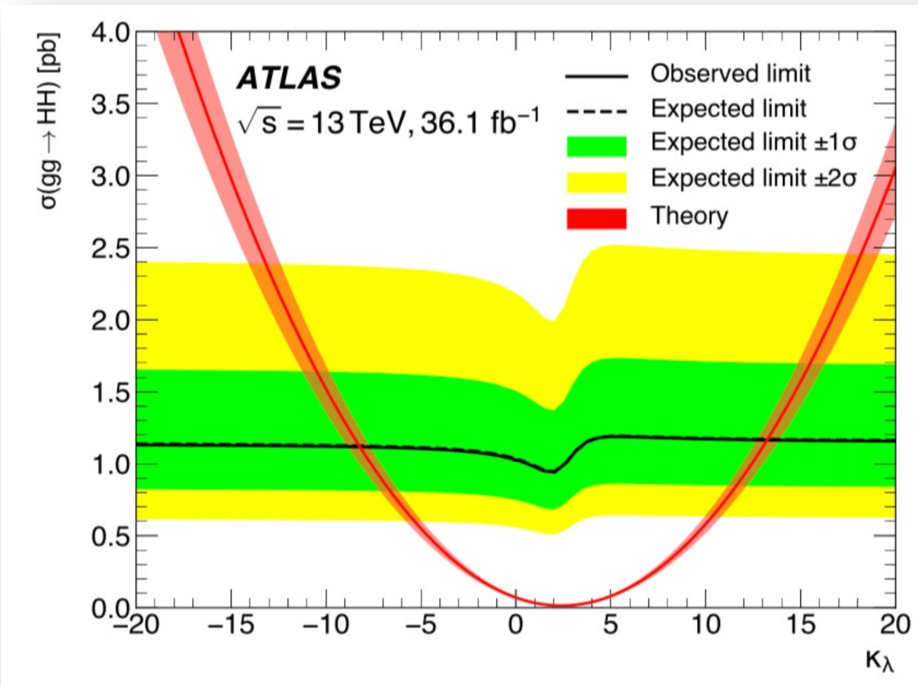

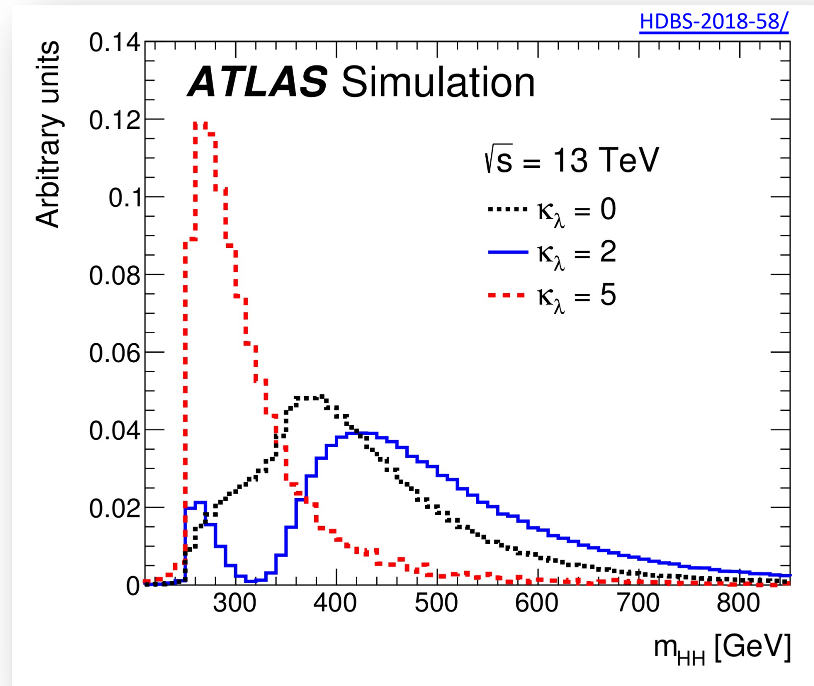

Maximum acceptance is obtained at $k_\lambda \sim 2$

The Higgs boson potential

https://atlas.web.cern.ch/Atlas/GROUPS/PHYSICS/PAPERS/HDBS-2018-58/

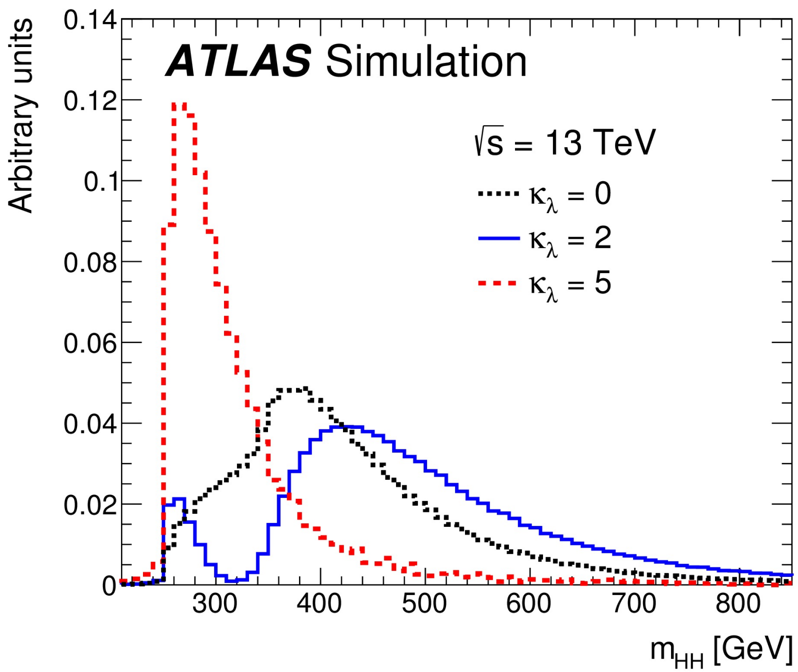

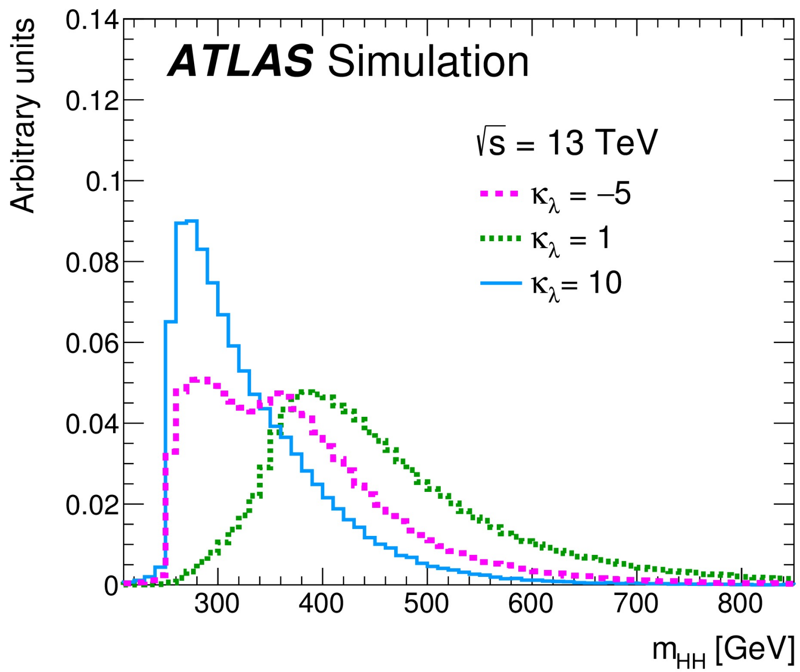

κ_λ=0 → no triangle contribution, m_{HH} shape characterised by the increase of the cross-section when $m_{HH} > 2\ m_t \approx 350$ GeV and by a large tail at high m_{HH} values.

κ_λ=10 → the triangle diagram dominates the cross-section, therefore the distribution peaks at the m_{HH} threshold being the Higgs boson propagator far off-shell on the upper side of the pole mass.

κ_λ = 2 → maximum interference between the box and the triangle diagram. The interference being destructive for positive κ_λ, it produces a deficit betwen $2m_H$ and $2m_t$.

κ_λ=5 → deficit less pronounced but still produces interference at high m_{HH} values, making the m_{HH} distribution narrower than in the κ_λ=10 case.

Di-Higgs Combination

Early Run 2 results

Non-resonant ggF production

ATLAS

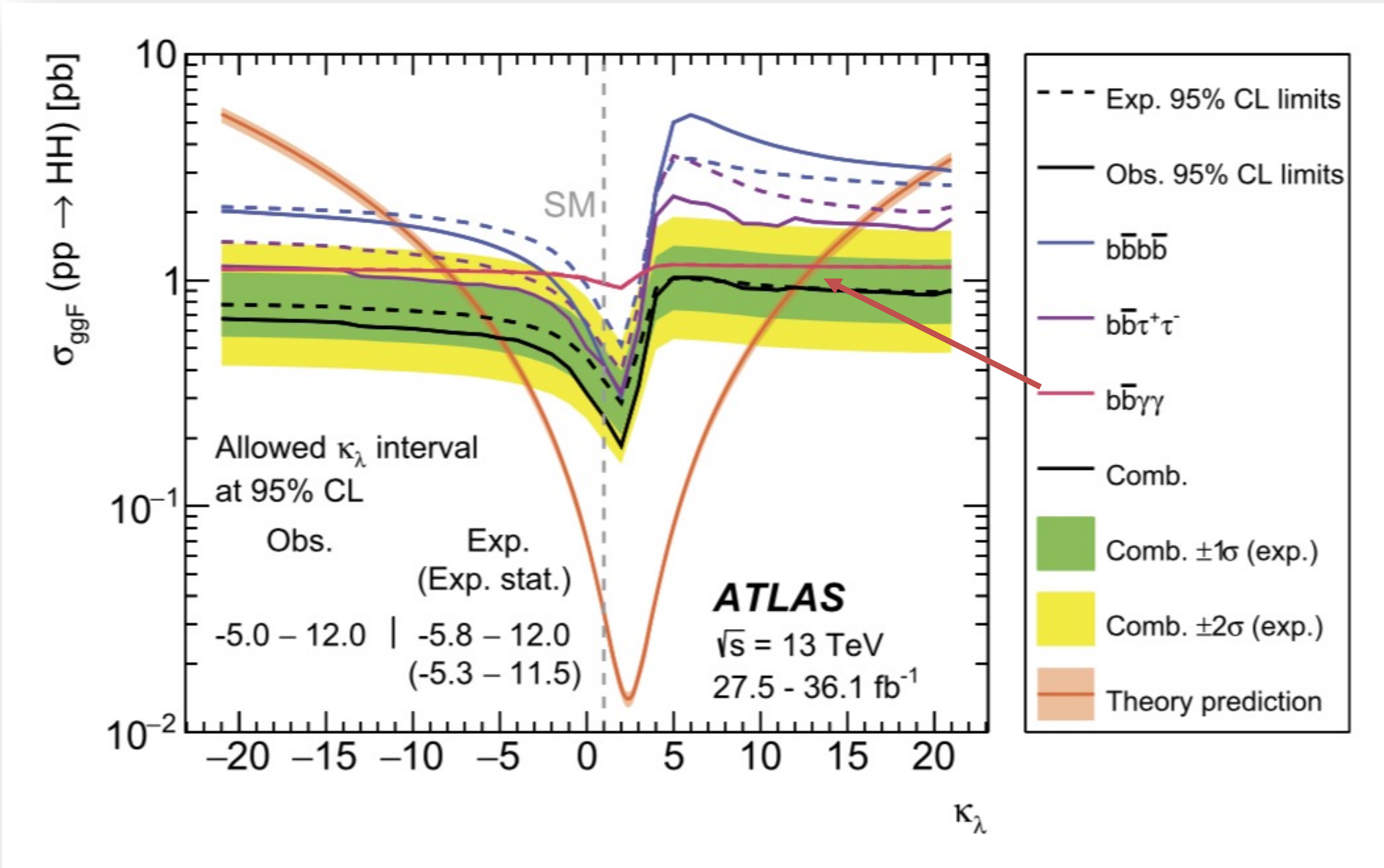

$HH \rightarrow b\bar{b}\gamma\gamma$ drives the sensitivity in the soft mass range (large k_λ)

Di-Higgs Combination

Early Run 2 results

Non-resonant ggF production

ATLAS

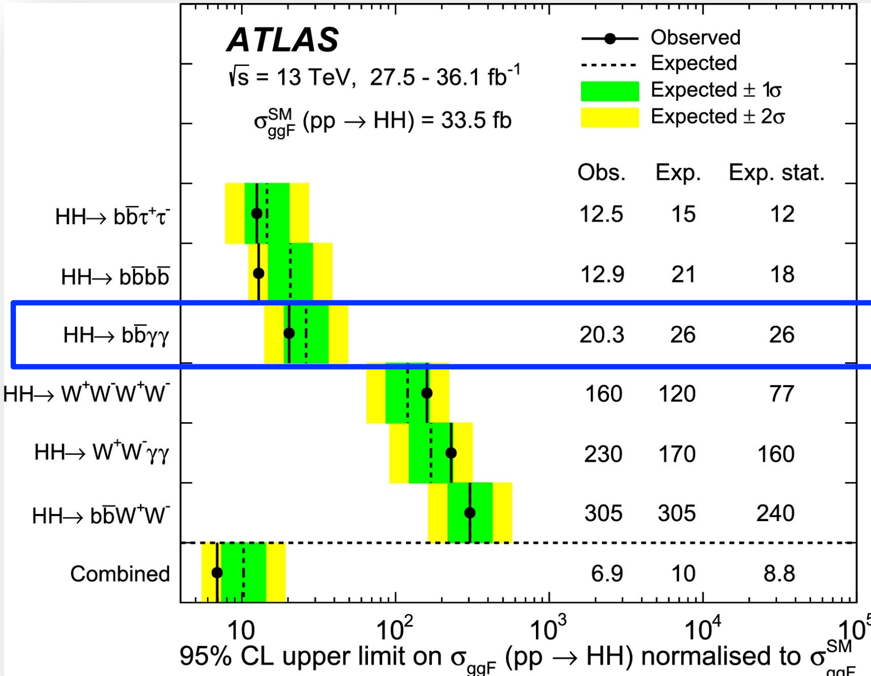

CMS

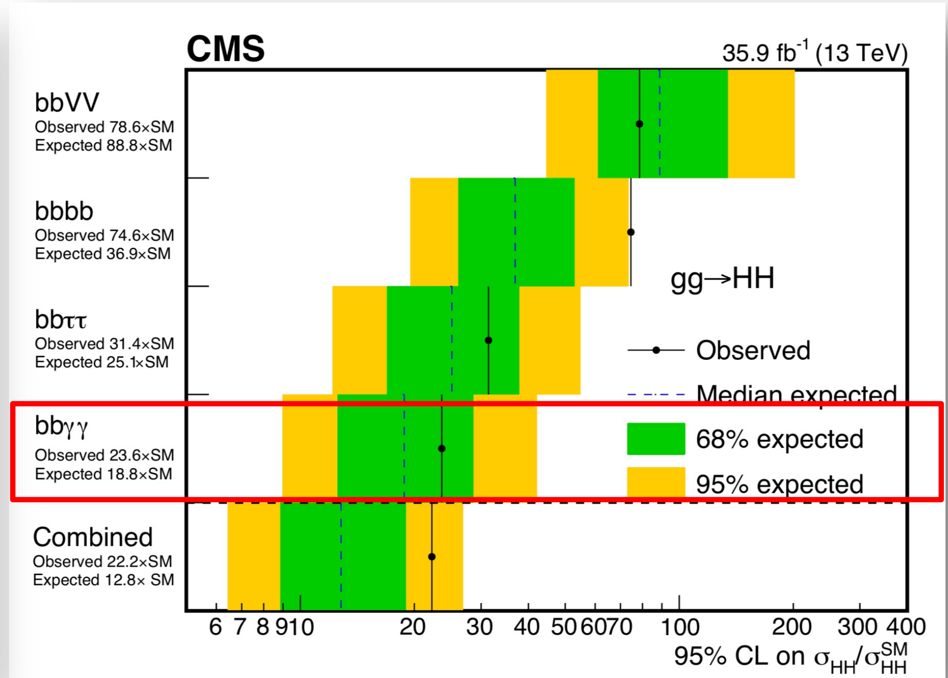

Different ATLAS-CMS “ranking” for the 3 most sensitive channels

Differences in analysis strategy can lead to large differences in sensitivity and final results…

Di-Higgs Combination

Early Run 2 results

Non-resonant ggF production

ATLAS

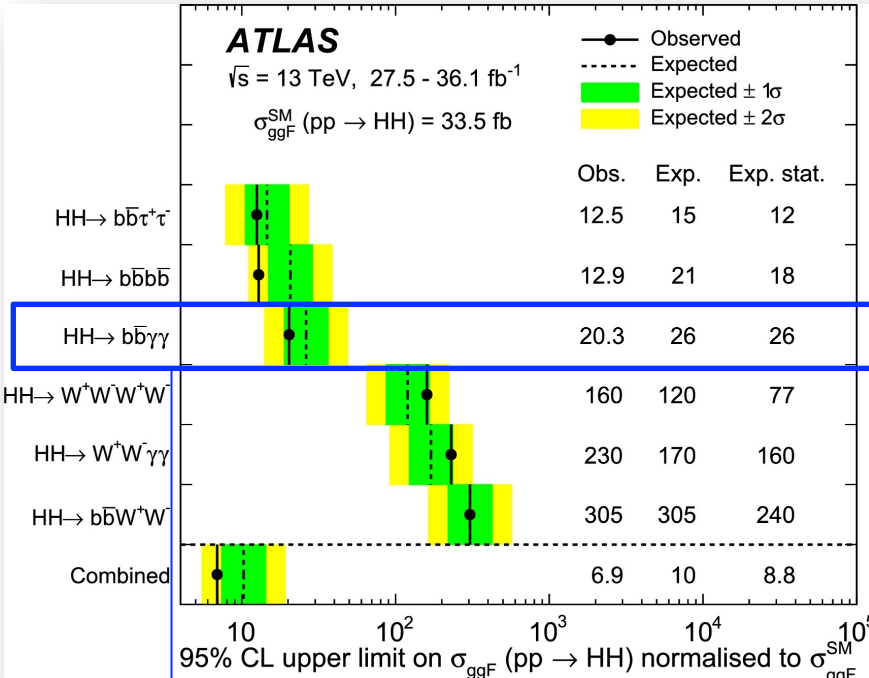

CMS

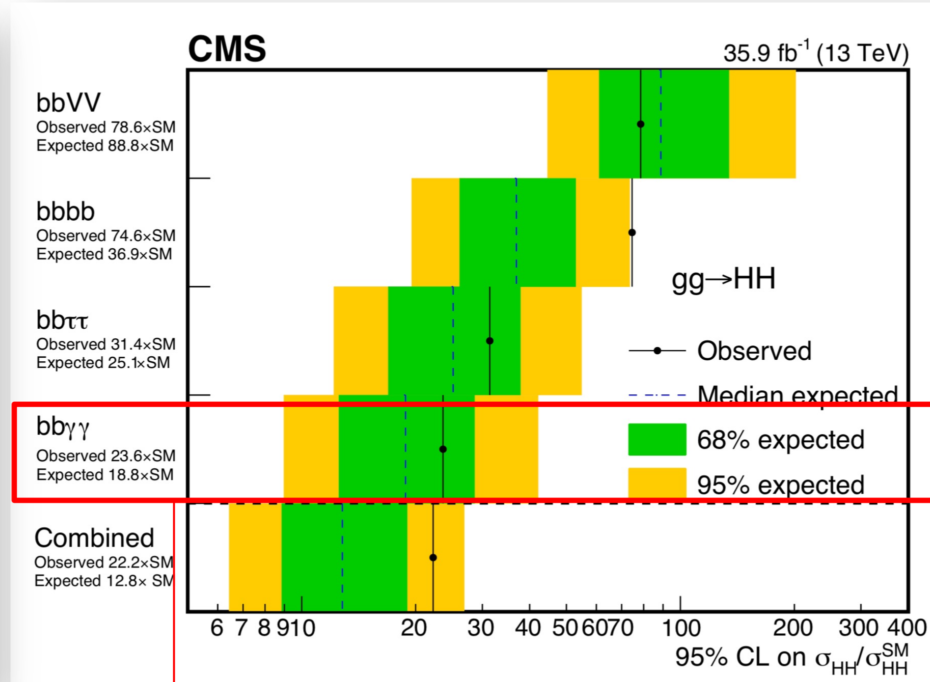

Ongoing in ATLAS

Stay tuned!

Recently updated by CMS (full Run 2 data-set)

7.7(5.2) x SM, $-3.3(-2.5) \leq k_{\lambda} \leq 8.5(8.2)$

2x better than a simple luminosity extrapolation!

Publication: ATL-PHYS-PUB-2021-031/

Summary

Non-resonant

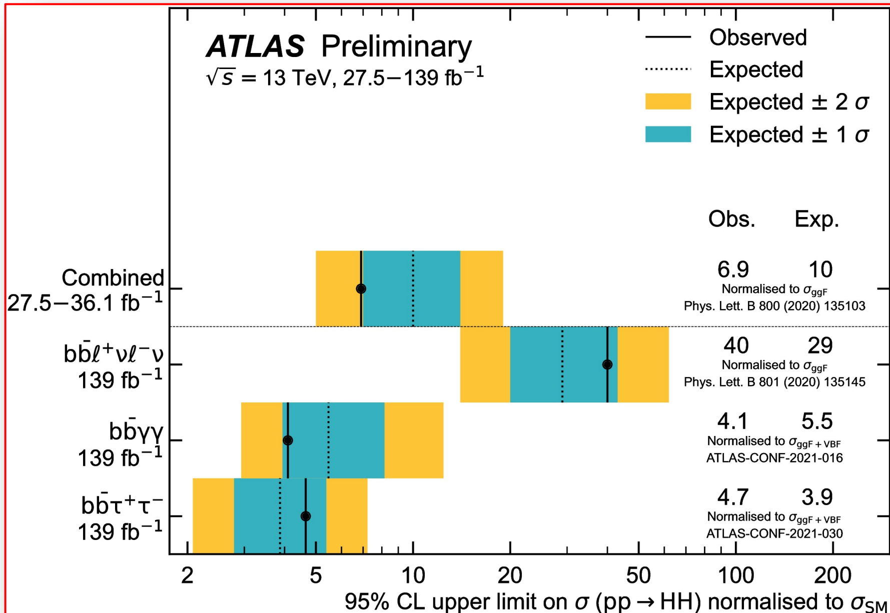

Resonant

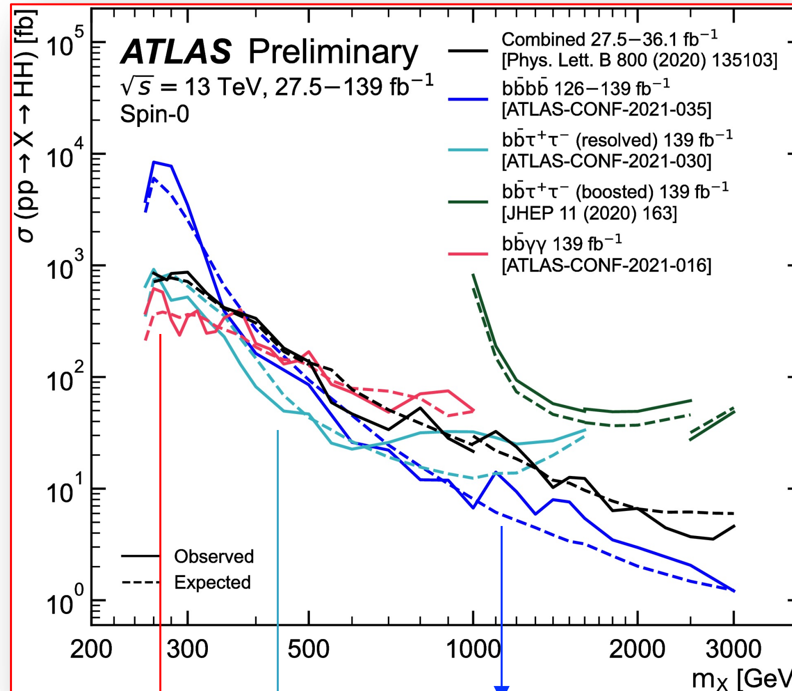

Single channels are now even better than the 36 fb^{-1} HH combination!

$b\bar{b}\gamma\gamma$ dominates the sensitivity at low m_X

$b\bar{b}b\bar{b}$ dominates the sensitivity at high m_X

$b\bar{b}\tau\tau$ dominates the sensitivity at medium m_X

- Great **analysis improvements** in all final states compared to early Run 2
- **Run 3 could already be a game changer** for a first statistically significant evidence of HH

(old) HL-LHC projections ATL-PHYS-PUB-2020-005

Channel	Statistical-only	Statistical + Systematic
$HH \to b\bar{b}b\bar{b}$	1.2	0.5
$HH \to b\bar{b}\tau^+\tau^-$	2.3	2.0
$HH \to b\bar{b}\gamma\gamma$	2.1	2.0
Combined	3.3 σ	2.9 σ

$HH \rightarrow b\bar{b}\gamma\gamma$: general considerations

ATLAS-CMS differences & potential improvements

- **Categorization**
  - Powerful variable: $\boldsymbol{m_{HH}}$
- **Signal extraction**
  - only $\boldsymbol{m_{\gamma\gamma}}$ in ATLAS
  - $m_{\gamma\gamma}$ vs $\boldsymbol{m_{b\bar{b}}}$ in CMS
- **Background modelling**
  - Largest uncertainty in ATLAS
- **b-tagging information**
  - Fixed WPs in ATLAS
  - All HH channels can benefit from direct improvements in b-tagging!

Di-Higgs VBF Production

[HIG-19-018-pas]

1.726 fb at 13 TeV

~20x smaller than ggF

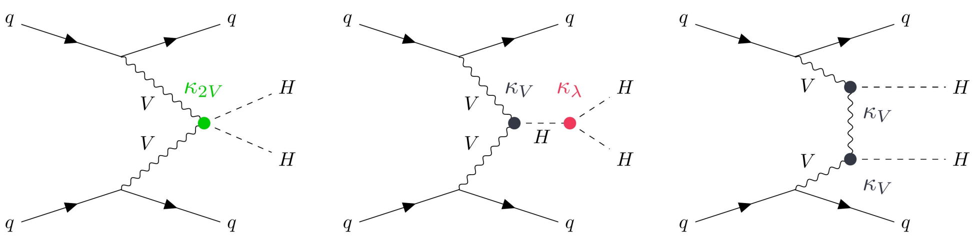

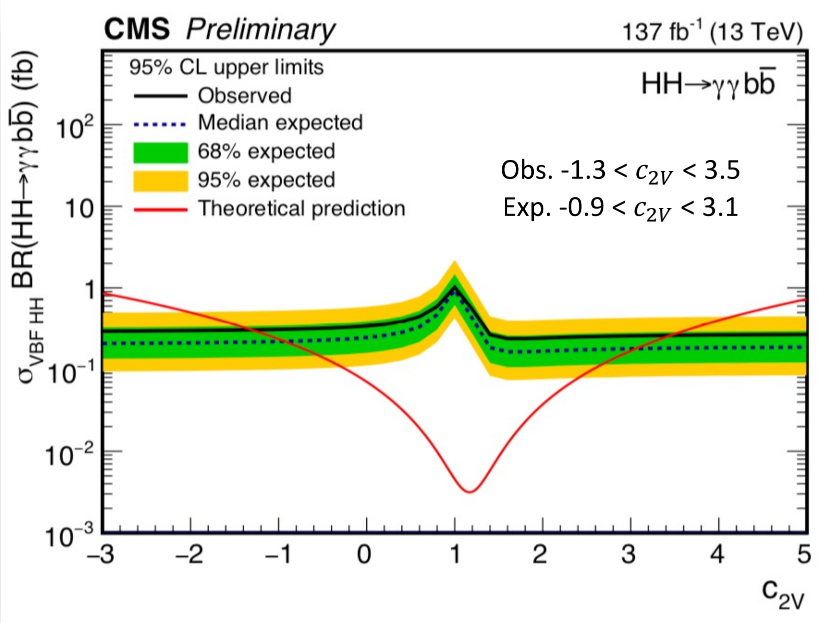

- Unique access to quartic VVHH coupling
- k_{2v} vs k_λ
- First Run 2 VBF HH analyses arriving
- No complete HL-LHC projections available
  - Forward acceptance & timing capabilities enhance analyses sensitivity!
    - $HH \rightarrow b\bar{b}\tau\tau$ in [HGCAL CMS-TDR-019]
    - 10–15%(4–8%) increase for the VBF(ggF) signal
    - 1.9-1.7 x SM → 1.5 x SM

Di-Higgs VBF Production

CMS PAS B2G-21-001

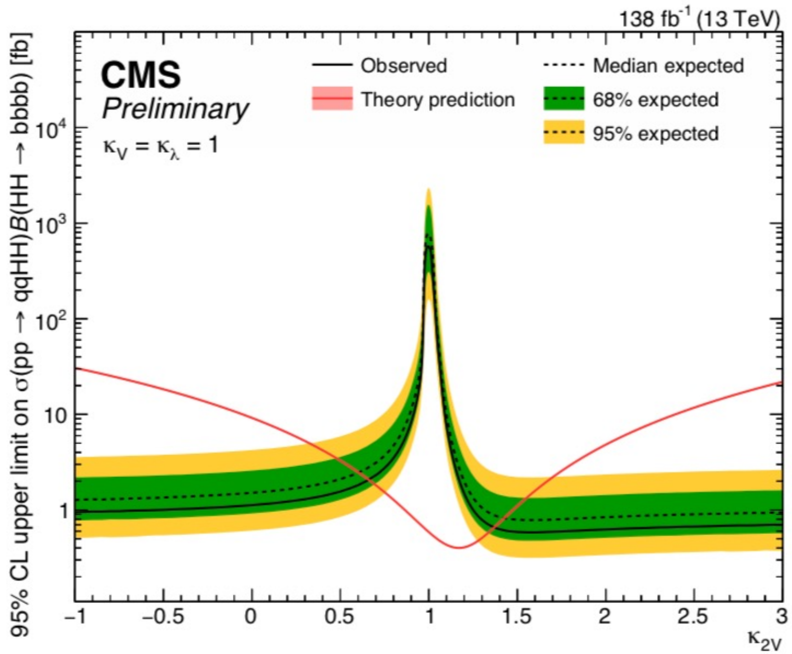

Figure 3: Observed (solid line) and expected (dashed line) 95% CL exclusion limit on the product of the VBF HH production cross section and the branching fraction into $b\bar{b}b\bar{b}$, as a function of the κ_{2V} coupling, with other couplings fixed to the SM values. The crossings of observed limit and the theoretical cross section (red line) indicate the ranges of the coupling values excluded at 95% CL.

The observed (expected) limits constrain κ2V within the range **0.6 < κ2V < 1.4 (0.6 < κ2V < 1.4)** and **κV within −1.2<κV <−0.8or0.8<κV <1.2(−1.2<κV <−0.8or0.8<κV <1.2)**at95%confidence level, when all other Higgs boson couplings are assumed equal to their standard model values. **The signal hypothesis with κ2V = 0 and other couplings equal to 1 is excluded at a CL higher than 99.99%**. **When both κ2V and κV are varied simultaneously, the observed limits exclude the hypothesis κ2V = 0 at a CL of 95% or higher for all κV coupling values above 0.5** (i.e. for all values compatible with previous measurements of the κV coupling), with other couplings assumed equal to their standard model values.

SMEFT

https://arxiv.org/pdf/1910.00012.pdf

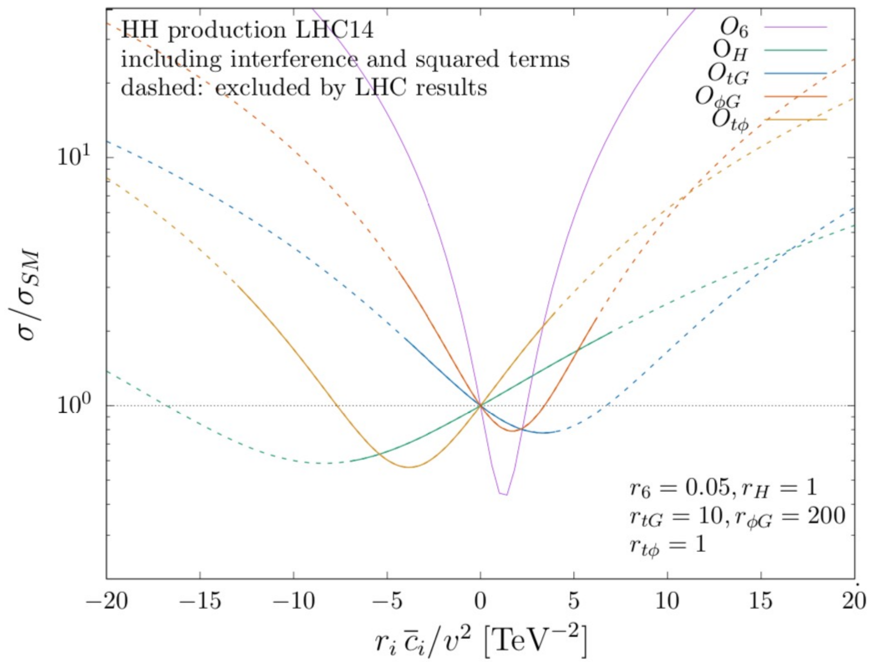

Figure 2.2: Dependence of double Higgs production cross-section on the Wilson coefficients of the relevant dimension-6 operators. The dashed part of the contours are excluded by LHC Run 1 Higgs and top quark measurements. Note that each coefficient $\bar{c}_i$ is multiplied by a different factor r_i, specified in the figure.

Given these bounds, only **the effect of *c*6 can lead to deviations of order 10 in the *HH* cross section from the SM predictions**. However, **to constrain *c*6 at levels of order 1, we will need precise constraints on all of other coefficients that enter the analysis**. This demands a global SMEFT interpretation.

Deviations

https://doi.org/10.1016/j.revip.2020.100045

Vacuum Stability:
While in low-scale inverse seesaw models one can find modifications in the trilinear Higgs self-coupling up to 30% [153], the scenarios providing such a large deviation of the trilinear Higgs self-coupling drive the Higgs potential into the unstable regime. Requesting that this does not occur within one order of magnitude from the mass scale of the right-handed neutrinos (hence not requiring any UV completion below that scale), **one can bound the trilinear Higgs self-coupling modifications to be smaller than = 0.1% [151] via metastability arguments** (see e.g. Ref. [154]).

Perturbativity:
Klambda<~6
Quartic coupling deviations < ~60

Deviations

(https://arxiv.org/pdf/1704.02311.pdf)

Maxi-sizing the trilinear Higgs self-coupling:how large could it be?

In order to answer the question on how much the trilinear Higgs self-coupling could deviate from its Standard Model value in weakly coupled models, we study both theoretical and phenomenological constraints. As a first step, we discuss this question by modifying the Standard Model using effective operators. Considering constraints from **vacuum stability and perturbativity**, we show that **only the latter can be reliably assessed in a model-independent way**. We then focus on UV models which receive constraints from Higgs coupling measurements, electroweak precision tests, vacuum stability and perturbativity. We find that the interplay of current measurements with perturbativity already **exclude self-coupling modifications above a factor of few with respect to the Standard Model value.**

The paper quotes $|\kappa\lambda| < 6$ and $-1.5 < \kappa\lambda < 8.7$

Deviations

(https://arxiv.org/pdf/1702.07678.pdf)

Electroweak oblique parameters as a probe of the trilinear Higgs boson self-interaction

In this paper, we evaluate how well electroweak precision data, expressed using the electroweak oblique parameters S and T[5, 6], can constrain modifications of the trilinear Higgs self-interaction.

In this paper, we consider only the effects of modifying of the trilinear and quartic couplings in isolation from the other Standard Model couplings

Quotes

$-14.0 \leq \kappa\lambda \leq 17.4$

Precision

properly include their effects (see Section 3.3).

We now provide an indicative summary of what experimental precision on the di-Higgs measurement is needed to probe the different BSM phenomena we have surveyed in this chapter:

- **Bronze: Precision of 100%:** Measurements at this level are sensitive to models with the largest new physics effects, in which new particles of few hundred GeV mass appear in tree diagrams or as *s*-channel resonances. Depending on the model, the heavy new resonance often has sizeable branching ratios also to *VV* final states. We have discussed in Section 3.1 models with singlets which allow for sizeable branching ratios of a heavy Higgs boson to light Higgs bosons, with values of maximally $BR(H \to hh) = 0.4$ for singlet models with Z_2 symmetry, while larger $BR(H \to hh)$ are possible without Z_2 symmetry.
- **Silver: Precision of 25–50%:** Measurements at this level are sensitive to mixing of the Higgs boson with a heavy scalar with a mass of order 1 TeV. Models of electroweak baryogenesis typically predict this level of deviation in the trilinear Higgs self-coupling. At this level of precision we are able to exclude a physical hypothesis with realistic deviations in the Higgs self-coupling, rather than just eliminating parts of parameter space.
- **Gold: Precision of 5–10%:** Measurements at this level are sensitive to a broad class of loop diagram effects that might be created by light top squarks and or other new particles with strong coupling to the Higgs sector. Measurements at this level could possibly complement measurements on new particles that could be discovered at the HL-LHC.
- **Platinum: Precision of 1%:** Measurements at percent level are sensitive to typical quantum corrections to the Higgs self-coupling generated by loop diagrams.

collider	single-H	HH	combined
HL-LHC	100-200%	50%	50%
CEPC_{240}	49%	–	49%
ILC_{250}	49%	–	49%
ILC_{500}	38%	27%	22%
ILC_{1000}	36%	10%	10%
CLIC_{380}	50%	–	50%
CLIC_{1500}	49%	36%	29%
CLIC_{3000}	49%	9%	9%
FCC-ee	33%	–	33%
FCC-ee (4 IPs)	24%	–	24%
HE-LHC	-	15%	15%
FCC-hh	-	5%	5%

The Higgs boson potential

arXiv:1907.02078v2

$$V(H) \simeq \begin{cases} -m^2 H^\dagger H + \lambda (H^\dagger H)^2 + \frac{c_6 \lambda}{\Lambda^2}(H^\dagger H)^3, & \text{Elementary Higgs} \\ -a \sin^2(\sqrt{H^\dagger H}/f) + b \sin^4(\sqrt{H^\dagger H}/f), & \text{Nambu-Goldstone Higgs} \\ \lambda (H^\dagger H)^2 + \epsilon (H^\dagger H)^2 \log \frac{H^\dagger H}{\mu^2}, & \text{Coleman-Weinberg Higgs} \\ -\kappa^3 \sqrt{H^\dagger H} + m^2 H^\dagger H, & \text{Tadpole-induced Higgs} \end{cases}$$

	a	b	c_1	c_2	c_3	d_3	d_4
relevant couplings	hVV	$hhVV$	$h\bar{t}t$	$hh\bar{t}t$	$hhh\bar{t}t$	hhh	$hhhh$
SM	1	1	1	0	0	1	1
SMEFT (with O_6)	1	1	1	0	0	$1 + c_6 \frac{v^2}{\Lambda^2}$	$1 + c_6 \frac{6v^2}{\Lambda^2}$
MCH_{5+5}	$1 - \frac{\xi}{2}$	$1 - 2\xi$	$1 - \frac{3}{2}\xi$	-2ξ	$-\frac{2}{3}\xi$	$1 - \frac{3}{2}\xi$	$1 - \frac{25}{3}\xi$
CTH_{8+1}	$1 - \frac{\xi}{2}$	$1 - 2\xi$	$1 - \frac{1}{2}\xi$	$-\frac{1}{2}\xi$	$-\frac{1}{6}\xi$	$1 - \frac{3}{2}\xi$	$1 - \frac{25}{3}\xi$
CW Higgs (doublet)	1	1	1	0	0	$\frac{5}{3}(1.75)$	$\frac{11}{3}(4.43)$
CW Higgs (singlets)	1	1	1	0	0	$\frac{5}{3}(1.91)$	$\frac{11}{3}(4.10)$
Tadpole-induced Higgs	$\simeq 1$	$\simeq 1$	$\simeq 1$	0	0	$\simeq 0$	$\simeq 0$

Table 1: Higgs couplings, defined in Eqs. (2.1) and (2.3), for the SM and various NP scenarios. For the Coleman-Weinberg (CW) Higgs scenario, we also present in the parenthesis the Higgs self-couplings up to the two-loop order, predicted in the two of the simplest conformal extensions of the scalar sector: SM Higgs doublet with another doublet [14], and SM Higgs doublet with two additional singlets [15].

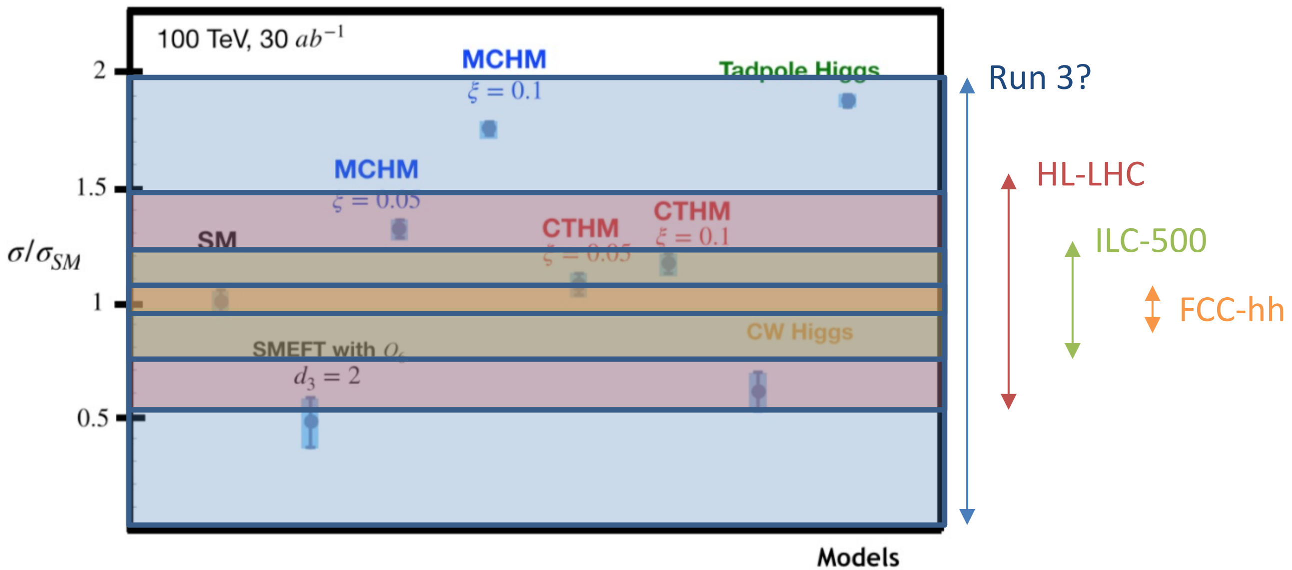

Light stops

- Section 3.5.6 of the White Paper mentions MSSM, focusing on the presence of light stops

https://atlas.web.cern.ch/Atlas/GROUPS/PHYSICS/PUBNOTES/ATL-PHYS-PUB-2021-019/fig_06.png

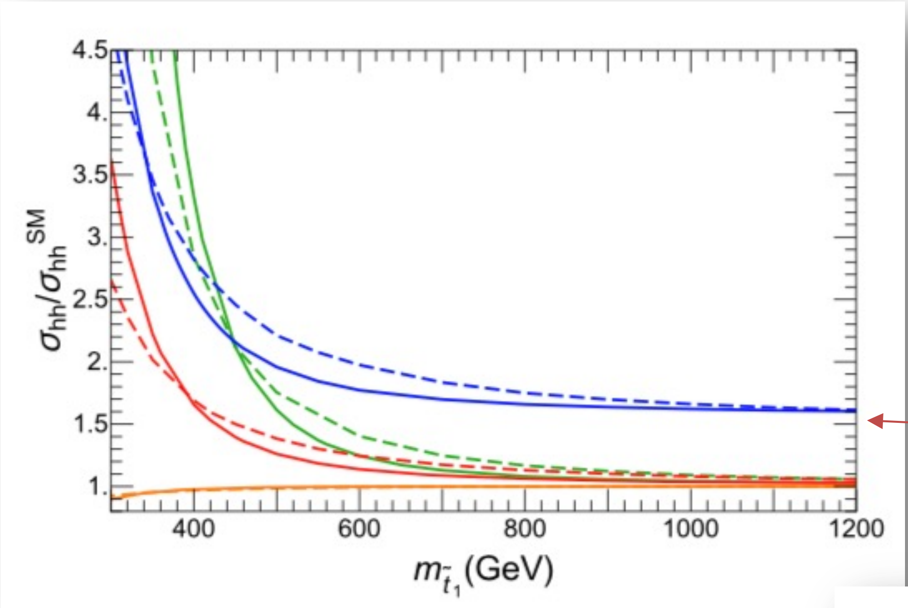

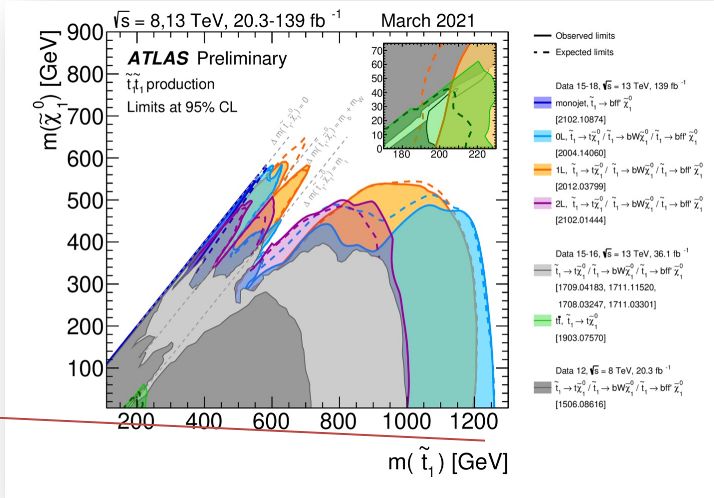

Double Higgs production cross section normalised to the SM values as a function of the lightest stop mass. Full one loop calculation (solid lines), and the EFT calculation (dashed lines). ***κt*** is chosen to be 1 for the orange, red and green lines, and **1.1 for the blue lines.**

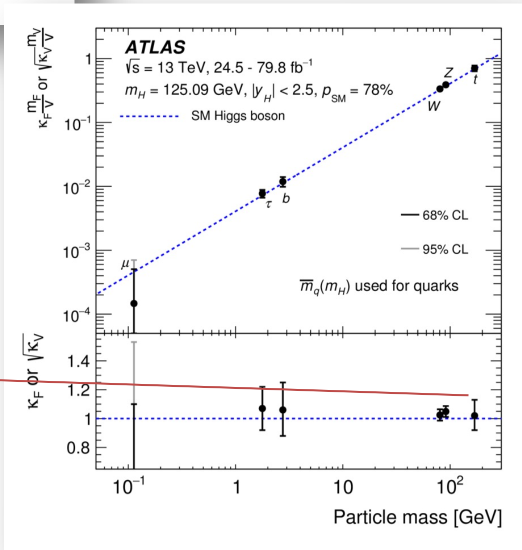

Given the current exclusion limits on the stop mass and the precision on kt, **a scenario with the stop mass > 1.2 TeV and kt 1.1 implies a xs enhancement of a factor 1.6**, not too far away from our combined limits, so it could be investigated and would be interesting also for future kt measurements

Lepton colliders

https://arxiv.org/pdf/1905.03764.pdf

Lepton collider

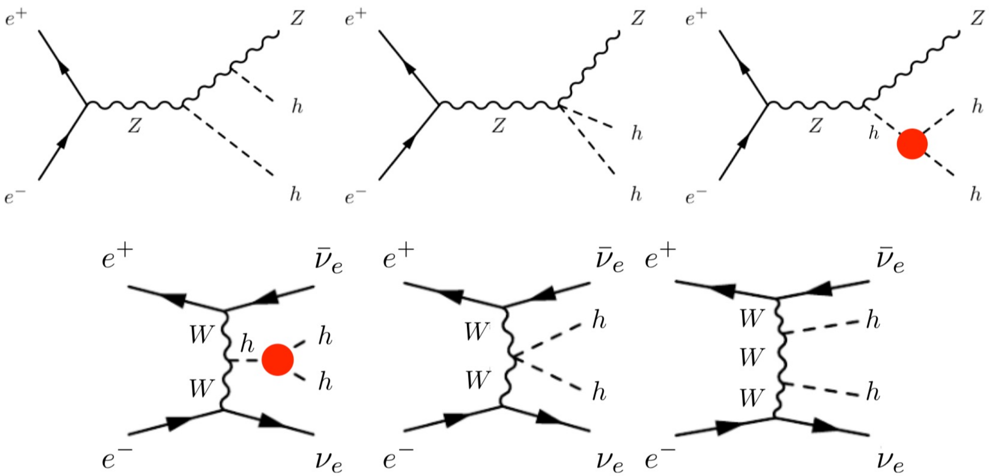

At lepton colliders, the production cross sections do depend on the polarisation but this dependence drops out in the ratios to the SM rates (beam spectrum and QED ISR effects have been included).

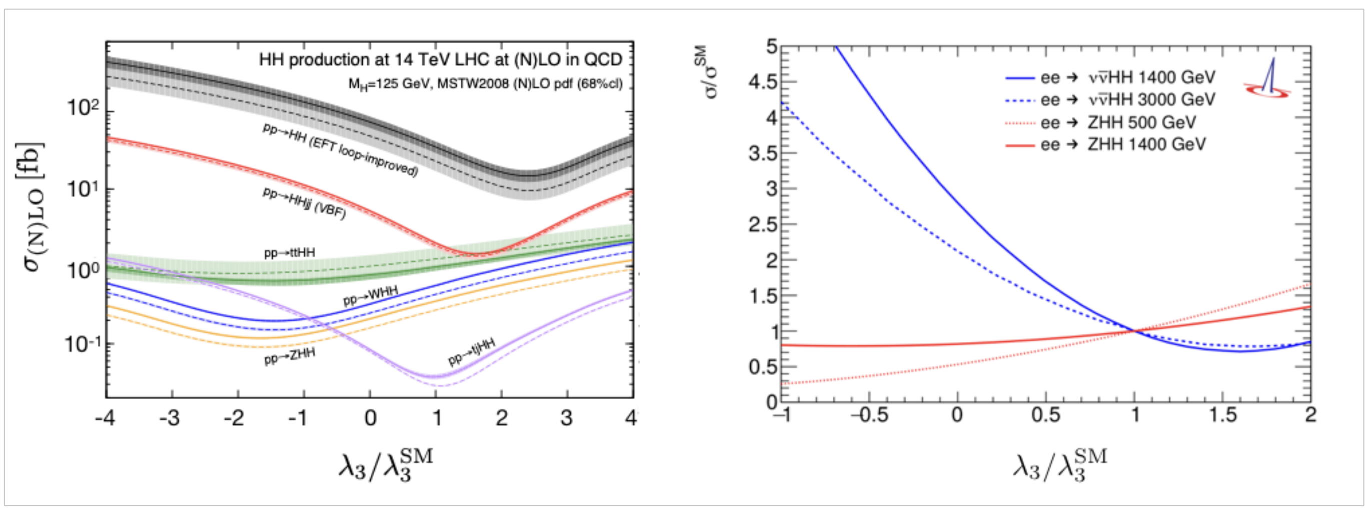

Tracking & Vertexing

ATLAS and CMS Trackers

ATLAS

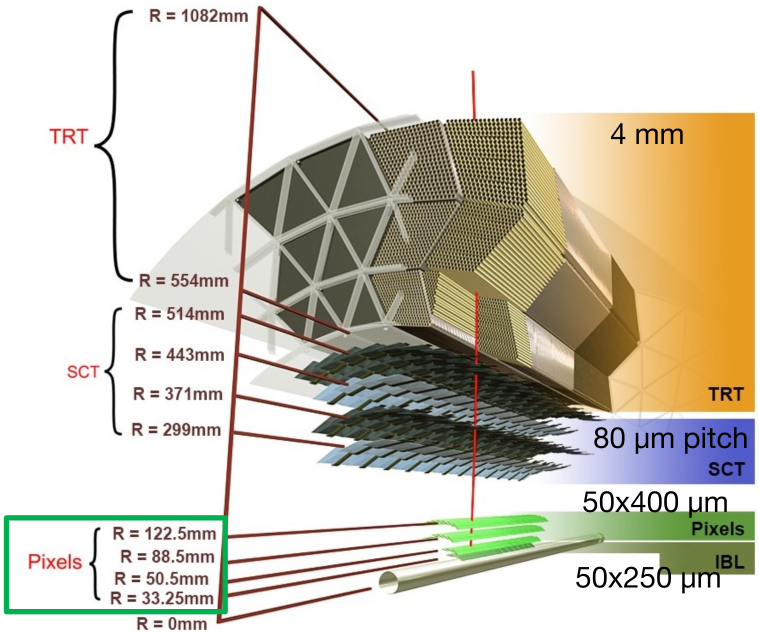

CMS

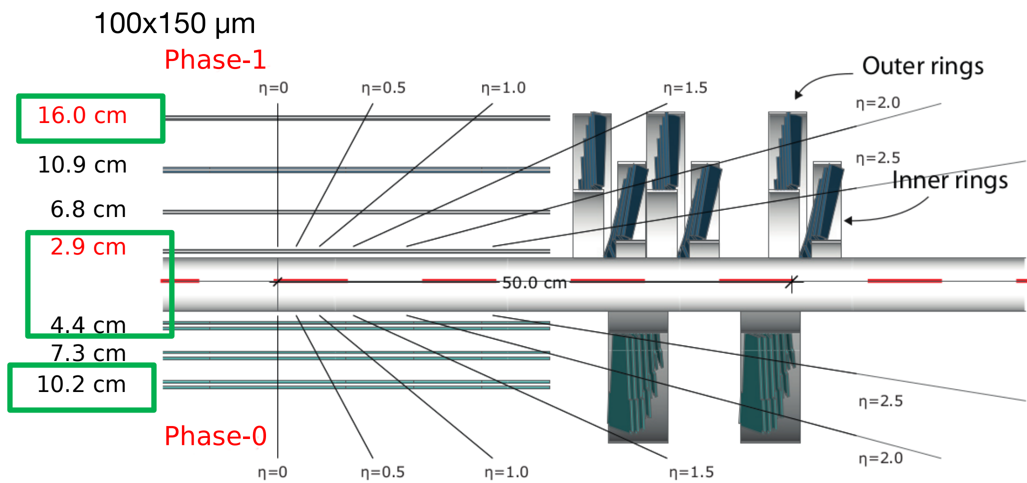

	Inner R [cm]	|eta|	B field [T]	X0 at eta 0	p_T resolution at 1 (100) GeV, $\|\eta\|=0$
ATLAS	3.3	2.5	2	0.3	1.3 (3.8)%
CMS	2.9	3.0	4	0.4	0.7 (1.5-2.0)%

The Tracking & Vertexing Challenge

Eur. Phys. J. C76 (2016)

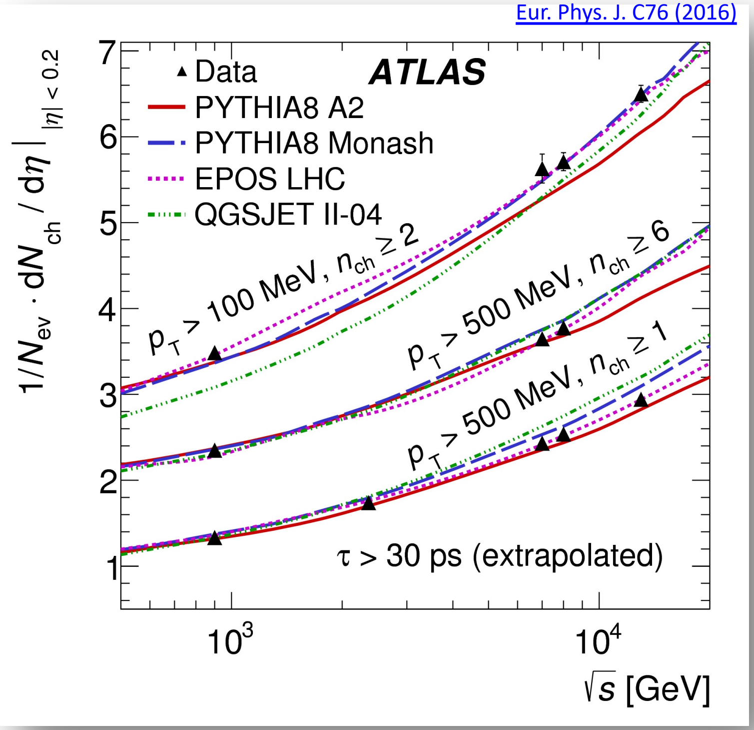

- At 13 TeV, O(15) charged particles per *pp* collision
- Run 2 <$\boldsymbol{\mu}$> ~ 40 , O(500-1000) tracks per event
- Tracking and vertexing designed for <$\boldsymbol{\mu}$> ~ 20
- Run 3 <$\boldsymbol{\mu}$> ~ 60
- Updates to retain high efficiency and low fake rate are mandatory!

d0/z0 resolutions

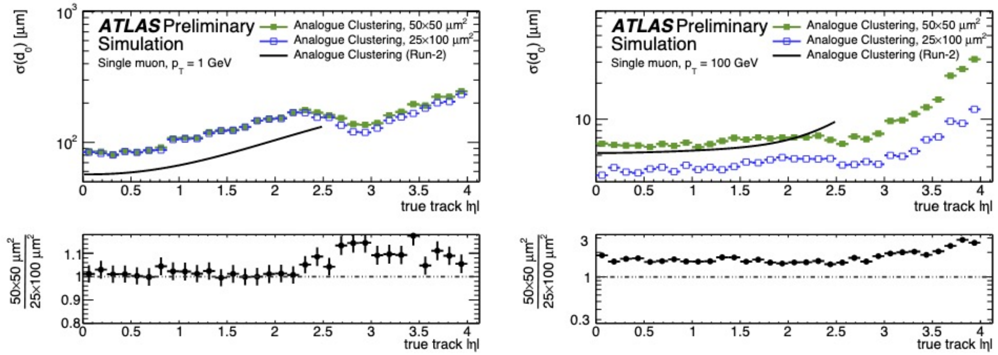

39 mm

Figure 10: Track parameter resolution in d_0 as a function of η for the ITk for muons with p_T = 1 GeV (**left**) and p_T = 100 GeV (**right**) and $\langle\mu\rangle = 0$. For comparison the results for the current Run-2 detector are shown as a line. The ratio in the lower part of the plots is defined as the results using 50×50 μm^2 pixels over those obtained using 25×100 μm^2 pixels.

http://cdsweb.cern.ch/record/26695http://cdsweb.cern.ch/record/2669540/files/ATL-PHYS-PUB-2019-014.pdf40/files/ATL-PHYS-PUB-2019-014.pdf

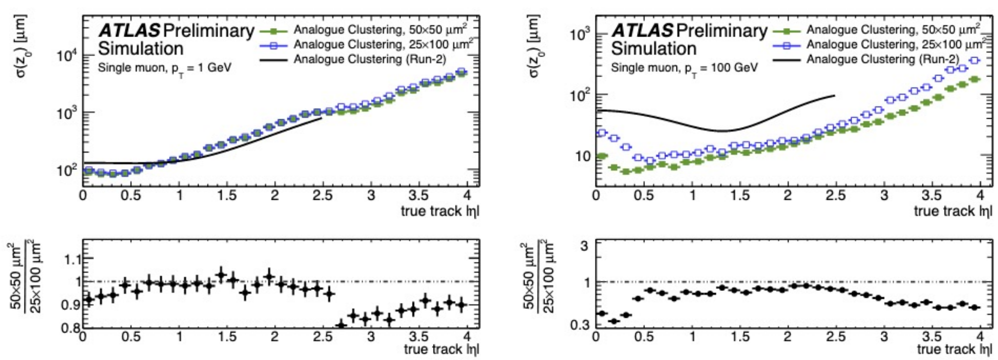

Figure 11: Track parameter resolution in z_0 as a function of η for the ITk for muons with p_T = 1 GeV (**left**) and p_T = 100 GeV (**right**) and $\langle\mu\rangle = 0$. For comparison the results for the current Run-2 detector are shown as a line. The ratio in the lower part of the plots is defined as the results using 50×50 μm^2 pixels over those obtained using 25×100 μm^2 pixels.

d0/z0 resolutions

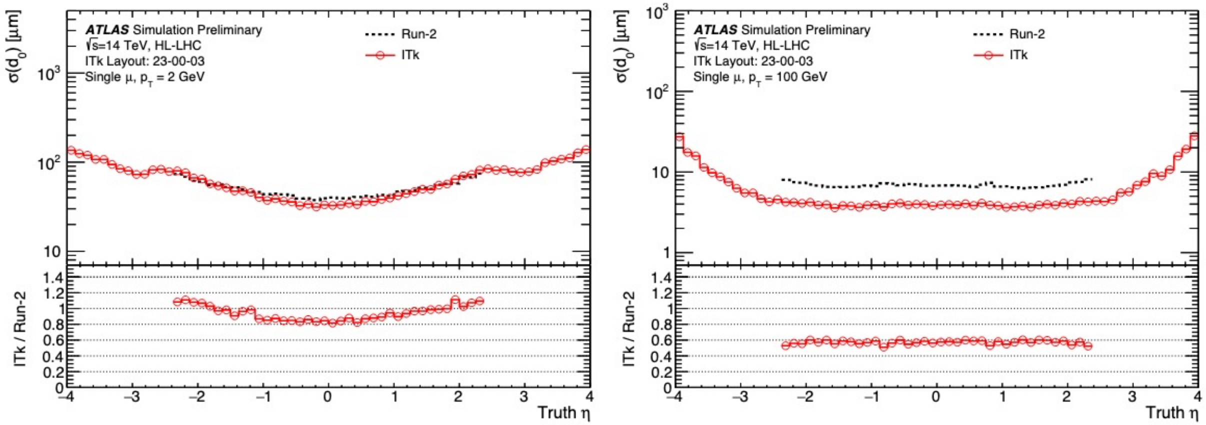

(a) (b)

Figure 12: Transverse impact parameter (d_0) resolution as a function of η for 2 GeV (a) and 100 GeV (b) muons without pileup, compared between the Run 2 detector and the updated ITk layout.

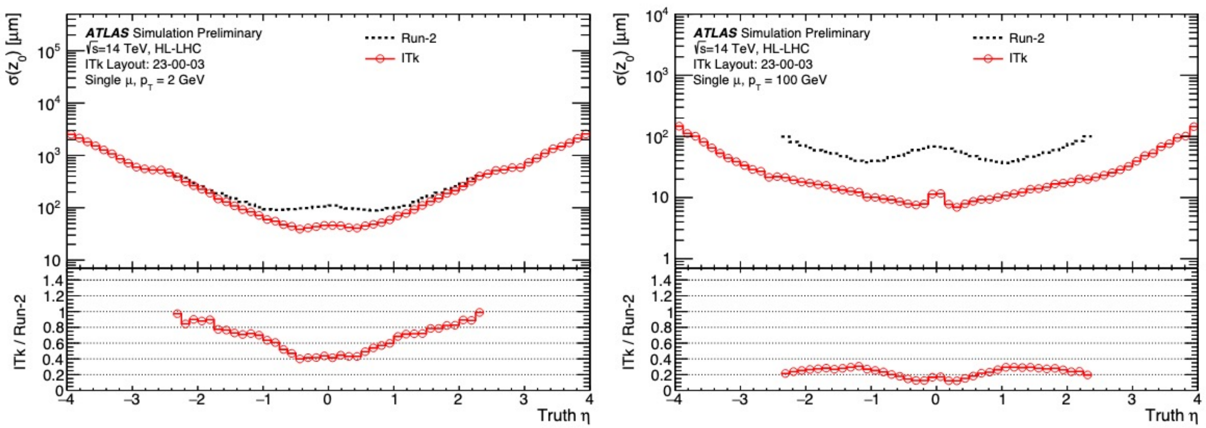

(a) (b)

Figure 13: Longitudinal impact parameter (z_0) resolution as a function of η for 2 GeV (a) and 100 GeV (b) muons without pileup, compared between the Run 2 detector and the updated ITk layout.

radius of the innermost pixel layer from 39 to 34 mm.

The pixel pitch in the barrel of the innermost layer was also fixed to 25 × 100 μm2 while a pixel pitch of 50 × 50 μm2 is used in the rest of the detector.

Tracking & Vertexing in a Nutshell

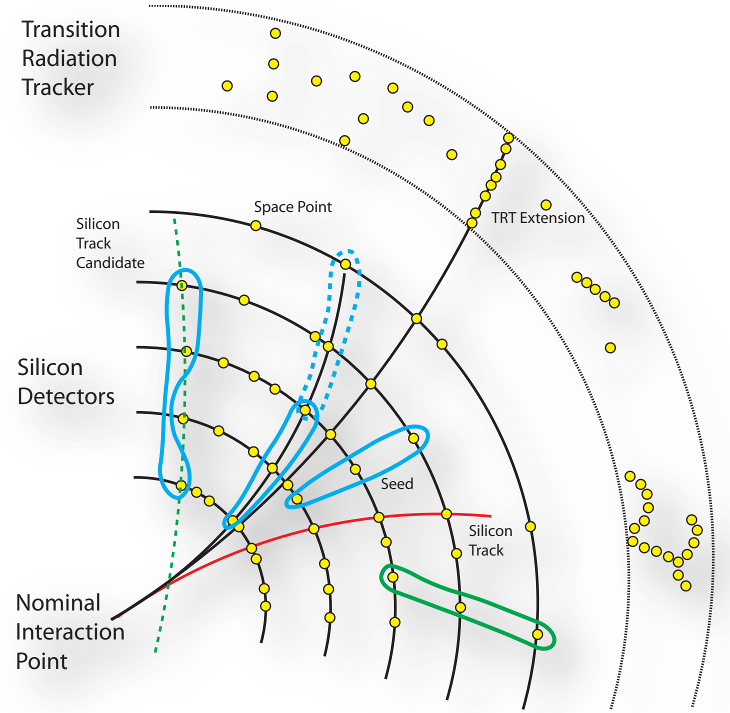

- Multi-step Inside-out:
  - **Space points**
  - **Seed finding**
  - **Track candidate**
  - **Ambiguity solving**
  - **TRT Extension**
- Additional outside-in step
- Special setups: pixel tracklets, tracks with large impact parameters, etc.

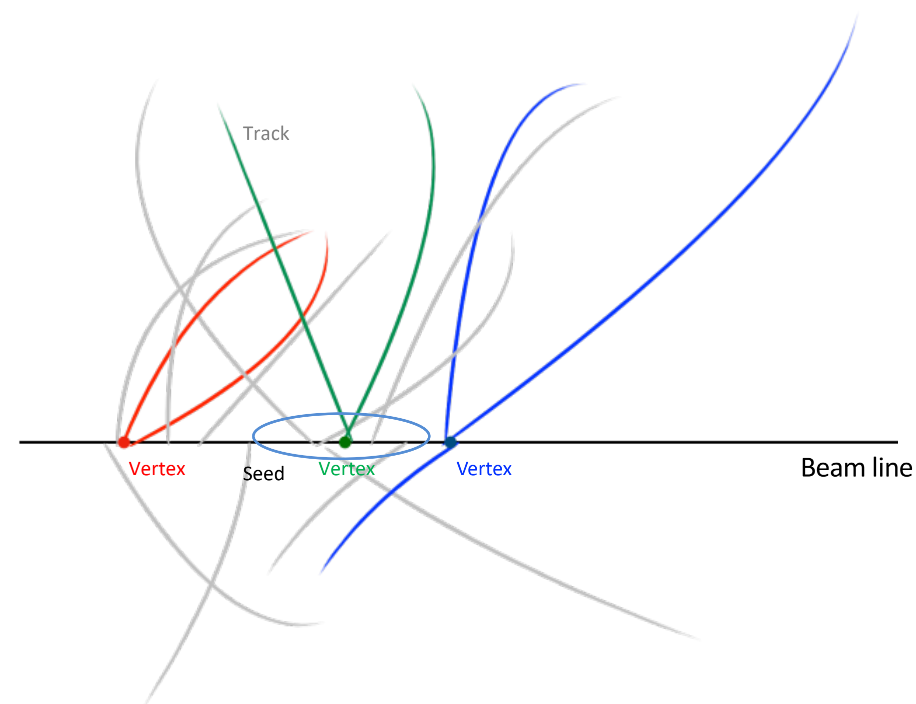

- **Seed finding**
- **Track-to-Seed assignment**
- **Fitting**
- **Acceptance/Rejection**

Track Parametrization

5 parameters describe the helical path of a charged particle in a solenoidal magnetic field:

- **Transverse d_0** and **longitudinal z_0** impact parameters,
- **Azimuthal Φ** (measured in the transverse plane [-π, π]) and **polar ϑ** (measured from the z axis [0, π]), pseudorapidity **η**=-ln(tanθ/2)
- **Charge/momentum q/p** defining orientation and curvature
- Track bending in magnetic field, sagitta measurement related to the inverse of the transverse momentum p_T=p cos(ϕ)

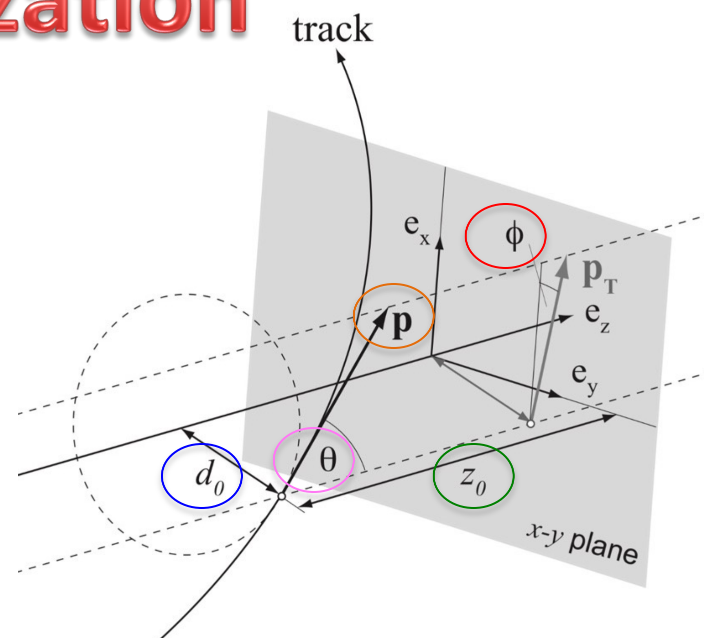

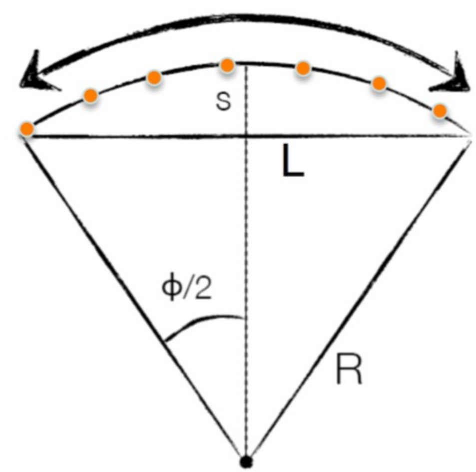

Track Reconstruction

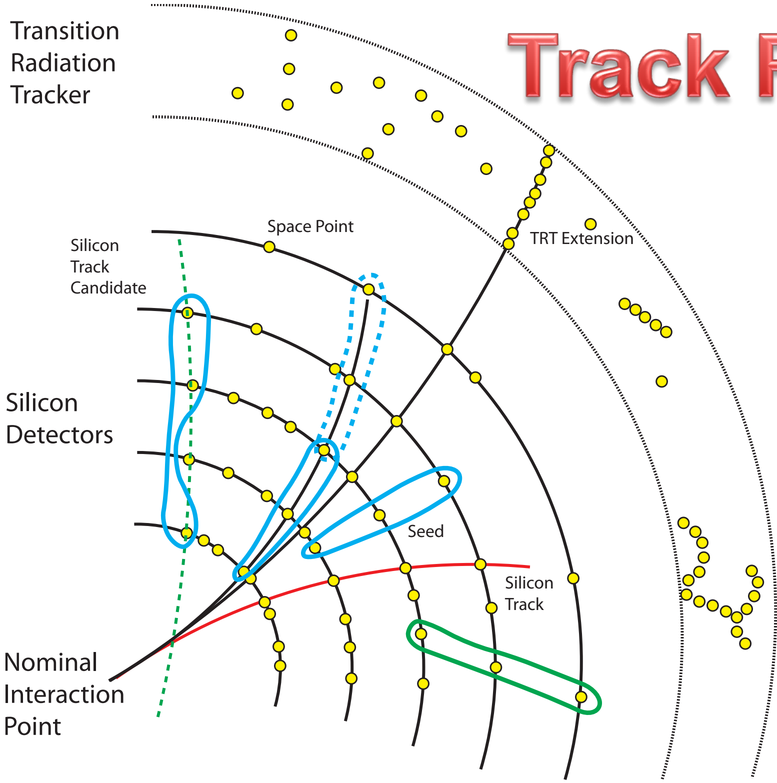

Inside-out

ATLAS

↓

Space Points

↓

Seed finding

↓

Track Candidates (Combinatorial Kalman Filter)

↓

Ambiguity solving

↓

TRT Extension

Track Reconstruction

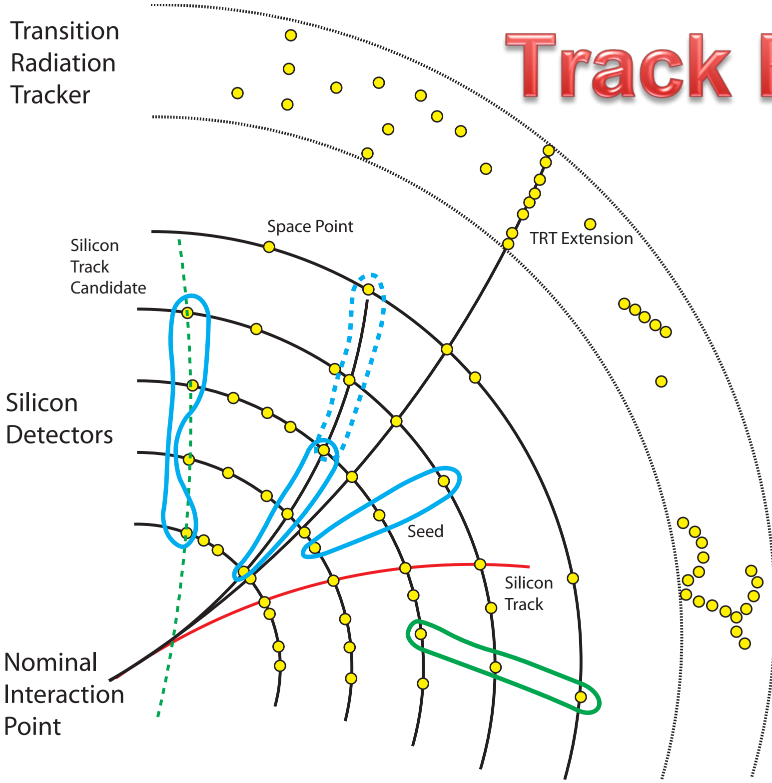

Inside-out

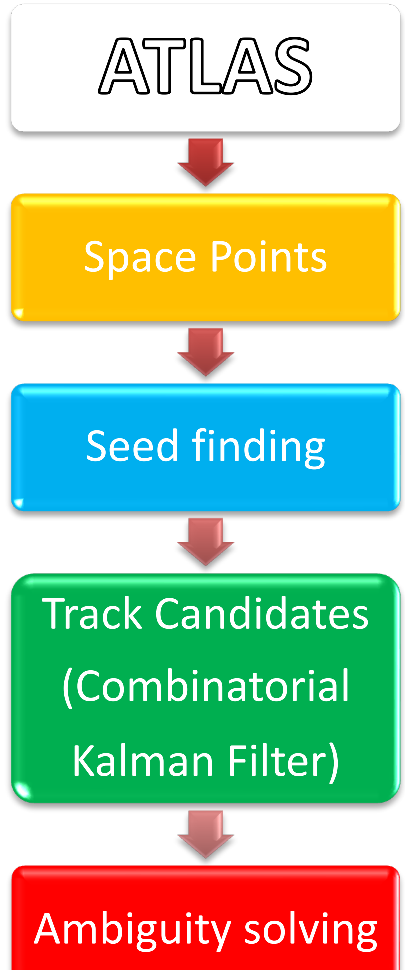

Quite a lot of reconstruction time spent here, and it scales dramatically with pile-up

ATL-PHYS-PUB-2019-041

Detector	$\langle\mu\rangle$	Cluster Finding	Space Points	Si Track Finding	Ambiguity Resolution	TRT+Back Tracking	Primary Vertex	Total ITk/ID
ITk Layout	200	22	6.5	78	97	-	6	219
Run-2	20	1.5	0.7	23	15	19	0.5	64

Track Reconstruction

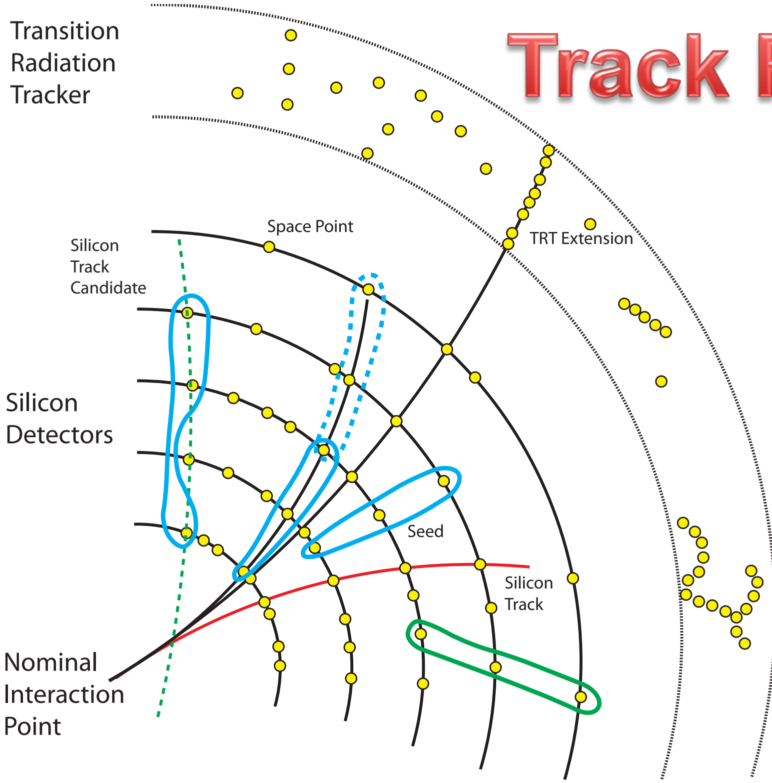

Inside-out

ATLAS

Space Points

Seed finding

Track Candidates (Combinatorial Kalman Filter)

Ambiguity solving

TRT Extension

Outside-in By default, enabled only in ROIs

Seed finding

Track Candidates (Combinatorial Kalman Filter)

Ambiguity solving

Track Reconstruction

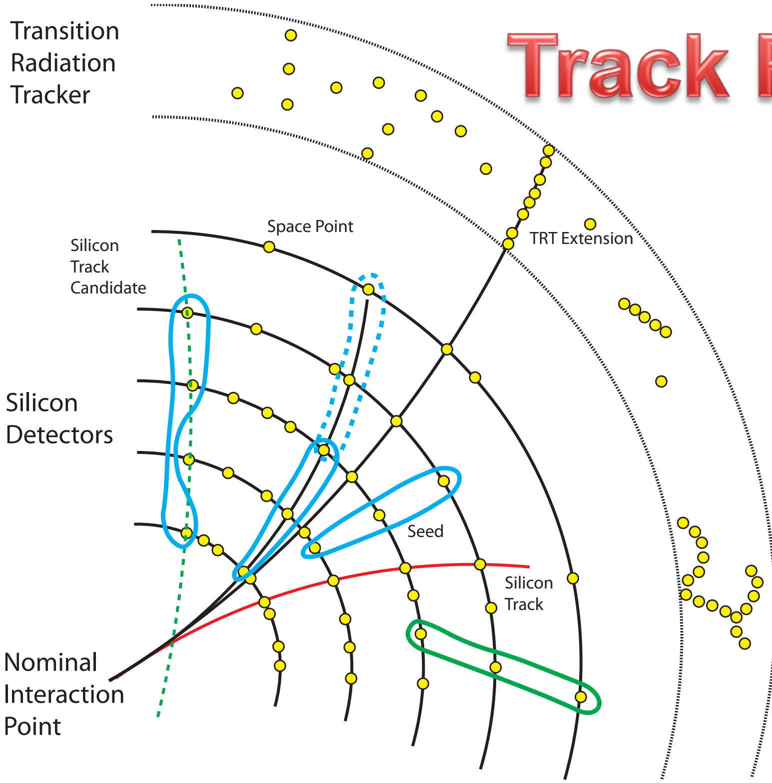

Inside-out

ATLAS

Space Points

Seed finding

Track Candidates (Combinatorial Kalman Filter)

Ambiguity solving

TRT Extension

Outside-in

Seed finding

Track Candidates (Combinatorial Kalman Filter)

Ambiguity solving

Specials

Large impact parameter tracks

Electron tracking

Pixel Tracklets

Impact parameter resolution

The transverse and longitudinal impact parameters, d_0 and z_0 respectively, are important to discriminate tracks originating from primary vertices from tracks originating from secondary vertices

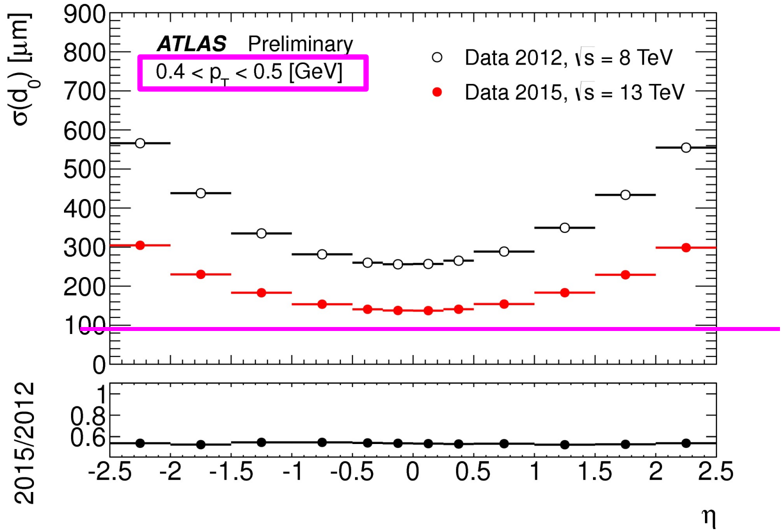

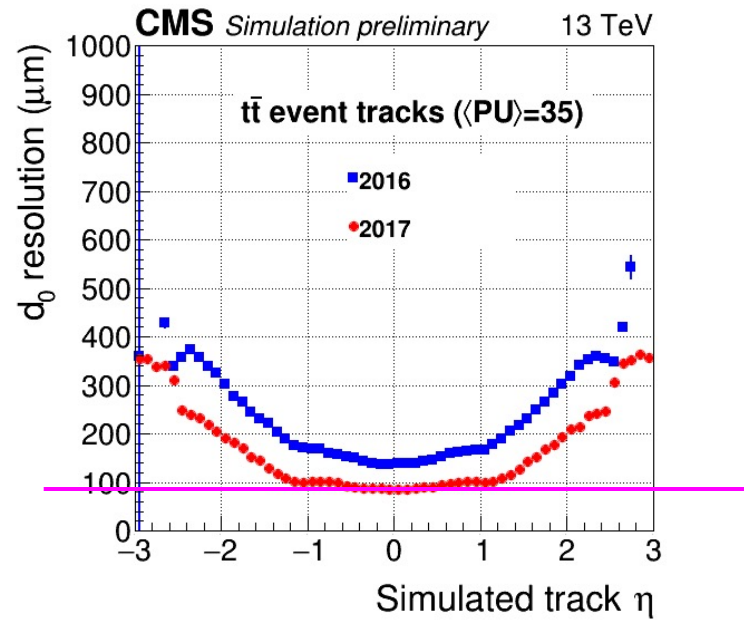

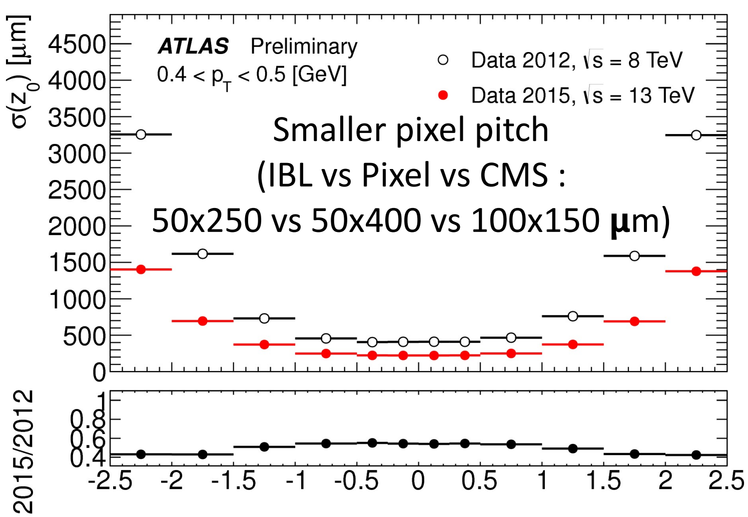

Smaller pixel pitch

(IBL vs Pixel vs CMS :

50x250 vs 50x400 vs 100x150 µm)

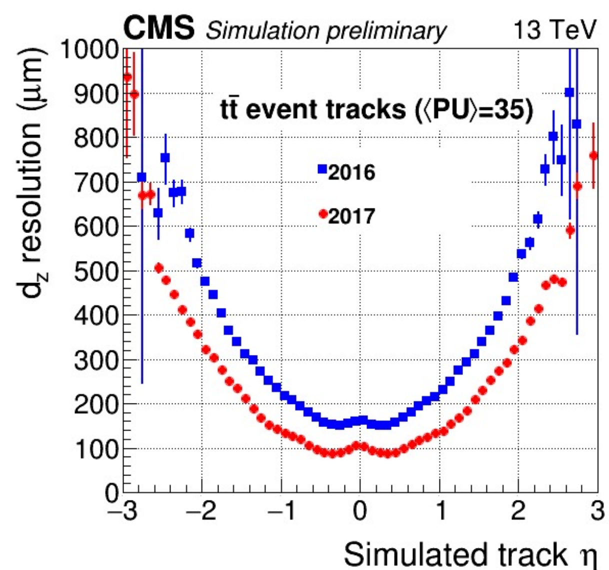

Primary Vertex Reconstruction for Run 3

Run 2 → **Run 3** : main innovation is an adaptive **multi-vertex** fitting procedure (**AMVF**)

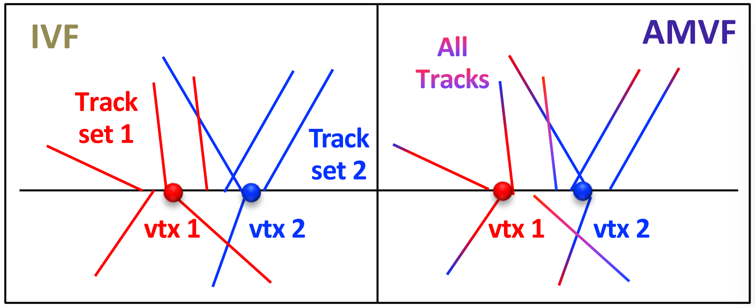

Significant performance improvements:

~**10**% better vertex selection efficiency

~**20**% better longitudinal resolution

~**30%** inclusive efficiency recovery

All relevant for **the HL-LHC ATLAS silicon Inner Tracker (ITk)**

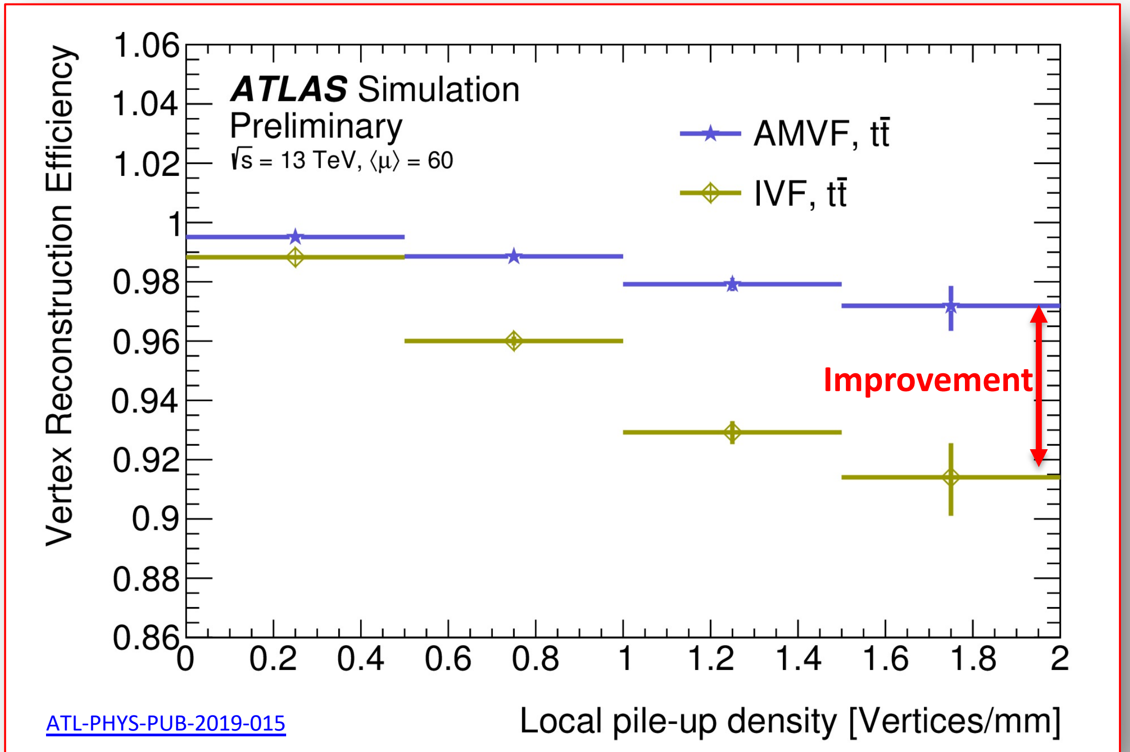

ATL-PHYS-PUB-2019-015

Performance Figures

Performance figures for vertex reconstruction are:

- **Merging probability**
  - Longitudinal separation between nearby vertices is an indicator of the ability in resolving vertices

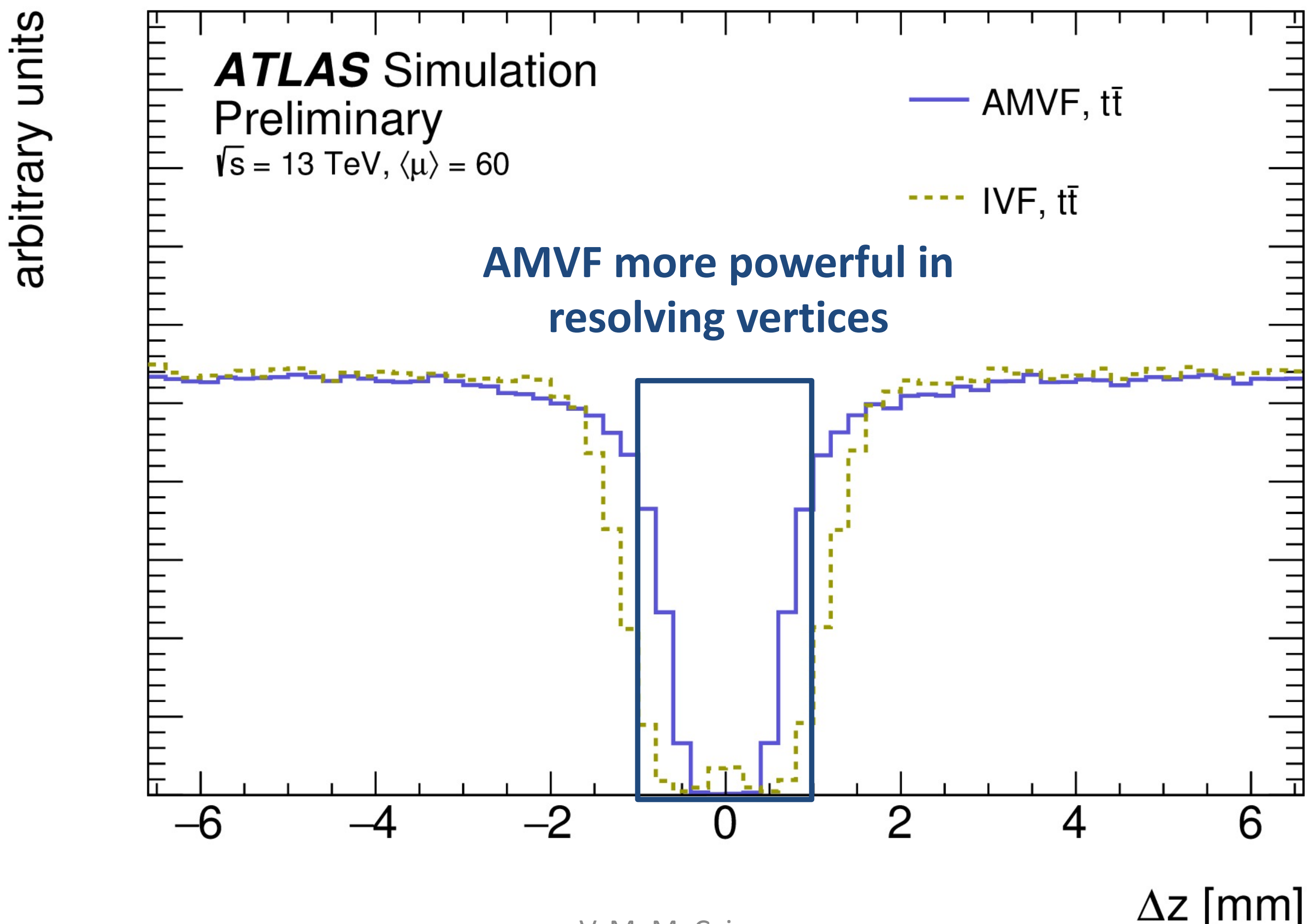

Performance Figures

Performance figures for vertex reconstruction are:

- **Efficiency**
  - **Reconstruction**: Fraction of events in which the hard scatter vertex is reconstructed and classified as Clean/Matched, LowPU and HighPU (see extra slides for details)
  - **Selection**: Fraction of events in which the highest SumPt2 vertex contains the largest total weight from the true HS tracks

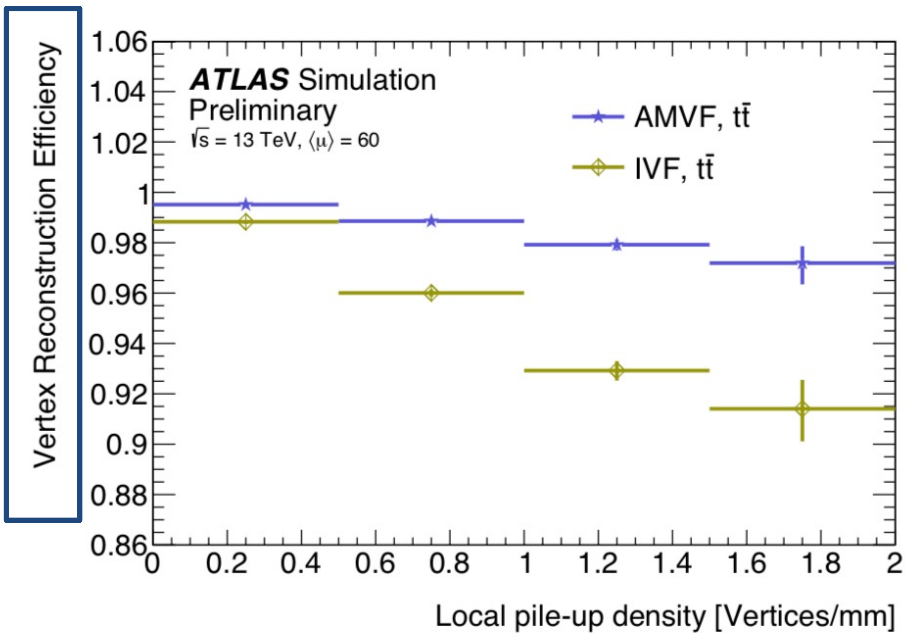

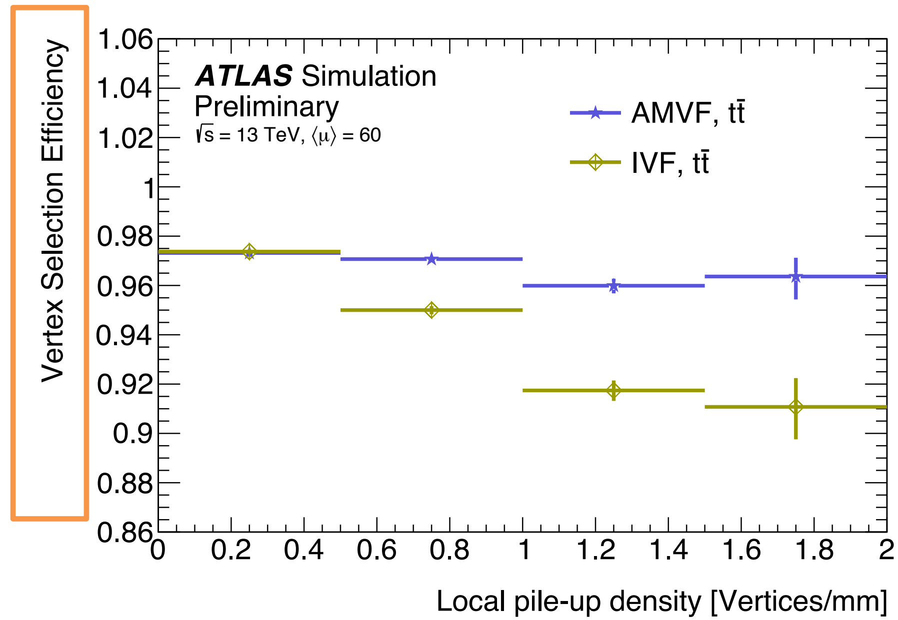

The AMVF improves the reconstruction efficiency for ttbar, in particular at high PU

The AMVF improves the selection efficiency for ttbar reducing the dependence on pile-up density

Performance Figures

Performance figures for vertex reconstruction are:

- **Spatial resolution**
  - Radial and longitudinal radial resolution calculated as the difference between the true and the reconstructed vertex position

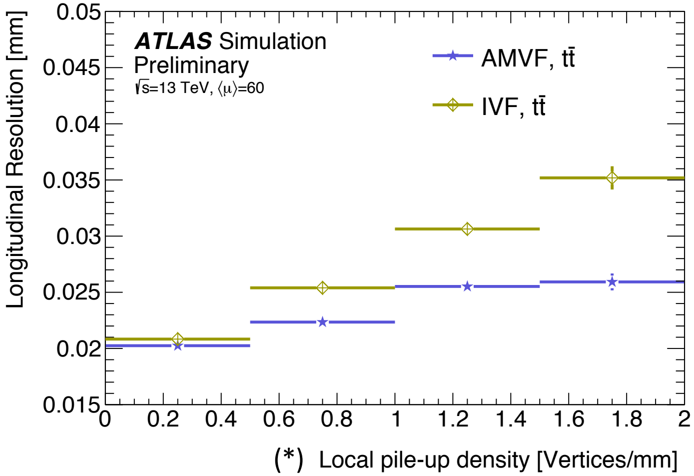

In the *z* direction, the **AMVF achieves 20% (10%) better resolution for ttbar (VBF *H* → 4ν).**

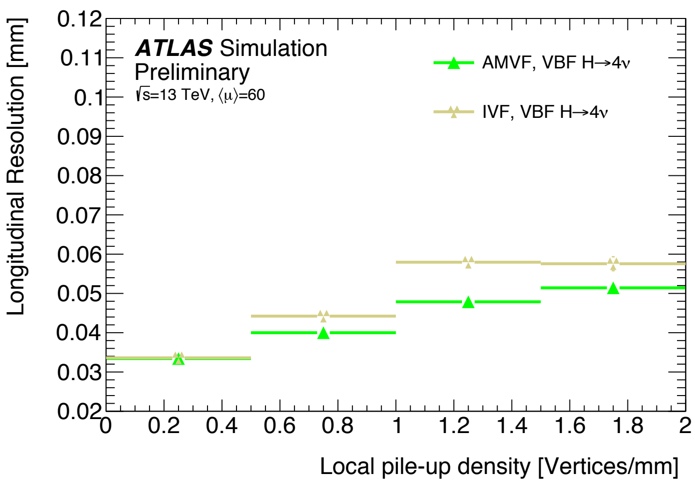

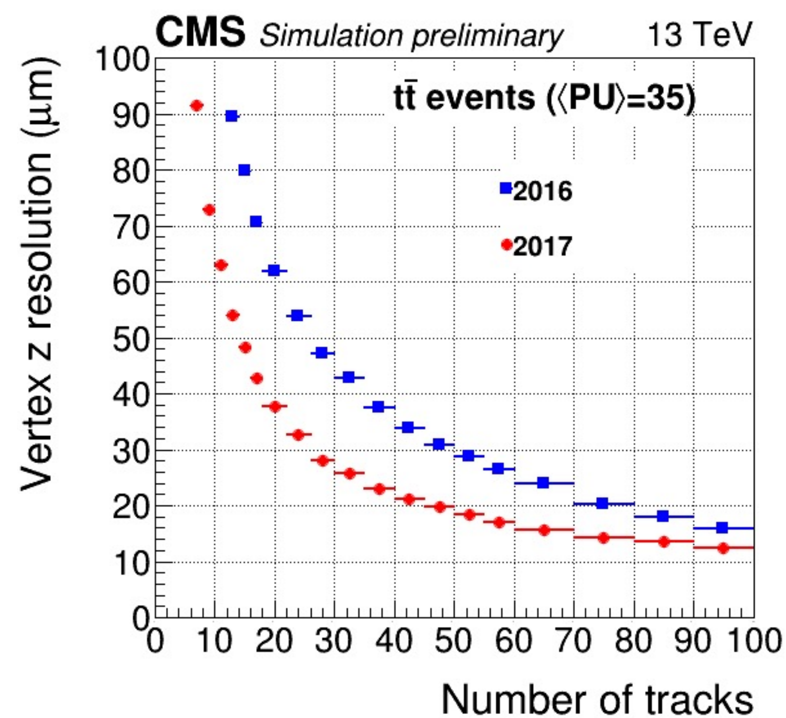

(*) number of generated vertices per unit length within a symmetrical ±2 mm longitudinal window.

Truth Matching Definitions

To study the performance of primary vertex reconstruction using MC simulation, a truth-matching algorithm is needed, based on the generator-level particles associated to tracks contributing to reconstructed vertices.

Reconstructed Vertices classification

CLEAN: >70% of the total track weight in the reconstructed vertex originates from a single simulated *pp* interaction.

MERGED: <70% of the total track weight in the reconstructed vertex originates from any single simulated *pp* interaction

SPLIT: A single simulated *pp* interaction contributes the largest track weight to two or more reconstructed vertices. The reconstructed vertex with the largest track Σp^2_T is classed as either CLEAN or MERGED, whilst the other(s) are labelled SPLIT.

FAKE: Fake tracks contribute more weight to the reconstructed vertex than any simulated *pp* interaction.

Event Classification

CLEAN/MATCHED: the event contains a CLEAN reconstructed vertex originating from the true HS interaction, and the HS interaction does not contribute more than 50% of the accumulated track weight to any other vertex.

LOWPU: the event contains a MERGED vertex with at least 50% of the accumulated track weight coming from the simulated HS interaction.

HIGHPU: the event contains a MERGED vertex with its main contribution coming from a simulated pile-up interaction, and in which the HS interaction contributes between 1% and 50% of the accumulated track weight.

PUREPU: The event does not contain any reconstructed vertex with at least 1% accumulated track weight from the HS interaction.

Primary Vertex Selection

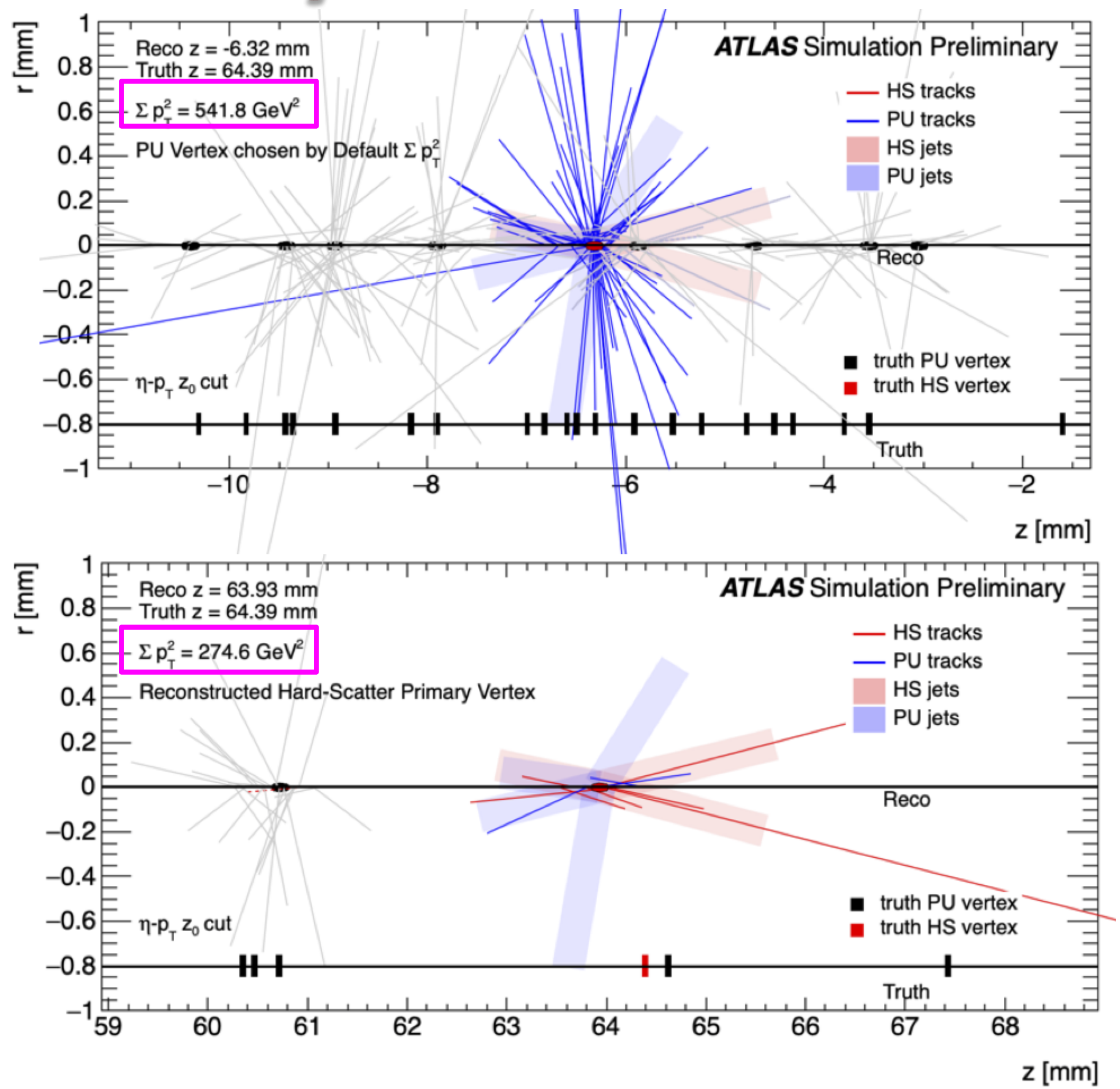

Pile up vertex harder than vertex of interest, wrongly selected by $\sum p_T^2$

Primary Vertex Selection

$$\mathrm{sumPT} = \sum_{\mathrm{tracks}} p_{\mathrm{T}}^2 \longrightarrow \mathrm{sumPTw} = \sum_{\mathrm{tracks}} p_{\mathrm{T}_w} = \sum_{\mathrm{tracks}} p^2_{\mathrm{T(track)}}\, p^2_{\mathrm{T(closest\ jet)}} \frac{1}{\Delta R} 1(\Delta R < 0.4) 1(p_{\mathrm{T(jet)}} > p_{\mathrm{T(threshold)}})$$

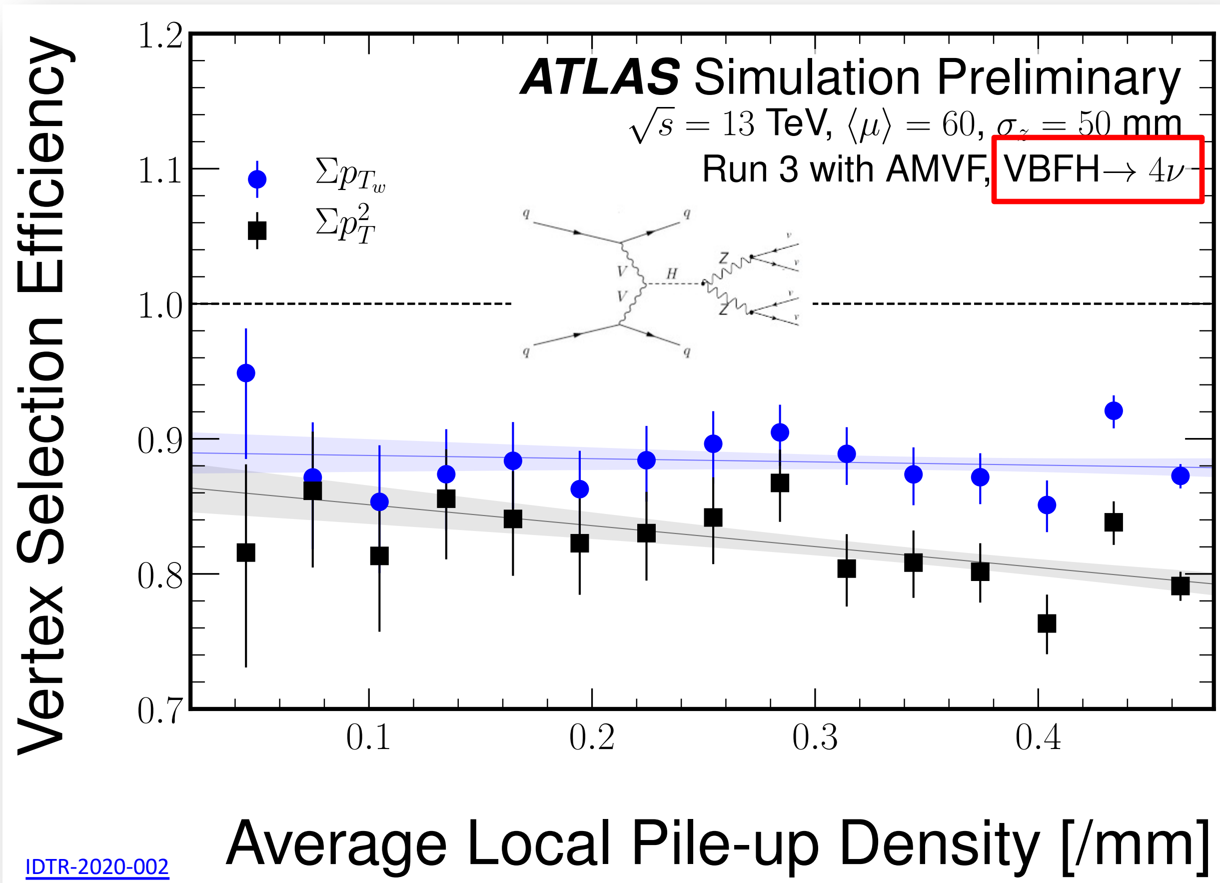

Benefits even more from the forward ITk acceptance…

The Modernization Phase

ATLAS Tracking & Vertexing infrastructure gave the basis to
A Common Tracking Software

http://acts.web.cern.ch/ACTS/

- **Open-source and detector independent platform for tracking & vertexing algorithms R&D**
- Collaboration across experiments + ML experts

Primary Vertex Reconstruction for Run 3

Run 2 → Run 3 : single iterative → **adaptive multi-vertex** fitting procedure (**AMVF**)

- All selected tracks available for fitting
  - Vertex candidates compete for tracks

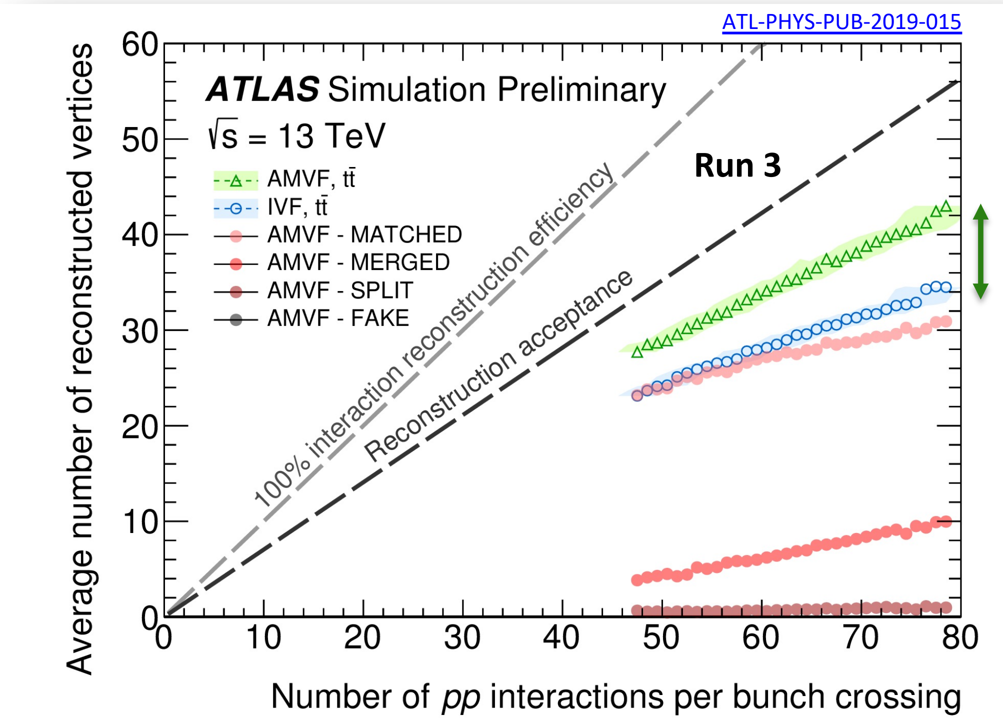

- ~**30% inclusive** efficiency recovery
- **~10%** better PV selection efficiency
- **~20%** better longitudinal resolution
- **Direct improvement** in **JetFitter**
- First deployed **ACTS** component

Being re-tuned for **the new ATLAS silicon Inner Tracker (ITk)**

Vertex Reconstruction

Run 2 → **Run 3** : from **single iterative** to **multi-vertex** fitting procedure (**AMVF**)

$$\omega_i(\chi_i^2, T) = \frac{e^{-\frac{1}{2}\chi_i^2/T}}{\sum_j e^{-\frac{1}{2}\chi_j^2/T} + e^{-\frac{1}{2}\chi_0^2/T}}$$

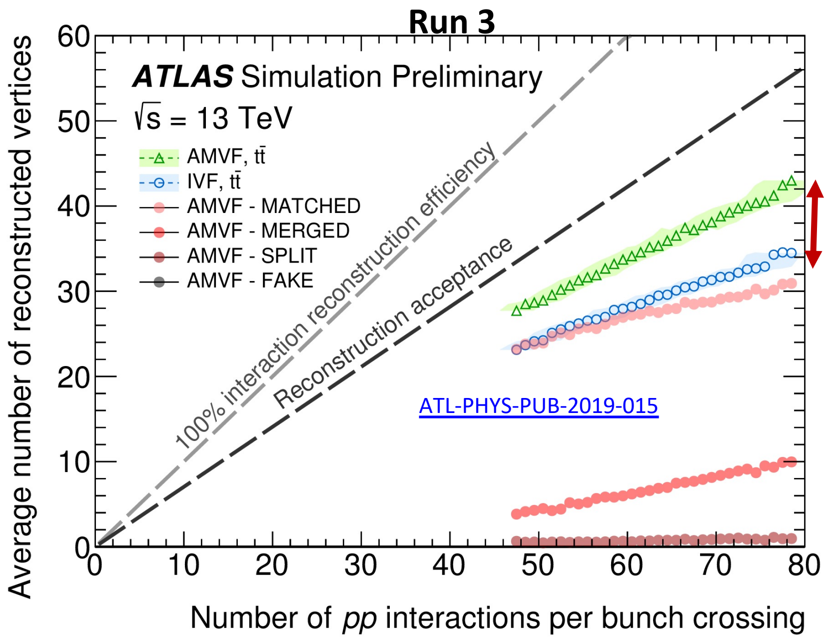

- ~**30% inclusive** efficiency recovery
- ~**10%** better vertex selection efficiency
- ~**20%** better longitudinal resolution
- Improved overall PU robustness, currently being re-tuned for ITk

First piece of *ACTS* included in the ATLAS: execution time **2x as fast**!

Opens-up opportunities for **new vertexing ideas in a flexible and detector independent way**...

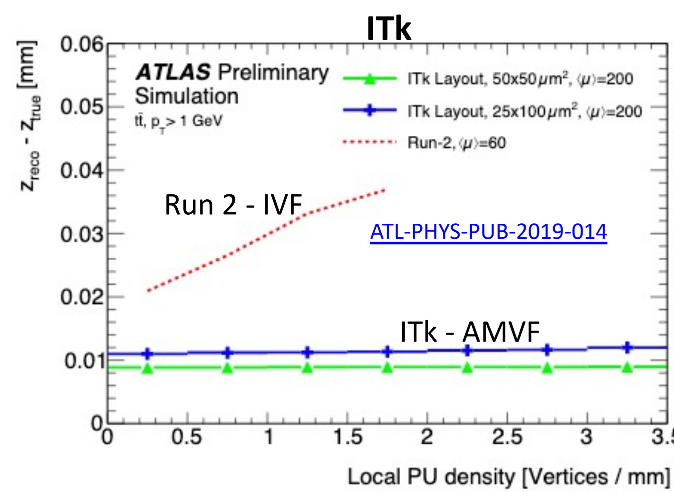

ACTS Vertexing

https://atlas.web.cern.ch/Atlas/GROUPS/PHYSICS/PLOTS/IDTR-2021-002/

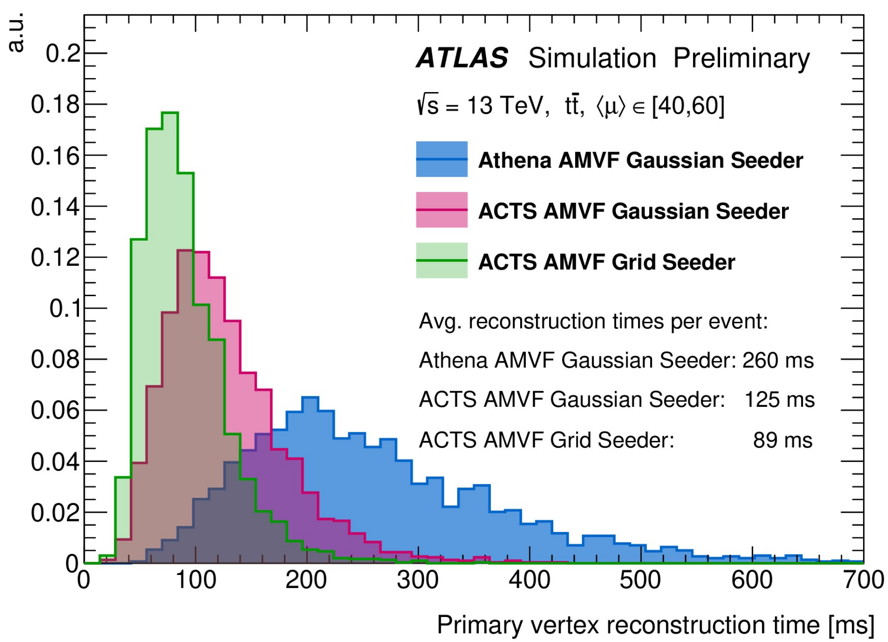

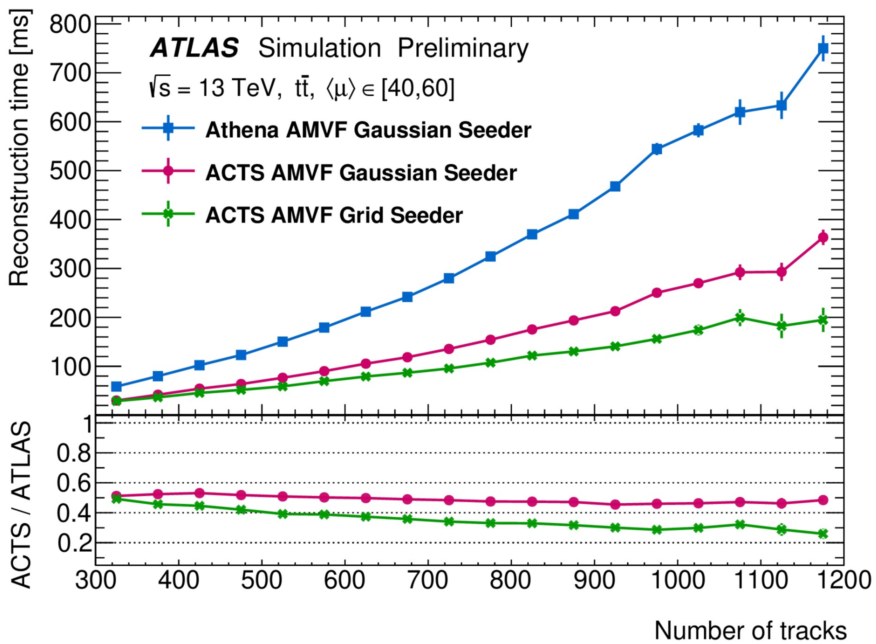

HGTD Impact

https://cds.cern.ch/record/2773619/files/ATL-COM-HGTD-2021-010.pdf?version=5

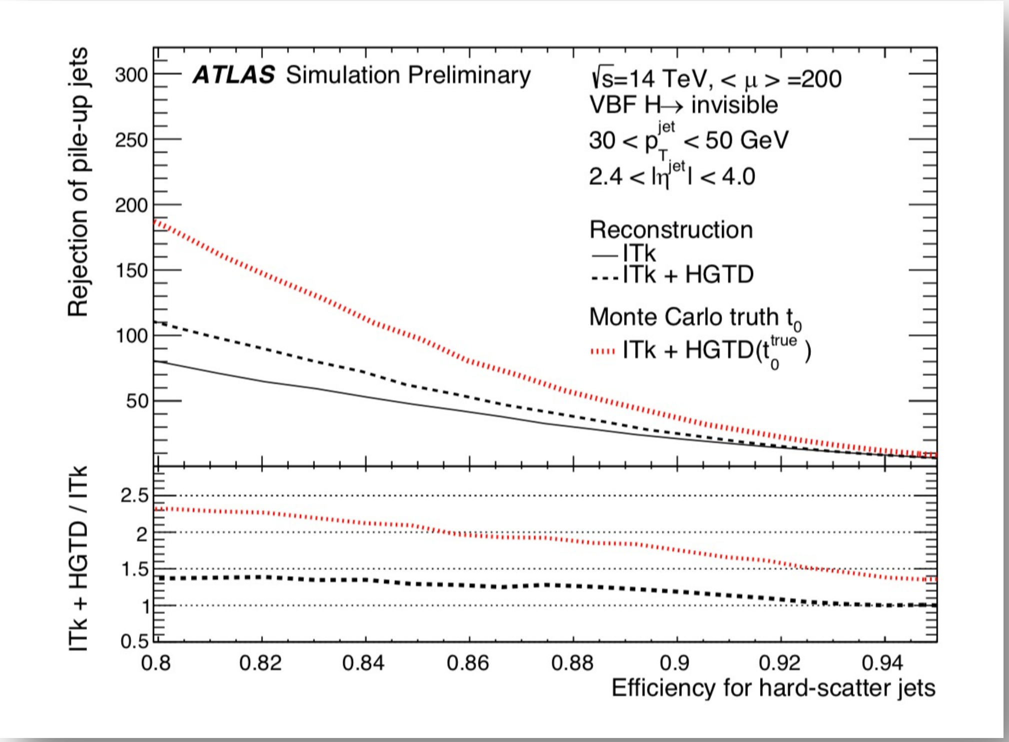

Rejection of pileup jets as a function of the efficiency for selecting hard-scatter jets with $30 < p_T < 50$ GeV using the R_{pT} discriminant in VBF H → invisible events with an average of 200 pile-up collisions per bunch crossing. The R_{pT} algorithm computes the ratio of track p_T within a jet to the fully calibrated jet p_T. Jets originating from the hard-scatter vertex have larger R_{pT} on average than those from pileup interactions. Typical working points use 85% of efficiency for hard-scatter jets. In order to compute the numerator of R_{pT}, tracks are required to be compatible with the hard-scatter vertex. The track-to-vertex association can be computed using the longitudinal impact parameter (z_0) with the tracker detector alone (ITk) or by combining it with the HGTD using the reconstructed time of the tracks (t) in addition to their impact parameter. In the case of ITk, the track-to-vertex association is performed by comparing the track z_0 to the z position of the hard-scatter vertex. For HGTD, the reconstructed time of the tracks are compared to the reconstructed time t_0 of the hard-scatter vertex.

In order to evaluate the impact that the reconstruction of the vertex t_0 has on the pileup jet suppression, this figure considers the case in which the reconstructed vertex t_0 is replaced by the Monte Carlo truth t_0. This gives an indication of the maximum (ideal) performance that could be achieved, as well as the effect of the current algorithm used to determine the vertex t_0 on the pileup jet identification performance. There are two sets of curves (black and red). The black curves use reconstructed quantities only and show the pileup suppression performance using ITk alone (solid) and the combined ITk and HGTD detectors (dashed) as it is shown in the HGTD TDR. The ITk+HGTD performance depends on the ability to reconstruct t_0, which includes both the efficiency to find a vertex t_0 in the event, and on its resolution. The red fine-dashed line was obtained using the Monte Carlo truth t_0 instead of the reconstructed t_0, indicating the ultimate (ideal) performance achievable under perfect efficiency and resolution to determine the vertex t_0.

Detector

The ITk Pixel System

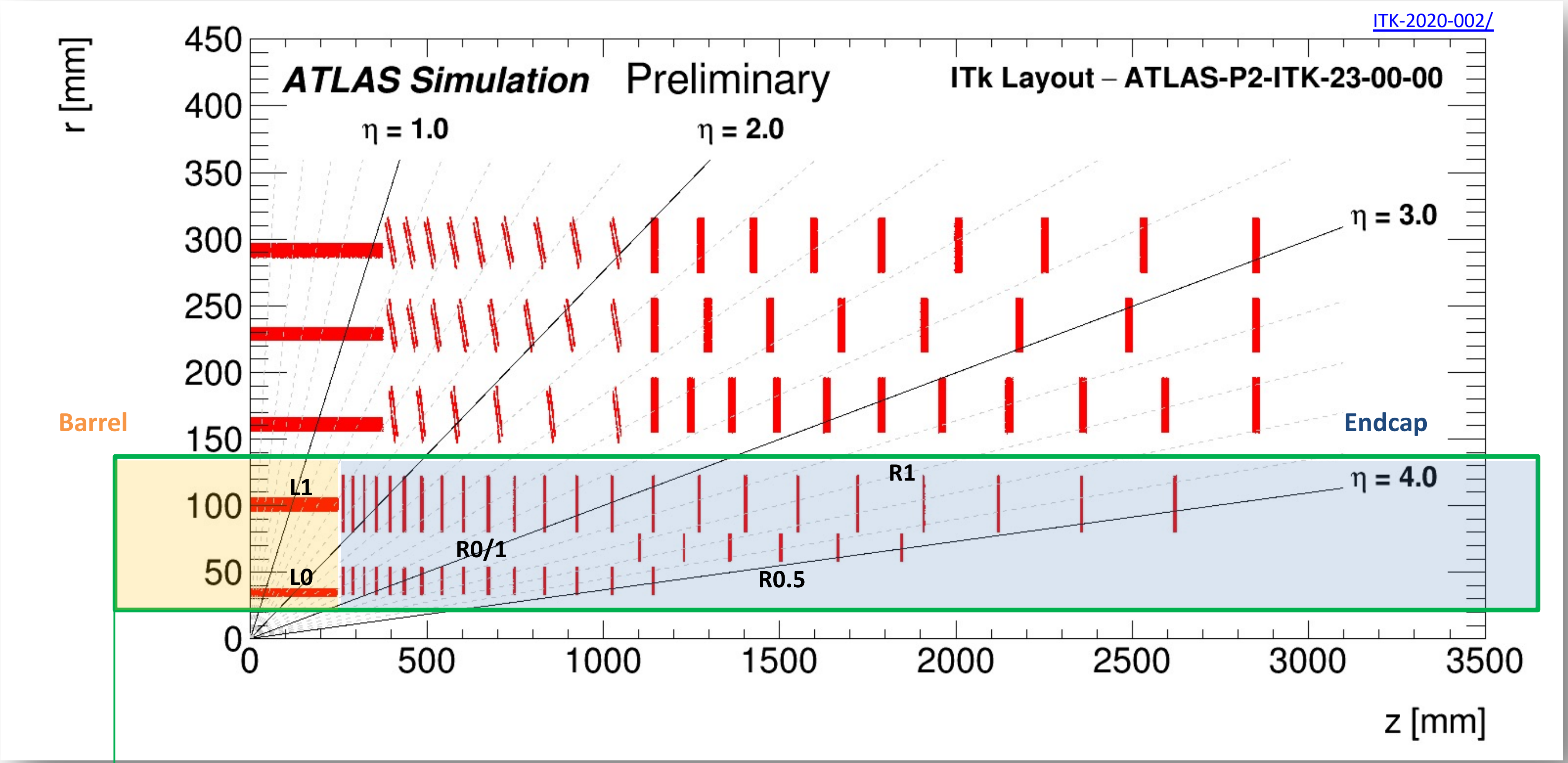

Inner System

Detector Part	Surface [m^2]
Inner Barrel Flat	0.48
Endcap Inner Rings	1.77
Inner Total	2.26

SLAC

is the Inner System (IS) Assembly & Integration

The Prototyping phase

Validate Local Support design and loading procedure

Thermo-mechanical prototype

- Load with dummy modules
  - silicon heaters with platinum coating
    - power to dissipate 0.7 W/cm^2 (chip end-of-life)
    - measure *Thermal Figure of Merit*
- R0/1 coupled ring and L0 stave

Heaters

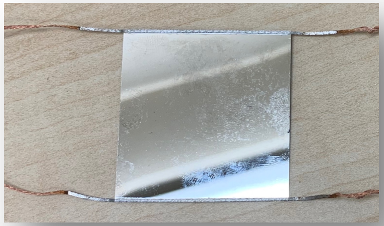

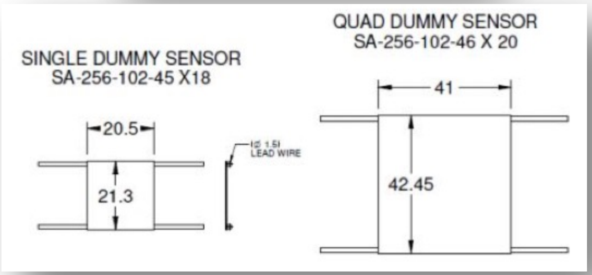

Electrical prototype

- Load with RD53A modules
- R0/1 coupled ring, L0 stave, L1 stave

Validate Local Support design and loading procedure

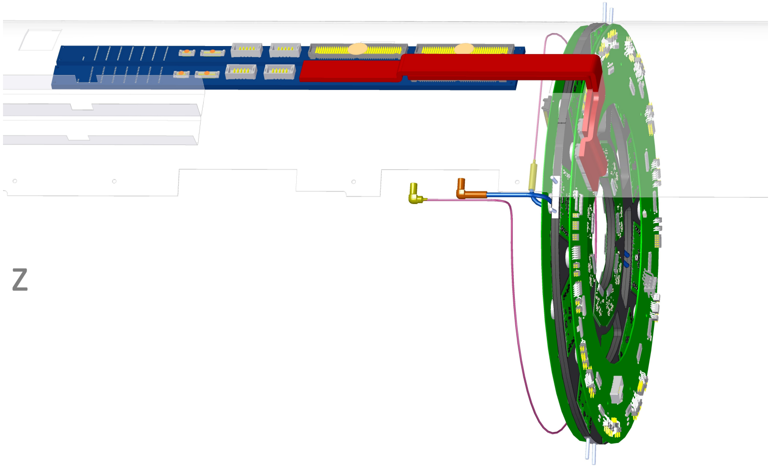

Integration prototypes

- Integrate electrical prototype in quarter shell at low z
- Integrate additional stave/ring flavors

The Prototyping phase

Thermo-mechanical characterization

- **Radiation hardness up to** 10-15 MGy, **operate cold**, prevent leakage current & thermal runaway

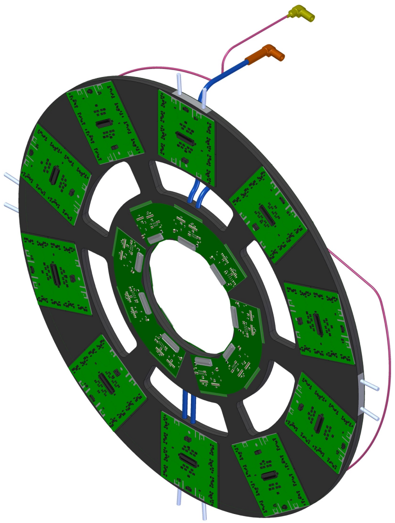

R0/1

coupled

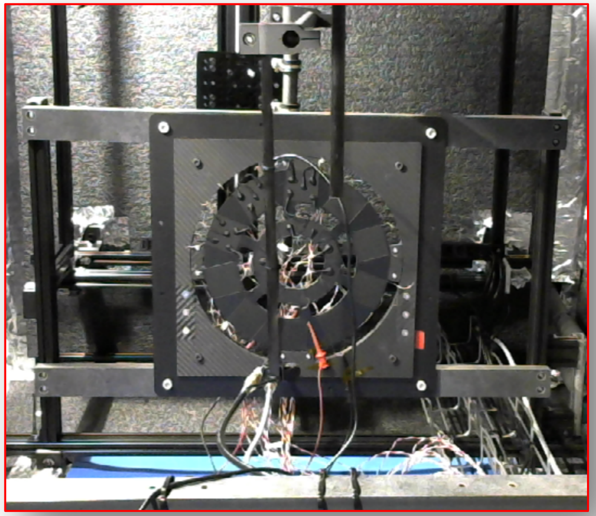

Lessons from the past…

- Every small detail in construction plays a role later on in performance
- **Large amount of material in the tracker from Pixel services and cooling**
- Estimated a priori, but requires data-driven methods during actual operation
- **Many lessons learned after IBL installation**
  - Hadronic interactions & photon conversions
  - Track extension efficiency

ITK-2019-001

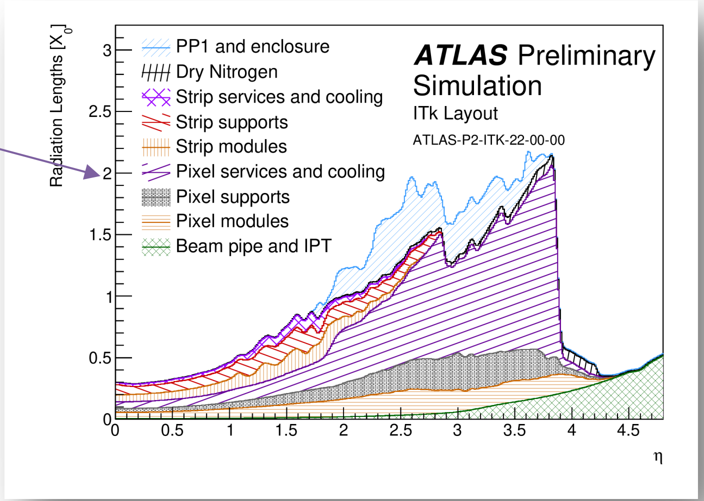

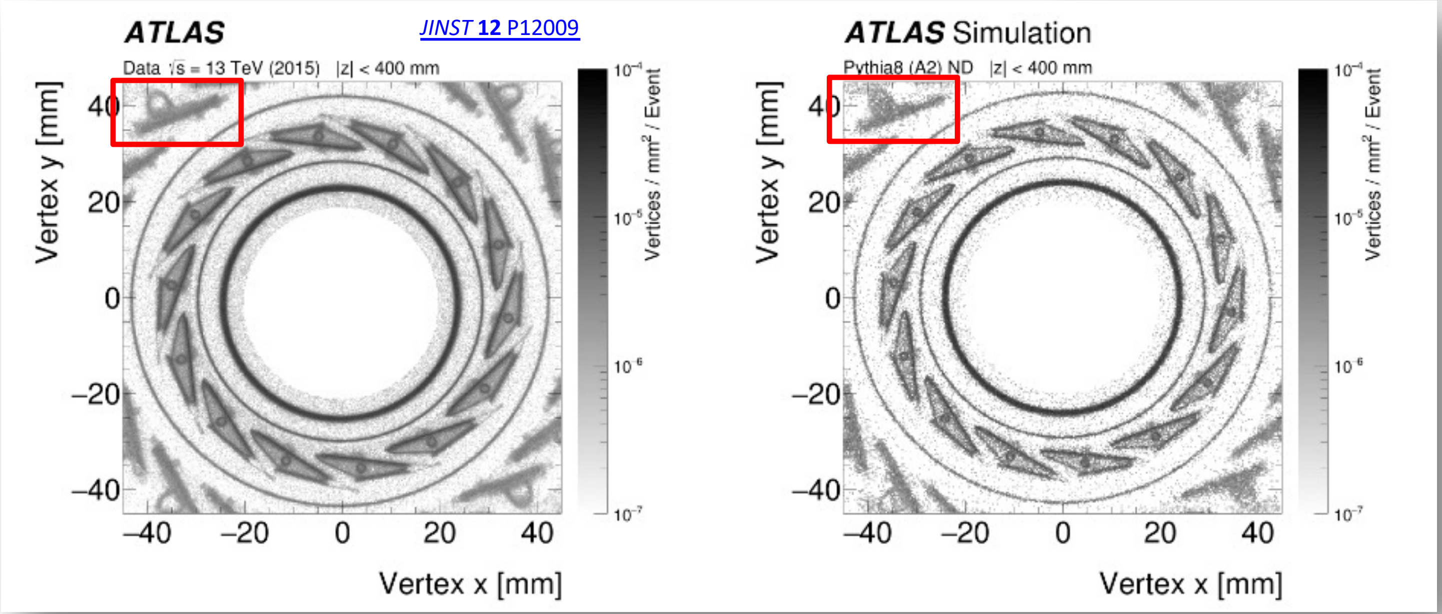

Cooling fluid incorrectly modelled in simulation

Lessons from the past…

- Every small detail in construction plays a role later on in performance
- **Large amount of material in the tracker from Pixel services and cooling**
- Estimated a priori, but requires data-driven methods during actual operation
- Many lessons learned after IBL installation
  - Hadronic interactions & photon conversions
  - Track extension efficiency
- **Largest source of uncertainty for track reconstruction**

ITK-2019-001

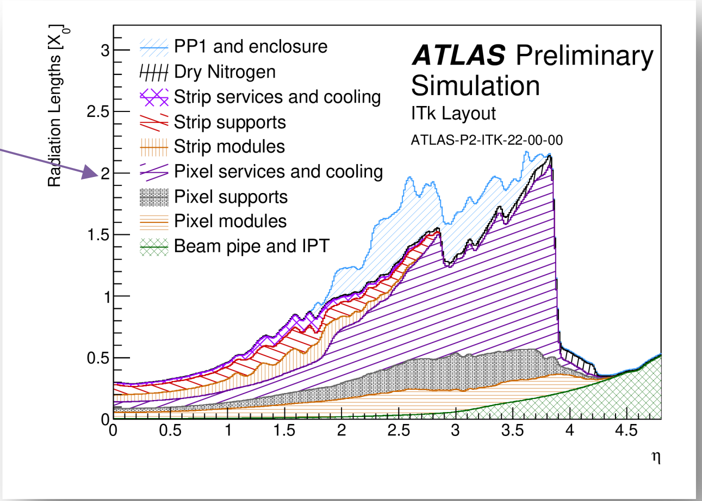

JINST **12** P12009

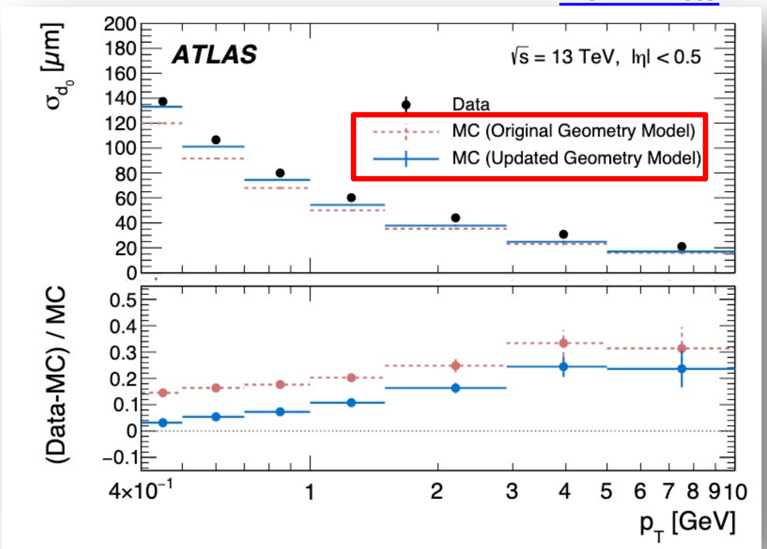

End of 2015

Track Reconstruction Efficiencies and Systematic Uncertainties				
Track Quality Selection	Loose		Tight Primary	
η Range	$\lvert\eta\rvert \leq 0.1$	$2.3 \leq \lvert\eta\rvert \leq 2.5$	$\lvert\eta\rvert \leq 0.1$	$2.3 \leq \lvert\eta\rvert \leq 2.5$
Track Reconstruction Efficiency	91%	73%	86%	63%
$\text{Sys}_{+5\% Extra}$	0.4%	0.9%	0.5%	1.1%
$\text{Sys}_{PixServExtra}$	—	2.0%	—	2.3%
$\text{Sys}_{+30\% IBLExtra}$	0.2%	0.5%	0.2%	0.5%
Total Systematic Uncertainty	0.4%	2.2%	0.5%	2.6%

Beginning of 2018

Updated (release 21) Track Reconstruction Efficiencies and Systematic Uncertainties				
Track Quality Selection	Loose		Tight Primary	
η Range	$\lvert\eta\rvert \leq 0.1$	$2.3 \leq \lvert\eta\rvert \leq 2.5$	$\lvert\eta\rvert \leq 0.1$	$2.3 \leq \lvert\eta\rvert \leq 2.5$
Track Reconstruction Efficiency	90%	71%	85%	61%
$\text{Sys}_{+5\% Extra}$	0.3%	1.0%	0.4%	1.2%
$\text{Sys}_{PixServExtra}$	—	1.1%	—	1.4%
$\text{Sys}_{IBLExtra}$	0.1%	0.2%	0.1%	0.1%
$\text{Sys}_{PhysModel}$	0.2%	0.1%	0.1%	0.1%
Total Systematic Uncertainty	0.4%	1.5%	0.5%	1.8%

Inner Trackers

- **Crucial components** in the event reconstruction chain
  Unprecedented challenges from **increasing pile-up**

- **Algorithms' optimization** and **detector construction** go hand-in-hand
  - **Constructability** and **optimal performance** must be ensured
    - **Material-budget is critical**
    - **Systematic effects propagate to all reconstructed objects (e.g. converted photons)**

- About **5 years to go** before the start of the **HL-LHC phase**
  - Building the trackers is **a major deliverable for ATLAS & CMS**
  - **Lessons from the past** are to be taken into account
    - The early operation phase will open opportunity for exciting **track- and vertex- based analysis!**

Barrel and Endcap Features

Barrel Staves

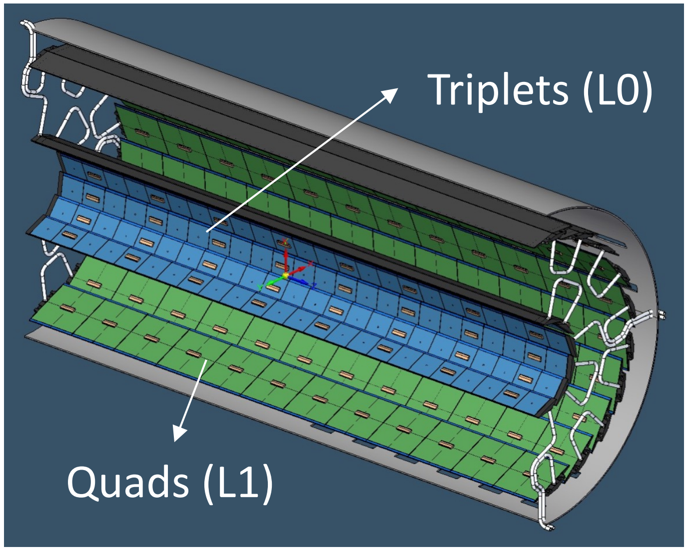

Quads (L1)

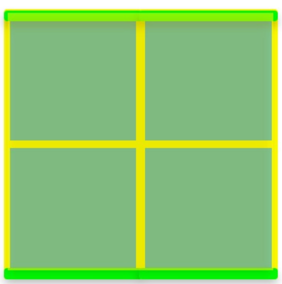

Triplets (L0)

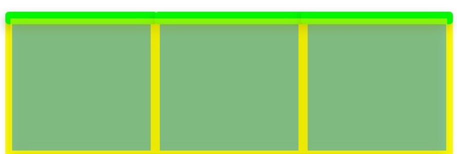

Endcap Rings

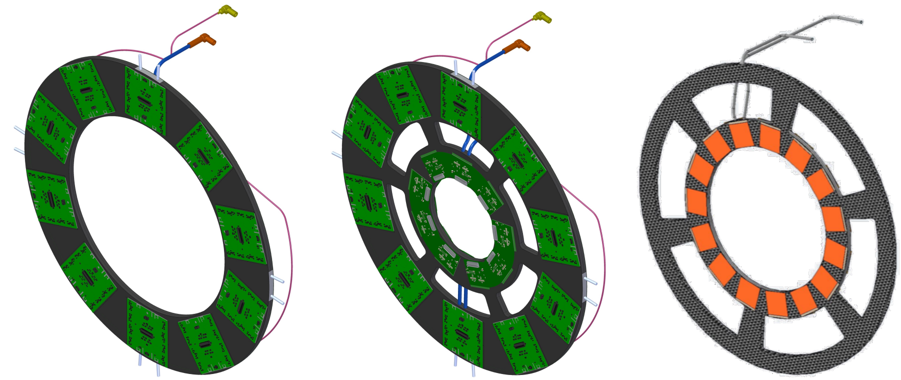

R1

R0/1
coupled

R0.5
intermediate

Quads (R1 & R0/1)

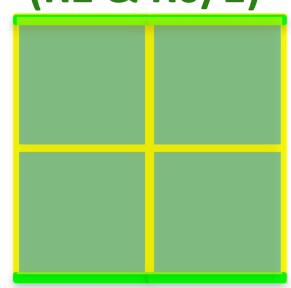

Triplets (R0.5 & R0/1)

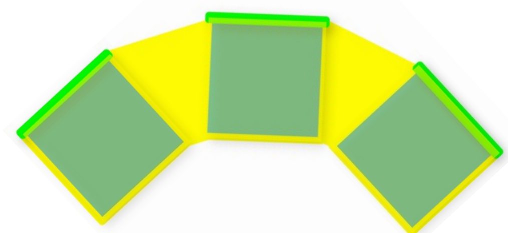

Testing Infrastructure

Will accommodate thermal and electrical testing

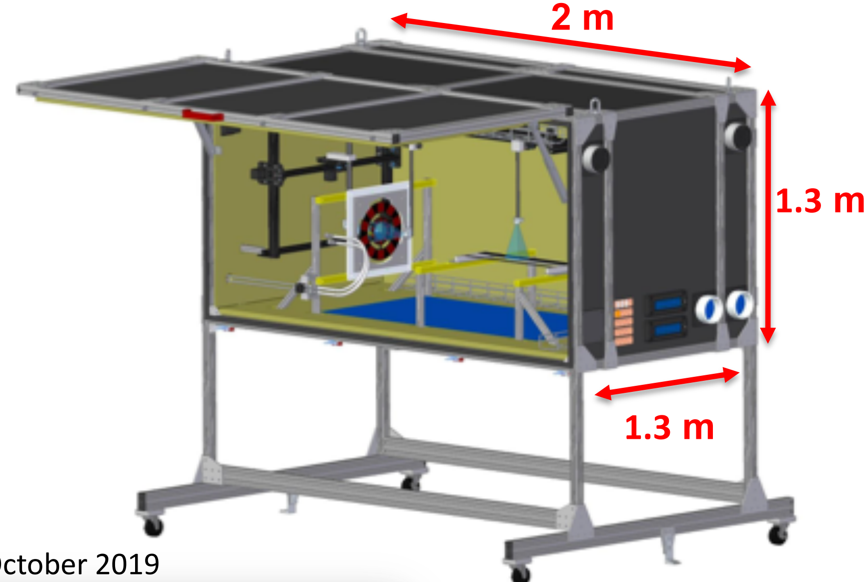

October 2019

January 2020

July 2020

Testing Infrastructure

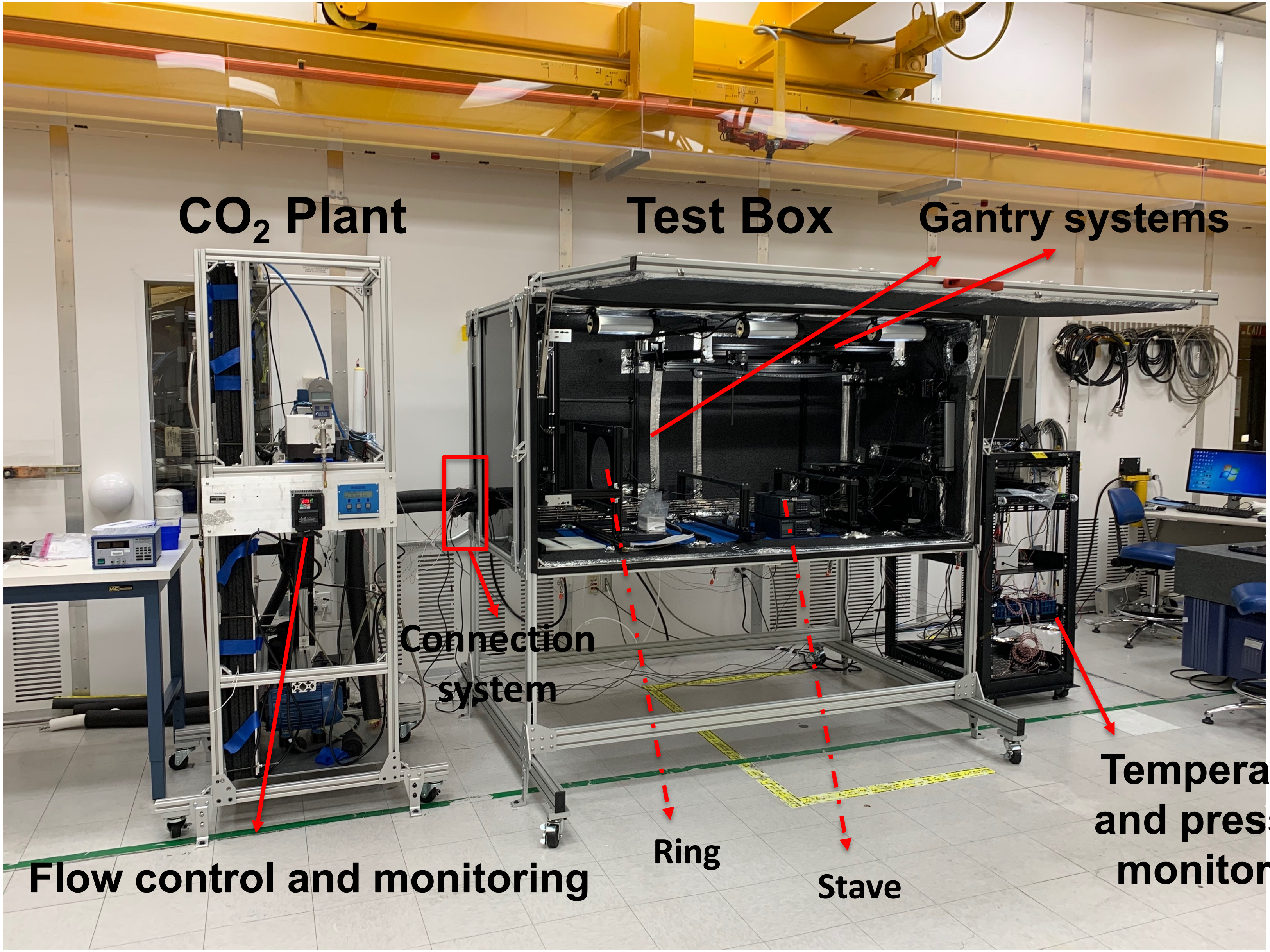

Testing the Bare Local Support

- **Bare local support** (R0/1) **tested in July 2020** - to be used for **thermo-mechanical prototype**
- Ongoing work on loading it with heaters

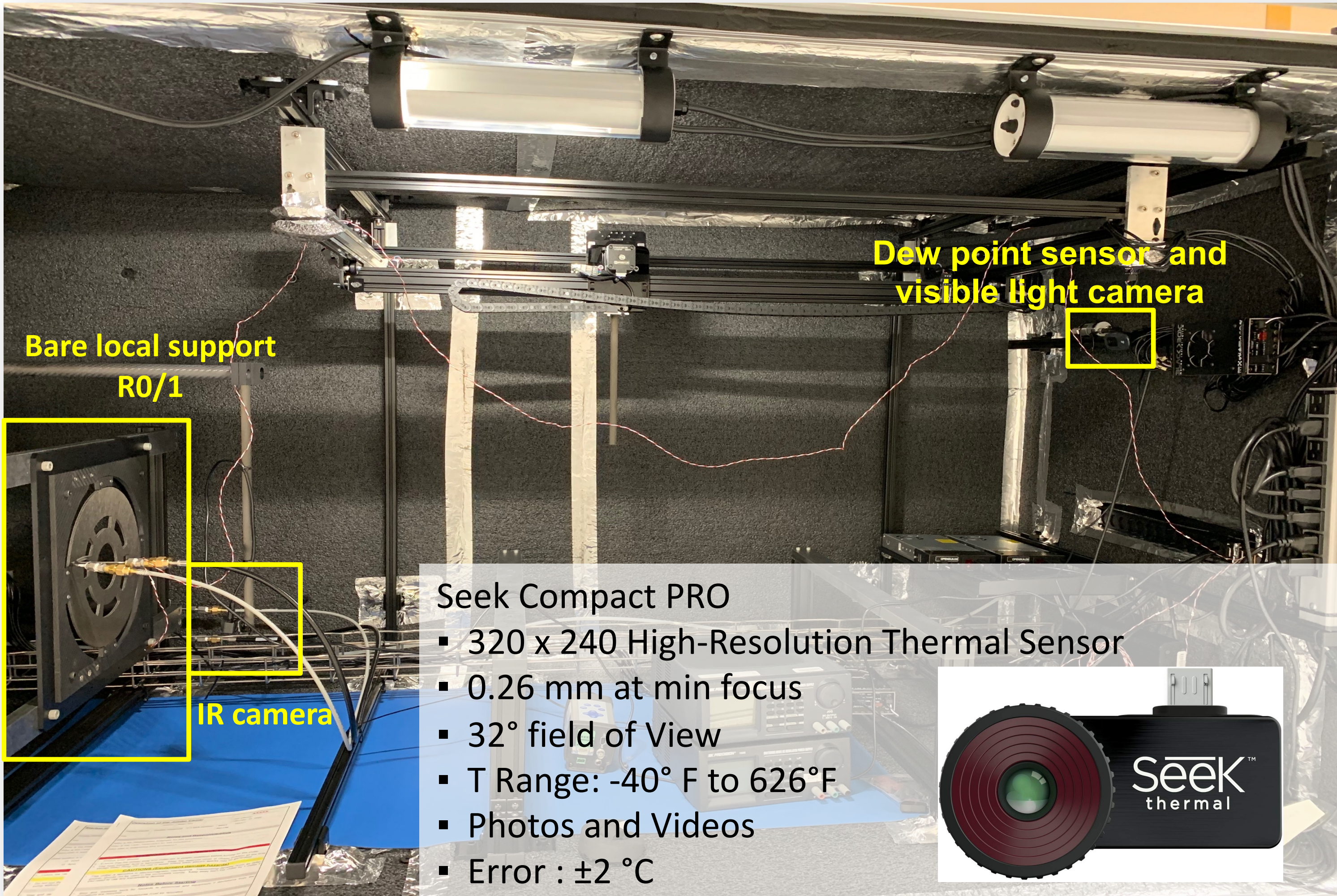

Testing the Bare Local Support

- **Bare local support** (R0/1) **tested in July 2020** - to be used for **thermo-mechanical prototype**
- Ongoing work on loading it with heaters

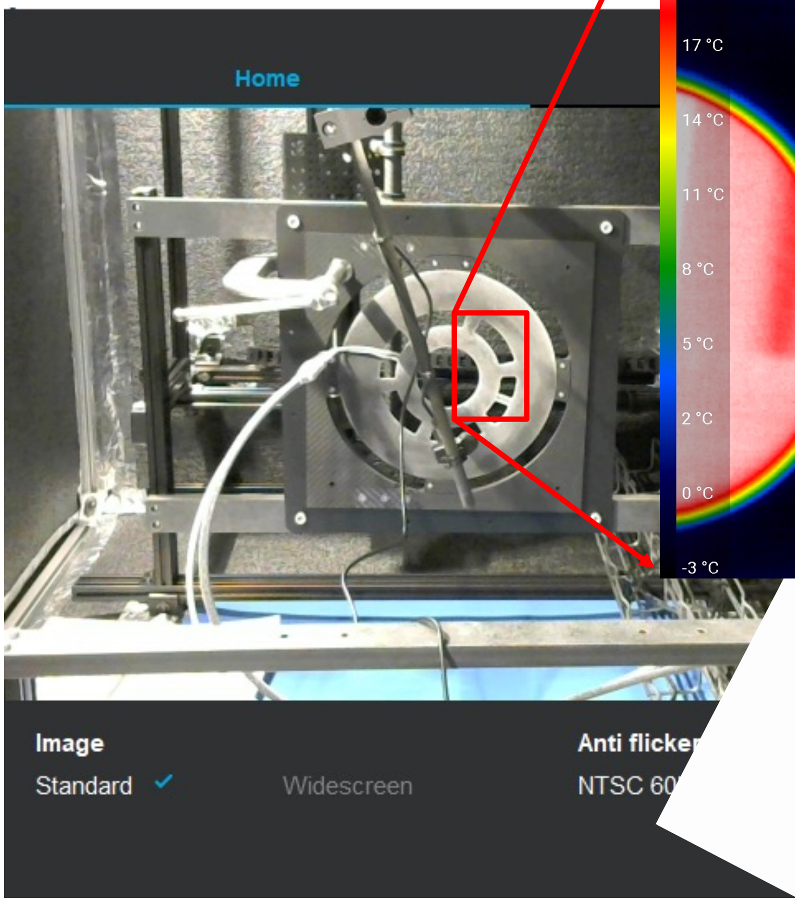

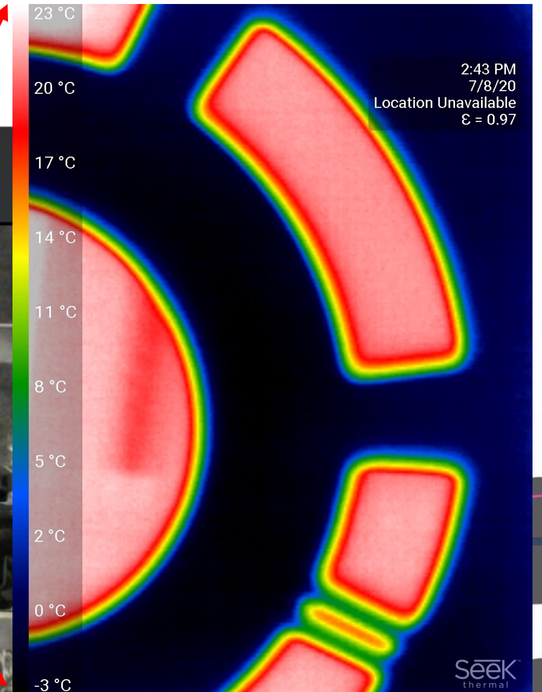

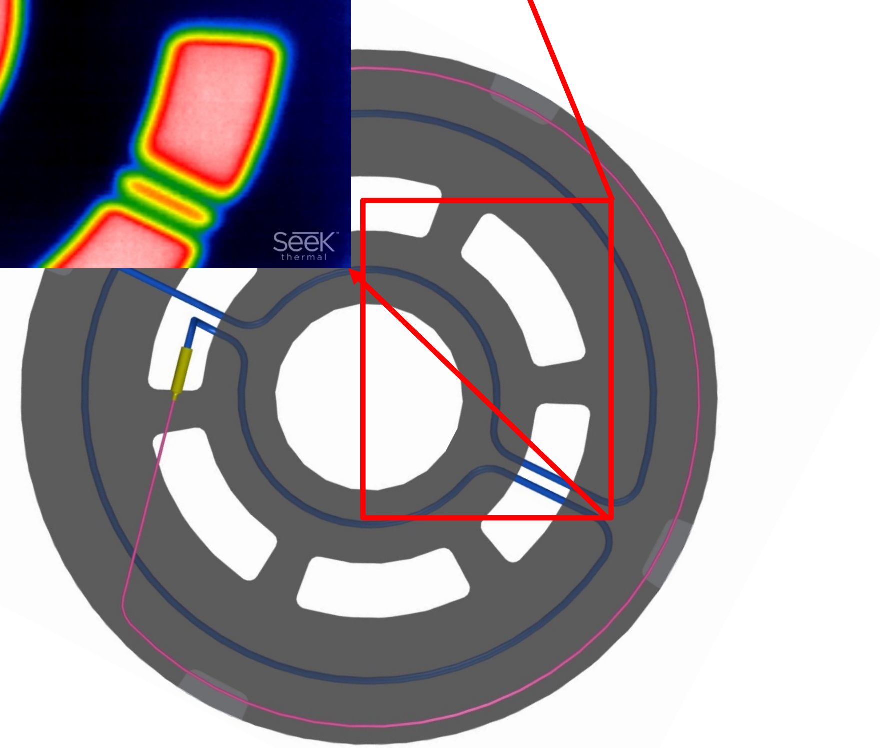

More on the offline image processing in the extra slides…

Testing the Bare Local Support

Cooled ring

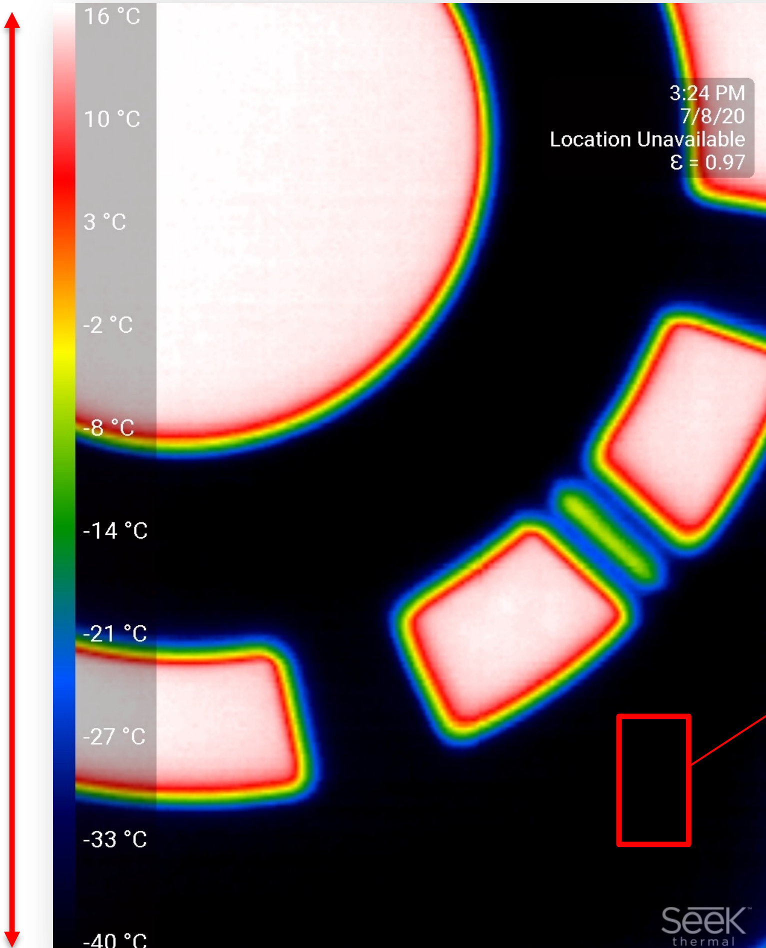

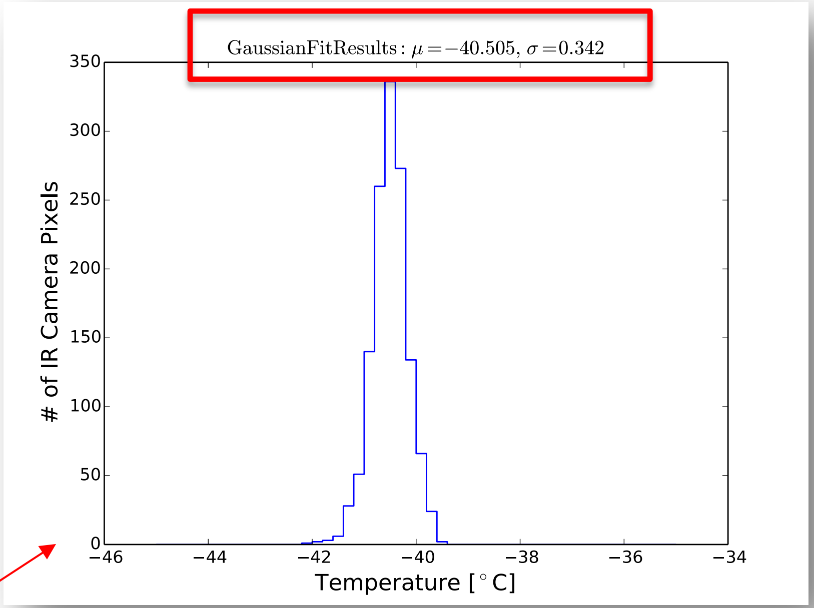

LS meets specifications

Preparing for the thermo-mechanical prototype

- **Thermal testing infrastructure ready, current emphasis on loading**

Thermally conductive epoxy (SE4445)

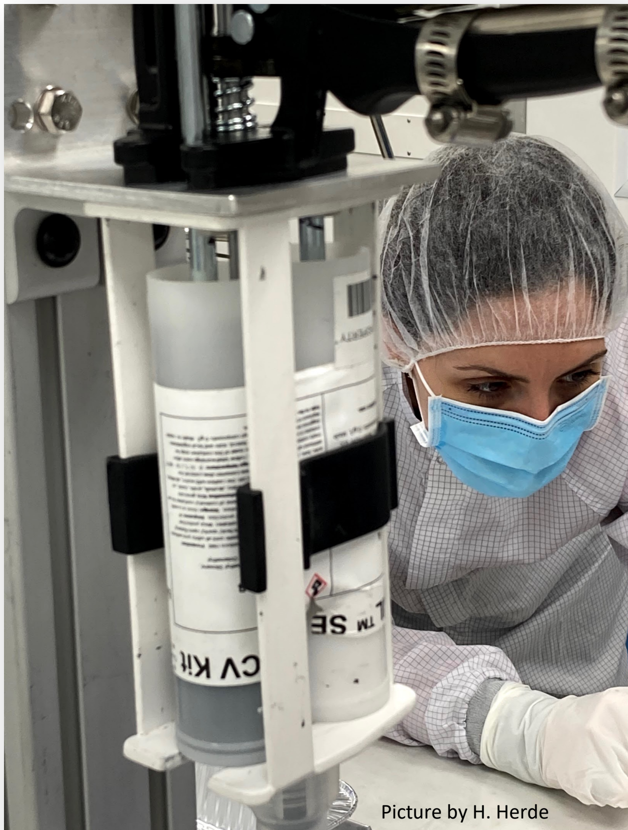

Syringes with SE4445 for glue robot

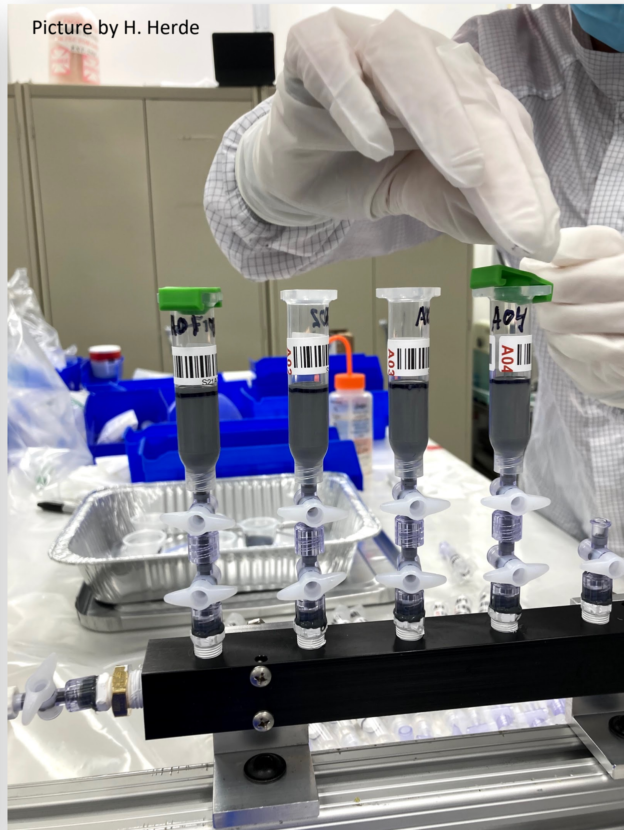

Nordson EFD Ultimus V

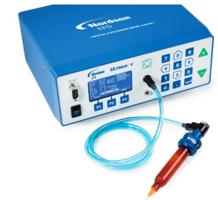

Example of glue dispensing on glass slides emulating quad modules

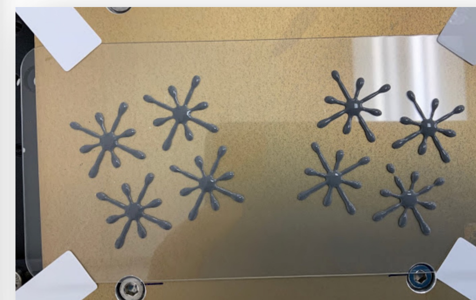

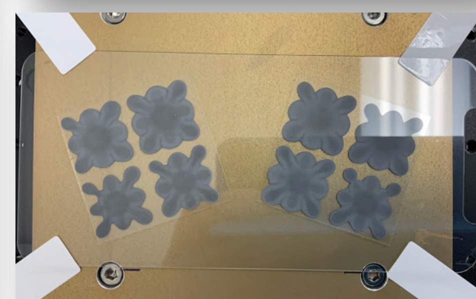

SLAC *loading team*

Closest layers to the interaction points: radiation effects are severe, adhesives must be rad-hard

Thermal Analysis